UNIVERSITAT POLITÈCNICA DE VALÈNCIA

Estudio de compuestos As_2X_3 bajo presión

TESIS DOCTORAL

Presentada por:

Vanesa Paula Cuenca Gotor

Dirigida por:

Francisco Javier Manjón Herrera

Juan Ángel Sans Tresserras

Junio 2019

Lo esencial es invisible a los ojos

[Saint-Exupéry 2010]

Resumen

El estudio de la materia sometida a condiciones extremas de presión y/o temperatura nos permite ampliar nuestros conocimientos sobre sus propiedades estructurales, elásticas, vibracionales, ópticas, eléctricas y magnéticas; comprender y predecir su comportamiento frente a estas condiciones; y valorar su aplicabilidad en ámbitos tan dispares como la computación cuántica, los semiconductores, la ciencia de materiales, la medicina o la farmacología.

La presión es una variable termodinámica relativamente rápida y fácil de modificar que nos permite avanzar en la comprensión del comportamiento de la materia en función de las múltiples propiedades que la definen. Cuando las propiedades de un material no estable en condiciones ambientales mejoran bajo presión, y se prevé que su utilización pueda desarrollar aplicaciones novedosas o mejorar las ya existentes, se puede estudiar la posibilidad de sintetizar este nuevo material a presión ambiente aprovechándonos de las barreras cinéticas entre las transiciones de fase.

El desarrollo tecnológico de las técnicas de caracterización de las propiedades de los materiales, así como de los modelos teóricos que permiten realizar cálculos *ab initio*, junto con la aplicación de altas presiones, han facilitado la consecución de los objetivos de análisis y comprensión de las propiedades estructurales, mecánicas, electrónicas y vibracionales de los compuestos de tipo As_2X_3 (sesquióxidos y sesquicalcogenuros de arsénico) de esta tesis doctoral.

Con este fin se recoge en la presente tesis el compendio de los trabajos realizados en varios compuestos de tipo As_2X_3, en concreto los compuestos estudiados han sido la arsenolita pura (As_4O_6), el compuesto resultante al medir la arsenolita con He como medio transmisor de presión (MTP) a altas presiones ($As_4O_6 \cdot 2He$), el oropimente (α-As_2S_3) y el telururo de arsénico (α-As_2Te_3).

El análisis y la comprensión de las propiedades de estos compuestos ha supuesto un avance en el estudio de los sesquióxidos y sesquicalcogenuros del grupo 15, y allana el camino para diseñar nuevos sesquicalcogenuros del grupo 15 y compuestos relacionados con propiedades termoeléctricas o aislantes topológicas, tanto a presión ambiente como en condiciones extremas.

Abstract

The study of matter under extreme conditions of pressure and/or temperature allows us to extend our knowledge about their structural, mechanical, vibrational, electrical, optical and magnetic properties; understand and predict their behaviour under these extreme conditions; and validate their possible application in several fields such as quantum computing, semiconductors, material science or pharmacology.

Pressure is a thermodynamic variable easy to modify which allows us to advance in the comprehension of the behaviour of the multiple properties of the matter. When the properties of a material unstable at ambient conditions show a significant progress, this material can be postulated as a possible candidate to develop novel properties or improve those already existing; then, the synthesis of this metastable compound can be studied by the application of pressure and temperature and taking advantage of the kinetic barriers that stabilize high pressure phases.

The technical development suffered by the characterization techniques, which are used to analyse the properties of materials, together with the theoretical models that allows to perform *ab initio* calculations, have facilitated to reach the objective of the analysis and understanding of the structural, mechanical, electronic and vibrational properties of the compounds belonging to the As_2X_3 family (arsenic sesquioxides and sesquichalcogenides) studied in this PhD thesis.

To this aim, the present PhD thesis collects a compendium of the works done about several As_2X_3 compounds. In particular, the compounds studied here have been: pure arsenolite (As_4O_6), the resulting material from expose the arsenolite with helium as pressure transmitting medium at extreme conditions of pressure ($As_4O_6 \cdot 2He$), orpiment (α-As_2S_3) and arsenic telluride (α-As_2Te_3).

The analysis and comprehension of the properties of these compounds have provided a significant advance in the study of sesquioxides and sesquichalcogenides belonging to the group 15, and pave the way to design new sesquichalcogenides of the same group and related compounds with thermoelectric or topological insulating properties, at ambient or under extreme conditions.

Resum

L'estudi de la matèria sotmesa a condicions extremes de pressió i/o temperatura ens permet ampliar els nostres coneiximents sobre les seus propietats estructurals, elàstiques, vibracionals, òptiques, eléctriques i magnétiques; comprendre i predir el seu comportament front a aquestes condicions; i valorar la seua aplicabilitat en àmbits tan dispars com la computació cuántica, els semiconductors, la ciència de materials, la medicina o la farmacologia.

La pressió és una variable termodinàmica relativament ràpida i fàcil de modificar que ens permet avançar en la comprensió del comportament de la matèria en funció de les múltiples propietats que la defineixen. Quan les propietats d'un material no estable en condicions ambientals milloren sota pressió, i es preveu que la seua utilització puga desenvolupar aplicacions novedoses o millorar les ja existents, es pot estudiar la posibilitat de sintetitzar aquest nou material a pressió ambient aprofitant-nos de les barreres cinètiques entre les transicions de fase.

El desenvolupament tecnològic de les técniques de caracterització de les propietats dels materials, així com dels models teòrics que permeten realitzar càlculs *ab initio*, junt amb l'aplicació d'altes pressions, han facilitat la consecució dels objectius d'análisi i comprensió de les propietats estructurals, mecàniques, electròniques i vibracionals dels compostos de tipus As_2X_3 (sesquiòxids i sesquicalcogenurs de arsenic) d'aquesta tesi doctoral.

Amb aquest fi s'arreplega en la present tesi un compendi dels treballs realitzats a varios compostos de tipus As_2X_3, en concret els compostos estudiats han segut l'arsenolita pura (As_4O_6), el compost resultant de mesurar l'arsenolita amb He com a mitjà transmisor de pressió (MTP) a altes pressions ($As_4O_6 \cdot 2He$), l'oropiment (α-As_2S_3) i el telurur d'arsenic (α-As_2Te_3).

L'anàlisi i la comprensió de les propietats d'aquestos compostos ha suposat un avanç a l'estudi dels sesquiòxids i sesquicalcogenurs del grup 15, i aplana el camí per a disenyar nous sesquicalcogenurs del grup 15 i compostos relacionats amb propietats termoelèctriques o de aillants topològics, tant a pressió ambient com en condicions extremes.

ÍNDICE

Agradecimientos

En primer lugar, y como no podría ser de otro modo, agradezco a mis directores, Javi y Juan Ángel, todo el apoyo que me han brindado. Sin ellos, esta labor simplemente habría resultado imposible. Han sido mis tutores, me han dirigido y enseñado, pero, lo que es aún más importante, han sido mis amigos, han tenido una paciencia infinita y me han ayudado en los momentos más duros, haciendo de estos cinco años una mezcolanza de medidas, análisis, estudios, descansos y risas a horas adecuadas y a horas intempestivas…

Por supuesto, agradezco de todo corazón el trabajo experimental y teórico desarrollado por todos los miembros de nuestro gran equipo, que forma una parte importante de esta tesis. A todos ellos les doy gracias mil, pero tengo que mencionar especialmente a Alfonso y Plácida, eficientes y adorables, y a mi querido Catalin, que siempre me ha hecho más llevaderas las estancias en el sincrotrón ALBA.

Mis compañeros de trabajo, Isa, Juan y Marcos, amigos también, han sido un gran referente y una mejor compañía. Desde que empecé a trabajar con ellos no ha habido un solo día en que no haya sido consciente de lo afortunada que soy por tenerlos.

Mis amigas y amigos, en especial Andrea, Silvia, Toni, Yoli y Pilar, me han permitido desconectar cuando era necesario, eso sí, siempre preguntándome qué tal iba la cosa. Muchísimas gracias por vuestra compañía y vuestro cariño. Bien sabéis que vosotros y los libros sois mi válvula de escape.

A mis padres, Luis y Rosa, no solo les debo la vida, les debo "mi" maravillosa vida. Me han dado amor, protección, cultura, estudios, viajes, una mente abierta… Han soportado a una hija difícil y han conseguido que me levante después de cada caída y que me supere una y otra vez. Gracias a ellos asumí este reto y gracias a ellos he podido llevarlo a cabo. Saben que los quiero con locura, pero no está de más que quede por escrito. Papás, OS QUIERO.

Gracias a mi hermano, Edu, por estar ahí, por haber pasado mil cosas juntos desde niños hasta ahora. Como todos los hermanos, hemos tenido nuestros más y nuestros menos, pero ahí seguimos, queriéndonos siempre.

A mi compañero, el hombre de mi vida, no hace falta que le diga nada, pues ya lo sabe todo. Con él espero seguir viajando, conversando, leyendo juntos en la cama antes de dormir y disfrutando por siempre de nuestras aficiones comunes. Gracias, Jorge, por tu compañía, tu amistad, tu amor y tus maravillosos y reconfortantes abrazos.

Por último, les agradezco a mis grandes amores, mis hijas Mar e Iris, que sean dos soles. Han soportado estoicamente mis ataques de nervios y mis horas de ausencia, y de presencia ausente, que espero poder compensar con creces. A pesar de que no terminan de entender lo que significa todo este berenjenal, sí que entienden que deben portarse bien y ayudarme en todo lo posible, aunque a veces lo olviden… Aun así, día tras día me complazco en su amor, me pierdo simplemente mirándolas y recupero la tranquilidad con sus besos de buenas noches.

Capítulo 1

Introducción

El arsénico es un elemento químico muy común en la Tierra, pudiéndose encontrar en la atmósfera, en la hidrosfera, en la geosfera y en la biosfera. El arsénico es popularmente conocido por su alta toxicidad, encontrando gran cantidad de referencias de su uso como veneno a lo largo de la historia, así como en la literatura, el cine y el teatro. A pesar de sus propiedades tóxicas [Pershagen 1981], se trata de un elemento necesario para el correcto funcionamiento de nuestro organismo, ya que su carencia provoca una inhibición del crecimiento. También es posible encontrar muchos ejemplos de su utilización con fines menos dramáticos, pues el arsénico puro no es tóxico, aunque se oxida fácilmente a trióxido de arsénico (As_2O_3), que es un fuerte veneno. No en vano el nombre del elemento deriva del griego *arsenikon*, que significa "varonil, macho", en referencia a las potentes propiedades de este elemento [Quadbeck 2007].

Por su situación en la tabla periódica, en el centro del bloque *p* y en la mitad de la diagonal de separación entre los metales y los no metales, el arsénico se comporta en unas ocasiones como metal y en otras como no-metal. Así, podemos encontrar en la naturaleza minerales de arsénico en los que este se encuentra como catión, formando óxidos y sulfuros como los metales; o minerales de arsénico [Drahota 2009] en los que se encuentra formando distintos tipos de aniones, como oxoaniones, arseniatos, arsenitos y arseniuros como los no-metales.

La ambivalencia del arsénico se refleja también en compuestos aparentemente simples, como el trióxido de arsénico, que se puede encontrar de varias formas en la naturaleza: el mineral conocido como *arsenolita* (As_4O_6) está formado por moléculas discretas, típico de los óxidos de los no-metales; mientras que el mineral conocido como *claudetita* (As_2O_3) forma redes, asemejándose a los óxidos metálicos [Gasque 2013].

Los minerales de arsénico más empleados desde la antigüedad han sido los sulfuros: el *realgar* (As_4S_4) y el *oropimente* (As_2S_3). Ambos presentan formas cristalinas muy llamativas, de color rojo sangre el primero y amarillo dorado (se creía que contenía oro) el segundo, que hizo que fueran muy apreciados. De hecho, el oropimente debe su

Imagen 1. Minerales de arsénico: realgar (izquierda) y oropimente (derecha). *Fuente: https://llorensminerals.com/*

nombre a su coloración dorada ("Aurum pigmentum" en latín) [Pliny 1938]. Se conoce la utilización ancestral de estos compuestos, empleados como medicamentos, para tratar dolencias tan diversas como las enfermedades venéreas, el asma, la tuberculosis, la diabetes, las úlceras de la piel y otros padecimientos (recetados por Aristóteles e Hipócrates en el siglo IV a.C.), y recomendados como antisépticos, sudoríficos, sedantes o tónicos. Además, estos compuestos han sido también empleados en la elaboración de pinturas y diversos tintes a lo largo de la historia. También han sido usados comúnmente los óxidos de arsénico previamente mencionados, especialmente como raticida y preservante de animales (hasta 1950) por lo que se encuentra en la piel de numerosos animales conservados en museos de Historia Natural [Bartrip 1992].

El arsénico y sus derivados se siguen empleando con regularidad, a día de hoy, en sus distintas formas como: aditivo en aleaciones de plomo y latones (arsénico puro); preservante de la madera (arseniato de plomo y cromo); componente de construcción de diodos de láser, LEDs y componentes de circuitos integrados (arseniuro de galio); pigmento y elemento para pirotecnia (disulfuro de arsénico); decolorante para la fabricación del vidrio (trióxido de arsénico); etc.

Utilización de compuestos minerales de arsénico en diferentes ámbitos y en diferentes épocas

PIGMENTOS, PINTURAS Y TINTES

Los estudios sobre los colores hallados en las tumbas faraónicas y templos del antiguo Egipto revelan que el oropimente y el realgar [Siddall 2018] ya eran empleados durante el reinado de la XVIII Dinastía, entre los años 1550 y 1295 a.C. aproximadamente.

En las pinturas de Amarna (Tell el Amarna, 1353-1336 a.C.) hay una del rey Akhenaton, su reina, y dos princesitas con sus asistentes. La piel de los representados se ilumina con una porción diminuta de oropimente, especialmente en las zonas de luz, donde aparece visible más claramente que en las partes sombreadas. También se aplicó una fina capa superficial de polvo sobre los pendientes de la realeza, como una idea de último momento, aparentemente para alegrarlos [Spurrell 1895].

El oropimente era un color raro, se usó en este período únicamente moliendo la cantidad justa a emplear, y nunca en grandes cantidades. El realgar, que se encuentra comúnmente con el oropimente, se usó con moderación al ser molido junto con él. Sin embargo, no se ha encontrado realgar puro aislado del oropimente en ninguna pintura de este período. El oropimente se aplicaba a la piedra y la cerámica, a veces cubriendo relativamente grandes superficies.

En el año 2000, durante el estudio de autenticidad de seis papiros egipcios, supuestamente datados entre los siglos XIII y I a.C., se compararon los resultados de los colores hallados en estos seis papiros con los obtenidos a partir del análisis de un auténtico papiro egipcio perteneciente al Museo Petrie y que data del siglo XIII a.C.,

que había sido conservado por el Museo Británico y colocado bajo vidrio [Burgio 2000]. Los pigmentos detectados en el papiro original fueron, entre otros, el pararealgar (As_4S_4), concentrado en las áreas brillantes de ladrillo "rojo", y el oropimente (As_2S_3), ambos tradicionalmente utilizados en Egipto en el siglo XIII a.C. La presencia del pararealgar (pigmento amarillo) es altamente significativa, ya que otros papiros datados en este período presentan el uso de este pigmento, producto de la degradación del realgar (pigmento rojo) inducida por la exposición a la luz. Todos estos resultados fueron obtenidos gracias al uso de la micro-espectroscopia Raman. Así, esta técnica demostró ser una herramienta de gran valor en la discriminación entre objetos de arte antiguos y modernos, siendo utilizada como método rápido y eficiente de autenticación y datación de estas obras.

En 1775 el químico sueco Carl Wilhelm Scheele preparó un pigmento verde, que tuvo una gran aceptación en la época, y que pasó a ser conocido como *verde de Scheele* [Eastaugh 2004]. Este pigmento estaba compuesto por arsenito ácido de cobre y se utilizó ampliamente en pinturas, así como en tintes de telas y papeles, incluyendo el papel tapiz. A principios del siglo XIX, este verde fue sustituido por otro compuesto, también en base a cobre y arsénico, al que se conoció como *verde de París*, que presentaba una mejor retención del color que el anterior, y que se utilizó hasta el siglo XX. Estos pigmentos también fueron empleados en las artes plásticas, especialmente por los impresionistas, como Cézzane, Monet o Van Gogh [Gasque 2013].

RATICIDAS Y CONSERVACIÓN DE ANIMALES

Como se ha mencionado anteriormente, los óxidos de arsénico son especialmente tóxicos. Es por ello que se han utilizado ampliamente durante muchos siglos como raticidas e insecticidas, fundamentalmente para preservar alimentos y enseres. Es más, el efecto tóxico de los óxidos de arsénico propició que los taxidermistas usaran una solución que contenía óxido de arsénico, conocida como el jabón arsenical de Bécoeur y que se utilizó desde mediados del s. XVIII hasta finales del s. XIX, para la conservación de animales e insectos que actualmente están presentes en numerosas colecciones de museos de Historia Natural de todo el mundo. El envenenamiento de personas con estos compuestos, así como muchos efectos tóxicos producidos después de exposiciones a corto y largo plazo han sido ampliamente estudiados [Bartrip 1992, National Research Council 1999, Agency for Toxic Substances and Disease Registry 2005, Liu 2007].

MEDICINA

Los compuestos minerales de arsénico han sido empleados en la medicina tradicional desde tiempos ancestrales, a pesar del conocimiento de su alta toxicidad. El uso del arsénico en este tipo de medicina proviene normalmente de la adición deliberada de compuestos minerales de arsénico para fines terapéuticos, empleando las formas comunes del oropimente, el realgar y la arsenolita [Liu 2008].

Ya durante los siglos XVIII y XIX los médicos occidentales prescribían tratamientos basados en fármacos compuestos por arsénico, tanto para uso interno como para uso externo [Waxman 2001, Miller 2002, Evens 2004]. En el s. XVIII Thomas Fowler inventó el *tónico de Fowler*, que consistía en una solución al 1% de arseniato de potasio, y que fue utilizada empíricamente para el tratamiento de gran variedad de dolencias. En el año 1878 se describió por primera vez la actividad del trióxido de arsénico sobre los leucocitos, al reportarse que el *tónico de Fowler* había producido un ligero descenso en los recuentos de glóbulos blancos en dos individuos normales y un descenso dramático en un paciente con leucemia mielógena crónica tratado con esta preparación durante 10 semanas. Después de la interrupción del tratamiento, el recuento de leucocitos aumentó progresivamente hasta que se restableció la terapia con arsénico [Cutler 1878].

Sin embargo, el arsénico es un carcinógeno humano conocido que puede llegar a producir cáncer de piel, pulmón, vejiga urinaria, hígado, riñón, y posiblemente otros tipos de cáncer [National Research Council 1999, IARC 2004].

La toxicidad de los compuestos minerales de arsénico depende fundamentalmente de la sustancia química formada, por lo tanto, es conveniente el estudio de la especiación del arsénico, pero también de la biodisponibilidad en el organismo y de la relación entre la toxicidad y el beneficio obtenido, para evaluar la aplicación de estos tratamientos. La conjunción de estos tres factores parece ser la respuesta a por qué los compuestos de arsénico tienen una historia de utilidad tan larga y notable en la farmacología.

Cientos de remedios de la medicina tradicional china empleaban oropimente, realgar o arsenolita en sus composiciones, y el realgar puro se incluyó en 22 remedios orales basados en el Comité de Farmacopea Chino (2005). El oropimente se utilizaba principalmente de forma externa como tratamiento contra piojos, cura para la sarna, mordeduras de serpientes, picaduras de insectos y enfermedades de la piel [Chinese Pharmacopoeia Committee 2005, Koch 2007]. Actualmente, las nanopartículas de oropimente son efectivas para matar las células K562 de la leucemia in vitro, pero se requieren estudios adicionales para evaluar su uso, ya que la absorción del arsénico de la preparación de las nanopartículas aumenta notablemente [Lin 2007, Lin 2008].

El realgar era ampliamente utilizado en las medicinas tradicionales tanto de forma externa, para el tratamiento de afecciones de la piel, como de forma interna, como ingrediente en remedios orales por sus propiedades antipiréticas, antiinflamatorias, antiulcerosas, anticonvulsivas y antiesquistosomiáticas [Chinese Pharmacopoeia Committee 2005]. Los usos terapéuticos de estas preparaciones variaban desde el tratamiento de resfriados comunes, dolor de muelas, amigdalitis, asma, y dolores abdominales, hasta espasmos, sedación, úlceras, golpes de calor, coma y delirio [Koch 2007].

Desde los años 60, preparaciones que contenían realgar han sido empleadas con éxito en el tratamiento de ciertos tipos de leucemia aguda y crónica, y más recientemente, las fórmulas de *Realgar - Indigo naturalis* han demostrado ser muy efectivas contra la leucemia promielocítica. Al ser menos tóxico que el óxido de

arsénico, se utiliza actualmente, puro o en combinación con otras sustancias, para el tratamiento de enfermedades hematológicas [Lu 2002].

La arsenolita pura se usaba tradicionalmente para eliminar nódulos o escrófulas (proceso infeccioso que afecta a los ganglios linfáticos, sobre todo los del cuello). Además, la arsenolita mezclada con otras sustancias es empleada para el tratamiento de la leucemia promielocítica aguda (LPA) [Shen 1997, Chinese Pharmacopoeia Committee 2005]. La evidencia científica del uso del trióxido de arsénico en el tratamiento de la leucemia ha permitido su aceptación por la medicina, y está convirtiendo este compuesto en un agente quimioterapéutico muy prometedor, en especial para el tratamiento de la LPA recidivante y farmacorresistente, además de otros tumores malignos y cánceres hematopoyéticos [Miller 2002, Evens 2004, Hede 2007].

El estudio de la LPA y el papel del arsénico en su tratamiento se encuentran entre las historias más interesantes de la oncología clínica. En la década de los 90, a pesar de los rápidos avances en la terapia de este subtipo común de leucemia aguda con ácido holo-transretinoico (ATRA) combinado con quimioterapia, aproximadamente el 20% -30% de los pacientes recaían y morían, a menos que fueran rescatados por un trasplante de médula ósea [Soignet 1998]. Los estudios iniciales del tratamiento con trióxido de arsénico (TOA) en la Harbin Medical University, seguidos de un cuidadoso ensayo clínico llevado a cabo en la Shanghai Second Medical University, documentaron una notable eficacia clínica en pacientes con LPA recién diagnosticado y recidivante. A diferencia de la terapia con ATRA, la terapia a largo plazo con TOA fue seguida por remisiones moleculares en algunos pacientes. La monoterapia con TOA produjo remisiones completas en 9 de los 10 pacientes tratados, mientras que el tratamiento produjo una respuesta completa en los 5 pacientes con LPA en recaída, que anteriormente habían sido tratados mediante la combinación de ATRA y quimioterapia [Shen 1997, Niu 1999]. Una extensión de los estudios chinos llevada a cabo por investigadores en los Estados Unidos confirmó la actividad del TOA en dosis bajas en pacientes con LPA recidivante. En este estudio, en 11 de los 12 pacientes tratados se produjo una remisión completa tras unas pocas semanas de tratamiento, con efectos adversos relativamente leves [Soignet 1998].

Al comprobarse la eficacia del TOA en el tratamiento de la LPA, renació el interés por la utilización de este compuesto como fármaco principal al inicio de la enfermedad, como terapia de inducción a la remisión y en la fase de consolidación de la misma, tanto en el tratamiento como monoterapia como en medicaciones asociadas. Varios grupos han realizado investigaciones clínicas al respecto, obteniendo resultados muy similares en cuanto a remisiones, efectos adversos y bajos índices de mortalidad; concluyendo que la mortalidad asociada a complicaciones hemorrágicas se ha producido cuando el diagnóstico y el tratamiento no se han efectuado de manera oportuna [Niu 1999, Miller 2002, Lazo 2003, Sanz 2005, De la Serna 2008, Grimwade 2009, Ramos 2009, Ablain 2011, Ghavamzadeh 2011, Suárez 2014].

En un estudio más reciente sobre la actividad conjunta de TOA y ATRA [Kozono 2018] se han confirmado los buenos resultados alcanzados anteriormente en el tratamiento contra la LPA. La combinación de ambos elementos es efectiva en la cura, en dosis clínicamente seguras, de la LPA mortal. El ATRA inhibe la leucemia, el cáncer de mama y el cáncer de hígado, al atacar a la isomerasa Pin1 (la cual actúa como regulador principal de las redes de señalización oncogénicas) [Lu 2014, Wei 2015, Zhou 2016]. El TOA también ataca a la Pin1, mediante su enlace no covalente con el sitio activo de Pin1 [Zhang 2010, Jeanne 2010, Shen 2013], y coopera con el ATRA para ejercer una potente actividad contra el cáncer, inhibiendo y degradando esta isomerasa, y suprimiendo su función oncogénica. Además, el ATRA aumenta la captación celular del TOA potenciando su acción inhibidora.

La combinación de TOA y ATRA, trabajando de manera cooperativa y eliminando la Pin1, no solo potencia su eficacia contra el cáncer, sino que también reduce la toxicidad del fármaco, lo cual es especialmente importante dada la conocida toxicidad de TOA en dosis altas. Por lo tanto, la inhibición cooperativa de Pin1 por TOA y ATRA bloquea potentemente numerosas vías de transmisión del cáncer, inhibe el crecimiento de células de cáncer de mama triple negativas y elimina las células iniciadoras de tumores en modelos celulares y animales, ofreciendo un enfoque prometedor y no tóxico para combatir el cáncer de mama y, probablemente, muchos otros cánceres.

La actividad apoptótica, antiproliferativa y angioinhibitoria del TOA, así como sus otras propiedades, pueden contribuir a la capacidad de este agente para tratar una variedad de otros tumores [Waxman 2001]. Además del uso efectivo para neoplasias hematológicas, (enfermedades malignas que afectan a la sangre, la médula ósea y los ganglios linfáticos), también es efectivo contra las células tumorales sólidas, en composición con la butionina sulfoximina [Maeda 2004], y contra los cánceres cervicales metastásicos [Yu 2007].

Los estudios toxicológicos muestran que la toxicidad cardiovascular es la principal preocupación en el uso del TOA y que los efectos adversos gastrointestinales y dérmicos pueden ocurrir después del uso prolongado de minerales compuestos de arsénico; sin embargo, los tratamientos controlados con dosis clínicamente seguras auguran un futuro prometedor para la utilización del arsénico. La selección de las terapias funcionales mediante la evidencia científica, con origen en la medicina tradicional, desembocan en tratamientos válidos en la medicina contemporánea. Lo que ha llevado a encontrar prometedores avances en la cura a una enfermedad mortal, a pesar de que la base farmacológica para la inclusión del arsénico mineral en la medicina actual aún necesite más estudios.

Estudio de compuestos sometidos a altas presiones

La aplicación de altas presiones en el estudio de la materia se ha convertido en un campo atractivo y multidisciplinar que ha experimentado un crecimiento extraordinario en las últimas décadas. Desde los distantes planetas y estrellas hasta nuestra Tierra, el estudio de las altas presiones nos permite avanzar en la

comprensión de los fenómenos que afectan directamente a nuestras vidas y sus implicaciones físicas, químicas, geológicas y biológicas, así como avanzar en el desarrollo de novedosas aplicaciones tecnológicas en diferentes ámbitos como las ciencias planetarias, ciencia y tecnología de los materiales, microbiología, química, geociencia o tecnología de alimentos.

La aplicación de las altas presiones en materiales líquidos y sólidos sufrió un importante auge gracias a Percy Williams Bridgman (laureado con el premio Nobel de Física en 1946). El Profesor Bridgman tuvo una prolífica carrera que le llevó a analizar más de 1000 sustancias bajo presión y establecer la primera calibración interna de presión. Además, su trabajo abrió las puertas a nuevas ramas científicas como la "pascalización" de los alimentos para eliminar bacterias, al someter a un huevo bajo presión y observar que se parecía a un huevo cocido [Bridgman 1914]. Bridgman dedicó también parte de su vida a la búsqueda de la síntesis del diamante, pero nunca lo logró; sin embargo, sus trabajos permitieron el desarrollo de tecnologías que allanarían el camino para su posterior consecución.

La primera síntesis de diamante artificial a partir de grafito, en principio, se adjudicó al equipo de General Electric en 1954, lo que transformó la alta presión en algo interesante desde el punto de vista tecnológico [Bundy 1955]. Sin embargo, luego se demostró que fue en realidad un trabajo individual de Howard Tracy Hall [Hall 1960]. Además, en 2008 se llegó al consenso de que fue un equipo sueco liderado por Anders Kämpe [Lundblad 1994] quien habría logrado su síntesis un año antes (1953) pero que la mantuvo en secreto por cuestiones de secreto empresarial. El uso de las altas presiones para sintetizar fases no conocidas o inestables en condiciones ambientales no solo abrió la posibilidad de crear compuestos con propiedades nuevas o desconocidas, sino que también ayudó a interpretar las propiedades del interior de la Tierra o de planetas distintos al nuestro. Es fundamental considerar que la mayor parte de la materia condensada se encuentra, de forma natural, sometida a altas presiones. De hecho, las que consideramos como *condiciones ambientales* (25ºC y 1 atm, es decir, 298,15 K y 1 bar aproximadamente) son precisamente las menos habituales en el Universo, en el que la materia se encuentra a una presión promedio de 10 GPa.

Los desarrollos producidos en el campo de las condiciones extremas durante los años 50, llevaron a un repunte de la tecnología disponible para aplicar mayores rangos de presión combinados con mayores rangos de temperatura. Sin embargo, no fue hasta el desarrollo de la celda de yunques de diamante por C. E. Weir, E. R. Lippincott, A. Van Valkenburg, y E. N. Bunting, del National Institute of Standards and Technology (NIST), que se tuvo acceso óptico al material sometido a las altas presiones [Weir 1959]. Esto permitió compatibilizar las altas presiones con multitud de técnicas de caracterización disponibles como la espectroscopia óptica, dispersión Raman, difracción de rayos X, etc. Así, fue Harry George Drickamer el pionero en el estudio de las relaciones físico-químicas de los materiales sometidos a alta presión, materiales que van desde semiconductores a proteínas [Edwards 1961, Weber 1983].

Toda esta revolución tecnológica produjo un mayor interés por parte de la academia y las compañías privadas por este campo, donde en los laboratorios, cada vez más se emplea la condición extrema de la alta presión como una variable añadida al estudio de la materia, junto con la temperatura, la composición química, los procesos físico-químicos, geológicos y/o biológicos. De esta manera se emula el comportamiento de la materia en el interior de la Tierra y de otros objetos planetarios, pudiendo estudiar transformaciones de fase, reacciones químicas, formación de minerales e hidrocarburos, actividad microbiana, etc.

Esta tesis mostrará cómo la aplicación de condiciones extremas de alta presión permite comprender y analizar las distintas propiedades de los sesquióxidos y sesquicalcogenuros de arsénico, que van desde materiales con claro carácter molecular (As_4O_6) a materiales cuasi-laminares (α-As_2S_3 y α-As_2Te_3).

Técnicas experimentales de caracterización

La respuesta de un compuesto al ser perturbado por una señal permite obtener información crucial para el conocimiento y caracterización de sus propiedades, pudiendo así valorar su utilidad en diversas aplicaciones. El desarrollo tecnológico producido en las técnicas de caracterización, y su combinación con las altas presiones, ha permitido un notable avance en el estudio de las propiedades de estos compuestos.

Las técnicas experimentales empleadas en el análisis de los compuestos objeto de esta tesis han sido principalmente la espectroscopia Raman y la difracción de rayos X (DRX).

ESPECTROSCOPIA RAMAN

El estudio de la interacción entre la materia y la radiación electromagnética generada por las diferencias de energía en las transiciones de los electrones de unos niveles atómicos a otros, es la base del análisis espectral, mediante el cual se detecta la absorción o la emisión de dicha radiación a ciertas frecuencias o longitudes de onda.

Las espectroscopias infrarroja (IR) y Raman son metodologías basadas en el estudio de vibraciones a nivel atómico y molecular. La espectroscopia vibracional es una técnica ampliamente utilizada en Física y Química gracias al desarrollo de espectrómetros IR y Raman fiables y sencillos en su manejo, así como a una gran versatilidad en su aplicación, ya que todos los materiales tienen un espectro vibracional característico. Estas técnicas permiten, por lo tanto, el estudio de sólidos, líquidos, disoluciones o gases, incluso en condiciones extremas de temperatura y presión.

La espectroscopia IR se caracteriza por detectar procesos de absorción de energía vibracional en los cuales los niveles de energía radiante son tan pequeños que resultan insuficientes para que se produzcan transiciones electrónicas, mientras que en la espectroscopia Raman se detectan los procesos de dispersión inelástica de una

fracción de luz monocromática incidente en la muestra, la cual sufre un cambio de frecuencia debido al intercambio de energía con la materia en dicha colisión.

Cuando un haz de luz incide sobre una muestra se producen los fenómenos ópticos de reflexión, absorción y transmisión. El haz absorbido, que es una parte del haz refractado al pasar la luz del medio externo al medio interno de la propia muestra, interactúa con el material provocando interacciones de la luz con los átomos, moléculas o iones que lo conforman, con la consiguiente modificación en la trayectoria del haz (fenómeno de dispersión). Estas colisiones pueden ser de carácter elástico, conservando el haz dispersado la energía del haz incidente y dando origen a la dispersión elástica o *de Rayleigh*; o de carácter inelástico, cuando el haz dispersado no conserva la energía, en cuyo caso se produce la dispersión inelástica. Si la dispersión inelástica se produce por vibraciones acústicas se denomina dispersión *Brillouin* y si se produce por vibraciones ópticas se denomina dispersión *Raman* (DR).

Al no conservarse la energía del haz incidente, existen dos tipos de dispersión inelástica posibles: la dispersión Stokes, en la cual la radiación dispersada tiene menor energía que la incidente; y la dispersión Anti-Stokes, en la que la radiación dispersada tiene mayor energía que la incidente. Ambas dispersiones son simétricas respecto a la dispersión de Rayleigh, apareciendo la dispersión Stokes hacia las frecuencias inferiores al pico Rayleigh, mientras que la dispersión Anti-Stokes aparece hacia las frecuencias superiores al pico Rayleigh. Sin embargo, la intensidad de la señal de recepción de la dispersión Stokes es superior a la Anti-Stokes, por lo que se suele utilizar la primera para analizar el espectro Raman generado.

La interacción entre la luz y la red atómica está en el origen de las bandas que se registran en los espectros Raman, las cuales se asocian a los distintos modos vibracionales y son características de una determinada sustancia y de una determinada estructura cristalina, lo cual nos permite obtener información química y estructural sobre el material objeto de estudio. La DR nos proporciona información precisa acerca de las vibraciones moleculares que experimentan los iones y átomos enlazados químicamente para formar moléculas y redes cristalinas. Las frecuencias de vibración dependen de las masas de los átomos involucrados y de la fuerza de los enlaces: los átomos pesados y los enlaces débiles presentan pequeños desplazamientos Raman, mientras que los átomos ligeros y los enlaces fuertes presentan grandes desplazamientos Raman.

La espectroscopia Raman consiste en la excitación de las vibraciones en la materia con luz y la recolección de la señal inelástica dispersada por la muestra utilizando un espectrómetro óptico [ver esquema del montaje óptico en **Imagen 2**]. El equipo empleado para la toma de datos de la señal de DR sobre las muestras estudiadas, a temperatura ambiente y a diferentes presiones, ha sido el espectrómetro Horiba Jobin Yvon LabRam HR, ubicado en la Universitat Politècnica de València [**Imágenes 3 y 4**].

Para la excitación de los distintos materiales se han utilizado los láseres monocromáticos de alta potencia de He:Ne (632,8 nm) de 50 mW y de estado sólido (532,0 nm) de 20 mW. Para eliminar la dispersión elástica de la excitación láser, se

sitúan unos filtros de interferencia a la entrada del espectrómetro que permiten filtrar la señal del láser incidente.

La luz láser se enfoca sobre la muestra contenida en la celda de yunques de diamante a través de las ventanas de diamante, empleando para ello un objetivo de microscopio refractivo confocal. La luz emitida por la muestra, que está formada por la señal Raman y la dispersión elástica del láser, sale de la celda a través de la misma ventana de diamante por retrodispersión, utilizándose el mismo objetivo para enfocar la luz láser de excitación y para recoger la luz láser reflejada por la muestra y las ventanas de diamante, así como los fotones dispersados elásticamente (Rayleigh) y los fotones dispersados inelásticamente (Raman).

Para eliminar la luz de dispersión reflejada y de Rayleigh, y así poder detectar la débil señal Raman, se han utilizado filtros *edge*. Estos son filtros de banda que bloquean todas las longitudes de onda cercanas a la línea del láser y a energías más altas, mientras transmiten la señal Raman, a energías más pequeñas que la línea de excitación del láser.

La señal Raman se enfoca en la rendija de entrada del espectrómetro, donde es dispersada utilizando una red de difracción y analizada con un detector multicanal, con un dispositivo de carga acoplada (en inglés charge-coupled device, CCD), que se encarga de la conversión de la señal luminosa en señal eléctrica.

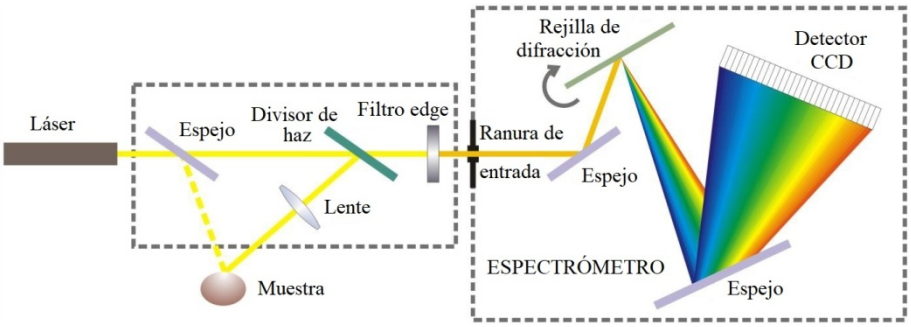

Imagen 2. Esquema del recorrido de la luz en la espectroscopia Raman [Castro 2013].

El equipo Horiba Jobin Yvon LabRam HR, ubicado en la Universitat Politècnica de València, incorpora un detector CCD multicanal enfriado termoeléctricamente, con una alta relación señal/ruido para la detección de señales Raman débiles, que calibra la posición de los píxeles con la frecuencia óptica. Las medidas de espectroscopia Raman realizadas con este equipo suelen tener una resolución inferior a 3 cm^{-1} gracias al uso de diversas redes de difracción según la longitud de onda escogida para las medidas Raman.

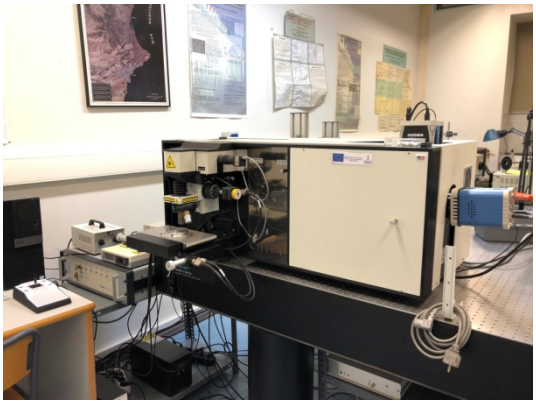

Imagen 3. Espectrómetro Horiba Jobin Yvon LabRam HR (Universitat Politècnica de València).

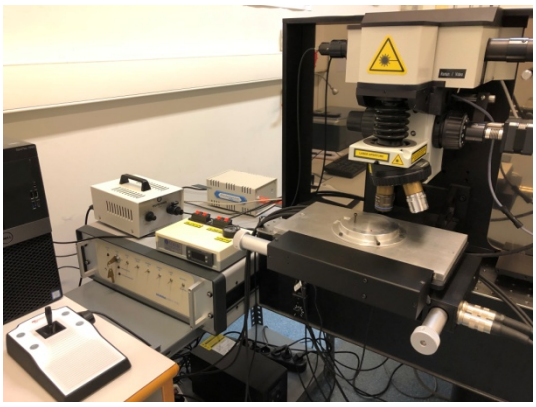

Imagen 4. Detalle del objetivo y la zona de colocación de la muestra. Espectrómetro Horiba Jobin Yvon LabRam HR (Universitat Politècnica de València).

DIFRACCIÓN DE RAYOS X

Los rayos X interactúan con la materia a través de los electrones que la forman de modo que, cuando la radiación X alcanza a un electrón cargado, este se convierte a su vez en fuente de radiación electromagnética dispersada. Según la longitud de onda y las relaciones de fase de esta radiación dispersada, nos podemos encontrar distintos fenómenos en la interacción entre los rayos X y la materia: reflexión, refracción, absorción, difracción, etc. La difracción de los rayos X es el fenómeno mediante el cual se estudia la interacción de los rayos X con la materia ordenada (cristales).

El fenómeno de difracción se produce cuando una onda encuentra un obstáculo o rendija cuyo tamaño es comparable a su longitud de onda. La longitud de onda de los rayos X está entre 0,1 y 100 Å (los rayos X utilizados en difracción tienen longitudes de onda entre 0,5 y 2,5 Å aproximadamente), mientras que las distancias interatómicas son del orden de 1 Å, así que la DRX permite el estudio del orden y espaciado de los átomos en las estructuras cristalinas.

Los compuestos cristalinos son agrupaciones periódicas y ordenadas de átomos. Cuando un haz de rayos X incide sobre un material cristalino, parte de este se dispersa sin pérdida de energía, conservando la misma longitud de onda que la radiación incidente, y dando lugar a diferentes tipos de interferencias que son constructivas en unas direcciones privilegiadas. Como los rayos X se dispersan por los electrones, el centro de dispersión activo para los rayos X no es el núcleo de los átomos sino la densidad electrónica, que también se distribuye periódicamente en la red cristalina.

La disposición periódica de los átomos permite que los puntos de la red cristalina que muestran la simetría traslacional de una estructura (repetición mediante traslación de la porción más simple de la estructura o celda unidad) puedan ser conectados mediante los planos de la red. Cada plano de red pertenece a un conjunto de planos equivalente que se nombra usando los *índices de Miller (h,k,l)*. Estos planos mantienen una separación constante entre ellos, que se conoce como *espaciado* d_{hkl}, y contienen a todos los puntos de red. La relación entre el espaciado d_{hkl} y los parámetros de red depende del sistema cristalino.

En el proceso de difracción los átomos dispersan la radiación incidente en todas las direcciones, pero solo en algunas de ellas los rayos dispersados están completamente en fase y se producen las interferencias constructivas necesarias para formar los rayos difractados. Si se estudia la reflexión de los rayos X incidentes con un ángulo θ sobre los planos de red, se puede observar cómo, para que exista reflexión cooperativa, los frentes de onda emergentes tras la reflexión deben seguir estando en fase, lo cual ocurrirá cuando la diferencia de caminos recorridos por los frentes de onda, antes y después de la reflexión, sea igual a un número entero de veces n la longitud de onda λ. El cumplimiento de esta condición es lo que se conoce como *Ley de Bragg*, según la cual $n\lambda = 2d_{hkl}sen\theta$, y demuestra que la caracterización geométrica de la difracción únicamente depende de la propia geometría de la red y no de la naturaleza de los átomos que la componen.

Cuando la incidencia de los rayos X se produce sobre una muestra de polvo de un material cristalino, la radiación dispersada se puede medir en función de una única variable, que es el *ángulo de Bragg* o 2θ. La proyección de las interferencias constructivas a lo largo de la distancia entre el detector y la muestra, teniendo en cuenta su simetría de revolución, se realiza mediante unos conos, conocidos como los conos de difracción o *conos de Debye-Scherrer*. Al situar un detector plano a una distancia fija de la muestra que difracta, tenemos un tipo de gráfico que se denomina patrón de difracción de polvo y que está formado por una serie de anillos, llamados *anillos de Debye-Scherrer*, de diferentes intensidades, diámetros y anchuras. Estos anillos están asociados a los índices de Miller (*hkl*) y vienen definidos por la

interacción constructiva de los planos característicos de un determinado espaciado d_{hkl}. En los patrones de difracción el radio de los anillos de Debye-Scherrer es proporcional a la tangente del ángulo de Bragg (*tan(θ)*) para una determinada distancia entre la muestra y el detector.

Para el análisis de los resultados de un experimento de difracción de polvo se integra angularmente el patrón de difracción bidimensional, obteniendo un gráfico unidimensional que se llama difractograma. En este difractograma, se representan la intensidad del anillo respecto a su posición respecto del centro del detector, ya sea en función del espaciado entre planos (*d-spacing*) o en función del ángulo (2θ). Los difractogramas nos permiten identificar la estructura cristalográfica de los materiales cristalinos y obtener información sobre la disposición de los átomos dentro de la celda unidad, así, la posición de los picos de Bragg estará relacionada con los parámetros de red, la intensidad de cada pico de Bragg con las posiciones atómicas relativas de los diferentes átomos constituyentes y su anchura con la calidad cristalina del material o su dimensionalidad. Un difractograma con picos de Bragg estrechos y bien definidos indicará que la mayoría de los granos que forman la muestra en polvo tienen los mismos parámetros de red, mientras que un difractograma con picos de Bragg anchos indica una variación muy grande entre los parámetros de red de cada grano en la muestra, llegando a ser tan anchos que describan un material amorfo, donde no hay orden de largo alcance.

Un patrón de difracción de calidad proporciona información precisa sobre la estructura de los materiales permitiendo refinar todos sus parámetros cristalográficos. Las diferentes características estructurales de un material tienen diferentes efectos sobre los parámetros de su patrón de difracción, siendo este la "huella dactilar" que posibilita la identificación del mismo. Es por ello que la aplicación de DRX al estudio de materiales se enfoca principalmente en la caracterización de huellas dactilares de materiales cristalinos y en la determinación de su estructura, siendo una de las técnicas de caracterización más importantes en la investigación en física del estado sólido, química y ciencia de materiales.

La DRX ha sido durante mucho tiempo el método más básico para la identificación *in situ* de fases de alta presión y/o temperatura, así como para la determinación de la ecuación de estado *P-T-V* y otras propiedades elásticas. En la aplicación de la DRX destaca el uso de grandes instalaciones como el sincrotrón, que proporciona los haces de rayos X de mayor energía, con mayor densidad de fotones, más penetrantes y versátiles para una amplia gama de estudios de muestras en celdas de yunques de diamante. La radiación sincrotrón (RS) es la radiación electromagnética emitida por una partícula cargada acelerada hasta una velocidad cercana a la de la luz cuando es desviada de su trayectoria mediante un campo magnético.

Este tipo de radiación se genera en grandes instalaciones llamadas sincrotrones donde la calidad del haz generado viene dada por el brillo espectral que es capaz de generar. Así, el brillo espectral de las fuentes de rayos X ha dado pasos agigantados en el desarrollo de las fuentes de RS, obteniendo ganancias de varios órdenes de magnitud en el brillo del haz conforme se han ido desarrollando las fuentes de 1ª, 2ª y 3ª generación. Una fuente de RS de 3ª generación viene determinada por el uso de

dispositivos de inserción (matriz de dipolos magnéticos de polaridades opuestas que genera un espectro más monocromático pero más intenso y que se puede regular variando el gap entre los imanes) y está formada por: un cañón de electrones, que genera el haz; un acelerador lineal, que acelera los paquetes de electrones a una fracción de GeV; un *booster*, acelerador circular o sincrotrón, que acelera los electrones a la energía máxima (2,5-3 GeV en el sincrotrón español ALBA); y un anillo de almacenamiento, en el que se inyectan los electrones, cuyos imanes de curvatura se utilizan también como fuentes de RS, y en cuyas secciones rectas se instalan los dispositivos de inserción como fuentes de línea de haz de alto brillo.

Imagen 5. Vista exterior de la línea BL04-MSPD en el sincrotrón ALBA.

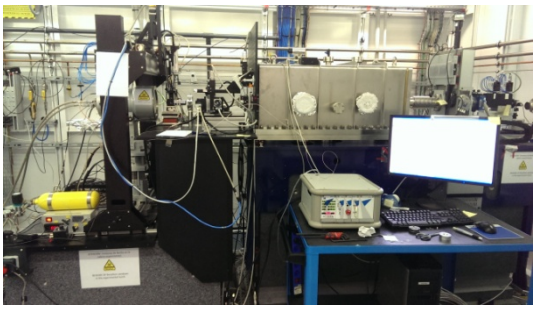

Imagen 6. Estación de alta presión en el interior de la cabaña experimental de la línea BL04-MSPD. *Imagen cedida por el Dr. Catalin Popescu.*

Para el estudio estructural de las muestras cristalinas se han realizado experimentos de difracción de polvo de alta presión, utilizando celdas de yunques de diamante, en la Línea de Haz de Ciencia de Materiales y de Difracción de Polvo (BL04-MSPD) del sincrotrón ALBA, ubicado en Cerdanyola del Vallès, en la provincia de Barcelona [**Imágenes 5 y 6**]. Esta línea opera con un rango de energías entre 8 y 50

keV, cubriendo adecuadamente el rango deseable para la realización de los experimentos, y permite la focalización del haz hasta un tamaño de 10 x 10 μm^2, creando una densidad de fotones de aproximadamente 10^8 ph/s.

En la **Imagen 7** se muestra el esquema del recorrido del haz partiendo del dispositivo de inserción de la línea en el anillo de almacenamiento del sincrotrón, su paso a través de los elementos ópticos de la línea BL04-MSPD y su posterior llegada a la estación de alta presión.

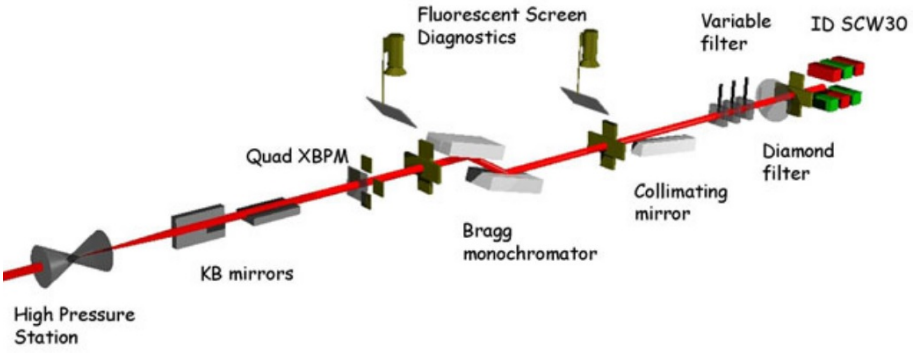

Imagen 7. Esquema del recorrido del haz en la línea BL04-MSPD. *Fuente: https://www.cells.es/en/beamlines/bl04-mspd*

La captura de la luz sincrotrón y entrega de los fotones de los rayos X, desde el anillo de almacenamiento a la cabaña óptica de la línea, se realiza mediante una serie de imanes que conforman el dispositivo de inserción tipo *wiggler* superconductor (SCW30). Estos imanes están diseñados para producir una desviación lateral y periódica del haz de partículas cargadas dentro del anillo de almacenamiento del sincrotrón. Las desviaciones de las partículas crean un cambio en la aceleración, que es el que produce la emisión de la radiación de sincrotrón tangente a la curva.

En el interior de la cabaña óptica se disponen varios dispositivos como filtros, atenuadores, espejos y monocromadores, que se usan para enfocar y seleccionar la intensidad y longitud de onda (energía) de la luz deseada para cada experimento, con la que pasará a la estación final o cabaña experimental. La estación de alta presión se encuentra en el interior de esta última cabaña, y es donde se llevan a cabo los experimentos por parte de los usuarios de la línea. La cabaña experimental está configurada como un recinto cerrado de apantallamiento frente a la radiación, de forma que usuarios y trabajadores estén protegidos frente a los rayos X nocivos mientras se desarrolla la recolección de datos.

En la estación de alta presión, la luz incide sobre la muestra cargada en la celda de yunques de diamante, que se coloca en un soporte que la permite rotar para mejorar la estadística de la medida, lo que repercute en la calidad del patrón de DRX. La

radiación difractada se proyecta sobre el detector CCD Rayonix, protegido con un *beamstop* (tope de haz), situado entre la celda y el detector, para evitar la incidencia directa del haz de rayos X sobre el mismo. La conversión de la señal luminosa en señal eléctrica permite la visualización de los resultados para su posterior análisis.

Dado que los científicos no pueden acceder a la cabaña experimental durante la recolección de los datos, el equipamiento está controlado remotamente desde la cabaña de control (Imagen 8), anexa a la experimental, vía motores y dispositivos robóticos. Además, la instalación de dos cámaras web en la estación permite visualizar la posición de todos los dispositivos experimentales desde esta cabaña.

Imagen 8. Vista de la cabaña de control de la línea BL04-MSPD.

Compuestos As_2X_3 estudiados en esta tesis

Al ser esta una tesis por compendio de artículos, las publicaciones incluidas en la misma pueden leerse de forma independiente, ya que contienen individualmente los aspectos necesarios para su comprensión. Sin embargo, el hilo conductor de este compendio de estudios ayudará al lector a integrar el conocimiento adquirido y a valorar el objetivo común de los mismos, que no es más que comprender y analizar las propiedades de los sesquióxidos y sesquicalcogenuros de arsénico mediante la aplicación de la condición extrema de alta presión.

La estructura de la tesis permite, en este primer capítulo de introducción, tener una visión general del elemento químico común a los compuestos estudiados, de las aplicaciones de estos compuestos, y de las técnicas fundamentales en el estudio de las altas presiones, así como del gran valor científico de este campo de estudio. En el segundo capítulo, el lector podrá profundizar en los detalles de análisis, discusión de resultados y conclusiones de las investigaciones llevadas a cabo sobre los compuestos estudiados en los diferentes artículos, cuyas ideas principales son mostradas en los siguientes párrafos.

En el **primer artículo**, titulado "*Ordered helium trapping and bonding in compressed arsenolite: Synthesis of $As_4O_6 \cdot 2He$*", la compresión de la arsenolita ha sido estudiada desde un punto de vista experimental y teórico conjuntamente. Los experimentos sobre este sólido molecular a altas presiones con diferentes medios de transmisión de presión (aceite de silicona, mezcla de metanol-etanol 4:1 y He), así como sin medio transmisor de presión, se han llevado a cabo combinando dos técnicas experimentales (DRX y DR). A su vez se han complementado las medidas experimentales con simulaciones teóricas *ab initio* y predicciones de enlace químico no covalente de vanguardia, proporcionando una caracterización completa de sus propiedades estructurales, electrónicas, elásticas y dinámicas de red de la arsenolita a diferentes presiones. La comparación de los resultados de los diferentes experimentos, y su comparación con los cálculos *ab initio*, revelan que la arsenolita es uno de los minerales no hidratados más compresibles conocidos, y proporcionan la evidencia del atrapamiento del He a más de 3 GPa entre las distintas unidades moleculares tipo-adamantano del As_4O_6. Además, nuestros cálculos indican que, a presiones relativamente pequeñas, el He establece enlaces con el As, de una intensidad similar a los puentes de hidrógeno, para formar un compuesto con estequiometría $As_4O_6 \cdot 2He$.

La revista de investigación periódica PHYSICAL REVIEW B, en la que se publicó este artículo, es de reconocido prestigio internacional. Así, en el 2016 JCR Science Edition, esta revista tiene acreditado un factor de impacto de 3,836, ocupando la posición 18 en el ámbito científico de PHYSICS, CONDENSED MATTER respecto al total de 67 títulos recogidos en esta misma área científica (primer tercil). Adicionalmente, y con el fin de evidenciar la contribución de esta aportación al desarrollo de posteriores estudios, es también oportuno señalar que, de acuerdo con el Science Citation Index (ISI Web of Knowledge), este artículo ha recibido a fecha de hoy 13 citas. Mi contribución particular a esta aportación ha consistido en la toma de medidas de DR y DRX del compuesto a diferentes presiones, y posterior análisis y discusión de los resultados.

Tras el descubrimiento de la formación del compuesto $As_4O_6 \cdot 2He$ en el estudio de la arsenolita (As_4O_6) bajo presión empleando el He como medio transmisor de presión y, con el fin de caracterizar mejor su comportamiento, se publicó el **segundo artículo** de esta tesis, titulado "*Vibrational and elastic properties of As_4O_6 and $As_4O_6 \cdot 2He$ at high pressures: Study of dynamical and mechanical stability*". Aquí se procede al estudio de las propiedades dinámicas de red de los compuestos As_4O_6 y $As_4O_6 \cdot 2He$ a altas presiones desde una perspectiva experimental y teórica, mediante mediciones de DR a temperatura ambiente y cálculos *ab initio*, y se reportan las propiedades elásticas teóricas de ambos compuestos bajo presión. Las medidas de DR muestran un comportamiento completamente diferente entre el As_4O_6 y el $As_4O_6 \cdot 2He$ a altas presiones, que es analizado exhaustivamente y que concuerda con los resultados obtenidos en los experimentos de DRX publicados en el artículo anterior. Además, el cálculo teórico de las curvas de dispersión de fonones y de los coeficientes de rigidez elástica a alta presión en ambos compuestos nos permite discutir su estabilidad dinámica y mecánica bajo compresión hidrostática, lo que permite explicar los resultados experimentales.

Este artículo se publicó en la revista de investigación periódica JOURNAL OF APPLIED PHYSICS, de reconocido prestigio internacional. En el 2016 JCR Science Edition, esta revista tiene acreditado un factor de impacto de 2,068, ocupando la posición 59 en el ámbito científico de PHYSICS, APPLIED respecto al total de 148 títulos recogidos en esta misma área científica (segundo tercil). De acuerdo con el Science Citation Index (ISI Web of Knowledge), este artículo ha recibido a fecha de hoy 3 citas. Mi contribución particular a esta aportación ha consistido en la toma de medidas de DR del compuesto a diferentes presiones y posterior análisis y discusión de los resultados de ambos compuestos.

En el **tercer artículo**, titulado "*Study of the orpiment and anorpiment phases of As_2S_3 under pressure*", se estudia el comportamiento del oropimente (monoclínico) y el anoropimente (triclínico), estructuras laminares del sulfuro de arsénico As_2S_3, sometidos a altas presiones. Este estudio teórico es llevado a cabo mediante cálculos *ab initio* realizados dentro de la teoría del funcional de la densidad, como parte de un esfuerzo conjunto teórico y experimental (en estudios posteriores) para proporcionar un conocimiento exhaustivo de la evolución de las interacciones interatómicas en este interesante material y de cómo varían sus propiedades estructurales, electrónicas y vibracionales bajo presión.

Este trabajo fue presentado en el congreso JOINT AIRAPT-25th & EHPRG-53rd INTERNATIONAL CONFERENCE ON HIGH PRESSURE SCIENCE AND TECHNOLOGY, en el año 2015, y publicado en la colección JOURNAL OF PHYSICS: CONFERENCE SERIES, publicación revisada por pares y de acceso abierto, de IOP Publishing, que ofrece a los lectores los últimos desarrollos en física presentados en conferencias internacionales. De acuerdo con el Science Citation Index (ISI Web of Knowledge), este artículo ha recibido a fecha de hoy 1 cita.

La continuación de los estudios sobre el oropimente se desarrolla en el **cuarto artículo** de esta tesis, titulado "*Orpiment under compression: metavalent bonding at high pressure*". En este trabajo se presenta un estudio conjunto experimental y teórico de las propiedades estructurales, vibracionales y electrónicas del oropimente (α-As_2S_3) bajo presión. Las medidas de DRX y DR realizadas en las muestras de oropimente a alta presión, combinadas con cálculos *ab initio*, nos han permitido determinar la ecuación de estado y la asignación tentativa de la simetría de muchos de los modos activos Raman de este compuesto, e investigar la posible aparición de las fases de alta presión y su relación con las de otros sesquióxidos y sesquicalcogenuros, aumentando nuestro conocimiento sobre el comportamiento del oropimente bajo presión. Los resultados muestran una compresión continua del material hasta 25 GPa con una pérdida del carácter van der Waals de las fuerzas intercapa por encima de 10 GPa. Además, los cálculos muestran que hay un aumento progresivo de la coordinación del As con la presión, cambiando de una coordinación 3 a 0 GPa a más de 5 por encima de 20 GPa, donde se produce una transición de fase isoestructural inducida por presión. Los cálculos de la estructura de bandas electrónicas sugieren que hay un cierre progresivo de la banda prohibida (gap) del α-As_2S_3 al aumentar la presión, que va desde un semiconductor trivial a un metal trivial muy por encima de 40 GPa. Todos los cambios observados en el oropimente bajo presión, como la fuerte disminución del gap, el ablandamiento de muchos

modos ópticos de vibración, la evolución de la función de localización de electrones a lo largo de los enlaces As-S, y el fuerte aumento del tensor dieléctrico y de las cargas efectivas de Born, pueden explicarse en el marco de la formación de enlaces metavalentes a altas presiones, habiendo sido propuesto recientemente este comportamiento para otros calcogenuros. En definitiva, el oropimente forma un metal incipiente (término acuñado para la denominación de compuestos que forman enlace metavalente) bajo presión.

Este artículo ha sido enviado a la revista de investigación periódica THE JOURNAL OF PHYSICAL CHEMISTRY C, de reconocido prestigio internacional, estando a la espera de los comentarios pertinentes para su publicación. En el 2017 JCR Science Edition, esta revista tiene acreditado un factor de impacto de 4,484, ocupando la posición 38 en el ámbito científico de CHEMISTRY, PHYSICAL respecto al total de 147 títulos recogidos en esta misma área científica, y la posición 54 de 285 en el ámbito científico de MATERIALS SCIENCE, MULTIDISCIPLINARY (ambas en el primer tercil). Mi contribución particular a este trabajo ha consistido en la toma de medidas de DR y DRX del compuesto a diferentes presiones, y posterior análisis y discusión de los resultados.

Finalmente, en el **quinto artículo**, titulado "*Structural, Vibrational, and Electronic Study of α-As_2Te_3 under Compression*", se presenta el estudio de las propiedades estructurales, vibracionales y electrónicas del telururo de arsénico monoclínico laminar (α-As_2Te_3) a altas presiones. Las medidas de DRX en polvo y de DR hasta 17 GPa se han complementado con cálculos *ab initio* de energía total, dinámica de red y estructura electrónica de bandas. Nuestras medidas, que incluyen medidas de DR no reportadas previamente para el α-As_2Te_3 cristalino, muestran que este compuesto experimenta una transición de fase reversible por encima de 14 GPa a temperatura ambiente. La estructura cristalina monoclínica del α-As_2Te_3 y su comportamiento bajo presión se analizan mediante el tensor de compresibilidad. Se observan importantes cambios estructurales y vibracionales en el rango entre 2 y 4 GPa, que pueden atribuirse al fortalecimiento de los enlaces entre capas, sin embargo no se ha observado ninguna evidencia de transición de fase isoestructural en el compuesto. La comparación con otros sesquicalcogenuros del grupo 15 permite comprender la estructura del α-As_2Te_3 y su comportamiento bajo presión en función de la actividad del par de electrones solitarios del catión (As) en estos compuestos. Finalmente, nuestros cálculos de la estructura de bandas electrónicas muestran que el α-As_2Te_3 es un semiconductor a 1 atm y experimenta una transición trivial semiconductor-metal por encima de 4 GPa. Asimismo, se discute la ausencia de una transición topológica electrónica inducida por presión en el compuesto.

La revista de investigación periódica en la que se publicó este artículo es THE JOURNAL OF PHYSICAL CHEMISTRY C, de reconocido prestigio internacional. En el 2016 JCR Science Edition tiene acreditado un factor de impacto de 4,536, ocupando la posición 43 en el ámbito científico de MATERIALS SCIENCE, MULTIDISCIPLINARY respecto al total de 275 títulos recogidos en esta misma área científica (primer tercil). También está indexada en el primer tercil del campo CHEMISTRY, PHYSICAL ocupando una posición relativa de 31/146. Adicionalmente, y con el fin de evidenciar la contribución de esta aportación al

desarrollo de posteriores estudios, es también oportuno señalar que, de acuerdo con el Science Citation Index (ISI Web of Knowledge), este artículo ha recibido a fecha de hoy 13 citas. Mi contribución particular a este trabajo ha consistido en la toma de medidas de DR y DRX del compuesto a diferentes presiones, y posterior análisis y discusión de los resultados.

Para concluir esta tesis, en los capítulos tercero y cuarto, se presentan la discusión general de los resultados obtenidos y las conclusiones y consecución de objetivos de los trabajos actuales, así como las perspectivas futuras de estudio. Por último, se muestra la bibliografía completa empleada a lo largo de la tesis.

Objetivos de esta tesis

El objetivo principal de esta tesis es el estudio de las propiedades estructurales, vibracionales, mecánicas y electrónicas de compuestos As_2X_3, es decir, sesquióxidos y sesquicalcogenuros de arsénico, en condiciones de alta presión.

Los objetivos específicos de la tesis son los siguientes:

i. Caracterización de las propiedades estructurales, vibracionales, electrónicas y elásticas de los compuestos As_4O_6 y $As_4O_6 \cdot 2He$ mediante la combinación de las técnicas experimentales de DRX y DR a altas presiones, complementadas con simulaciones teóricas *ab initio*.

ii. Estudio de las propiedades vibracionales de los compuestos As_4O_6 y $As_4O_6 \cdot 2He$ a altas presiones desde una perspectiva conjunta experimental (DR) y teórica (cálculos *ab initio*), así como de las propiedades elásticas teóricas de ambos compuestos bajo presión.

iii. Caracterización de las propiedades estructurales, vibracionales y electrónicas del compuesto α-As_2S_3 bajo presión, empleando las técnicas experimentales de DRX y DR combinadas con cálculos *ab initio*.

iv. Caracterización de las propiedades estructurales, vibracionales y electrónicas del compuesto α-As_2Te_3 bajo presión, empleando las técnicas experimentales de DRX y DR, complementadas con los cálculos *ab initio* de energía total, dinámica de red y estructura electrónica de bandas.

Referencias

[Ablain 2011] J. Ablain and H. The. Revisiting the differentiation paradigm in acute promyelocytic leukemia. *Blood*. **2011**, *117(22)*, 5795.

[Agency for Toxic Substances and Disease Registry 2005] Agency for Toxic Substances and Disease Registry. *Toxicological Profile for Arsenic (Update)*. (Atlanta, **2005**).

[Bartrip 1992] P. Bartrip. A "Pennurth of Arsenic for rat poison ": The Arsenic Act, 1851 and the prevention of secret poisoning. *Medical History*. **1992**, *36*, 53-69.

[Bridgman 1914] P. W. Bridgman. The Coagulation of Albumen by Pressure. *Journal of Biological Chemistry.* **1914**, 19, 511-512.

[Bundy 1955] F.P. Bundy, H.T. Hall, H.M. Strong, and R.H. Wentorf, Jr. Man-Made Diamonds. *Nature*. **1955**, *176*, 51.

[Burgio 2000] L. Burgio and R. J. H. Clark. Comparative pigment analysis of six modern Egyptian papyri and an authentic one of the 13th century BC by Raman microscopy and other techniques. *Journal of Raman Spectroscopy*. **2000**, *31*, 395.

[Castro 2013] J. Castro Ramos, A.E. Villanueva Luna, y C.M. Ortiz Lima. Espectroscopia Raman y sus aplicaciones. *Óptica Pura y Aplicada*. **2013**, *46-1*, 83.

[Chinese Pharmacopoeia Committee 2005] Chinese Pharmacopoeia Committee. *Pharmacopoeia of China*. (People's Press, Beijing, China, **2005**)

[Cutler 1878] E. G. Cutler and E. H. Bradford. Action of iron, cod-liver oil, and arsenic on the globular richness of the blood. *The American Journal of the Medical Sciences*. **1878**, *75*, 74.

[De la Serna 2008] J. De la Serna, P Montesinos, E. Vellenga, C. Rayón, R. Parody, A. León, . Causes and prognostic factors of remission induction failure in patients with acute promyelocytic leukemia treated with all-trans retinoic acid and idarubicin. *Blood*. **2008**, *111(7)*, 3395.

[Drahota 2009] P. Drahota and M. Filippi. Secondary arsenic minerals in the environment: A review. *Environment International*. **2009**, *35*, 1243.

[Eastaugh 2004] N. Eastaugh, V. Walsh, T. Chaplin, and R. Sidall. *The Pigment Compendium. A Dictionary of Historical Pigments*. (Elsevier Butterworth-Heinemann, **2004**).

[Edwards 1961] A. L. Edwards and H. G. Drickamer. Effect of Pressure on the Absorption Edges of Some III-V, II-VI, and I-VII Compounds. *Physical Review*. **1961**, 122, 1149.

[Evens 2004] A. M. Evens, M. S. Tallman, and R. B. Gartenhaus. The potential of arsenic trioxide in the treatment of malignant disease: past, present, and future. *Leukemia Research*. **2004**, *28*, 891.

[Gasque 2013] L. Gasque Silva. Arsénico, el elemento inclasificable. *Educación Química*. **2013**, *24-2*, 495.

[Ghavamzadeh 2011] A. Ghavamzadeh, K. Alimoghaddam, S. Rostami, S.H. Ghaffari, M. Jahani, M. Iravani, S.A. Mousavi, B. Bahar, and M. Jalili. Phase II study of single-agent arsenic trioxide for the front-line therapy of acute promyelocytic leukemia. *Journal of Clinical Oncology*. **2011**, *29(20)*, 2753.

[Grimwade 2009] D. Grimwade, J.V. Jovanovic, R.K. Hills, E.A. Nugent, Y. Patel, R. Flora, D. Diverio, K. Jones, H. Aslett, E. Batson, K. Rennie, R. Angell, R.E. Clark, E. Solomon, F. Lo-Coco, K. Wheatley, and A.K. Burnett. Prospective minimal residual disease monitoring to predict relapse of acute promyelocytic leukemia and direct pre-emptive arsenic trioxide therapy. *Journal of Clinical Oncology*. **2009**, *27(22)*, 3650.

[Hall 1960] H. T. Hall. Ultra-High-Pressure, High-Temperature Apparatus: the "Belt". *Review of Scientific Instruments.* **1960**, 31, 125.

[Hede 2007] K. Hede. Chinese folk treatment reveals power of arsenic to treat cancer, new studies under way. *Journal of the National Cancer Institute*. **2007**, *99*, 667.

[IARC 2004] International Agency for Research on Cancer. Some Drinking Water Disinfectants and Contaminants, including Arsenic. *Monographs on Evaluation of Carcinogenic Risk to Humans*. **2004**, *84*, 269.

[Jeanne 2010] M. Jeanne, V. Lallemand-Breitenbach, O. Ferhi, M. Koken, M. Le Bras, S. Duffort, L. Peres, C. Berthier, H. Soilihi, B. Raught, and H. de Thé. PML/RARA oxidation and arsenic binding initiate the antileukemia response of As_2O_3. *Cancer Cell*. **2010**, *18*, 88.

[Koch 2007] I. Koch, S. Sylvester, V. W. Lai, A. Owen, K. J. Reimer, and W. R. Cullen. Bioaccessibility and excretion of arsenic in Niu Huang Jie Du Pian pills. *Toxicology and Applied Pharmacology*. **2007**, *222*, 357.

[Kozono 2018] S. Kozono, Y-M. Lin, H-S. Seo, B. Pinch, X. Lian, C. Qiu, M.K. Herbert, C-H. Chen, L. Tan, Z.J. Gao, W. Massefski, Z.M. Doctor, B.P. Jackson, Y. Chen, S. Dhe-Paganon, K.P. Lu, and X.Z. Zhou. Arsenic targets Pin1 and cooperates with retinoic acid to inhibit cancer-driving pathways and tumor-initiating cells. *Nature Communications*. **2018**, *9*, 3069.

[Lazo 2003] G. Lazo, H. Kantarjian, E. Estey, D. Thomas, S. O'Brien, and J. Cortes. Use of arsenic trioxide (As_2O_3) in the treatment of patients with acute promyelocytic leukemia. *Cancer*. **2003**, *97*, 2218.

[Lin 2007] M. Lin, Z. Wang, and D. S. Zhang. Preparation of orpiment nanoparticles and their cytotoxic effect on cultured leukemia K562 cells. *Journal of Nanoscience and Nanotechnology*. **2007**, *7*, 490.

[Lin 2008] M. Lin, D. S. Zhang, H. Li, J. Ye, and L. X. Zhang. Anticancer effect of orpiment nanoparticles on K562 cells in vitro and its mechanism. *Nanotechnology and Precision Engineering*. **2008**, *6(1)*, 14.

[Liu 2007] J. Liu, R. Goyer, and M. P. Waalkes. "Toxic effects of metals." in *Casarett and Doull's Toxicology – The Basis of Poisons, 7th Ed*. Ed. C. D. Klaassen (McGraw Hill, New York, **2007**, 931-979).

[Liu 2008] J. Liu, Y. Lu, Q. Wu, R. A. Goyer, and M. P. Waalkes. Mineral Arsenicals in Traditional Medicines: Orpiment, Realgar, and Arsenolite. *The Journal of Pharmacology and Experimental Therapeutics*. **2008**, *326*, 2.

[Lu 2002] D. P. Lu, J. Y. Qiu, B. Jiang, Q. Wang, K. Y. Liu, Y. R. Liu, and S. S. Chen. Tetra-arsenic tetra-sulfide for the treatment of acute promyelocytic leukemia: a pilot report. *Blood*. **2002**, *99*, 3136.

[Lu 2014] Z. Lu and T. Hunter. Pin 1 and cancer. *Cell Research*. **2014**, *24*, 1033.

[Lundblad 1994] E. W. Lundblad. High pressure synthesis of diamond in Sweden in 1953. *AIP Conference Proceedings.* **1994**, 309, 503.

[Maeda 2004] H. Maeda, S. Hori, H. Ohizumi, T. Segawa, Y. Kakehi, O. Ogawa, and A. Kakizuka. Effective treatment of advanced solid tumors by the combination of arsenic trioxide and L-buthionine-sulfoximine. *Cell Death & Differentiation*. **2004**, *11*, 737.

[Miller 2002] W. H. Jr. Miller, H. M. Schipper, J. S. Lee, J. Singer, and S. Waxman. Mechanism of action of arsenic trioxide. *Cancer Research*. **2002**, *62*, 3893.

[National Research Council 1999] National Research Council, Subcommittee on Arsenic in Drinking Water, Committee on Toxicology, Board on Environmental Studies and Toxicology, and Commission on Life Sciences. *Arsenic in the Drinking Water*. National Academy Press (Washington, DC, **2005**).

[Niu 1999] C. Niu, H. Yan, T. Yu, H.P. Sun, J.X. Liu, X-S. Li, W. Wu, F.Q. Zhang, Y. Chen, L. Zhou, J.M. Li, X.Y. Zeng, R.R. Yang, M.M. Yuan, M.Y. Ren, F.Y. Gu, Q. Cao, B.W. Gu, X.Y. Su, G-Q. Chen, S.M. Xiong, T.D. Zhang, S. Waxman, Z-Y. Wang, Z. Chen, J. Hu, Z-X. Shen, and S.J. Chen. Studies on treatment of acute promyelocytic leukemia with arsenic trioxide: remission induction, follow-up, and molecular monitoring in 11 newly diagnosed and 47 relapsed acute promyelocytic leukemia patients. *Blood*. **1999**, *94*, 3315.

[Pershagen 1981] G. Pershagen. The Carcionogenicity of Arsenic. *Enviromental Health Perspectives*. **1981**, *40*, 93.

[Pliny 1938] Pliny the Elder. *Natural History I*, ed. by E. H. Warmington (Harvard University Press, Cambridge, **1938**, 147).

[Quadbeck 2007] H.-J. Quadbeck-Seeger. *World of the Elements – Elements of the World*. (Wiley-VCH, Weinheim, **2007**, 51).

[Ramos 2009] C.O. Ramos Peñafiel, H. Castellanos Sinco, E. Montaño, C. Martínez Murillo, P. Lavielle, y V. García Vidrios. Experiencia del tratamiento de leucemia promielocítica aguda (LAP) en el Hospital General de México: protocolo LAP 2001. *Revista de Hematología Mexicana*. **2009**, *10 (supl2)*, 57.

[Sanz 2005] M. Sanz, P. Fenaux, and F. Lo-Coco. Arsenic trioxide in the treatment of acute promyelocytic leukemia. A review of current evidence. *Haematologica*. **2005**, *90*, 1231.

[Shen 1997] Z-X. Shen, G-Q. Chen, J-H. Ni, X-S Li, S.M. Xiong, Q.Y. Qiu, J. Zhu, W. Tang, G.L. Sun, K.Q. Yang, Y. Chen, L. Zhou, Z-W. Fang, Y.T. Wang, J. Ma, P. Zhang, T-D- Zhang, S.J. Chen, and Z-Y Wang. Use of arsenic trioxide (As2O3) in the treatment of acute promyelocytic leukemia (APL): II. Clinical efficacy and pharmacokinetics in relapsed patients. *Blood*. **1997**, *89*, 3354.

[Shen 2004] J. C. Shen, K. Y. Liu, B. Jiang, X. J. Lu, and D. P. Lu. Effect of the tetra-arsenic tetra-sulfide (As_4S_4) on the corrected QT interval in the treatment of acute promyelocytic leukemia. *Zhonghua Xue Ye Xue Za Zhi*. **2004**, *25*, 359.

[Shen 2013] S. Shen, X-F. Li, W.R. Cullen, M. Weinfeld, and X.C. Le. Arsenic binding to proteins. *Chemical Reviews*. **2013**, *113*, 7769.

[Siddall 2018] R. Siddall. Mineral Pigments in Archaeology: Their Analysis and the Range of Available Materials. *Minerals*. **2018**, *8*, 201.

[Soignet 1998] S. L. Soignet, P. Maslak, Z-G. Wang, S. Jhanwar, E. Calleja, L.J. Dardashti, D. Corso, A. DeBlasio, J. Gabrilove, D.A. Scheinberg, P.P. Pandolfi, and R.P. Warrell. Complete remission after treatment of acute promyelocytic leukemia with arsenic trioxide. *The New England Journal of Medicine*. **1998**, *339*, 1341.

[Spurrell 1895] F. C. J. Spurrell. Notes on Egyptian Colours. *Archaeological Journal*. **1895**, *52:1*, 222.

[Suárez 2014] L. Suárez, Y.N. Tamayo, I. Rodríguez, G. Hernández, y B.O. de la Uz. Tratamiento con trióxido de arsénico en pacientes con leucemia promielocítica aguda. *Medisan*. **2014**, *18(1)*, 25.

[Waxman 2001] S. Waxman and K. C. Anderson. History of the development of Arsenic Derivatives in Cancer Therapy. *The Oncologist*. **2001**, *6-2*, 3.

[Weber 1983] G. Weber and H. G. Drickamer. The effecxt of high pressure upon proteins and other biomolecules. *Quarterly Reviews of Biophysics.* **1983**, 16, 89-112.

[Wei 2015] S. Wei. Active Pin1 as a target of all-trans retinoic acid in acute promyelocytic leukemia and breast cancer. *Nature Medicine*. **2015**, *21*, 457.

[Weir 1959] C. E. Weir, E. R. Lippincott, A. Van Valkenburg, and E. N. Bunting, Infrared Studies in the 1- to 15-Micron Region to 30,000 Atmospheres. *Journal of Research of the Natural Bureau of Standards.* **1959**, 63A, 55-62.

[Yu 2007] J. Yu, H. Qian, Y. Li, Y. Wang, X. Zhang, X. Liang, M. Fu, and C. Lin. Arsenic trioxide (As_2O_3) reduces the invasive and metastatic properties of cervical cancer cells in vitro and in vivo. *Gynecologic Oncology*. **2007**, *106*, 400.

[Zhang 2010] X.W. Zhang, X.J. Yan, Z.R. Zhou, F.F. Yang, Z.Y. Wu, H.B. Sun, W.X. Liang, A.X. Song, V. Lallemand-Breitenbach, M. Jeanne, Q.Y. Zhang, H.Y. Yang, Q.H. Huang, G.B. Zhou, J.H. Tong, Y. Zhang, J.H. Wu, H.Y. Hu, H. de Thé, S.J. Chen, and Z. Chen. Arsenic trioxide controls the fate of the PML-RARalpha oncoprotein by directly binding PML. *Science*. **2010**, *328*, 240.

[Zhou 2016] X.Z. Zhou and K.P. Lu. The isomerase Pin1 controls numerous cancer-driving pathways and is a unique drug target. *Nature Reviews Cancer*. **2016**, *16*, 463.

Capítulo 2

Publicaciones

PHYSICAL REVIEW B **93**, 054102 (2016)

Ordered helium trapping and bonding in compressed arsenolite: Synthesis of $As_4O_6 \cdot 2He$

Juan A. Sans,[1,*] Francisco J. Manjón,[1,†] Catalin Popescu,[2] Vanesa P. Cuenca-Gotor,[1] Oscar Gomis,[3] Alfonso Muñoz,[4] Plácida Rodríguez-Hernández,[4] Julia Contreras-García,[5,6] Julio Pellicer-Porres,[7] Andre L. J. Pereira,[1,8] David Santamaría-Pérez,[7] and Alfredo Segura[7]

[1]*Instituto de Diseño para la Fabricación y Producción Automatizada, Universitat Politècnica de València, 46022, Valencia, Spain*
[2]*ALBA-CELLS, 08290, Cerdanyola, Spain*
[3]*Centro de Tecnologías Físicas, MALTA Consolider Team, Universitat Politècnica de València, 46022, Valencia, Spain*
[4]*Departamento de Física, Instituto de Materiales y Nanotecnología, Universidad de La Laguna, 38205, La Laguna, Spain*
[5]*Sorbonne Universités, UPMC Univ Paris 06, UMR 7616, Laboratoire de Chimie Théorique, F-75005, Paris, France*
[6]*CNRS, UMR 7616, Laboratoire de Chimie Théorique, F-75005, Paris, France*
[7]*ICMUV-Departamento de Física Aplicada, Universitat de València, 46100, Burjassot, Spain*
[8]*Laboratório de Materiais Cerâmicos Avançados, Faculdade de Ciências Exatas e Tecnologia, Universidade Federal da Grande Dourados, Dourados, Brazil*

(Received 23 April 2015; revised manuscript received 30 December 2015; published 1 February 2016)

Compression of arsenolite has been studied from a joint experimental and theoretical point of view. Experiments on this molecular solid at high pressures with different pressure-transmitting media have been interpreted thanks to *state-of-the-art ab initio* calculations. Our results confirm arsenolite as one of the most compressible minerals and provide evidence for ordered helium trapping above 3 GPa between adamantane-type As_4O_6 cages. Our calculations indicate that, at relatively small pressures, helium establishes rather localized structural bonds with arsenic forming a compound with stoichiometry $As_4O_6 \cdot 2He$. All properties of $As_4O_6 \cdot 2He$ are different from those of parent As_4O_6. In particular, pressure-induced amorphization, which occurs in arsenolite above 15 GPa, is impeded in $As_4O_6 \cdot 2He$, thus resulting in a mechanical stability of $As_4O_6 \cdot 2He$ beyond 30 GPa. Our work paves the way to explore the formation of alternative compounds by pressure-induced trapping and reaction of gases, small atomic or molecular species, in the voids of molecular solids containing active lone electron pairs.

DOI: 10.1103/PhysRevB.93.054102

Molecular solids are very soft materials with open-framework structures composed of molecular units, exhibiting strong covalent interatomic forces, which are linked by weak intermolecular forces, such as van der Waals interactions or hydrogen bonding forces. Pressure is a thermodynamic variable that allows tuning interatomic distances and consequently is a powerful tool to study atomic interactions and the connectivity of different molecular units – hence, the possibility of molecular solids to trap small atoms or molecules. In this sense, molecule trapping has received a lot of interest from the scientific community due to its potential industrial applications covering hydrogen storage [1] and CO_2 segregation from other organic compounds [2], among others. Recently, the small size of helium has triggered the study of pressure-induced helium trapping and how this effect affects the compressibility of host compounds. Those first studies were focused on helium trapping in silica glass [3–5] that is an amorphous compound with disordered interstitial voids large enough to host and trap helium. However, more studies need to be made of pressure-induced helium trapping in ordered crystallographic compounds, such as molecular solids.

Helium reaction is a challenge since it is one of the most inert elements in nature [6]. Previous studies of helium trapping in glasses have not revealed the pressure-induced reactivity of helium with the glass structure. On the search of the formation of solid structures with helium, the study of mixtures of helium with other noble gases at high pressures has exhibited successful results. The mix of those fluids under pressure allows the formation of solid van der Waals compounds with exotic stoichiometries [7,8] [$He(N_2)_{11}$, $Ne(He)_2$] given by the solubility of helium and dominated by the crystallization process of the other noble gases. On the other hand, it is noteworthy to highlight the low reactivity of helium with solid compounds, which has required the use of extremely high pressures (more than 1 Mbar) to form solid alloys, such as Na_2He [9].

In this work, we provide experimental and theoretical proofs of the pressure-induced helium trapping and reactivity in a molecular solid (arsenolite) at relatively low pressures. Our results could trigger the formation of alternative compounds by pressure-induced trapping and bonding of gases, small atomic and molecular species, with molecular solids containing active lone electron pairs.

Arsenic oxide (As_2O_3) belongs to the sesquioxide family of group 15 elements, which also includes P_2O_3, Sb_2O_3, and Bi_2O_3. In particular, As_2O_3 crystallizes either in a cubic structure [space group (SG) 227, $Fd\text{-}3m$, $Z = 16$] (which corresponds to mineral named arsenolite) [10] or in monoclinic structures [SG 14, $P2_1/c$, $Z = 4$] (which corresponds to mineral named claudetite I and claudetite II) [11–13]; however, it can also be obtained in an amorphous (glass) phase [14,15]. Most of the polymorphs of group 15 sesquioxides [16] show close structural connections since many structures could be derived from a defective fluorite structure through symmetry breaking and local distortions [17,18]. A few of those polymorphs constitute molecular solids, like arsenolite

*juasant2@upv.es
†fjmanjon@upv.es

Ordered helium trapping and bonding in compressed arsenolite: Synthesis of $As_4O_6 \cdot 2He$

Juan A. Sans,[1] Francisco J. Manjón,[1] Catalin Popescu,[2] Vanesa P. Cuenca-Gotor,[1] Óscar Gomis,[3] Alfonso Muñoz,[4] Plácida Rodríguez-Hernández,[4] Julia Contreras-García,[5,6] Julio Pellicer-Porres,[7] Andre L. J. Pereira,[1,8] David Santamaría-Pérez,[7] and Alfredo Segura[7]

[1] *Instituto de Diseño para la Fabricación y Producción Automatizada, MALTA Consolider Team, Universitat Politècnica de València, 46022 València, Spain*

[2] *ALBA-CELLS, 08290, Cerdanyola, Spain*

[3] *Centro de Tecnologías Físicas: Acústica, Materiales y Astrofísica, MALTA Consolider Team, Universitat Politècnica de València, 46022 València, Spain*

[4] *Departamento de Física, Instituto de Materiales y Nanotecnología, MALTA Consolider Team, Universidad de La Laguna, 38205 Tenerife, Spain*

[5] *Sorbonne Universités, UPMC Univ Paris 06, UMR 7616, Laboratoire de Chimie Théorique, F-75005, Paris, France*

[6] *CNRS, UMR 7616, Laboratoire de Chimie Théorique, F-75005, Paris, France*

[7] *ICMUV-Departamento de Física Aplicada, MALTA Consolider Team, Universitat de València, 46100, Burjassot, Spain*

[8] *Laboratòrio de Materiais Cerâmicos Avançados, Faculdade de Ciências Exatas e Tecnologia, Universidade Federal da Grande Dourados, Dourados, Brazil*

Abstract

Compression of arsenolite has been studied from a joint experimental and theoretical point of view. Experiments on this molecular solid at high pressures with different pressure-transmitting media have been interpreted thanks to *state-of-the-art ab initio* calculations. Our results confirm arsenolite as one of the most compressible minerals and provide evidence for ordered helium trapping above 3 GPa between adamantane-type As_4O_6 cages. Our calculations indicate that, at relatively small pressures, helium establishes rather localized structural bonds with arsenic forming a compound with stoichiometry $As_4O_6 \cdot 2He$. All properties of $As_4O_6 \cdot 2He$ are different from those of parent As_4O_6. In particular, pressure-induced amorphization, which occurs in arsenolite above 15 GPa, is impeded in $As_4O_6 \cdot 2He$, thus resulting in a mechanical stability of $As_4O_6 \cdot 2He$ beyond 30 GPa. Our work paves the way to explore the formation of alternative compounds by pressure-induced trapping and reaction of gases, small atomic or molecular species, in the voids of molecular solids containing active lone electron pairs.

Molecular solids are very soft materials with open-framework structures composed of molecular units, exhibiting strong covalent interatomic forces, which are linked by weak intermolecular forces, such as van der Waals interactions or hydrogen bonding forces. Pressure is a thermodynamic variable that allows tuning interatomic distances and consequently is a powerful tool to study atomic interactions and the connectivity of different molecular units – hence, the possibility of molecular solids to trap small atoms or molecules. In this sense, molecule trapping has received a lot of interest from the scientific community due to its potential industrial applications covering hydrogen storage [Song 2013] and CO_2 segregation from other organic compounds [Xiang 2012], among others. Recently, the small size of helium has triggered the study of pressure-induced helium trapping and how this effect affects the compressibility of host compounds. Those first studies were focused on helium trapping in silica glass [Sato 2011, Shen 2011, Weigel 2012] that is an amorphous compound with disordered interstitial voids large enough to host and trap helium. However, more studies need to be made of pressure-induced helium trapping in ordered crystallographic compounds, such as molecular solids.

Helium reaction is a challenge since it is one of the most inert elements in nature [Herman 2012]. Previous studies of helium trapping in glasses have not revealed the pressure-induced reactivity of helium with the glass structure. On the search of the formation of solid structures with helium, the study of mixtures of helium with other noble gases at high pressures has exhibited successful results. The mix of those fluids under pressure allows the formation of solid van der Waals compounds with exotic stoichiometries [Vos 1992, Loubeyre 1993] [$He(N_2)_{11}$, $Ne(He)_2$] given by the solubility of helium and dominated by the crystallization process of the other noble gases. On the other hand, it is noteworthy to highlight the low reactivity of helium with solid compounds, which has required the use of extremely high pressures (more than 1 Mbar) to form solid alloys, such as Na_2He [Dong 2014].

In this work, we provide experimental and theoretical proofs of the pressure-induced helium trapping and reactivity in a molecular solid (arsenolite) at relatively low pressures. Our results could trigger the formation of alternative compounds by pressure-induced trapping and bonding of gases, small atomic and molecular species, with molecular solids containing active lone electron pairs.

Arsenic oxide (As_2O_3) belongs to the sesquioxide family of group 15 elements, which also includes P_2O_3, Sb_2O_3, and Bi_2O_3. In particular, As_2O_3 crystallizes either in a cubic structure [space group (SG) 227, Fd-3m, Z = 16] (which corresponds to mineral named arsenolite) [Pertlik 1978a] or in monoclinic structures [SG 14, P 2$1/c$, Z = 4] (which corresponds to mineral named claudetite I and claudetite II) [Frueh 1951, White 1967, Pertlik 1978b]; however, it can also be obtained in an amorphous (glass) phase [Bertoluzza 1972, Papatheodorou 1976]. Most of the polymorphs of group 15 sesquioxides [**1**] show close structural connections since many structures could be derived from a defective fluorite structure through symmetry breaking and local distortions [Matsumoto 2010, Matsumoto 2011]. A few of those polymorphs constitute molecular solids, like arsenolite (As_4O_6). This compound is a very soft and toxic mineral with an intermediate hardness between that of talc and gypsum, i.e., the softest minerals in the Mohs scale. In fact, arsenolite is

composed of pseudotetrahedral units consisting of an arsenic atom surrounded by three oxygen ligands and a very active lone electron pair (LEP). Pseudotetrahedral units in arsenolite are configured in closed-compact adamantane-type As_4O_6 molecular cages [**Fig. 1, left**], which are bonded together by weak van der Waals forces and with LEPs pointing towards the exterior of the molecular unit. Interestingly, the formation of molecular cages is also found in other sesquioxides and sesquichalcogenides of group 15 elements [**2**].

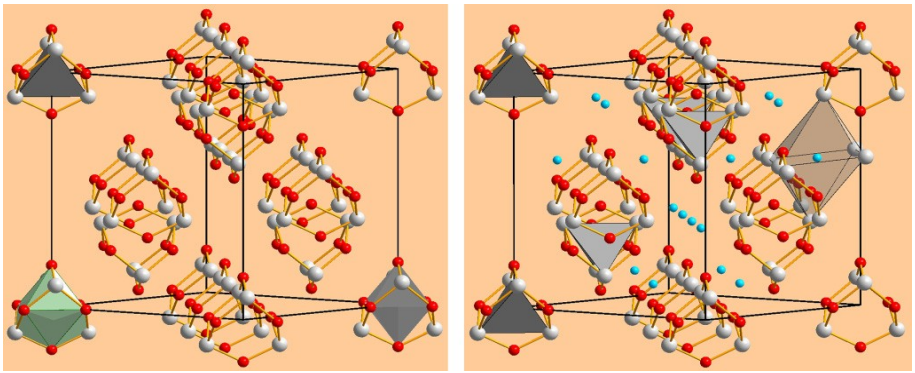

Figure 1. Detail of the cubic unit cell of arsenolite (As_4O_6) (left) and $As_4O_6 \cdot 2He$ (right). $As_4O_6 \cdot 2He$ is a compound formed above 3 GPa by arsenolite with He atoms inserted into 16*d* Wyckoff sites. Large gray balls, medium-size red balls, and small blue balls represent As, O, and He atoms, respectively.

High-pressure (HP) Raman scattering (RS) and HP Fourier transform infrared measurements of arsenolite [Grzechnik 1999]; HP RS measurements of arsenolite, claudetite, and glass [Mei 2007a, Soignard 2008]; and HP x-ray diffraction (XRD) studies of arsenolite, claudetite, and glass As2O3 [Mei 2007a, Soignard 2008, Weir 1965, Mei 2007b] have been published. On the other hand, the atomic structure of arsenolite and its equation of state under different pressure transmitting media (PTM) were firstly reported in Ref. [Sans 2015] and later by Ref. [Guńka 2015b]. However, the possible reaction between those PTM and arsenolite studied from a joint experimental and theoretical approach have not been studied yet.

In this work, we provide a comprehensive understanding of the compression of arsenolite using different PTM (silicone oil, 4:1 methanol-ethanol mixture, and He) and without PTM. For this purpose, we combine two experimental techniques (XRD and RS) and *state-of-the-art ab initio* calculations providing structural, electronic, elastic, and lattice dynamical properties of arsenolite at different pressures. The comparison of the results of different experiments and its understanding on the light of *ab initio* calculations reveals that arsenolite is one of the most compressible minerals and provides evidence for helium trapping above 3 GPa between adamantane-type As_4O_6 cages. Furthermore, our calculations indicate that, at relatively small pressures,

He establishes localized structural bonds with As to form a compound with $As_4O_6 \cdot 2He$ stoichiometry [**Fig. 1, right**].

Experimental XRD patterns of arsenolite compressed with different PTM (see **Fig. S1** in Supplemental Material [**3**]) reveal a progressive shift of the Bragg diffraction peaks of the cubic structure towards higher angles under compression, as expected for a decrease in the unit cell volume with increasing pressure. Absence of new peaks at HP indicates that no phase transition occurs along the pressure range studied. The pressure dependence of the lattice parameter and atomic positions of arsenolite was obtained by Rietveld refinement along a large pressure range due to the relatively high quality of our experimental XRD patterns (see **Fig. S2** in Supplemental Material [**3**]) [**4**]. EOS of As_4O_6 obtained from experiments using no PTM and silicone oil or methanol-ethanol as PTM yield an average bulk modulus of 7(2) GPa. This value is in good agreement with the theoretical EOS **(**see **Fig. 2(a)** and **Table S1** in Supplemental Material [**3**]) [**5**] and with the bulk modulus obtained from experimental data of As_4O_6 compressed with He below 4 GPa [**6**].

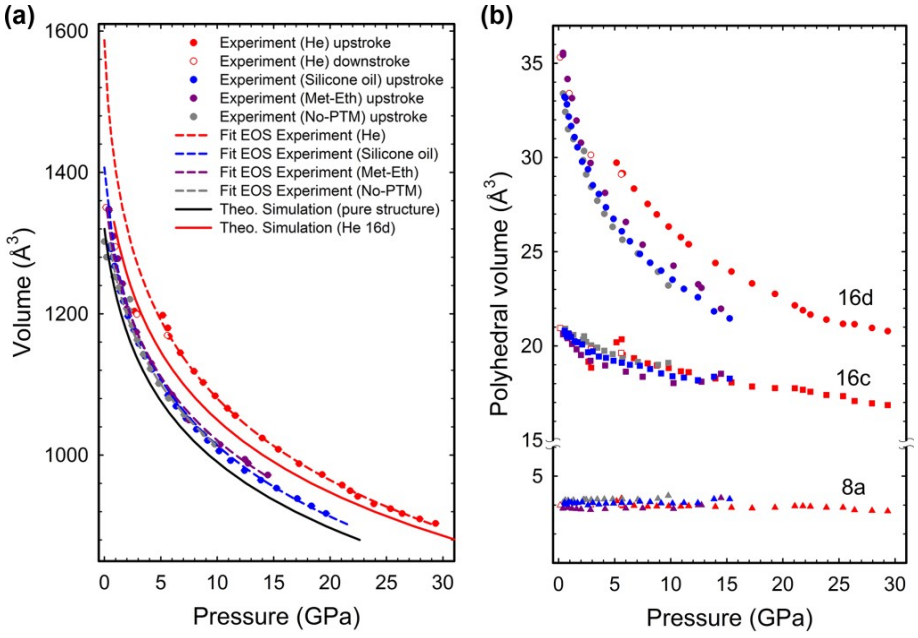

Figure 2. Evolution of the structural parameters of arsenolite under pressure for different PTM. Gray, blue, purple, and red symbols correspond to experimental data of arsenolite compressed without PTM, with silicone oil, with methanol-ethanol mixture, and with He, respectively. Black (red) solid lines correspond to theoretical data of pure (He inserted in 16*d* sites) arsenolite. Dashed lines correspond to fit of experimental data. (a) EOS of arsenolite compressed with different PTM. (b) Compression of the polyhedral volume around different Wyckoff crystallographic sites: 16*d* (circles), 16*c* (squares), and 8*a* (triangles).

Notably, arsenolite's bulk modulus is smaller than those known for other sesquioxides of group 15 elements, which are well below 90 GPa, and much smaller than those of sesquioxides of group 13 elements, whose bulk moduli are well above 160 GPa (**Table S2** in Supplemental Material [**3**]). Moreover, arsenolite's bulk modulus is in the range of the softest molecular crystals [Mei 2007b, Vaidya 1971, Chattopadhyay 1982, Tuktabiev 2009, Lepore 2012] and smaller than related molecular solids, like minerals realgar (α-As_4S_4, B_0 = 8.1 GPa, and B_0' = 9.0) [Tuktabiev 2009] and pararealgar (β- As_4S_4, B_0 = 10.9 GPa, and B_0' = 8.9) [Lepore 2012]. These similar compounds [Kyono 2013] have a cagelike structure based on As tetrahedra [**Fig. 1, left**] surrounded by anions in a closed-compact configuration. The reason for the small bulk moduli of sesquioxides and related molecular crystals of group 15 elements is the presence of the cation LEP which favors the formation of voids in the structural units resulting in open-framework low-compact structures with high compressibility.

Compression of arsenolite with He leads to a striking behavior above 3 GPa [**Fig. 2(a)**]. Unit cell volume decreases with increasing pressure in a normal fashion below 3 GPa and above 5 GPa, but volumes at 3 and 5 GPa are rather similar, resulting in a jump of the *P-V* curve of As_4O_6 compressed with He with respect to *P-V* curves of arsenolite compressed with other PTM. These results can be interpreted as a signature of He entering arsenolite's structure between 3 and 5 GPa and the consequent He trapping between As_4O_6 cages above 5 GPa. The similar volume observed at 3 and 5 GPa can be explained as a compensation between the decrease of volume with pressure and the increase of volume due to He incorporation and trapping.

In order to understand where He gets trapped, we show in **Figure 2(b)** the compressibility of arsenolite's constituting polyhedral units (see **Fig. S4** in Supplemental Material [**3**]): (i) adamantane-type As_4O_6 cage, centered around the 8*a* (0,0,0) Wyckoff site; (ii) the quasioctahedral unit centered around the 16*c* site [**7**]; and (iii) the distorted octahedron centered around the 16*d* site. A clear change in the compressibility of the volume of the distorted octahedron around the 16*d* Wyckoff site is observed depending on the PTM used. A jump in the volume of this polyhedral unit (also in that of the 16*c* site but at a smaller rate) between 3 and 5 GPa is observed when He is used as PTM. This result is nicely explained by theoretical calculations including He in 16*d* sites (a different experimental result would be found if He enters in 16*c* sites according to calculations). Therefore, our measurements and calculations show a clear evidence of He entering in the largest voids of the structure (16*d* sites).

Helium does not enter into the smallest polyhedral units, and in particular into 16*c* sites, which feature the smallest distances between neighboring As_4O_6 cages and the smallest intermolecular As-As distance. This is a somewhat striking result since the smallest intermolecular As-As distance (around the 16*c* site) is well above the van der Waals diameter of He [Bondi 1968], so one could expect the occupation of 16*c* sites because He has been proved to be inserted in interstitials voids of similar or slightly larger diameter than He in amorphous silica [Sato 2011, Shen 2011, Weigel 2012].

In this respect, we want to stress that small He atoms can be diffused along the whole structure due to the existence of big connected spaces between 16*d* sites without the need to enter in 16*c* sites (see paths between He atoms at 16*d* sites in **Fig. S4** in Supplemental Material [**3**]).

The hypothesis of He incorporation and trapping in arsenolite above 3 GPa can also be checked by theoretically simulating the bulk compression of arsenolite with He located at 8*a*, 16*c*, and 16*d* Wyckoff positions (**Fig. S2a** in Supplemental Material [**3**]). Theoretical EOS of He trapped in 16*d* Wyckoff sites shows rather good agreement with experimental data in the range between 5 and 30 GPa [**Fig. 2(a)**]. Therefore, our joint experimental and theoretical study of the bulk and polyhedral compressibilities with different PTM clearly points to the incorporation and trapping of He in 16*d* sites of arsenolite above 3 GPa. Additional proofs confirming He trapping in arsenolite at HP are provided by HP RS measurements (see Supplemental Material [**3**]) performed with similar PTM as those used in HP XRD measurements (**Fig. S5** in Supplemental Material [**3**]). Experimental HP RS spectra without PTM or with (4:1) methanol-ethanol mixture as PTM are similar to those already reported and agree with theoretical calculations for pure arsenolite [Grzechnik 1999, Soignard 2008]. Remarkably, a different pressure dependence of the Raman-active mode frequencies in arsenolite is observed above 3 GPa when He is used as PTM (**Fig. S6** in Supplemental Material [**3**]).

A remarkable broadening of Bragg peaks was observed in XRD experiments without PTM and with silicone oil or methanol-ethanol mixture above 15 and 20 GPa, respectively (**Fig. S1** in Supplemental Material [**3**]). This feature can be ascribed to the onset of pressure-induced amorphization (PIA), as previously reported [Mei 2007a]. Comparison of XRD patterns of samples before and after compression reveal that recovered samples do not exhibit a good crystalline quality after the pressure cycle, which also suggests PIA of arsenolite. It is noteworthy that As_4O_6 compressed with He shows no evidence of PIA up to the maximum pressure reached (29.4 GPa), as confirmed by the comparable crystalline quality of the sample before and after the pressure cycle (**Fig. S1a** in Supplemental Material [**3**]).

To understand the different mechanical stability of As_4O_6 at HP depending on the PTM used we have analyzed the experimental and theoretical evolution of the two characteristic As-As and As-O distances with increasing pressure (see **Fig. S3a** in Supplemental Material [**3**] and related discussion). It can be concluded that the main modification upon entering He in the arsenolite structure is the enlargement of the closest As-As distance between adjacent molecular units (external As-As distance). Under compression of pure arsenolite, both internal and external As-As distances become nearly equal around 20 GPa, leading to strong steric repulsions between the different molecular units which result in PIA. Nevertheless, He trapping in arsenolite above 3 GPa leads to a considerable increase of the external As-As distance, thus avoiding the increase of the intermolecular interactions which turn the crystalline structure of arsenolite unstable. This feature explains the stability of arsenolite beyond 30 GPa when compressed with He and suggests that the stability of

the molecular structure of arsenolite is related to the steric repulsion between the cationic As sublattice governing the formation of the cagelike structure.

Theoretical calculations of the pressure dependence of the elastic constants and stiffness coefficients in As_4O_6 and As_4O_6 with He at 16*d* sites (**Fig. S7** in Supplemental Material [**3**]) allow us to understand the different mechanical stability of arsenolite compressed with different PTM. Generalized Born stability criteria reveal a Born instability in arsenolite due to the violation of the M_2 criterion at 19.7 GPa (**Fig. S8a** in Supplemental Material [**3**]), a pressure close to that experimentally observed for the onset of PIA in our HP XRD measurements using no PTM or using a PTM different from He. On the other hand, no mechanical instability is observed in As_4O_6 with He at 16*d* sites even at 30 GPa (**Fig. S8b** in Supplemental Material [**3**]) which is in very good agreement with our experimental results.

Finally, we have theoretically studied whether He trapping in arsenolite could lead to modification of other properties of arsenolite and even if He at 16*d* sites could react with arsenolite to form a compound with $As_4O_6{\cdot}2He$ stoichiometry above 3 GPa [**8**]. Our calculations indicate a strong decrease of the indirect band gap of As_4O_6 from 4 to 3 eV between 1 atm and 15 GPa, whereas they predict a very small increase of the indirect band gap of $As_4O_6{\cdot}2He$ (also around 4 eV) as a function of pressure between 5 and 30 GPa. In fact, our theoretical calculations of the projected density of states in $As_4O_6{\cdot}2He$ at 14 and 31 GPa (**Fig. S9** in Supplemental Material [**3**]) show bonding and antibonding contributions to the valence band, with He 1*s* orbital character. The bonding contribution mainly concentrates in the extra band group, appearing just below the As 4*s* band group as He is incorporated into the structure, while the antibonding He 1*s* contribution concentrates mainly inside the As 4*s* band group. The presence of As 4*s* and O 2*p* contributions in this band group is a clear evidence of the new bonds formed by the He reaction with arsenolite. Three features provide further evidence of the reaction of He with As_4O_6: (i) a downward (upward) shift in energy of the bonding (antibonding) bands with increasing pressure, (ii) an increase of the bandwidth of both band groups with increasing pressure, and (iii) an increase in the projected density of states of the band group with antibonding He 1*s* character with increasing pressure.

Furthermore, we have analyzed our calculated charge density for pure arsenolite and arsenolite with He at 16*d* sites at different pressures looking for small interactions of He with surrounding atoms. For that purpose, we have used the NCI (noncovalent interaction) index [Johnson 2010] which is more adapted for identifying weak noncovalent bonds than the electron localization function (ELF). **Figure 3** shows that there are both localized and delocalized van der Waals interactions of He with its neighbors. In particular, localized interactions (revealed as compact surfaces) appear between He and six As neighbors. These interactions are strong enough to claim that He plays a role in the structure rather than simply occupying the 16*d* site, just like crystalline hydrogen bonded waters do. The low electronic density and the positive but weak values of the electronic Laplacian in this pressure range (**Fig. S12** in Supplemental Material [**3**]) allow us to classify the

character of the bonds established between He and As atoms as weak in nature, but the compact circular shapes obtained in NCI classify it as a localized structural type of bond. All these features allow us to conclude that there is a pressure-induced He bonding with As_4O_6 resulting in the formation of $As_4O_6 \cdot 2He$. This notation, taken from crystalline water, stands for the fact that He is structurally added to the arsenolite structure. This bonding of He at pressures as small as 3 GPa is striking since the formation of helium-containing compounds has been recently reported only at extremely high pressures: Na_2He (113 GPa) [Dong 2014].

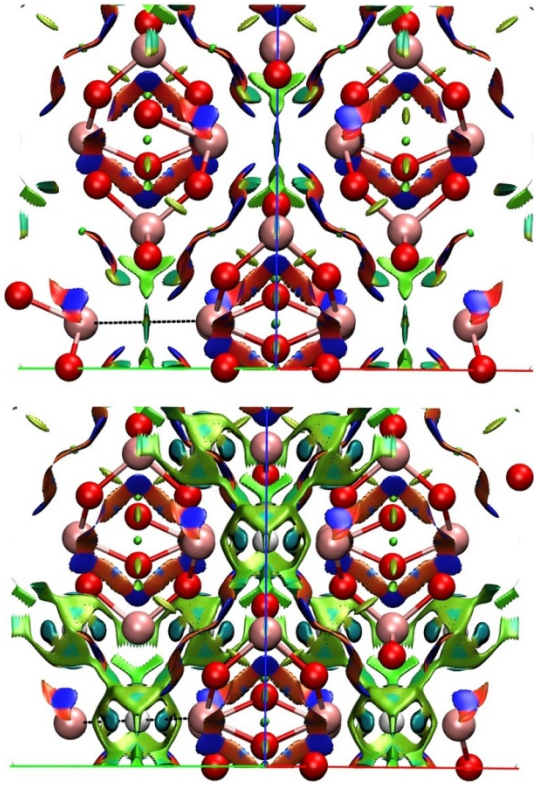

Figure 3. Isosurfaces of the reduced density gradient (revealed by NCI index) evidencing noncovalent interactions in As_4O_6 (top) and $As_4O_6 \cdot 2He$ (bottom) near 16 GPa. As expected for a noble gas, van der Waals (green) interactions around the He atoms are revealed. However, unexpectedly localized interactions (in turquoise blue) also make their appearance along the He-As interaction lines.

The hypothesis of amorphization due to steric repulsion between neighboring As atoms is confirmed by theoretical calculations which show a strong increase of the repulsive interaction between low pressures and 15 GPa when arsenolite is compressed in the absence of He (**Fig. S13** in Supplemental Material [**3**]).

In summary, we have proved that arsenolite is one of the nonhydrated molecular solids with the smallest bulk modulus and that He incorporates above 3 GPa into the arsenolite lattice at ordered 16*d* positions. He trapping helps to stabilize the arsenolite molecular structure keeping As_4O_6 units separated and avoiding PIA at least up to 30 GPa. Furthermore, calculations indicate that He trapping in arsenolite modifies all the properties of arsenolite because there is a pressure-induced He bonding with arsenolite at relatively low pressures. The interaction of He and As atoms results in the formation of a compound with $As_4O_6 \cdot 2He$ stoichiometry (only stable above 3 GPa since He exits arsenolite structure below this pressure) whose properties are different from those of As_4O_6. The present results pave the way to explore the formation of compounds by pressure-induced trapping and bonding of gases, small atomic and molecular species, with molecular solids having open-framework structures like those featuring active lone electron pairs. Moreover, these results suggest that compression of molecular solids with noble gases, such as helium, must be performed with caution since they may result in unexpected results compared to other pressure-transmitting media due to entry (and possible reaction) of these elements with the structure of the molecular compounds.

We acknowledge financial support from the Spanish Consolider Ingenio 2010 Program (Project No. MAT2015- 71070-REDC). The work was also supported by Spanish MINECO under Projects No. MAT2014-46649-C4-1/2/3-P and from Vicerrectorado de Investigación de la Universitat Politècnica de València under Projects No. SP20140701 and No. SP20140871. Supercomputer time has been provided by the Red Española de Supercomputación (RES) and the MALTA cluster. J.A.S. acknowledges Juan de la Cierva fellowship program for his financial support. A.M. and P.R.-H. acknowledge S. Muñoz Rodríguez for providing them with a data parsing application. A.L.J.P. acknowledges financial support through Brazilian CNPq (Project No. 201050/2012-9).

References

[1] P_2O_3 is not stable in solid form at ambient conditions.

[2] The reason for the molecular character of these materials is the strong activity of LEPs in group 15 elements and also in O and S.

[3] See Supplemental Material at:

http://link.aps.org/supplemental/10.1103 /PhysRevB.93.054102

for XRD patterns and RS spectra at different pressures and with different PTM; Rietveld analysis of data including atomic positions and bond distances; charge density analysis and electronic structure of pure arsenolite and compressed As_4O_6·2He.

[4] Rietveld refinement was not possible above 15 and 20 GPa due to loss of hydrostaticity in the experiments without PTM and with silicone oil and methanol-ethanol, respectively.

[5] Slightly larger deviations between the experimental and the- oretical pressure dependence are observed at pressures above 15 GPa likely due to the onset of PIA.

[6] EOS for arsenolite compressed with He below 3 GPa was not obtained because of the few data points mainly taken during downstroke due to He loading constraints.

[7] To establish the compressibility around the 16*c* site we have taken the volume of the octahedron defined by the closest As atoms to a 16*c* site.

[8] Taking into account that He incorporates into 16*d* sites, while As and O are in 32*e* and 48*f* sites, the stoichiometry of the new compound must be AsO·2He.

[Bertoluzza 1972] A. Bertoluzza, M. A. Morelli, and C. Fogano. C. Investigation Using Raman and Infrared Spectroscopy of As_2O_3 Glass in Relation to Crystalline Polymorphous Changes of Trioxide. *Lincei Rend. Sin. Fis. Mat. Nat.* **1972**, *52*, 932.

[Bondi 1968] A. Bondi. Van der Waals volumes and radii. *J. Phys. Chem.* **1968**, *68*, 441.

[Chattopadhyay 1982] T. Chattopadhyay, A. Werner, and H. G. von Schnering. Thermal expansion and compressibility of β-As_4S_3. *J. Phys. Chem. Solids*. **1982**, *43*, 919.

[Dong 2014] X. Dong *et al*. Stable Compound of Helium and Sodium at High Pressure. **2014**, arXiv:1309.3827v3.

[Frueh 1951] A. J. Frueh, Jr. The Crystal Structure of Claudetite (Monoclinic As_2O_3). *American Mineralogist*. **1951**, *36*, 833.

[Grzechnik 1999] A. Grzechnik. Compressibility and Vibrational Modes in Solid As_4O_6. *J. Solid State Chem.* **1999**, *144*, 416.

[Guńka 2015b] P. A. Guńka, K. F. Dziubek, A. Gladysiak, M. Dranka, J. Piechota, M. Hanfland, A. Katrusiak, and J. Zachara. Compressed Arsenolite As_4O_6 and Its Helium Clathrate $As_4O_6 \cdot 2He$. *Cryst. Growth Des*. **2015**, *15*, 3740.

[Herman 2012] C. Herman. Cool as Helium. *Nat. Chem*. **2012**, *4*, 140.

[Johnson 2010] E. Johnson, S. Keinan, P. Mori-Sánchez, J. Contreras-García, A. Cohen, and W. Yang. Revealing noncovalent interactions. *J. Am. Chem. Soc*. **2010**, *132*, 6498.

[Kyono 2013] A. Kyono. Ab initio quantum chemical investigation of arsenic sulfide molecular diversity from As_4S_6 and As_4. *Phys. Chem. Miner*. **2013**, *40*, 717.

[Lepore 2012] G. O. Lepore, T. Boffa Ballaran, F. Nestola, L. Bindi, D. Pasqual, and P. Bonazzi. Compressibility of β-As_4S_4: an in situ high-pressure single-crystal X-ray study. *Mineral. Mag*. **2012**, *76*, 963.

[Loubeyre 1993] P. Loubeyre, M. Jean-Louis, R. LeToullec, and L. Charon-Gerard. High pressure measurements of the He-Ne binary phase diagram at 296 K: Evidence for the stability of a stoichiometric $Ne(He)_2$ solid. *Phys. Rev. Lett*. **1993**, *70*, 178.

[Matsumoto 2010] A. Matsumoto, Y. Koyama, and I. Tanaka. Structures and energetics of Bi_2O_3 polymorphs in a defective fluorite family derived by systematic first-principles lattice dynamics calculations. *Phys. Rev. B*. **2010**, *81*, 094117.

[Matsumoto 2011] A. Matsumoto, Y. Koyama, and I. Tanaka. Electronic structures of dynamically stable As_2O_3, Sb_2O_3, and Bi_2O_3 crystal polymorphs. *Phys. Rev. B*. **2011**, *83*, 214110.

[Mei 2007a] Q. Mei, R. T. Hart, C. J. Benmore, S. Amin, K. Leinenweber, and J. L. Yarger. The structure of densified As_2O_3 glasses. *J. Non-Cryst. Solids*. **2007**, *353*, 1755.

[Mei 2007b] Q. Mei, C. J. Benmore, E. Soignard, S. Amin, and J. L. Yarger. Analysis of high-energy X-ray diffraction data at high pressure: the case of vitreous As_2O_3 at 32 GPa. *J. Phys.: Condens. Matter*. **2007**, *19*, 415103.

[Papatheodorou 1976] G. N. Papatheodorou and S. A. Solin. Vibrational excitations of As_2O_3. I. Disordered phases. *Phys. Rev. B*. **1976**, *13*, 1741.

[Pertlik 1978a] F. Pertlik. Strukturverfeinerung von Kubischem As_2O_3 (Arsenolith) mit Einkristalldaten. *Czech. J. Phys. B*. **1978**, *28*, 170.

[Pertlik 1978b] F. Pertlik. Verfeinerung der Kristallstruktur des Minerals Claudetit, As_2O_3 ("Claudetit I"). *Monatsh. Chem*. **1978**, *109*, 277.

[Sans 2015] J. A. Sans, F. J. Manjón, C. Popescu, V. P. Cuenca-Gotor, O. Gomis, A. Muñoz, P. Rodríguez-Hernández, J. Pellicer- Porres, A. L. J.

Pereira, D. Santamaría-Pérez, and A. Segura. Helium ordered trapping in arsenolite under compression: Synthesis of $He_2As_4O_6$. **2015**, arXiv:1502.04279.

[Sato 2011] T. Sato, N. Funamori, and T. Yagi. Helium penetrates into silica glass and reduces its compressibility. *Nat. Commun*. **2011**, *2*, 345.

[Shen 2011] G. Shen, Q. Mei, V. B. Prakapenka, P. Lazor, S. Sinogeikin, Y. Meng, and C. Park. Effect of helium on structure and compression behavior os SiO_2 glass. *Proc. Natl. Acad. Sci. U. S. A*. **2011**, *108*, 6004.

[Soignard 2008] E. Soignard, S. A. Amin, Q. Mei, C. J. Benmore, and J. L. Yarger. High-Pressure Behavior of As_2O_3: Amorphous-Amorphous and Crystalline-Amorphous Transitions. *Phys. Rev. B*. **2008**, *77*, 144113.

[Song 2013] Y. Song. New perspectives on potential hydrogen storage materials using high pressure. *Phys. Chem. Chem. Phys*. **2013**, *15*, 14524.

[Tuktabiev 2009] M. A. Tuktabiev, S. V. Popova, V. V. Brazhkin, A. G. Lyapin, and Y. Katayama. Compressibility and polymorphism of α-As_4S_4 realgar under high pressure. *J. Phys.: Condens. Matter*. **2009**, *21*, 385401.

[Vaidya 1971] S. N. Vaidya and G. C. Kennedy. Compressibility of 18 Molecular Organic Solids to 45 kbar. *J. Chem. Phys*. **1971**, *55*, 987.

[Vos 1992] W. L. Vos, L. W. Finger, R. J. Hemley, J. Z. Hu, H. K. Mao, and J. A. Schouten. A high-pressure van der Waals compound in solid nitrogen-helium mixtures. *Nature*. **1992**, *358*, 46.

[Weigel 2012] C. Weigel, A. Polian, M. Kint, B. Rufflé, M. Foret, and R. Vacher. Vitreous Silica Distends in Helium Gas: Acoustic Versus Static Compressibilities. *Phys. Rev. Lett*. **2012**, *109*, 245504.

[Weir 1965] C. E. Weir. Compressibility of 11 Inorganic Materials. *J. Res. Natl. Bur. Stand., Sect. A*. **1965**, *69A*, 29.

[White 1967] W. B. White, F. Dachille, and R. Roy. High-pressure polymorphism of As_2O_3 and Sb_2O_3. *Z. Kristall*. **1967**, *125*, 450.

[Xiang 2012] S. Xiang, Y. He, Z. Zhang, H. Wu, W. Zhou, R. Krishna, and B. Chen. Microporous metal-organic framework with potential for carbon dioxide capture at ambient conditions. *Nat. Commun*. **2012**, *3*, 954.

SUPPLEMENTAL MATERIAL

Ordered helium trapping and bonding in compressed arsenolite: Synthesis of $As_4O_6 \cdot 2He$

Juan A. Sans, Francisco J. Manjón, Catalin Popescu, Vanesa P. Cuenca-Gotor, Óscar Gomis, Alfonso Muñoz, Plácida Rodríguez-Hernández, Julia Contreras-García, Julio Pellicer-Porres, Andre L. J. Pereira, David Santamaría-Pérez, and Alfredo Segura

Angle-dispersive X-ray diffraction (XRD) measurements under pressure

Highly pure arsenolite (As_4O_6) powder (99.999%) was commercially obtained from Sigma-Aldrich Company. High-pressure angle-dispersive XRD experiments at room temperature up to pressures between 15 and 30 GPa were conducted in a membrane-type diamond anvil cell (DAC) using commercial powder crushed in a mortar with a pestle to obtain a micron-sized powder. Measurements were performed with silicone oil (Rhodorsil 47V1000), methanol-ethanol (4:1 ratio) mixture, or He gas as quasihydrostatic pressure transmitting medium (PTM) and also without any PTM. Pressure inside DAC was estimated from the equation of state (EOS) of copper [Dewaele 2014]. Experiments were performed at the BL04-MSPD beamline of ALBA synchrotron with an incident monochromatic wavelength of 0.4246 Å focused to 20 x 20 μm^2 [Fauth 2013]. Pinhole of 50 μm was used to clean the x-ray beam tail. Images covering a 2θ range up to 20° were collected using a SX165 CCD located at 240 mm from sample. One-dimensional diffraction profiles of intensity as a function of 2θ were obtained by integration of observed intensities with Fit2D software [Hammersley 1996]. Lattice parameters of powder XRD patterns were obtained by Rietveld refinements performed using GSAS program package [Larson 1994, Toby 2001]. Interatomic distances were extracted thanks to VESTA software [Momma 2011].

High-quality XRD patterns of arsenolite under compression using helium, (4:1) methanol-ethanol mixture and silicone oil as PTM and without PTM are displayed in **Fig. S1**. A progressive increase of the angle for all diffraction peaks of the cubic structure with increasing pressure is observed, as expected for a decrease in the unit cell volume under compression. Absence of new peaks at high pressure clearly indicates that no phase transition occurs along the pressure range studied. In the experiment with silicone oil, the increase of the intensity of the (200) Bragg peak and the decrease of the relative intensity of the peak corresponding to the lowest angle (111) reveal an increase of preferential orientation along the c-axis with increasing pressure. This preferential orientation has been considered during the Rietveld refinement by the addition of the spherical harmonics preferential orientation coefficients giving a texture index of 1.8-2.0, which is considered an intermediate value between 1 (no texturized) and 3 (strongly texturized). This feature is not observed in the rest of the experiments using He, (4:1) methanol-

ethanol as PTM or without PTM. Furthermore, As_4O_6 compressed with (4:1) methanol-ethanol mixture, silicone oil and without PTM reveal the appearance of a progressive pressure-induced amorphization (PIA). On the contrary, arsenolite compressed with He shows no evidence of PIA up to the maximum pressure reached (29.4 GPa), even though there is a small increase of the width of the Bragg peaks at the highest pressures, likely due to a partial loss of hydrostaticity.

Rietveld refinement performed in the experimental XRD patterns of arsenolite allowed us to obtain the evolution of the lattice parameter and the Wyckoff sites of As and O with pressure. The evolution of the compressibility of the lattice parameter is equivalent to the EOS since it is a cubic structure. The experimental EOS of As_4O_6 compressed with different PTM and the comparison with the theoretically simulated compression curve of arsenolite and of He-trapped arsenolite with He located either at *8a*, *16c* or *16d* Wyckoff sites are displayed in **Fig. S2a**. The experimental EOS obtained in the experiments using no PTM and silicone oil or methanol-ethanol as PTM yield a bulk modulus at ambient pressure around 7(2) GPa which is in good agreement with the theoretical EOS for arsenolite. However, the EOS of arsenolite compressed with He (using data above 5 GPa) yields a bulk modulus at ambient pressure of 4(2) GPa [see **Table S1**]. This result is a little bit surprising since we expected a larger value of the bulk modulus of He-trapped arsenolite than the one obtained in bare arsenolite. This discrepancy could be an artifact due to the lack of experimental data of He-trapped As_4O_6 at low pressures (He exits *16d* sites below 3 GPa) since data at low pressures strongly influence the obtained value of the bulk modulus at ambient pressure. In order to stress the extraordinary small arsenolite's bulk modulus, its bulk modulus is compared to those of other sesquioxides of group-15 elements [see **Table S2**].

Evolution under pressure of the experimental and theoretical atomic coordinates of As and O is presented in **Fig. S2b**. Good agreement is found between experiments and theoretical curves for As Wyckoff sites, but a larger discrepancy is found for O Wyckoff sites. This result is due to the difficulty to accurately obtain the atomic position of light elements from Rietveld refinement of XRD data.

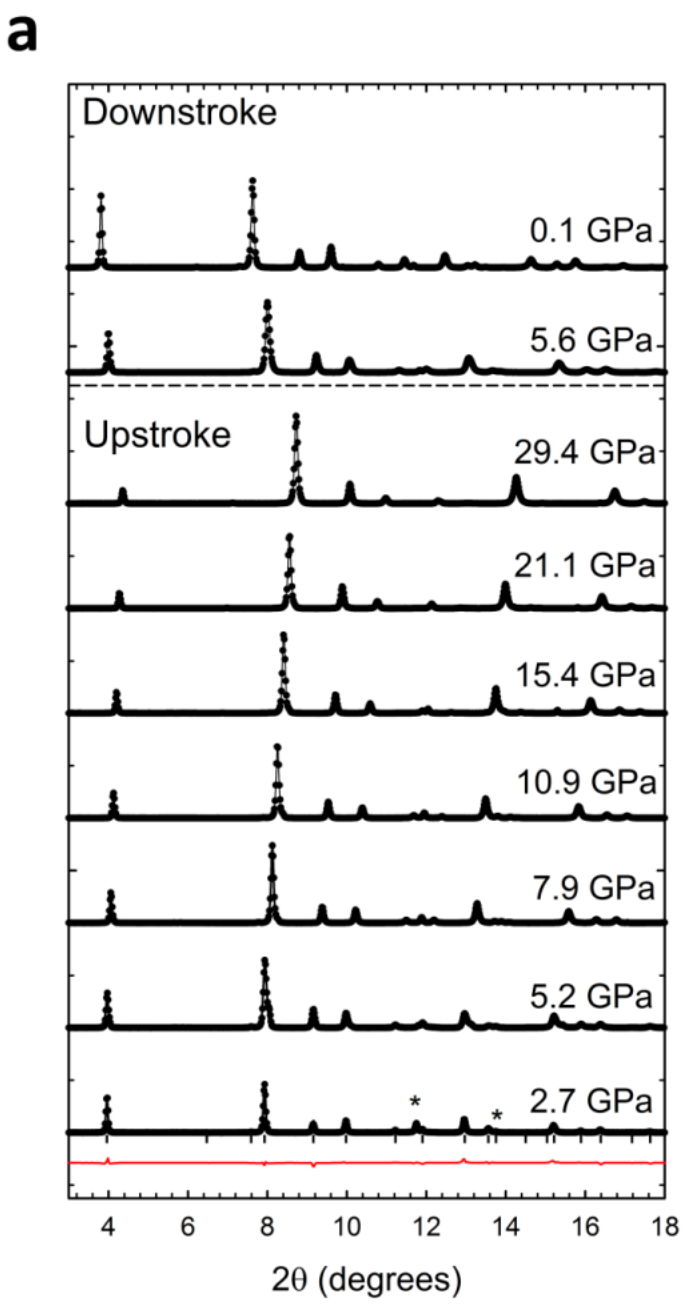
a
Downstroke
0.1 GPa
5.6 GPa
Upstroke
29.4 GPa
21.1 GPa
15.4 GPa
10.9 GPa
7.9 GPa
5.2 GPa
2.7 GPa
*
*
4
6
8
10
12
14
16
18
2θ (degrees)

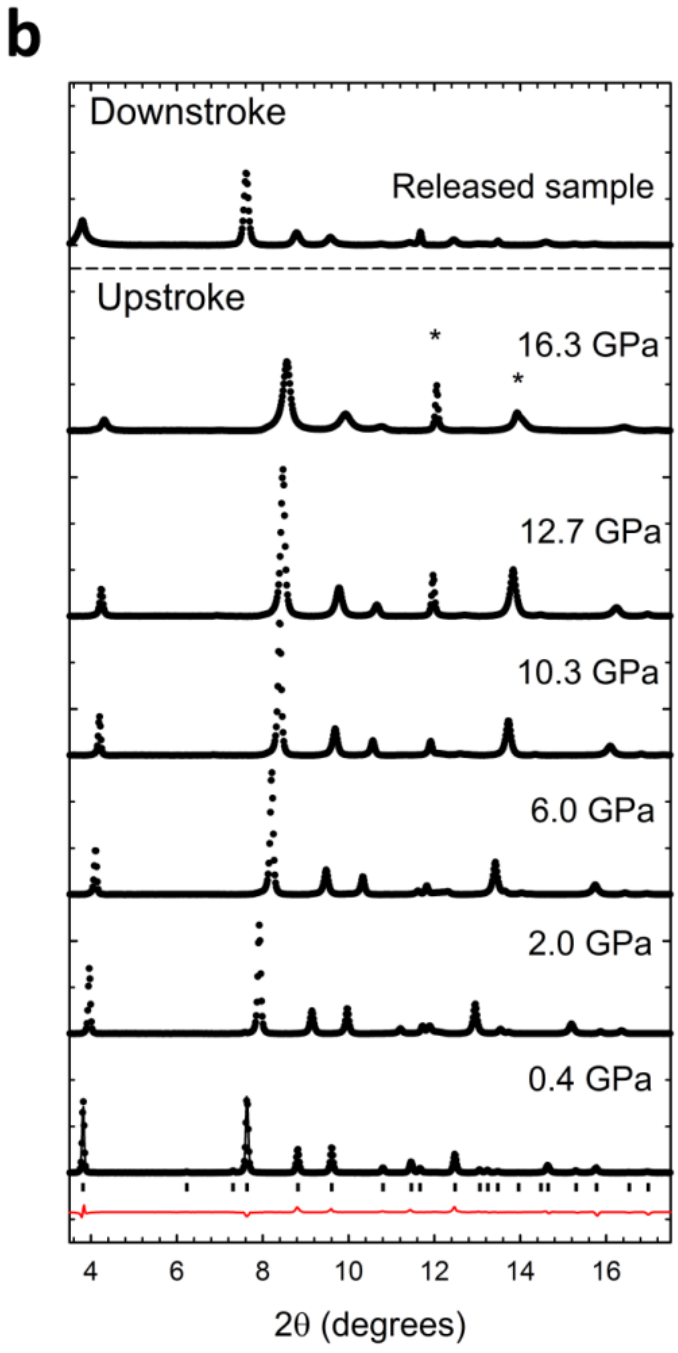
b
Downstroke
Released sample
Upstroke
16.3 GPa
*
*
12.7 GPa
10.3 GPa
6.0 GPa
2.0 GPa
0.4 GPa
4
6
8
10
12
14
16
2θ (degrees)

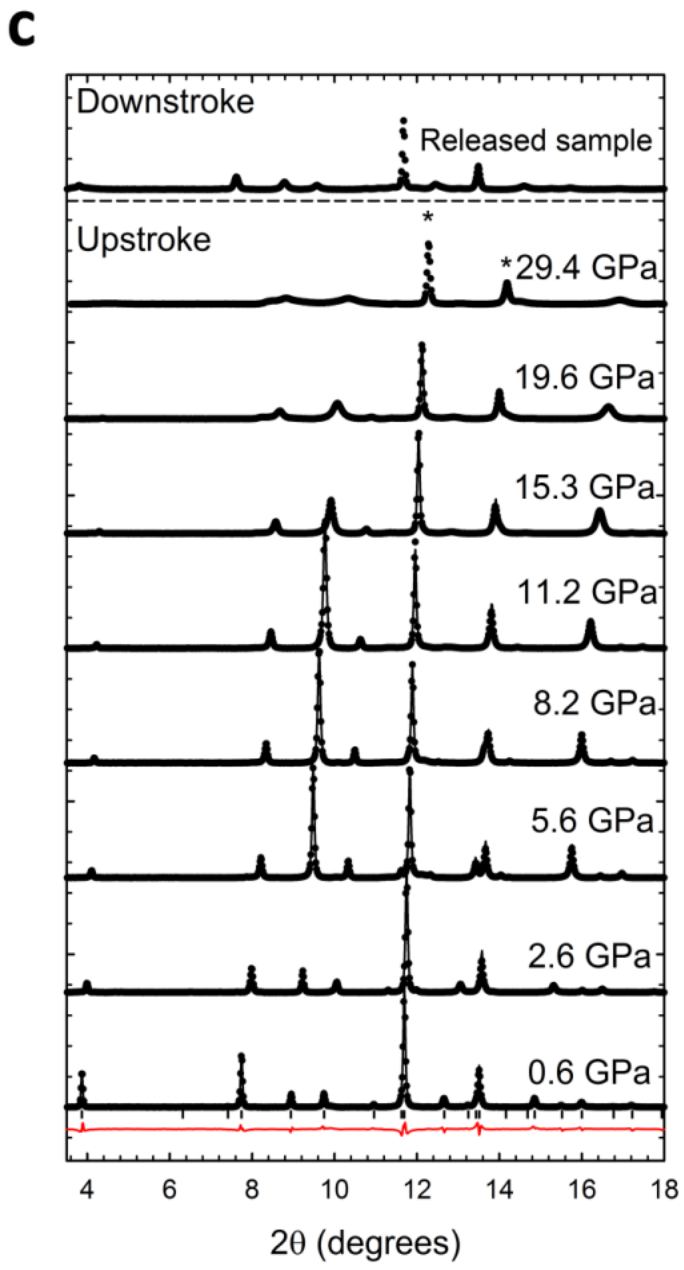
c
Downstroke
Released sample
Upstroke
*
*29.4 GPa
19.6 GPa
15.3 GPa
11.2 GPa
8.2 GPa
5.6 GPa
2.6 GPa
0.6 GPa
4
6
8
10
12
14
16
18
2θ (degrees)

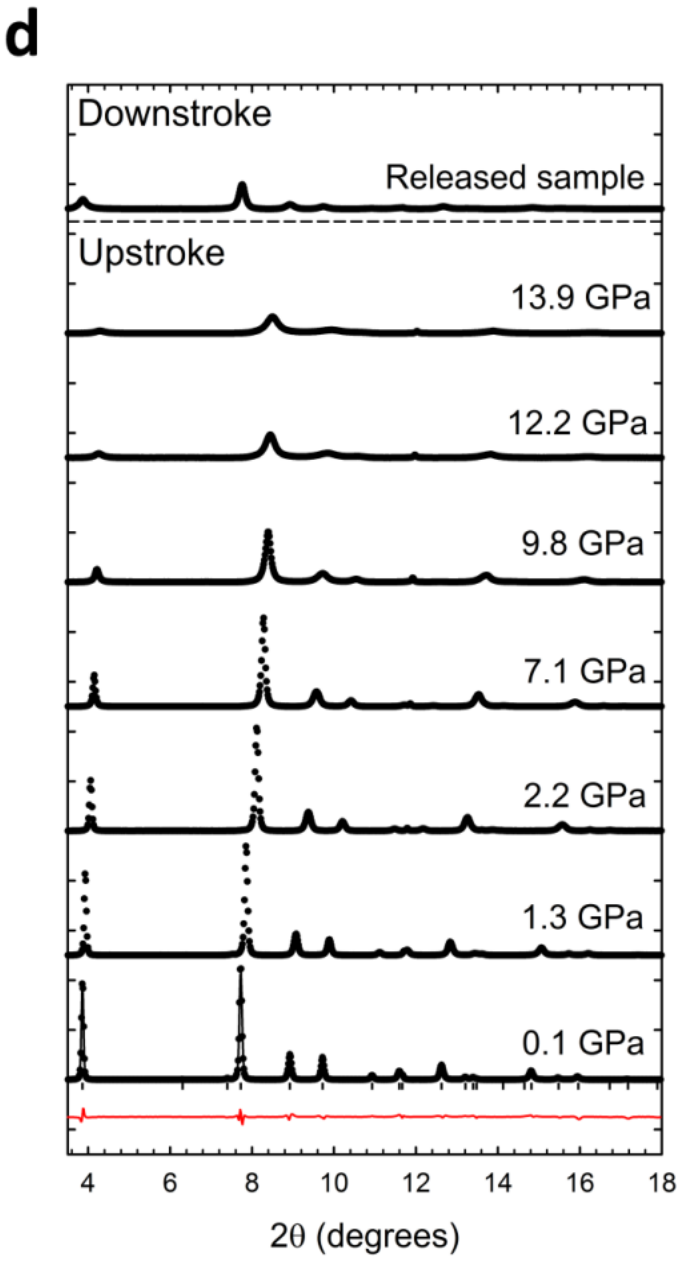

Figure S1. Experimental XRD patterns (vertically shifted for the sake of clarity) of arsenolite compressed with: a) helium; b) methanol-ethanol mixture; c) silicone oil and d) no PTM. Asterisks correspond to peaks of Cu. Red lines correspond to the residuals of the Rietveld refinement at low pressures. Vertical ticks correspond to the position of the Bragg peaks included in the refinement.

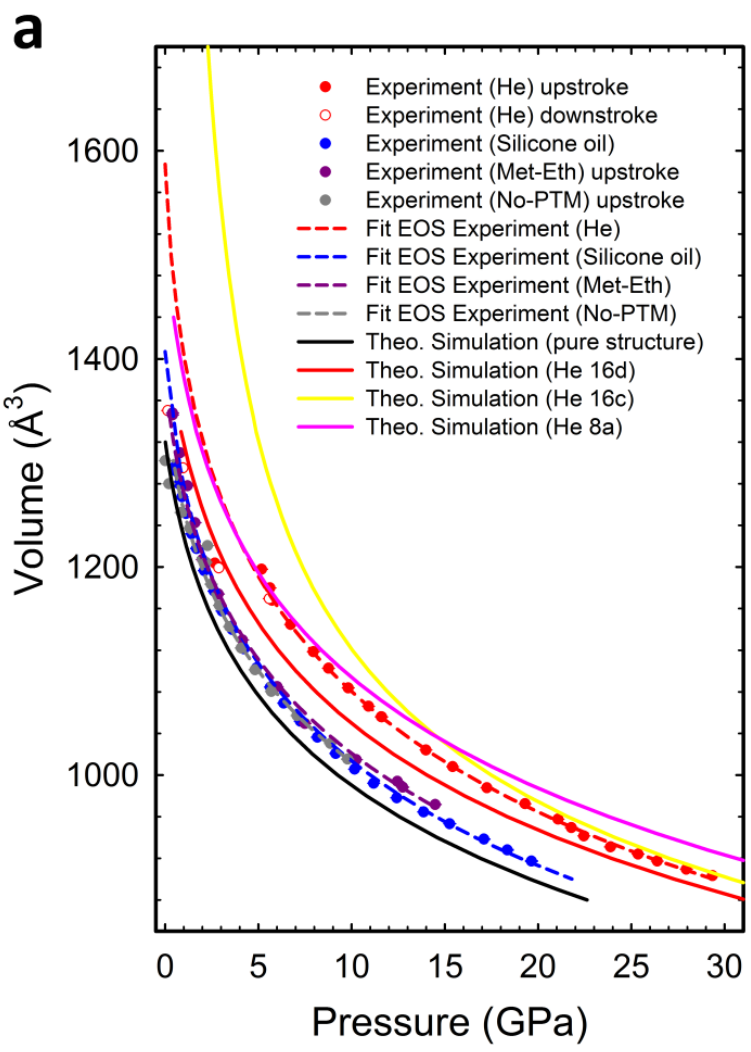
a
Experiment (He) upstroke
Experiment (He) downstroke
Experiment (Silicone oil)
Experiment (Met-Eth) upstroke
Experiment (No-PTM) upstroke
Fit EOS Experiment (He)
Fit EOS Experiment (Silicone oil)
Fit EOS Experiment (Met-Eth)
Fit EOS Experiment (No-PTM)
Theo. Simulation (pure structure)
Theo. Simulation (He 16d)
Theo. Simulation (He 16c)
Theo. Simulation (He 8a)
Volume (Å3)
1600
1400
1200
1000
0
5
10
15
20
25
30
Pressure (GPa)

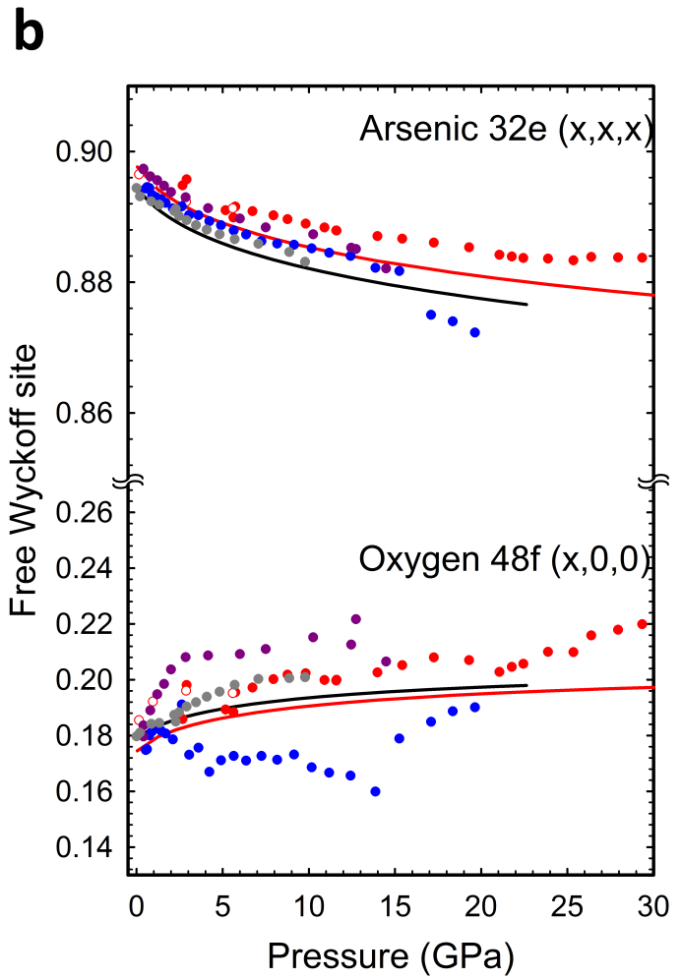

Figure S2. EOS and evolution of atomic positions of arsenolite under pressure. a) Experimental and theoretically simulated EOS under different conditions. b) Pressure dependence of the free Wyckoff coordinates of As and O atoms. Grey, blue, purple, and red correspond to data of arsenolite compressed without PTM, with silicone oil, with methanol-ethanol mixture and with He, respectively. Black (red) solid line corresponds to theoretical data of pure (He-inserted at *16d* sites) arsenolite. Yellow (pink) solid line corresponds to theoretical data of arsenolite with He inserted at *16c* (*8a*) sites.

Table S1. Experimental and theoretical EOS of arsenolite.

	V_0 [Å^3]	B_0 [GPa]	B_0'
Experimental (He)[a)]	1587(26)	4(2)	12.9
Experimental (Sil. Oil)	1407(2)	6(1)	12.9
Experimental (Met-Eth)	1385(15)	7(2)	12.9
Experimental (No-PTM)	1361(20)	7(2)	12.9
Theo. Sim. (He 16d)	1444(5)	6.4(4)	12.9
Theo. sim. (pure)	1331(2)	7.6(3)	12.9(3)

[a)] Data fitted above 5 GPa.

Table S2. EOS of different group-15 sesquioxides.

	V_0 [Å^3]	B_0 [GPa]	B_0'
Pure-As_2O_3 (arsenolite)[a)]	1361(20)	7(2)	12.9
As_2O_3 (claudetite)[b)]	308(2)	18(2)	3.5(5)
Sb_2O_3 (senarmontite)[c)]	1386(5)	16.5(2)	13.5
α-Bi_2O_3 (bismite)[d)]	329(1)	85.4(5)	2.6(5)
β-Bi_2O_3 (beta-phase)[e)]	338.2(5)	34(5)	8(5)
β-Ga_2O_3 (beta-phase)[f)]	209	202(7)	2.4(6)
In_2O_3 (Bixbyite)[g)]	64.28(13)	184(10)	4.0
Tl_2O_3 (Bixbyite)[h)]	1170.6(1)	147(13)	5(2)

[a)] This work; [b)] [Soignard 2008]; [c)] [Pereira 2012]; [d)] [Pereira 2013]; [e)] [Pereira 2014b]; [f)] [Machon 2006]; [g)] [García-Domene 2014]; [h)] [Gomis 2014]

Lattice parameters and atomic Wyckoff positions obtained from Rietveld refinement allows calculating the experimental pressure dependence of intramolecular (internal) and intermolecular (external) As-As and As-O distances [see **Fig. S3**]. Again, a good agreement is found between experimental and theoretical data for both distances except for As-O distances in the experiment with silicone oil. A slight shift of the atomic positions for As and O, but with the same pressure dependence, is theoretically predicted when He is located at *16d* sites of arsenolite and indeed experimentally observed when He is used as PTM. The compression of the

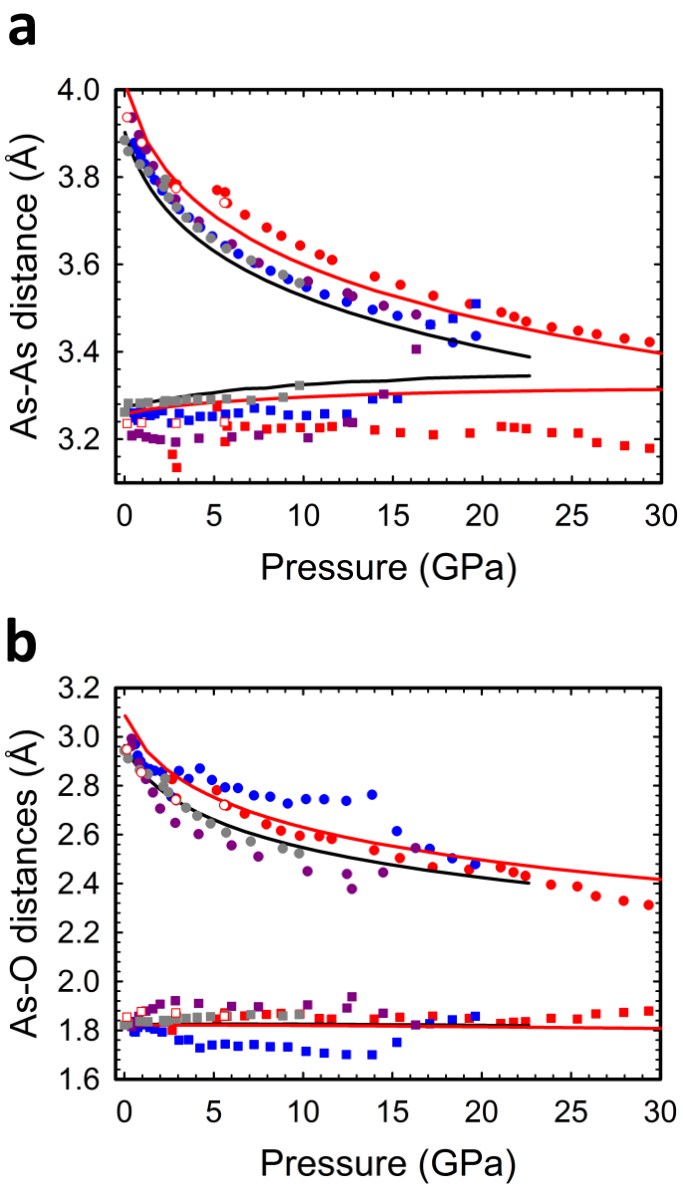

Figure S3. Pressure dependence of interatomic distances in arsenolite. Compression of the shortest interatomic distances belonging to the same molecular unit (squares) and different molecular units (circles): a) arsenic-arsenic and b) arsenic-oxygen. Grey, blue, purple, and red correspond to experimental data of arsenolite compressed without PTM, with silicone oil, with (4:1) methanol-ethanol mixture and with He, respectively. Black (red) solid line corresponds to theoretical data of pure (He-inserted at *16d* sites) arsenolite.

experimental external and internal As-O distances with the different PTM used is less affected with the inclusion of He in *16d* sites than As-As distances (in good agreement with theoretical calculations). Internal As-As distance corresponds to the distance between As cations inside the tetrahedron of the cage-like molecular unit, while external As-As distance corresponds to the minimum distance between As atoms of two neighboring cages. In pure As_4O_6 under compression, the external As-As distance tends to decrease monotonously (due to the closing of the gap between As_4O_6 molecules), whereas the internal As-As distance tends to slightly increase. Around 20 GPa, both internal and external As-As distances become nearly equal (external As-As distance is less than 3% longer than the internal As-As distance at 15 GPa when PIA starts to occur). Our calculations could suggest that the similarity of external and internal As-As distances above 15 GPa results in strong intermolecular interactions that make the cubic structure of arsenolite unstable. Nevertheless, He trapping in arsenolite above 3 GPa leads to a considerably increase of the external As-As distance [see the jump in **Fig. S2a**], thus avoiding the intermolecular interactions which turn the crystalline structure of arsenolite unstable. This feature allows to explain the stability of arsenolite beyond 30 GPa when compressed with He (the experimental external As-As distance is still 6% larger than the internal As-As distance at 30 GPa).

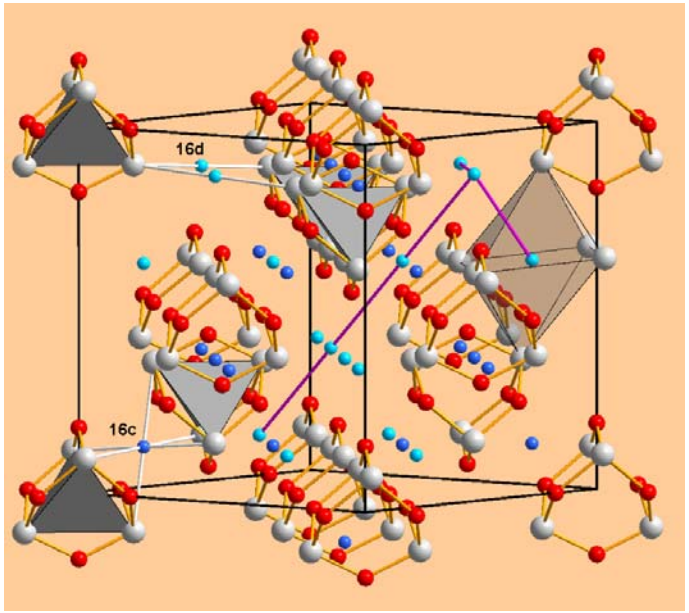

Figure S4. He-trapped arsenolite with He inserted into the two possible Wyckoff sites (16c and 16d). Big gray balls, medium-size red balls and small dark and light blue balls represent As, O, He(16c) and He(16d) atoms, respectively. Pink lines correspond to 3D diffusion paths for He along 16d sites.

Raman scattering (RS) measurements under pressure

High-pressure RS measurements at room temperature were performed in a backscattering geometry using a Horiba Jobin-Yvon LabRam HR UV spectrometer in combination with a thermoelectrically-cooled multichannel CCD detector (resolution below 2 cm^{-1}). RS spectra of arsenolite powder inside a DAC were excited either with 532.0 or 632.8 nm laser lines and laser power below 10 mW up to pressures between 12 and 22 GPa. RS measurements were performed with the same PTM as XRD measurements except for silicone oil. A few ruby balls of about 2 μm in diameter evenly distributed in the pressure chamber were employed as a pressure sensor [Mao 1986]. RS measurements were analyzed by fitting Raman peaks with a Voigt profile fixing the Gaussian line width (1.6 cm^{-1}) to the experimental setup resolution [Debernardi 2001].

High-quality RS spectra of arsenolite under compression using helium, (4:1) methanol-ethanol mixture as PTM and without PTM are displayed in **Fig. S5**. A progressive shift of the Raman-active mode frequencies of all peaks of the cubic structure with increasing pressure is observed. Absence of new peaks at high pressure clearly indicates that no phase transition occurs along the pressure range studied. Only splitting of some modes is observed in samples compressed without PTM. These results and those obtained for arsenolite compressed with the methanol-ethanol mixture are similar to those already reported using CsI as PTM [Grzechnik 1999]. Furthermore, many Raman modes, especially in the experiments without PTM and with the methanol-ethanol mixture, undergo a progressive asymmetric broadening above 10 GPa. This broadening is likely caused by the increase of intermolecular interactions; i.e., the increase of interactions among As_4O_6 cages, which finally results in the onset of PIA above 15 GPa. No such broadening of Raman modes is observed in the experiment performed with He up to 30 GPa.

Splitting and broadening of several Raman modes above 3-6 GPa (depending on the PTM used) are observed and attributed to the strong intermolecular interactions of compressed arsenolite. The different features observed in RS measurements depending on the PTM used can be explained by the different intermolecular interactions, related to external As-As and As-O distances, taking place in arsenolite compressed with or without He.

The experimental pressure dependence of the frequencies of the first-order Raman-active modes measured (only the soft mode E_{g2} has not been observed as it has occurred in previous measurements) [Grzechnik 1999] when arsenolite is compressed without PTM or with a PTM different from He is well reproduced by our theoretical calculations for As_4O_6 [**Fig. S6**]. In the case of the arsenolite compressed with He as PTM, frequencies follow the same pressure dependence as in the previous experiments below 3 GPa. However, above 3 GPa almost all Raman modes suffer a small shift in frequency which is consistent with a volume increase at around 3 GPa: for modes with a positive pressure coefficient the shift is negative and vice versa. Additionally, some Raman-active modes of arsenolite show a completely different behavior when compressed with He above 3 GPa due to the incorporation of He in *16d* sites. Above this pressure, it is possible to observe a

change of the phonon anticrossing affecting T_{2g}^{3} and T_{2g}^{4} modes corresponding to As-O bending modes. These two T_g modes undergo a phonon anticrossing around 4.5 GPa when (4:1) methanol-ethanol mixture is used as PTM in good agreement with our lattice dynamics calculations of As_4O_6 and similar results can be observed in the experiment without PTM [**Fig. S6**]. However, they shift apart above 3 GPa when arsenolite is compressed with He, thus resulting in a delay of the phonon anticrossing up to 11 GPa, which is nicely described by our theoretical calculations including He in *16d* Wyckoff sites [**Fig. S6c**]. The incorporation of He at *16d* sites does not result in new Raman-active modes, but it results in two new infrared active modes whose frequencies are close to the A_{1g}^{1} mode. Detailed analysis of Raman data with the different PTM are out of the scope of the present paper.

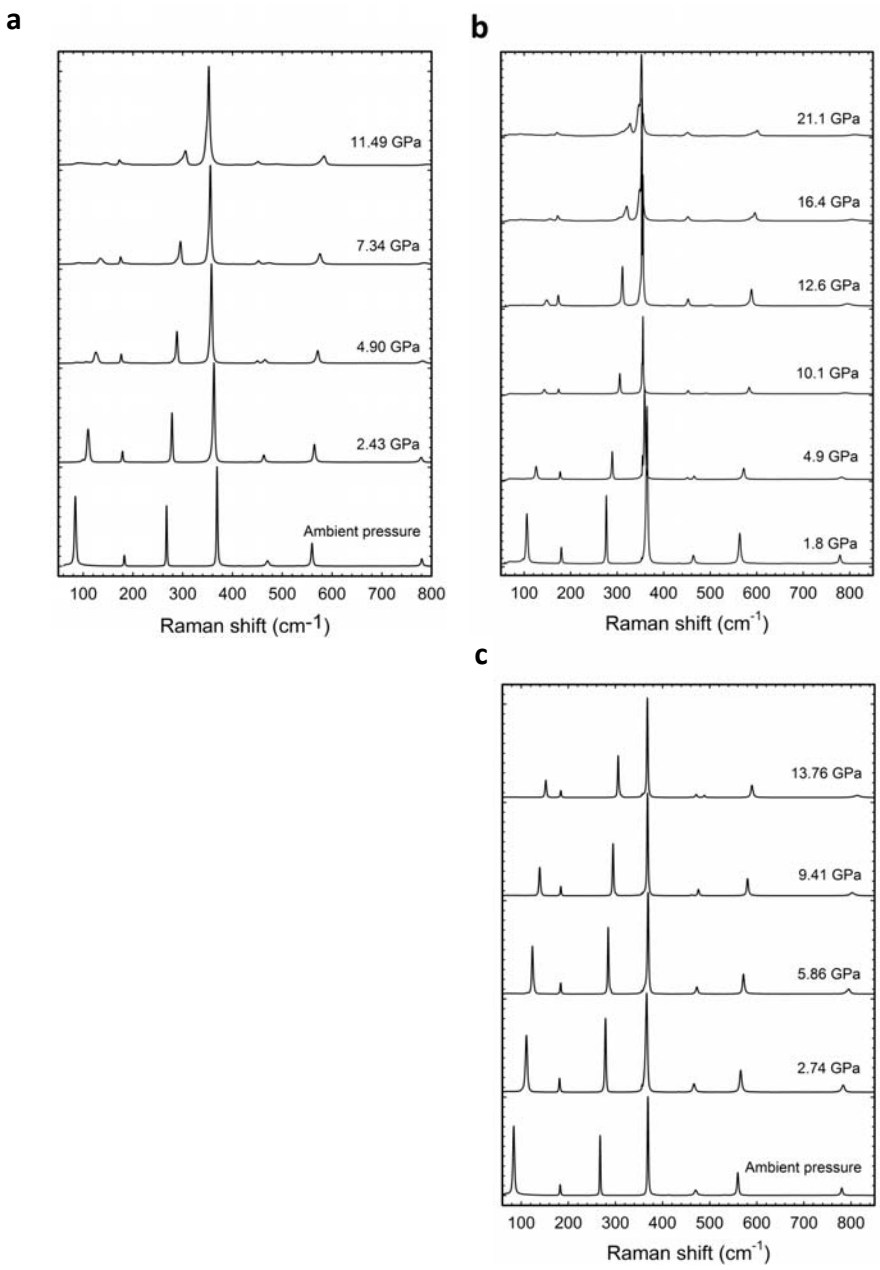

Figure S5. RS spectra at selected pressures of arsenolite compressed with different PTM: a) no PTM; b) (4:1) methanol-ethanol mixture; and c) helium. RS spectra are vertically shifted for the sake of clarity.

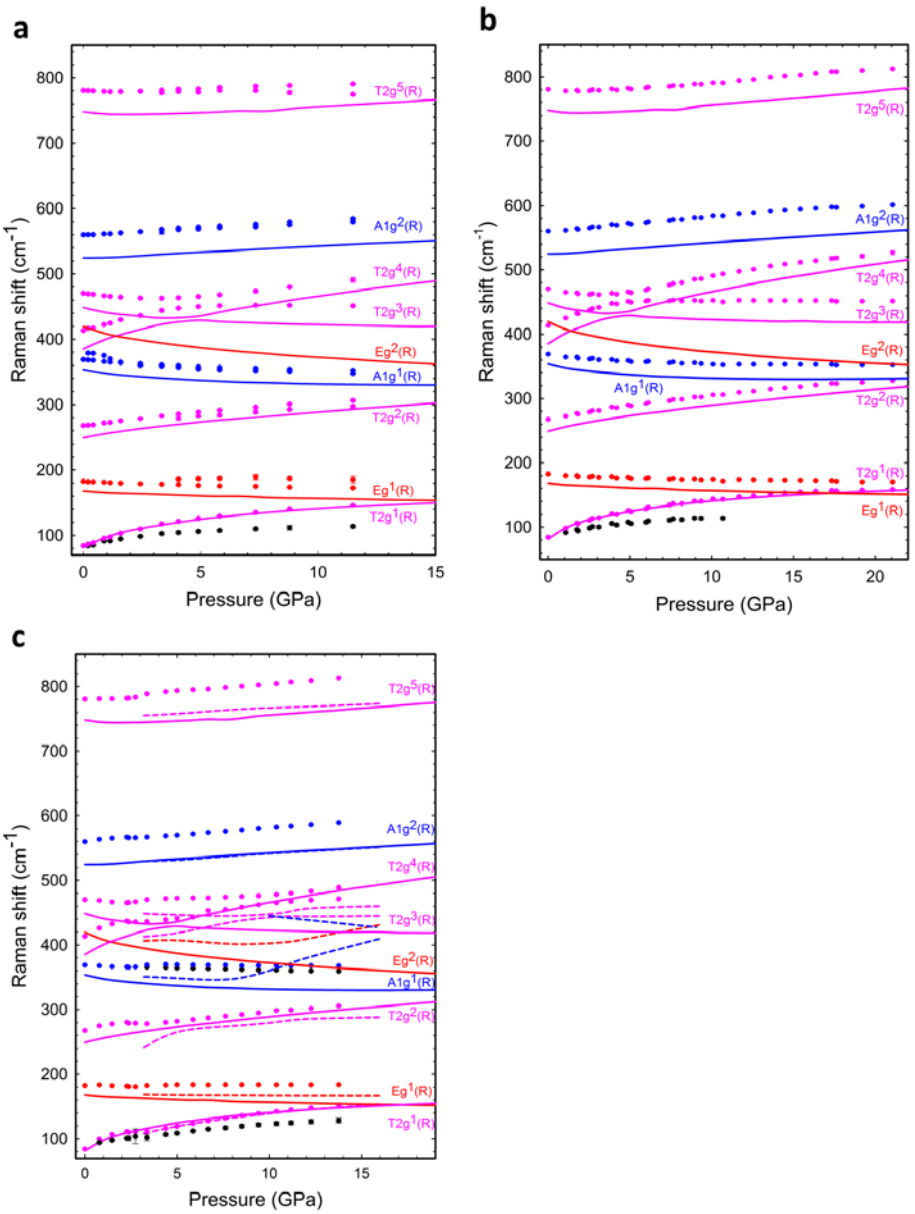

Figure S6. Experimental (symbols) and theoretical (lines) pressure dependence of first-order Raman-active mode frequencies of arsenolite compressed with different PTM: a) no PTM; b) (4:1) methanol-ethanol mixture; and c) helium. Solid and dashed lines correspond to calculations of pure arsenolite and arsenolite with He-inserted at *16d* sites, respectively.

Theoretical calculations

Ab initio total-energy calculations of arsenolite (As_4O_6) were performed within the framework of density functional theory (DFT) [Hohenberg 1964]. Vienna *Ab initio* Simulation Package (VASP) was used to carry out calculations with the pseudopotential method and the projector augmented wave (PAW) scheme, which replace the core electrons, make smoothed pseudovalence wave functions and take into account the full nodal character of the all-electron charge density in the core region [Blöchl 1994]. Exchange and correlation term was computed through PBE for solids prescription [Perdew 2008]. Lattice-dynamics calculations at the zone center (Γ point) of the Brillouin zone were performed using the direct force constant approach [Parlinski 1997]. The elastic constants can be obtained by computing the macroscopic stress for a small strain with the use of the stress theorem [Chetty 1989]. In the present work, we have performed the evaluation of the elastic constants of arsenolite as implemented in the VASP package [Le Page 2002]. Hereafter, we will show that a new compound is formed (As_4O_6·2He) when He is trapped at 16d sites. Therefore, hereafter the notation As_4O_6 and As4O6·2He is used to distinguish calculations in both compounds.

Theoretical calculations have allowed us to obtain the evolution of the three independent elastic constants (C_{11}, C_{12} and C_{44}) of cubic As_4O_6 and As_4O_6·2He as a function of pressure [see **Fig. S7**]. From the pressure dependence of the elastic constants, the pressure dependence of the elastic stiffness coefficients (B_{11}, B_{12} and B_{44}) can be calculated [see **Fig. S7**] [Wallace 1970] and defined as:

$$B_{11} = C_{11} - P; \quad B_{12} = C_{12} + P; \quad B_{44} = C_{44} - P$$

Once the elastic stiffness constants of a material in a given structure are known as a function of pressure the mechanical stability of the structure at high pressures can be evaluated by means of the generalized Born stability criteria [Born 1940, Wang 1993]. For the mechanical stability of a cubic structure these criteria are:

$$M_1 = B_{11} + 2B_{12} > 0; \quad M_2 = B_{11} - B_{12} > 0; \quad M_3 = B_{44} > 0$$

The mechanical stability of As_4O_6 and As_4O_6·2He can be discussed by the inspection of the generalized Born stability criteria plotted in **Fig. S8**. A Born instability in arsenolite due to the violation of the M_2 criterion occurs at 19.7 GPa; i.e., at a pressure close to that experimentally observed for the onset of PIA in our HP-XRD measurements using no PTM or using a PTM different from He. On the other hand, no mechanical instability is observed in As_4O_6·2He even at 30 GPa in good agreement with our experimental results.

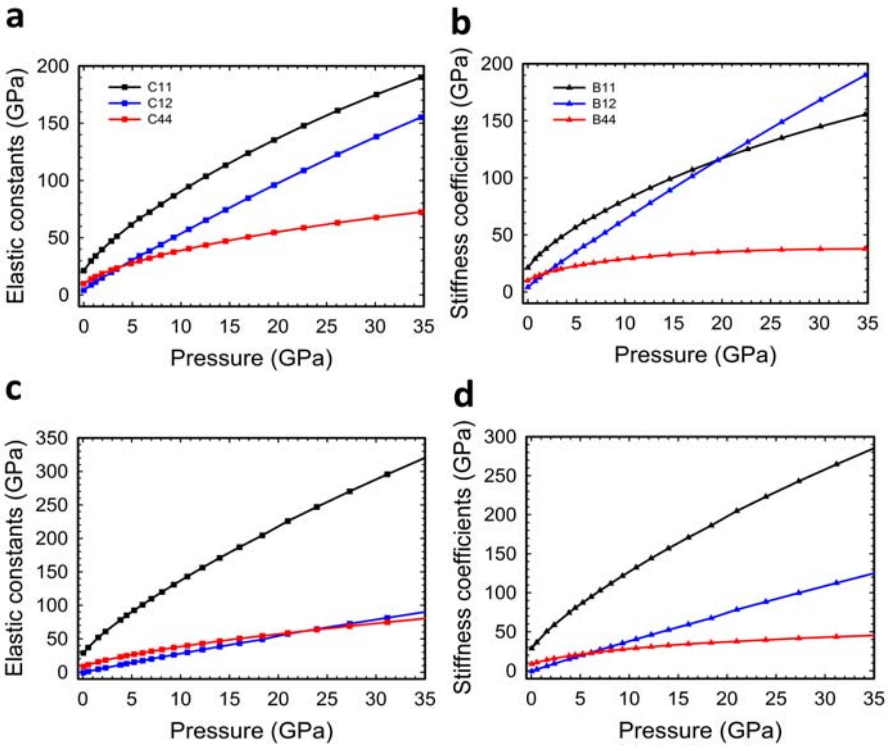

Figure S7. Pressure dependence of the theoretical elastic constants and elastic stiffness coefficients of As_4O_6 and $As_4O_6 \cdot 2He$. Elastic constants C_{11}, C_{12}, and C_{44} of: a) As_4O_6; b) $As_4O_6 \cdot 2He$. Elastic stiffness coefficients B_{11}, B_{12}, and B_{44} of: c) As_4O_6; d) $As_4O_6 \cdot 2He$.

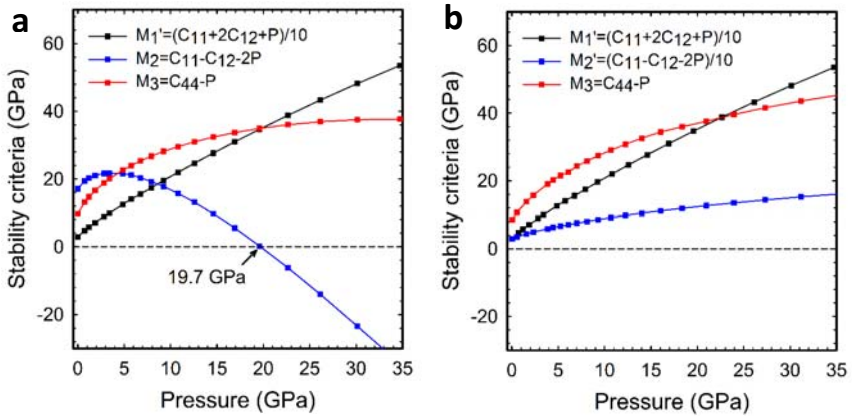

Figure S8. Generalized Born criteria for mechanical stability under hydrostatic pressure in As_4O_6 (a) and $As_4O_6 \cdot 2He$ (b).

Theoretical calculations of the electronic band structure of $As_4O_6 \cdot 2He$ shows the projected orbital distribution along the conduction and the valence band at 14 and 31 GPa [**Fig. S9**]. The most relevant result is how He *1s* orbitals, located deep in the valence band (red lines), behave under compression. The shape and evolution of their contribution evidences that they constitute bonding and antibonding orbitals with *s* orbitals of As and *p* orbitals of O, respectively. Three features that clearly indicate the reaction of He with As_4O_6 are: i) a downward (upward) shift in energy of the bonding (antibonding) band with increasing pressure; ii) an increase of the bandwidth of both bands with increasing pressure; and iii) an increase in the density of states of the antibonding band of He with increasing pressure. All these features allow us to conclude that there is a pressure-induced reaction of He with As_4O_6 resulting in the formation of $As_4O_6 \cdot 2He$.

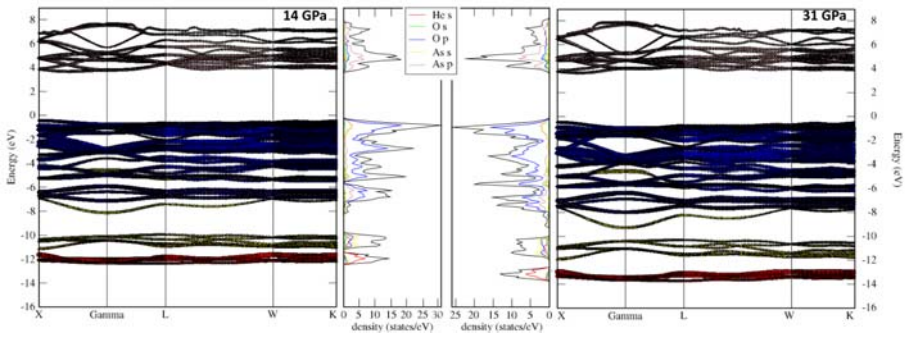

Figure S9. Pressure dependence of the band structure and projected distribution of orbitals of $He_2As_4O_6$ at 14 GPa (left) and 31 GPa (right).

In order to further show evidence of the interaction of He with arsenolite and the formation of $As_4O_6 \cdot 2He$ once He is trapped above 3 GPa, we have also conducted analysis of the electron density, ρ, using the *state-of-the-art* noncovalent interactions (NCI) index [Johnson 2010, Contreras-García 2011a, Contreras-García 2011b, Otero-de-la-Roza 2012, Saleh 2012]. The recently disclosed NCI method relies on the relationship between the reduced density gradient *s* [Johnson 2010]:

$$s = \frac{|\nabla \rho|}{c_F \rho^{4/3}}$$

and the electron density ρ, to discriminate between various types of non-bonding interactions, such as attractive, van der Waals (vdW)-dispersive and repulsive ones. The two-dimensional plot of *s* vs the electron density ρ, gives rise to a plot where interactions appear as peaks. Their location in the diagram identifies the strength of the interaction, with stronger interactions appearing at higher densities.

These plots are shown in **Fig. S10** for arsenolite (As_4O_6) and for $As_4O_6 \cdot 2He$ both at 14 and 31 GPa. The comparison of the structure upon inclusion of He atoms [**Fig. S10a**] enables to identify the new interactions as strongly attractive in nature. Moreover, when the evolution of the peaks is analyzed under pressure [**Fig. S10b**], we see that they are strengthened under pressure (they move to higher absolute values). NCI can be visualized by representing *s* isosurfaces, colored in order to reveal their nature and stregth: attractive interactions appear in blue turquoise, vdW interactions are revealed in green and steric clashes are colored in red. Within this representation, localized interactions appear as compact isosurfaces whereas delocalized ones appear as extended flat surfaces. This result is in contrast with the "charge-shift" bonding suggested by Rzepa for He atoms in stressed environments [Rzepa 2010].

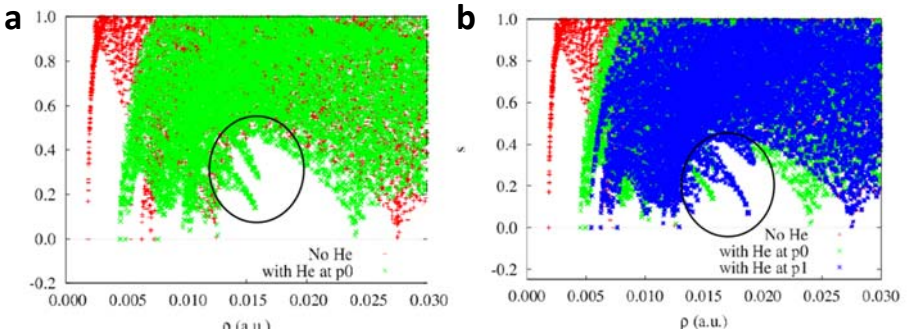

Figure. S10. Comparison of $s(\rho)$ for As_4O_6 and $As_4O_6 \cdot 2He$ at 14 GPa (a) and at 31GPa (b).

As expected for a noble gas, **Figure S11** shows the appearance of van der Waals interactions around He atoms. However, unexpected localized interactions also make their appearance along the He-As interaction lines. In agreement with the $s(\rho)$ plot in **Fig. S10**, these interactions are strengthened (more intense in their blue color) with increasing pressure.

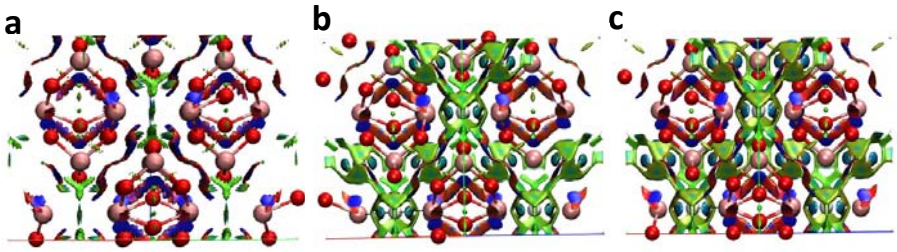

Figure S11. Comparison of *s*(r) isosurfaces for As_4O_6 at 14 GPa (a), $As_4O_6 \cdot 2He$ at 14 GPa (b) and $As_4O_6 \cdot 2He$ at 31 GPa (c).

In order to give quantitative details regarding the He-As interaction, we plot in **Fig. S12** the pressure dependence of the electronic density and its Laplacian at the bond critical point of He-As. As observed, the interaction is small with an electronic density between 0.01 and 0.045 from 1 atm to 150 GPa. The small interaction between He and As atoms is different to the relatively strong "charge-shift" bonds recently predicted for He in stressed environments with electronic densities between 0.06 and 0.15 [Rzepa 2010].

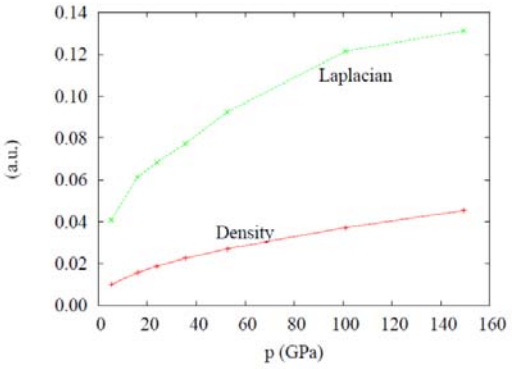

Figure S12. Pressure dependence of the electronic density and its Laplacian at the bond charge point of He-As.

Finally, we want to mention that theoretical calculations give support to the amorphization of arsenolite as due to repulsion between As atoms in neighbor molecular units. **Figure S13** shows a considerable increase of the repulsive forces between As atoms from 5.7 to 14 GPa which result in amorphization above 15-20 GPa.

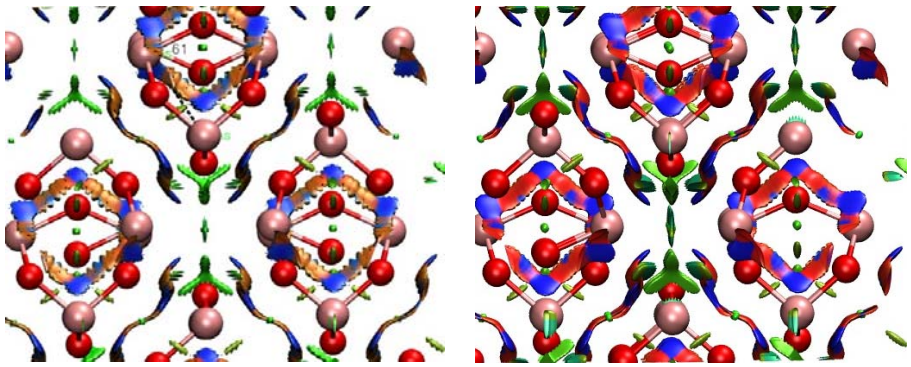

Figure S13. Comparison of *s*(r) isosurfaces for As_4O_6 (left) at 5.7 GPa and for As_4O_6 at 14 GPa (right). Repulsive forces (red zigzag chains) between adamantane-type molecular units increase in intensity with increasing pressure.

References

[Blöchl 1994] P. E. Blöchl. Projector augmented-wave method. *Phys. Rev. B: Condens. Matter Mater. Phys*. **1994**, *50*, 17953.

[Born 1940] M. Born. On the stability of crystal lattices. I. *I. Proc. Cambridge Philos. Soc.* **1940**, *36*, 160.

[Chetty 1989] N. Chetty, A. Muñoz, and R. M. Martin. First-principles calculation of the elastic constants of AlAs. *Phys. Rev. B*. **1989**, *40*, 11934.

[Contreras-García 2011a] J. Contreras-García, E. Johnson, S. Keinan, R. Chaudret, J. Piquemal, D. Beratan, and W. Yang. NCIPLOT: a program for plotting non-covalent interaction regions. *J. Chem. Theory Comput*. **2011**, *7*, 625.

[Contreras-García 2011b] J. Contreras-García, W. Yang, and E. Johnson. Analysis of Hydrogen-Bond Interaction Potentials from the Electron Density: Integration of Non-covalent Interaction Regions. *J. Phys. Chem. A* **2011**, *115*, 12983.

[Debernardi 2001] A. Debernardi, C. Urlich, M. Cardona, and K. Syassen. Pressure Dependence of Raman Linewidth in Semiconductors. *Phys. Status Solidi B*. **2001**, *223*, 213.

[Dewaele 2014] A. Dewaele, P. Loubeyre, and M. Mezouar. Equations of state of six metals above 94GPa. *Phys. Rev. B*. **2014**, *70*, 094112.

[Fauth 2013] F. Fauth, I. Peral, C. Popescu, and M. Knapp. The New Material Science Powder Diffraction Beamline at ALBA Synchrotron. *Powder. Diffr*. **2013**, *28*, S360.

[García-Domene 2014] B. García-Domene, J. A. Sans, O. Gomis, F. J. Manjón, H. M. Ortiz, D. Errandonea, D. Santamaría-Pérez, D. Martínez-García, R. Vilaplana, A. L. J. Pereira, A. Morales-García, P. Rodríguez-Hernández, A. Muñoz, C. Popescu, and A. Segura. *Pbca*-Type In_2O_3: The High-Pressure Post-Corundum phase at Room Temperature. *J. Phys. Chem. C*. **2014**, *118*, 20545.

[Gomis 2014] O. Gomis, D. Santamaría-Pérez, J. Ruiz-Fuertes, J. A. Sans, R. Vilaplana, H. M. Ortiz, B. García-Domene, F. J. Manjón, D. Errandonea, P. Rodríguez-Hernández, A. Muñoz, and M. Mollar. High-Pressure Structural and Elastic Properties of Tl_2O_3. *J. App. Phys.* **2014**, *116*, 133521.

[Grzechnik 1999] A. Grzechnik. Compressibility and Vibrational Modes in Solid As_4O_6. *J. Solid State Chem.* **1999**, *144*, 416.

[Hammersley 1996] A. P. Hammersley, S. O. Svensson, M. Hanfland, A. N. Fitch, and D. Hausermann. Two-Dimensional Detector Software: From Real Detector to Idealized Image or Two-Theta Scan. *High Pressure Res*. **1996**, *14*, 235.

[Hohenberg 1964] P. Hohenberg and W. Kohn. Inhomogeneous Electron Gas. *Phys. Rev*. **1964**, *136*, 3864.

[Johnson 2010] E. Johnson, S. Keinan, P. Mori-Sánchez, J. Contreras-García, A. Cohen, and W. Yang. Revealing noncovalent interactions. *J. Am. Chem. Soc*. **2010**, *132*, 6498.

[Larson 1994] A. C. Larson and R. B. von Dreele. General Structure Analysis System (GSAS). *LANL Report*. **1994**, *86*, 748.

[Le Page 2002] Y. Le Page and P. Saxe. Symmetry-general least-squares extraction of elastic data for strained materials from ab initio calculations of stress. *Phys. Rev. B*. **2002**, *65*, 104104.

[Machon 2006] D. Machon, P. F. McMillan, B. Xu, and J. J. Dong. High-Pressure Study of the β-to-α Transition in Ga_2O_3. *Phys. Rev. B.* **2006**, *73*, 094125.

[Mao 1986] M. K. Mao, J. Xu, and P. M. Bell. Calibration of the Ruby Pressure Gauge to 800 kbar under Quasi-Hydrostatic Conditions. *J. Geophys. Res*. **1986**, *91*, 4673.

[Momma 2011] K. Momma and F. Izumi. VESTA 3 for three-dimensional visualization of crystal, volumetric and morphology data. *J. Appl. Crystallogr*. **2011**, *44*, 1272.

[Otero-de-la-Roza 2012] A. Otero-de-la-Roza, J. Contreras-Garcia, and E. R. Johnson. Revealing non-covalent interactions in solids: NCI plots revisited. *Phys. Chem. Chem. Phys.* **2012**, *14*, 12165.

[Parlinski 1997] K. Parlinski, Z. Q. Li, and Y. Kawazoe. First-Principles Determination of the Soft Mode in Cubic ZrO_2. *Phys. Rev. Lett*. **1997**, *78*, 4063.

[Perdew 2008] J. P. Perdew, A. Ruzsinszky, G. I. Csonka, O. A. Vydrow, G. E. Scuseria, L. A. Constantin, X. Zhou, and K. Burke. Restoring the Density-Gradient Expansion for Exchange in Solids and Surfaces. *Phys. Rev. Lett*. **2008**, *100*, 136406.

[Pereira 2012] A. L. J. Pereira, L. Gracia, D. Santamaria-Perez, R. Vilaplana, F. J. Manjon, D. Errandonea, M. Nalin, and A. Beltran. Structural and vibrational study of cubic Sb_2O_3 under high pressure. *Phys. Rev. B*. **2012**, *85*, 174108.

[Pereira 2013] A. L. J. Pereira, D. Errandonea, A. Beltran, L. Gracia, O. Gomis, J. A. Sans, B. Garcia-Domene, A. Miquel-Veyrat, F. J. Manjon, A. Muñoz, and C. Popescu. Structural study of α-Bi_2O_3 under pressure. *J. Phys.: Condens. Matter.* **2013**, *25*, 475402.

[Pereira 2014b] A. L. J. Pereira, J. A. Sans, R. Vilaplana, O. Gomis, F. J. Manjon, P. Rodriguez-Hernandez, A. Muñoz, C. Popescu, and A. Beltran. Isostructural Second-Order Phase Transition of β-Bi_2O_3 at High Pressures: An Experimental and Theoretical Study. *J. Phys. Chem. C.* **2014**, *118*, 20545.

[Rzepa 2010] H. S. Rzepa.The rational design of helium bonds. *Nat. Chem*. **2010**, *2*, 390.

[Saleh 2012] G. Saleh, C. Gatti, L. Lo Presti, and J. Contreras-Garcia. Revealing Non-covalent Interactions in Molecular Crystals through Their Experimenatl Electron Densities. *Chem. Eur. J.* **2012**, *18*, 15523.

[Soignard 2008] E. Soignard, S. A. Amin, Q. Mei, C. J. Benmore, and J. L. Yarger. High-Pressure Behavior of As_2O_3: Amorphous-Amorphous and Crystalline-Amorphous Transitions. *Phys. Rev. B*. **2008**, *77*, 144113.

[Toby 2001] B. H. Toby. EXPGUI, A Graphical User Interface for GSAS. *J. Appl. Crystallogr*. **2001**, *34*, 210.

[Wallace 1970] D. C. Wallace, "Thermoelastic theory of stressed crystals and higher-order elastic constants," in *Solid State Physics*, edited by F. S. Henry Ehrenreich, D. Turnbull, and F. Seitz (Academic Press, **1970**), vol. *25*, pp. 301–404.

[Wang 1993] J. Wang, S. Yip, S. R. Phillpot, and D. Wolf. Crystal instabilities at finite strain. *Phys. Rev. Lett*. **1993**, *71*, 4182.

JOURNAL OF APPLIED PHYSICS **120**, 155901 (2016)

Vibrational and elastic properties of As_4O_6 and $As_4O_6 \cdot 2He$ at high pressures: Study of dynamical and mechanical stability

V. P. Cuenca-Gotor,[1] O. Gomis,[2,a)] J. A. Sans,[1] F. J. Manjón,[1] P. Rodríguez-Hernández,[3] and A. Muñoz[3]
[1]*Instituto de Diseño para la Fabricación y Producción Automatizada, MALTA Consolider Team, Universitat Politècnica de València, 46022 València, Spain*
[2]*Centro de Tecnologías Físicas: Acústica, Materiales y Astrofísica, MALTA Consolider Team, Universitat Politècnica de València, 46022 València, Spain*
[3]*Departamento de Física, Instituto de Materiales y Nanotecnología, MALTA Consolider Team, Universidad de La Laguna, 38205 Tenerife, Spain*

(Received 25 August 2016; accepted 4 October 2016; published online 18 October 2016)

The formation of a new compound with stoichiometry $As_4O_6 \cdot 2He$ at relatively low pressure (3 GPa) has been recently reported when arsenolite (As_4O_6) powder is compressed with helium as a pressure-transmitting medium. In this work, we study the lattice dynamics of As_4O_6 and $As_4O_6 \cdot 2He$ at high pressures from an experimental and theoretical perspective by means of Raman scattering measurements and *ab initio* calculations and report the theoretical elastic properties of both compounds at high pressure. Raman scattering measurements show a completely different behaviour of As_4O_6 and $As_4O_6 \cdot 2He$ at high pressures. Furthermore, the theoretical calculation of phonon dispersion curves and elastic stiffness coefficients at high pressure in both compounds allow us to discuss their dynamical and mechanical stability under hydrostatic compression. Both compounds are dynamically stable even above 35 GPa, but As_4O_6 becomes mechanically unstable at pressures beyond 19.7 GPa. These results allow explaining the pressure-induced amorphization of As_4O_6 found experimentally above 15–20 GPa and the lack of observation of any instability in $As_4O_6 \cdot 2He$ up to the highest studied pressure (30 GPa). *Published by AIP Publishing.*
[http://dx.doi.org/10.1063/1.4964875]

I. INTRODUCTION

Arsenic trioxide (As_2O_3) is a commercially important compound since it is the main precursor to other arsenic compounds, like organoarsenic compounds used in forestry products and pharmaceuticals. The oxide is also used in colorless glass production and in electronics as the precursor to elemental arsenic, arsenic alloys, and arsenide semiconductors.[1] Despite the well known toxicity of arsenic, arsenic trioxide has long been of biomedical interest, dating to traditional Chinese medicine, and is still used to treat cancer and other diseases.[2,3]

Arsenolite (α-As_2O_3, indeed As_4O_6) is a mineral which is formed by oxidation of As-rich ore deposits as arsenic sulfide or by hydrolysis of arsenic chloride.[4] This mineral constitutes the cubic polymorph [space group 227, *Fd*-3*m*, Z = 16] of arsenic oxide and is a molecular 3D solid with an open framework structure composed of closed-compact adamantane-type As_4O_6 molecular cages (with strong covalent interatomic As-O bonds) bonded together by weak van der Waals forces and directional intermolecular interactions[5,6] [see Fig. 1(a)]. In particular, the structure of the As_4O_6 molecular cage can be described by the overlap of four pseudo–tetrahedral units consisting of an As atom surrounded by three O ligands and a cationic lone electron pair (LEP) in such a way that they form a ball with all cation (also anion) LEPs pointing towards the external part of the cage.[7]

Apart from the structural characterization of As_4O_6 at high pressures (HPs),[8–10] the vibrational properties of arsenolite under compression have been also reported.[11,12] In Ref. 11, the pressure dependence of all (except one) Raman-active modes was reported as well as the pressure dependence of all infrared (IR)-active modes. Furthermore, additional modes were observed above 6 GPa, which were suggested to occur due to a cubic-to-tetragonal phase transition in As_4O_6. However, this phase transition has not been confirmed in the HP structural studies already performed.[8–10] Therefore, it is timely to revisit the vibrational properties of As_4O_6 at HP.

Several, previous works have reported the structural characterization of As_4O_6 under compression by means of angle dispersive x-ray diffraction (XRD) measurements using different pressure-transmitting media (PTMs).[8,10] In those works, it was shown that arsenolite is one of the most compressible non-hydrated minerals. Furthermore, it was shown that when this compound is compressed with He, this PTM enters into the largest voids of the structure (16d sites) above 3 GPa to form a stable compound with stoichiometry $As_4O_6 \cdot 2He$ [Fig. 1(b)].[8–10] In this regard, it is worth mentioning that it has been reported that As_4O_6 undergoes pressure-induced amorphization (PIA) above 15–20 GPa depending on the PTM used;[8,10–12] however, it was also shown that $As_4O_6 \cdot 2He$ remained stable at least up to 30 GPa showing no sign of PIA.[8–10]

a)Author to whom correspondence should be addressed. Electronic mail: osgohi@fis.upv.es

Vibrational and elastic properties of As_4O_6 and $As_4O_6 \cdot 2He$ at high pressures: Study of dynamical and mechanical stability

V.P. Cuenca-Gotor,[1] O. Gomis,[2] J.A. Sans,[1] F. J. Manjón,[1]
P. Rodríguez-Hernández,[3] and A. Muñoz [3]

[1] *Instituto de Diseño para la Fabricación y Producción Automatizada, MALTA Consolider Team, Universitat Politècnica de València, 46022 València, Spain*

[2] *Centro de Tecnologías Físicas: Acústica, Materiales y Astrofísica, MALTA Consolider Team, Universitat Politècnica de València, 46022 València, Spain*

[3] *Departamento de Física, Instituto de Materiales y Nanotecnología, MALTA Consolider Team, Universidad de La Laguna, 38205 Tenerife, Spain*

Abstract

The formation of a new compound with stoichiometry $As_4O_6 \cdot 2He$ at relatively low pressure (3 GPa) has been recently reported when arsenolite (As_4O_6) powder is compressed with helium as a pressure-transmitting medium. In this work, we study the lattice dynamics of As_4O_6 and $As_4O_6 \cdot 2He$ at high pressures from an experimental and theoretical perspective by means of Raman scattering measurements and *ab initio* calculations and report the theoretical elastic properties of both compounds at high pressure. Raman scattering measurements show a completely different behavior of As_4O_6 and $As_4O_6 \cdot 2He$ at high pressures. Furthermore, the theoretical calculation of phonon dispersion curves and elastic stiffness coefficients at high pressure in both compounds allow us to discuss their dynamical and mechanical stability under hydrostatic compression. Both compounds are dynamically stable even above 20 GPa, but As_4O_6 becomes mechanically unstable at pressures beyond 19.7 GPa. These results allow explaining the pressure-induced amorphization of As_4O_6 found experimentally above 15-20 GPa and the lack of observation of any instability in $As_4O_6 \cdot 2He$ up to the highest studied pressure (30 GPa).

I. INTRODUCTION

Arsenic trioxide (As_2O_3) is a commercially important compound since it is the main precursor to other arsenic compounds, like organoarsenic compounds used in forestry products and pharmaceuticals. The oxide is also used in colorless glass production and in electronics as the precursor to elemental arsenic, arsenic alloys, and arsenide semiconductors [Grund 2005]. Despite the well known toxicity of arsenic, arsenic trioxide has long been of biomedical interest, dating to traditional Chinese medicine, and is still used to treat cancer and other diseases [Gielen 2005, Liu 2008].

Arsenolite (α-As_2O_3, indeed As_4O_6) is a mineral which is formed by oxidation of As-rich ore deposits as arsenic sulfide or by hydrolysis of arsenic chloride [Brauer 1963]. This mineral constitutes the cubic polymorph [space group 227, *Fd-3m*, Z=16] of arsenic oxide and is a molecular 3D solid with an open framework structure composed of closed-compact adamantane-type As_4O_6 molecular cages (with strong covalent interatomic As-O bonds) bonded together by weak van der Waals forces and directional intermolecular interactions [Gibbs 2009, Guńka 2015a] [see **Fig. 1(a)**]. In particular, the structure of the As_4O_6 molecular cage can be described by the overlap of four pseudo–tetrahedral units consisting of an As atom surrounded by three O ligands and a cationic lone electron pair (LEP) in such a way that they form a ball with all cation (also anion) LEPs pointing towards the external part of the cage [Pertlik 1978].

Apart from the structural characterization of As_4O_6 at high pressures (HP) [Sans 2015, Guńka 2015b, Sans 2016a], the vibrational properties of arsenolite under compression have been also reported [Grzechnik 1999, Soignard 2008]. In Grzechnik (1999), the pressure dependence of all (except one) Raman-active modes were reported as well as the pressure dependence of all infrared (IR)-active modes. Furthermore, additional modes were observed above 6 GPa which were suggested to occur due to a cubic-to-tetragonal phase transition in As_4O_6. However, this phase transition has not been confirmed in the HP structural studies already performed [Sans 2015, Guńka 2015b, Sans 2016a]. Therefore, it is timely to revisit the vibrational properties of As_4O_6 at HP.

Additionally, previous works have reported the structural characterization of As_4O_6 under compression by means of angle dispersive X-ray diffraction (XRD) measurements using different pressure-transmitting media (PTMs) [Sans 2015, Guńka 2015b, Sans 2016a]. In those works it was shown that arsenolite is one of the most compressible non-hydrated minerals. Furthermore, it was shown in several previous works that when this compound is compressed with He, this PTM enters into the largest voids of the structure (16d sites) above 3 GPa to form a stable compound with stoichiometry $As_4O_6{\cdot}2He$ [**Fig. 1(b)**] [Sans 2015, Guńka 2015b, Sans 2016a]. In this regard, it is worth to mention that it has been reported that As_4O_6 undergoes pressure-induced amorphization (PIA) above 15-20 GPa depending on the PTM used [Sans 2015, Sans 2016a, Grzechnik 1999, Soignard 2008]; however, it was also shown that $As_4O_6{\cdot}2He$ remained stable at least up to 30 GPa showing no sign of PIA [Sans 2015, Guńka 2015b, Sans 2016a].

In order to further understand the different behavior of As_4O_6 and $As_4O_6{\cdot}2He$, we study in this work the lattice dynamics of both compounds by means of Raman scattering (RS) measurements at room temperature and *ab initio* calculations of the elastic properties for both compounds at HP. Some thermodynamic properties are also reported in the supplementary material. In this way, we have theoretically studied the dynamical and mechanical stability of As_4O_6 and $As_4O_6{\cdot}2He$ at HP, which allows explaining prior experimental results. Note that partial results of the lattice dynamics and mechanical stability of both compounds were already reported in [Sans 2015, Sans 2016a].

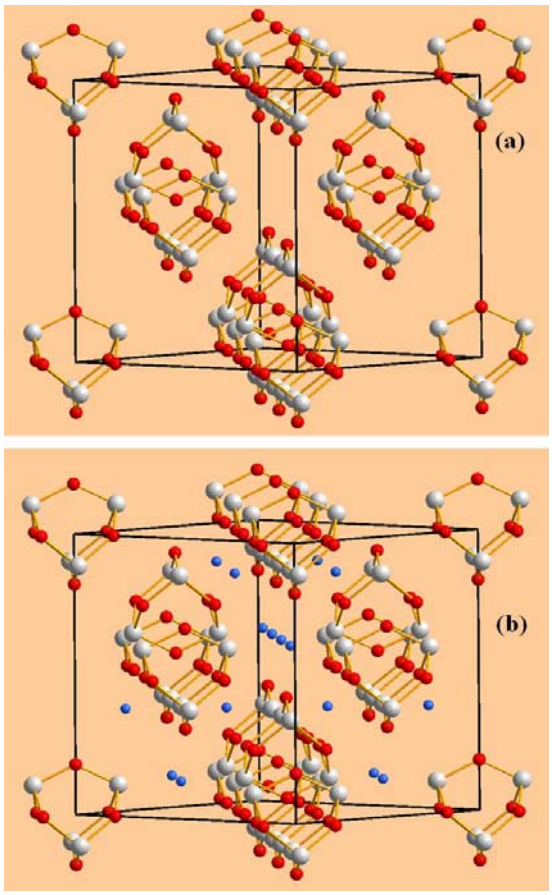

Figure 1. Cubic unit cell of As_4O_6 (a) and $As_4O_6 \cdot 2He$ (b). Grey (big), red (medium) and blue(small) balls correspond to As, O and He atoms, respectively.

II. EXPERIMENTAL DETAILS

Highly pure arsenolite (As_4O_6) powder (99.999%) was commercially obtained from Sigma Aldrich Company. As_4O_6 powder was loaded together with several ruby balls inside a membrane-type diamond anvil cell (DAC) and was pressurized with different PTM (4:1 metanol-ethanol mixture (MEM) and He) but also without any PTM. The ruby photoluminescence was used for pressure calibration in all measurements [Mao 1986].

HP-RS measurements at room temperature were performed in a backscattering geometry using a Horiba Jobin-Yvon LabRam HR UV spectrometer in combination with a thermoelectrically-cooled multichannel CCD detector (resolution below 2 cm^{-1}). RS spectra of arsenolite powder were excited either with 532.0 or 632.8 nm

laser lines and laser power below 10 mW up to pressures between 12 and 22 GPa. RS measurements were analyzed by fitting Raman peaks with a Voigt profile fixing the Gaussian line width to the experimental setup resolution.

III. THEORETICAL CALCULATIONS DETAILS

Ab initio total-energy calculations were performed within the density functional theory (DFT) [Hohenberg 1964] using the plane-wave method [Blochl 1994] and the pseudopotential theory with the Vienna *ab initio* simulation package (VASP) [Kresse 1993, Kresse 1994, Kresse 1996a, Kresse 1996b] as in a previous work [Sans 2016a]. Convergence tests show that in order to have accurate results, the plane wave basis requires an energy cutoff of 520 eV. The integrations in the Brillouin zone were performed using a special k-point sampling, with dense (4x4x4) grid of k-points in order to have high accurate and converged results. Total energies were converged up to 0.001 eV/atom and forces acting on atoms were converged up to 0.003 eV/Å. Exchange and correlation term was computed through PBE for solids prescription [Perdew 2008]. In this way, lattice dynamics *ab initio* calculations at the zone center (Γ point) of the Brillouin zone (BZ) were performed using the direct force constant approach [Parlinski 1997]. To obtain the phonon dispersion curves (PDCs) along high-symmetry directions of the BZ we performed similar calculations using appropriate supercells, which allow the phonon dispersion at k-points to be obtained commensurate with the supercell size [Parlinski 1997].

On the other hand, *ab initio* calculations allow the study of the mechanical properties of materials. In particular, the elastic constants describe the mechanical properties of materials in the region of small deformations where the stress-strain relations are still linear. The elastic constants can be obtained by computing the macroscopic stress for a small strain with the use of the stress theorem [Chetty 1989]. In the present work, we perform the evaluation of the elastic constants of As_4O_6 and $As_4O_6 \cdot 2He$ with the use of the DFT as implemented in the VASP package [Le Page 2002]**.** The ground state and fully relaxed structures were strained in different directions according to their symmetry [Le Page 2002]. The total-energy variations were evaluated according to a Taylor expansion for the total energy with respect to the applied strain [Beckstein 2001]. Due to this fact, it is important to check that the strain used in the calculations guarantees the harmonic behavior. This procedure allows us to obtain the C_{ij} elastic constants in the Voigt notation. The number of independent elastic constants is reduced by crystalline symmetry [Nye 1957].

IV. RESULTS AND DISCUSSION

A. Lattice dynamics

Arsenolite has a primitive unit cell containing two As_4O_6 adamantanoid molecules situated on the T_d sites of the unit cell [Ballirano 2002]. According to the factor group analysis, arsenolite, as well as senarmontite, has 60 vibrational modes at zone

center [Kroumova 2003]: $\Gamma = 2A_{1g} + 2A_{2u} + 2E_g + 2E_u + 3T_{1g} + 3T_{2u} + 5T_{2g} + 5T_{1u}$, where E and T modes are double and triple degenerated, respectively. In this way, there are nine Raman-active modes: $2A_{1g} + 2E_g + 5T_{2g}$, four IR-active modes: $4T_{1u}$, ten inactive modes: $2A_{2u} + 2E_u + 3T_{1g} + 3T_{2u}$, and one acoustic mode: T_{1u} [Beattie 1970]. Most of the above optical modes come from the internal modes of the isolated As_4O_6 molecule: $\Gamma_{vib} = 2A_1 + 2E + 2T_1 + 4T_2$ due to crystal field (or Davydov) splitting [Jensen 2003]. From now on, we will add to the optical vibrational modes of a given symmetry a superscript in order of increasing frequency for the sake of clarity.

To date, several studies have been published on arsenolite's Raman spectra at room conditions [Beattie 1970, Jensen 2003, Szymansky 1968, Brumbach 1972, Lockwood 2000, Gilliam 2003] and only two at HP [Grzechnik 1999, Soignard 2008]. In the first works there was some disagreement on the assignment of T_{2g} and E_g modes, which has been finally clarified [Jensen 2003, Gilliam 2003]; however, there remains one E_g vibrational mode yet to be clearly observed and identified [Jensen 2003, Gilliam 2003]. In the following we will report the pressure dependence of the different Raman-active modes with different PTM and will show the identification of the lost E_g mode.

1. As_4O_6 pressurized with MEM as a PTM

MEM is a good quasi-hydrostatic PTM up to 20 GPa which is not expected to enter into the open framework structure of arsenolite. **Figure 2(a)** shows the RS spectra of As_4O_6 with MEM as a PTM measured up to 21 GPa. As observed, our RS spectra are similar to those already reported [Grzechnik 1999, Soignard 2008]. **Figure 2(b)** shows the pressure dependence of the experimental and theoretical Raman-active modes of As_4O_6. Upon compression, several modes shift to upper wavenumbers: the T_{2g}^1 mode at 84 cm^{-1}; the T_{2g}^2 mode at 268 cm^{-1}; the T_{2g}^3 at 413 cm^{-1}; the A_{1g}^2 mode at 560 cm^{-1} and the T_{2g}^5 mode at 780 cm^{-1}. On the other hand, there are a few modes which shift to lower wavenumbers: the E_g^1 mode at 183 cm^{-1}; the A_{1g}^1 mode at 369 cm^{-1} and the T_{2g}^4 at 470 cm^{-1}. Due to the closeness of the T_{2g}^3 and T_{2g}^4 modes these two modes undergo a phonon anticrossing around 4.5 GPa; i.e., these two modes repel each other at around 4.5 GPa, then the T_{2g}^3 band gains intensity and shifts to lower wavenumbers, while the T_{2g}^4 band loses intensity and shifts to upper wavenumbers. Our symmetry assignments performed on the basis of our theoretical calculations agree with those of Grzechnik and Gilliam et al. [Grzechnik 1999, Gilliam 2003]. Furthermore, our *ab initio* calculations indicate that there is an E_g mode at 420 cm^{-1}, which is the only Raman-active mode that was not clearly found in previous Raman works. Taking into account that our calculated frequencies underestimate the experimental frequencies, it is expected that the lost E_g mode could be the weak mode near 443 cm^{-1} observed as a shoulder of the intense T_{2g}^4 mode by Lockwood and Gilliam et al. [Lockwood 2000, Gilliam 2003]. However, we have not observed this mode in RS measurements of As_4O_6 at room conditions or using MEM as a PTM.

Apart from the first-order Raman-active modes, other modes are observed in the RS spectrum of arsenolite as noted by many authors. In particular, we have observed a

very weak peak at about 80 cm^{-1}, also seen in Grzechnik (1999), close to the T_{2g}^{1} mode at 84 cm^{-1}. In our opinion this extra mode can be tentatively assigned to one of the inactive librational modes, likely T_{1g}^{1}, of the As_4O_6 molecule due to the close similarity of the theoretical frequencies and pressure coefficients of this mode [see **Fig. 2(b)**], where the theoretical pressure dependence of the two lowest frequency inactive modes is also plotted. We think that this inactive mode could be observed due to local loss of translational periodic conditions in As_4O_6 as pressure increases. Furthermore, with increasing pressure, many Raman modes undergo a progressive asymmetric broadening resulting in split modes mainly above 10 GPa.

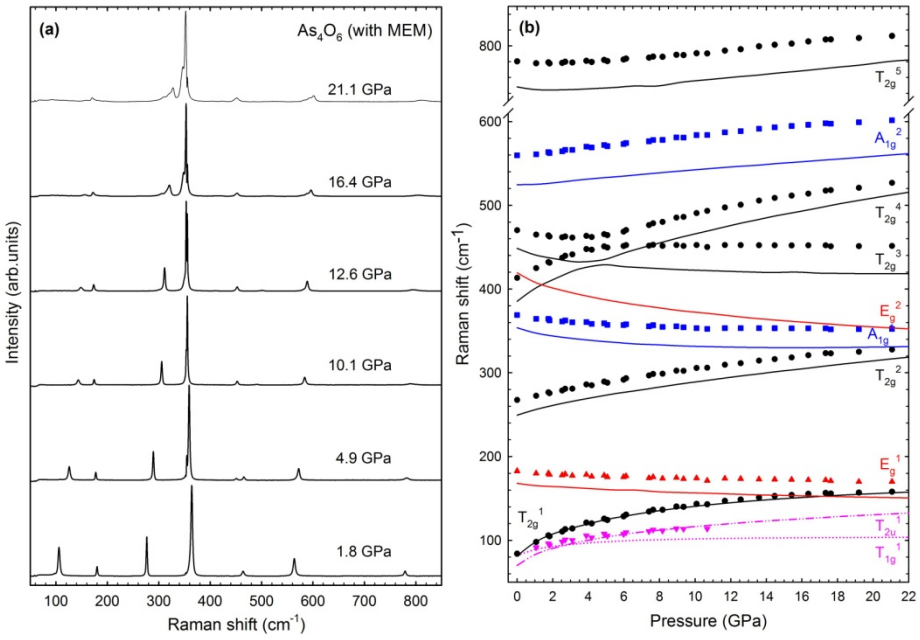

Figure 2. (a) Raman spectra of As_4O_6 up to 21 GPa when pressurized with a 4:1 methanol-ethanol mixture. (b) Pressure dependence of the experimental (symbols) and theoretical (solid lines) Raman-mode frequencies. The theoretical T_{1g}^{1} (T_{2u}^{1}) inactive mode is shown with a dotted (dash-dotted) line. Pink symbols represent the extra Raman modes observed or used to fit the profile of broadened asymmetric peaks on increasing pressure.

These features, which were also noted in Grzechnik (1999), are likely caused by the increase of intermolecular interactions; i.e., the increase of interactions among As_4O_6 cages, which finally results in the onset of PIA above 15-20 GPa depending on the PTM used. On the other hand, the reversibility of the changes in the RS spectra above 10 GPa shows little or no hysteresis. We must note that the increase of intermolecular interactions does not result in a reversible phase transition above 6

GPa as suggested by Grzechnik [Grzechnik 1999]. Previous X-ray diffraction measurements confirmed that the cubic symmetry is maintained up to the onset of PIA [Sans 2015, Guńka 2015b, Sans 2016a]. **Table I** summarizes the experimental and theoretical zero-pressure frequencies, pressure coefficients, and derivative of the pressure coefficients for the Raman-active modes of arsenolite. As observed, our results for the Raman-active modes at zero pressure compare well with previous results reported by Grzechnik [Grzechnik 1999] and also with those of Gilliam et al. [Gilliam 2003] at ambient pressure.

Table I. Experimental and theoretical frequencies and pressure coefficients of Raman- active (R) modes in As_4O_6 at 0 GPa. The inactive modes $T_{2u}{}^1$ and $T_{1g}{}^1$ are also included.

	Ab initio calculations		Experiments					
Mode (Sym)	ω_0 (cm^{-1})	$\frac{\partial\omega}{\partial P}$ $\left(\frac{cm^{-1}}{GPa}\right)$	ω_0^a (cm^{-1})	$\frac{\partial\omega^a}{\partial P}$ $\left(\frac{cm^{-1}}{GPa}\right)$	ω_0^b (cm^{-1})	$\frac{\partial\omega^b}{\partial P}$ $\left(\frac{cm^{-1}}{GPa}\right)$	ω_0^c (cm^{-1})	$\frac{\partial\omega^c}{\partial P}$ $\left(\frac{cm^{-1}}{GPa}\right)$
$T_{2u}{}^1$	70.7	11.9						
$T_{1g}{}^1$	81.8	7.8	85.5	6.0	82.3	8.9		
$T_{2g}{}^1$ (R)	82.1	15.2	84.7	12.9	83.8	13.2	81.0	10.0
$E_g{}^1$ (R)	168.0	-2.5	182.5	-2.3	182.6	-2.0	181.1	-1.0
$T_{2g}{}^2$ (R)	249.4	6.4	267.5	4.9	267.1	5.0	265.2	3.9
$A_{1g}{}^1$ (R)	353.4	-5.7	368.6	-3.6	368.7	-3.0	367.2	-2.0
$T_{2g}{}^3$ (R)	385.4	16.0	413.4	11.8	413.2	11.6	410.6	10.0
$E_g{}^2$ (R)	418.9	-10.4			449.2	-6.4		
$T_{2g}{}^4$ (R)	448.5	-8.7	470.3	-5.6	470.5	-5.1	469.8	-3.0
$A_{1g}{}^2$ (R)	524.6	0.5	559.4	1.7	559.3	2.0	558.8	1.4
$T_{2g}{}^5$ (R)	747.9	-3.7	780.0	-1.5	780.5	-2.3	780.5	-0.6

[a] Experiment with MEM.
[b] Experiment without any PTM.
[c] Experiment with CsI (data from Grzechnik (1999)).

For completeness, we have compared the theoretical pressure dependence of the IR-active modes of As_4O_6 with the experimental data taken from Grzechnik (1999) [see **Fig. S1** in the supplementary material]. As observed, there is a rather good agreement between the experimental and theoretical data, so our calculations confirm the four IR-active modes already reported for arsenolite [Grzechnik 1999, Brumbach 1972]. The experimental and theoretical zero-pressure frequencies,

pressure coefficients, and derivative of the pressure coefficients for the IR-active modes of arsenolite are given in **Table SI** of the supplementary material.

2. As_4O_6 pressurized without any PTM

For a better comparison of our HP-RS measurements on As_4O_6 with those of Grzechnik (1999), which were performed with CsI as a PTM, and with those of Soignard (2008), which were performed without any PTM, we performed measurements without any PTM since arsenolite is a rather good quasi-hydrostatic PTM at low pressures (in fact slightly better than CsI) [Sans 2016b]. RS spectra of As_4O_6 without PTM were measured up to 12 GPa [see **Fig. S2** in the supplementary material]. A detail of the Raman spectra in the region between 400 and 500 cm^{-1}, where the E_g mode is expected to be observed, is plotted in **Fig. 3(a)** and the pressure dependence of the frequencies of its Raman-active modes is reported [**Fig. 3(b)**]. The frequencies and pressure coefficients of the Raman-active modes in As_4O_6 pressurized without any PTM are also shown in **Table I**.

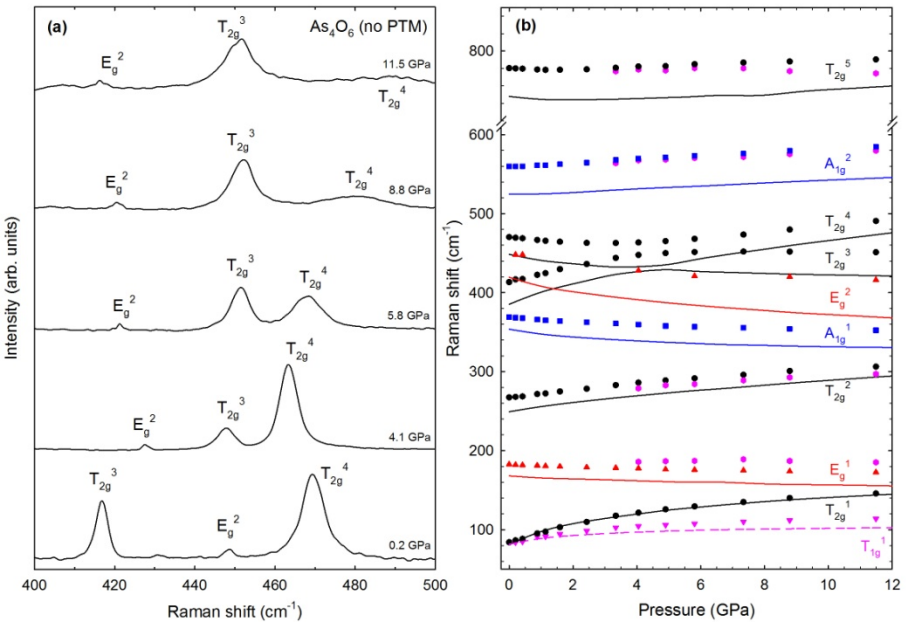

Figure 3. (a) Detail of the Raman spectra of As_4O_6 up to 12 GPa when pressurized without any pressure-transmitting medium. (b) Pressure dependence of the experimental (symbols) and theoretical (solid lines) Raman-mode frequencies. The theoretical T_{1g}^{1} inactive mode is shown with a dashed line. Pink symbols represent the extra Raman modes observed or used to fit the profile of asymmetric peaks.

Raman-active modes of As_4O_6 pressurized without any PTM show a similar behavior with increasing pressure as in the case of As_4O_6 pressurized with MEM as a PTM. However, the width of the Raman-active modes increases with pressure at a much faster rate; i.e., at smaller pressures, than using MEM as a PTM. Curiously, we have found a weak mode near 448 cm^{-1} at room pressure whose pressure dependence is consistent with the theoretical evolution of the E_g^2 mode [see **Figs. 3(a), 3(b)** and **Table I**]. Therefore, we have tentatively attributed this weak mode to the lost E_g^2 mode. We have to note that this means that there are three Raman-active modes in the RS of arsenolite in the region from 400 to 500 cm^{-1}. In this respect, previous RS measurements of arsenolite compressed without any PTM already reported three Raman active modes in this region in the RS spectrum at 11 GPa [Soignard 2008]. However, this work does not report any analysis of the experimental Raman-active mode frequencies of arsenolite as a function of pressure. We have also to note that the frequency we have found is slightly larger than the one reported by Gilliam et al. [Gilliam 2003], but in very good agreement with Hartree-Fock calculations of Jensen et al. [Jensen 2003]. At present, we don't know why it has been easier to find this mode under quasi-hydrostatic conditions than under truly hydrostatic conditions (this mode was also not observed when pressurizing with He). We can speculate that the small RS cross section already known for this mode [Jensen 2003] can be enhanced by altering selection rules under non-hydrostatic conditions.

3. As_4O_6 pressurized with helium as a PTM

Helium provides the most hydrostatic conditions for HP experiments, but He is so a small atom that it can enter into the cavities of open framework structures present in porous and molecular materials. We have performed a study of As_4O_6 pressurized with He in order to study the effect of He into the compression of this molecular solid. In this regard, we showed in a previous work that He enters into the 16d sites of As_4O_6 and reacts with this molecular solid forming a new compound with stoichiometry $As_4O_6{\cdot}2He$ above 3 GPa [Sans 2016a].

$As_4O_6{\cdot}2He$ has the same cubic structure as As_4O_6 with two formula units per primitive cell. Therefore, according to group theory, $As_4O_6{\cdot}2He$ has 62 vibrational modes at zone center [Kroumova 2003]: $\Gamma = 2A_{1g} + 2A_{2u} + 2E_g + 2E_u + 3T_{1g} + 3T_{2u} + 5T_{2g} + 7T_{1u}$. In this way, there are nine Raman-active modes: $2A_{1g} + 2E_g + 5T_{2g}$, six IR-active modes: $6T_{1u}$, ten inactive modes: $2A_{2u} + 2E_u + 3T_{1g} + 3T_{2u}$, and one (triply degenerated) acoustic mode: T_{1u}. In summary, there are only two additional IR-active modes in $As_4O_6{\cdot}2He$ than in As_4O_6.

Figure 4(a) shows the pressure dependence of the RS spectra of As_4O_6 compressed with He up to 3 GPa and of $As_4O_6{\cdot}2He$ from 3 GPa up to 12 GPa. The experimental and theoretical pressure dependence of the different Raman-active modes is presented in **Fig. 4(b)**. The frequencies and pressure coefficients of the Raman-active modes in $As_4O_6{\cdot}2He$ are shown in **Table II**. As observed, the pressure dependence of Raman-active modes up to 2 GPa follows the same behavior as As_4O_6 modes studied in sections IV A 1 and IV A 2. However, between 2 and 3 GPa many Raman modes undergo a sudden change in frequency. No further sudden

change in frequencies is observed above 3 GPa and RS modes from 3 GPa on behave in a different way to Raman-active modes of As_4O_6. Noteworthy, the anticrossing between the two T_{2g} modes, which occurs in As_4O_6 around 4-5 GPa is retarded up to 11 GPa in As_4O_6·2He. The good agreement of our experimental and theoretical data in this regard is a clear confirmation of the entrance of He into 16d sites of the arsenolite structure. Since we have not performed IR measurements in As_4O_6·2He, the pressure dependence of the theoretically IR-active modes of As_4O_6·2He is reported in **Fig. S3** in the supplementary material for comparison with future experimental works. As observed, there are two extra IR-active modes in As_4O_6·2He between 200 and 300 cm^{-1} whose pressure coefficient is much larger than those coming from As_4O_6.

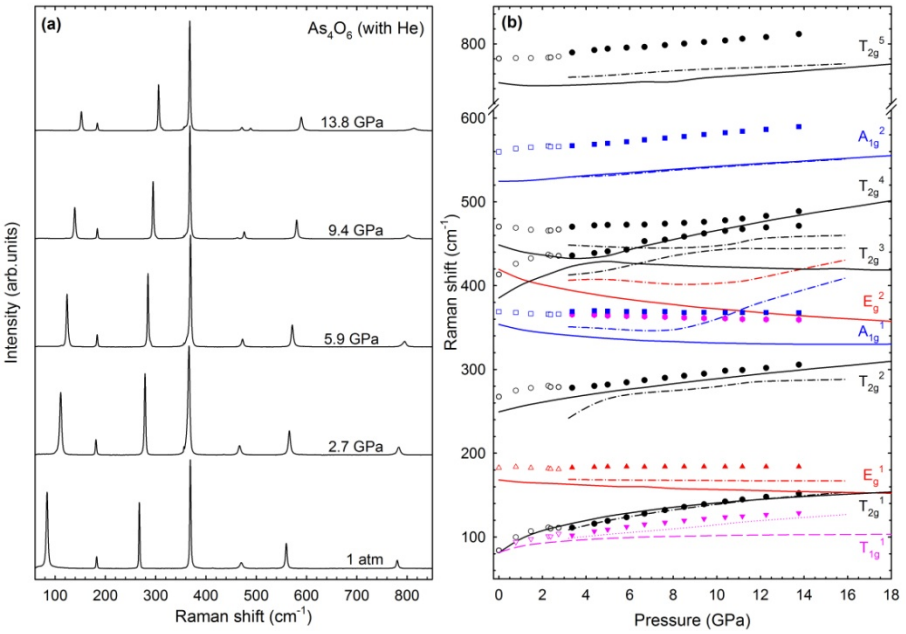

Figure 4. (a) Raman spectra of As_4O_6 up to 3 GPa and of As_4O_6·2He from 3 GPa up to 14 GPa. (b) Pressure dependence of the experimental (full symbols) and theoretical (dash-dotted lines) Raman-mode frequencies of As_4O_6·2He. Experimental Raman-mode frequencies for As_4O_6 up to 3 GPa are shown with empty symbols. Theoretical data for As_4O_6 (solid lines) are also shown for comparison with those of As_4O_6·2He to note the effect of He entrance in 16d sites of As_4O_6. The theoretical T_{1g}^1 inactive mode is shown in pink with a dashed line for As_4O_6 and with a dotted line for As_4O_6·2He. Pink symbols represent the extra Raman modes observed or used to fit the profile of asymmetric peaks.

Table II. Experimental and theoretical frequencies and pressure coefficients of Raman-active (R) modes in $As_4O_6 \cdot 2He$ at 3 GPa. The inactive mode $T_{1g}^{\ 1}$ is also included.

	Ab initio calculations		Experiments	
Mode (Sym)	ω_0 (cm^{-1})	$\frac{\partial\omega}{\partial P}$ $\left(\frac{cm^{-1}}{GPa}\right)$	ω_0 (cm^{-1})	$\frac{\partial\omega}{\partial P}$ $\left(\frac{cm^{-1}}{GPa}\right)$
$T_{1g}^{\ 1}$	98.9	2.3	102.0	3.6
$T_{2g}^{\ 1}$ (R)	108.2	6.6	108.8	6.7
$E_g^{\ 1}$ (R)	168.7	-0.3	183.1	0.4
$T_{2g}^{\ 2}$ (R)	244.3	10.0	276.4	3.3
$A_{1g}^{\ 1}$ (R)	349.7	-4.9	369.8	-0.3
$T_{2g}^{\ 3}$ (R)	412.3	-0.7	435.0	-1.3
$E_g^{\ 2}$ (R)	409.2	-5.9		
$T_{2g}^{\ 4}$ (R)	448.7	-2.4	469.7	3.7
$A_{1g}^{\ 2}$ (R)	528.8	1.8	565.7	2.2
$T_{2g}^{\ 5}$ (R)	754.7	2.2	788.6	2.0

B. Dynamical stability

To finish the study of the lattice dynamics of As_4O_6 and $As_4O_6 \cdot 2He$ at HP, we report the calculation of PDCs for both compounds at selected pressures which allows the discussion of their dynamical stability under hydrostatic compression [Born 1940]. **Figure 5** shows the PDCs of As_4O_6 at 0 GPa and 34.7 GPa, while **Figure 6** shows the PDCs of $As_4O_6 \cdot 2He$ at 5.2 GPa and 35.5 GPa. It can be observed that there is no phonon dispersion relation that undergoes softening to zero frequency on increasing pressure neither in As_4O_6 up to 34.7 GPa nor in $As_4O_6 \cdot 2He$ up to 35.5 GPa. Therefore, we safely conclude that the cubic structure of both compounds is dynamically stable at least up to those pressures.

C. Elastic properties

Since the cubic structures of As_4O_6 and $As_4O_6 \cdot 2He$ belong to the Fd-3m space group, they have point group 4/m-3 2/m, also known as m-3m (or O_h), and belong to the cubic Laue group m-3m (or C I) [Clayton 2010] which has three independent second order elastic constants: C_{11}, C_{12}, and C_{44}. When a non-zero uniform stress is

applied to the crystal, the elastic properties are described by the elastic stiffness (or stress-strain) coefficients, which are defined as:

$$B_{ijkl} = C_{ijkl} + 1/2\,[\,\delta_{ik}\sigma_{jl} + \delta_{jk}\sigma_{il} + \delta_{il}\sigma_{jk} + \delta_{jl}\sigma_{ik} - 2\,\delta_{kl}\sigma_{ij}], \quad (1)$$

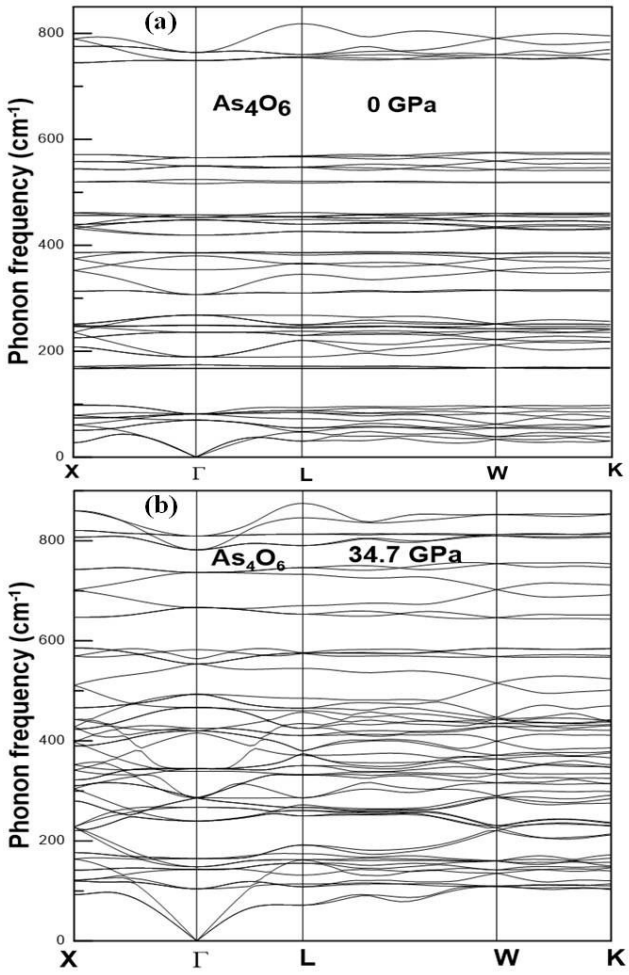

Figure 5. Phonon dispersion curves of As_4O_6 at 0 GPa (a) and 34.7 GPa (b).

with C_{ijkl} being the elastic constants evaluated at the current stressed state, σ_{ij} correspond to the external stresses, and δ_{kl} is the Kronecker delta [Wallace 1970, Wang 1993, Wang 1995]**.** In the special case of hydrostatic pressure ($\sigma_{11} = \sigma_{22} = \sigma_{33} = -P$) applied to a cubic crystal, the elastic stiffness coefficients in the Voigt notation

B_{ij} are: $B_{11} = C_{11} - P$, $B_{12} = C_{12} + P$, and $B_{44} = C_{44} - P$ where P is the hydrostatic pressure. Note that the B_{ij} and C_{ij} are equal at 0 GPa. When the elastic stiffness coefficients B_{ij} are used, all relationships of the elasticity theory can be applied for the crystal under any loading, including Born's stability conditions which are identical in both loaded and unloaded states [Wang 1993, Wang 1995, Zhou 1996, Karki 2001, Krasil'nikov 2014]**. Table III** summarizes the values of the three elastic constants C_{ij} in As_4O_6 and $As_4O_6 \cdot 2He$ at 0 GPa as obtained from our *ab initio* calculations. As observed, C_{11} is larger in $As_4O_6 \cdot 2He$ than in As_4O_6 while C_{12} and C_{44} are smaller in $As_4O_6 \cdot 2He$ than in As_4O_6.

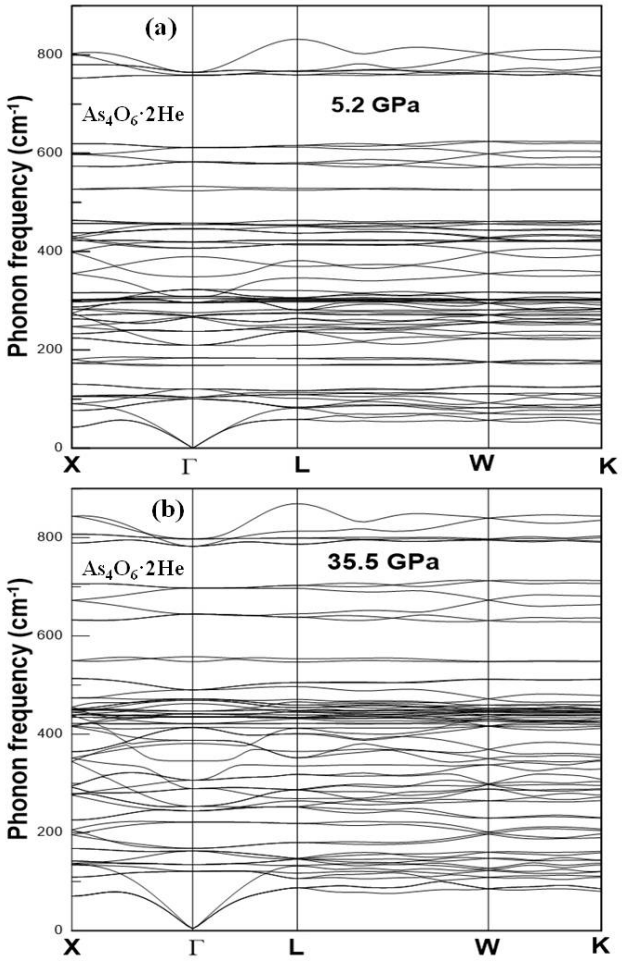

Figure 6. Phonon dispersion curves of $As_4O_6 \cdot 2He$ at 5.2 GPa (a) and 35.5 GPa (b).

Table III. C_{ij} elastic constants (in GPa) for As_4O_6 and $As_4O_6{\cdot}2He$ at 0 GPa. Elastic moduli B_H, G_H, and E_H (in GPa), Possion's ratio (ν_H) given in the Hill approximation, labeled with subscript H in As_4O_6 and $As_4O_6{\cdot}2He$ at 0 GPa. The B_H/G_H ratio, Zener anisotropy factor (A), Vickers hardness (H_v in GPa), density (ρ in g/cm^3), and longitudinal (v_{lon}), transverse (v_{trans}) and averaged (v_m) elastic wave velocities (all in m/s) are also included.

	As_4O_6	$As_4O_6{\cdot}2He$
C_{11}	21.2	28.8
C_{12}	4.0	-0.6
C_{44}	9.8	8.7
B_H	9.8	9.2
G_H	9.3	10.7
E_H	21.2	23.1
ν_H	0.14	0.08
B_H/G_H	1.05	0.86
A	1.15	0.59
H_v	4.2	5.8
ρ	3.982	3.766
v_{lon}	2359.8	2495.3
v_{trans}	1529.6	1684.1
v_m	1678.0	1838.1

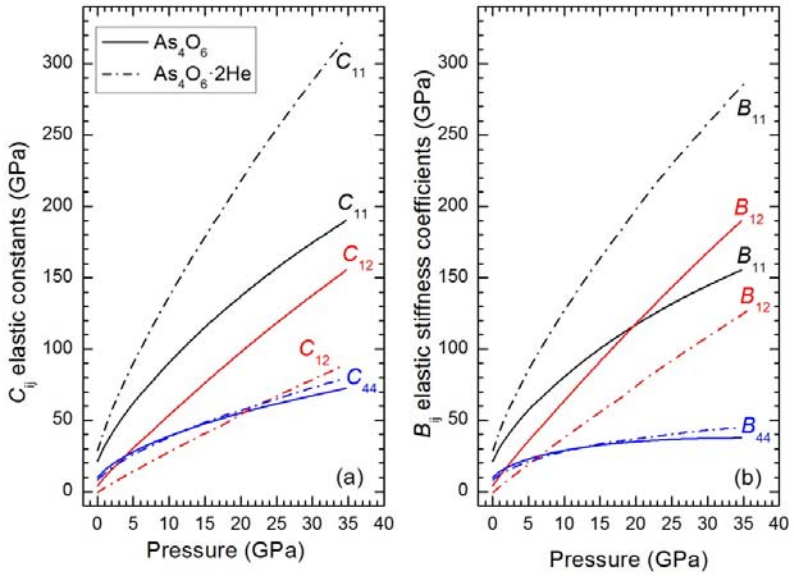

Figure 7. Pressure dependence of the theoretical elastic constants (a) and elastic stiffness coefficients (b) in As_4O_6 and $As_4O_6{\cdot}2He$.

Figure 7 shows the pressure dependence of the elastic constants, C_{ij}, and elastic stiffness coefficients, B_{ij}, in As_4O_6 and $As_4O_6{\cdot}2He$. Despite only B_{ij} are meaningful at any pressure, we report also the pressure dependence of C_{ij} because they are the original magnitudes computed from which B_{ij} are obtained. As observed, C_{11} (and B_{11}) has a larger pressure coefficient in $As_4O_6{\cdot}2He$ than in As_4O_6 while C_{12} (and B_{12}) and C_{44} (and B_{44}) have smaller pressure coefficients in $As_4O_6{\cdot}2He$ than in As_4O_6. Besides, C_{11} (and B_{11}) and C_{12} (and B_{12}) increase with increasing pressure both in As_4O_6 and $As_4O_6{\cdot}2He$ while C_{44} (and B_{44}) tend to saturate with increasing pressure in As_4O_6 but not in $As_4O_6{\cdot}2He$. These results will be discussed later in relation with the mechanical stability of both compounds.

Standard analytical formulas for the bulk (B) and shear (G) moduli in the Voigt [Voigt 1928], Reuss [Reuss 1929], and Hill [Hill 1952] approximations, labeled with subscripts V, R, and H, respectively, can be obtained from the set of B_{ij} for any loading in As_4O_6 and $As_4O_6{\cdot}2He$ [Gomis 2014]**:**

$$B_V = B_R = \frac{B_{11}+2B_{12}}{3} \tag{2}$$

$$B_H = \frac{B_V+B_R}{2} \tag{3}$$

$$G_V = \frac{B_{11}-B_{12}+3B_{44}}{5} \tag{4}$$

$$G_R = \frac{5(B_{11}-B_{12})B_{44}}{4B_{44}+3(B_{11}-B_{12})} \tag{5}$$

$$G_H = \frac{G_V+G_R}{2} \tag{6}$$

In the Voigt (Reuss) approximation, uniform strain (stress) is assumed throughout the polycrystal [Voigt 1928, Reuss 1929]. Hill has shown that the Voigt and Reuss averages are limits and suggested that the actual effective B and G elastic moduli can be approximated by the arithmetic mean of the two bounds [Hill 1952]. The Young (E) modulus and the Poisson's ratio (ν) are calculated with the expressions [Caracas 2010, Liu 2011]:

$$G_X = \frac{9B_XG_X}{3B_X+G_X} \tag{7}$$

$$\nu_X = \frac{1}{2}\left(\frac{3B_X-2G_X}{3B_X+G_X}\right) \tag{8}$$

where the subscript X refers to the symbols V, R, and H. In this work, we report the elastic moduli in the Hill approximation. We summarize in **Table III** all the values obtained for B_H, G_H and E_H in As_4O_6 and $As_4O_6{\cdot}2He$ at 0 GPa. Note that our calculated value for the bulk modulus in the Hill approximation is 9.8 (9.2) GPa for As_4O_6 ($As_4O_6{\cdot}2He$); which is in rather good agreement with the value of B_0= 7.6 (6.4) GPa obtained from our PBEsol structural calculations via a fit to a third-order Birch Murnaghan equation of state [Sans 2015, Sans 2016a] and with those of Birch-Murnaghan EoS fit to p(V) data computed within the PAW_PBE-D2

approach in Guńka (2015b). Furthermore, both values are comparable to experimental values of B_0= 7(2) GPa and 4(2) GPa obtained via a fit to a third-order Birch Murnaghan equation of state for As_4O_6 and As_4O_6·2He, respectively [Sans 2015, Sans 2016a]. Note that the bulk modulus of As_4O_6·2He at zero pressure was extrapolated from data above 3 GPa since this compound is not stable below this pressure.

The above results give us confidence about the correctness of our elastic constants calculations. With this subject in mind, we have compared the bulk modulus and shear modulus in both compounds, which is indicative of the difference between the elastic behavior of both compounds. In As_4O_6 the bulk modulus is larger than the shear modulus, while in As_4O_6·2He the contrary is observed. This means that As_4O_6 is more resistive to compression than to shear stresses while the contrary is observed in As_4O_6·2He.

Table III also includes the values of the Poisson's ratio (v_H), the ratio between the bulk and shear modulus, B_H/G_H, and the Zener elastic anisotropy factor A at 0 GPa for both compounds. The Poisson's ratio provides information about the characteristics of the bonding forces and chemical bonding. The value of the Poisson's ratio in the Hill approximation is v = 0.14 (0.08) in As_4O_6 (As_4O_6·2He). This value indicates that the interatomic bonding forces are predominantly non central (v < 0.25) and that directional intramolecular and intermolecular bonding is predominant at 0 GPa [Gibbs 2009, Brazhkin 2002, Greaves 2011].

The B_H/G_H ratio is a simple relationship given by Pugh [Pugh 1954], empirically linking the plastic properties of a material with its elastic moduli. According to the Pugh criterion, a high B_H/G_H ratio is associated with ductility, whereas a low ratio corresponds to brittleness. The critical value for the B_H/G_H ratio is around 1.75, which separates ductile and brittle materials. In our study, we have found values of B/G at 0 GPa below 1.75 for As_4O_6 and As_4O_6·2He. Therefore, both compounds are fragile at zero pressure, being As_4O_6·2He more fragile than As_4O_6.

One of the elastic properties of crystals with more importance for both engineering science and crystal physics is the elastic anisotropy, because it is highly correlated to the possibility of inducing microcraks in materials [Tvergaard 1988]. This anisotropy can be quantified with the Zener anisotropy factor A, which is defined as $A=2B_{44}/(B_{11}-B_{12})$. If A is equal to 1, no anisotropy exists. On the other hand, the more this parameter differs from 1 the more elastically anisotropic is the crystalline structure. The value of A for As_4O_6 is closer to 1 than for the case of As_4O_6·2He. Therefore, the latter is more elastically anisotropic than the former at 0 GPa.

Figures 8 and 9 show the pressure dependence of B, G, and E elastic moduli, ν Poisson's ratio, B/G ratio and Zener anisotropy, A, in As_4O_6 and As_4O_6·2He. It can be noted that the Hill bulk modulus, B_H, increases with pressure reaching a maximum value close to 115 GPa in both compounds at 20 GPa. Contrarily, the G_H and E_H moduli increase with pressure up to 9 GPa in As_4O_6 and decrease for larger pressures. This behavior is different to that of As_4O_6·2He where both G_H and E_H increase with pressure up to the maximum calculated pressure (35.5 GPa).

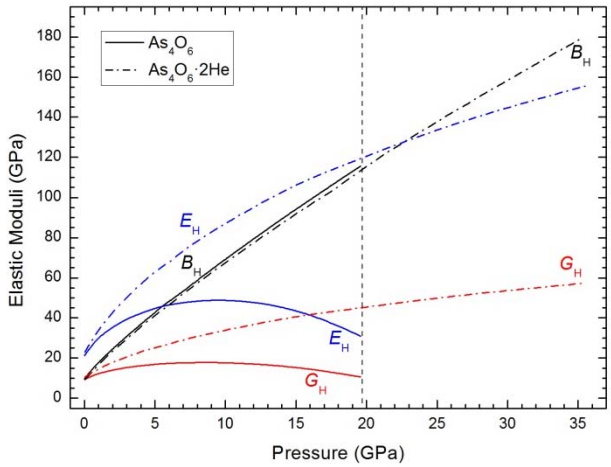

Figure 8. Pressure dependence of the elastic moduli B_H, G_H, and E_H in As_4O_6 and $As_4O_6{\cdot}2He$.

On the other hand, the Poisson's ratio shows a curious pressure dependence in both compounds. It strongly increases with pressure up to 2 GPa and then tends to saturate above this pressure. It reaches a value of 0.46 (0.32) at 20 GPa for As_4O_6 ($As_4O_6{\cdot}2He$). These values indicate an increment of the ductility and of the metallic behavior; i.e., the progressive loss of interatomic bond directionality, with increasing pressure in both compounds. It must be stressed that the approximation of the Poisson's ratio of As_4O_6 to 0.5 (superior limit of the Poisson's ratio) near 20 GPa is likely due to the tendency of As_4O_6 towards a mechanical instability [Greaves 2011]. Note that the *B/G* ratio, which is related to the Poisson's ratio [Greaves 2011], also increases with pressure in the two compounds; however the increase is moderate in $As_4O_6{\cdot}2He$ and abrupt in As_4O_6 above 10 GPa; thus suggesting the presence of a mechanical instability in this later compound. Finally, the Zener anisotropy factor also shows a quite different behavior in both compounds. It increases considerably in As_4O_6 especially above 10 GPa while it stays nearly constant (around 0.6) in $As_4O_6{\cdot}2He$. Again, these results indicate that the elastic anisotropy strongly increases in As_4O_6 with pressure, but it remains constant in $As_4O_6{\cdot}2He$. Therefore, the strong increase of the elastic anisotropy in As_4O_6 with pressure could be also understood as a signal of a mechanical instability in arsenolite at high pressure.

One of the most common elastic properties and less easy to handle is hardness, which is a property generally related to both the elastic and plastic properties of a material. Hardness is an unusual physical property because it is not an intrinsic materials property, but the result of a defined measurement procedure susceptible to precise definitions in terms of fundamental units of mass, length, and time. In practice, hardness is measured by the size of the indentation made on a specimen by

a load of a specified shape when a force is applied during a certain time. In this way, there are three principal standard methods for expressing the relationship between hardness and the size of the indentation, these being Brinell, Rockwell, and Vickers. The Vickers hardness, H_v, can be calculated by the formula proposed by Tian et al. [Tian 2012]:

$$H_v = 0.92(G/B)^{1.137}G^{0.708} \quad (9)$$

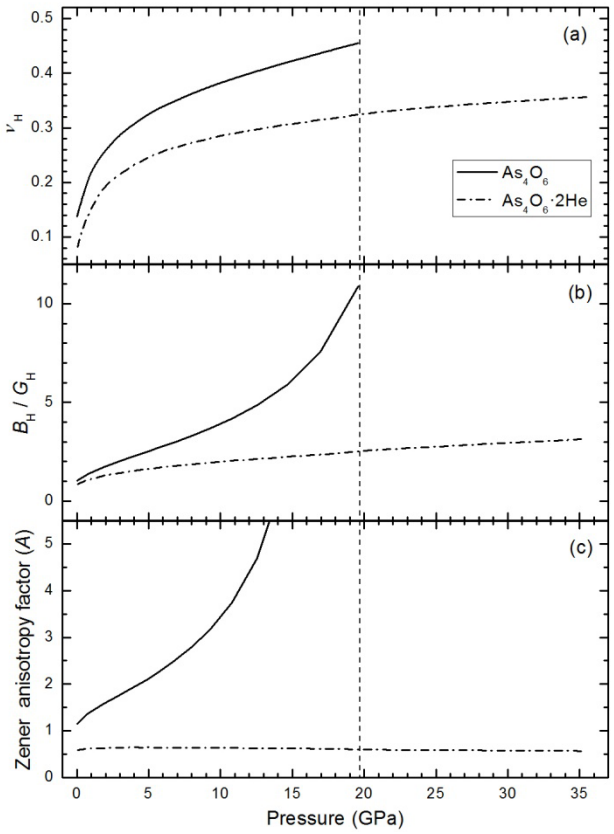

Figure 9. Pressure dependence of the Poisson's ratio (ν_H), B_H/G_H ratio, and Zener anisotropy factor (A), in As_4O_6 and As_4O_6·2He.

We used this formula as it eliminates the possibility of unrealistic negative hardness. The values of H_v for As_4O_6 and As_4O_6·2He at 0 GPa are included in **Table III**. As observed, As_4O_6·2He is harder than As_4O_6 and both have values of H_v are approximately between 4-6 GPa at 0 GPa when using elastic moduli in the Hill

approximation. Since H_v at 0 GPa is smaller than 10 GPa, both compounds can be classified as relatively soft materials.

Figure 10 shows the pressure evolution of the Vickers hardness with pressure. It is observed that H_v decreases as pressure increases for both oxides. This is related to the fact that the B/G ratio increases with pressure. In this way, both compounds become softer as pressure increases in good agreement with the increase of their ductility (B/G ratio) as stated above. We note that H_v for $As_4O_6 \cdot 2He$ decreases notably with pressure approaching 0 GPa at 20 GPa.

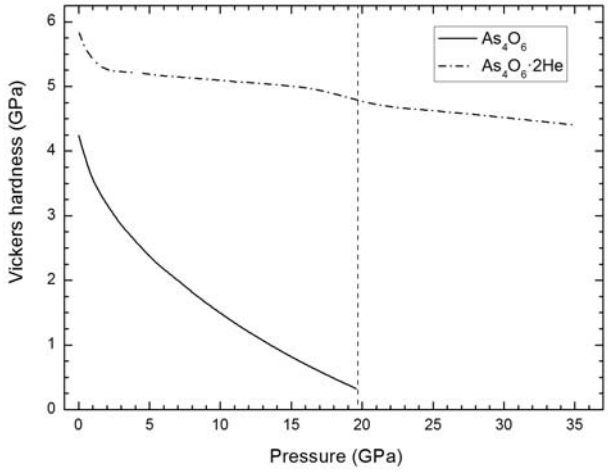

Figure 10. Evolution with pressure of the Vickers hardness in As_4O_6 and $As_4O_6 \cdot 2He$.

Finally, one elastic property which is fundamental for Earth Sciences in order to interpret seismic waves is the average sound velocity, v_m [Poirier 2000]. In polycrystalline materials v_m is given by [Anderson 1963]:

$$v_m = \left[\frac{1}{3}\left(\frac{2}{v_{trans}^3} + \frac{1}{v_{lon}^3}\right)\right]^{-1/3} \tag{10}$$

where v_{trans} and v_{lon} are the transverse and longitudinal elastic wave velocities of the polycrystalline material which are given by:

$$v_{lon} = \left(\frac{B+\frac{4}{3}G}{\rho}\right)^{1/2} \tag{11}$$

$$v_{trans} = \left(\frac{G}{\rho}\right)^{1/2} \tag{12}$$

where *B* and *G* are the elastic moduli and ρ the density. Values of the density and wave velocities v_m, v_{lon} and v_{trans} at 0 GPa are given for both oxides in **Table III**. Wave velocities are greater for $As_4O_6 \cdot 2He$ than for As_4O_6 because of the higher value of the shear modulus *G* in the former than in the later and the slightly smaller density of the former than in the later.

Figure 11 reports the evolution with pressure of the elastic wave velocities for both oxides. Using elastic moduli in the Hill approximation, the calculated v_{lon} increases with pressure reaching a value larger than 4725 m/s (5580 m/s) at 20 GPa in As_4O_6 ($As_4O_6 \cdot 2He$). A similar behavior is observed for velocities v_{trans} and v_m in $As_4O_6 \cdot 2He$. However, the corresponding velocities v_{trans} and v_m increase in As_4O_6 reaching a maximum value around 6 GPa and decrease above this pressure.

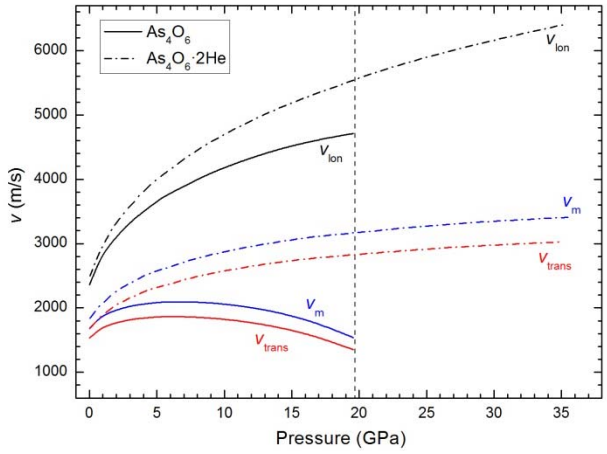

Figure 11. Pressure dependence of the longitudinal (v_{lon}), transverse (v_{trans}), and average (v_m) elastic wave velocity in As_4O_6 and $As_4O_6 \cdot 2He$.

In order to finish this section, where different magnitudes derived from the elastic constants have been obtained and analysed, we refer the reader to the supplementary material in order to get information on a few thermodynamic properties (Debye temperature and minimum thermal conductivity) obtained for As_4O_6 and $As_4O_6 \cdot 2He$.

D. Mechanical stability

To finish this work, we study the mechanical stability of the cubic structure in As_4O_6 and $As_4O_6 \cdot 2He$ at HP. For that purpose, we make use of the elastic stiffness coefficients reported in the previous section. The mechanical stability of a crystal at zero pressure can be studied with the Born stability criteria [Born 1954]. However, the study of the mechanical stability of a crystal at HP requires the generalization of the Born stability criteria to the case when an external load is applied [Wallace 1967,

Grimvall 2012, Wang 2012]. These generalized stability criteria for cubic crystals with three independent elastic constants are given by the following conditions:

$$M_1 = B_{11} + 2B_{12} > 0 \quad (13)$$

$$M_2 = B_{11} - B_{12} > 0 \quad (14)$$

$$M_3 = B_{44} > 0 \quad (15)$$

where B_{11}, B_{12}, and B_{44} are the elastic stiffness coefficients at the considered pressure. These generalized stability criteria are plotted in **Fig. 12**. It is found that **Eq. (14)**, called the Born instability [Grimvall 2012], is violated at 19.7 GPa in As_4O_6; however, none of the three generalized stability criteria is violated in As_4O_6·2He up to 35.5 GPa. Therefore, our theoretical study of the mechanical stability suggests that the cubic structure of As_4O_6 becomes mechanically unstable beyond 19.7 GPa, in good agreement with the observation of PIA in the pressure range between 15 and 20 GPa depending on the PTM used [Sans 2015, Sans 2016a, Grzechnik 1999, Soignard 2008]. On the other hand, our calculations show that there is no mechanical instability of As_4O_6·2He up to 35.5 GPa, in good agreement with the observation of the cubic phase of this new compound up to 30 GPa [Sans 2015, Sans 2016a]. Finally, it must be noted that our theoretical results on the mechanical instability of As_4O_6 above 19.7 GPa do not agree with results on single crystals of As_4O_6 pressurized with He, where He partially entered into the pores of As_4O_6 [Guńka 2015b].

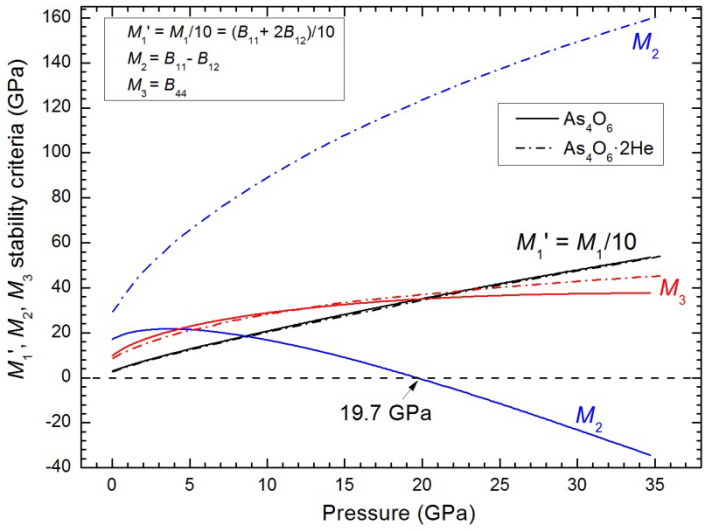

Figure 12. General stability criteria in As_4O_6 and As_4O_6·2He. The pressure at which As_4O_6 becomes mechanically unstable is indicated.

V. CONCLUSIONS

We have experimentally and theoretically studied the lattice dynamics of As_4O_6 and $As_4O_6 \cdot 2He$ at HP and found a different HP behavior in the Raman-active modes of both compounds which support the inclusion of He into 16d sites of the arsenolite structure above 2-3 GPa. On the other hand, we have studied the dynamical stability of the cubic structure of both compounds and it has been found that As_4O_6 and $As_4O_6 \cdot 2He$ are dynamically stable at least up to 34.7 and 35.5 GPa, respectively.

Additionally, we have theoretically studied the elastic and thermodynamic behavior of both compounds at HP. It has been found that most of the properties of both compounds are similar at low pressures. The elastic constants and the elastic stiffness coefficients increase with increasing pressure in all the pressure range; however, the pressure coefficients of the elastic stiffness coefficients B_{11} and B_{12} are quite different in both compounds, thus resulting in a completely different HP behavior of shear and Young moduli, *B/G* ratio, Poisson's ratio, Vickers hardness and Zener anisotropy in both compounds. In this context, both compounds are more resistive to volume compression than to shear deformation ($B > G$) at all pressures. The average elastic wave velocity, Debye temperature and minimum thermal conductivity of both compounds are also similar at low pressures, but show a different behavior at HP. From the behavior of the elastic stiffness coefficients at HP we have studied the mechanical stability of the cubic structure at HP in both compounds and have found that the cubic structure becomes mechanically unstable at 19.7 GPa in As_4O_6, while there is no mechanical instability in $As_4O_6 \cdot 2He$ at least up to 35.5 GPa. These results are in good agreement with experiments which show PIA in As_4O_6 above 15-20 GPa (depending on the PTM used) and with the experimental observation of the cubic structure of $As_4O_6 \cdot 2He$ up to 30 GPa without signs of PIA.

Supplementary material

See supplementary material for IR-active modes and thermodynamic properties in As_4O_6 and $As_4O_6 \cdot 2He$ along with the Raman scattering spectra of arsenolite at selected pressures without any PTM.

Acknowledgments

This study is supported by the Spanish Ministerio de Economía y Competitividad under projects MAT2013-46649-C4-2-P/3-P and MAT2015-71070-REDC. A.M. and P.R-H. acknowledge computing time provided by Red Española de Supercomputación (RES) and MALTA-Cluster.

References

[Anderson 1963] O. L. Anderson. A simplified method for calculating the Debye temperature from elastic constants. *J. Phys. Chem. Solids*. **1963**, *24*, 909.

[Ballirano 2002] P. Ballirano and A. Maras. Refinement of the crystal structure of arsenolite, AS_2O_3. *Z. Kristallogr. NCS*. **2002**, *217*, 177.

[Beattie 1970] I.R. Beattie, K.M.S. Livingston, G. A. Ozin, and D.J. Reynolds. Single-crystal Raman spectra of arsenolite (As_4O_6) and senarmonite (Sb_4O_6). The gas-phase Raman spectra of P_4O_6, P_4O_{10}, and As_4O_6. *J. Chem. soc. A*. **1970**, *449*.

[Beckstein 2001] O. Beckstein, J. E. Klepeis, G. L. W. Hart, and O. Pankratov. First-principles elastic constants and electronic structure of α-Pt_2Si and PtSi. *Phys. Rev. B*. **2001**, *63*, 134112.

[Blochl 1994] P. E. Blochl. Projector augmented-wave method. *Phys. Rev. B*. **1994**, *50*, 17953.

[Born 1940] M. Born. On the stability of crystal lattices. *I. Proc. Cambridge Philos. Soc.* **1940**, *36*, 160.

[Born 1954] M. Born and K. Huang. *Dynamical Theory of Crystal Lattices* (Oxford University Press, **1954**) p. 140.

[Brauer 1963] G. Brauer. *Handbook of Preparative Inorganic Chemistry* (Academic Press, **1963**).

[Brazhkin 2002] V. V. Brazhkin, A. G. Lyapin, and R. J. Hemley. Harder than diamond: Dreams and reality. *Philos. Mag. A*. **2002**, *82*, 231.

[Brumbach 1972] S.B. Brumbach and G.M. Rosenblatt. In-cavity Laser Raman Spectroscopy of Vapors at Elevated Temperatures. As_4 and As_4O_6. *J. Chem. Phys*. **1972**, *56*, 3110.

[Caracas 2010] R. Caracas and T. B. Ballaran. Elasticity of (K,Na)·$AlSi_3O_8$ hollandite from lattice dynamics calculations. *Phys. Earth Planet. Int*. **2010**, *181*, 21.

[Chetty 1989] N. Chetty, A. Muñoz, and R. M. Martin. First-principles calculation of the elastic constants of AlAs. *Phys. Rev. B*. **1989**, *40*, 11934.

[Clayton 2010] J.D. Clayton. *Nonlinear Mechanics of Crystals, Solid Mechanics and Its Applications* (Springer, New York, **2010**) p. 177.

[Gibbs 2009] G. V. Gibbs, A. F. Wallace, D. F. Cox, P. M. Dove, R. T. Downs, N. L. Ross, and K. M. Rosso. Role of directed van der Waals bonded interactions in the determination of the structures of molecular arsenate solids. *J. Phys. Chem. A*. **2009**, *113*, 736.

[Gielen 2005] M. Gielen and E. R. Tiekink. *Metallotherapeutic Drugs and Metal-Based Diagnostic Agents.* (John Wiley & Sons, **2005**) p. 298.

[Gilliam 2003] S. J. Gilliam, C. N. Merrow, S. J. Kirkby, J. O. Jensen, D. Zeroka, and A. Banerjee. Raman spectroscopy of arsenolite: crystalline cubic As_4O_6. *J. Solid State Chem*. **2003**, *173*, 54.

[Gomis 2014] O. Gomis, D. Santamaría-Pérez, J. Ruiz-Fuertes, J. A. Sans, R. Vilaplana, H. M. Ortiz, B. García-Domene, F. J. Manjón, D. Errandonea, P. Rodríguez-Hernández, A. Muñoz, and M. Mollar. High-Pressure Structural and Elastic Properties of Tl_2O_3. *J. App. Phys.* **2014**, *116*, 133521.

[Greaves 2011] G. N. Greaves, A. L. Greer, R. S. Lakes, and T. Rouxel. Poisson's ratio and modern materials. *Nat. Mater*. **2011**, *10*, 823.

[Grimvall 2012] G. Grimvall, B. Magyari-Köpe, V. Ozolinš, and K. A. Persson. Lattice instabilities in metallic elements. *Rev. Mod. Phys*. **2012**, *84*, 945.

[Grund 2005] S. C. Grund, K. Hanusch, and H. Wolf. "Arsenic and Arsenic Compounds" in *Ullmann's Encyclopedia of Industrial Chemistry* (Wiley-VCH, **2005**). doi:10.1002/14356007.a03_113.pub2

[Grzechnik 1999] A. Grzechnik. Compressibility and Vibrational Modes in Solid As_4O_6. *J. Solid State Chem.* **1999**, *144*, 416.

[Guńka 2015a] P. A. Guńka, Z. Gontarz, and J. Zachara. Spatial dispersion of lone electron pairs?--experimental charge density of cubic arsenic(III) oxide. *Phys. Chem. Chem. Phys*. **2015**, *17*, 11020.

[Guńka 2015b] P. A. Guńka, K. F. Dziubek, A. Gladysiak, M. Dranka, J. Piechota, M. Hanfland, A. Katrusiak, and J. Zachara. Compressed Arsenolite As_4O_6 and Its Helium Clathrate $As_4O_6{\cdot}2He$. *Cryst. Growth Des*. **2015**, *15*, 3740.

[Hill 1952] R. Hill. The Elastic Behaviour of a Crystalline Aggregate. *Proc. Phys. Soc. London A*. **1952**, *65*, 349.

[Hohenberg 1964] P. Hohenberg and W. Kohn. Inhomogeneous Electron Gas. *Phys. Rev*. **1964**, *136*, 3864.

[Jensen 2003] J. O. Jensen, S. J. Gilliam, A. Banerjee, D. Zeroka, S. J. Kirkby, and C. N. Merrow. A theoretical study of As_4O_6: vibrational analysis, infrared and Raman spectra. *J. Mol. Str.: THEOCHEM*. **2003**, *664-665*, 145.

[Karki 2001] B. B. Karki, L. Stixrude, and R. M. Wentzcovitch. High-pressure elastic properties of major materials of Earth's mantle from first principles. *Reviews of Geophysics*. **2001**, *39*, 507.

[Krasil'nikov 2014] O. M. Krasil'nikov, M. P. Belov, A. V. Lugovskoy, I. Yu. Mosyagin, and Yu. Kh. Vekilov. Elastic properties, lattice dynamics and structural transitions in molybdenum at high pressures. *Computational Materials Science*. **2014**, *81*, 313.

[Kresse 1993] G. Kresse and J. Hafner. Ab initio molecular dynamics for liquid metals. *Phys. Rev. B*. **1993**, *47*, 558.

[Kresse 1994] G. Kresse and J. Hafner. Ab initio molecular-dynamics simulation of the liquid-metal–amorphous-semiconductor transition in germanium. *Phys. Rev. B*. **1994**, *49*, 14251.

[Kresse 1996a] G. Kresse and J. Furthmüller. Efficiency of ab-initio total energy calculations for metals and semiconductors using a plane-wave basis set. *Comput. Mater. Sci*. **1996**, *6*, 15.

[Kresse 1996b] G. Kresse and J. Furthmüller. Efficient iterative schemes for ab initio total-energy calculations using a plane-wave basis set. *Phys. Rev. B*. **1996**, *54*, 11169.

[Kroumova 2003] E. Kroumova, M.I. Aroyo, J.M. Perez-Mato, A. Kirov, C. Capillas, S. Ivantchev, and H. Wondratschek. Bilbao Crystallographic Server: Useful Databases and Tools for Phase-Transition Studies. *Phase Trans*. **2003**, *76*, 155.

[Le Page 2002] Y. Le Page and P. Saxe. Symmetry-general least-squares extraction of elastic data for strained materials from ab initio calculations of stress. *Phys. Rev. B*. **2002**, *65*, 104104.

[Liu 2008] J. Liu, Y. Lu, Q. Wu, R. A. Goyer, and M. P. Waalkes. Mineral Arsenicals in Traditional Medicines: Orpiment, Realgar, and Arsenolite. *J. Pharmacol. Exp. Therap*. **2008**, *326*, 363.

[Liu 2011] Q. J. Liu, Z. T. Liu, and L. P. Feng. First-Principles Calculations of Structural, Elastic and Electronic Properties of Tetragonal HfO_2 under Pressure. *Commun. Theor. Phys*. **2011**, *56*, 779.

[Lockwood 2000] D.J. Lockwood. Raman Spectroscopy of Oxides of GaAs Formed in Solution. *J. Sol. Chem*. **2000**, *29*, 1039.

[Mao 1986] M. K. Mao, J. Xu, and P. M. Bell. Calibration of the Ruby Pressure Gauge to 800 kbar under Quasi-Hydrostatic Conditions. *J. Geophys. Res*. **1986**, *91*, 4673.

[Nye 1957] J. F. Nye. *Physical Properties of Crystals. Their Representation by Tensor and Matrices* (Oxford University Press, **1957**).

[Parlinski 1997] K. Parlinski, Z. Q. Li, and Y. Kawazoe. First-Principles Determination of the Soft Mode in Cubic ZrO_2. *Phys. Rev. Lett*. **1997**, *78*, 4063.

[Perdew 2008] J. P. Perdew, A. Ruzsinszky, G. I. Csonka, O. A. Vydrow, G. E. Scuseria, L. A. Constantin, X. Zhou, and K. Burke. Restoring the Density-Gradient Expansion for Exchange in Solids and Surfaces. *Phys. Rev. Lett*. **2008**, *100*, 136406.

[Pertlik 1978a] F. Pertlik. Strukturverfeinerung von Kubischem As_2O_3 (Arsenolith) mit Einkristalldaten. *Czech. J. Phys. B*. **1978**, *28*, 170.

[Poirier 2000] J. P. Poirier. *Introduction to the Physics of the Earth's Interior* (Cambridge University Press, **2000**).

[Pugh 1954] S. F. Pugh. XCII. Relations between the elastic moduli and the plastic properties of polycrystalline pure metals. *Philos. Mag*. **1954**, *45*, 823.

[Reuss 1929] A. Reuss. Berechnung der Fließgrenze von Mischkristallen auf Grund der Plastizitätsbedingung für Einkristalle. *Z. Angew. Math. Mech*. **1929**, *9*, 49.

[Sans 2015] J. A. Sans, F. J. Manjón, C. Popescu, V. P. Cuenca-Gotor, O. Gomis, A. Muñoz, P. Rodríguez-Hernández, J. Pellicer- Porres, A. L. J. Pereira, D. Santamaría-Pérez, and A. Segura. Helium ordered trapping in arsenolite under compression: Synthesis of $He_2As_4O_6$. **2015**, arXiv:1502.04279.

[Sans 2016a] J.A. Sans, F.J. Manjón, C. Popescu, V.P. Cuenca-Gotor, O. Gomis, A. Muñoz, P. Rodríguez-Hernández, J. Contreras-García, J. Pellicer-Porres, A.L.J. Pereira, D. Santamaría-Pérez, and A. Segura. Ordered helium trapping and bonding in compressed arsenolite: Synthesis of $As_4O_6 \cdot 2He$. *Phys. Rev. B*. **2016**, *93*, 054102.

[Sans 2016b] J.A. Sans, F.J. Manjón, C. Popescu, A. Muñoz, P. Rodríguez-Hernández, J.L. Jordá, and F. Rey. Arsenolite: a quasi-hydrostatic solid pressure-transmitting medium. *J. Phys: Condens. Matter*. **2016**, *28*, 475403.

[Soignard 2008] E. Soignard, S. A. Amin, Q. Mei, C. J. Benmore, and J. L. Yarger. High-Pressure Behavior of As_2O_3: Amorphous-Amorphous and Crystalline-Amorphous Transitions. *Phys. Rev. B*. **2008**, *77*, 144113.

[Szymansky 1968] H.A. Szymansky, L. Marabella, J. Hoke, and J. Harter. Infrared and Raman Studies of Arsenic Compounds. *Appl. Spectros*. **1968**, *22*, 297.

[Tian 2012] Y. Tian, B. Xu, and Z. Zhao. Microscopic theory of hardness and design of novel superhard crystals. *Int. J. Refract. Met. H*. **2012**, *33*, 93.

[Tvergaard 1988] V. Tvergaard and J. W. Hutchinson. Microcracking in Ceramics Induced by Thermal Expansion or Elastic Anisotropy. *J. Am. Ceram. Soc*. **1988**, *71*, 157.

[Voigt 1928] W. Voigt. *Lehrbuch der Kristallphysik* (B. G. Teubner, Leipzig, Germany, **1928**).

[Wallace 1967] D.C. Wallace. Thermoelasticity of Stressed Materials and Comparison of Various Elastic Constants. *Phys. Rev*. **1967**, *162*, 776.

[Wallace 1970] D. C. Wallace, "Thermoelastic theory of stressed crystals and higher-order elastic constants," in *Solid State Physics*, edited by F. S. Henry Ehrenreich, D. Turnbull, and F. Seitz (Academic Press, **1970**), vol. *25*, pp. 301–404.

[Wang 1993] J. Wang, S. Yip, S. R. Phillpot, and D. Wolf. Crystal instabilities at finite strain. *Phys. Rev. Lett*. **1993**, *71*, 4182.

[Wang 1995] J. Wang, J. Li, S. Yip, S. Phillpot, and D. Wolf. Mechanical instabilities of homogeneous crystals. *Phys. Rev. B*. **1995**, *52*, 12627.

[Wang 2012] H. Wang and M. Li. Unifying the criteria of elastic stability of solids. *J. Phys. Condens. Matter*. **2012**, *24*, 245402.

[Zhou 1996] Z. Zhou and B. Joós. Stability criteria for homogeneously stressed materials and the calculation of elastic constants. *Phys. Rev. B*. **1996**, *54*, 3841.

SUPPLEMENTARY MATERIAL

Vibrational and elastic properties of As_4O_6 and $As_4O_6 \cdot 2He$ at high pressures: study of dynamical and mechanical stability

V.P. Cuenca-Gotor, O. Gomis, J.A. Sans, F. J. Manjón,
P. Rodríguez-Hernández, and A. Muñoz

A. Lattice dynamics

A progressive shift of the Raman-active mode frequencies of all peaks of the cubic structure with increasing pressure is observed in As_4O_6 compressed without any PTM. Absence of new peaks at high pressure clearly indicates that no phase transition occurs along the pressure range studied. Many Raman modes undergo a progressive asymmetric broadening with increasing pressure. This broadening is likely caused by the increase of intermolecular interactions; i.e., the increase of interactions among As_4O_6 cages, which finally results in the onset of PIA above 15 GPa.

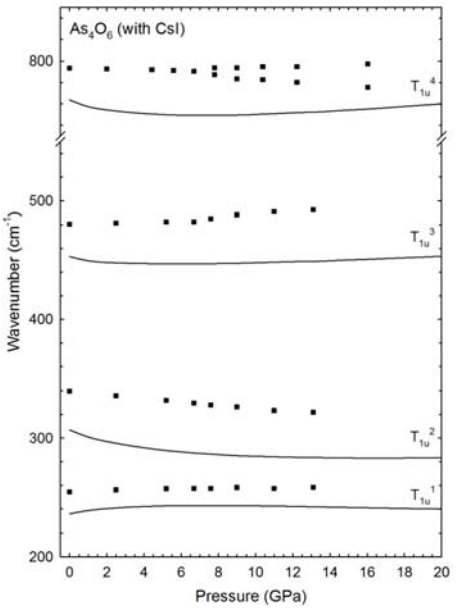

Figure S1. Experimental and theoretical pressure dependence of the IR-active modes in As_4O_6. Experimental data measured using CsI as a PTM are taken from Grzechnik (1999).

Table SI. Theoretical and experimental zero-pressure frequencies and pressure coefficients of IR-active modes in As_4O_6 at 0 GPa. Experimental data are taken from Grzechnik (1999).

	Ab initio calculations		Experimental	
Mode (Sym)	ω_0 (cm^{-1})	$\frac{\partial\omega}{\partial P}$ $\left(\frac{cm^{-1}}{GPa}\right)$	ω_0 (cm^{-1})	$\frac{\partial\omega}{\partial P}$ $\left(\frac{cm^{-1}}{GPa}\right)$
T_{1u}^{1} (IR)	236.0	2.7	254.5	0.8
T_{1u}^{2} (IR)	306.7	-5.7	339.8	-1.5
T_{1u}^{3} (IR)	453.1	-3.8	480.4	0.1
T_{1u}^{4} (IR)	763.5	-6.6	793.4	-0.2

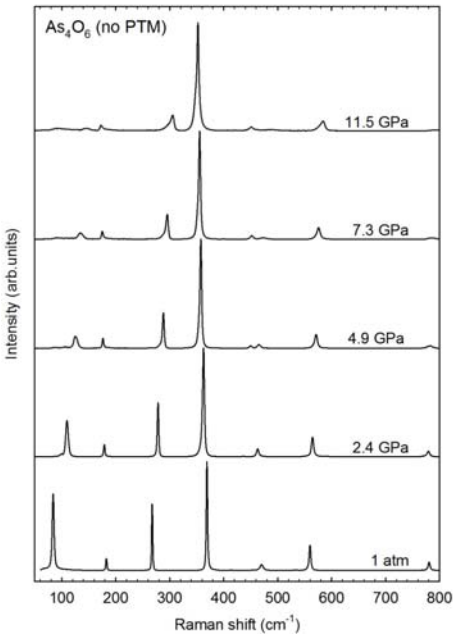

Figure S2. Raman scattering spectra of arsenolite at selected pressures without any PTM. Raman spectra are vertically shifted for the sake of clarity.

There are two additional IR-active modes in $As_4O_6 \cdot 2He$ than in As_4O_6. The two extra modes are located between the two lowermost IR-active modes of As_4O_6 and

have a much larger pressure coefficient than IR-active modes of As_4O_6 thus leading to anticrossings with the mode above 300 cm-1.

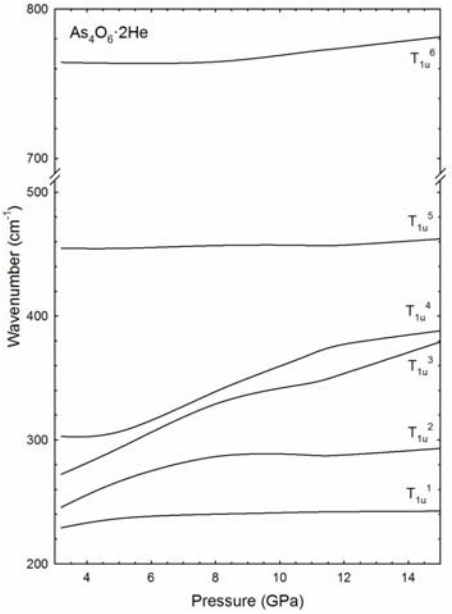

Figure S3. Theoretical pressure dependence of the IR-active modes in As_4O_6·2He.

Table SII. Theoretical frequencies and pressure coefficients of IR-active modes in As_4O_6·2He at 3 GPa.

	Ab initio calculations	
Mode (Sym)	ω_0 (cm^{-1})	$\frac{\partial\omega}{\partial P}$ $\left(\frac{cm^{-1}}{GPa}\right)$
T_{1u}^{1} (IR)	230.0	3.3
T_{1u}^{2} (IR)	247.5	11.2
T_{1u}^{3} (IR)	271.6	12.5
T_{1u}^{4} (IR)	300.3	0.3
T_{1u}^{5} (IR)	455.1	-0.7
T_{1u}^{6} (IR)	763.8	-1.1

B. Thermodynamic properties

The Debye temperature is a fundamental parameter that correlates with many physical properties of solids, such as specific heat, elastic constants, and melting temperature. One of the standard methods to calculate the Debye temperature, θ_D, is from elastic constant data using the semi-empirical formula [Anderson 1963]:

$$\theta_D = \frac{h}{k_B}\left[\frac{3n}{4\pi}\left(\frac{N_A\rho}{M}\right)\right]^{1/3} v_m$$

where h is the Planck's constant, k_B is the Boltzmann's constant, n is the number of atoms in the molecule, N_A is the Avogadro's number, ρ is the density, M is the molecular weight, and v_m is the averaged sound velocity. As reported in **Table SIII**, the values of θ_D at 0 GPa using the Hill approximation are 196.2 K (222.7 K) in As_4O_6 (As_4O_6·2He). We note that the Debye temperature in As_4O_6·2He is slightly greater than that of As_4O_6. **Figure S4(a)** reports the evolution with pressure of the Debye temperature, θ_D, for both oxides. It is observed that θ_D follows a similar dependence than v_m with increasing pressure; i.e., increases at low pressures in both oxides and decreases above 8 GPa in As_4O_6 while it increases in As_4O_6·2He at least up to 35 GPa.

The thermal conductivity is the property of a material that indicates its ability to conduct heat. In order to estimate the theoretical minimum of the thermal conductivity, we have used the following expression [Clarke 2003]:

$$\kappa_{\min} = k_B v_m \left(\frac{M}{n\rho N_A}\right)^{-2/3}$$

The values of κ_{min} in As_4O_6 (As_4O_6·2He) at 0 GPa using the Hill approximation are 0.36 (0.42) W m^{-1} K^{-1} [see **Table SIII**]. Therefore, both oxides are low κ materials [Levi 2004]. **Figure S4(b)** reports the evolution with pressure of the minimum thermal conductivity, κ_{min}, for both oxides. As in the case of θ_D, κ_{min} first increases with pressure and latter it decreases with pressure because of the decreasing of v_m with pressure for As_4O_6, while κ_{min} increases with pressure up to 35 GPa in As_4O_6·2He. On the other hand, if we use the simplified formula for κ_{min} that considers $v_m = 0.87\sqrt{E/\rho}$ [Clarke 2003], the decreasing of κ_{min} with pressure in As_4O_6 can be explained by the decreasing of the tensile stiffness of As_4O_6 as pressure increases above 9 GPa.

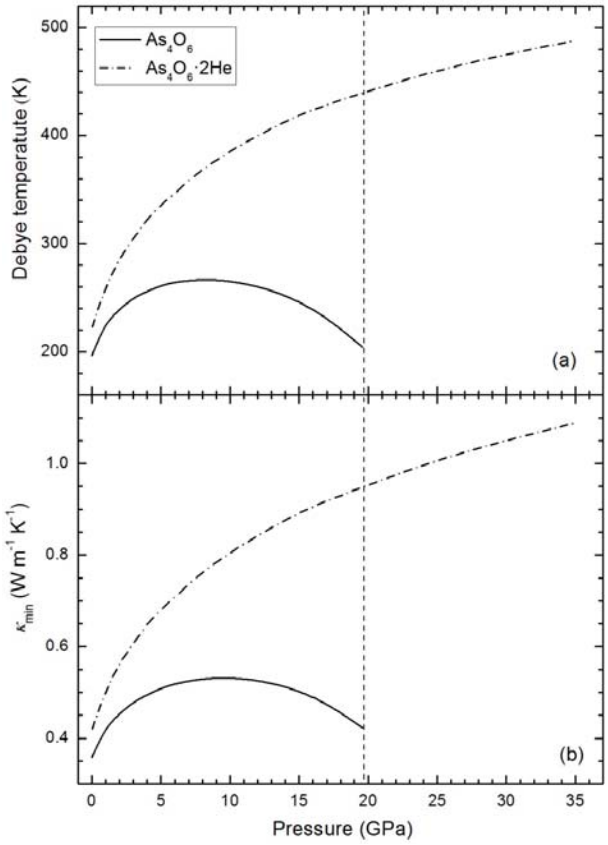

Figure S4. Evolution with pressure of the theoretical Debye temperature (a) and theoretical minimum thermal conductivity, κ_{min}, (b) in As_4O_6 and $As_4O_6 \cdot 2He$.

Table SIII. Debye temperature (θ_D in K), and minimum thermal conductivity (κ_{min} in W m^{-1} K^{-1}) in As_4O_6 and $As_4O_6 \cdot 2He$ at 0 GPa. Data are given in the Hill approximation.

	As_4O_6	$As_4O_6 \cdot 2He$
θ_D	196.2	222.7
κ_{min}	0.36	0.42

References

[Anderson 1963] O. L. Anderson. A simplified method for calculating the Debye temperature from elastic constants. *J. Phys. Chem. Solids*. **1963**, *24*, 909-917.

[Clarke 2003] D. R. Clarke. Materials selection guidelines for low thermal conductivity thermal barrier coatings. *Surf. Coat. Technol*. **2003**, *163*, 67-74.

[Grzechnik 1999] A. Grzechnik. Compressibility and Vibrational Modes in Solid As_4O_6. *J. Solid State Chem.* **1999**, *144*, 416.

[Levi 2004] C. G. Levi. Emerging materials and processes for thermal barrier systems. *Curr. Opin. Solid State Mater. Sci*. **2004**, *8*, 77-91.

AIRAPT IOP Publishing
IOP Conf. Series: Journal of Physics: Conf. Series **950** (2017) 042018 doi:10.1088/1742-6596/950/4/042018

Study of the orpiment and anorpiment phases of As_2S_3 under pressure

S Radescu[1], A Mujica[1], P Rodríguez Hernández[1], A Muñoz[1], J Ibáñez[2], J A Sans[3], V P Cuenca-Gotor[3] and F J Manjón[3]

[1] Departamento de Física and Instituto Universitario de Materiales y Nanotecnología, MALTA Consolider Team, Universidad de La Laguna, La Laguna 38200, Tenerife, Spain
[2] Consejo Superior de Investigaciones Científicas, Instituto Jaume Almera, Barcelona 08028, Spain
[3] Instituto de Diseño para la Fabricación y Producción Automatizada, and MALTA Consolider Team, Universitat Politècnica de València, Camí de Vera s/n, 46022 València, Spain

E-mail: sradescu@ull.es

Abstract. In this work we study the pressure behaviour of the orpiment (monoclinic) and anorpiment (triclinic) layered structures of As_2S_3 by means of *ab initio* calculations performed within the density functional theory, as part of an ongoing theoretical and experimental joint effort to provide a comprehensive picture of the bonding of this interesting material and the evolution of its structural, electronic, and vibrational properties under pressure.

1. Introduction

Arsenic sulfide binary compounds with different stoichiometries have been researched in the past following interest in their optical, electronic, and structural properties, and in particular As_2S_3 has been found to be an excellent glass former at high temperatures, with some significant properties [1-5]. Under normal conditions, the stable phase of As_2S_3 is a semiconductor named orpiment with a crystalline layered structure in which each atom of As is surrounded by three atoms of S whereas each atom of S is surrounded by two atoms of As. Despite efforts to synthesize new polymorphs of this material no other crystalline metastable phases at normal conditions could be artificially produced in laboratories for a long time. Quite recently however, a low symmetry (triclinic) new phase of As_2S_3 named anorpiment has been naturally discovered analyzing the mineral specimens of an old peruvian mine [3]. The structure of this anorpiment phase is similar to that of the long known orpiment phase in that it is made of covalently bonded layers of As and Se atoms with a similar coordination (though the interlayer pattern is not exactly the same) arranged in a different stacking sequence, with interlayer van der Waals forces playing a significant role in the structural properties. In this work we study the orpiment and anorpiment phases of As_2S_3 theoretically (within the first-principles framework of the density functional theory) as part of an ongoing theoretical and experimental joint effort to provide a comprehensive picture of the bonding of this interesting material and the evolution of its structural, electronic, and vibrational properties under pressure.

Study of the orpiment and anorpiment phases of As_2S_3 under pressure

S. Radescu,[1] A. Mujica,[1] P. Rodríguez-Hernández,[1] A. Muñoz,[1] J. Ibáñez,[2] J. A. Sans,[3] V. P. Cuenca-Gotor,[3] and F. J. Manjón[3]

[1] *Departamento de Física, Instituto de Materiales y Nanotecnología, MALTA Consolider Team, Universidad de La Laguna, 38205 Tenerife, Spain*

[2] *Consejo Superior de Investigaciones Científicas, Instituto Jaume Almera, 08028, Barcelona, Spain*

[3] *Instituto de Diseño para la Fabricación y Producción Automatizada, MALTA Consolider Team, Universitat Politècnica de València, 46022 València, Spain*

Abstract

In this work we study the pressure behaviour of the orpiment (monoclinic) and anorpiment (triclinic) layered structures of As_2S_3 by means of *ab initio* calculations performed within the density functional theory, as part of an ongoing theoretical and experimental joint effort to provide a comprehensive picture of the bonding of this interesting material and the evolution of its structural, electronic, and vibrational properties under pressure.

I. INTRODUCTION

Arsenic sulfide binary compounds with different stoichiometries have been researched in the past following interest in their optical, electronic, and structural properties, and in particular As_2S_3 has been found to be an excellent glass former at high temperatures, with some significant properties [Brazhkin 2010, Gibbs 2010, Kampf 2011, Bolotina 2013a, Bolotina 2013b]. Under normal conditions, the stable phase of As_2S_3 is a semiconductor named orpiment with a crystalline layered structure in which each atom of As is surrounded by three atoms of S whereas each atom of S is surrounded by two atoms of As. Despite efforts to synthesize new polymorphs of this material no other crystalline metastable phases at normal conditions could be artificially produced in laboratories for a long time. Quite recently however, a low symmetry (triclinic) new phase of As_2S_3 named anorpiment has been naturally discovered analyzing the mineral specimens of an old peruvian mine [Kampf 2011]. The structure of this anorpiment phase is similar to that of the long known orpiment phase in that it is made of covalently bonded layers of As and S atoms with a similar coordination (though the interlayer pattern is not exactly the same) arranged in a different stacking sequence, with interlayer van der Waals forces playing a significant role in the structural properties. In this work we study the orpiment and anorpiment phases of As_2S_3 theoretically (within the first-principles framework of the density functional theory) as part of an ongoing theoretical and experimental joint effort to provide a comprehensive picture of the

bonding of this interesting material and the evolution of its structural, electronic, and vibrational properties under pressure.

II. DETAILS OF THE CALCULATIONS

All the calculations were done within the first-principles theoretical framework of the density functional theory (DFT) implemented in the computational scheme of pseudopotentials and plane waves. The Vienna Ab Initio Simulation Package (VASP) code was used [Kresse 1993, Kresse 1996a, Kresse 1996b]. Both the Perdew-Burke-Ernzerhof (PBE) [Perdew 1996] and its PBEsol modified version [Perdew 2008] of the generalized gradient approximations to the exchange and correlation (XC) energy were used as well as the projector-augmented wave scheme [Kresse 1999, Blöchl 1994]. The *4s* and *4p* outermost electrons of As and the *3s* and *3p* electrons of S were dealt with explicitly in the valence, the rest of the electrons being considered frozen at the core. The cutoff in the kinetic energy of the plane-waves basis set was 360 eV which together with the use of dense Monkhorst-Pack grids of k-points for integrations in reciprocal space [Monkhorst 1976] (6×4×2 for orpiment and 4×2×2 for anorpiment), ensured a convergence in the energy differences between phases of around 1 meV. The van der Waals (vdW) corrections to the total energy were taken into account within the DFT using Grimme's so-called D2 method [Grimme 2006, Grimme 2010].

All the results that we present in this short communication correspond to zero temperature, with zero-point energy neglected, and hydrostatic pressure conditions (that is, diagonal and isotropical stress tensor). For each phase, a full structural optimization at fixed volumes (of both internal parameters and cell shape) was performed through the calculation of the forces on atoms and the components of the stress tensor. The structural relaxation was deemed complete when the forces on atoms were less than 0.005 $eV \cdot Å^{-1}$ and the anisotropy in the diagonal components of the stress tensor was less than 0.1 GPa. The calculated total energy E as a function of volume V for the fully relaxed configurations were fitted using a Birch-Murnaghan equation of state (EoS) [Birch 1947] from which the pressure p, enthalpy $H = E + pV$, and properties at zero pressure (equilibrium volume V_0, bulk modulus B_0, etc) were obtained [Mujica 2003].

For the calculation of phonons at the zone center we used the small-displacements method as implemented in the PHON code [Alfè 2009] followed by the symmetry analysis of the eigenvectors for each mode in order to identify its possible Raman or infrared activity. These calculations were done at a range of volumes (and respective pressures) allowing the study of the pressure evolution of the frequencies of the different modes.

III. RESULTS AND DISCUSSION

Both structural evolution and the change in energetics, lattice vibrations, and electronic structure have been studied under compression, of which we will give here a very brief account.

The orpiment structure is monoclinic with space group (SG) $P2_1/c$, No. 14, with Z=4 and As and S atoms at 2e positions whereas, the recently discovered anorpiment structure is triclinic, SG P-1, No. 2, Z=4 and As and S atoms at 2i positions. The orpiment and anorpiment structures are plotted in projection in **Figures 1 and 2**, respectively, and **Figures 3 and 4** show the calculated evolution of the first few neighbours distances under compression.

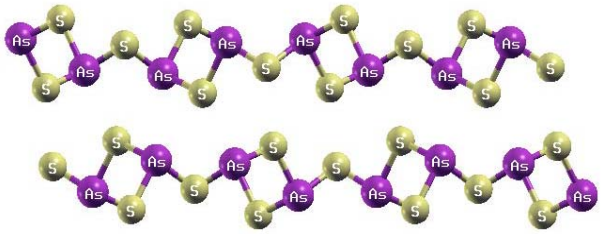

Figure 1. Plot of the orpiment structure, showing the positions of As and S atoms in projection, perpendicularly to the layers.

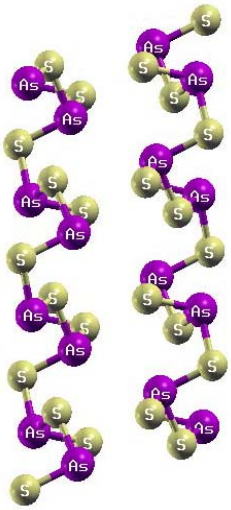

Figure 2. Plot of the anorpiment structure, showing the positions of As and S atoms in projection, perpendicularly to the layers.

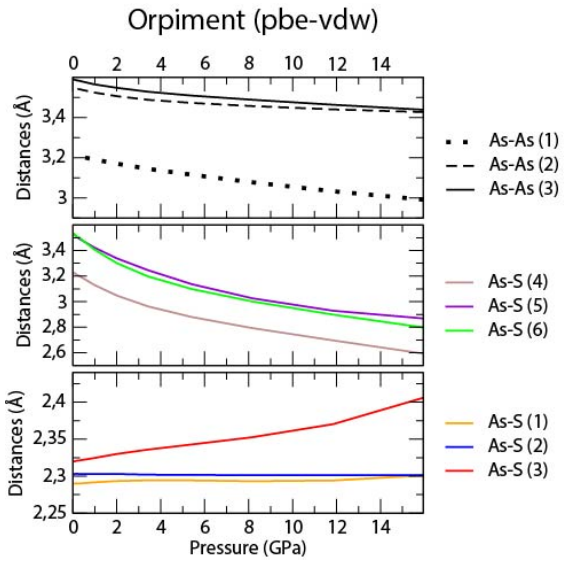

Figure 3. Calculated evolution of the inter-atomic distances between near neighbours of the orpiment phase obtained using the PBE funtional and van der Waals corrections. The species for each neighbour is specified in the labels to each curve.

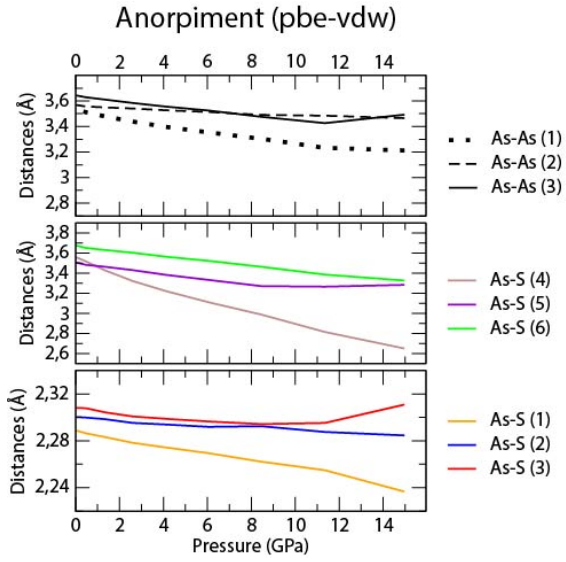

Figure 4. Calculated evolution of the inter- atomic distances between near neighbours of the anorpiment phase obtained using the PBE funtional and van der Waals corrections. The species for each neighbour is specified in the labels to each curve.

Figure 5 shows the calculated energy-volume (*E*-*V*) curves of the orpiment and anorpiment phases of As_2S_3 obtained using different XC functionals with and without van der Waals corrections, which shows the effects of the different approximations. Thus, for example, for the orpiment phase the zero-pressure equilibrium volumes V_0 (per cell) obtained using the PBE functional are 477.8 Å^3 and 584.8 Å^3, with and without van der Waals corrections, respectively, whereas using the PBEsol functional the values obtained are 418.6 Å^3 (with vdW) and 445.1 Å^3 (without vdW), cf. the experimental value of 467.7(4) Å^3 [Kampf 2011]. For the anorpiment phase the results for the equilibrium volume are 502.0 Å^3 (PBE with vdW), 582.3 Å^3 (PBE without vdW), 454.5 Å^3 (PBEsol with vdW), and 485.2 Å^3 (PBEsol without vdW), cf. the experimental value of 488.4 Å^3 [Kampf 2011]. In general, including vdW corrections decreases the equilibrium volume and results in *E*-*V* curves with a better defined minimum, in comparison to those *E*-*V* curves obtained without vdW, that is, the vdW corrections enhance the stability of the zero-pressure state. On the other hand, the PBEsol XC functional and the PBE XC functional with vdW corrections provide the results that are closer to the experimental values of V_0, and for this last functional the calculated bulk moduli at zero pressure are 14 GPa and 19 GPa for the orpiment and anorpiment phases, respectively.

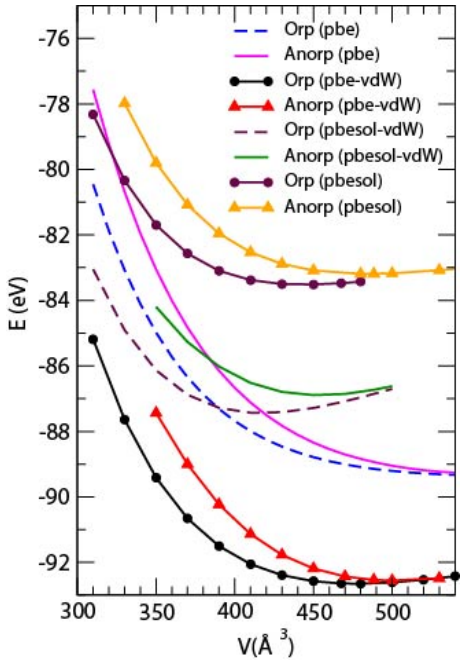

Figure 5. Calculated energy-volume (*E*-*V*) curves for the orpiment (Orp) and anorpiment (Anorp) phases of As_2S_3 obtained using the PBE and PBEsol XC functionals, with and without van der Waals (vdW) corrections. Both *E* and *V* are given per cell.

Finally, in this brief account of our theoretical results we show in **Figures 6-8** the evolution of the calculated frequencies of the phonon modes at Γ under pressure for the two phases. The mechanical representation of the orpiment structure yields the following multiplicities for the symmetry of the modes at the zone center: 15*Ag* + 15*Bg* + 15*Au* + 15*Bu*, of which the *Ag* and *Bg* modes are active in Raman and the *Au* and *Bu* modes are infrared-active (two *Bu* and one *Au* acoustic modes excepted). For the triclinic anorpiment phase, the symmetry analysis results in 30*Ag* + 30*Au* modes, of which the *Ag* modes are Raman active and the 27 non-acoustic *Au* modes are infrared active. The results of our assignment will be useful for the experimental study of the modes, as this information is not easy to obtain experimentally.

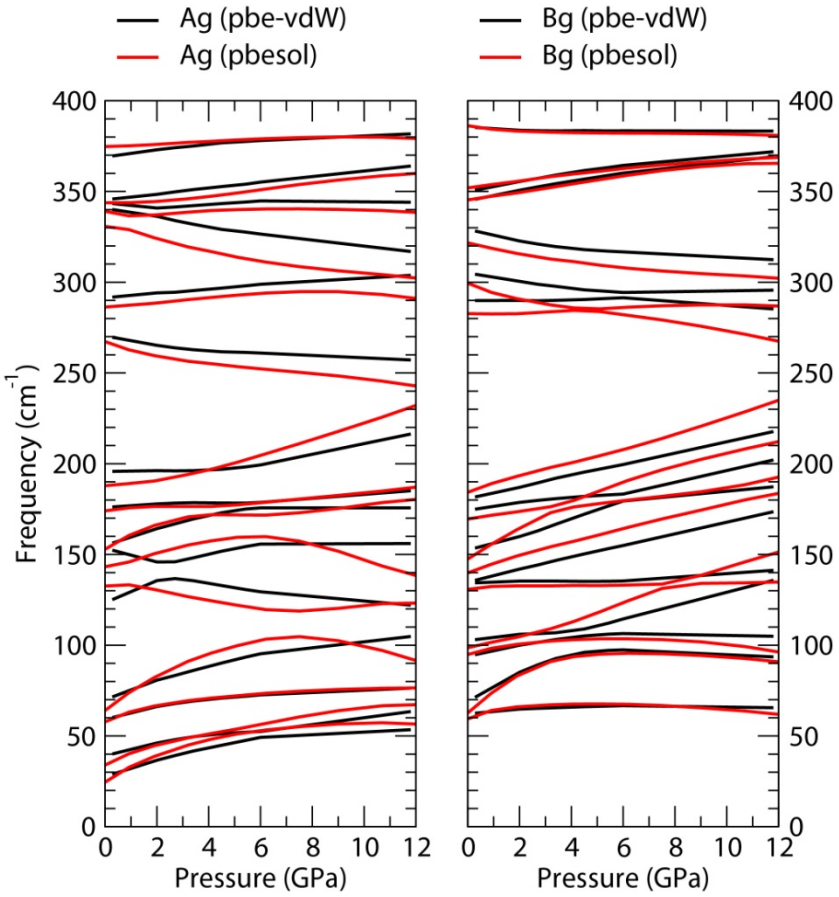

Figure 6. Calculated pressure evolution of the phonon frequencies of the Raman-active modes of the orpiment phase (*Ag* and *Bg* modes), obtained using the PBE XC functional with vdW corrections (pbe-vdW) and the PBEsol XC functional (pbesol).

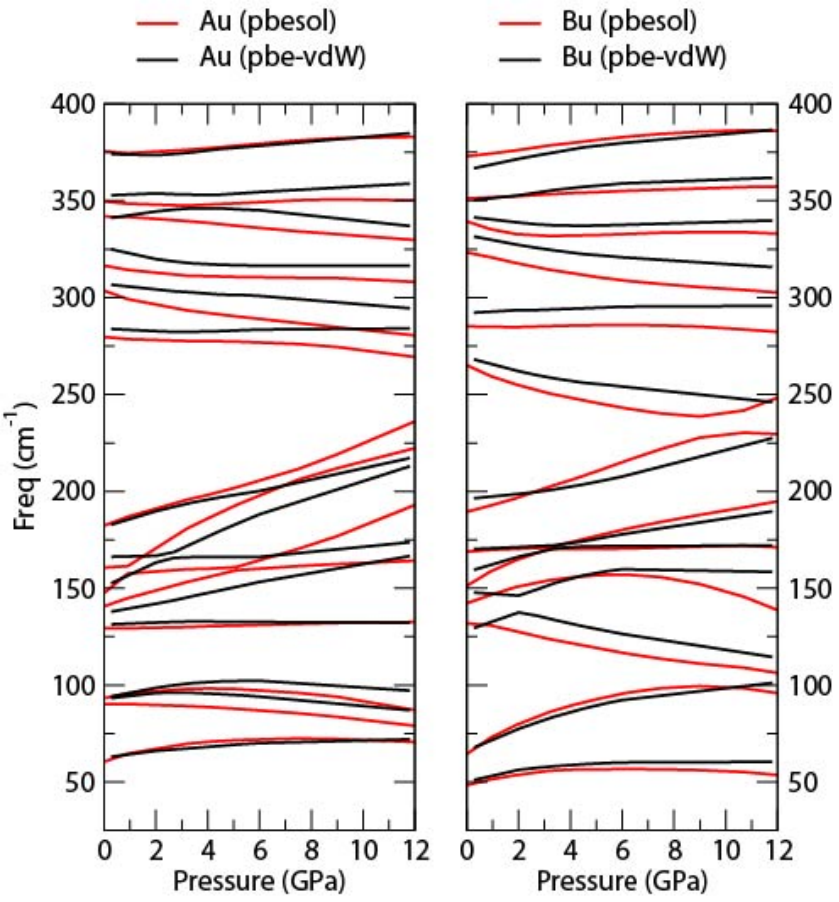

Figure 7. Calculated pressure evolution of the phonon frequencies of the infrared-active modes of the orpiment phase (*Au* and *Bu* modes), obtained using the PBE XC functional with vdW corrections (pbe-vdW) and the PBEsol XC functional (pbesol).

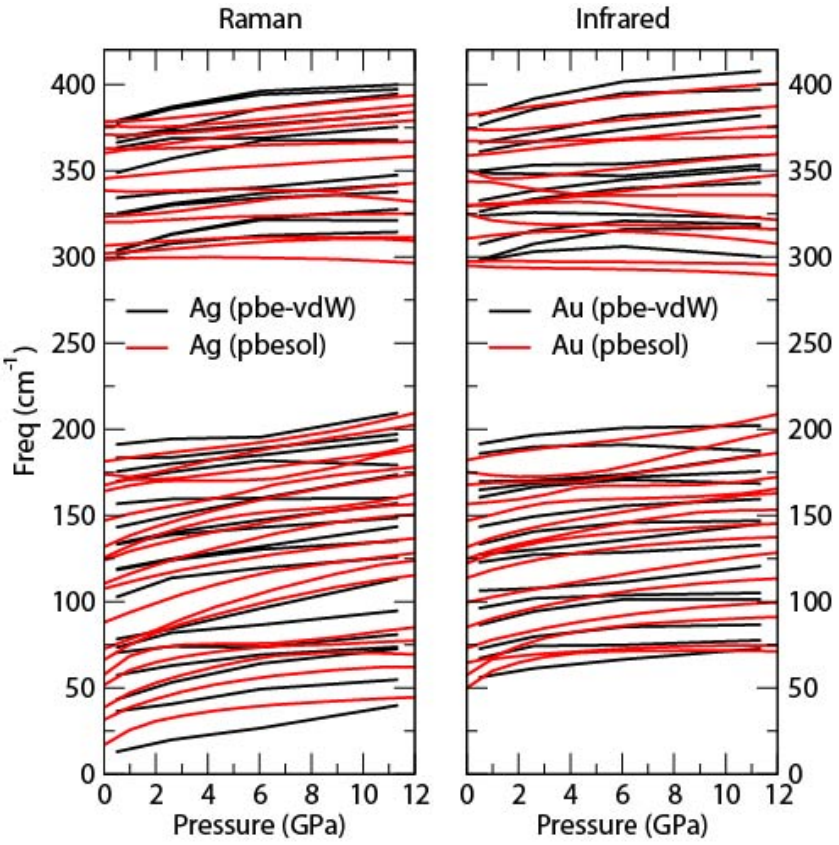

Figure 8. Calculated pressure evolution of the phonon frequencies of the Raman-active (*Ag*) and infrared-active (*Au*) modes of the anorpiment phase, obtained using the PBE XC functional with vdW corrections (pbe-vdW) and the PBEsol XC functional (pbesol).

IV. SUMMARY

The pressure behaviour of the orpiment and anorpiment layered structures of As_2S_3 has been investigated by means of *ab initio* calculations performed within the density functional theory.

The phonon frequencies at the zone center were calculated using the finite displacements method, and the symmetry of the modes were assigned, which will help in future Raman and infrared experimental studies of these phases under compression. The effect of van der Waals interactions was especifically investigated and found to be important for the structural response of these layered structures, enhancing their stability. These results are part of an ongoing comprehensive effort

to shed further light on the properties of As_2S_3, with a particular emphasis on their pressure evolution.

Acknowledgments

The authors acknowledge the financial support from the Ministerio de Economía y Competitividad (MINECO) of Spain through Projects No. MAT2013-46649-C04-02-P and MAT2013-46649-C04-03-P. Computer time in the MALTA computer cluster at the University of Oviedo, Spain, is also gratefully acknowledged (MINECO Project No. CSD2007-00045).

References

[Alfè 2009] D. Alfè. PHON: A program to calculate phonons using the small displacement method. *Comput. Phys. Commun*. **2009**, *180*, 2622.

[Birch 1947] F. Birch. Finite Elastic Strain of Cubic Crystals. *Phys. Rev*. **1947**, *71*, 809.

[Blöchl 1994] P. E. Blöchl. Projector augmented-wave method. *Phys. Rev. B: Condens. Matter Mater. Phys*. **1994**, *50*, 17953.

[Bolotina 2013a] N. B. Bolotina, V. V. Brazhkin, T. I. Dyuzheva, Y. Katayama, L. F. Kulikova, L. V. Lityagina, and N. A. Nikolaev. High-pressure polymorphism of As_2S_3 and new AsS_2 modification with layered structure. *JETP Letters*. **2013**, *98*, 539.

[Bolotina 2013b] N. B. Bolotina, V. V. Brazhkin, T. I. Dyuzheva, L. M. Lityagina, L. F. Kulikova, N. A. Nikolaev, and I. A. Verin. Crystal structure of new AsS_2 compound. *Crystallogr. Rep*. **2013**, *58*, 61.

[Brazhkin 2010] V. V. Brazhkin, Y. Katayama, M. V. Kondrvin, A. G. Lyapin, and H. Saitoh. Structural transformation yielding an unusual metallic state in liquid As_2S_3 under high pressure. *Phys. Rev. B*. **2010**, *82*, 140202(R).

[Gibbs 2010] G. V. Gibbs, A. F. Wallace, R. Zallen, R. T. Downs, N. L. Ross, D. F. Cox, and K. M. Rosso. Bond paths and van der Waals interactions in orpiment, As_2S_3. *J. Phys. Chem. A*. **2010**, *114*, 6550.

[Grimme 2006] S. Grimme. Semiempirical GGA-type density functional constructed with a long-range dispersion correction. *J. Comp. Chem*. **2006**, *27*, 1787.

[Grimme 2010] S. Grimme, J. Antony, S. Ehrlich, and S. Krieg. A consistent and accurate *ab initio* parametrization of density functional dispersion correction (DFT-D) for the 94 elements H-Pu. *J. Chem. Phys*. **2010**, *132*, 154104.

[Kampf 2011] A. R. Kampf, R. T. Downs, R. M. Housley, R. A. Jenkins, and J. Hyršl. Anorpiment, As_2S_3, the triclinic dimorph of orpiment. *Mineral. Mag*. **2011**, *75*, 2857.

[Kresse 1993] G. Kresse and J. Hafner. Ab initio molecular dynamics for liquid metals. *Phys. Rev. B*. **1993**, *47*, 558.

[Kresse 1996a] G. Kresse and J. Furthmüller. Efficiency of ab-initio total energy calculations for metals and semiconductors using a plane-wave basis set. *Comput. Mater. Sci*. **1996**, *6*, 15.

[Kresse 1996b] G. Kresse and J. Furthmüller. Efficient iterative schemes for ab initio total-energy calculations using a plane-wave basis set. *Phys. Rev. B*. **1996**, *54*, 11169.

[Kresse 1999] G. Kresse and D. Joubert. From ultrasoft pseudopotentials to the projector augmented-wave method. *Phys. Rev. B*. **1999**, *59*, 1758.

[Monkhorst 1976] H. J. Monkhorst and J. D. Pack. Special points for Brillouin-zone integrations. *Phys. Rev. B*. **1976**, *13*, 5188.

[Mujica 2003] A. Mujica, A. Rubio, A. Muñoz, and R. J. Needs. High-pressure phases of group-IV, III–V, and II–VI compounds. *Rev. Mod. Phys*. **2003**, *75*, 863, and references therein.

[Perdew 1996] J. P. Perdew, K. Burke, and M. Ernzerhof. Generalized Gradient Approximation Made Simple. *Phys. Rev. Lett*. **1996**, *77*, 3865.

[Perdew 2008] J. P. Perdew, A. Ruzsinszky, G. I. Csonka, O. A. Vydrow, G. E. Scuseria, L. A. Constantin, X. Zhou, and K. Burke. Restoring the Density-Gradient Expansion for Exchange in Solids and Surfaces. *Phys. Rev. Lett*. **2008**, *100*, 136406.

Artículo enviado a la revista de investigación periódica THE JOURNAL OF PHYSICAL CHEMISTRY C, a la espera de los comentarios pertinentes para su publicación.

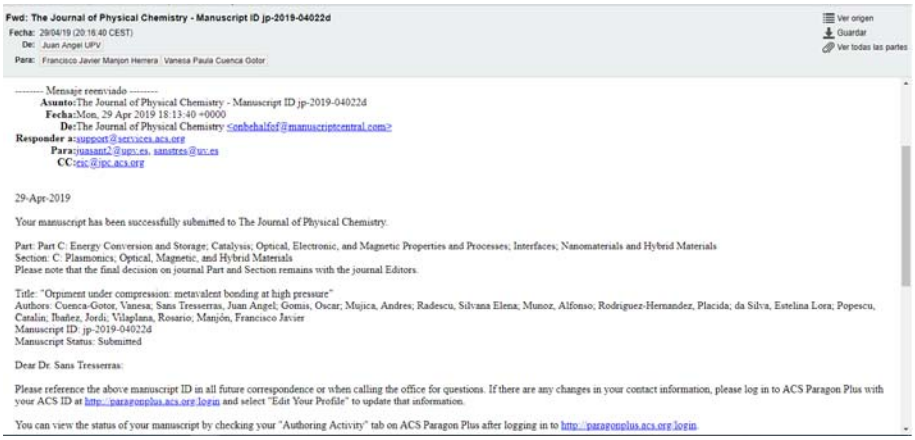

Fwd: The Journal of Physical Chemistry - Manuscript ID jp-2019-04022d

Fecha: 29/04/19 (20:16:40 CEST)
De: Juan Angel UPV
Para: Francisco Javier Manjon Herrera | Vanesa Paula Cuenca Gotor

Ver origen | Guardar | Ver todas las partes

-------- Mensaje reenviado --------
Asunto: The Journal of Physical Chemistry - Manuscript ID jp-2019-04022d
Fecha: Mon, 29 Apr 2019 18:13:40 +0000
De: The Journal of Physical Chemistry <onbehalfof@manuscriptcentral.com>
Responder a: support@services.acs.org
Para: juasant2@upv.es, sanstres@uv.es
CC: eic@jpc.acs.org

29-Apr-2019

Your manuscript has been successfully submitted to The Journal of Physical Chemistry.

Part: Part C: Energy Conversion and Storage; Catalysis; Optical, Electronic, and Magnetic Properties and Processes; Interfaces; Nanomaterials and Hybrid Materials
Section: C: Plasmonics; Optical, Magnetic, and Hybrid Materials
Please note that the final decision on journal Part and Section remains with the journal Editors.

Title: "Orpiment under compression: metavalent bonding at high pressure"
Authors: Cuenca-Gotor, Vanesa; Sans Tresserras, Juan Angel; Gomis, Oscar; Mujica, Andres; Radescu, Silvana Elena; Munoz, Alfonso; Rodriguez-Hernandez, Placida; da Silva, Estelina Lora; Popescu, Catalin; Ibañez, Jordi; Vilaplana, Rosario; Manjón, Francisco Javier
Manuscript ID: jp-2019-04022d
Manuscript Status: Submitted

Dear Dr. Sans Tresserras:

Please reference the above manuscript ID in all future correspondence or when calling the office for questions. If there are any changes in your contact information, please log in to ACS Paragon Plus with your ACS ID at http://paragonplus.acs.org/login and select "Edit Your Profile" to update that information.

You can view the status of your manuscript by checking your "Authoring Activity" tab on ACS Paragon Plus after logging in to http://paragonplus.acs.org/login.

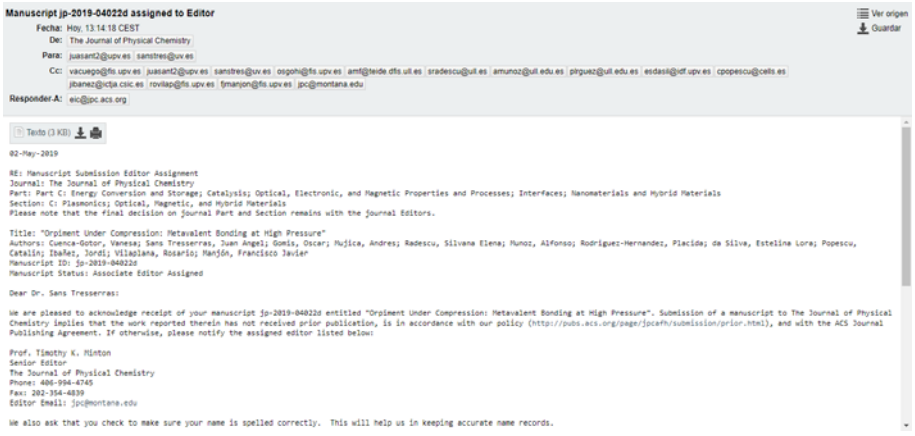

Manuscript jp-2019-04022d assigned to Editor

Fecha: Hoy, 13:14:18 CEST
De: The Journal of Physical Chemistry
Para: juasant2@upv.es | sanstres@uv.es
Cc: vacuego@fis.upv.es | juasant2@upv.es | sanstres@uv.es | osgohi@fis.upv.es | amf@teide.dfis.ull.es | sradescu@ull.es | amunoz@ull.edu.es | plrguez@ull.edu.es | esdasi@idf.upv.es | cpopescu@cells.es | jbanez@ictja.csic.es | rovilap@fis.upv.es | fjmanjon@fis.upv.es | jpc@montana.edu
Responder A: eic@jpc.acs.org

Ver origen | Guardar

Texto (3 KB)

02-May-2019

RE: Manuscript Submission Editor Assignment
Journal: The Journal of Physical Chemistry
Part: Part C: Energy Conversion and Storage; Catalysis; Optical, Electronic, and Magnetic Properties and Processes; Interfaces; Nanomaterials and Hybrid Materials
Section: C: Plasmonics; Optical, Magnetic, and Hybrid Materials
Please note that the final decision on journal Part and Section remains with the journal Editors.

Title: "Orpiment Under Compression: Metavalent Bonding at High Pressure"
Authors: Cuenca-Gotor, Vanesa; Sans Tresserras, Juan Angel; Gomis, Oscar; Mujica, Andres; Radescu, Silvana Elena; Munoz, Alfonso; Rodriguez-Hernandez, Placida; da Silva, Estelina Lora; Popescu, Catalin; Ibañez, Jordi; Vilaplana, Rosario; Manjón, Francisco Javier
Manuscript ID: jp-2019-04022d
Manuscript Status: Associate Editor Assigned

Dear Dr. Sans Tresserras:

We are pleased to acknowledge receipt of your manuscript jp-2019-04022d entitled "Orpiment Under Compression: Metavalent Bonding at High Pressure". Submission of a manuscript to The Journal of Physical Chemistry implies that the work reported therein has not received prior publication, is in accordance with our policy (http://pubs.acs.org/page/jpcafh/submission/prior.html), and with the ACS Journal Publishing Agreement. If otherwise, please notify the assigned editor listed below:

Prof. Timothy K. Minton
Senior Editor
The Journal of Physical Chemistry
Phone: 406-994-4745
Fax: 202-354-4839
Editor Email: jpc@montana.edu

We also ask that you check to make sure your name is spelled correctly. This will help us in keeping accurate name records.

Orpiment under compression: metavalent bonding at high pressure

V. P. Cuenca-Gotor,[1] J. A. Sans,[1,*] O. Gomis,[2] A. Mujica,[3] S. Radescu,[3] A. Muñoz,[3] P. Rodríguez-Hernández,[3] E. Lora da Silva,[1] C. Popescu,[4] J. Ibañez,[5] R. Vilaplana,[2] and F. J. Manjón[1,*]

[1] *Instituto de Diseño para la Fabricación y Producción Automatizada, Universitat Politècnica de València, 46022 València, Spain*

[2] *Centro de Tecnologías Físicas, Universitat Politècnica de València, 46022 Valencia (Spain)*

[3] *Departamento de Física, Instituto de Materiales y Nanotecnología, MALTA Consolider Team, Universidad de La Laguna, 38200 San Cristóbal de La Laguna (Spain)*

[4] *ALBA-CELLS, 08290 Cerdanyola, Barcelona (Spain)*

[5] *Institute of Earth Sciences Jaume Almera, CSIC, 08028 Barcelona (Spain)*

Abstract

We report a joint experimental and theoretical study of the structural, vibrational, and electronic properties of layered monoclinic arsenic sulfide (α-As_2S_3), aka mineral orpiment, under compression. X-ray diffraction and Raman scattering measurements performed in orpiment samples at high pressure and combined with *ab initio* calculations have allowed us to determine the equation of state and the tentative assignment of the symmetry of many Raman-active modes of orpiment. From our results, we conclude that no first-order phase transition occurs up to 25 GPa at room temperature; however, compression leads to an isostructural phase transition above 20 GPa. In fact, As coordination increases from threefold at room pressure to more than fivefold above 20 GPa. This increase in coordination can be understood as the formation of metavalent bonding at high pressure, which results in a progressive decrease of the electronic and optical bandgap, an increase of the dielectric tensor and Born effective charges, and a considerable softening of many high-frequency optical modes with pressure. The formation of metavalent bonding may also explain the behavior of other group-15 sesquichalcogenides under compression. Moreover, our results suggest that group-15 sesquichalcogenides either show metavalent bonding at room pressure or undergo a transition from p-type covalent bonding at room pressure towards metavalent bonding at high pressure, as a preceding phase towards metallic bonding at very high pressure.

KEYWORDS: group-15 sesquichalcogenides, high-pressure, X-ray diffraction, Raman scattering, electronic band structure, *ab initio* calculations, metavalent or resonant bonding.

I. INTRODUCTION

Arsenic sulfide (As_2S_3) and in particular the monoclinic polymorph (α-As_2S_3), aka mineral orpiment, is one of the ores of As together with minerals realgar (α-As_4S_4) and arsenopyrite (FeAsS) [Smith 1973]. In particular, orpiment and realgar have been known since ancient times, with realgar being used as an orange-red pigment and orpiment as a gold-like pigment, hence his mineral name orpiment (*Aurum pigmentum* in latin) [Pliny the Elder 1855]. Due to the high chemical stability of α-As_2S_3, the canary yellow or King's yellow pigment was obtained from molten orpiment and has been extensively used in papyrus and objects of ancient Egypt that date back to 3.1 millennia BC [Fitzhugh 1997, Spurrell 1895, Burgio 2000]. Additionally, As_2S_3 crystals and glasses have been used as drugs to treat different illnesses, such as prophylactic diseases, asthma, tuberculosis or diabetes, and were also prescribed as antiseptics and sedative by Aristotle and Hippocrates (IV century BC). Moreover, orpiment has been used since ancient times in traditional Chinese medicine for the treatment of inflammation, ulcers, convulsions, and schistosomiasis [Waxman 2001]. Nowadays, arsenic trisulfide has proved to exhibit an excellent activity and positive effects in cancer therapy [Ding 2016]. Finally, it must be stressed that in the last decades arsenic sulfides have been investigated for different applications in photonics and non-linear optics since they possess high values of the refractive index, high IR transparency, high optical non-linearity, stability to crystallization, the possibility to be modified by a femtosecond laser irradiation, and an inertness to environment [Heo 2014, Hewak 2014].

As_2S_3 usually crystallizes in the monoclinic α polymorph (space group (SG) $P2_1/n$ or $P2_1/c$, No. 14) [Morimoto 1954, Mullen 1972]; although a triclinic dimorph of orpiment, called anorpiment (SG $P\bar{1}$, No. 2) was recently discovered and approved as a new mineral by the International Mineralogical Association [Kampf 2011]. The crystalline structure of the monoclinic α phase [see **Fig. 1**] is composed by corrugated or zigzag layers piled up mainly along the *b* axis [see **Fig. 1(a)**], which are linked by weak van der Waals (vdW) forces [Gibbs 2010].

(a)

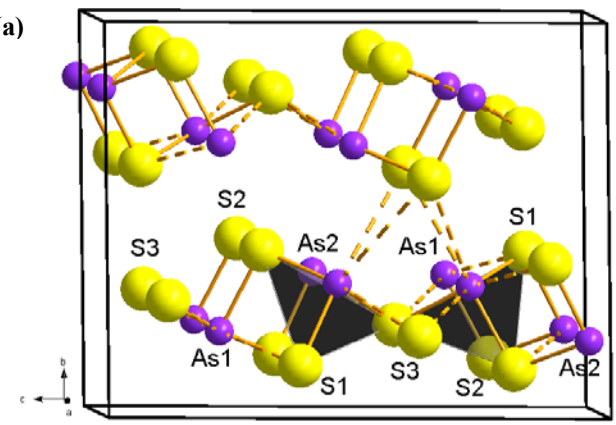

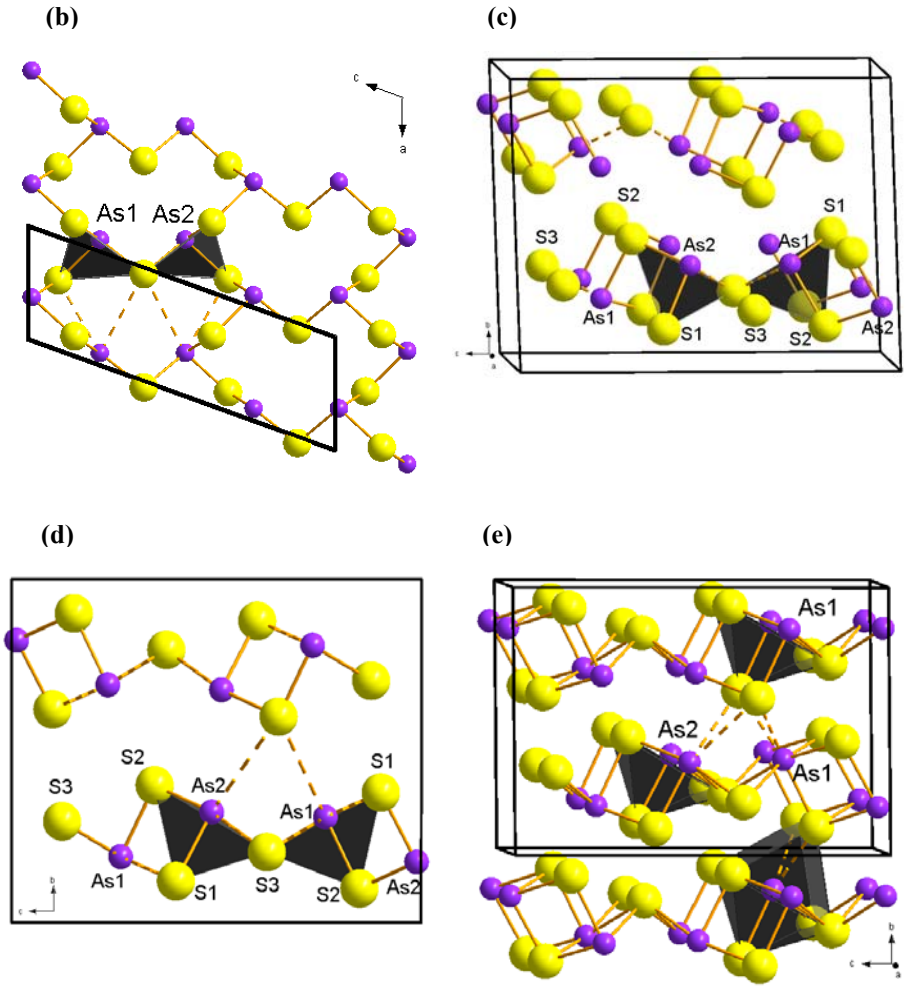

Figure 1. α-As_2S_3 structure at room pressure. Big yellow and small purple spheres correspond to S and As atoms, respectively. **(a)** 3D structure. All solid lines correspond to bonds of similar length (~2.3 Å) and dashed lines correspond to longer As-S distances (> 3.0 Å). **(b)** Structure of the layer in the *ac* plane showing the heart-shaped rings. The upper part shows the AsS_3 pyramids due to the short bonds that result in the threefold coordination of As and twofold coordination of S at room pressure. Inside the cell edges, we show the long intralayer bonds that would contribute to fivefold coordination of As above 25 GPa. **(c)** Structure viewed as AsS spiral chains (in As1-S1-As2-S2 sequence) joined by inter-chain S3 atoms. Only short bonds are displayed. Solid (dashed) lines correspond to intra (inter)-chain bonds. **(d)** Projection of the α-As_2S_3 structure onto the *bc* plane. **(e)** 3D structure of α-As_2S_3 at 30 GPa, showing polyhedral units with fivefold coordination of As1 and As2 atoms (up and middle) and with 5+2 coordination for As1 atoms (down).

The properties of arsenic sulfides have been extensively studied, mainly for melts and glasses, because As_2S_3 ranks first among chalcogenides from the viewpoint of the production of amorphous and glass-like industrial materials. However, many properties of their crystalline phases, orpiment, and anorpiment, are not yet well known likely due to the complex monoclinic and triclinic crystalline structures of these compounds. For instance, a definitive symmetry assignment of the vibrational modes of orpiment is still under debate [Cheng 2017] despite a number of papers reporting Raman scattering (RS) measurements, as well as infrared (IR) measurements, since the advent of laser-based Raman spectroscopy [Cheng 2017, Porto 1962, Weber 1965, Ward 1968, Forneris 1969, Scheuermann 1969, Mathieu 1970, Zallen 1971, Zallen 1974a, Zallen 1974b, DeFonzo 1978, Razzetti 1979, Besson 1980, Besson 1981, Frost 2002, Mamedov 2018].

In this context, pressure is a valuable tool to study the properties of materials and several high-pressure (HP) studies have been performed in glassy As_2S_3 and α-As_2S_3 in order to help us to understand their properties. In particular, results obtained from HP optical absorption, HP X-ray absorption spectroscopy (XAS), HP Raman scattering (RS) measurements, HP electrical measurements and also from a few *ab initio* calculations have been reported for α-As_2S_3 [Zallen 1974b, Besson 1980, Besson 1981, Itié 1992, Zallen 2004, Bolotina 2013a, Liu 2019, Kravchenko 1980, Radescu 2017]. Moreover, a HP and high-temperature (HT) polymorph of orpiment (γ-As_2S_3), whose structure has not been resolved yet, has been found [Kravchenko 1980]. This is not surprising because little is also known about the structure of orpiment and its behavior under compression. It is only known that the remarkable high packing of layers in orpiment is responsible for its high stability under pressure as suggested by previous experiments. Besides, HP-XAS measurements suggested some structural changes above 10 GPa and an increase in As coordination above 30 GPa. On the other hand, recent electrical measurements and calculations suggest an isostructural phase transition (IPT) around 25 GPa [Liu 2019].

To verify the above hypotheses, it would be desirable to perform HP X-ray diffraction (XRD) measurements on α-As_2S_3 at room temperature. In this way, we will obtain the equation of state of orpiment and explore the origin of the changes proposed in the literature. Such measurements will allow us to investigate the possible appearance of HP phases and its relationship mainly with those of other sesquioxides and sesquichalcogenides. On the other hand, it will be important to perform new HP-RS measurements in order to correlate the structural and vibrational changes in orpiment and to aid in the assignment of the symmetries and the origin of the different vibrational modes with the help of *ab initio* calculations. All these measurements and calculations would allow us to understand the behavior of orpiment under compression.

For all the mentioned reasons, we report in this work a joint experimental and theoretical study of the structural, vibrational, and electronic properties of α-As_2S_3 under compression at room temperature by means of powder HP-XRD and HP-RS measurements in orpiment. Experimental results are complemented with theoretical *ab initio* electronic and lattice-dynamics calculations. Our results show a continuous

compression of orpiment up to 25 GPa with a loss of the vdW character of the interlayer forces above 10 GPa. Moreover, our calculations show that there is a progressive increase of As coordination with pressure, changing from threefold coordination at 0 GPa to more than fivefold coordination above 20 GPa, where a pressure-induced IPT occurs. Additionally, we provide a tentative symmetry assignment of the Raman-active modes in orpiment and explain their behavior under compression.

Our electronic band structure calculations suggest that there is a progressive closing of the bandgap of α-As_2S_3 with increasing pressure leading from a trivial semiconductor to a trivial metal well above 40 GPa, which is in rather good agreement with previous optical absorption and resistivity measurements [Besson 1980, Besson 1981, Zallen 2004, Liu 2019]. Finally, we show that all the changes observed in orpiment under compression, such as the strong decrease of the bandgap, the softening of many optical vibrational modes, the evolution of the electron localization function (ELF) along the As-S bonds, and the strong increase of the dielectric tensor and Born effective charges, can been explained in the framework of the formation of metavalent bonding at HP. This behavior has been recently proposed for other chalcogenides [Shportko 2008, Lee 2014, Li 2015, Xu 2017, Wuttig 2018, Raty 2018]. In summary, we show in the present paper that orpiment under compression is an example, together with GeSe [Xu 2017], of a compound that develops a pressure-induced transition from covalent to metavalent bonding without the need of undergoing a first-order structural phase transition. This feature contrasts to Se and Te, which undergo this transition after being subject of a first-order phase transition. Moreover, we propose that the formation of metavalent bonding may explain the behavior under compression of other group-15 chalcogenides, so our results pave the way for extending the study of the transformation from covalent to metavalent bonding to other group-15 chalcogenides and related compounds.

II. EXPERIMENTAL DETAILS

Almost pure mineral orpiment from Hunan province (China) was used in the present study. Powder XRD measurements at ambient pressure were performed with a Rigaku Ultima IV diffractometer. Angle-dispersive powder HP-XRD experiments at room temperature up to 25 GPa were conducted in a membrane-type diamond anvil cell (DAC) at the BL04-MSPD beamline of ALBA synchrotron. Incident monochromatic beam with wavelength of 0.4246 Å was focused to 20 x 20 μm^2 using a pinhole of 50 μm to cut the X-ray beam tail [Fauth 2013]. Images covering a 2θ range up to 18° were collected using a SX165 CCD detector located at 240 mm from the sample. One-dimensional diffraction profiles of intensity as a function of 2θ were obtained by integration of the observed intensities with the Fit2D software [Hammersley 1996]. Le Bail refinements were carried out with GSAS package software for synchrotron measurements [Larson 2004, Toby 2001]. Interatomic distances were obtained with the Visualization for Electronic and Structural Analysis (VESTA) software [Momma 2011]. The equation of state (EoS) of copper

[Dewaele 2004], which powder was mixed with the sample powder, was used for pressure calibration.

Room-temperature unpolarized HP-RS measurements up to 14.5 GPa were carried out with a Horiba Jobin Yvon LabRAM HR spectrometer equipped with a thermoelectrically cooled multichannel CCD detector. RS measurements with a spectral resolution better than 2 cm^{-1} were excited using the 632.8 nm line of a He:Ne laser. The use of an edge filter limited the observation of Raman-active modes below 40 cm^{-1}. Pressure was determined with the ruby fluorescence method [Mao 1986]. In both HP-XRD and HP-RS measurements, a methanol-ethanol (4:1 ratio) mixture was used as a pressure-transmitting medium with hydrostatic conditions up to 10 GPa and quasi-hydrostatic conditions up to 25 GPa [Piermarini 1973, Klotz 2009].

III. THEORETICAL DETAILS

Ab initio calculations within the density functional theory (DFT) [Hohenberg 1964] were performed to compute the electronic and structural properties of α-As_2S_3 by using the plane-wave Vienna Ab initio Simulation Package (VASP) [Kresse 1993, Kresse 1996a, Kresse 1996b]. The projector-augmented wave scheme (PAW) [Blöchl 1994, Kresse 1999] was considered to treat the valence and the semi-core states, more explicitly by including the 4s and 4p outermost electrons of As and the 3s and 3p electrons of S as valence electrons, with the remaining of the electrons being considered frozen at the core. In this work, the generalized gradient approximation (CGA) with the Perdew-Burke-Ernzerhof (PBE) [Perdew 1996] parametrization was used for the exchange and correlation energy, after evaluating calculations performed also with the PBEsol modified version [Perdew 2008] in Radescu (2017). The plane-wave kinetic-energy cutoff was defined with 360 eV, which together with the use of a dense Monkhorst-Pack grid [Monkhorst 1976] with a 6×4×2 k-point reciprocal space sampling mesh, ensured a convergence of the total energy around 1 meV with deviations of the stress tensor from a diagonal hydrostatic form of less than 1 kbar (0.1 GPa). The vdW corrections to the total energy were taken into account within DFT by using the D2 method [Grimme 2006, Grimme 2010]. Electronic band-structure calculations were carried out at different pressures along selected high-symmetry k-points on the first Brillouin-zone (BZ). Additionally, analysis of the electron density topology and of the ELF were accomplished with the VESTA program employing data from the VASP code [Contreras-García 2008, Contreras-García 2009].

Lattice-dynamics calculations were performed at the zone center (Γ-point) and along high-symmetry segments of the BZ as a function of pressure, by using the direct-force constant approach [Parlinski 1997, Alfè 2009]. The separate calculations of the forces, which result from a fixed displacement away from equilibrium of the atoms in the primitive cell, necessary to the construction of the dynamical matrix at the Γ-point of the BZ were achieved with VASP. The diagonalization of the dynamical matrix provides the normal-mode frequencies and allows identifying the irreducible representations and the character of the vibrational phonon modes at the Γ-point.

IV. RESULTS AND DISCUSSION

Structural and vibrational characterization of α-As_2S_3 at room conditions

As already commented, α-As_2S_3, with monoclinic $P2_1/c$ space group at room conditions, is a layered material with corrugated (or zigzag) layers extended along the *ac*-plane that are linked by vdW interlayer interactions along the *b*-axis [**Fig. 1(a)**]. Each corrugated layer is formed by heart-shaped six-member rings of corner-sharing AsS_3 pyramids [**Fig. 1(b)**]. Traditionally, the zigzag layers have been understood as formed by spiral AsS chains extended along the *a*-axis and held together by inter-chained S atoms, which allow the link between the chains along the *c*-axis [see **Fig. 1(c)**]. On the other hand, zigzag layers can also be seen as a W-shape formation of molecules (S1-As2-S3-As1-S2) where each molecule is linked with four adjacent inverted W-shape molecules, mostly along the *c*-axis due to covalent bonding [see **Fig. 1(d)**].

At room conditions, each As1 and As2 atom is linked by covalent bonds to one S1, one S2 and one S3 atom at distances around 2.3 Å, leading to an As threefold-coordination [see pyramids in **Fig. 1(a)**]. Additionally, each As1 and As2 atom has two farther S neighbors on the same layer at distances above 3.0 Å [see dashed lines inside the layers in **Fig. 1(a)** and **1(b)**] and other two S neighbors on an adjacent layer at distances above 3.5 Å [see dashed lines between the layers at the top part of **Fig. 1(a)** and **1(d)**]. In the following section, we will discuss the importance of these long As-S intra- and inter-layer distances (above 3 Å at room pressure) in orpiment at high pressure.

According to the difference of the As-S distances, we can consider orpiment as an arrangement of AsS_3 pyramids forming AsS_3E tetrahedral units, where E refers to the lone electron pair (LEP) of the As atoms. Therefore, each layer can be described alternatively by an arrangement of two tetrahedral AsS_3E units; i.e. those formed by the two inequivalent As atoms, each surrounded by three S atoms and the corresponding cation LEP that points towards the interlayer space. The strong As LEP distorts the electronic distribution and the geometry of the polyhedral units leading to the layered structure of orpiment.

The layered structure of orpiment bears similarities with the chain-like structure of the valentinite mineral (β-Sb_2O_3), where the W-shape molecules (linked through a helical form) lead to the formation of an acicular or quasimolecular crystal [Svensson 1974]. On the other hand, the layered structure of orpiment is isostructural to that of α-As_2Se_3 [Stergiou 1985b] and belongs to the same space group that the claudetite mineral (β-As_2O_3); however, claudetite is not isostructural to orpiment, because the layered structure of the former is due to the arrangement of AsO_3 molecules in a buckled structure [Pertlik 1978] as in black phosphorous [Brown 1965]. The layered structure of orpiment also bears some resemblance to the zigzag layered structure recently described for Sb_2S_3, Sb_2Se_3, and Bi_2S_3 [Efthimiopoulos 2013, Efthimiopoulos 2014, Ibáñez 2016], crystallizing in the orthorhombic *Pnma* structure, and to that of α-As_2Te_3, crystallizing in the monoclinic *C2/m* phase [Cuenca-Gotor 2016]. In these former group-15 A_2X_3

sesquichalcogenides, the layers are clearly composed by spiral chains held together through long and weak *A-X* bonds, whereas in As_2S_3 the chains are connected through short and strong *A-X* bonds. Another difference found between these systems, is regarding the cation coordination in the different structures at room pressure. In α-As_2S_3, the two inequivalent As atoms are threefold-coordinated; in Sb_2S_3, Bi_2S_3 and Sb_2Se_3, there is an average fourfold coordination because one cation has threefold coordination and the other has fivefold coordination; and in α-As_2Te_3, As atoms have a coordination between five and six. This means that the larger cation or the larger anion favors an increase of cation coordination probably due to the smaller cation LEP effect [Walsh 2011].

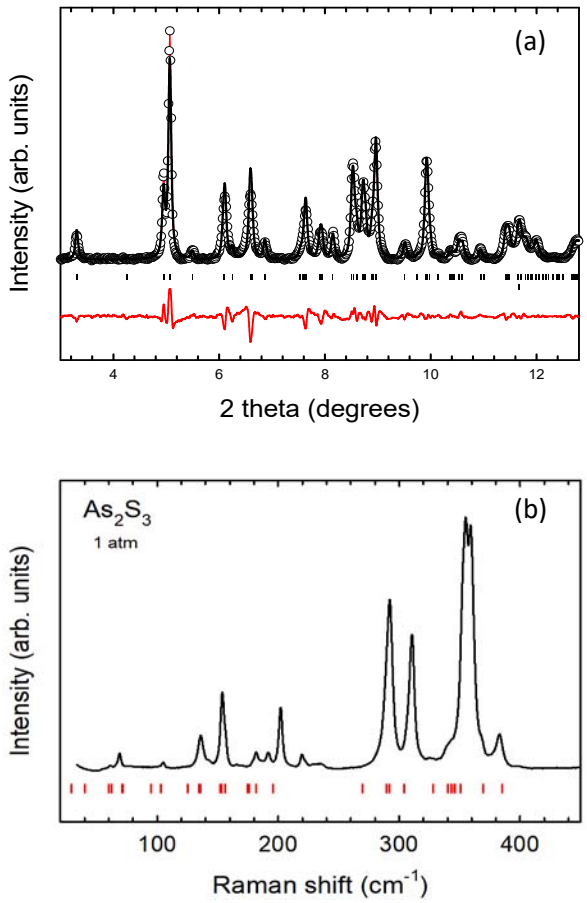

Figure 2. Structural and vibrational characterization of α-As_2S_3 at room conditions: **(a)** Powder XRD pattern. Le Bail analysis and residuals are also plotted. **(b)** RS spectrum. Bottom marks indicate the theoretical Raman-active mode frequencies from calculations including vdW interactions.

The experimental XRD pattern of our sample at room conditions [see **Figure 2(a)**] shows that the sample corresponds to the α phase without the presence of additional phases or impurities. The pattern was fitted to a monoclinic structure ($P2_1/c$ space group), with small residuals and a correlation factor R_{wp} of 10%, yielding the following lattice parameters: a = 4.2626(5) Å, b = 9.6056(7) Å, c = 12.1836(12) Å and β = 110.054(7) º with V_0 = 468.61(5) Å^3. In **Table 1** we can observe that these values are in good agreement with previously reported experimental values [Morimoto 1954, Mullen 1972, Gibbs 2010], with our theoretical calculated lattice parameters and with other previously published theoretical data [Liu 2019, Srivastava 2011]. The theoretical atomic parameters of the five inequivalent atomic sites (three S and two As atoms) of α-As_2S_3 are also given in **Table S1** in the Supporting Information (SI) section for comparison with experimental and theoretical values.

Table 1. Experimental and theoretical (with vdW) lattice parameters (LP) corresponding to the $P2_1/c$ phase of α-As_2S_3 at ambient conditions. Experimental (Exp.) and theoretical (The.) values from Morimoto (1954) **(a)**, Mullen (1972) **(b)**, Liu (2019) **(c)** and Srivastava (2011) **(d)** are given for comparison. All data have been expressed in the standard $P2_1/c$ setting for comparison.

LP	Exp. (This work)	The. (This work)	Exp. **(a)**	Exp. **(b)**	Exp. **(c)**	Exp. **(d)**
a (Å)	4.2626(5)	4.2608	4.256(2)	4.22(5)	4.22	4.22
b (Å)	9.6056(7)	9.6289	9.577(5)	9.57(2)	9.65	9.57
c (Å)	12.1836(12)	12.3084	12.191(5)	12.18(4)	12.27	12.1839
β (º)	110.054(7)	109.84	109.75(8)	109.8(5)	109.59	109.85
V_0 (Å^3)	468.61(5)	475.00	467.68	462.8	471.2	462.80

As regards to the vibrational properties of α-As_2S_3, group theory predicts sixty vibrational modes at the BZ center with the following mechanical representation [Kroumova 2003]:

$$\Gamma_{60} = 15A_g\,(R) + 13B_u\,(IR) + 15B_g\,(R) + 14A_u\,(IR) + 1A_u + 2B_u \qquad (1)$$

where g (gerade) modes are Raman-active (R) and u (ungerade) modes are infrared-active (IR), except one A_u and two B_u modes, which are acoustic modes. Therefore, α-As_2S_3 has 30 Raman-active modes and 27 IR-active modes.

Figure 2(b) shows the unpolarized RS spectrum of orpiment at room conditions together with the theoretically-predicted Raman-active mode frequencies (including vdW interactions) at room pressure. The values of the experimental and theoretical frequencies of the Raman-active modes of α-As_2S_3 at room pressure are summarized in **Table 2**. The RS spectrum of orpiment at room pressure clearly shows 19 out of

the 30 theoretically-predicted Raman-active modes and a quite good agreement between our experimental and theoretical frequencies. The spectrum is similar to those previously reported, with a doublet between 60 and 70 cm^{-1}, a phonon gap between 200 and 290 cm^{-1} and a triplet around 360 cm^{-1} [Cheng 2017, Porto 1962, Weber 1965, Ward 1968, Forneris 1969, Scheuermann 1969, Mathieu 1970, Zallen 1971, Zallen 1974a, Zallen 1974b, DeFonzo 1978, Razzetti 1979, Besson 1980, Besson 1981, Frost 2002, Mamedov 2018, Liu 2019]. Unfortunately, we have not been able to observe modes below 40 cm^{-1} due to the limit imposed by the edge filter of our spectrometer.

Table 2. Theoretical (with vdW interactions) and experimental Raman-active mode frequencies and their respective pressure coefficients for α-As_2S_3 at room temperature, as fitted with equation $\omega(P) = \omega_0 + \alpha \cdot P$. Experimental values from Zallen (1974b), Razzetti (1979) and Liu (2019) have been added for comparison.

	Theoretical		Experimental			
Mode	$\omega_0\ (cm^{-1})$ [a]	$\alpha\left(\frac{cm^{-1}}{GPa}\right)$ [a]	$\omega_0\ (cm^{-1})$ [a]	$\alpha\left(\frac{cm^{-1}}{GPa}\right)$ [a]	$\omega_0\ (cm^{-1})$	$\alpha\left(\frac{cm^{-1}}{GPa}\right)$
A_g^1	27 (1)	5.1 (3)	26 (1)	6.32 (37)	25 [b], 26 [c]	9.0 [b]
A_g^2	38 (1)	4.5 (2)	37 (1)	4.9 (3)	36 [b], 37 [c]	7.2 [b]
A_g^3	59 (1)	4.1 (2)	62 (1)	3.7 (1)		
B_g^1	62 (1)	1.6 (2)			62 [b,c]	5.0 [b]
B_g^2	68 (1)	10.3 (4)	69 (3)	10.5 (8)	69 [b], 70 [c]	11.0 [b]
A_g^4	70 (1)	5.9 (3)	70 (3)	8.1 (3)		
B_g^3	94 (2)	3.1 (1)	103 (2)	2.9 (1)		
B_g^4	103 (2)	2.1 (5)	106 (2)	2.8 (1)	107 [b], 106 [c]	4.9 [b]
A_g^5	124 (2)	7.7 (7)	138 (5)	5.1 (4)	136 [b], 137 [c], 135 [d]	7.3 [b], -0.42 [d]
B_g^5	134 (2)	0.7 (2)	120 (1)	2.9 (5)		
B_g^6	135 (2)	3.6 (1)	144 (1)	3.9 (2)	145 [c]	
B_g^7	152 (3)	3.7 (2)				
A_g^6	153 (3)	-4.6 (7)	155 (2)	-0.3 (3)	158 [c]	
A_g^7	155 (3)	5.5 (3)	156 (2)	6.9 (4)	154 [b,c], 153 [d]	8.5 [b], 0.24 [d]
B_g^8	174 (3)	2.5 (2)	179 (2)	2.2 (1)	180 [c], 177 [d]	-2.22 [d]
A_g^8	176 (3)	1.2 (1)	185 (2)	2.3 (1)		
B_g^9	181 (3)	3.3 (2)	188 (2)	4.6 (9)	188 [c]	
A_g^9	196 (3)	1.3 (1)	202 (1)	2.5 (2)	202 [b], 204 [c], 201 [d]	3.2 [b]

A_g^{10}	270 (4)	-3.1 (2)	291 (1)	-2.6 (3)	292 [b], 293 [c], 290 [d]	-3.8 [b], -0.89 [d]
B_g^{10}	290 (4)	0.3 (1)	306 (2)	0.5 (1)	307 [c], 308 [d]	-0.2 [d]
A_g^{11}	291 (4)	1.3 (1)	310 (2)	1.4 (1)	310 [b], 312 [c]	1.0 [b]
B_g^{11}	305 (4)	-2.7 (1)	325 (2)	-3.5 (4)	326 [b,c]	-4.6 [b]
B_g^{12}	329 (5)	-3.7 (1)			343 [c]	
A_g^{12}	341 (5)	1.0 (5)	356 (4)	-0.7 (6)*	357 [b], 360 [c]	0.96 [b]
A_g^{13}	343 (5)	3.4 (3)	354 (4)	1.8 (4)*	356 [c]	
B_g^{13}	345 (5)	3.1 (1)				
A_g^{14}	346 (5)	-0.5 (1)	353 (4)	4.1 (6)*	354 [c], 353 [d]	-0.19 [d]
B_g^{14}	350 (5)	3.1 (4)	369 (2)	2.2 (3)	370 [c]	
A_g^{15}	369 (5)	2.4 (1)	383 (2)	2.2 (2)	383 [b], 384 [c], 380 [d]	1.7 [b], 0.47 [d]
B_g^{15}	385 (5)	-0.9 (2)	400 (2)	-0.7 (3)	401 [c]	

[a] This work. [b] [Zallen 1974b]. [c] [Razzetti 1979]. [d] [Liu 2019]. * The pressure coefficient of these modes has been measured above 2 GPa.

The vibrational spectrum of orpiment at room pressure is separated between a low-frequency region (below 200 cm^{-1}) and a high-frequency region (above 260 cm^{-1}) with a phonon gap between these regions. Some Raman features are observed inside the phonon gap of α-As_2S_3, which are assumed to be second-order modes, so they will not be further commented in this work. Among the measured RS modes below 250 cm^{-1} and above 280 cm^{-1}, the more intense modes are those of the high-frequency region between 350 and 360 cm^{-1}. Due to the large number of Raman-active modes located within a small frequency region of the RS spectrum at room pressure and the broadening of experimental peaks, it is almost impossible to identify the modes by solely using the RS spectrum at room pressure and its comparison with lattice-dynamics *ab initio* calculations. Therefore, a tentative assignment of experimental peaks will be performed in a forthcoming section taking into account the HP dependence of the experimental and theoretical Raman-active mode frequencies.

The atomic vibrations of several characteristic Raman- and IR-active modes of α-As_2S_3 have been visualized and discussed in the SI with the aid of the Jmol Interface for Crystallographic and Electronic Properties (J-ICE) software [Canepa 2011] [see **Fig. S1 to S14** in the SI]. An interesting feature is that many vibrations evidence that atoms of the same chain (As1, S1, As2, and S2) vibrate in-phase or out-of-phase, whereas S3 atoms interconnecting the chains vibrate in a quite different fashion than the other four inequivalent atoms. This observation clearly evidences the chain-like nature of the layers of orpiment in good agreement with a previous vibrational study [DeFonzo 1978].

As a layered material, some of the most important vibrational modes of α-As_2S_3 are the rigid layer modes. Our calculations confirm that the two lowest-frequency modes

located at 27 and 38 cm^{-1}, and attributed to the A_g^1 and A_g^2 modes, correspond to the rigid shear layer modes of orpiment [**Fig. S1** in the SI]. Moreover, our calculations show that the compressional or longitudinal rigid layer mode is the B_g^1 mode theoretically predicted at 62 cm^{-1} [**Fig. S2** in the SI]. This frequency value is in good agreement with previous estimations of the compressional mode [Zallen 1974a]. At room pressure, we have observed this mode in a region where it is overlapped with inter-chain vibrational modes [see comments in the SI], as previously suggested [DeFonzo 1978].

As regards other vibrational modes of orpiment, those of the high-frequency region mainly correspond to As-S stretching modes located between 350 and 400 cm^{-1} and to a mixture of As-S stretching and bending modes between 260 and 350 cm^{-1}. On the other hand, modes located below 200 cm^{-1} correspond to pure As-S bending modes, being those below 100 cm^{-1} mainly related to rotations and translations of the spiral chains, which can be seen as rigid units. This distribution of modes agrees well with previous works, that assigned the As-S bending modes and As-S stretching modes near 200 and 400 cm^{-1}, respectively [Forneris 1969, Siebert 1954]. In fact, the modes close to 380 and 350 cm^{-1} can be assigned to the antisymmetric and symmetric As-S stretching vibrations inside the spiral chains, respectively, in good agreement with previous estimations [Frost 2002].

Structural characterization of α-As_2S_3 at HP

Figure 3 shows powder HP-XRD patterns of orpiment at selected pressures up to 26.6 GPa. XRD patterns were analyzed by means of Le Bail fits to the monoclinic $P2_1/c$ structure, which is stable up to the maximum achievable pressure. Le Bail analysis of this material allowed the possibility of obtaining the structural parameters of α-As_2S_3 at different pressures [see **Fig. 4**]. A progressive increase of the Bragg peaks width was observed and explained in the framework of a progressive loss of the hydrostatic conditions.

A monotonous decrease of the unit-cell volume of orpiment up to 26.6 GPa is observed in **Figure 4(a)**, where experimental volume data at several pressures have been compared with DFT calculations, both including and without including vdW interactions. At low pressures, the pressure dependence of the experimental volume agrees quite well with the theoretical simulation when vdW interactions are included. However, experimental data above 10 GPa show a smaller agreement with these calculations and much better agreement with calculations that do not include vdW interactions. The above experimental result indicates that orpiment is more incompressible above 10 GPa. This fact is likely due to the loss of quasi-hydrostatic conditions of the pressure-transmitting medium above this pressure.

The fit of pressure vs. experimental volume up to 10 GPa through a third-order Birch-Murnaghan Equation of State (BM-EoS) [Birch 1938] yields a zero-pressure volume, bulk modulus and pressure derivative of the bulk modulus of: V_0=468.61(5) $Å^3$, B_0=13.3(5) GPa and B_0'=8.9(5), respectively. For the fit, the volume at zero pressure, V_0, was fixed to the value measured outside the DAC and the order of the

BM-EoS was determined by the monotonously positive slope of the Eulerian strain vs normalized pressure plot of the theoretically simulated data. This plot agrees with highly compressible non-purely covalent compounds with large cation LEP activity, as it has been observed for structurally-related sesquichalcogenides, such as Sb_2S_3, Sb_2Se_3, Bi_2S_3 and α-As_2Te_3, which are characterized by bulk modulus pressure derivatives larger than 4 [Ibáñez 2016, Cuenca-Gotor 2016].

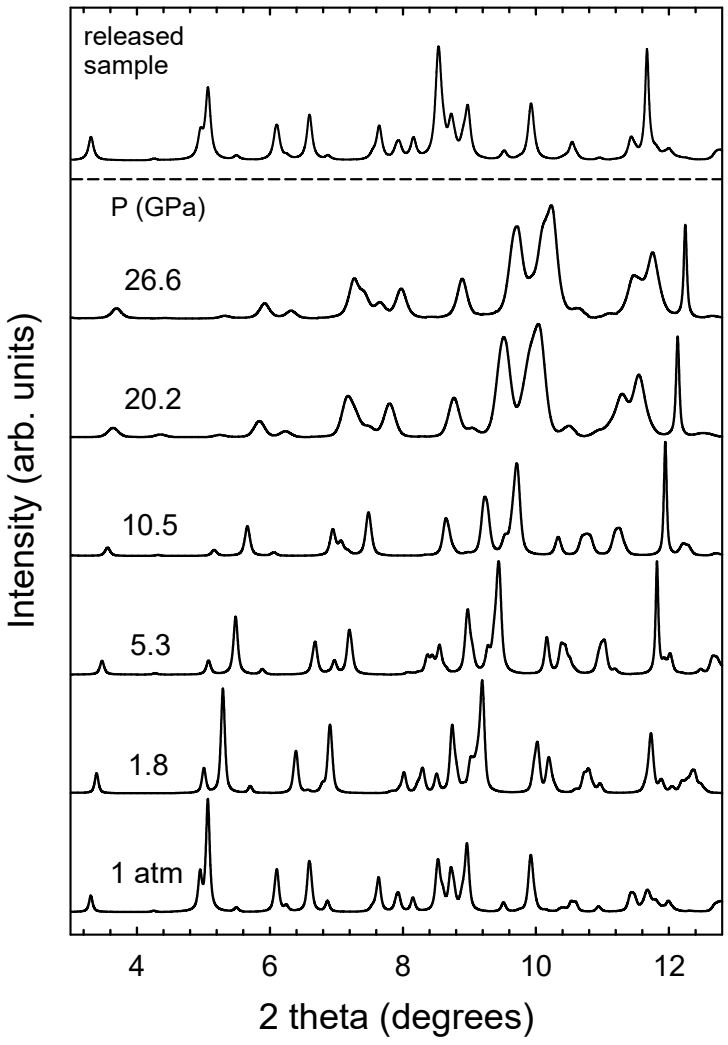

Figure 3. Powder HP-XRD patterns of α-As_2S_3 at selected pressures up to 26.6 GPa. Patterns are shifted vertically for comparison.

Our experimental bulk modulus and its pressure derivative under hydrostatic conditions for orpiment can be compared to our theoretical data with and without vdW interactions. As expected in the description of **Figure 4(a)**, the theoretical bulk modulus is closer to the experimental one when calculations include vdW interactions (B_0= 12.7(5) GPa) than when calculations do not include them (B_0= 16.1(12) GPa). Nevertheless, the theoretical pressure derivative of the bulk modulus at zero pressure is smaller than the experimental value (B_0'= 8.9(5)) in the case of simulations with vdW interactions (B_0'=7.0(14)) than in simulations without vdW interactions (B_0'= 7.9(6)). A comparison of these results with similar compounds, such as the claudetite polymorph of As_2O_3 or α-As_2Te_3, indicates that orpiment presents a similar value of the bulk modulus to the former (B_0= 15.5(4) GPa) [Guńka 2015c], but a much smaller value to the bulk modulus than the latter (B_0= 24(3) GPa) [Cuenca-Gotor 2016]. This result is consistent with the higher LEP activity of As atom in oxides and sulfides than in selenides and tellurides [Walsh 2011].

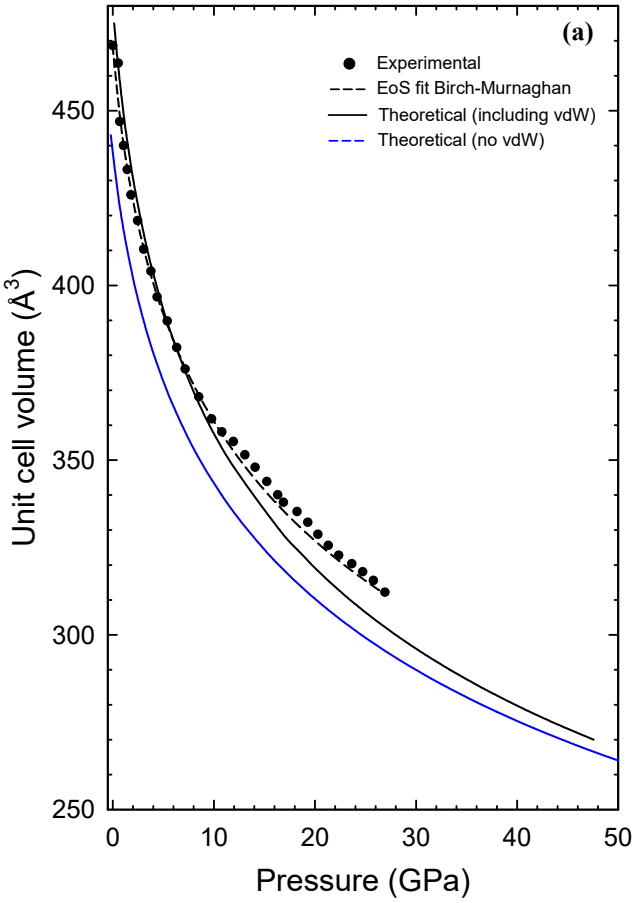

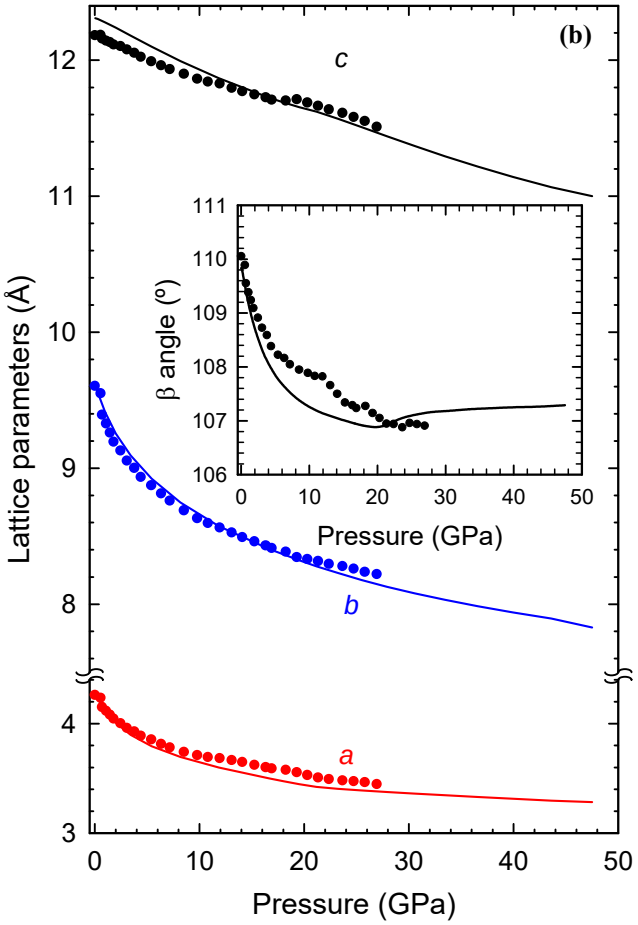

Figure 4. (a) Experimental (symbols) and theoretical (solid lines) pressure dependence of the unit-cell volume in α-As_2S_3. Black (blue) solid lines represent data from calculations including (do not including) vdW interactions. Dashed lines correspond to experimental data fit to a 3rd order BM-EoS. **(b)** Experimental (symbols) and theoretical (solid lines) pressure dependence of the lattice parameters and monoclinic β angle (inset) in α-As_2S_3. All calculations include vdW interactions.

The pressure dependence of the experimental and theoretical lattice parameters of α-As_2S_3 up to 26.6 GPa also shows a monotonous and smooth decrease [see **Fig. 4(b)**]. The good agreement of the theoretical behavior of volume and lattice parameters with our experimental data at room temperature allows us to conclude that no first-order phase transition occurs throughout the whole range of studied pressures. Furthermore, the pressure dependence of our lattice parameters do not

evidence anomalies at the region close to 10 GPa, which could be indicative of any structural transition as already suggested [Itié 1992]. Therefore, our results are in good agreement with recently published theoretical data [Liu 2019].

The analysis of the axial compressibility in monoclinic structures requires a more complex analysis than for more symmetric phases because the β-angle is not 90º, so the directions of maximum and minimum compressibility of the compound are usually not along any of the three crystallographic axes. Therefore, we have analyzed the compressibility of the material by calculating and diagonalizing the experimental and theoretical isothermal compressibility tensor β_{ij} at different pressures [details are given in the SI]. This tensor is a symmetric second rank tensor that relates the state of strain of a crystal to the pressure change that induced it [Haussühl 2007] and it has been obtained with the finite Eulerian approximation as implemented in the Win_Strain package [Angel 2004-2011].

Figures 5(a) and **5(b)** describe the pressure dependence of the tensor elements [numerical data are provided in **Tables S2**, **S3(a)** and **S3(b)** in the SI] corresponding to the compressibilities along the different axis and the direction of maximum compressibility with respect to the *c*-axis (Ψ) or to the *a*-axis (θ), respectively. According to these figures, the *a*-axis (the spiral axis) is more compressible than the *b*-axis (the axis perpendicular to the layers) up to 23 GPa. This is a surprising result for layered materials, where the axis perpendicular to the layers is usually the most compressible one; however, it is coherent with the spiral chain-like nature of the layers in orpiment and the small connectivity of the spiral layers along the *a*-axis.

The compressibility trend among the different crystallographic directions remains constant ($\beta_{11}>\beta_{22}>\beta_{33}$) up to 23 GPa, being all axial compressibilities positive, thus indicating a compression of the structure along the three main crystallographic axes up to 23 GPa. This result is somewhat in disagreement with previous visual estimations of Besson *et al.* [Besson 1980], who found positive and negative values for the compressibilities along the *a*- and *c*-axis of the layer plane, respectively, and suggested a compression of the orpiment layers in the direction perpendicular to the spiral chains and an expansion of the spiral chains along the helicoidal axis, similar to what occurs in trigonal Se and Te [Minomura 1979, Bandyophadhay 1999].

The reliability of our theoretical calculations allowed us to obtain the theoretical compressibility tensor up to 32 GPa. A sudden regularization of the three axial compressibilities to roughly the same value is attained around 23 GPa, with a quick change of the direction of maximum compressibility around this pressure. At 24 GPa, the direction of maximum compressibility is found to be along the *b*-axis ([010] direction); reason why we do not display any value on **Figure 5**. However, above 27 GPa, the direction of maximum compressibility is again found to be within the *ac*-plane, but now it is close to the *c*-axis. In particular, Ψ = 15(4)º and θ =92(4)º at 32 GPa. The drastic change of the direction of the maximum compressibility observed above 23 GPa can be considered as a more significant feature of the variation of properties associated to the low-pressure structure.

For completeness, the experimental and theoretical pressure dependence of the axial ratios in α-As_2S_3 is shown in **Figure S15** in the SI. The monotonous trend of all the

axial ratios is well reproduced by our theoretical calculations including vdW interactions. A closer look into the slopes reveals a clear change of tendency above 20 GPa, where all three ratios seem to become insensitive to pressure up to 50 GPa.

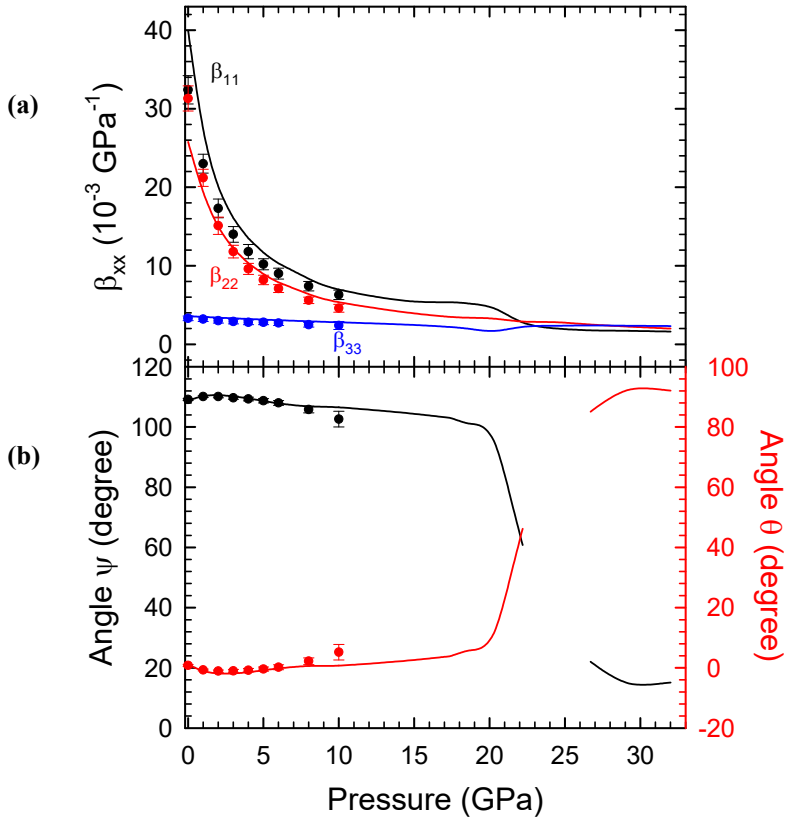

Figure 5. (a) β_{xx} coefficients of the compressibility tensor that indicates the compressibility along the different crystallographic axes. **(b)** Angle of maximum compressibility ψ relative to the *c*-axis (from *c* to *a*) or equivalently θ relative to the *a*-axis (from *a* to *c*). Solid lines represent data from calculations and symbols data from our experiments.

A similar behavior is observed in the pressure dependence of the β-angle [inset of **Fig. 4(b)**]. In some previous works, the change in the axial ratios of several group-15 sesquichalcogenides has been considered as a proof for the occurrence of a pressure-induced electronic topological transition (ETT) [Efthimiopoulos 2013, Sorb 2016, Efthimiopoulos 2016], since a minimum of the *c/a* ratio has previously been observed to be coincident with the occurrence of a pressure-induced ETT in α-Bi_2Se_3, α-Sb_2Te_3, and α-Bi_2Te_3 [Manjón 2013]. However, in recent works [Ibáñez

2016, Sans 2016c], this fact has been put into question because the minimum of the *c/a* ratio can be simply originated by a change of the ratio of inter-layer/intra-layer forces. Therefore, the change of the minimum of the *c/a* ratio does not necessarily warrant a change in the electronic density of states near the Fermi level leading to an ETT; however, it can be indicative of an IPT, as recently suggested for orpiment [Liu 2019].

To prove that the change of the axial ratios is indicative of a pressure-induced IPT, we have analyzed the pressure dependence of the internal atomic parameters of the five inequivalent atomic sites in α-As_2S_3 [see **Fig. S16** in the SI]. The most noticeable results are those observed for the three coordinates of the two inequivalent As atoms, which show a clear trend towards certain fixed coordinates above 18 (25) GPa, as obtained for calculations without (with) vdW interactions. This result occurs at similar pressures where the change of the direction of the maximum compressibility was observed. This result clearly indicates a modification of the HP behavior of the low-pressure phase.

A remarkable featura, derived from the pressure dependence of the atomic coordinates, is the grouping and regularization of many theoretical As-S interatomic distances around 18 (25) GPa, as observed in calculations without (with) vdW interactions [see **Fig. 6**]. As a consequence, there is an increase of As1 coordination from threefold at 0 GPa to more than fivefold (5+2) above 20 GPa [see **Fig. 1(e)**]. The increase in As1 coordination is because, on one hand, all As1-S1 and As1-S3 intra-layer distances become similar, thus giving a fivefold coordination and, on the other hand, two additional As1-S2 inter-layer distances become smaller than 3 Å. Similarly, there is an increase of As2 coordination from threefold at 0 GPa to fivefold above 20 GPa that stems from the equalization of the As2-S2 and As2-S3 intra-layer distances. In summary, we can conclude that above 20 GPa the As1 (As2) polyhedral units of orpiment pass from a threefold coordination towards a sevenfold (fivefold) coordination without a change in the space group.

A more detailed analysis of the As polyhedral units [see **Fig. S17 to S19** in the SI] shows how both As1 and As2 polyhedral units remain in a threefold effective coordination below 10 GPa. Above this critical pressure, there is a progressive increase of the effective coordination up to 22 GPa, where the As2 polyhedron remains in fivefold effective coordination, whereas that of the As1 polyhedral unit increases up to sixfold effective coordination [**Fig. S19** in the SI]. We must note that in distorted polyhedral units [values very different from 0 in **Fig. S18** in the SI], the effective coordination number does not describe properly the coordination of the polyhedral unit because some of the interatomic distances are longer than others, thus leading to an effective coordination dominated by the next neighbors [**Fig. S19** in the SI] but with large polyhedral volumes [**Fig. S17** in the SI]. Above 20 GPa, the effective coordination of As1 is slightly larger than five despite there is a higher real coordination of (5+2) due to the strong distortion of the polyhedral unit around As1, whereas for As2 the effective coordination (five) coincides with the real coordination due to the proximity of the interatomic distances.

The above results between 0 and 20 GPa are consistent with: i) the regularization of the axial compressibilities, ii) the trend found towards the fixed As coordinates, and iii) the similar *x* and *z* coordinates showed by the Wyckoff sites of As1, S2, and S3 atoms, above 18 (25) GPa in our calculations without (with) vdW interactions. All these results indicate the presence of an IPT above 20 GPa, in agreement with a recent paper [Liu 2019] and also with by HP-XAS results that reported a change in the As environment above 10 GPa and an increase of As coordination above 30 GPa [Itié 1992].

In summary, HP-XRD measurements and DFT calculations carried out up to 32 GPa show that the effect of pressure upon the structure of α-As_2S_3 does not result in a first-order phase transition, but triggers a change of the trend of atomic coordinates, of axial ratios, and an increase of coordination of As atoms above 20 GPa; as well as a drastic change of the direction of the maximum compressibility above 23 GPa. All these features are in good agreement with published data [Itié 1992, Liu 2019] and could be attributed to a pressure-induced IPT in orpiment above 20 GPa.

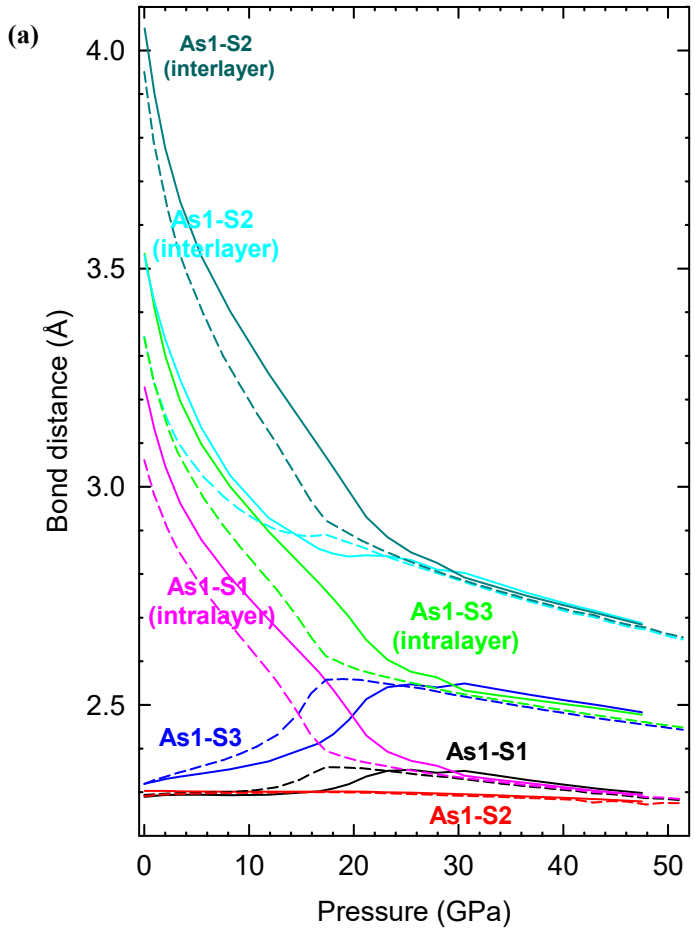

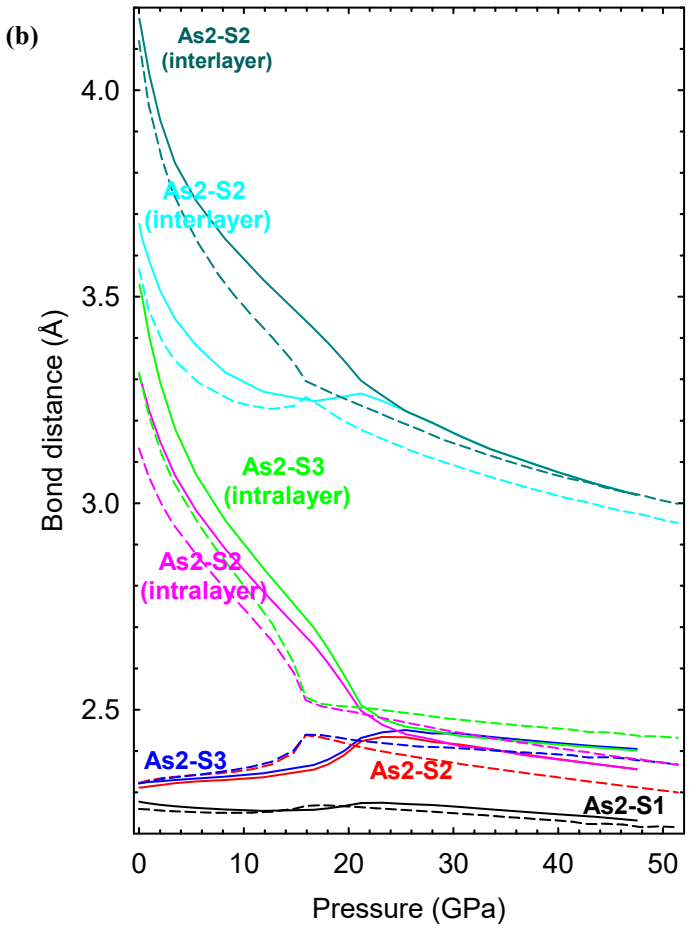

Figure 6. Evolution under pressure of the theoretical As-S interatomic distances of α-As_2S_3. **(a)** As1 and its next-neighbor S atoms. **(b)** As2 and its next-neighbor S atoms. Dashed (solid) lines represent data from theoretical calculations that include (do not include) vdW interactions.

Vibrational characterization of α-As_2S_3 at HP

In order to study the effect of pressure on the vibrational properties of orpiment and better understand its HP behavior, we have carried out HP-RS measurements on orpiment samples up to 14.5 GPa that have been compared to lattice-dynamics calculations of α-As_2S_3. On **Figure 7**, we show the room-temperature RS spectra of orpiment at selected pressures under hydrostatic conditions. We may observe that the highest-frequency mode of the low-frequency region, located close to 200 cm^{-1} at room pressure, shows an increase of the intensity as pressure increases. This fact

supports the argument of the absence of any first-order PT in orpiment up to 14.5 GPa, in good agreement with our HP-XRD measurements and previously published results [Itié 1992, Liu 2019].

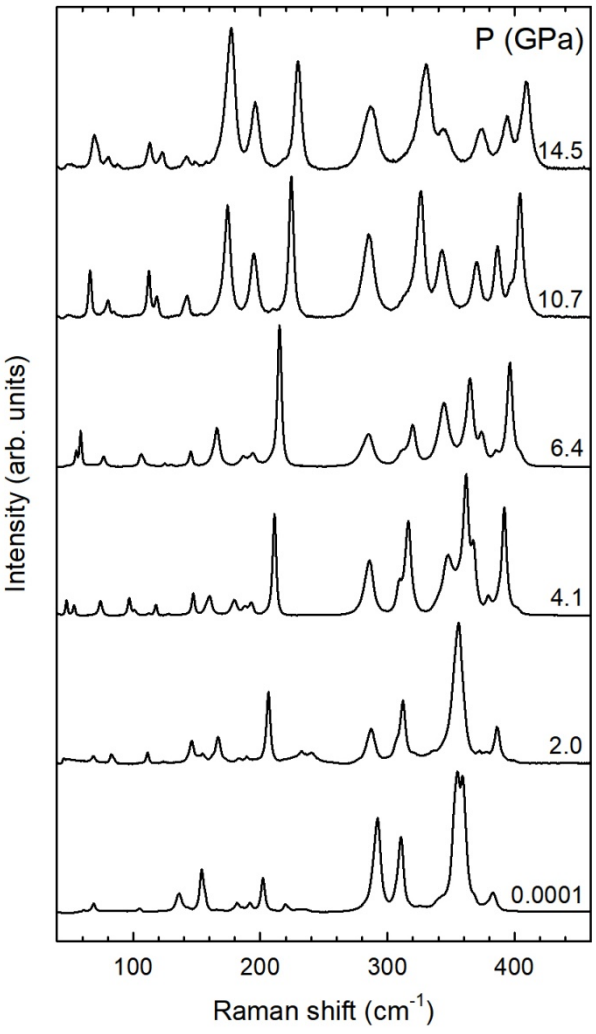

Figure 7. Room-temperature RS spectra of orpiment at selected pressures up to 15 GPa.

RS spectra show a much larger number of Raman modes between 2.0 and 4.1 GPa. A much larger number of Raman modes are observed at 4.1 GPa than at 2.0 GPa, despite the disappearance of the Raman modes in the phonon gap between 210 and

250 cm^{-1}. As already commented, these modes in the phonon gap, together with a mode observed above 1 GPa near 120 cm^{-1}, are assumed to be second-order modes and will not be further discussed. No major changes of the RS spectra are observed between 4.1 and 14.5 GPa. In this context, it must be noted that the bandgap of orpiment (2.7 eV at room pressure) decreases under pressure at a rate of -0.14 eV/GPa [Besson 1980, Zallen 2004]. This means that the bandgap equals the HeNe laser energy (1.96 eV) at 5.3 GPa, so some resonance effects could be observed above ca. 4 GPa.

As already mentioned, it is very difficult to assign the features that show up in the room-pressure RS spectrum of α-As_2S_3. However, it is possible to perform a tentative peak assignment by studying the pressure dependence of the Raman-active modes in combination with lattice-dynamics calculations taking into account the correlation of the frequencies and their pressure coefficients [see **Table 2** and **Fig. 8(a)**]. Our observed frequencies and pressure coefficients are in good agreement with previous HP-RS studies [Zallen 1974b, Besson 1980, Besson 1981, Liu 2019]. Notably, the shear or transverse rigid modes A_g^1 and A_g^2 at 26 and 37 cm^{-1} and the B_g^2 mode at 69 cm^{-1} show the three largest relative frequency pressure coefficients at zero pressure (0.24, 0.13 and 0.15 GPa^{-1}, respectively). Moreover, the B_g^2 mode shows the experimental and theoretical largest pressure coefficient and mode Grüneisen parameter of all Raman-active modes (around 10.5 cm^{-1}/GPa and 1.97, respectively).

While the above results regarding the shear rigid layer A_g modes are rather common in layered materials, the result regarding the B_g^2 mode is quite surprising because the largest pressure coefficient is indeed expected for the compressional or longitudinal layer mode B_g^1 located at 62 cm^{-1} [see **Fig. S2** in the SI]. It is well known that the compressional layer mode usually shows higher frequencies and pressure coefficients than those of the shear rigid layer modes in layered materials with vdW interactions between the layers. This common trend is due to the extraordinary increase of the stretching force constant between neighboring layers caused by the strong decrease of the interlayer distance, as discussed in a recent paper [Pereira 2018]. However, we have found that the B_g^1 mode in orpiment (not observed experimentally) shows a rather small theoretical pressure coefficient [see **Table 2**]. This anomalous pressure dependence of the compressional mode of orpiment can be understood by considering a frequency anticrossing (occurring already at room pressure) between the B_g^1 and B_g^2 modes. In fact, the large pressure coefficient of the "bare" B_g^1 mode [see dashed line in **Fig. 8(b)**] is so large, when compared to other Raman modes, that this mode undergoes anticrossings with up to four B_g modes (up to B_g^5) in the pressure range between 0 and 15 GPa. This anticrossing allows us to explain the small pressure coefficient of the B_g^1 mode and the large pressure coefficient of the B_g^2 mode of orpiment. Moreover, this puzzling behavior may explain why the compressional mode was not previously assigned, despite the frequency of the compressional mode was well identified in a previous work [Zallen 1974a] as well as the pressure coefficient of the B_g^2 mode [Zallen 1974b].

As observed in **Figure 8(a)**, experimental and theoretical frequencies of Raman-active modes do not show a simple monotonic behavior with increasing pressure. In

fact, many Raman active modes exhibit a complex behavior under pressure with crossings and anticrossings of modes with different and equal symmetries, respectively. This complex behavior stems from the presence of 30 Raman-active modes in a small frequency region between 30 and 400 cm^{-1}, similarly to what has been found in monoclinic α-As_2Te_3 [Cuenca-Gotor 2016]. Despite the complex behavior observed in our theoretical Raman-active modes, several experimental modes have shown a behavior consistent with the theoretical modes. In particular, we have found an experimental reduction of the phonon gap with pressure, an anticrossing of Raman modes close to 150 cm^{-1} around 2 GPa, and the splitting of several Raman modes located near 350 cm^{-1}, which are in good agreement with previous results [Besson 1980, Besson 1981, Liu 2019]. Such behaviors are supported by our lattice-dynamics calculations for the pressure dependence of the A_g^9 and A_g^{10} modes, the A_g^5 and A_g^6 modes and the A_g^{12}, A_g^{13} and A_g^{14} modes, respectively [see **Fig. 8(a)**].

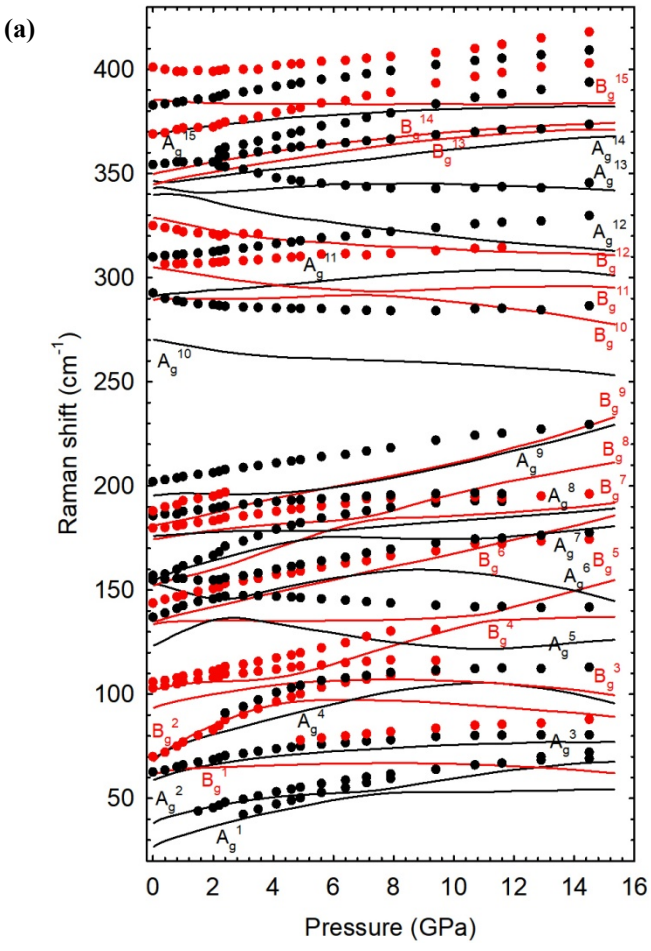

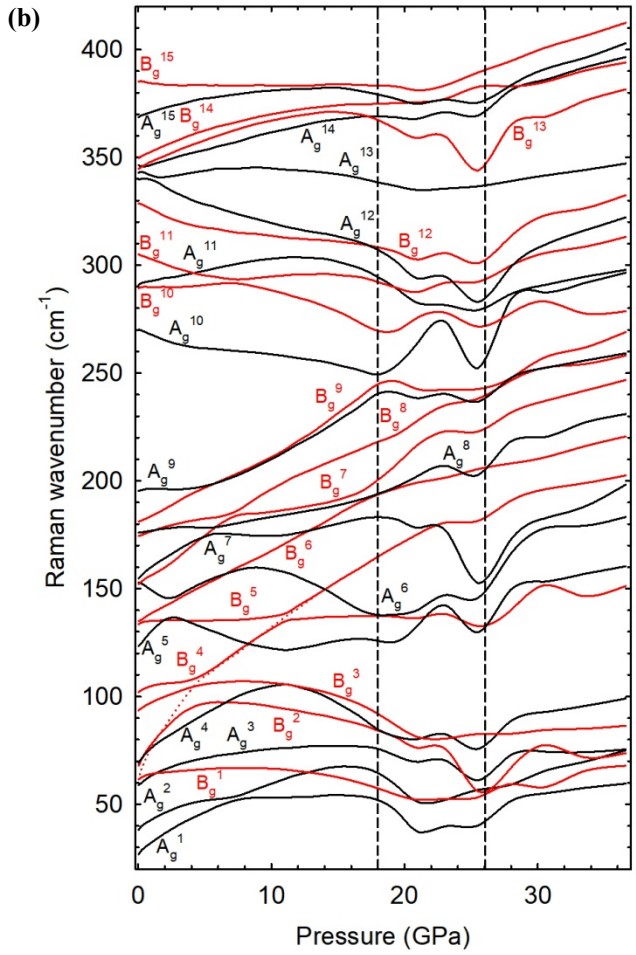

Figure 8. (a) Experimental (symbols) and theoretical (lines) pressure dependence of the Raman-active mode frequencies of As_2S_3 up to 16 GPa. Black (red) color represents A_g (B_g) Raman-active modes. Theoretical curves correspond to calculations with vdW interaction. **(b)** Pressure dependence of the theoretical Raman-active mode frequencies of As_2S_3 up to 36 GPa. Red dotted line represents the tentative pressure dependence of the "bare" B_g^1 mode (the compressional rigid layer mode) if no anticrossing would occur with other modes of the same symmetry. Note that a change in the pressure coefficient of the "bare" B_g^1 mode observed near 4 GPa and that a considerable softening of some vibrational modes is observed between 18 and 26 GPa.

A striking feature of orpiment is the large number of Raman modes with negative pressure coefficients at room pressure. This is confirmed by both experimental and theoretical data. In particular, modes located at 155, 291, 325, 356 and 400 cm^{-1} show softening under pressure in rather good agreement with previous

measurements [Zallen 1974b, Liu 2019]. As noted by Besson et al. [Besson 1980], negative pressure coefficients of internal modes have been observed in Raman measurements of other chain-like structures, such as trigonal S, Se and Te [Degtyareva 2007, Richter 1973, Aoki 1980], but never for ring molecules, like those found in orthorhombic S [Zallen 1974b]. In trigonal S, Se and Te, the soft Raman phonon is the A_1 mode (the breathing mode of the chains at the *ab*-plane [Lucogsky 1972]) and it can be related to the expansion of the *c*-axis, caused by the increase of the Se-Se intra-chain distance, at the expense of the contraction of the *a*-axis, caused by the decrease of the Se-Se inter-chain distance. In orpiment, the situation is quite different because all three *a*-, *b*-, and *c*-axes suffer a contraction under compression so the explanation for the negative pressure coefficients is not related to the elongation of any axis.

Figure 6 shows that As1-S3, As2-S2, and As2-S3 (As1-S1) intra-layer distances increase above 0 (10) GPa, thus providing an explanation for the softening of several phonons in different pressure ranges. Notably, changes of the pressure coefficient of some experimental and theoretical Raman-active modes have been observed around 4 GPa in α-As_2S_3, which could be attributed to the strong changes of the interatomic distances around these pressures. The changes can be clearly observed in the experimental B_g^1 and A_g^{10} modes and in the theoretical A_g^2, B_g^1, A_g^8, A_g^9, A_g^{10} and A_g^{15} modes [see **Fig. 8**]. They can also be observed in the theoretical B_u^1, A_u^2, A_u^3, A_u^8, B_u^7, B_u^8 and A_u^9 modes [see **Fig. S20** in the SI], which do not evidence anticrossings between 0 and 6 GPa.

Figures 8(b) and **S20** show a notable softening of the theoretical vibrational modes of orpiment in the region between 18 and 26 GPa, where the pressure-induced IPT occurs according to our calculations. In order to probe the possibility of a second-order IPT occurring in α-As_2S_3, we have studied the phonon dispersion curves calculated at different pressure values, ranging up to 30 GPa [see **Fig. S21 and S22** in the SI], because a second-order IPT is related to the presence of a soft phonon mode according to Landau theory. Since we do not observe any soft mode up to 30 GPa, we can conclude that the pressure-induced IPT occurring in α-As_2S_3 above 20 GPa must be of order higher than 2; i.e. an IPT of electronic origin, such as the pressure-induced ETTs observed in other group-15 sesquichalcogenides [Manjón 2013].

Electronic band structure calculations of α-As_2S_3 at HP

To complete the picture of the behavior of orpiment at HP and in order to assess whether a pressure-induced ETT could be observed in orpiment, we have performed *ab initio* electronic band-structure calculations of α-As_2S_3 at different pressures to identify possible changes of the band extrema that could be related to a pressure-induced ETT [see **Fig. 9**]. Our calculations show that orpiment is an indirect bandgap (1.7 eV) semiconductor at 0 GPa, with the valence band maximum (VBM) and conduction band minimum (CBM) being located along the high-symmetry segment of Y-Γ and Γ-Z directions, respectively. The value of the bandgap is clearly

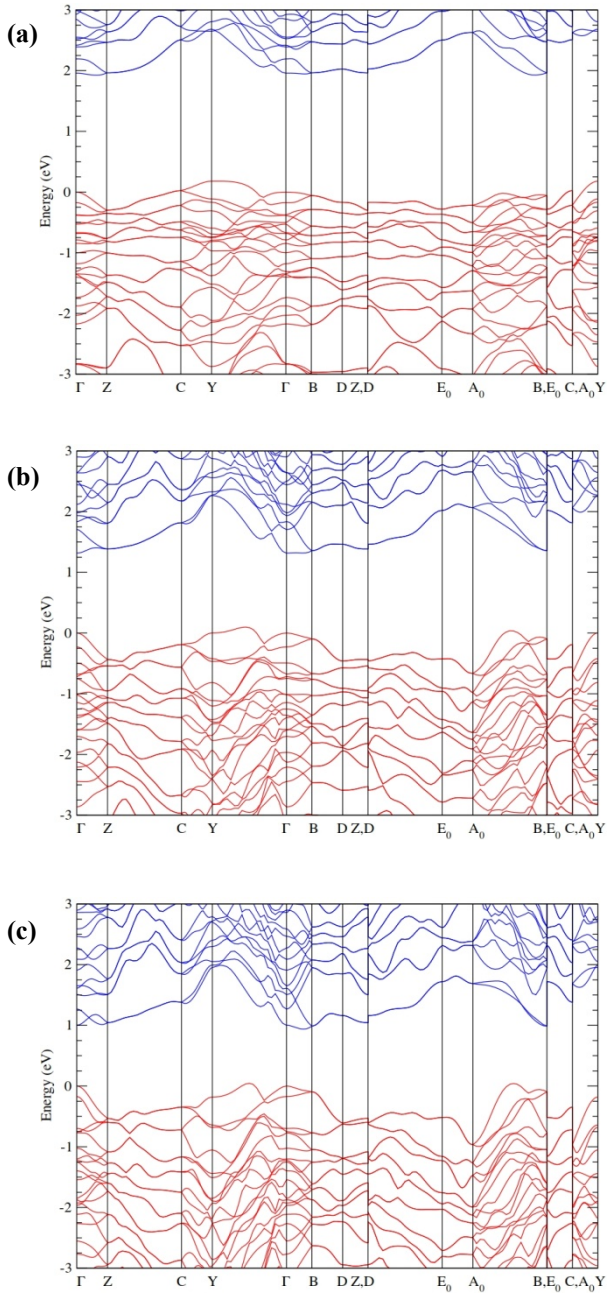
(a)
(b)
(c)
Energy (eV)
3
2
1
0
-1
-2
-3
Γ Z C Y Γ B D Z,D E0 A0 B,E0 C,A0 Y

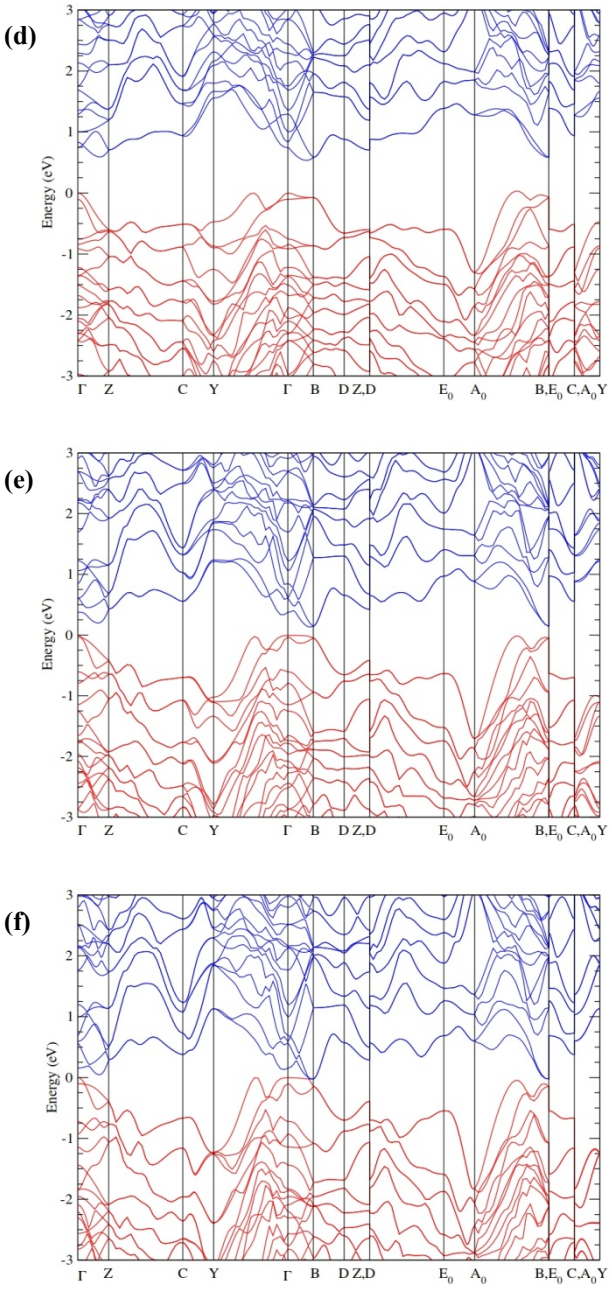

Figure 9. Calculated band structure of α-As_2S_3 at different pressures: **(a)** 0 GPa, **(b)** 5 GPa, **(c)** 10 GPa, **(d)** 15 GPa, **(e)** 20 GPa, and **(f)** 30 GPa.

underestimated by our DFT calculations, since orpiment is known to have a bandgap around 2.7 eV at room pressure [Besson 1980, Zallen 2004], but the structure of the electronic bands and the bandgap evolution with pressure are correctly described by this method. The bandgap energy value in our calculations is similar to the values of recent *ab initio* calculations, however differing in the precise locations of the VBM and CBM [Liu 2019, Srivastava 2011].

There are considerable changes in the VBM and CBM of α-As_2S_3 at HP. Both valence and conduction bands show a low dispersion across the BZ at 0 GPa, but a high dispersion above 20 GPa. The flat bands at 0 GPa reflect the 2D character of orpiment, while the highly-dispersed bands above 20 GPa reflect the 3D character of orpiment above this pressure. It can be observed that above 20 GPa, the VBM shifts to the Γ-point and along the Γ-B direction, whereas the CBM moves to the B-point. Additionally, a variation of the VBM occurs between 20 and 30 GPa, with the VBM at 30 GPa shifted along the high-symmetry Γ-Y direction. Since we observe the crossing of an extremum through the Fermi level above 20 GPa, thus modifying of the topology of the Fermi-surface, we thus suggest a possible pressure-induced ETT above this pressure in α-As_2S_3.

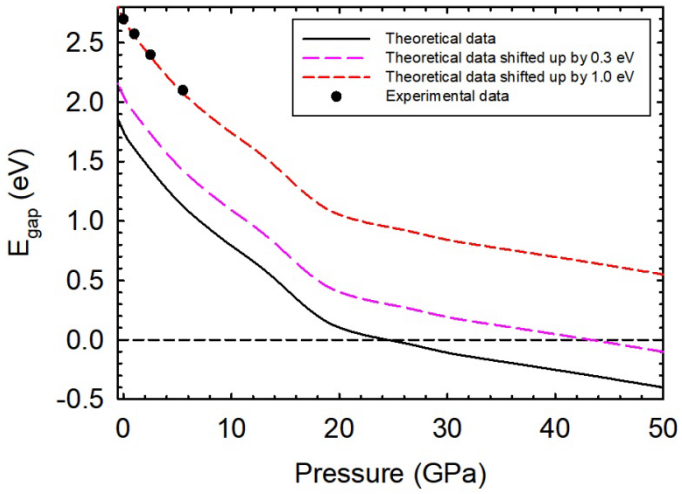

Figure 10. Pressure dependence of the energy bandgap of orpiment. Solid, long dashed and short dashed lines correspond to results of theoretical calculations including vdW interaction, theoretical calculations shifted by 0.3 eV (to match the metallization observed above 42 GPa in Liu (2019)) and theoretical calculations shifted by 1.0 eV (to match the optical bandgap at 0 GPa as in Besson (1980) and Besson (1981)), respectively. Symbols correspond to experimental data from Besson (1980) and Besson (1981).

The calculated indirect bandgap exhibits a strong decrease at HP from 1.7 eV at 0 GPa to 0 eV at 26 GPa [see solid line in **Fig. 10**]. Therefore, our calculations provide evidence for a semiconducting-metallic transition in orpiment above 26 GPa. A

recent experiment suggests that metallization in orpiment should occur above 42 GPa [Liu 2019]. However, if metallization occurred above 42 GPa, the underestimation of the bandgap should be only 0.3 eV in our calculations [see long dashed line in **Fig. 10**]. On the other hand, if we take into account the value of the experimental optical bandgap at room pressure (2.7 eV) and shift the calculated bandgap to match the latter, the evolution of the bandgap [see short dashed line in **Fig. 10**] matches remarkably well with the behavior of the optical bandgap [symbols in **Fig. 10**] [Besson 1980, Besson 1981] and the extrapolation of the shifted calculated bandgap to 0 eV yields a closure of the bandgap to 0 eV at pressures that go beyond the studied range (above 50 GPa). In fact, the decrease of the electronic bandgap shows a theoretical pressure coefficient of -0.11 eV/GPa, which is in very good agreement with a previous experimental estimation of the optical bandgap pressure coefficient (-0.14 eV/GPa) [Besson 1980, Besson 1981, Zallen 2004]. Therefore, our theoretical estimation of the pressure dependence of the bandgap suggests that metallization should actually occur at much higher pressure values of 40 GPa, so we suggest that the metallization of orpiment, observed above 42 GPa [Liu 2019], could be due to non-hydrostatic conditions in the sample during electric measurements.

In summary, α-As_2S_3 is a semiconductor with a rather wide indirect bandgap (2.7 eV at room pressure) that decreases at HP at a considerable rate until it becomes a metal well above 50 GPa. A clear change in the VBM is observed above 20 GPa that could lead to a pressure-induced ETT; i.e. an IPT of order $2^{1/2}$ according to Ehrenfest notation [Lifshitz 1960].

Metavalent bonding in α-As_2S_3

In this section, we will show that the results obtained so far for the pressure dependence of the structural, vibrational, optical and electric properties of α-As_2S_3 can be understood on the light of a special case of resonant bonding formalism [Shportko 2008, Lee 2014, Li 2015, Xu 2017, Wuttig 2018, Raty 2018], recently termed as metavalent bonding in order to distinguish it from the resonant bonding occurring in benzene and graphite [Wuttig 2018]. In particular, the HP behavior of orpiment between 0 and 20 GPa can be considered as the process of change from p-type covalent bonding towards metavalent bonding at HP. Moreover, we will show that the concept of metavalent bonding could be extended to understand the pressure behavior of other group-15 sesquichalcogenides and of trigonal Se and Te.

Metavalent bonding is a recently proposed new class of bonding formalism, mainly located between p-type covalent bonding and metallic bonding, which is characteristic of a new type of materials termed as “incipient metals” [Wuttig 2018]. This kind of bonding occurs in materials where there is a deficiency of valence electrons in the unit cell to form a large number of bonds, such as in octahedrally-coordinated rocksalt-related structures as those found for GeTe, SnTe, PbSe, PbTe, Sb, Bi, Sb_2Te_3, Bi_2Se_3, Bi_2Te_3, $AgSbTe_2$, $AgBiSe_2$, $AgBiTe_2$, and $GeSb_2Te_4$ [Lee 2014, Wuttig 2018, Raty 2018]. Under these circumstances, the few valence

electrons available in the formula unit must be shared (resonate) between several bonds.

The main characteristics of this type of bonding are: i) a cation coordination much higher than that assumed with the 8-N rule; ii) high Born effective charges that are much larger than the valence of the atoms; iii) higher optical dielectric constants than typical covalent materials; iv) high mode Grüneisen parameters of phonons and lower wavenumbers of optical phonons than typical covalent materials, thus revealing a high lattice anharmonicity causing a very small thermal conductivity; and v) a moderately high electrical conductivity caused by a very small bandgap. All these features stem from the partial delocalization of electrons that are shared between several bonds. Due to these characteristics, materials featuring metavalent bonding have been named "incipient metals" because they show characteristics close to those of metals. In fact, they exhibit extraordinary properties that make them ideal candidates for phase-change materials, thermoelectric materials, and topological insulators.

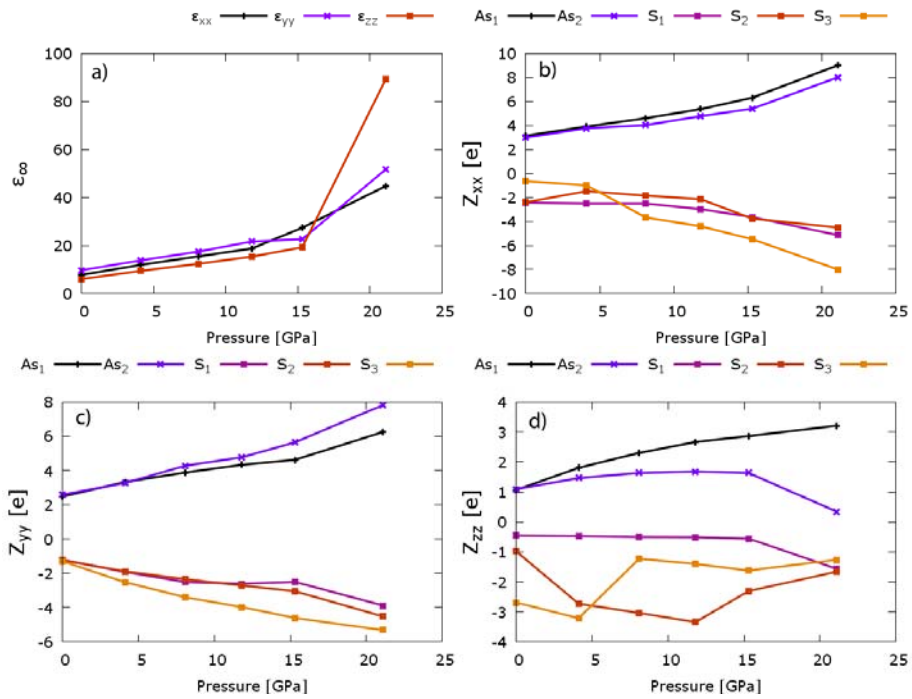

Figure 11. Pressure dependence of the dielectric functions **(a)** along the main crystallographic axes and Born effective charges **(b,c,d)** of the different As1, As2, S1, S2 and S3 atoms along the main crystallographic axes.

Regarding orpiment, the equalization of the As-S intralayer distances above 18 (25) GPa, according to our calculations without (with) vdW interactions, is in agreement with the bonding variation nature of As-S bonds from covalent to metavalent [Xu 2017, Wuttig 2018, Raty 2018]. To prove such fact, we have probed the bonding character of orpiment at different pressures; e.g. the electron localization function (ELF) along the seven next-neighbor As-S distances, the dielectric tensor, and the Born effective charges, as suggested in Wuttig (2018).

The increase of the metavalent bonding in orpiment under compression can be traced by the increase of the theoretical dielectric constants and the Born effective charges [see **Fig. 11**], as commented in Shportko (2008) and Wuttig (2018). A strong increase in the absolute value of most of these magnitudes is observed between 0 and 20 GPa [see **Fig. 11**] [**1**]. The only Born effective charge component that does not show similar behavior within the range of 0 and 20 GPa is the Z_{zz} component, which is related to the *c*-axis, the direction of smallest change in bonding character because it is the direction of smaller compressibility [see **Fig. 5**]. These changes are a clear indication of the decrease (increase) of the covalent (metavalent) bonding of the layers of orpiment. Besides, the strong decrease of the optical bandgap with pressure and the metallization of orpiment well above 50 GPa is consistent with the metavalent bonding observed for chalcogenides [Wuttig 2018, Raty 2018]. The rapid delocalization of the electron charge density over the plane of the layers caused by the steep increase of coordination of As atoms due to the strong compression of the chains mainly along the *a*-axis is the origin of the pronounced negative slope of the bandgap with increasing pressure.

Figure 12 shows the ELF values along the seven next-neighbor As1-S and As2-S distances obtained from our theoretical results at 0 and 25 GPa. At 0 GPa, both the As1 and As2 atoms have high ELF values (around 0.8) close to the center of the As-S bonds for each of the three bonds of each As atom (As1-S1, As1-S2, As1-S3, As2-S1, As2-S2, and As2-S3); thus evidencing the threefold coordination of As1 and As2 atoms and the covalent bonding in orpiment at room pressure. However, at 25 GPa there are five intra-layer As2-S bonds with high ELF values (As2-S1 bond above 0.8 and two As2-S2 and two As2-S3 bonds above 0.6) showing fivefold coordination for As2 in orpiment. A similar situation occurs for the As1 atoms at 25 GPa, with five intra-layer As1-S bonds with a relatively high ELF (As1-S2 bond near 0.8, two As1-S1 above 0.7 and two As1-S3 above 0.5), but also with two inter-layer As1-S2 bonds with an intermediate value of the ELF (slightly above 0.2), which can be considered to support 5+2 coordination. Note that the typical metavalent bonding in the layer plane (*ac*-plane) of orpiment is clear for the As2 atoms, where all four intra-layer bonds (As2-S2, As2-S3, As2-S4, and As2-S5) have the same ELF value because they have the same As2-S length. A similar behavior of the ELF at HP has been found in GeSe at HP and ascribed to the onset of metavalent bonding [Xu 2017]. On the other hand, the character of As1-S bonds is more complex because the ELF values and lengths of all the intra-layer bonds are not equal. Such behavior suggest that the intra-layer metavalent bonding of As1 atoms is sacrificed by a larger coordination number taking into account S atoms of adjacent layers. Note that these S atoms are not linked to As2 atoms of the monoclinic

structure even up to 50 GPa, what evidences the different behavior of As1 and As2 atoms on increasing pressure. The larger coordination of As1 atoms at HP is indicative of a tendency of As1 atoms to metallic bonding, which is usually characterized by a much larger effective coordination number than covalent and metavalent bondings [Wuttig 2018, Raty 2018].

The decrease of the bond force (ELF value) of some As-S bonds in orpiment is likely related to the length increase of those bonds [see **Fig. 6]**, because the charge of valence electrons in As atoms must progressively be redistributed among several equidistant As-S bonds within the context of metavalent bonding [Xu 2017, Wuttig 2018, Raty 2018]. Therefore, the charge at each of the short bonds at low pressure is redistributed between two equal bonds at HP leading to a smaller ELF for the initial short bonds at HP than room pressure. Such a feature is confirmed by the equal values of the ELF in As-S bonds of equal length at HP already commented. Therefore, the decrease of the ELF of the original covalent bonds at HP clearly shows the delocalization of electronic charge in these bonds to form metavalent bonds at HP.

This bond enlargement and charge redistribution typical of the formation of metavalent bonds is expected to cause a decrease of some of the optical phonon frequencies. In particular, a softening of the transverse optical (TO) and longitudinal optical (LO) modes has been predicted in rocksalt compounds with metavalent

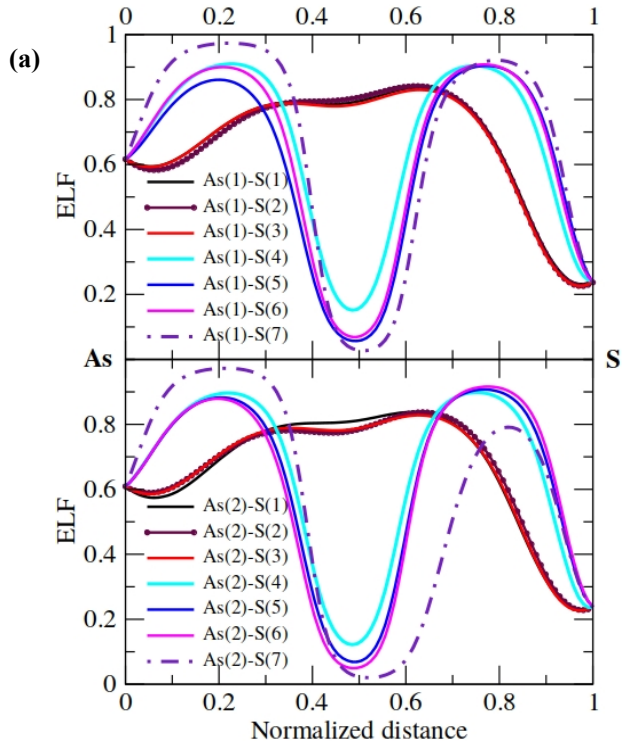

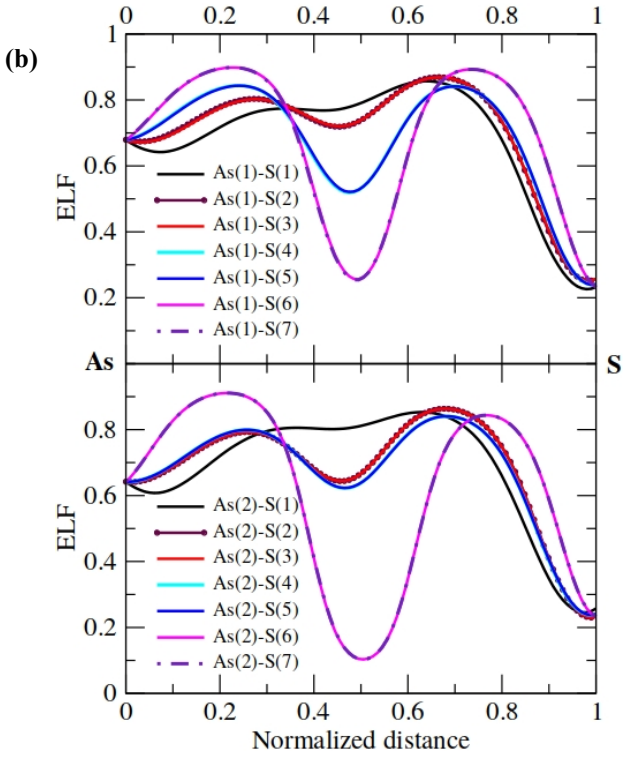

Figure 12. Pressure dependence of the ELF along the As1-S (top) and As2-S (bottom) bonds at 0 GPa **(a)** and 25 GPa **(b)**.

bonding as compared to the same compound in absence of metavalent bonding [Lee 2014, Li 2015]. For a monoclinic compound, such as orpiment, the situation is more complex, because the TO and LO modes of the rocksalt structure are split into many components due to the decrease in symmetry. Therefore, we expect that many optical modes of orpiment will soften with increasing pressure due to the establishment of long-range interactions between neighboring atoms upon increasing the metavalent bonding at increasing pressure. In fact, **Table 2** and **Figure 8** show that one of the most characteristic modes that exhibit a negative pressure coefficient is the A_g^{10} mode [see atomic vibrations in **Fig. S11** in the SI], that is experimentally observed at 291 cm^{-1} at room pressure. Other soft Raman- and IR-active modes can be observed in **Figures 8(b)** and **S20** in the SI, respectively. Moreover, these last figures show a clear decrease of the phonon bandgap (between A_g^9 and A_g^{10} and between B_u^7 and B_u^8) from 0 to 20 GPa. This decrease of the phonon bandgap is also expected in the context of metavalent bonding [Lee 2014, Li 2015, Wuttig 2018]. Finally, we observed a considerable softening of several modes taking place between 18 and 26 GPa and clear positive slopes of most vibrational modes above 26 GPa; i.e. once the bonding transition to metavalent bonding takes over. These

features are in agreement with the development of metavalent bonding since low-frequency values of optical vibrational modes and positive slopes of all Raman-active and IR-active modes have been observed in Bi_2Se_3, Sb_2Te_3 and Bi_2Te_3, which are metavalent compounds at room pressure [Manjón 2013].

A closer look into the HP behavior of other chalcogenides evidences that the softening of optical modes at HP has been observed in a number of chalcogenides, thus suggesting that metavalent bonding is more common than expected at HP in these compounds. Several modes of the low-pressure trigonal phase of Se and Te exhibit a pronounced softening at HP. However, no softening has been found in the HP phases of these two elements [Properzi 2013, Marini 2012], as it happens in Bi_2Se_3, Bi_2Te_3 and Sb_2Te_3 [Manjón 2013]. This result is consistent with the formation of metavalent bonding in both materials at HP [Wuttig 2018]. Therefore, we expect a similar increase of dielectric constants and Born effective charges at HP in the low-pressure trigonal phase of Se and Te, as it has been shown in orpiment and other compounds [Shportko 2008, Wuttig 2018, Raty 2018].

Finally, we want to emphasize that the analysis of the different group-15 sesquichalcogenides [**Table S5** in the SI] reveals that their behavior at HP can also be understood in the framework of metavalent bonding. In particular, some of these materials possess metavalent bonding at room pressure and some others tend to a metavalent bonding at HP. For instance, a similar situation to that of α-As_2S_3 is expected to occur for isostructural α-As_2Se_3 and for β-As_2Se_3 at HP since both compounds feature a threefold coordination at room pressure. Unfortunately, there are almost no HP studies of these compounds. On the other hand, α-Sb_2S_3, α-Sb_2Se_3 and α-Bi_2S_3, which crystallize in the orthorhombic *Pnma* phase, feature an average fourfold cation coordination, because one cation has threefold coordination and the other has fivefold coordination. Therefore, they show an intermediate cation coordination between the threefold coordination of α-As_2S_3 and the sixfold coordination of α-Sb_2Te_3. They exhibit softening of some high-frequency modes [Efthimiopoulos 2013, Efthimiopoulos 2014, Ibáñez 2016]. In particular, softening of two high-frequency modes has been observed in α-Sb_2S_3 up to 12 GPa; pressure at which Sb1 and Sb2 can be considered to have almost a sevenfold coordination due to a pressure-induced metavalent bonding of both Sb atoms [Ibáñez 2016].

An intermediate case between covalent and metavalent bonding is also that of α-As_2Te_3, which shows an average cation coordination of 5.5, because one cation has 3+2 coordination and the other has 3+3 coordination. Therefore, it shows an intermediate coordination between the fivefold coordination of α-Sb_2Se_3 and the sixfold coordination of α-Sb_2Te_3. Consequently, α-As_2Te_3 shows almost no soft phonons. Only a few of high-frequency phonons show a soft behavior with almost negligible pressure coefficient between 0 and 4 GPa and a notable hardening above this pressure [Cuenca-Gotor 2016]. An inspection of the evolution of the As-Te distances in this pressure range shows that the As1 (As2) coordination changes from almost five (six) at room pressure to real six (six) above 4 GPa. Therefore, the changes observed in the pressure coefficients of zone-center vibrational modes in α-As_2Te_3 are indicative of a change of bonding type from an almost metavalent bonding inside the layers to a full metavalent bonding that takes into account also

interactions between the layers. Finally, β-As_2Te_3 with $R\bar{3}m$ symmetry and sixfold coordination is expected to show no soft modes, as α-Bi_2Se_3, α-Bi_2Te_3 and α-Sb_2Te_3 [Manjón 2013].

It must be noted that a notable decrease of the bandgap with pressure has also been obtained in DFT calculations for α-Sb_2S_3, α-Sb_2Se_3 and α-Bi_2S_3 [Ibáñez 2016], and at a smaller rate also for α-As_2Te_3 [Manjón 2013] and Bi_2Te_3 [Vilaplana 2011a]. In fact, we have observed a metallization around 26 GPa in our DFT calculations for α-As_2S_3, similar to the metallization found around 4 GPa for α-As_2Te_3 and above 12 GPa for α-Sb_2S_3. Therefore, it is expected that a similar increase of dielectric tensors and the Born effective charges at HP occurs in these group-15 sesquichalcogenides, thus supporting the occurrence of metavalent bonding in these compounds at HP.

V. CONCLUSIONS

The monoclinic structure of orpiment (α-As_2S_3) at room conditions is composed of layers formed by AsS spiral chains, where the As atoms have threefold coordination. We have studied the structural, vibrational, and electronic properties of orpiment at room temperature and HP and have found that orpiment undergoes a strong compression up to 20 GPa, followed by an IPT of electronic origin, that leads to a coordination of As which is higher than five above that pressure. The most striking feature of the pressure-induced IPT is that several As-S bond distances become equal above 20 GPa.

The lattice dynamics of orpiment has been studied and all the rigid layer modes and the main inter-chain and intra-chain modes have been fully described. Our measurements and calculations evidence the softening of many vibrational modes and the decrease of the phonon gap at HP (it closes above 20 GPa) at HP. Moreover, our calculations confirm the metallization of orpiment above 26 GPa due to the strong decrease of the optical bandgap, thus supporting metallization in laboratory under hydrostatic conditions well above 50 GPa when taking into consideration the underestimation of the energy bandgap in DFT calculations. All these changes are related to the formation of metavalent bonding occurring in orpiment above 20 GPa due to the delocalization of electronic clouds, mainly in the *ac*-plane of the layers, without the need for a first-order structural phase transition as in Se and Te but similar to GeSe [Xu 2017].

It has been shown that metavalent bonding already occurs in other group-15 sesquichalcogenides at room pressure. Full metavalent bonding occurs in topological insulators and good thermoelectric materials as α-Bi_2Se_3, α-Bi_2Te_3 and α-Sb_2Te_3 with tetradymite layered structure that feature a sixfold cation coordination. In these compounds, metallic bonding is formed at HP after a first-order phase transition to a structure with a cation coordination larger than the original sixfold one. On the other hand, a partial metavalent bonding occurs in α-Bi_2S_3, α-Sb_2S_3 and α-Sb_2Se_3, with an orthorhombic *Pnma* structure, and in α-As_2Te_3. These compounds show an intermediate coordination between three and six. In all these compounds, pressure increases cation coordination leading to a considerable bandgap reduction and

partial phonon softening consistent with metavalent bonding. Finally, we predict that a similar situation than for As_2S_3 is expected for As_2Se_3 polymorphs and also in the low-pressure trigonal Se and Te at HP. These compounds featuring threefold coordination at room pressure are expected to exhibit metavalent bonding at HP.

In summary, our present results on α-As_2S_3 confirm that pressure is able to tune the metavalent bonding in group-15 sesquichalcogenides with strong LEP activity, such as occurs for orpiment, thus turning common semiconductors into "incipient metals" with promising phase-change, thermoelectric and topological insulating properties at extreme conditions. Since Sb_2Te_3 and Bi_2Te_3 are topological insulators and two of the best known thermoelectric materials at room conditions due to metavalent bonding, this work paves the way to design new group-15 sesquichalcogenides and related compounds with thermoelectric or topological insulating properties both at room pressure and at extreme conditions.

Supporting Information

Supporting Information provides an analysis of the structural and vibrational properties of As_2S_3 at ambient and high pressure. Details of the structural evolution of compressed As_2S_3 show the evolution of the axial ratios, the theoretical Wyckoff free coordinates and the polyhedral distortion under pressure. On the other hand, an extensive description of the experimental and theoretical isothermal compressibility tensor is given. Details of atomic vibrations of many zone-center phonons are provided and the pressure dependence of the theoretical Raman- and IR-active modes are given. Finally, a table with the known group-15 sesquichalcogenides and their particular cation coordination and type of bonding is provided. This material is available free of charge via the Internet at http://pubs.acs.org.

Acknowledgments

Authors thank the financial support from Spanish Ministerio de Economía y Competitividad (MINECO) through MAT2016-75586-C4-2/3-P and FIS2017-83295-P and from Generalitat Valenciana under project PROMETEO/2018/123-EFIMAT. ELDS acknowledges the European Union Horizon 2020 research and innovation programme under Marie Sklodowska-Curie for grant agreement No. 785789-COMEX. JAS also acknowledges Ramón y Cajal program for funding support through RYC-2015-17482. AM, SR and ELDS thank interesting discussions with J. Contreras-García who taught them how to analyze the ELF. Finally, authors thank ALBA Light Source for beam allocation at beamline MSPD (Experiment No. 2013110699) and acknowledge computing time provided by MALTA-Cluster and Red Española de Supercomputación (RES) through computer resources at MareNostrum with technical support provided by the Barcelona Supercomputing Center (QCM-2018-3-0032).

References

[**1**] No value is obtained at higher pressure since the metallization of the monoclinic structure above 25 GPa in our calculations yields unreasonably high values of these parameters.

[Alfè 2009] D. Alfè. PHON: A program to calculate phonons using the small displacement method. *Computer Physics Communications*. **2009**, *180*, 2622−2633.

[Angel 2004-2011] R. J. Angel. http://www.rossangel.com/text_strain.htm

[Aoki 1980] K. Aoki, O. Shimomura, S. Minomura, N. Koshizuka, and T. Tsushima. Raman Scattering of Trigonal Se and Te at Very High Pressure. *Journal of the Physical Society of Japan*. **1980**, *48*, 906−911.

[Bandyophadhay 1999] A. K. Bandyophadhay and D. B. Singh. Pressure induced phase transformations and band structure of different high pressure phases in tellurium. *Pramana*. **1999**, *52*, 303−319.

[Besson 1980] J. M. Besson, J. Cernogora, and R. Zallen. Effect of pressure on optical properties of crystalline As_2S_3. *Physical Review B*. **1980**, *22*, 3866−3876.

[Besson 1981] J. M. Besson, J. Cernogora, M. L. Slade, B. A. Weinstein, and R. Zallen. Pressure effects on the absorption edge, refractive index, and Raman spectra of crystalline and amorphous As_2S_3. *Physica B*. **1981**, *105*, 319−323.

[Birch 1938] F. Birch. The Effect of Pressure Upon the Elastic Parameters of Isotropic Solids, According to Murnaghan's Theory of Finite Strain. *Journal of Applied Physics*. **1938**, *9*, 279−288.

[Blöchl 1994] P. E. Blöchl. Projector Augmented-Wave Method. *Physical Review B*. **1994**, *50*, 17953−17979.

[Bolotina 2013a] N. B. Bolotina, V. V. Brazhkin, T. I. Dyuzheva, Y. Katayama, L. F. Kulikova, L. V. Lityagina, and N. A. Nikolaev. High-pressure polymorphism of As_2S_3 and new AsS_2 modification with layered structure. *JETP Letters*. **2013**, *98*, 539-543.

[Brown 1965] A. Brown and S. Rundqvist. Refinement of the crystal structure of black phosphorus. *Acta Crystallographica*. **1965**, *19*, 684–685.

[Burgio 2000] L. Burgio and R. J. H. Clark. Comparative pigment analysis of six modern Egyptian papyri and an authentic one of the 13th century BC by Raman microscopy and other techniques. *Journal of Raman Spectroscopy*. **2000**, *31*, 395-401.

[Canepa 2011] P. Canepa, R. M. Hanson, P. Ugliengo, and M. Alfredsson. J-ICE: a new Jmol interface for handling and visualizing crystallographic and electronic properties. *Journal of Applied Crystallography*. **2011**, *44*, 225−229.

[Cheng 2017] H. F. Cheng, Y. Zhou, and R. L. Frost. Structure comparison of Orpiment and Realgar by Raman spectroscopy. *Spectroscopy Letters*. **2017**, *50*, 23−29.

[Contreras-García 2008] J. Contreras-García, A. Martín Pendás, B. Silvi, and J. M. Recio. Useful applications of the electron localization function in high-pressure crystal chemistry. *Journal of Physics and Chemistry of Solids*. **2008**, *69*, 2204−2207.

[Contreras-García 2009] J. Contreras-García, B. Silvi, A. Martín Pendás, and J. M. Recio. Computation of local and global properties of the electron localization function topology in crystals. *Journal of Chemical Theory and Computation*. **2009**, *5*, 164–173.

[Cuenca-Gotor 2016] V. P. Cuenca-Gotor, J. A. Sans, J. Ibáñez, C. Popescu, O. Gomis, R. Vilaplana, F. J. Manjón, A. Leonardo, E. Sagasta, A. Suárez-Alcubilla, I. G. Gurtubay, M. Mollar, and A. Bergara. Structural, Vibrational, and Electronic Study of α-As_2Te_3 under Compression. *Journal of Physical Chemistry C*. **2016**, *120*, 19340−19352.

[DeFonzo 1978] A. P. DeFonzo and J. Tauc. Network dynamics of 3:2 coordinated compounds, *Physical Review B*. **1978**, *18*, 6957−6972.

[Degtyareva 2007] O. Degtyareva, E. R. Hernández, J. Serrano, M. Somayazulu, H-K. Mao, E. Gregoryanz, and R. J. Hemley. Vibrational dynamics and stability of the high-pressure chain and ring phses in S and Se. *Journal of Chemical Physics*. **2007**, *126*, 084503.

[Dewaele 2004] A. Dewaele, P. Loubeyre, and M. Mezouar. Equations of State of Six Metals above 94 GPa. *Physical Review B*. **2004**, *70*, 094112.

[Ding 2016] W. Ding, Y. Tong, X. Zhang, M. Pan, and S. Chen. Study of Arsenic Sulfide in Solid Tumor Cells Reveals Regulation of Nuclear Factors of Activated T-cells by PML and p53, *Scientific Reports*. **2016**, *6*, 19793.

[Efthimiopoulos 2013] I. Efthimiopoulos, J. M. Zhang, M. Kucway, C. Park, R. C. Ewing, and Y. Wang. Sb_2Se_3 under Pressure. *Scientific Reports.* **2013**, *3*, 2665-2672.

[Efthimiopoulos 2014] I. Efthimiopoulos, J. Kemichick, X. Zhou, S. V. Khare, D. Ikuta, and Y. Wang. High-Pressure Studies of Bi_2S_3. *Journal of Physical Chemistry A*. **2014**, *118*, 1713-1720.

[Efthimiopoulos 2016] I. Efthimiopoulos, C. Buchan, and Y. Wang. Structural Properties of Sb_2S_3 under Pressure: Evidence of an Electronic Topological Transition. *Scientific Reports.* **2016**, *6*, 24246.

[Fauth 2013] F. Fauth, I. Peral, C. Popescu, and M. Knapp. The New Material Science Powder Diffraction Beamline at ALBA Synchrotron. *Powder Diffraction*. **2013**, *28*, S360−S370.

[Fitzhugh 1997] E. W. Fitzhugh. *Orpiment and Realgar, in Artists' Pigments*. A Handbook of Their History and Characteristics, Vol 3, pp. 47−80 (Oxford University Press, **1997**).

[Forneris 1969] R. Forneris. The infrared and Raman spectra of realgar and orpiment. *American Mineralogist*. **1969**, *54*, 1062−1074.

[Frost 2002] R. L. Frost, W. N. Martens, and J. T. Kloprogge. Raman spectroscopic study of cinnabar (HgS), realgar (As_4S_4), and orpiment (As_2S_3) at 298 and 77K. *Neues Jahrbuch für Mineralogie. Mh. Jg*. **2002**, *10*, 469− 480.

[Gibbs 2010] G. V. Gibbs, A. F. Wallace, R. Zallen, R. T. Downs, N. L. Ross, D. F. Cox, and K. M. Rosso. Bond paths and van der Waals interactions in orpiment, As_2S_3. *J. Phys. Chem. A*. **2010**, *114*, 6550-6557.

[Grimme 2006] S. Grimme. Semiempirical GGA-type density functional constructed with a long-range dispersion correction. *Journal of Computational Chemistry*. **2006**, *27*, 1787-1799.

[Grimme 2010] S. Grimme, J. Antony, S. Ehrlich, and S. Krieg. A consistent and accurate *ab initio* parametrization of density functional dispersion correction (DFT-D) for the 94 elements H-Pu. *Journal of Chemical Physics*. **2010**, *132*, 154104.

[Guńka 2015c] P. A. Guńka, M. Dranka, M. Hanfland, K. F. Dziubek, A. Katrusiak, and J. Zachara. Cascade of High-Pressure Transitions of Claudetite II and the First Polar Phase of Arsenic(III) Oxide. *Crystal Growth & Design*. **2015**, *15*, 3950−3954.

[Hammersley 1996] A. P. Hammersley, S. O. Svensson, M. Hanfland, A. N. Fitch, and D. Hausermann. Two-Dimensional Detector Software: From Real Detector to Idealized Image or Two-Theta Scan. *High Pressure Research*. **1996**, *14*, 235−248.

[Haussühl 2007] S. Haussühl. *Physical Properties of Crystals. An Introduction*. (Wiley-VCH, **2007**).

[Heo 2014] J. Heo and W. J. Chung. *Rare-earth-doped chalcogenide glass for lasers and amplifiers*, in Chalcogenide Glasses: Preparation, Properties and Applications. (Woodhead Publishing, **2014**), pp. 347−380.

[Hewak 2014] D. W. Hewak, N. I. Zheludev, and K. F. MacDonald. *Controlling light on the nanoscale with chalcogenide thin films*, in Chalcogenide Glasses: Preparation, Properties and Applications. (Woodhead Publishing, **2014**), pp. 471−508.

[Hohenberg 1964] P. Hohenberg and W. Kohn. Inhomogeneous Electron Gas. *Physical Review*. **1964**, *136*, B864−B871.

[Ibáñez 2016] J. Ibáñez, J. A. Sans, C. Popescu, J. López-Vidrier, J. J. Elvira-Betanzos, V. P. Cuenca-Gotor, O. Gomis, F. J. Manjón, P. Rodríguez-Hernández, and A. Muñoz. Structural, Vibrational, and Electronic Study of

Sb_2S_3 at High Pressure. *Journal of Physical Chemistry C*. **2016**, *120*, 10547-10558.

[Itié 1992] J. P. Itié, A. Polian, M. Grimsditch, and S. Susman. X-ray absorption spectroscopy Investigation of Amorphous and Crystalline As_2S_3. *Japanese Journal of Applied Physics*. **1992**, *32, Suppl. 2*, 719−721.

[Kampf 2011] A. R. Kampf, R. T. Downs, R. M. Housley, R. A. Jenkins, and J. Hyršl. Anorpiment, As_2S_3, the triclinic dimorph of orpiment. *Mineral. Mag*. **2011**, *75*, 2857-2867.

[Klotz 2009] S. Klotz, J-C. Chervin, P. Munsch, and G. Le Marchand. Hydrostatic limits of 11 pressure transmitting media. *Journal of Physics D: Applied Physics*. **2009**, *42*, 075413.

[Kravchenko 1980] E. A. Kravchenko, A. V. Timofeeva, and G. Z. Virogradova. Crystals Modifications of Arsenic and Antimony Sulphides at High Pressure and Temperature. *Journal of Molecular Structure*. **1980**, *58*, 253−262.

[Kroumova 2003] E. Kroumova, M. I. Aroyo, J. M. Pérez-Mato, A. Kirov, C. Capillas, S. Ivantchev, and H. Wondratschek. Bilbao Crystallographic Server: Useful Databases and Tools for Phase-Transition Studies. *Phase Transitions*. **2003**, *76*, 155−170.

[Kresse 1993] G. Kresse and J. Hafner. Ab Initio Molecular Dynamics for Liquid Metals. *Physical Review B*. **1993**, *47*, 558−561.

[Kresse 1996a] G. Kresse and J. Furthmüller. Efficiency of *ab initio* Total-Energy Calculations for Metals and Semiconductors Using a Plane-wave Basis Set. *Computational Materials Science*. **1996**, *6*, 15-50.

[Kresse 1996b] Kresse and J. Furthmüller. Efficient Iterative Schemes for *ab initio* Total-energy Calculations Using a Plane-wave Basis Set. *Physical Review B: Condensed Matter and Materials Physics.* **1996**, *54*, 11169-11186.

[Kresse 1999] G. Kresse and D. Joubert. From Ultrasoft Pseudopotentials to the Projector Augmented-wave Method. *Physical Review B: Condensed Matter and Materials Physics.* **1999**, *59*, 1758-1775.

[Larson 2004] A. C. Larson and R. B. von Dreele. General Structure Analysis System (GSAS). *LANL Report*. **2004**, *86*, 748.

[Lee 2014] S. Lee, K. Esfarjani, T. F. Luo, J. W. Zhou, Z. T. Tian, and G. Chen. Resonant bonding leads to low lattice thermal conductivity. *Nature Communications*. **2014**, *5*, 3525.

[Li 2015] C. W. Li, J. Hong, A. F. May, D. Bansal, S. Chi, T. Hong, G. Ehlers, and O. Delaire. Orbitally driven giant phonon anharmonicity in SnSe. *Nature Physics*. **2015**, *11*, 1063–1069.

[Lifshitz 1960] I. M. Lifshitz. Anomalies of Electron Characteristics of a Metal in the High Pressure Region. *Sov. Phys. JETP*. **1960**, *11*, 1130.

[Liu 2019] K. X. Liu, L. D. Dai, H. P. Li, H. Y. Hu, L. F. Yang, C. Pu, M. L. Hong, and P. F. Liu. Phase Transition and Metallization of Orpiment by Raman Spectroscopy, Electrical Conductivity and Theoretical Calculation under High Pressure. *Materials*. **2019**, *12*, 784.

[Lucogsky 1972] G. Lucogsky. Comparison of the Long Wave Optical Phonons in Se and Te. *Physica Status Solidi B*. **1972**, *49*, 633−641.

[Mamedov 2018] S. Mamedov and N. Drichko. Characterization of 2D As_2S_3 crystal by Raman spectroscopy. *MRS Advances*. **2018**, *3*, 385−390.

[Manjón 2013] F. J. Manjón, R. Vilaplana, O. Gomis, E. Pérez-González, D. Santamaría-Pérez, V. Marín-Borrás, A. Segura, J. González, P. Rodríguez-Hernández, and A. Muñoz. High-Pressure Studies of Topological Insulators Bi_2Se_3, Bi_2Te_3, and Sb_2Te_3. *Physica Status Solidi B*. **2013**, *250*, 669-676.

[Mao 1986] M. K. Mao, J. Xu, and P. M. Bell. Calibration of the Ruby Pressure Gauge to 800 kbar under Quasi-Hydrostatic Conditions. *Journal of Geophysical Research.* **1986**, *91*, 4673−4676.

[Marini 2012] C. Marini, D. Chermisi, M. Lavagnini, D. Di Castro, C. Petrillo, L. Degiorgi, S. Scandolo, and P. Postorino. High-pressure phases of crystalline tellurium: A combined Raman and ab initio study. *Physical Review B*. **2012**, *86*, 064103.

[Mathieu 1970] J. M. Mathieu and H. Poulet. Spectres de vibration de l'orpiment As_2S_3. *Bulletin de la Société Française de Minéralogie et de Cristallographie*. **1970**, *93*, 532−535.

[Minomura 1979] S. Minomura, K. Aoki, N. Koshizuka, and T. Tsushima. *The Effect of Pressure on The Raman Spectra in Trigonal Se and Te*. in High-Pressure Science and Technology (Springer, **1979**), p. 435.

[Momma 2011] K. Momma and F. Izumi. VESTA 3 for Three-dimensional Visualization of Crystal, Volumetric and Morphology Data. *Journal of Applied Crystallography*. **2011**, *44*, 1272−1276.

[Monkhorst 1976] H. J. Monkhorst and J. D. Pack. Special points for Brillouin-zone integrations. *Physical Review B*. **1976**, *13*, 5188.

[Morimoto 1954] N. Morimoto. The crystal structure of orpiment (As_2S_3) refined. *Mineralogical Journal*. **1954**, *1(3)*, 160-169.

[Mullen 1972] D. J. E. Mullen and W. Nowacki. Refinement of the crystal structures of realgar, AsS and orpiment, As_2S_3. *Zeitschrift für Kristallographie*. **1972**, *136*, 48-65.

[Parlinski 1997] K. Parlinski, Z. Q. Li, and Y. Kawazoe. First-Principles Determination of the Soft Mode in Cubic ZrO_2. *Physical Review Letters.* **1997**, *78*, 4063−4066.

[Perdew 1996] J. P. Perdew, K. Burke, and M. Ernzerhof. Generalized Gradient Approximation Made Simple. *Physical Review Letters*. **1996**, *77*, 3865−3868.

[Perdew 2008] J. P. Perdew, A. Ruzsinszky, G. I. Csonka, O. A. Vydrov, G. E. Scuseria, L. A. Constantin, X. Zhou, and K. Burke. Restoring the Density-Gradient Expansion for Exchange in Solids and Surfaces. *Physical Review Letters*. **2008**, *100*, 136406.

[Pereira 2018] A. L. J. Pereira, D. Santamaría-Pérez, J. Ruíz-Fuertes, F. J. Manjón, V. P. Cuenca-Gotor, R. Vilaplana, O. Gomis, C. Popescu, A. Muñoz, P. Rodríguez-Hernández, A. Segura, L. Gracia, A. Beltrán, P. Ruleova, C. Drasar, and J. A. Sans. Experimental and Theoretical Study of Bi_2O_2Se Under Compression. *Journal of Physical Chemistry C*. **2018**, *122*, 8853−8867.

[Pertlik 1978b] F. Pertlik. Verfeinerung der Kristallstruktur des Minerals Claudetit, As_2O_3 ("Claudetit I"). *Monatshefte für Chemie*. **1978**, *109*, 277-282.

[Piermarini 1973] G. J. Piermarini, S. Block, and J. D. Barnett. Hydrostatic limits in liquids and solids to 100 kbar. *Journal of Applied Physics*. **1973**, *44*, 5377−5382.

[Pliny the Elder 1855] Pliny the Elder. *Naturalis Historia, Chapter 22*, edited by J. Bostock MD FRS, H. T. Riley, Esq., B.A. London. (Taylor and Francis, London, **1855**).

[Porto 1962] S. P. S. Porto and D. L. Wood. Ruby Optical Maser as a Raman source. *Journal of the Optical Society of America*. **1962**, *52*, 251−252.

[Properzi 2013] L. Properzi, A. Polian, P. Munsch, and A. Di Cicco. Investigation of the phase diagram of selenium by means of Raman spectroscopy. *High Pressure Research*. **2013**, *33*, 35−39.

[Radescu 2017] S. Radescu, A. Mujica, P. Rodríguez-Hernández, A. Muñoz, J. Ibáñez, J. A. Sans, V. P. Cuenca-Gotor, and F. J. Manjón. Study of the orpiment and anorpiment phases of As_2S_3 under pressure. *Journal of Physics: Conference Series*. **2017**, *950*, 042018.

[Raty 2018] J-Y. Raty, M. Schumacher, P. Golub, V. L. Deringer, C. Gatti, and M. Wuttig. A Quantum-Mechanical Map for Bonding and Properties in Solids. *Advanced Materials*. **2018**, *31*, 1806280.

[Razzetti 1979] C. Razzetti and P. P. Lottici. Polarization analysis of the Raman spectrum of As_2S_3 crystals. *Solid State Communications*. **1979**, *29*, 361−364.

[Richter 1973] W. Richter, J. B. Renucci, and M. Cardona. Hydrostatic Pressure Dependence of First-Order Raman Frequencies in Se and Te. *Physica Status Solidi B*. **1973**, *56*, 223−229.

[Sans 2016c] J. A. Sans, F. J. Manjón, A. L. J. Pereira, R. Vilaplana, O. Gomis, A. Segura, A. Muñoz, P. Rodríguez-Hernández, C. Popescu, C. Drasar, et al. Structural, Vibrational, and Electrical Study of Compressed BiTeBr. *Physical Review B: Condensed Matter and Materials Physics.* **2016**, *93*, 024110.

[Scheuermann 1969] W. Scheuermann and G. J. Ritter. Raman spectra of cinnabar (HgS), realgar (As_4S_4) and orpiment (As_2S_3). *Zeitschrift für Naturforschung*. **1969**, *A 24*, 408−411.

[Shportko 2008] K. Shportko, S. Kremers, M. Woda, D. Lencer, J. Robertson, and M. Wuttig. Resonant bonding in crystalline phase-change materials. *Nature Materials*. **2008**, *7*, 653−658.

[Siebert 1954] H. Siebert. Struktur der Sauerstoffsäuren. *Zeitschrift für anorganische und allgemeine Chemie*. **1954**, *275*, 225−240.

[Smith 1973] J. D. Smith, J. C. Bailar, H. J. Emeléus, and R. Nyholm. *The Chemistry of Arsenic, Antimony and Bismuth*. (Pergamon Texts in Inorganic Chemistry, **1973**).

[Sorb 2016] Y. A. Sorb, V. Rajaji, P. S. Malavi, U. Subbarao, P. Halappa, S. C. Peter, S. Karmakar, and C. Narayana. Pressure-induced electronic topological transition in Sb_2S_3. *Journal of Physics: Condensed Matter*. **2016**, *28*, 015602.

[Spurrell 1895] F. C. J. Spurrell. Notes on Egyptian Colours. *Archaeological Journal*. **1895**, *52:1*, 222-239.

[Srivastava 2011] P. Srivastava, H. Singh Mund, and Y. Sharma. Investigation of electronic properties of crystalline arsenic chalcogenides: Theory and experiment. *Physica B*. **2011**, *406*, 3083−3088.

[Stergiou 1985b] A. C. Stergiou and P. J. Rentzeperis. The crystal structure of arsenic selenide, As_2Se_3. *Z-Kristall*. **1985**, *173*, 185−191.

[Svensson 1974] C. Svensson. The crystal structure of orthorhombic antimony trioxide, Sb_2O_3. *Acta Crystallographica B*. **1974**, *30*, 458−461.

[Toby 2001] B. H. Toby. EXPGUI, A Graphical User Interface for GSAS. *Journal of Applied Crystallography*. **2001**, *34*, 210−213.

[Vilaplana 2011a] R. Vilaplana, O. Gomis, F. J. Manjón, A. Segura, E. Pérez-González, P. Rodríguez-Hernández, A. Muñoz, J. González, V. Marín-Borrás, V. Muñoz-Sanjosé, C. Drasar, and V. Kucek. High-pressure vibrational and optical study of Bi_2Te_3. *Physical Review B*. **2011**, *84*, 104112.

[Walsh 2011] A. Walsh, D. J. Payne, R. G. Egdell, and G. W. Watson. Stereochemistry of post-transition metal oxides: revision of the classical lone pair model. *Chemical Society Reviews*. **2011**, *40*, 4455−4463.

[Ward 1968] A. T. Ward. Raman spectroscopy of sulfur, sulfur-selenium, and sulfur-arsenic mixtures. *Journal of Physical Chemistry*. **1968**, *72*, 4133−4139.

[Waxman 2001] S. Waxman and K. C. Anderson. History of the development of Arsenic Derivatives in Cancer Therapy. *The Oncologist*. **2001**, *6-2*, 3-10.

[Weber 1965] A. Weber and S. P. S. Porto. He-Ne Laser as a Light Source for High Resolution Raman Spectroscopy. *Journal of the Optical Society of America*. **1965**, *55*, 1033−1034.

[Wuttig 2018] M. Wuttig, W. L. Deriger, X. Gonze, C. Bichara, and J-Y. Raty. Incipient Metals: Functional Materials with a Unique Bonding Mechanism. *Advanced Materials*. **2018**, *30*, 1803777.

[Xu 2017] M. Xu, S. Jakobs, R. Mazzarello, J-Y. Cho, Z. Yang, H. Hollermann, D. S. Shang, X. S. Miao, Z. H. Yu, L. Wang, and M. Wuttig. Impact of Pressure on the Resonant Bonding in Chalcogenides. *Journal of Physical Chemistry C*. **2017**, *121*, 25447−25454.

[Zallen 1971] R. Zallen, M. L. Slade, and A. T. Ward. Lattice Vibrations and Interlayer Interactions in Crystalline As_2S_3 and As_2Se_3. *Physical Review B.* **1971**, *3*, 4257-4273.

[Zallen 1974a] R. Zallen and M. L. Slade. Rigid-layer modes in chalcogenide crystals. *Physical Review B*. **1974**, *9*, 1627−1637.

[Zallen 1974b] R. Zallen. Pressure-Raman effects and vibrational scaling laws in molecular crystals: S8 and As_2S_3. *Physical Review B*. **1974**, *9*, 4485−4496.

[Zallen 2004] R. Zallen. Effect of Pressure on Optical Properties of Crystalline As_2S_3. *High Pressure Research*. **2004**, *24*, 117−118.

SUPPORTING INFORMATION

Orpiment under compression: metavalent bonding at high pressure

V. P. Cuenca-Gotor, J. A. Sans, O. Gomis, A. Mujica, S. Radescu, A. Muñoz, P. Rodríguez-Hernández, E. Lora da Silva, C. Popescu, J. Ibañez, R. Vilaplana, and F. J. Manjón

Structural properties of orpiment at room conditions

Table S1. Theoretical (the, with vdW) and experimental (exp) atomic parameters of the $P2_1/c$ structure of α-As_2S_3 at room conditions.

atoms	site	*x*	*y*	*z*
As1	*4e*	0.10723 (the) [a]	0.30752 (the) [a]	0.23420 (the) [a]
		0.09805 (exp) [b]	0.30829 (exp) [b]	0.23531 (exp) [b]
As2	*4e*	0.38070 (the) [a]	0.17785 (the) [a]	0.01176 (the) [a]
		0.37395 (exp) [b]	0.17878 (exp) [b]	0.01323 (exp) [b]
S1	*4e*	0.61732 (the) [a]	0.37901 (the) [a]	0.09901 (the) [a]
		0.60660 (exp) [b]	0.37872 (exp) [b]	0.09849 (exp) [b]
S2	*4e*	0.1719 (the) [a]	0.0999 (the) [a]	0.15133 (the) [a]
		0.16272 (exp) [b]	0.10277 (exp) [b]	0.15262 (exp) [b]
S3	*4e*	0.05703 (the) [a]	0.70532 (the) [a]	0.12304 (the) [a]
		0.06338 (exp) [b]	0.70646 (exp) [b]	0.12234 (exp) [b]

[a] This work. [b] Data from Mullen (1972) converted with VESTA from the original $P2_1/n$ setting to the standard $P2_1/c$ setting with coordinate standardization.

Vibrational properties of orpiment at room conditions

Group theory predicts sixty zone-center vibrational modes at the BZ center for α-As_2S_3 with mechanical representation [DeFonzo 1978]:

$$\Gamma_{60} = 15A_g\,(R) + 13B_u\,(IR) + 15B_g\,(R) + 14A_u\,(IR) + 1A_u + 2B_u \qquad (1)$$

where g (gerade) modes are Raman-active (R) and u (ungerade) modes are infrared-active (IR). Note that all modes are paired up, (A_g,B_u) and (B_g,A_u), where the first is R and the second is IR. Therefore, α-As_2S_3 has 30 Raman-active modes and 27 IR-active modes because one A_u and two B_u modes are acoustic modes. A_g and B_u

modes correspond mainly to vibrations of atoms in the *ac*-plane, while B_g and A_u modes correspond mainly to atomic vibrations along the *b*-axis.

It is well-known that in layered materials with layers piled along the *c*-axis, which usually crystallize either in a hexagonal or tetragonal space groups, the lowest-frequency E (doubly degenerated) and A (or B) modes at the Γ-point can be classified as inter-layer modes (out-of-phase vibrations of atoms corresponding to adjacent layers), also known as rigid layer modes, or intra-layer modes (out-of-phase vibrations of atoms inside the layers) [Zallen 1974a]. Inter-layer E and A (or B) modes are usually related to shear or transversal vibrations between adjacent layers along the *a*- or *b*-direction of the *ab*-layer plane and to longitudinal vibrations of one layer against the adjacent ones (along the *c*-axis), respectively.

Both E and A (or B) inter-layer modes arise from the transverse acoustic (TA) and longitudinal acoustic (LA) modes, respectively, due to the band folding of the Brillouin zone boundaries into the Γ-point due to the decrease of symmetry from cubic to hexagonal or tetragonal. Similarly, E and A (or B) intra-layer modes originate from the transverse optical (TO) and longitudinal optical (LO) modes at Γ-point and from additional modes due to the folding of the BZ boundaries into the Γ-point [Zallen 1974a].

The number of inter-layer and intra-layer modes in layered materials depends on the complexity of the unit cell. In the simplest case, there should be two inter-layer modes and four intra-layer modes. For α-As_2S_3, which crystallizes on the monoclinic phase, there are only modes with A and B symmetry, therefore there are three inter-layer rigid modes. Since the acoustic modes are one A_u and two B_u modes, corresponding to inter-layer rigid modes where both layers of the unit cell have in-phase translations, the out-of-phase translations of the two layers corresponding to the three optical inter-layer rigid modes must be Raman-active and must be two A_g and one B_g modes. We have visualized the atomic motions of the normal vibrations of α-As_2S_3 with the use of J-ICE program [Canepa 2011]. Two of these are the two shear rigid modes with lowest-frequency (27 and 389 cm^{-1}) represented in **Figure S1** and that are attributed to the A_g^1 and A_g^2 modes as indicated in previous papers [see Mullen (1972) and references therein]. On the other hand, the compressional or longitudinal rigid mode is the B_g^1 mode located around 62 cm^{-1} [see **Fig. S2**]. As commented in previous papers, this compressional rigid mode has a similar frequency to other optical modes; i.e. there is a mix between this inter-layer mode and several inter-chain modes [see **Fig. S3**] as previously suggested [DeFonzo 1978].

Intra-layer modes can be divided into high-frequency intra-chain modes and low-frequency inter-chain modes [DeFonzo 1978]. The mixture of inter-layer and inter-chain modes found is in agreement with the analysis of Defonzo and Tauc [DeFonzo 1978]. In fact, low-frequency inter-chain modes mixed with the compressional rigid mode are those related to the rotation of the AsS spiral chains around the *a*-axis [see **Fig. S3** and **S4**], and there are also modes related to the translation of the spiral chains inside each layer [see **Fig. S5** to **S8**].

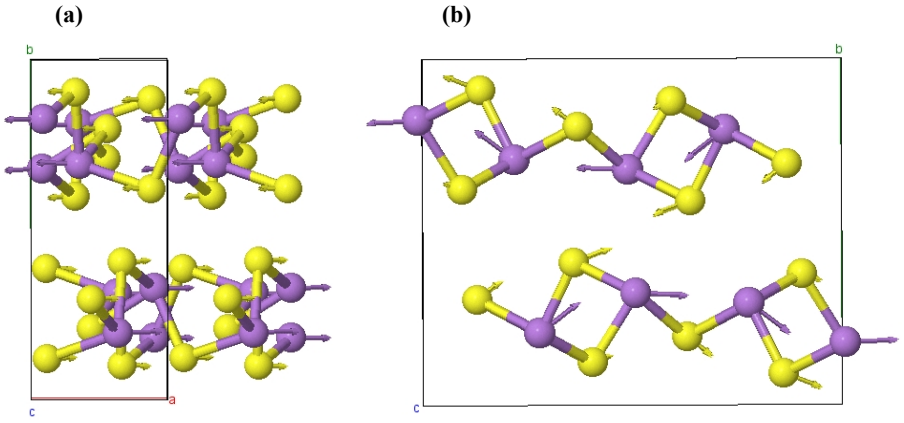

Figure S1. Atomic vibrations of the A_g^1 **(a)** and A_g^2 **(b)** inter-layer modes located around 27 and 38 cm^{-1} in the *ab*- (*bc*)-plane. These are the shear rigid layer modes in α-As_2S_3. As: Purple spheres, S: yellow spheres.

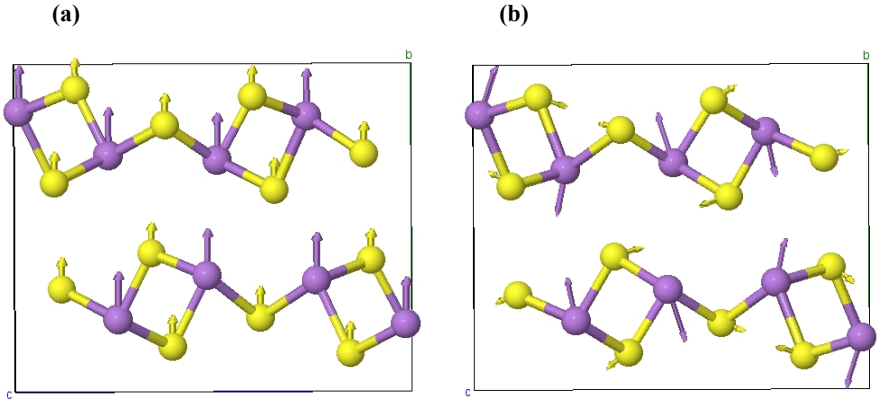

Figure S2. Atomic vibrations of the acoustic A_u inter-layer mode **(a)** and the related B_g^1 inter-layer mode located around 62 cm^{-1} **(b)** in the *bc*-plane. The B_g^1 mode is the longitudinal or compressional rigid layer mode in α-As_2S_3. As: Purple spheres, S: yellow spheres.

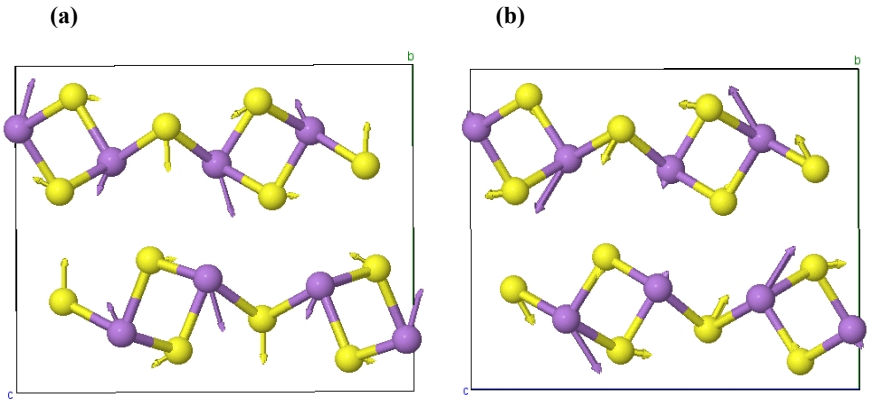

Figure S3. Atomic vibrations of the B_u^1 **(a)** and A_g^3 **(b)** modes located around 50 and 59 cm^{-1}, respectively, in the *bc*-plane. These are inter-chain modes of α-As_2S_3 corresponding to rotational modes of the spiral AsS chains around the *a*-axis (perpendicular to the page). Atoms of one chain rotate around the *a*-axis in the opposite sense (clockwise vs. counter-clockwise) than the neighbour chains inside the same layer. Rotations of the neighbour chains in the adjacent layers are in the same direction in the B_u mode and in the opposite direction in the A_g mode. These are two of the "inter-chain rolling" modes defined in DeFonzo (1978). As: Purple spheres, S: yellow spheres.

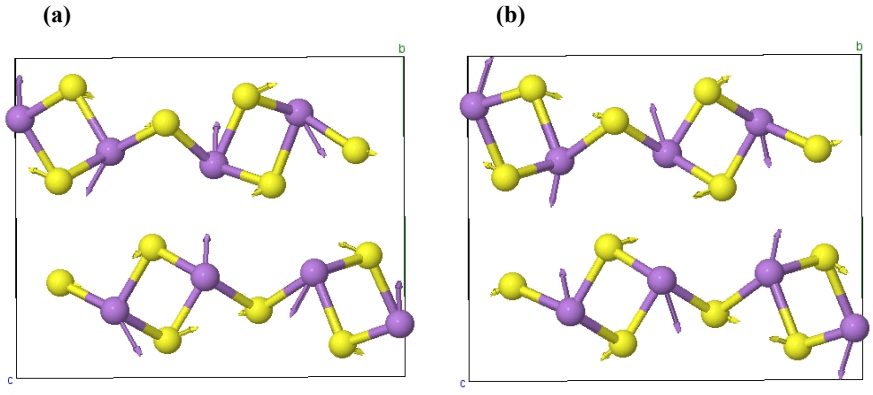

Figure S4. Atomic vibrations of the A_u^2 mode **(a)** and the B_g^4 mode **(b)** located around 93 and 103 cm^{-1}, respectively, in the *bc*-plane. These are inter-chain modes corresponding to rotational modes of the AsS spiral chains around the *a*-axis. Atoms of one chain rotate around the *a*-axis in the same direction as the neighbour chains inside the same layer. Rotations of the chains in the adjacent layers are in opposite direction (clockwise vs. counterclockwise) in the A_u mode and in the same direction in the B_g mode. These are other two "inter-chain rolling" modes defined in DeFonzo (1978). As: Purple spheres, S: yellow spheres.

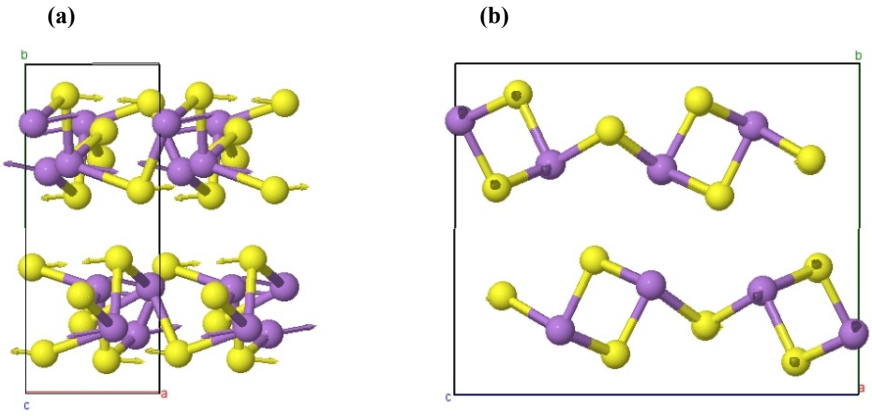

Figure S5. Atomic vibrations of the mode A_g^4 located around 70 cm^{-1} in the *ba*- **(a)** and *bc*-planes **(b)**. This is an inter-chain mode corresponding to translations of the spiral chains along the *a*-axis. Atoms of one spiral chain translate along the *a*-axis in opposite phase with respect to those of the neighbour chains inside the same layer. Translations in the neighbour layers are opposite to those of the first layer. The S atoms linking the chains (S3 atoms) are almost at rest. As: Purple spheres, S: yellow spheres.

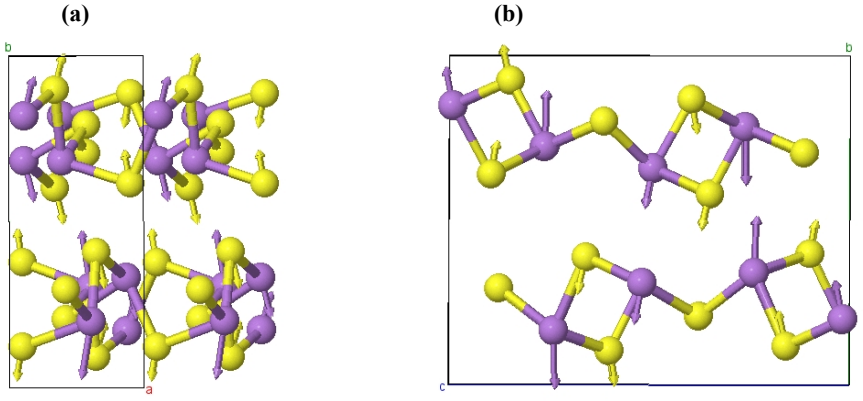

Figure S6. Atomic vibrations of the A_u^1 mode located around 63 cm^{-1} in the *ba*- **(a)** and *bc*-planes **(b)**. This is an inter-chain mode corresponding to translations of the spiral chains mainly along the *b* axis, together with a minor rotation around the *a*-axis. Atoms of one chain translate in opposite phase with respect to those of the neighbour chains both in the same layer and in neighbour layers. The S atoms (S3) linking the chains are almost at rest. As: Purple spheres, S: yellow spheres.

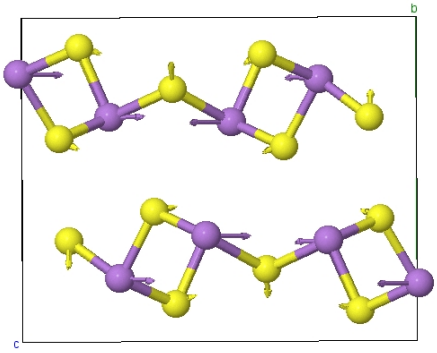

Figure S7. Atomic vibrations of the B_u^2 mode located around 94 cm^{-1} in the *bc* plane. This is an inter-chain mode corresponding to translations of the spiral chains along the *c*-axis. Atoms of one chain translate in opposite phase with respect to atoms of the neighbour chains in the same layer. This is the "inter-chain beating" mode of orpiment [DeFonzo 1978] and it is the pair of the A_g^4 mode around 70 cm^{-1}. As: Purple spheres, S: yellow spheres.

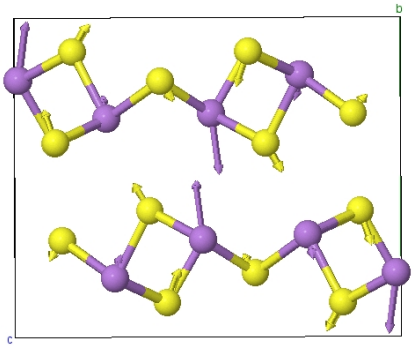

Figure S8. Atomic vibrations of the B_g^2 mode located around 69 cm^{-1} in the *bc*-plane. This is an inter-chain mode corresponding to a mixture of translations of the spiral chains mainly along the *b*-axis together with a small rotation around the *a*-axis. Atoms of one chain translate in opposite phase with respect to those of the neighbour chains in the same layer. The S atoms linking the chains are almost at rest. This is the pair of the A_u^1 mode around 63 cm^{-1}. As: Purple spheres, S: yellow spheres.

Several modes located around 150 cm^{-1} are related to vibrations of the S3 atoms (outside the chains), which vibrate in a completely different manner to the S1 and S2 atoms (inside the chains). These modes evidence the chain-like nature of the layers [see **Fig. S9**]. Finally, it can be stressed that there are typical bending modes in the intermediate-frequency region [**Fig. S10**], modes involving partial bending and stretching [**Fig. S11**] and typical stretching modes in the high-frequency region [**Fig. S12**, **S13**, and **S14**].

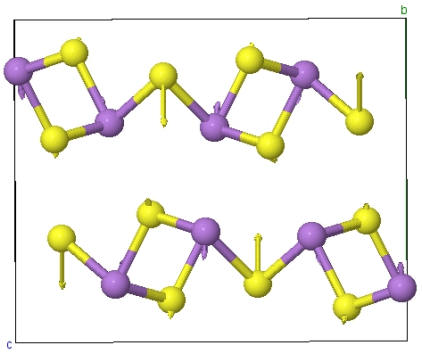

Figure S9. Atomic vibrations of the A_g^6 mode located at 153 cm^{-1} in the *bc* plane. This mode corresponds to an intra-layer mode mainly characterized by vibrations of the S atoms between the chains (S3 atoms).

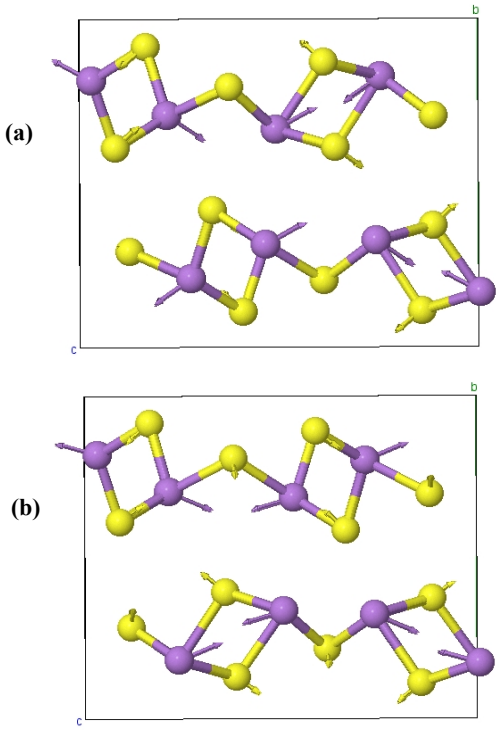

Figure S10. Atomic vibrations of the A_u^7 mode **(a)** and B_u^7 mode **(b)** located at 167 and 196 cm^{-1}, respectively, in the *bc* plane. They correspond to intra-chain modes where atoms of a semi-rod vibrate in opposite phase against the other semi-rod. As: Purple spheres, S: yellow spheres.

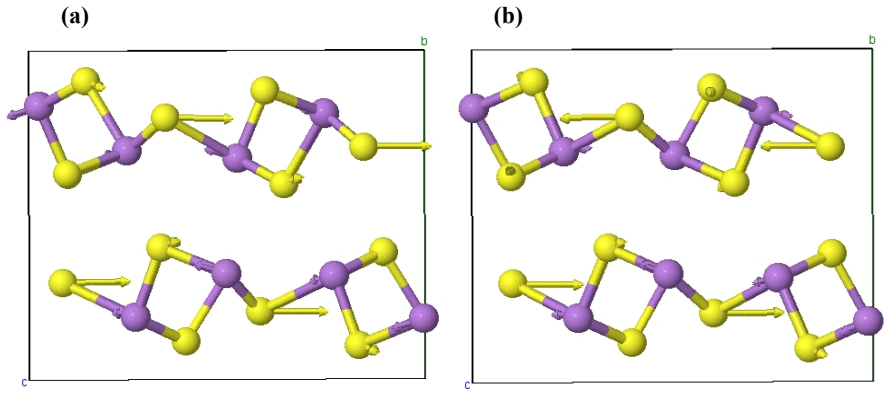

Figure S11. Atomic vibrations of the B_u^{8} mode **(a)** and the A_g^{10} mode **(b)** located around 269 and 270 cm^{-1}, respectively, in the *bc* plane. These high-frequency modes correspond to intra-layer modes mainly characterized by bending As-S vibrations. In particular, these two modes are related to vibrations of S3 atoms in the plane of the layers.

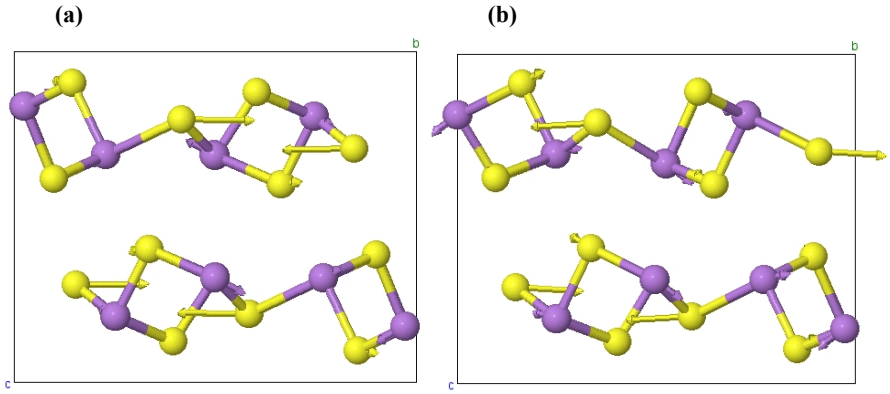

Figure S12. Atomic vibrations of the B_g^{11} mode **(a)** and the A_u^{10} mode **(b)** located around 305 and 307 cm^{-1}, respectively, in the *bc* plane. These high-frequency modes correspond to intra-layer modes mainly characterized by bending As-S vibrations. In particular, these two modes are related to vibrations of S3 atoms in the plane of the layers.

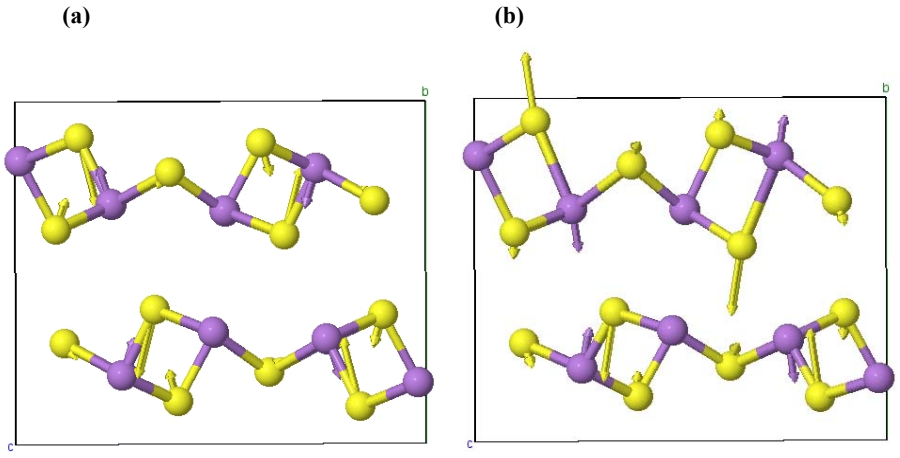

Figure S13. Atomic vibrations of the A_g^{14} mode **(a)** and the B_u^{12} mode **(b)** located around 346 and 350 cm^{-1}, respectively, in the *bc* plane. These high-frequency modes correspond to intra-chain modes mainly characterized by symmetric stretching As-S vibrations. All vibrational modes around 340-350 cm^{-1} are characterized by similar symmetric stretching intra-chain As-S vibrations.

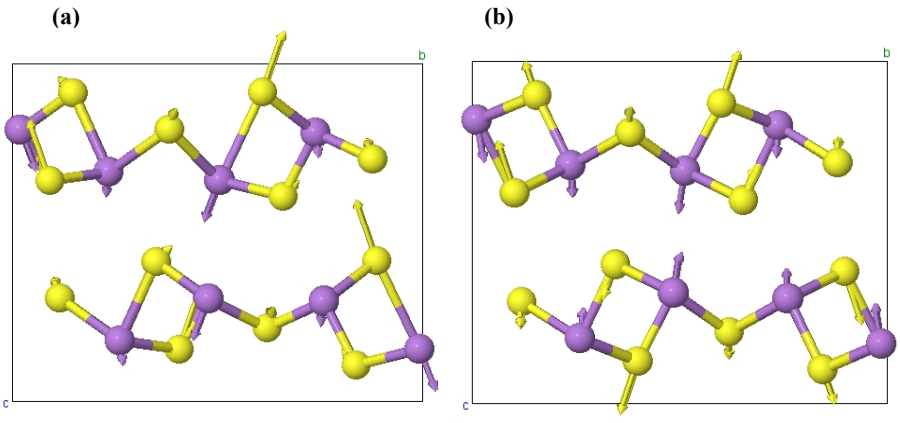

Figure S14. Atomic vibrations of the A_u^{14} mode **(a)** and the B_g^{15} mode **(b)** located around 374 and 385 cm^{-1}, respectively, in the *bc* plane. These high-frequency modes correspond to intra-chain modes mainly characterized by stretching As-S vibrations. All four vibrational modes located above 370 cm^{-1} are characterized by similar asymmetric stretching intra-chain As-S vibrations.

Structural properties of orpiment under high pressure

Calculation of the experimental and theoretical compressibility tensor at different pressures

The isothermal compressibility tensor, β_{ij}, is a symmetric second rank tensor that relates the state of strain of a crystal to the change in pressure that induced it [Haussühl 2007]. The tensor coefficients for a monoclinic crystal with *b* as the unique crystallographic axis are:

$$\beta_{ij} = \begin{pmatrix} \beta_{11} & 0 & \beta_{13} \\ 0 & \beta_{22} & 0 \\ \beta_{13} & 0 & \beta_{33} \end{pmatrix}$$

We have obtained the isothermal compressibility tensor coefficients for monoclinic α-As_2S_3 at several pressures using the Institute of Radio Engineers (IRE) convention for the orthonormal basis for the tensor: $e_3 \| c$, $e_2 \| b^*$, $e_1 \| e_2 \times e_3$. The tensor has been obtained with the finite Eulerian approximation as implemented in the Win_Strain package [Angel 2004-2011].

The change of the β monoclinic angle (always perpendicular to the *b*-axis) with pressure implies that, in this monoclinic compound, the direction of the *a*-axis changes with pressure assuming both *b*- and *c*-axis constant. Furthermore, the variation of this monoclinic angle from 90º indicates that the direction of maximum compressibility is not exactly that of the *a*-axis. Therefore, in order to evaluate the direction of maximum compressibility as a function of pressure, we have calculated and diagonalized the experimental and theoretical isothermal compressibility tensor, β_{ij}, at different pressures.

The experimental and theoretical elements of this tensor at different pressures are reported in **Tables S2**, **S3(a)** and **S3(b)**, up to 10.0 and 32.0 GPa, respectively, where the directions of the maximum, intermediate and minimum compressibility and the values of the compressibility along those directions are given by the eigenvectors (ev_i, i=1-3) and eigenvalues (λ_i, i=1-3), respectively.

First of all, we have to note that there is a reasonable good agreement between the experimental and calculated axial compressibilities (β_{ii} coefficients) at room pressure because $\beta_{11} \geq \beta_{22} > \beta_{33}$ in both cases. This result shows that the compressibility along the *a*-axis (layer plane) is greater or similar than that of the *b*-axis (axis perpendicular to the layer) and much larger than the *c*-axis. This is an unexpected result for a layered crystal whose layers extend in the *ac*-plane and it is also a clear indication of the acicular (quasi-molecular) character of the layers.

Diagonalization of the β_{ij} tensor at room pressure yields for our experiments the maximum, intermediate and minimum compressibilities $36.4(1.8)\cdot10^{-3}$, $31.3(1.6)\cdot10^{-3}$ and $-0.7(3)\cdot10^{-3}$ GPa^{-1}, respectively; whereas for the case of our calculations the obtained values for the compressibilities are $44.7(2.4)\cdot10^{-3}$, $25.8(1.3)\cdot10^{-3}$ and $-1.14(15)\cdot10^{-3}$ GPa^{-1}. These experimental (theoretical) results indicate that around

48% (58%) of the total compression at room pressure is being accommodated along the direction of maximum compressibility. The direction of the maximum compressibility at zero pressure, given by the eigenvector ev_1, occurs at the (0 1 0) plane and it is defined by angle Ψ [see **Tables S2**, **S3(a)** and **S3(b)**] relative to the *c*-axis (from *c* to *a*) or equivalently by an angle θ relative to the *a*-axis (from *a* to *c*). The direction of intermediate compressibility at zero pressure, given by eigenvector ev_2, is along the *b*-axis. Finally, the direction of minimum compressibility at zero pressure, given by eigenvector ev_3, is at the (0 1 0) plane and perpendicular to the direction of maximum compressibility within the same plane. In particular, the experimental direction of maximum compressibility at room pressure is at θ=0.8(3)º from the *a*-axis, whereas the calculated one is at 1.12(20)º. This means that the direction of maximum (minimum) compressibility at room pressure is close to the *a*-axis (*c*-axis).

Table S2. Experimental isothermal compressibility tensor coefficients, β_{ij}, and their eigenvalues, λ_i, and eigenvectors, ev_i, for α-As_2S_3 at several pressures. The results are given using the finite Eulerian method. The eigenvalues are given in decreasing value along a column.

P(GPa)	0.0	1.0	2.0	3.0	4.0
β_{11} (10^{-3} GPa^{-1})	32.4(1.8)	23.0(1.2)	17.3(1.2)	14.0(1.0)	11.8(9)
β_{22} (10^{-3} GPa^{-1})	31.3(1.6)	21.2(1.1)	15.1(1.1)	11.8(0.8)	9.6(7)
β_{33} (10^{-3} GPa^{-1})	3.3(3)	3.2(3)	3.0(3)	2.9(3)	2.8(3)
β_{13} (10^{-3} GPa^{-1})	-11.5(5)	-8.4(4)	-6.0(4)	-4.5(3)	-3.5(3)
λ_1 (10^{-3} GPa^{-1})	36.4(1.8)	26.1(1.3)	19.5(1.4)	15.6(1.1)	13.0(9)
ev_1 (λ_1)	(0.94,0,-0.33)	(0.94,0,-0.34)	(0.94,0,-0.34)	(0.94,0,-0.34)	(0.94,0,-0.33)
λ_2 (10^{-3} GPa^{-1})	31.3(1.6)	21.2(1.1)	15.1(1.1)	11.8(8)	9.6(7)
ev_2 (λ_2)	(0,1,0)	(0,1,0)	(0,1,0)	(0,1,0)	(0,1,0)
λ_3 (10^{-3} GPa^{-1})	-0.7(3)	0.09(24)	0.84(25)	1.3(3)	1.6(3)
ev_3 (λ_3)	(0.33,0,0.94)	(0.34,0,0.94)	(0.34,0,0.94)	(0.34,0,0.94)	(0.33,0,0.94)
Ψ, θ(°)[a]	109.1(3), 0.8(3)	110.1(3), -0.7(3)	110.1(4), -1.1(4)	109.7(5), -1.0(5)	109.3(6), -0.8(6)

P(GPa)	5.0	6.0	8.0	10.0
β_{11} (10^{-3} GPa^{-1})	10.2(7)	9.0(7)	7.4(6)	6.3(6)
β_{22} (10^{-3} GPa^{-1})	8.2(6)	7.1(5)	5.6(4)	4.6(5)
β_{33} (10^{-3} GPa^{-1})	2.8(3)	2.7(3)	2.5(3)	2.4(5)
β_{13} (10^{-3} GPa^{-1})	-2.84(23)	-2.31(20)	-1.51(15)	-0.94(22)
λ_1 (10^{-3} GPa^{-1})	11.2(8)	9.8(7)	7.8(6)	6.6(6)
ev_1 (λ_1)	(0.95,0,-0.32)	(0.95,0,-0.31)	(0.96,0,-0.27)	(0.98,0,-0.22)
λ_2 (10^{-3} GPa^{-1})	8.2(6)	7.1(5)	5.6(4)	4.6(5)
ev_2 (λ_2)	(0,1,0)	(0,1,0)	(0,1,0)	(0,1,0)
λ_3 (10^{-3} GPa^{-1})	1.8(3)	1.9(3)	2.1(3)	2.2(5)
ev_3 (λ_3)	(0.32,0,0.95)	(0.31,0,0.95)	(0.27,0,0.96)	(0.22,0,0.98)
Ψ, θ(°)[a]	108.7(7), -0.4(7)	108.0(8), 0.2(8)	105.8(1.1), 2.2(1.1)	102.6(2.6), 5.2(2.6)

[a] The major compression direction occurs in the (0 1 0) plane at the given angles Ψ to the *c* axis (from *c* to *a*) and θ to the *a* axis (from *a* to *c*).

As regards the behaviour of the experimental (theoretical) compressibility tensor under pressure, we start with the study between 0 and 10 GPa where both the theoretical and experimental β_{ij} values have been obtained. The most notable feature is that $\beta_{11} \geq \beta_{22} > \beta_{33}$ is maintained as pressure increases. Therefore, our experiment (*ab initio* calculations) shows that the *a*-axis has compressibility greater or similar (greater) than that of the *b*-axis. In this sense, a greater or similar compressibility in a direction along the layer with respect to that of the inter-layer (along the *b*-axis) is maintained with compression. On the other hand, the eigenvalue λ_3 is negative below 0.9 (1.3) GPa in the case of the experimental (theoretical) β_{ij} tensor. This means that the material slightly expands under compression (positive strain) along the direction of minimum compressibility, given by the eigenvector ev_3. On the other hand, the direction of major compression is close to the *a*-axis under compression.

Table S3(a). Theoretical isothermal compressibility tensor coefficients, β_{ij}, and their eigenvalues, λ_i, and eigenvectors, ev_i, for α-As_2S_3 at several pressures. The results are given using the finite Eulerian method. The eigenvalues are given in decreasing value along a column.

P(GPa)	0.0	1.0	2.0	3.0	4.0
β_{11} (10^{-3} GPa^{-1})	40.0(2.2)	27.4(1.4)	20.1(1.4)	16.1(1.2)	13.5(1.0)
β_{22} (10^{-3} GPa^{-1})	25.8(1.4)	19.4(1.0)	15.0(1.1)	12.2(0.9)	10.3(7)
β_{33} (10^{-3} GPa^{-1})	3.58(24)	3.49(21)	3.4(3)	3.3(0.3)	3.2(3)
β_{13} (10^{-3} GPa^{-1})	-13.9(7)	-10.2(5)	-7.3(5)	-5.4(0.4)	-4.2(3)
λ_1 (10^{-3} GPa^{-1})	44.7(2.4)	31.1(1.6)	22.8(1.6)	18.1(1.3)	15.0(1.1)
ev_1 (λ_1)	(0.95,0,-0.32)	(0.94,0,-0.35)	(0.94,0,-0.35)	(0.94,0,-0.35)	(0.94,0,-0.33)
λ_2 (10^{-3} GPa^{-1})	25.8(1.3)	19.4(1.0)	15.0(1.1)	12.2(0.9)	10.3(7)
ev_2 (λ_2)	(0,1,0)	(0,1,0)	(0,1,0)	(0,1,0)	(0,1,0)
λ_3 (10^{-3} GPa^{-1})	-1.14(15)	-0.27(0.13)	0.67(13)	1.31(16)	1.76(18)
ev_3 (λ_3)	(0.32,0,0.95)	(0.35,0,0.94)	(0.35,0,0.94)	(0.35,0,0.94)	(0.33,0,0.94)
Ψ, θ (°)[a]	108.73(20), 1.12(20)	110.25(20), -1.03(20)	110.56(20), -1.84(20)	110.2(3), -1.9(3)	109.5(4), -1.4(4)

P(GPa)	5.0	6.0	8.0	10.0
β_{11} (10^{-3} GPa^{-1})	11.7(8)	10.3(8)	8.3(6)	7.0(6)
β_{22} (10^{-3} GPa^{-1})	9.0(6)	7.9(6)	6.4(5)	5.4(4)
β_{33} (10^{-3} GPa^{-1})	3.1(3)	3.07(24)	2.93(24)	2.8(3)
β_{13} (10^{-3} GPa^{-1})	-3.25(24)	-2.60(20)	-1.80(15)	-1.36(17)
λ_1 (10^{-3} GPa^{-1})	12.8(9)	11.2(8)	8.9(7)	7.4(7)
ev_1 (λ_1)	(0.95,0,-0.32)	(0.95,0,-0.31)	(0.96,0,-0.29)	(0.96,0,-0.28)
λ_2 (10^{-3} GPa^{-1})	9.0(6)	7.9(6)	6.3(5)	5.4(4)
ev_2 (λ_2)	(0,1,0)	(0,1,0)	(0,1,0)	(0,1,0)
λ_3 (10^{-3} GPa^{-1})	2.05(19)	2.23(20)	2.39(21)	2.4(3)
ev_3 (λ_3)	(0.32,0,0.95)	(0.31,0,0.95)	(0.29,0,0.96)	(0.28,0,0.96)
Ψ, θ (°)[a]	108.6(4), -0.8(4)	107.9(5), -0.2(5)	106.8(7), 0.6(7)	106.5(1.7), 0.7(1.7)

[a] The major compression direction occurs in the (0 1 0) plane at the given angles Ψ to the *c* axis (from *c* to *a*) and θ to the *a* axis (from *a* to *c*).

Above 10 GPa, the theoretical compressibility tensor has been obtained up to 32.0 GPa. In this case, the direction of maximum compressibility changes rapidly for

pressures greater than 20 GPa. For instance, θ =46(13)º at 22.2 GPa and the direction of maximum compressibility is along the *b*-axis ([010] direction) at 24.3 GPa. However, the direction of maximum compressibility is again at the *ac* plane above 26.7 GPa, but it is close to the *c*-axis instead. In particular, Ψ = 15(4) and θ =92(4)º at 32.0 GPa.

Table S3(b). Theoretical isothermal compressibility tensor coefficients, β_{ij}, and their eigenvalues, λ_i, and eigenvectors, ev_i, for α-As_2S_3 at several pressures. The results are given using the finite Eulerian method. The eigenvalues are given in decreasing value along a column.

P(GPa)	14.3	17.4	18.8	20.4	22.2
β_{11} (10^{-3} GPa^{-1})	5.57 (21)	5.4(8)	5.2(7)	4.5(6)	2.8(5)
β_{22} (10^{-3} GPa^{-1})	4.11 (13)	3.5(4)	3.4(4)	3.3(3)	2.90(24)
β_{33} (10^{-3} GPa^{-1})	2.53(9)	2.2(4)	1.9(4)	1.7(3)	2.2(3)
β_{13} (10^{-3} GPa^{-1})	-0.86(4)	-0.77(16)	-0.65(14)	-0.23(12)	0.46(10)
λ_1 (10^{-3} GPa^{-1})	5.80(22)	5.5(8)	5.3(8)	4.6(6)	3.0(4)
ev_1 (λ_1)	(0.97,0,-0.25)	(0.97,0,-0.23)	(0.98,0,-0.19)	(1.00,0,-0.08)	(0.87,0,0.49)
λ_2 (10^{-3} GPa^{-1})	4.11(13)	3.5(4)	3.4(4)	3.3(3)	2.90(24)
ev_2 (λ_2)	(0,1,0)	(0,1,0)	(0,1,0)	(0,1,0)	(0,1,0)
λ_3 (10^{-3} GPa^{-1})	2.30(9)	2.0(4)	1.8(4)	1.7(3)	2.0(3)
ev_3 (λ_3)	(0.25,0,0.97)	(0.23,0,0.97)	(0.19,0,0.98)	(0.08,0,1.00)	(0.49,0,-0.87)
Ψ, θ(°)[a]	104.8(6), 2.3(6)	103.1(1.8), 3.8(1.8)	101.1(1.6), 5.8(1.6)	94.7(1.8), 12.2(1.8)	61(13), 46(13)

P(GPa)	24.3[b]	26.7	29.3	32.0
β_{11} (10^{-3} GPa^{-1})	2.0(4)	1.8(4)	1.7(3)	1.6(3)
β_{22} (10^{-3} GPa^{-1})	2.82(21)	2.52(18)	2.26(16)	2.00(14)
β_{33} (10^{-3} GPa^{-1})	2.4(3)	2.40(24)	2.37(23)	2.32(21)
β_{13} (10^{-3} GPa^{-1})	0.38(9)	0.30(8)	0.19(7)	0.20(20)
λ_1 (10^{-3} GPa^{-1})	2.82(21)	2.52(18)	2.42(23)	2.37(21)
ev_1 (λ_1)	(0,1,0)	(0.38,0,0.93)	(0.26,0,0.97)	(0.26,0,0.97)
λ_2 (10^{-3} GPa^{-1})	2.6(3)	2.52(18)	2.26(16)	2.00(14)
ev_2 (λ_2)	(0.55,0,0.84)	(0,1,0)	(0,1,0)	(0,1,0)
λ_3 (10^{-3} GPa^{-1})	1.8(3)	1.7(3)	1.7(3)	1.6(3)
ev_3 (λ_3)	(0.84,0,-0.55)	(0.93,0,-0.38)	(0.97,0,-0.26)	(0.97,0,-0.26)
Ψ, θ(°)[a]		22.0(1), 85.1(1)	15(5), 92(5)	15(4), 92(4)

[a] The major compression direction occurs in the (0 1 0) plane at the given angles Ψ to the *c* axis (from *c* to *a*) and θ to the *a* axis (from *a* to *c*).

[b] At 24.3 GPa, the direction of maximum compressibility is along *b*-axis; i.e. the [010] direction.

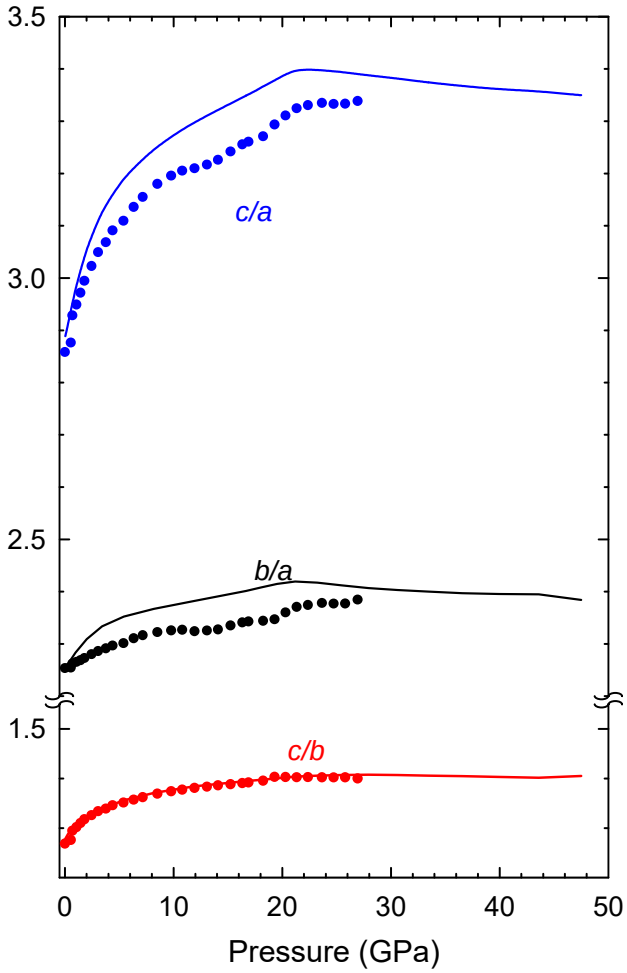

Figure S15. Pressure dependence of the experimental (symbols) and theoretical (lines) lattice parameter ratios as a function of pressure. Theoretical calculations include vdW dispersion corrections.

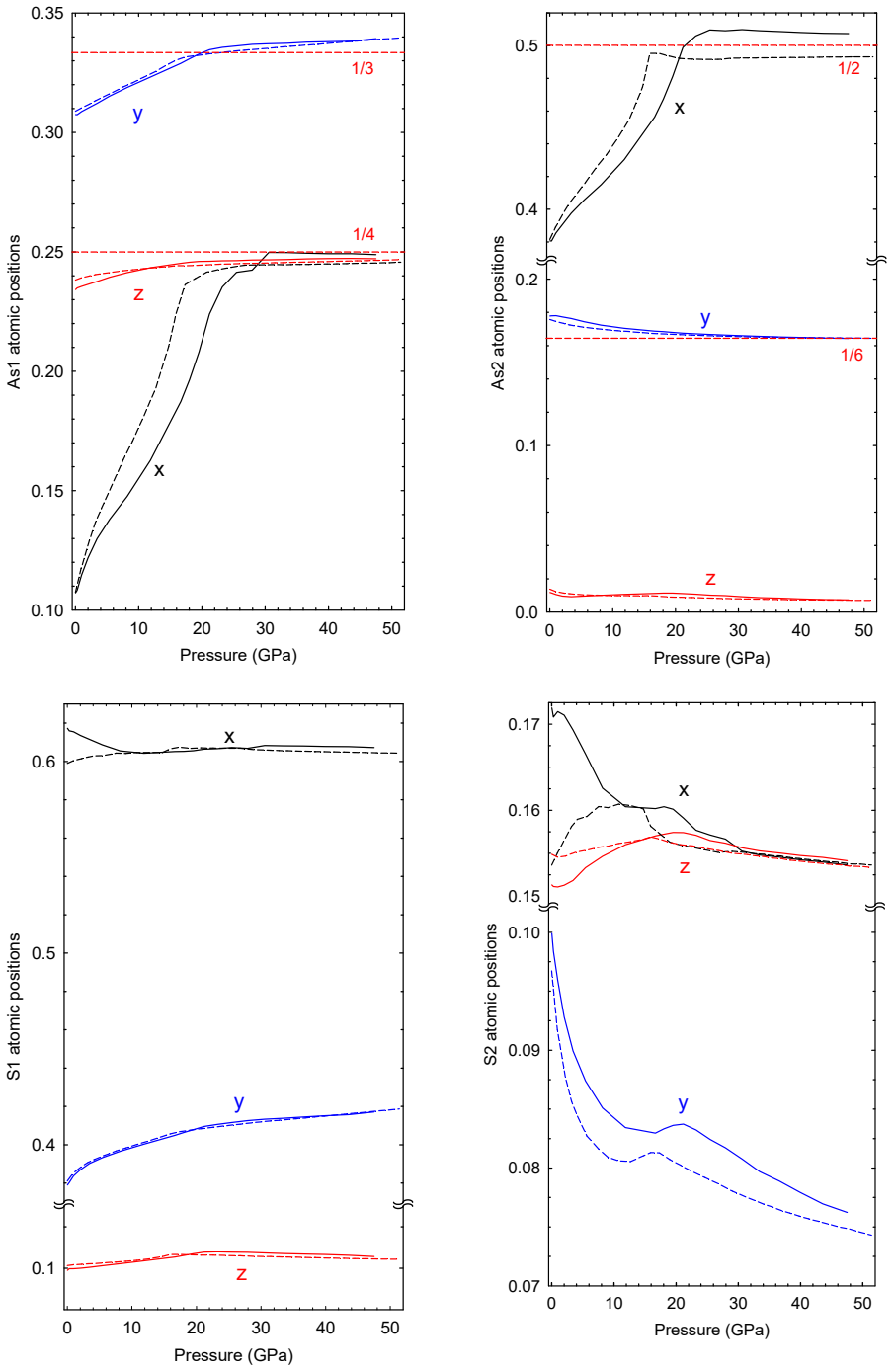
As1 atomic positions
Pressure (GPa)
1/3
1/4
y
z
x
As2 atomic positions
1/2
1/6
S1 atomic positions
S2 atomic positions

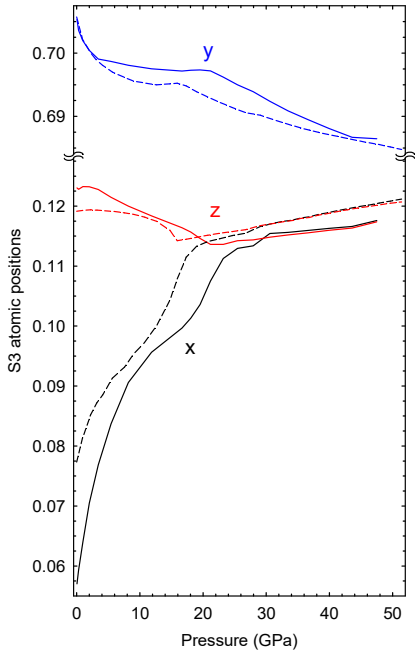

Figure S16. Pressure dependence of the theoretical free coordinates belonging to the different Wyckoff sites of the α-As_2S_3. Calculations with (without) vdW interactions are depicted as solid (dashed) lines. Compared to the As atomic coordinates, the S atomic coordinates show a very complex tendency with pressure. However, all of these show considerable changes above 18 and 25 GPa for calculations that do not consider and consider vdW interactions, respectively. Curiously, the erratic behavior of the S atomic coordinates is not reflected in the smooth HP dependence of the As-S interatomic distances [see **Fig. 6** in the main paper] that are mainly dominated by the strong changes of the x coordinate of As atoms.

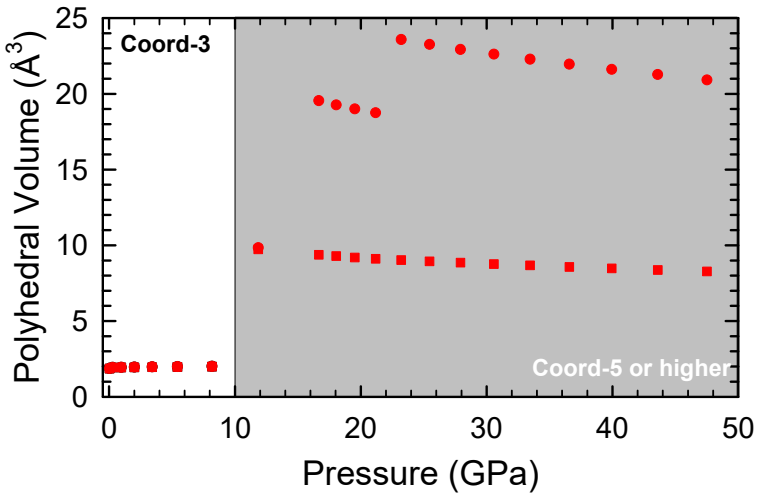

Figure S17. Pressure dependence of the theoretically predicted polyhedral unit volume around As1 (circles) and As2 (squares).

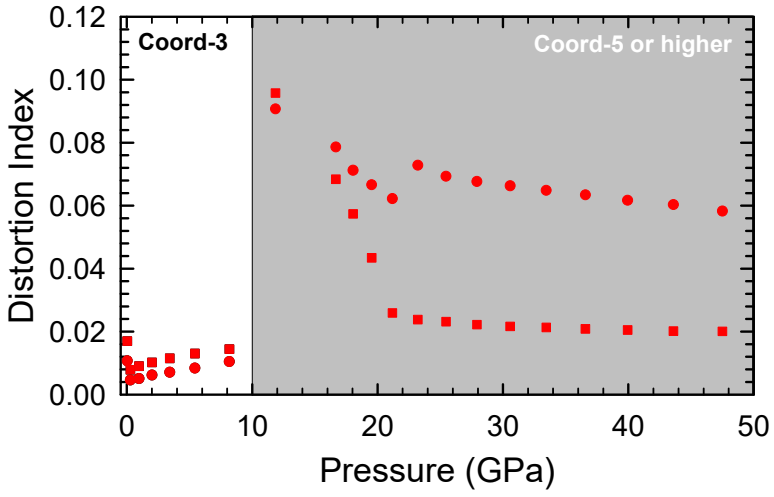

Figure S18. Pressure dependence of the theoretically predicted distortion index of the polyhedral units around As1 (circles) and As2 (squares).

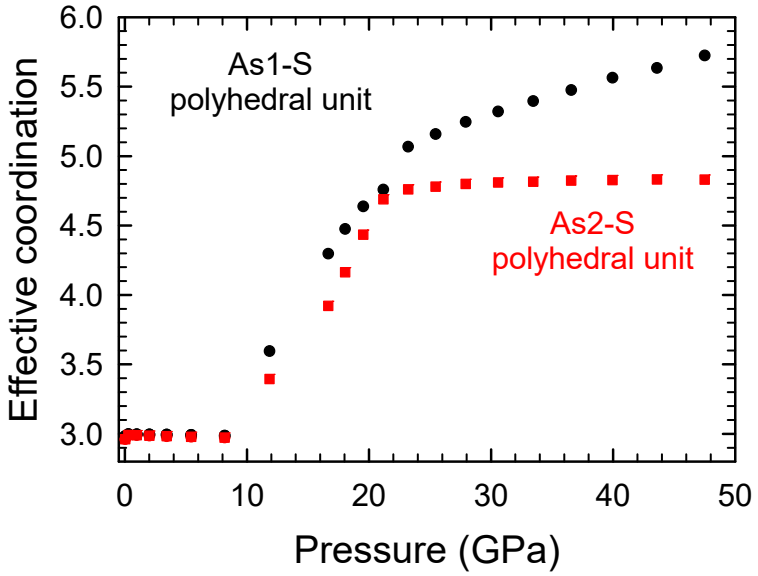

Figure S19. Pressure dependence of the theoretically predicted effective coordination number of polyhedral units around As1 (circles) and As2 (squares). Effective coordination number is calculated according to Hoppe (1979).

Vibrational properties of orpiment under compression

In layered compounds with typical van der Waals gap between the layers, the low-frequency inter-layer shear mode exhibits a much smaller pressure coefficient than other modes, whereas the low-frequency A (or B) mode displays the largest pressure coefficient. For example, the E and A modes with frequencies around 40 (60) cm^{-1} and 116 (133) cm^{-1} in InSe (GaSe) have pressure coefficients of 0.68 (0.85) cm^{-1}/GPa and 5.41 (5.78) cm^{-1}/GPa, respectively [Ulrich 1996, Kulibekov 2003]. Similar behavior is found for layered topological insulators Bi_2Se_3, Bi_2Te_3 and Sb_2Te_3 [Vilaplana 2011a, Vilaplana 2011b, Gomis 2011].

Usually, the small pressure coefficient of the low-frequency E mode in layered materials is ascribed to the weak bending force constant due to weak van der Waals forces between the neighboring layers. On the other hand, the large pressure coefficient of the low-frequency A mode is due to the extraordinary increase of the stretching force constant between neighboring layers due to the strong decrease of the inter-layer distance [Ulrich 1996, Kulibekov 2003].

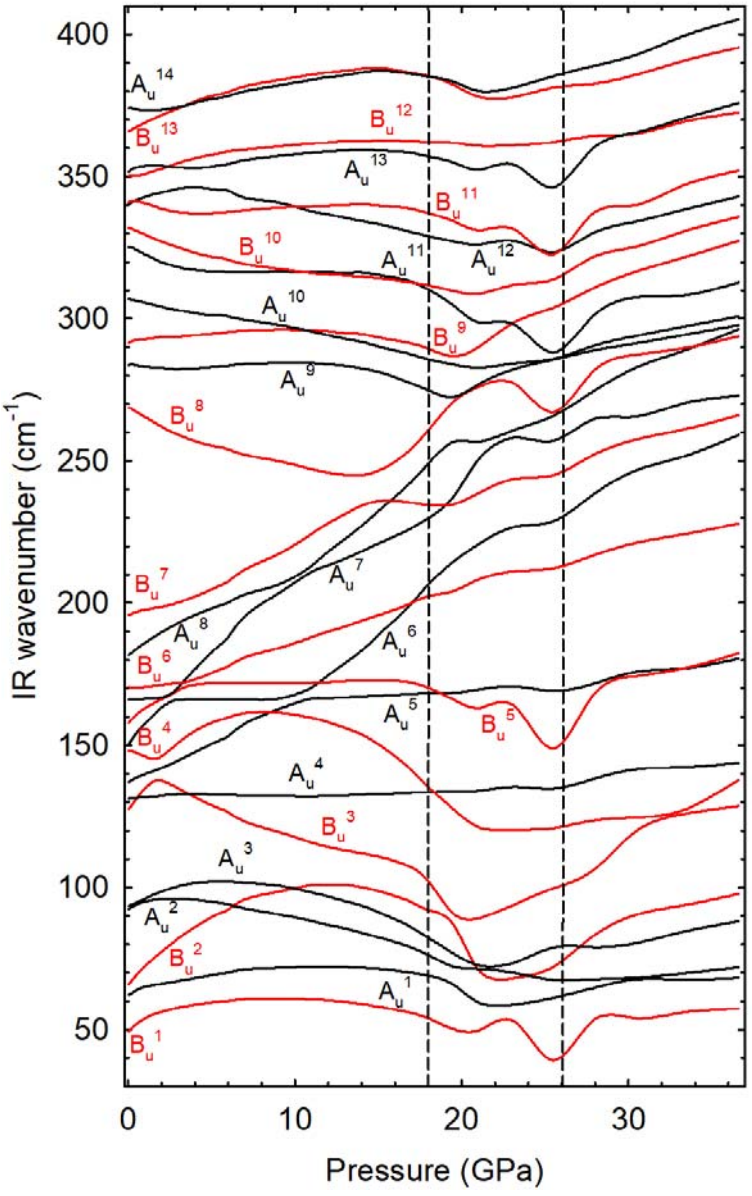

Figure S20. HP dependence of the theoretical wavenumbers of the IR-active modes in α-As_2S_3. Considerable softening of some vibrational modes is observed above 4 GPa and between 18 and 26 GPa.

(a)

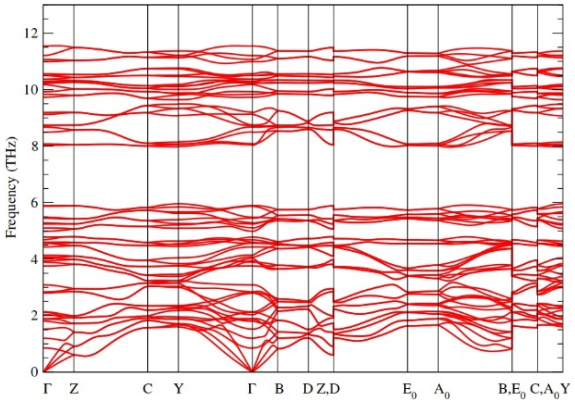
Frequency (THz)
0
2
4
6
8
10
12
Γ Z C Y Γ B D Z,D E0 A0 B,E0 C,A0 Y

(b)

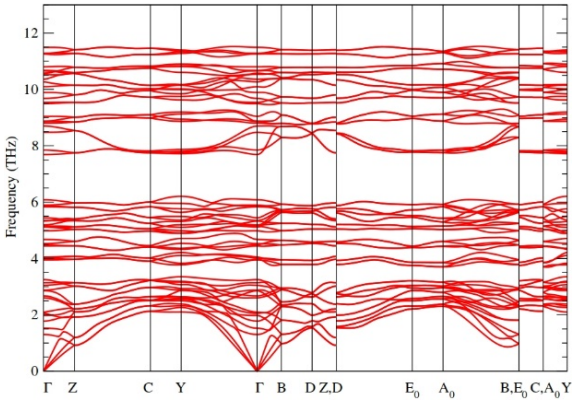
Frequency (THz)
0
2
4
6
8
10
12
Γ Z C Y Γ B D Z,D E0 A0 B,E0 C,A0 Y

(c)

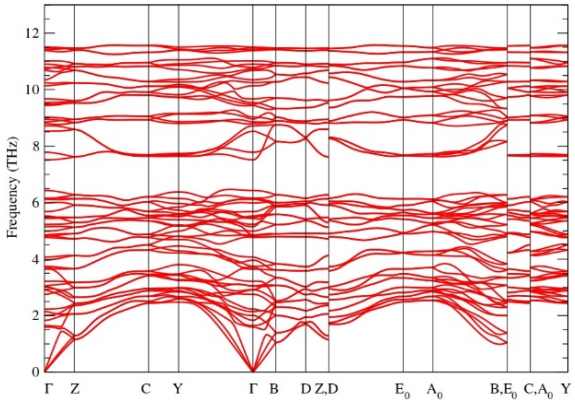
Frequency (THz)
0
2
4
6
8
10
12
Γ Z C Y Γ B D Z,D E0 A0 B,E0 C,A0 Y

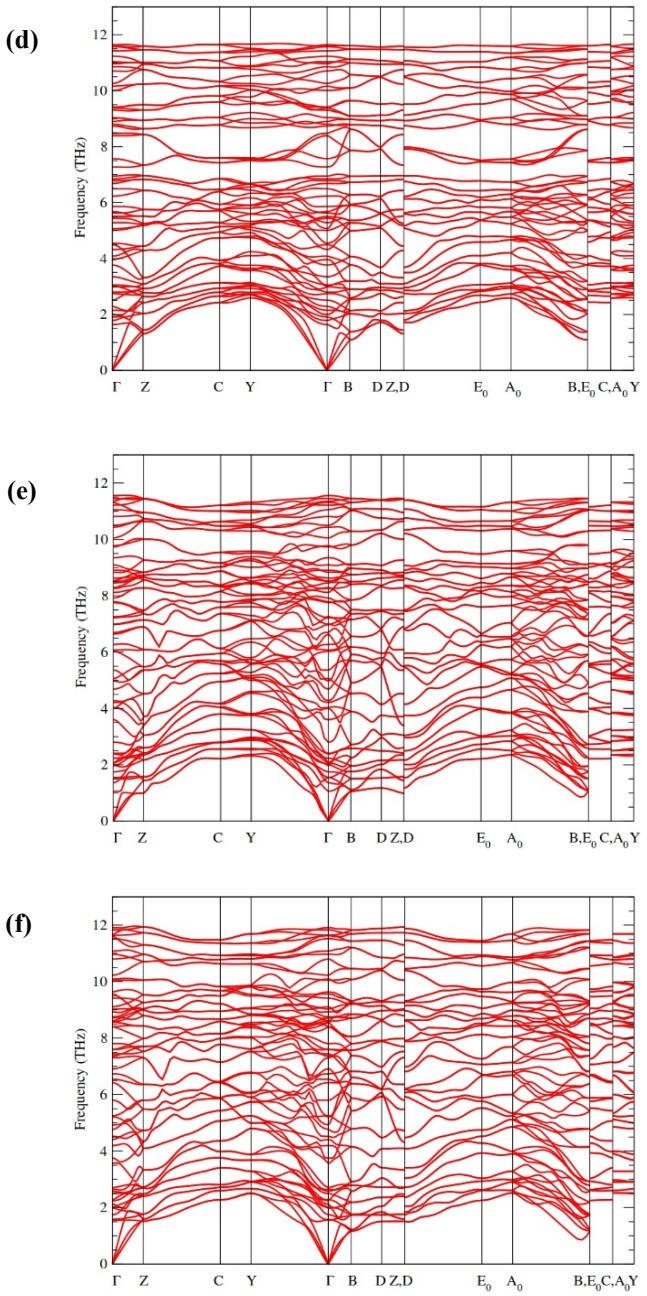

Figure S21. Calculated phonon dispersion curves of As_2S_3 at different pressures: **(a)** 0 GPa, **(b)** 5 GPa, **(c)** 10 GPa, **(d)** 15 GPa, **(e)** 21 GPa, and **(f)** 30 GPa.

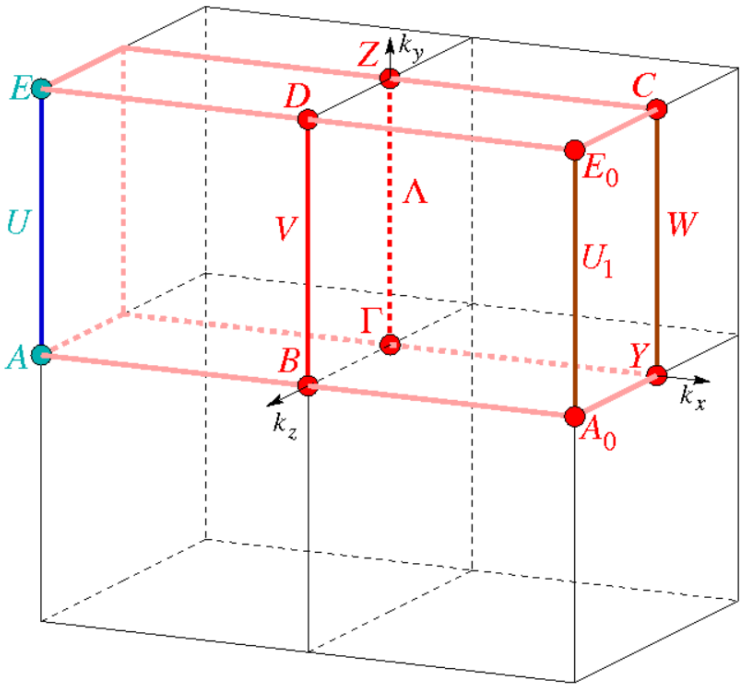

Figure S22. Representation of the points and paths used in the first Brillouin zone of monoclinic α-As_2S_3 in order to perform calculations of phonon dispersion curves and electronic band structures. Taken from the Bilbao Crystallographic Server database [Aroyo 2014].

Table S4. Theoretical (with vdW interactions) and experimental IR-active mode frequencies and their respective pressure coefficients for α-As_2S_3 at room temperature, as fitted with equation $\omega(P) = \omega_0 + \alpha \cdot P$. Experimental values have been added for comparison.

	Theoretical		Experimental
Mode (Sym)	$\omega_0\ (cm^{-1})$ [a]	$\alpha\ \left(\frac{cm^{-1}}{GPa}\right)$ [a]	$\omega_0\ (cm^{-1})$
B_u^1	50 (1)	4.3 (3)	52 [c]
A_u^1	63 (1)	2.3 (3)	
B_u^2	66 (1)	6.5 (2)	
A_u^2	93 (1)	2.5 (2)	
A_u^3	94 (1)	3.2 (1)	
B_u^3	128 (2)	8 (1)	
A_u^4	131 (2)	0.7 (1)	
A_u^5	137 (2)	2.3 (1)	
B_u^4	148 (2)	-2.5 (9)	140 [b], 139 [c]
A_u^6	150 (2)	8.8 (3)	
B_u^5	158 (2)	5.2 (3)	159 [b], 160[c]
A_u^7	167 (2)	-1.8 (4)	
B_u^6	170 (2)	-0.1 (2)	
A_u^8	182 (2)	4.6 (1)	181 [b], 183 [c]
B_u^7	196 (2)	1.1 (2)	198 [b], 202 [c]
B_u^8	269 (3)	-4.0 (1)	279 [b]
A_u^9	284 (3)	-1.0 (1)	299 [b]
B_u^9	292 (3)	1.1 (2)	311 [b], 305 [c]
A_u^{10}	307 (4)	-1.6 (1)	
A_u^{11}	326 (4)	-3.5 (2)	345 [b], 348 [c]
B_u^{10}	332 (4)	-2.8 (1)	354 [b,c]
A_u^{12}	340 (4)	2.7 (1)	
B_u^{11}	342 (4)	-1.7 (4)	
B_u^{12}	350 (4)	1.2 (3)	361 [c]
A_u^{13}	352 (4)	1.2 (4)	375 [b]
B_u^{13}	366 (4)	3.1 (1)	383 [b], 381 [c]
A_u^{14}	374 (4)	-1.0 (1)	393 [c]

[a] This work. [b] Ref. 14. [c] Ref. 15.

Table S5. Known crystalline phases of group-15 A_2B_3 sesquichalcogenides at room pressure, their space groups, stability at room pressure, average cation coordination and bonding type.

Compound	Space group	Stability at room pressure	Average cation coordination	Bonding-type
α-As_2S_3	*$P2_1/c$*	Stable	3	p-type covalent
α-As_2Se_3	*$P2_1/c$*	Stable	3	p-type covalent
β-As_2Se_3	*C2/m*	Metastable	3	p-type covalent
γ-As_2Se_3	*R-3m*	Metastable	6	metavalent
α-As_2Te_3	*C2/m*	Stable	5.5	mixed*
β-As_2Te_3	*R-3m*	Metastable	6	metavalent
α-Sb_2S_3	*Pnma*	Stable	4	mixed*
α-Sb_2Se_3	*Pnma*	Stable	4	mixed*
α-Sb_2Te_3	*R-3m*	Stable	6	metavalent
α-Bi_2S_3	*Pnma*	Stable	4	mixed*
α-Bi_2Se_3	*R-3m*	Stable	6	metavalent
α-Bi_2Te_3	*R-3m*	Stable	6	metavalent

* It is a mixture between p-type covalent and metavalent

References

[Angel 2004-2011] R. J. Angel. http://www.rossangel.com/text_strain.htm

[Aroyo 2014] M. I. Aroyo, D. Orobengoa, G. de la Flor, E. S. Tasci, J. M. Pérez-Mato, and H. Wondratschek. Brillouin-zone database on the Bilbao Crystallographic Server. *Acta Crystallographica A*. **2014**, *70*, 126.

[Canepa 2011] P. Canepa, R. M. Hanson, P. Ugliengo, and M. Alfredsson. J-ICE: a new Jmol interface for handling and visualizing crystallographic and electronic properties. *Journal of Applied Crystallography*. **2011**, *44*, 225−229.

[DeFonzo 1978] A. P. DeFonzo and J. Tauc. Network dynamics of 3:2 coordinated compounds, *Physical Review B*. **1978**, *18*, 6957−6972.

[Forneris 1969] R. Forneris. The infrared and Raman spectra of realgar and orpiment. *American Mineralogist*. **1969**, *54*, 1062−1074.

[Haussühl 2007] S. Haussühl. *Physical Properties of Crystals. An Introduction*. (Wiley-VCH, **2007**).

[Gomis 2011] O. Gomis, R. Vilaplana, F. J. Manjón, P. Rodríguez-Hernández, E. Pérez-González, A. Muñoz, C. Drasar, and V. Kucek. Lattice Dynamics of Sb_2Te_3 at High Pressures. *Physical Review B: Condensed Matter and Materials Physics*. **2011**, *84*, 174305.

[Hoppe 1979] R. Hoppe. Effective coordination numbers (ECoN) and mean Active fictive ionic radii (MEFIR). *Zeitschrift für Kristallographie*. **1979**, *150*, 23-52.

[Kulibekov 2003] A. M. Kulibekov, H. P. Olijnyk, A. P. Jephcoat, Z. Y. Salaeva, S. Onari, and K. R. Allakverdiev. Raman Scattering under Pressure and the Phase Transition in ε-GaSe. *Physica Status Solidi B*. **2003**, *235*, 517.

[Mullen 1972] D. J. E. Mullen and W. Nowacki. Refinement of the crystal structures of realgar, AsS and orpiment, As_2S_3. *Zeitschrift für Kristallographie*. **1972**, *136*, 48-65.

[Ulrich 1996] C. Ulrich, M. Mroginski, A. R. Goñi, A. Cantarero, U. Schwarz, V. Muñoz, and K. Syassen. Vibrational Properties of InSe under Pressure: Experiment and Theory. *Physica Status Solidi B*. **1996**, *198*, 121.

[Vilaplana 2011a] R. Vilaplana, O. Gomis, F. J. Manjón, A. Segura, E. Pérez-González, P. Rodríguez-Hernández, A. Muñoz, J. González, V. Marín-Borrás, V. Muñoz-Sanjosé, C. Drasar, and V. Kucek. High-pressure vibrational and optical study of Bi_2Te_3. *Physical Review B: Condensed Matter and Materials Physics*. **2011**, *84*, 104112.

[Vilaplana 2011b] R. Vilaplana, D. Santamaría-Pérez, O. Gomis, F. J. Manjón, J. González, A. Segura, A. Muñoz, P. Rodríguez-Hernández, E. Pérez-González, V. Marín-Borrás, et al. Structural and Vibrational Study of Bi_2Se_3 under High Pressure. *Physical Review B: Condensed Matter and Materials Physics.* **2011**, *84*, 184110.

[Zallen 1971] R. Zallen, M. L. Slade, and A. T. Ward. Lattice Vibrations and Interlayer Interactions in Crystalline As_2S_3 and As_2Se_3. *Physical Review B.* **1971**, *3*, 4257-4273.

[Zallen 1974a] R. Zallen and M. L. Slade. Rigid-layer modes in chalcogenide crystals. *Physical Review B*. **1974**, *9*, 1627−1637.

THE JOURNAL OF PHYSICAL CHEMISTRY C

Article

pubs.acs.org/JPCC

Structural, Vibrational, and Electronic Study of α-As_2Te_3 under Compression

V. P. Cuenca-Gotor,[†] J. A. Sans,[*,†] J. Ibáñez,[‡] C. Popescu,[§] O. Gomis,[∥] R. Vilaplana,[∥] F. J. Manjón,[†] A. Leonardo,[⊥,#] E. Sagasta,[¶] A. Suárez-Alcubilla,[ζ,ψ] I. G. Gurtubay,[#,ζ] M. Mollar,[†] and A. Bergara[#,ζ,ψ]

[†]Instituto de Diseño para la Fabricación y Producción Automatizada, Universitat Politècnica de València, 46022 Valencia, Spain
[‡]ICTJA-CSIC, Barcelona, Spain
[§]ALBA-CELLS, 08290 Cerdanyola, Barcelona, Spain
[∥]Centro de Tecnologías Físicas, Universitat Politècnica de València, 46022 Valencia, Spain
[⊥]Departamento de Física Aplicada II, Universidad del País Vasco, UPV/EHU, 48080 Bilbao, Spain
[#]Donostia International Physics Center (DIPC), 20018 Donostia, Spain
[¶]CIC NanoGUNE, E-20018, Donostia, Spain
[ζ]Departamento de Física de la Materia Condensada, Universidad del País Vasco, UPV/EHU, 48080 Bilbao, Spain
[ψ]Centro de Física de Materiales CFM, Centro Mixto CSIC-UPV/EHU, 20018 Donostia, Spain

Supporting Information

ABSTRACT: We report a study of the structural, vibrational, and electronic properties of layered monoclinic arsenic telluride (α-As_2Te_3) at high pressures. Powder X-ray diffraction and Raman scattering measurements up to 17 GPa have been complemented with *ab initio* total-energy, lattice dynamics, and electronic band structure calculations. Our measurements, which include previously unreported Raman scattering measurements for crystalline α-As_2Te_3, show that this compound undergoes a reversible phase transition above 14 GPa at room temperature. The monoclinic crystalline structure of α-As_2Te_3 and its behavior under compression are analyzed by means of the compressibility tensor. Major structural and vibrational changes are observed in the range between 2 and 4 GPa and can be ascribed to the strengthening of interlayer bonds. No evidence of any isostructural phase transition has been observed in α-As_2Te_3. A comparison with other group 15 sesquichalcogenides allows understanding the structure of α-As_2Te_3 and its behavior under compression based on the activity of the cation lone electron pair in these compounds. Finally, our electronic band structure calculations show that α-As_2Te_3 is a semiconductor at 1 atm, which undergoes a trivial semiconducting−metal transition above 4 GPa. The absence of a pressure-induced electronic topological transition in α-As_2Te_3 is discussed.

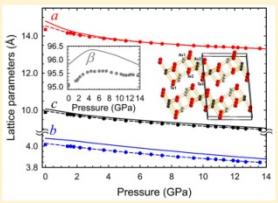

INTRODUCTION

Arsenic telluride (As_2Te_3) and other group 15 sesquichalcogenides with generic formula A_2X_3 (A = As, Sb, Bi; X = S, Se, Te) have been widely studied because of their outstanding thermoelectric properties.[1−3] In this regard, the most stable phase of arsenic telluride at ambient conditions (α-As_2Te_3) is a quasi-layered structure with monoclinic $C2/m$ symmetry[4−6] and a smaller figure of merit than Sb- and Bi-based tellurides;[7] however, the metastable β-As_2Te_3 polymorph, known for many years[8−11] and with layered tetradymite-like rhombohedral $R\bar{3}m$ symmetry, exhibits notable thermoelectric properties.[12,13] Additionally, As_2Te_3 glasses have also been extensively studied due to their interesting applications as IR devices, electric and optical switches, memory devices, high-resolution displays, acousto-optic devices, optical fibers, and amplifiers.[14−19]

The recent discovery of 3D topological insulators (TIs) among group 15 sesquichalcogenides[20−22] has stimulated in the last years the study of these materials, which crystallize in a number of polymorphs depending on the activity of the cation lone electron pair (LEP). Many of the group 15 sesquichalcogenides that behave as 3D TIs crystallize in the layered tetradymite $R\bar{3}m$ structure, like α-Sb_2Te_3, α-Bi_2Se_3, and α-Bi_2Te_3. Since this phase has been found in several sesquichalcogenides at high pressures (HP) and/or high temperatures (HT), HP studies of these materials are extremely interesting in order to search for new 3D TIs. Consequently, a number of HP experimental and theoretical studies have been conducted in recent years in group 15 sesquichalcogenides looking for an improvement of thermoelectrical properties or for the discovery

Received: June 15, 2016
Revised: August 2, 2016
Published: August 2, 2016

DOI: 10.1021/acs.jpcc.6b06049
J. Phys. Chem. C 2016, 120, 19340−19352

Structural, Vibrational, and Electronic Study of α-As_2Te_3 under Compression

V.P. Cuenca-Gotor,[1] J.A. Sans,[1] J. Ibáñez,[2] C. Popescu,[3] O.Gomis,[4] R. Vilaplana,[4] F.J. Manjón,[1] A. Leonardo,[5,6] E. Sagasta,[7] A. Suárez-Alcubilla,[8,9] I.G. Gurtubay,[6,8] M. Mollar,[1] and A. Bergara [6,8,9]

[1] *Instituto de Diseño para la Fabricación y Producción Automatizada, MALTA Consolider Team, Universitat Politècnica de València, 46022 València, Spain*

[2] *Consejo Superior de Investigaciones Científicas, Instituto Jaume Almera, 08028, Barcelona, Spain*

[3] *ALBA-CELLS, 08290, Cerdanyola, Spain*

[4] *Centro de Tecnologías Físicas: Acústica, Materiales y Astrofísica, MALTA Consolider Team, Universitat Politècnica de València, 46022 València, Spain*

[5] *Dpto. de Física Aplicada II, Universidad del País Vasco, UPV/EHU, 48080 Bilbao, Spain*

[6] *Donostia International Physics Center (DIPC), 20018 Donostia (Spain)*

[7] *CIC NanoGUNE, E-20018, Donostia, San Sebastián, Spain*

[8] *Dpto. de Física de la Materia Condensada, Universidad del País Vasco, UPV/EHU, 48080 Bilbao, Spain*

[9] *Centro de Física de Materiales CFM, Centro Mixto CSIC-UPV/EHU, 20018 Donostia, Spain*

Abstract

We report a study of the structural, vibrational, and electronic properties of layered monoclinic arsenic telluride (α-As_2Te_3) at high pressures. Powder X-ray diffraction and Raman scattering measurements up to 17 GPa have been complemented with *ab initio* total-energy, lattice dynamics, and electronic band structure calculations. Our measurements, which include previously unreported Raman scattering measurements for crystalline α-As_2Te_3, show that this compound undergoes a reversible phase transition above 14 GPa at room temperature. The monoclinic crystalline structure of α-As_2Te_3 and its behavior under compression are analyzed by means of the compressibility tensor. Major structural and vibrational changes are observed in the range between 2 and 4 GPa and can be ascribed to the strengthening of interlayer bonds. No evidence of any isostructural phase transition has been observed in α-As_2Te_3. A comparison with other group-15 sesquichalcogenides allows understanding the structure of α-As_2Te_3 and its behavior under compression based on the activity of the cation lone electron pair in these compounds. Finally, our electronic band structure calculations show that α-As_2Te_3 is a semiconductor at 1 atm, which undergoes a trivial semiconducting-metal transition above 4 GPa. The

absence of a pressure-induced electronic topological transition in α-As_2Te_3 is discussed.

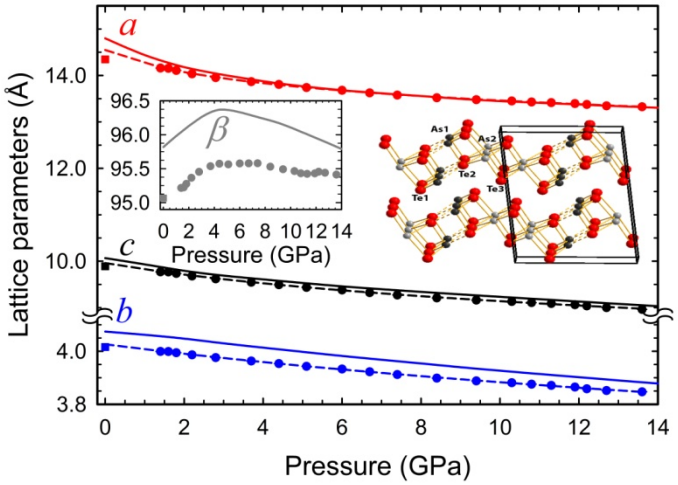

I. INTRODUCTION

Arsenic telluride (As_2Te_3) and other group-15 sesquichalcogenides with generic formula A_2X_3 (A=As, Sb, Bi; X= S, Se, Te) have been widely studied because of their outstanding thermoelectric properties [Nolas 2001, Scherrer 2005, Stordeur 1995]. In this regard, the most stable phase of arsenic telluride at ambient conditions (α-As_2Te_3) is a layered structure with monoclinic *C2/m* symmetry [Carron 1963, Kanishcheva 1982, Stergiou 1985a]. This structure has a smaller figure of merit than Sb- and Bi-based tellurides [Scheidemantel 2005]; however, the metastable β-As_2Te_3 polymorph, known for many years [Yakushev 1986, Kirkinskii 1974, Shu 1986, Toscani 1991] and with layered tetradymite-like rhombohedral $R\bar{3}m$ symmetry, exhibits notable thermoelectric properties [Scheidemantel 2003, Vaney 2015]. Additionally, As_2Te_3 glasses have also been extensively studied due to their interesting applications as IR devices, electric and optical switches, memory devices, high-resolution displays, acousto-optic devices, optical fibers and amplifiers [Thornburg 1973, Madan 1988, Hwang 2001, Aggarwal 2002, Kovanda 2003, Sanghera 2006].

The recent discovery of 3D topological insulators (TIs) among group-15 sesquichalcogenides [Chen 2009, Zhang 2009, Hsieh 2009] has stimulated in the last years the study of these materials, which crystallize in a number of polymorphs depending on the activity of the cation lone electron pair (LEP). Many of the group-15 sesquichalcogenides that behave as 3D TIs crystallize in the layered tetradymite $R\bar{3}m$ structure, like α-Sb_2Te_3, α-Bi_2Se_3 and α-Bi_2Te_3. Since this phase has been found in several sesquichalcogenides at high pressures (HP) and/or high temperatures (HT), HP studies of these materials are extremely interesting in order to search for new 3D TIs. Consequently, a number of HP experimental and

theoretical studies have been conducted in recent years in group-15 sesquichalcogenides looking for an improvement of thermoelectrical properties or for the discovery of topological properties [Manjón 2013, Liu 2013, Zhao 2013, Kirshenbaum 2013, Zhu 2013, Efthimiopoulos 2013, Efthimiopoulos 2014, Zhang 2014, Kong 2014, Brazhkin 2014, Zhao 2015a, Nielsen 2015, Wang 2015, Ovsyannikov 2015, Yu 2015, Zhang 2015, Sorb 2016, Efthimiopoulos 2016, Ibáñez 2016, Zhao 2016, Zhang 2016] [see Manjón (2013) for studies prior to 2013].

Despite the interest in group-15 sesquichalcogenides from both fundamental and technological points of view, many properties of crystalline As_2Te_3 are unknown. In particular, there is no report on the vibrational properties of crystalline phases of As_2Te_3 even at room conditions up to our knowledge and only a few HP studies have been devoted to crystalline As_2Te_3. In this respect, synthesis at HP/HT conditions explored the phase boundary between the α and β phases up to 2 GPa three decades ago [Yakushev 1986, Kirkinskii 1974]. Much later, changes in the thermoelectric power of α-As_2Te_3 were reported above 2 and 6 GPa and a structural transformation to β-As_2Te_3 between 6 and 8 GPa was claimed without reporting full structural details of the high-pressure phase [Scheidemantel 2005]. Finally, two recent studies of α-As_2Te_3 up to 40 and 47 GPa have been reported. In these two works, two isostructural phase transitions (IPTs) of α-As_2Te_3 and a progressive first-order phase transition to the γ-Bi_2Te_3 phase above 13-15 GPa have been reported [Zhao 2016, Zhang 2016]. In this regard, it must be noted that a new monoclinic $P2_1/m$ (named β') has also been recently found at low temperatures [Morin 2015].

As regards the electronic structure, recent *ab initio* calculations have reported that uniaxially-strained β-As_2Te_3 should undergo a pressure-induced electronic topological transition (ETT) leading from a trivial insulator to a Weyl semimetal and then to a topological insulator [Pal 2014]. While there is still no experimental result on β-As_2Te_3 under pressure, a recent work has reported electrical measurements at HP combined with theoretical *ab initio* calculations and observed the metallization of α-As_2Te_3 above 5 GPa [Zhao 2016]. Noteworthy, another recent work has suggested on the basis of theoretical calculations that there is no metallization of α-As_2Te_3 on increasing pressure but there are two second-order electronic transitions [Zhang 2016]. These recent studies contrast with previous studies of amorphous and liquid semiconductors As_2S_3, As_2Se_3 and As_2Te_3 at HP that suggested a decrease of the optical and electronic bandgap with increasing pressure, leading to a common semiconductor-metal transition and glass transitions [Sakai 1977, Kristofik 1985, Parthasarathy 1985, Hoshino 1996, Shimojo 2002, Struzhkin 2008, Ramesh 2014].

In light of the cited works and the interesting properties found in other group-15 sesquioxides and sesquichalcogenides, it is interesting to study the properties of α-As_2Te_3 at HP. They will provide information in order to: i) understand the stability of their different polymorphs; ii) check if there is any IPT or ETT in α-As_2Te_3; iii) verify if α-As_2Te_3 undergoes metallization under compression; and iv) explore if α-As_2Te_3 can behave as a 3D-TI at HP. For those reasons, here we report a HP study of structural, vibrational, and electronic properties of α-As_2Te_3 at room temperature by means of powder X-ray diffraction (XRD) and Raman scattering (RS) measurements up to 17 GPa, which are complemented with *ab initio* total energy,

lattice dynamics, and electronic structure calculations. We will show that our measurements show a reversible phase transition above 14 GPa to the γ phase in good agreement with recent reports [Zhao 2016, Zhang 2016], but no IPTs are found in α-As_2Te_3 contrary to the same recent reports [Zhao 2016, Zhang 2016]. The crystalline structure of α-As_2Te_3 and its compressibility is analyzed by calculating the compressibility tensor at HP and explained on the light of its comparison to that of other group-15 sesquichalcogenides; in particukar, taking into account the activity of the cation LEP. The RS spectrum of α-As_2Te_3 at room conditions is reported for the first time, and its HP behavior has been discussed. Finally, our electronic band structure calculations suggest that there is a progressive closing of the bandgap of α-As_2Te_3 with increasing pressure leading from a trivial semiconductor to a trivial metal above 4 GPa with no evidence for a pressure-induced ETT. Taking into account that the calculated bandgap is slightly underestimated in our calculations, we suggest the closing of the experimental bandgap above 6-7 GPa in good agreement with a recent work [Zhao 2016], but in disagreement with another recent study [Zhang 2016]. Therefore, our results are consistent with the changes in resistivity and thermopower measurements previously reported [Scheidemantel 2005, Zhao 2016].

II. EXPERIMENTAL DETAILS

Commercially available polycrystalline As_2Te_3 powder (Alfa-Aesar, 99.999%) was used in the present study. XRD measurements at ambient pressure performed with a Rigaku Ultima IV diffractometer showed that samples correspond to the α phase with no presence of other phases or impurities. HP angle-dispersive powder XRD experiments at room temperature up to 17 GPa were conducted in a membrane-type diamond anvil cell (DAC) at the BL04-MSPD beamline of ALBA synchrotron. Incident monochromatic beam with wavelength of 0.4246 Å was focused to 20 x 20 μm using a pinhole of 50 μm to cut the X-ray beam tail [Fauth 2013]. Images covering a 2θ range up to 18° were collected using a SX165 CCD located at 240 mm from sample. One-dimensional diffraction profiles of intensity as a function of 2θ were obtained by integration of the observed intensities with the Fit2D software [Hammersley 1996]. Rietveld refinement of the experimental diffraction patterns gave reliable correlation factors up to 6 GPa. Above this pressure, the atomic positions have not been included in the fit and the lattice parameters were extracted through a Le Bail analysis of the experimental diffraction patterns. Rietveld and Le Bail refinements were carried out with GSAS package software for synchrotron measurements [Larson 2004, Toby 2001]. Interatomic distances were extracted with VESTA software [Momma 2011]. The equation of state (EoS) of copper [Dewaele 2004], whose powder was mixed with the sample powder, was used for pressure calibration.

Room-temperature unpolarized RS measurements up to 12 GPa were carried out with a Horiba Jobin Yvon LabRAM HR spectrometer equipped with a thermoelectrically cooled multichannel CCD detector that enables a spectral resolution better than 2 cm^{-1}. RS measurements were excited using the 6328 Å line

of a He:Ne laser with an output power below 0.3 mW in order to avoid laser heating since these samples are very prone to laser damage both outside and inside the DAC. This fact could explain why RS measurements, even at ambient conditions, have not been previously reported for this compound to our knowledge. Pressure was determined with the ruby fluorescence method [Mao 1986]. In both HP-XRD and HP-RS measurements, methanol-ethanol (4:1 ratio) mixture was used as a pressure-transmitting medium with hydrostatic conditions up to 10 GPa and quasi-hydrostatic conditions up to 17 GPa [Piermarini 1973, Klotz 2009].

III. THEORETICAL DETAILS

Ab initio total-energy calculations were performed for α-As_2Te_3 and β-As_2Te_3 within the density functional theory (DFT) [Hohenberg 1964] using the plane-wave method and the pseudopotential theory with the Vienna Ab initio Simulation Package (VASP) [Kresse 1993] including scalar relativistic effects and spin-orbit interaction (SOI). The projector-augmented wave scheme (PAW) [Kresse 1996a, Kresse 1996b, Blöchl 1994, Kresse 1999] was used as implemented in this package and the basis set of plane waves extended up to an energy cutoff of 440 eV in order to achieve highly converged results and accurate description of the electronic properties. The exchange-correlation energy was described in the generalized gradient approximation (GGA) with the PBE prescription [Perdew 1996]. In order to obtain very well converged energies and forces, the integration over the Brillouin zone (BZ) was performed using dense meshes of special *k*-points. At selected volumes, the structures were fully relaxed to their optimized configuration through the calculation of the forces on atoms and the stress tensor. In the optimized configurations, the forces on the atoms are less than 0.002 eV/Å and the deviations of the stress tensor from a diagonal hydrostatic form are less than 1 kbar (0.1 GPa).

Electronic band-structure calculations were carried out at different pressures along selected paths on the first BZ. In turn, lattice-dynamics calculations were performed at the zone center (Γ point) and along high-symmetry directions of the BZ as a function of pressure using the direct-force constant approach [Parlinski 1997]. The construction of the dynamical matrix at the Γ point of the BZ involves separate calculations of the forces that result from a fixed displacement away from equilibrium of the atoms in the primitive cell. The diagonalization of the dynamical matrix provides the normal-mode frequencies. Moreover, these calculations allow identifying the irreducible representations and the character of the vibrational phonon modes at the Γ point.

IV. RESULTS AND DISCUSSION

Structural and vibrational characterization of α-As_2Te_3 at room conditions

As_2Te_3 usually crystallizes in the α polymorph with monoclinic *C2/m* space group. The crystalline structure of the α phase [**Fig. 1**] is composed of zigzag layers piled up mainly along the *a* axis, which are linked by very weak van der Waals forces. In

turn, zigzag layers are formed by rods extending along the *b* axis, which are linked by weak ionic-covalent As-Te forces mainly along the *c* axis. This zigzag layered structure is similar to that recently described for Sb_2S_3, Sb_2Se_3, and Bi_2S_3 [Ibáñez 2016]. In α-As_2Te_3, there are five atoms occupying independent 4i Wyckoff sites (As1, As2, Te1, Te2 and Te3); i.e., all atoms are located in the planes $y = 0$ and $y = 1/2$. The two independent As1 and As2 atoms have 5-fold and 6-fold coordination, respectively. In particular, Te atoms around As2 form a distorted octahedron with As-Te distances around 2.8 Å, while Te atoms around As1 form a square-based pyramid in a 3+2 coordination with three As-Te distances around 2.7 Å and two distances around 3.2 Å. This 5-fold and 6-fold coordination of As atoms in α-As_2Te_3 contrasts with the pure 6-fold coordination of As atoms in β-As_2Te_3.

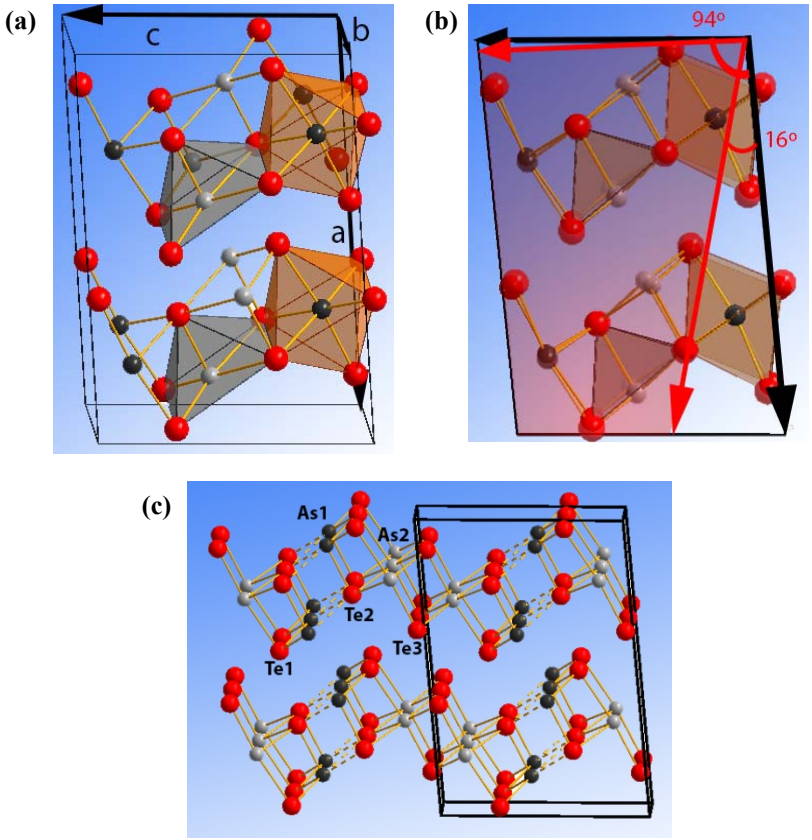

Figure 1. (a) Scheme of α-As_2Te_3 structure at room pressure. **(b)** Representation of the effect of pressure in the α-As_2Te_3 structure at 1 atm (base scheme) and 14 GPa (scaled and superimposed, transparent scheme). Atoms at 14 GPa seem greater than at 1atm due to rescaling of cell axes to match the values at 1 atm. Dark grey, light grey and red colors correspond to As1, As2 and Te atoms, respectively. Red arrow indicates the direction of maximum compressibility of the compound at room and high pressure. **(c)** Layer and rod layout.

In this regard, we must note that a higher 5+2 coordination has been proposed for As1 in α-As_2Te_3 (with two long (> 4Å) As-Te distances between As1 atoms and Te atoms corresponding to the adjacent layer) [Stergiou 1985a]. We will show later in the discussion of HP-XRD results that the right coordination of As1 in α-As_2Te_3 at room conditions is five.

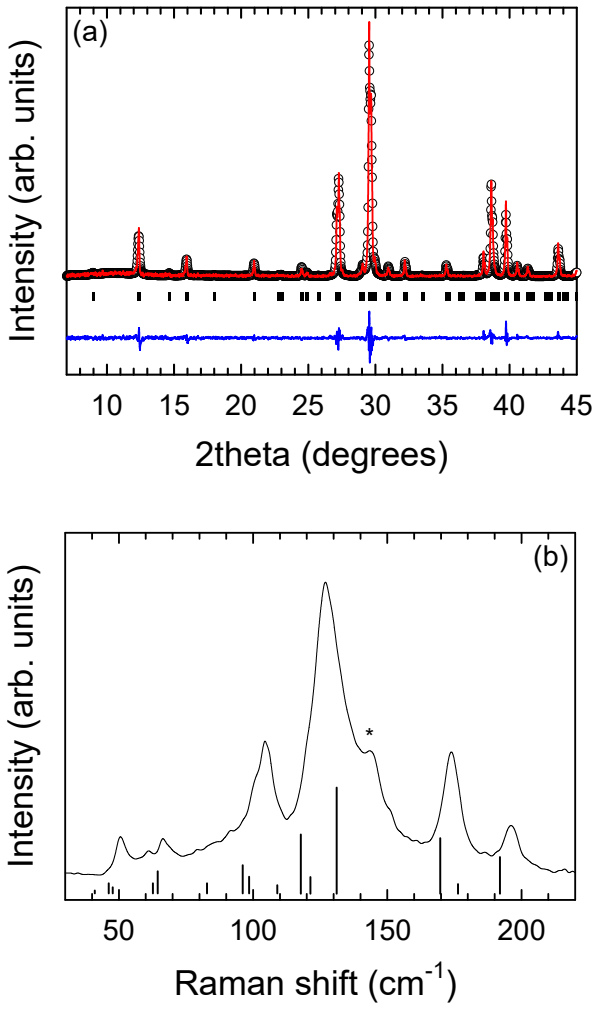

Figure 2. Structural and vibrational characterization of α-As_2Te_3 at room conditions: **(a)** Powder XRD pattern. Rietveld refinement and residuals are also plotted. **(b)** RS spectrum. Bottom marks show theoretical Raman-active mode frequencies whose length scales with the calculated intensity for each mode. The asterisk indicates a peak from crystalline Te.

The experimental XRD pattern of our sample at ambient conditions [**Fig. 2(a)**] can be refined with a Gd_2Cl_3-type structure (*C2/m* space group), with small residuals and a correlation factor R_{wp} of 10%, yielding the following lattice parameters: a = 14.3441(4) Å, b = 4.01627(19) Å, c = 9.8895(4) Å and β = 95.053(3)º with V_0 = 567.52(3) Å^3. These values show good agreement with our theoretical lattice parameters [see **Table 1**] and with previously reported experimental values [Carron 1963, Kanishcheva 1982, Stergiou 1985a, Zhao 2016, Zhang 2016]. Furthermore, our theoretical values at room pressure compare also well to those of recently reported *ab initio* calculations including SOI [Deng 2015]. Therefore, our XRD analysis at room conditions shows that our sample corresponds to pure α-As_2Te_3. No traces of crystalline Te have been observed in our samples.

Table 1. Experimental and theoretical fractional coordinates corresponding to the *C2/m* phase of α-As_2Te_3 at ambient conditions. Experimental (Exp) lattice parameters and volume are: a = 14.3441(4) Å, b = 4.01627(19) Å, c = 9.8895(4) Å, β = 95.053(3)º and V_0 = 567.52(3) Å^3. Theoretical (The) lattice parameters and volume are: a = 14.7995 Å, b = 4.0744 Å, c = 10.0667 Å, β = 95.8181º and V_0 = 603.88 Å^3.

atoms	site	character	*x*	*y*	*z*
As1	4i	Exp	0.6117(4)	0	0.4436(9)
		The	0.6218		0.4408
As2	4i	Exp	0.7917(7)	0	0.8608(13)
		The	0.7962		0.8593
Te1	4i	Exp	0.972(3)	0	0.7143(6)
		The	0.9619		0.7137
Te2	4i	Exp	0.778(3)	0	0.3391(7)
		The	0.7812		0.3371
Te3	4i	Exp	0.623(3)	0	0.9682(6)
		The	0.6284		0.9664

As regards the vibrational properties of α-As_2Te_3, group theory predicts 30 zone-center vibrational modes at the BZ center with mechanical representation [Kroumova 2003]:

$$\Gamma_{30} = 10(A_g + B_u) + 5(A_u + B_g) \quad (1)$$

where g (gerade) modes are Raman active and u (ungerade) modes are infrared (IR) active, except one Au and two Bu modes, which are acoustic modes. Therefore, α-As_2Te_3 has 15 Raman-active modes and 12 IR-active modes. A_u and B_g modes correspond to atom vibrations along the *b*-axis while A_g and B_u modes correspond to vibrations of atoms in the *a*-*c* plane.

Figure 2(b) shows unpolarized RS spectrum of α-As_2Te_3 at room conditions together with the theoretically predicted frequencies (bottom marks) scaled in intensity according to theoretical calculations of the Raman scattering cross section. The values of the experimental and theoretical frequencies of the Raman-active modes of α-As_2Te_3 at room pressure are summarized in **Table 2**. It can be observed that our RS spectrum clearly shows 10 out of the 15 Raman-active modes with a rather good agreement between our experimental and theoretical frequencies and intensities. However, the large number of Raman-active modes in a small frequency region of the RS spectrum at room pressure and the broadening of experimental peaks makes their identification, using only the RS spectrum at room pressure with the help of *ab initio* calculations, almost impossible. Therefore, a tentative assignment of experimental peaks has been performed on the basis of HP-RS measurements and calculations commented in a posterior section.

Table 2. Theoretical and experimental Raman mode frequencies and their pressure coefficients in α-As_2Te_3 at room temperature as fitted with equation $\omega(P) = \omega_0 + \alpha P + \beta P^2$.

	Ab initio calculations			Experiment		
Mode	$\omega_0\ (cm^{-1})$	$\alpha\left(\frac{cm^{-1}}{GPa}\right)$	$\beta\left(\frac{cm^{-1}}{GPa^2}\right)$	$\omega_0\ (cm^{-1})$	$\alpha\left(\frac{cm^{-1}}{GPa}\right)$	$\beta\left(\frac{cm^{-1}}{GPa^2}\right)$
A_g^1	43.0(6)	1.2(5)	-0.10(4)	49.0(2)	2.5(5)	-0.19(5)
A_g^2	47.4(5)	3.4(3)	-0.070(17)	67.0(4)	4.3(2)	-0.15(3)
B_g^1	48.3(7)	1.5(2)	-0.077(19)	66.0(4)	0.15(6)	-0.014(4)
B_g^2	62.4(2)	2.0(1)	-0.011(5)			
A_g^3	63.8(1)	3.8(2)	-0.08(1)			
A_g^4	83.0(5)	2.9(1)	-0.08(1)	90.6(3)	1.8(1)	-0.037(9)
B_g^3	95.6(3)	4.5(3)	-0.15(2)	99.0(8)	6.0(8)	-0.7(2)
A_g^5	99.1(4)	2.6(1)	-0.068(9)			
B_g^4	107.9(2)	3.2(2)	-0.04(1)	119.2(2)	2.2(1)	-0.045(9)
A_1(Te)				123.1(4)	-3.4(3)	0.13(5)
A_g^6	117.7(2)	1.9(3)	-0.005(2)			
A_g^7	121.0(3)	2.8(3)	-0.018(3)	128.0(8)	2.3(4)	-0.02(3)
B_g^5	130.9(4)	1.5(1)	0.05(1)	137.0(9)	-0.8(4)	0.16(2)
E''(Te)				142.0(3)	-0.6(2)	0.11(4)
A_g^8	170.2(4)	-1.3(2)	0.17(2)	171.4(3)	-0.3(1)	0.13(3)
A_g^9	177.3(2)	0.22(6)	0.074(5)			
A_g^{10}	192.0(1)	-1.3 (3)	0.14(2)	193.2(3)	0.13(5)	0.066(8)

The RS spectrum of α-As_2Te_3 is dominated by a mode close to 120 cm^{-1} and two characteristic high-frequency modes between 170 and 200 cm^{-1}. Unfortunately, our RS spectrum of crystalline α-As_2Te_3 cannot be compared to previous measurements since this is the first time this RS spectrum is reported to the best of our knowledge. However, we must note that our RS spectrum is consistent with RS spectra reported in glasses containing As and Te [see discussion in the Supporting Information], which show vibrational frequencies [Mendoza-Galván 2000, Usuki 1996, Tverjanovich 2012, Alekberov 2014, Taylor 1975, Lukic 2003, Zallen 1971] below 200 cm^{-1}. In this regard, it must be stressed that the RS spectrum of α-As_2Te_3 resembles that of crystalline Te since the most intense mode of the RS spectrum of α-As_2Te_3 (the A_g^7 mode around 120 cm^{-1}) occurs at a similar frequency as the most intense mode (A_1 mode) of crystalline Te [Pine 1971]. We will show latter in our HP-RS study that the RS spectrum of α-As_2Te_3 at several pressures shows two Raman-active modes of crystalline Te: the A_1 mode of Te which is overlapped with the A_g^7 mode near 120 cm^{-1} and the E″ mode of Te around 140 cm^{-1} (marked with an asterisk in **Fig. 2(b)**). Since XRD peaks of crystalline Te do not appear in our XRD pattern at ambient conditions, laser heating appears to be responsible for the presence of these Te-related modes, even at the small powers used in this work for exciting RS measurements. Further discussion of the vibrational properties of α-As_2Te_3 is given in the Supporting Information, where four characteristic Raman-active modes have been discussed and visualized and with the J-ICE software [see **Fig. S1** in the Supporting Information] [Canepa 2011] in the same way as was previously reported for monoclinic α-Bi_2O_3 [Pereira 2014a].

HP-XRD measurements

Figure 3 shows powder HP-XRD patterns of α-As_2Te_3 at selected pressures up to 17.2 GPa. It can be observed that the low-pressure monoclinic *C2/m* structure is stable up to 14 GPa. Above this pressure, a reversible structural transition to a HP phase is evidenced by new peaks [marked by asterisks in **Fig. 3**] in the pattern of 17.2 GPa and by the recovery of the XRD pattern of α-As_2Te_3 on releasing pressure to room pressure (see pattern at the top of **Fig. 3**). This result is in agreement with two recent works [Zhao 2016, Zhang 2016], but contrasts with a previous work that reported a phase transition to β-As_2Te_3 between 6 and 8 GPa under non-hydrostatic conditions [Scheidemantel 2005]. The peaks of the new phase can be assigned neither to β-As_2Te_3 nor to β'-As_2Te_3. Our XRD pattern at 17.2 GPa match with the γ-Bi_2Te_3 and γ-Bi_2Se_3 phases (monoclinic *C2/c*) phase in good agreement with the two recent works [Zhao 2016, Zhang 2016]. The study of the HP phase of α-As_2Te_3 is out of the scope of this work.

Rietveld refinements performed up to 6 GPa and Le Bail analysis at higher pressures [see examples in **Fig. S2** of the Supporting Information] allowed us to get the structural parameters of α-As_2Te_3 at different pressures. A monotonous decrease of the unit cell volume of α-As_2Te_3 up to 14 GPa is observed [**Fig. 4(a)**]. Fit of pressure vs. experimental volume to a third-order Birch-Murnaghan equation of state (BM-EoS) [Birch 1938] yields a zero-pressure volume, bulk modulus and pressure

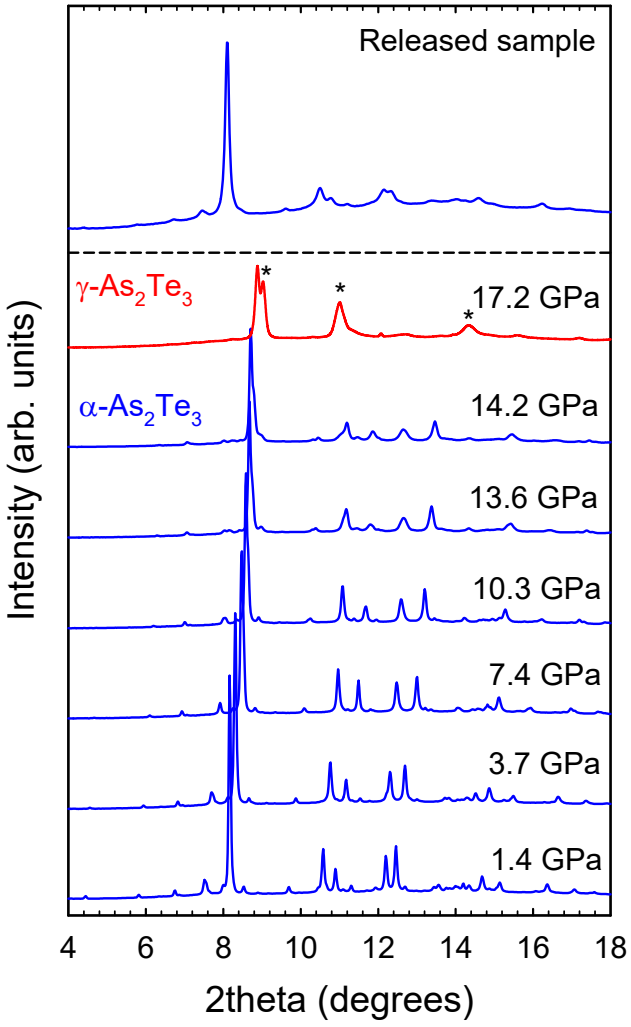

Figure 3. Powder HP-XRD patterns of α-As_2Te_3 at selected pressures up to 17.2 GPa where the sample transits to a α-As_2Te_3. Patterns are shifted in vertical for comparison.

derivative of the bulk modulus of: V_0=579(4) Å^3, B_0=24(3) GPa and B_0'=7.9(9), respectively. The volume at zero pressure, V_0, obtained from the BM-EoS fit is similar, but slightly different to the value measured outside the DAC. This is a common fact noted in many experimental works when XRD measurements outside the DAC are performed with commercial equipment by using the Kα1 and Kα2 lines of Cu, whereas HP-XRD patterns are measured using synchrotron radiation

[Errandonea 2014]. In any case, both results are comparable with those of literature [Carron 1963, Kanishcheva 1982, Stergiou 1985a, Zhao 2016, Zhang 2016]. On the other hand, our bulk modulus and pressure derivative under hydrostatic conditions are similar to those recently reported (B_0= 26 GPa, B_0'=9.0) under quasi-hydrostatic conditions [Zhao 2016], but different to those recently reported (B_0= 38.4 GPa, B_0'=4.0 fixed) under hydrostatic conditions [Zhang 2016]. In this respect, we must note that all these results are comparable since fixing B_0' leads to an increase of B_0. In fact, it seems to be unreliable to fix the bulk modulus pressure derivative to 4 in order to fit the volume vs pressure in highly compressible non-covalent compounds with a large cation LEP activity, as it has been observed for structurally-related sesquichalcogenides Sb_2S_3, Sb_2Se_3, and Bi_2S_3 characterized by bulk modulus pressure derivatives larger than 4 [Ibáñez 2016].

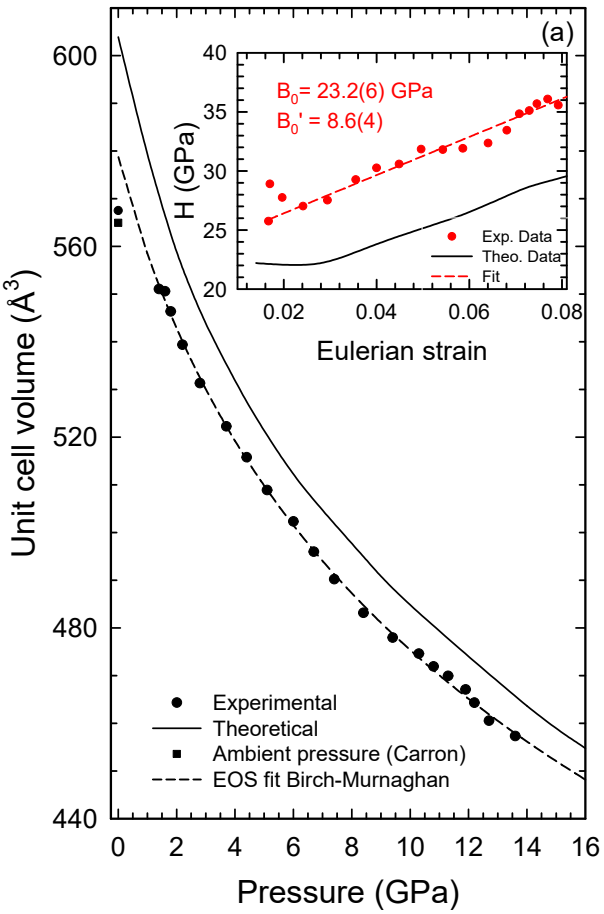

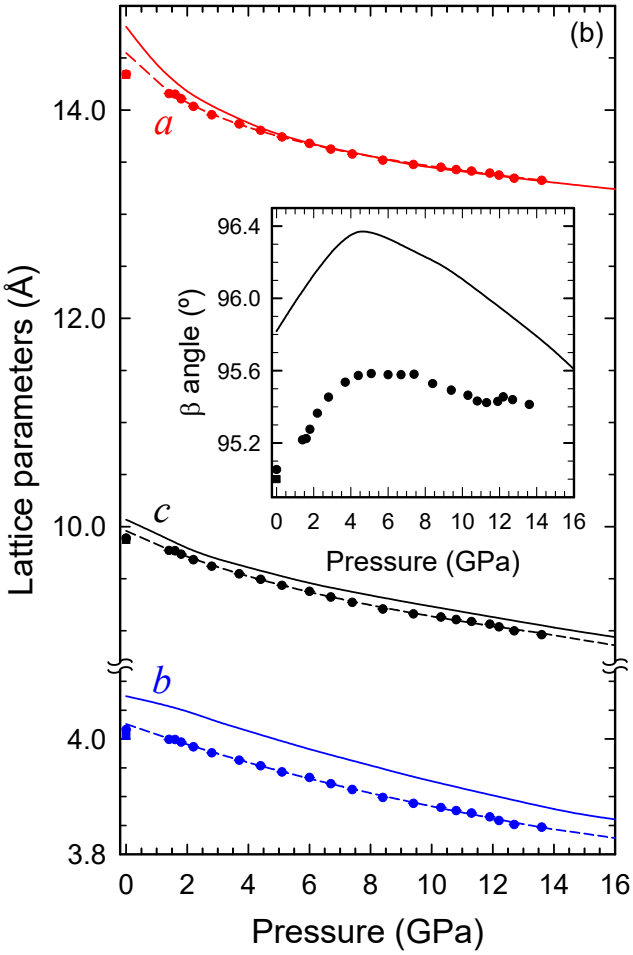

Figure 4. Experimental (symbols) and theoretical (solid lines) pressure dependence of the unit-cell volume **(a)** and lattice parameters **(b)** in α-As_2Te_3. Experimental data are fit to a BM-EoS (dashed lines) and compared to theoretical data. Inset of panel (a) shows the reduced pressure vs Eulerian strain plot for both experimental and theoretical data. Inset of panel (b) shows the pressure dependence of the monoclinic β angle. Squares correspond to data at ambient pressure taken from Brazhkin (2014).

It must be also stressed that our results from our experimental BM-EoS are in good agreement with our theoretical BM-EoS: V_0= 603.2(6) Å3, B_0= 19.7(3) GPa and B_0'=8.1(4). The theoretical bulk modulus is slightly smaller than the experimental one, which can be explained by the overestimation of the theoretical volume at zero pressure in the GGA-PBE approximation. As expected, our experimental and

theoretical values for the bulk modulus of the α phase are larger than those deduced for As_2Te_3 glass (~15 GPa) from ultrasonic measurements [Parthasarathy 1985]. However, it must be noted that our bulk moduli are much smaller than the value recently reported (42.7 GPa) from elastic constant calculations on the basis of GGA-PBE calculations [Deng 2015].

The lattice parameters of α-As_2Te_3 up to 16 GPa also show a monotonous and smooth decrease as pressure increases [**Fig. 4(b)**]. The nice agreement of the theoretical behavior of volume and lattice parameters with experimental results gives support to the absence of a first-order phase transition between 6 and 8 GPa at room temperature under hydrostatic conditions, unlike assumed in a previous work [Scheidemantel 2005] and in agreement with recent works [Zhao 2016, Zhang 2016]. Furthermore, the pressure dependence of our lattice parameters do not show evidence of anomalies in the region close to 13 GPa which could be indicative of any IPT as recently suggested [Zhang 2016]. In this regard, it is possible that the anomalous changes of correlated *a* and *c* parameters observed in literature [Zhang 2016] could be due to mistakes in the fit due to the mixture of the low and high-pressure phases coexisting above 13 GPa.

For completeness, the experimental and theoretical pressure dependence of the axial ratios of α-As_2Te_3 are shown in **Fig. S3** of the Supporting Information. As it can be observed, there is a monotonous behavior of the experimental *c/b* axial ratio, which is well reproduced by our calculations. On the other hand, the theoretical *a/b* and *a/c* axial ratios display a non-monotonic dependence showing changes in the region between 2 and 4 GPa. Our axial ratios are similar to those recently reported [Zhao 2016, Zhang 2016], but we have not observed the anomalies found at some pressures in these two last works. In some recent works, changes in the pressure dependence of the axial ratios of several group-15 sesquichalcogenides have been considered as a proof for the occurrence of a pressure-induced ETT [Efthimiopoulos 2014, Sorb 2016, Efthimiopoulos 2016]. Authors argue that a minimum of the *c/a* ratio was previously observed to be coincident with the occurrence of a pressure-induced ETT in α-Bi_2Se_3, α-Sb_2Te_3, and α-Bi_2Te_3 [Manjón 2013]. This fact has been put into question in recent works [Ibáñez 2016, Sans 2016c], because the minimum of the *a/c* ratio can be originated by a change in the ratio of interlayer/intralayer forces. Therefore, it cannot be taken for granted that this change should be necessarily translated into a change in the electronic density of states near the Fermi level.

The inset of **Fig. 4(b)** shows a change of the slope of the β monoclinic angle (always perpendicular to the *b*-axis) above 4 GPa. This result implies that in α-As_2Te_3 the direction of the *a*-axis changes with pressure; i.e., assuming that the directions of both *b* and *c* axis remain constant. The departure of β from 90º indicates that the direction of maximum compressibility at room pressure is not exactly that of the *a* axis; i.e., the main direction in which layers are piled up [see **Fig. 1**]. The change in the slope of the β angle together with the change of the compressibility of the *a* axis (correlated with a change in the *a/b* ratio) near 4-5 GPa has been interpreted in a recent work as a proof of the occurrence of a second-order IPT [Zhao 2016]. Similarly, changes of the β angle together with the changes in the electronic band structure near 3 and 6 GPa have been interpreted in a recent work as a proof of the

occurrence of two second-order IPTs [Zhang 2016]. In the following we will demonstrate that no pressure-induced IPT occurs in α-As_2Te_3 up to the first-order phase transition above 14 GPa; however, we will first analyze the compressibility tensor of our monoclinic material.

In order to evaluate the change in the direction of maximum compressibility as a function of pressure we have calculated and diagonalized the experimental and theoretical isothermal compressibility tensor, β_{ij}, at different pressures [details are given in the Supporting Information]. This tensor is a symmetric second rank tensor which relates the state of strain of a crystal to the change in pressure that induced it [Haussühl 2007], and it has been obtained with the finite Eulerian approximation as implemented in the Win_Strain package [Angel 2004-2011]. Diagonalization of the β_{ij} tensor at room pressure yields for our experiments the maximum, intermediate and minimum compressibilities $27.3(21)\cdot10^{-3}$, $14.0(11)\cdot10^{-3}$, and $4.7(4)\cdot10^{-3}$ GPa^{-1}, respectively; whereas for the case of our calculations the obtained values for the compressibilities are $38(3)\cdot10^{-3}$, $14.6(11)\cdot10^{-3}$, and $4.3(5)\cdot10^{-3}$ GPa^{-1}. As observed, the *a* axis is the most compressible one, the *b* axis is by far the less compressible axis, and the compressibility of the *c* axis is intermediate between that of the *a* and *b* axes. The experimental (theoretical) axial compressibilities indicate that around 59% (67%) of the total compression at room pressure is accommodated along the direction of maximum compressibility. The major compression direction at room pressure occurs in the (0 1 0) plane at the given angle Ψ [see **Tables S1** and **S2** in the Supporting Information] relative to the *c* axis (from *c* to *a*) or equivalently at an angle θ relative to the *a* axis (from *a* to *c*). In particular, the experimental major compression direction at room pressure is at θ=16.0(1.4)º from the *a* axis whereas our calculations predict that it is at 5.5(7)º from the *a* axis (see red arrow in **Fig. 1(b)**).

As regards the behavior of the compressibility tensor at HP, the evolution under pressure of the β_{xx} tensor coefficients (related to the axial compressibilities) are shown in **Fig. S4**. Note that the evolution of the experimental and theoretical compressibility tensors at HP is very similar. The most notable feature is that the experimental compressibility of the *a* axis is higher than that of the *c* axis ($\beta_{11}>\beta_{33}$) below 2.0 GPa; however, both compressibilities are similar at 2 GPa and $\beta_{11}<\beta_{33}$ beyond 3 GPa within experimental uncertainties. Moreover, the decrease of the compressibility of the *a* axis with increasing pressure is so large that the compressibilities of the *a* and *b* axes become equal around 13 GPa ($\beta_{11}=\beta_{22}$). These results imply that the *c* axis becomes more compressible than the *a* axis above 3 GPa. In this way, the direction of maximum compressibility moves away the *a* axis and approaches the *c* axis with increasing pressure; i.e., the θ angle increases. At 3 GPa the direction of maximum compressibility is closer to the *c* axis than to the *a* axis and at pressures beyond 5 GPa the direction of maximum compressibility is already very close to the *c* axis.

From the experimental and theoretical compressibility tensors at different pressures we can obtain the experimental and theoretical volume compressibility (trace of the tensor) at each pressure, which is plotted in **Fig. S5**. As observed, there is a

continuous evolution of the compressibility as a function of pressure so no one can infer the presence of any pressure-induced second-order IPT. This result contrasts with the pressure-induced second-order IPTs suggested in recent works [Zhao 2016, Zhang 2016]. In this respect, an IPT near 5 GPa on the basis of a change of the β angle, a change in the slope of the compressibility at HP, and a change in the reduced pressure vs the Eulerian strain (*F-f*) plot has been suggested [Zhao 2016]. We plot in the inset of **Fig. 4(a)** the *F-f* plot of our experiments and calculations. As observed, no change of the slope is observed when using the unit cell volume obtained from our fitted EoS. Therefore, our measurements and calculations do not support the existence of any IPT up to 14 GPa. In any case, we have to note that the results of the *F-f* plot are not completely reliable because they are very sensitive to errors in the volume at room pressure and the dispersion of data measured at HP, as already discussed regarding the structural behavior of α-Bi_2Se_3, a compound that shows a pressure-induced second-order phase transition [Vilaplana 2011b]. Further support to the absence of pressure-induced second-order IPTs in α-As_2Te_3 is provided below.

In order to better understand the HP behavior of the structural parameters in α-As_2Te_3 previously described, we have studied the experimental and theoretical pressure dependence of the *x* and *z* atomic parameters of the Wyckoff positions for the five non-equivalent As (As1 and As2) and Te (Te1, Te2 and Te3) atoms [see **Fig. S6**] and the main interatomic distances [see **Figs. S7 to S10**]. As can be seen in **Fig. S6**, all atomic parameters evolve in a monotonous way between ambient pressure and 14 GPa. This result means that all atomic positions are located at planes $b = 0$ and 1/2 ($y = 0$ or $y = 1/2$ atomic coordinate) at all pressures up to 14 GPa and that the changes of the atomic parameters do not show evidence for any phase transition up to 14 GPa. No increase or decrease of the symmetry of our theoretical atomic positions is observed in the whole pressure range studied unlike in the case of β-Bi_2O_3 where an increase of symmetry has been observed along the $\beta - \beta'$ IPT [Pereira 2014b]. Therefore, our theoretical calculations do not support the existence of any IPT in α-As_2Te_3.

Similarly, **Figures S7 to S10** show an overall monotonous decrease of the experimental and theoretical As-Te, As-As and Te-Te distances as pressure increases. In general, there is a good agreement between the behavior of experimental and theoretical interatomic distances. Note that the values of the refined distances are of the same order as those theoretically calculated, which indicates that the refinement is correct; however, errors in Rietveld refinement positions propagate when calculating interatomic distances, especially with increasing pressure, which accounts for the differences between experimental and theoretical data. Therefore, in the following the discussion of the evolution of interatomic distances with pressure is going to be based on the evolution of the theoretical distances, which have been calculated in the whole range of pressure from 1 atm to 14 GPa.

Regarding the coordination of As1 atoms in α-As_2Te_3, **Figure S7** shows that As1 is 5-fold (3+2) coordinated at room pressure if one considers all intralayer As-Te bonds; i.e., intrarod As-Te bonds below 3.0 Å and interrod bonds above 3.2 Å. At

pressures above 6 GPa, As1 atoms can be considered to become truly 5-fold coordinated (all intralayer As-Te bonds below 3.0 Å). On the other hand, As1 polyhedral units only tend towards a 5+2 coordination at pressures far from the stability range of the low-pressure phase if interlayer As1-Te1 distances (> 3.5 Å at 14 GPa) are considered. Regarding the coordination of As2 atoms, **Figure S8** shows that As2 is 6-fold coordinated at room pressure and all six As2-Te distances tend to similar values above 6-7 GPa, thus indicating a regularization of the distorted As2 octahedron on increasing pressure. Finally, **Figures S9 and S10** show that intralayer and interlayer As-As and Te-Te distances show different behaviors under pressure. Intralayer distances show a small compression, while interlayer distances show a large contraction up to around 3-4 GPa and a considerable saturation above this pressure range. **Figures S7 to S10** allow us to understand the different compressibilities of *a*, *b* and *c* axes at HP. At room pressure, the *a* axis is considerably more compressible than *b* and *c* axes at room pressure, as it was expected from the strong initial compression of the weak van der Waals forces present in the space between adjacent layers that are piled up mainly along the *a* axis [**Fig. 1(a)**]. This strong compression of the *a* axis below 3 GPa is related to the strong compressibility of interlayer Te-Te distances in this pressure range. On the contrary, the *b* axis is the less compressible axis at any pressure because of strong intralayer As-Te covalent bonds (< 3.0 Å) which extend along the *b* axis. Finally, the compressibility of the *c* axis is intermediate between that of the *a* and *b* axes because of the presence of long As1-Te2 distances (> 3.2 Å) at room pressure. On the other hand, interlayer Te-Te distances at pressures above 3-4 GPa decrease at a similar rate as intralayer Te-Te distances with the exception of Te2-Te2 distances which extend mainly along the *c* axis. This result evidences the hardening of interlayer bonds and explains why the *a* axis is no more the most compressible axis above this pressure range and why the most compressible axis approaches the *c* axis as pressure increases as evidenced from the analysis of the compressibility tensor.

To finish this section regarding the structural properties of α-As_2Te_3, it is interesting to compare the structure of α-As_2Te_3 and its pressure behavior with that of other group-15 sesquichalcogenides. This family of compounds crystallize in a number of distorted crystalline structures due to the activity of the cation LEP, which increases in the series Bi-Sb-As [Walsh 2011]. Therefore, the study of the behavior of the As LEP in α-As_2Te_3 at HP is crucial in order to understand the properties of this compound and other group-15 sesquichalcogenides under compression. **Figures S11(a) and S12(a)** in the Supporting Information show the decrease of the volume of the different Te polyhedra around As1 and As2 atoms, respectively. As observed, a good agreement is obtained between experiment and theoretically simulated evolution of these polyhedral units. The decrease of the distortion index [**Figs. S11(b) and S12(b)**] shows that these polyhedra become more regular with increasing pressure and evidences a decrease of the As LEP activity with increasing pressure, in good agreement with previous results in a number of Sb- and Bi-related materials [Efthimiopoulos 2014, Ibáñez 2016, Pereira 2014b, Lundegaard 2003, Lundegaard 2005]. A comparison of the structure of α-As_2Te_3 with that of α-Sb_2Te_3, α-Bi_2Te_3 and orthorhombic Sb_2Se_3 (isostructural to Sb_2S_3 and Bi_2S_3) and their pressure dependences is provided in the Supporting Information taking into account

the cation LEP activity. We can conclude that the structure of α-As_2Te_3 and its pressure behavior can be understood as intermediate between that of α-Sb_2Te_3 and Sb_2Se_3 in good agreement with what is expected from the activity of cation LEP in group-15 sesquichalcogenides. In this way, the non-observation of a pressure-induced second-order IPT in α-As_2Te_3 is consistent with the fact that no IPT has also been found in Sb_2Se_3 [Efthimiopoulos 2013], Bi_2S_3 [Efthimiopoulos 2014], or Sb_2S_3 [Ibáñez 2016] with a similar zigzag layered structure. We speculate that the reason for the lack of pressure-induced IPTs in these compounds is due to the large structural flexibility of orthorhombic and monoclinic structures. These structures have many free atomic parameters able to accommodate changes in the cation LEP activity due to pressure, unlike cubic, tetragonal, and rhombohedral structures of α-Sb_2O_3, β-Bi_2O_3 and α-Sb_2Te_3, respectively, which already show pressure-induced second-order IPTs [Pereira 2014b, Pereira 2012, Zhao 2015b].

In summary, the effect of pressure in the structure of α-As_2Te_3 is a progressive contraction of the interlayer space and a slight rotation of polyhedral units (see the main difference between the structure of α-As_2Te_3 at 1 atm and 14 GPa in **Fig. 1(b)**). This leads to an increase of the average coordination of As ions and to a decrease of the distortion of the polyhedral units around As ions (due to the decrease of the cation LEP), but without modifying the *y* parameter of the initial Wyckoff sites of the five non-equivalent atoms of the unit cell. No evidence for a pressure-induced IPT has been found in α-As_2Te_3.

HP-RS measurements

As already discussed, HP-XRD measurements at room temperature under quasi-hydrostatic conditions show no phase transition to the β phase either above 8 or above 14 GPa, unlike expected from previous results [Scheidemantel 2005]. In order to clarify the stability of both α-As_2Te_3 and β-As_2Te_3 phases, we have performed *ab initio* calculations of the enthalpy vs pressure for both phases [**Fig. S13** in the Supporting Information]. Unlike previous calculations [Zhao 2016], our calculations suggest that the α-to-β phase transition in As_2Te_3 could occur at relatively small pressures (>1 GPa). This means that perhaps, the α-to-β phase transition in As_2Te_3 is hindered at room temperature and at quasi-hydrostatic conditions by a high kinetic energy barrier. Therefore, some additional thermal energy is needed in order to overcome this energy barrier. This result is in agreement with experiments reporting the existence of β-As_2Te_3 at relatively low pressures and high temperatures [Yakushev 1986, Kirkinskii 1974, Shu 1986, Toscani 1991]. In this regard, a possible transition above 6 GPa as previously suggested from thermopower measurements [Scheidemantel 2005] and expected from extrapolation of experimental HP/HT data at relatively low pressures [Yakushev 1986, Kirkinskii 1974], could correspond to the non-hydrostatic conditions in Scheidemantel (2005) or to thermal activation at HP derived from the increase in temperature inherent to thermo-power measurements. Additionally, it can be observed from **Fig. S13** that the enthalpy of the β phase is higher than that of the α phase above 15 GPa; therefore, our calculations show that the β phase is not a competitive phase at very

HP as it was previously assumed. This may explain why we have observed a new phase above 14 GPa different to that of the β phase in good agreement with two recent works [Zhao 2016, Zhang 2016].

In order to study the possible effect of hydrostaticity on the appearance of the α-to-β phase transition we have conducted HP-RS measurements at both hydrostatic and non-hydrostatic conditions, which have been compared to lattice-dynamical calculations in order to better understand the HP behavior of α-As_2Te_3. **Figure 5** shows room-temperature RS spectra of α-As_2Te_3 at selected pressures under hydrostatic conditions up to 12 GPa. It can be observed that RS spectra clearly correspond to α-As_2Te_3 in this pressure range.

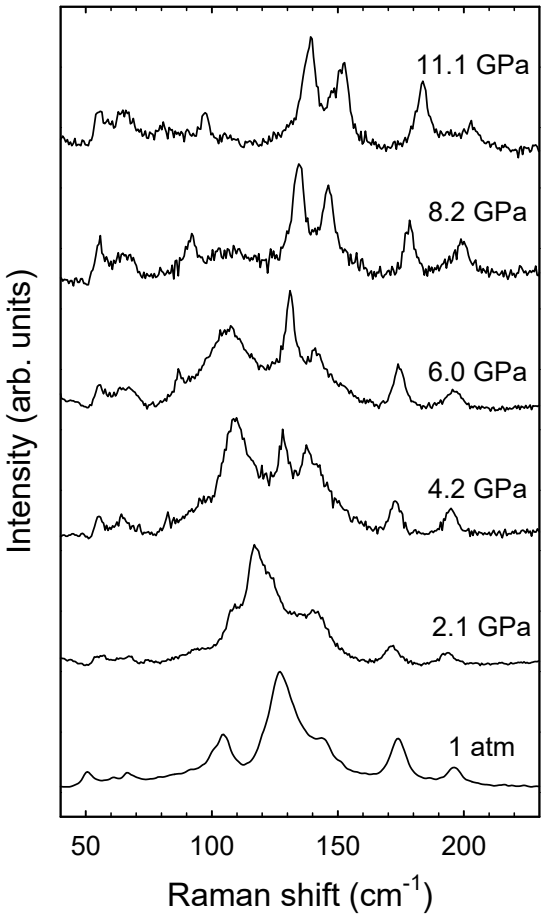

Figure 5. Room-temperature Raman scattering spectra of α-As_2Te_3 at selected pressures.

As already mentioned, it is very difficult to assign the features that show up in the room-pressure RS spectrum of α-As_2Te_3. However, it is possible to perform a tentative peak assignment by studying the behavior of the Raman-active peaks at HP in combination with the results of lattice-dynamical calculations. **Figure 6** shows the pressure dependence of the experimental and theoretical Raman-active mode frequencies of α-As_2Te_3 measured up to 12 GPa under hydrostatic conditions.

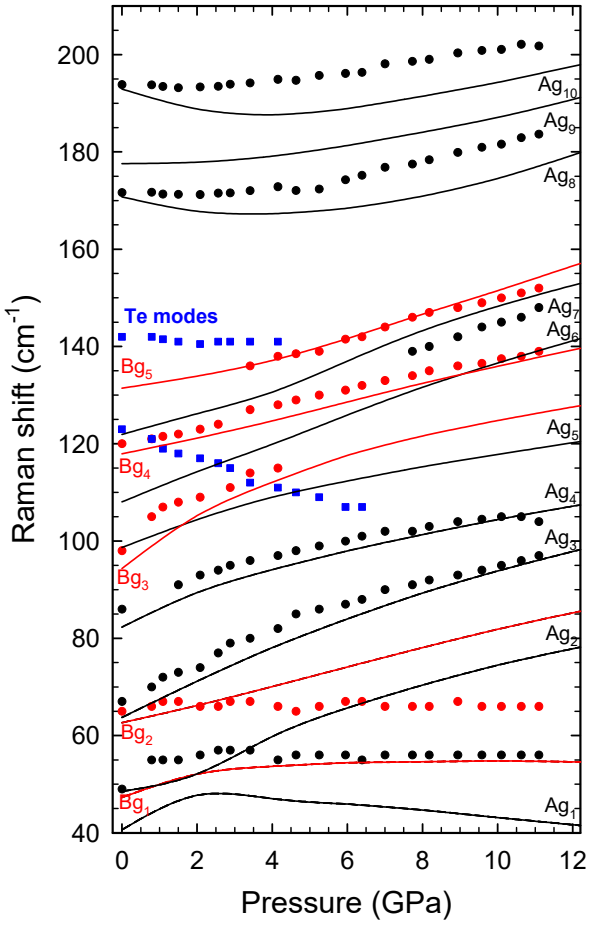

Figure 6. Experimental (symbols) and theoretical (lines) pressure dependence of the Raman-mode frequencies of α-As_2Te_3. Different colors represent Raman-active modes of different symmetries. Blue squares represent the modes corresponding to crystalline Te.

In general, theoretical frequencies of Raman-active modes do not show a simple monotonic behavior with increasing pressure. In fact, they show a complex behavior

with crossings and anticrossings of modes with different and equal symmetries, respectively. This complex behavior is caused by the presence of 15 Raman-active modes in a small region between 50 and 200 cm^{-1} similar to that found in orthorhombic Sb_2S_3, Sb_2Se_3 and Bi_2S_3 [Ibáñez 2016]. Apart from crossings and anticrossings already observed in related orthorhombic compounds Sb_2S_3, Sb_2Se_3 and Bi_2S_3 [Ibáñez 2016], small changes in the pressure coefficient of some theoretical Raman-active modes have been observed in the range between 2 and 4 GPa in α-As_2Te_3. They could be attributed to the strong changes observed in the interatomic distances around these pressures as already commented in the previous section.

Despite the complex behavior observed in theoretical Raman-active modes, several experimental modes are found to show a behavior consistent with the theoretical ones. In particular, the two high-frequency theoretical Raman modes above 160 cm^{-1} show small negative pressure coefficients at room pressure in rather good agreement with the almost negligible pressure coefficient of our two highest-frequency modes. These small negative or even negligible pressure coefficients are consistent with the small or even negligible increase of the shorter intralayer As1-Te distances [**Fig. S7**] at low pressures. Therefore, tentative assignments of the experimental Raman-active modes of α-As_2Te_3 reported in **Fig. 6** have been made by comparing the experimental and theoretical values of frequencies and pressure coefficients. The tentative assignments are summarized in **Table 2**.

As observed in **Fig. 6**, we have additionally observed two experimental Raman modes in the range from 120 to 145 cm^{-1} (see blue symbols in **Fig. 6**) whose frequency decreases with increasing pressure. The frequencies of these two modes are close to those previously reported for crystalline Te [Pine 1971], as already mentioned. Furthermore, the negative pressure coefficients shown by these two modes is in agreement with those reported for crystalline Te [Lundegaard 2005, Pereira 2012, Richter 1973, Aoki, 1980]. Consequently, we have attributed the modes near 120 cm^{-1} and near 140 cm^{-1} to the A_1 and E″ (marked with an asterisk in **Fig. 2(b)**) modes of crystalline Te. In this regard, we have to note that Raman-active modes associated to Te have been already observed in non-stoichiometic samples of Bi_2Te_3 nanowires and were assigned to Te clusters in Te-rich regions in nanowires [Rodríguez-Fernández 2016]. Furthermore, segregation of Se nanoclusters caused by laser-induced damage during HP-RS measurements has also been observed in several chalcogenides [Lindberg 2013, Vilaplana 2013]. In our experiments, it is highly difficult to avoid such damage when performing experimental RS measurements, at least with the red He:Ne laser. These modes are no longer observed at pressures beyond 4-5 GPa likely because of the improvement in the thermal conductivity inside the DAC with increasing pressure in part due to the metallization of α-As_2Te_3 as will be commented in the next section.

Room-temperature HP-RS spectra and the pressure dependence of the Raman-active modes under non-hydrostatic conditions (without pressure transmitting medium) are shown in **Figs. S14 and S15** in the Supporting Information, respectively. As observed, no phase transition near 6-8 GPa is observed either under hydrostatic or under non-hydrostatic conditions, thus supporting the hypothesis that thermal

activation at HP is needed in order to force the α-to-β phase transition in α-As_2Te_3 at relatively low pressures [Yakushev 1986, Kirkinskii 1974].

In order to check if there could be any pressure-induced second-order IPT in α-As_2Te_3, we have also studied the phonon dispersion curves theoretically calculated at different pressures up to 14 GPa [see **Fig. S16** in the Supporting Information] since second-order IPTs must be related to the presence of a soft phonon mode according to Landau theory. As observed, there is no soft mode along the whole BZ at any pressure either in the range from 3 to 5 GPa or in the range from 6 to 13 GPa, unlike in β-Bi_2O_3 [Pereira 2014b]. Therefore, we can safely conclude that there is no pressure-induced IPT in α-As_2Te_3 up to 14 GPa, unlike recently reported [Zhao 2016, Zhang 2016].

Finally, we must mention that in order to check if there could be a possible occurrence of a pressure-induced ETT in α-As_2Te_3, we have also studied the pressure dependence of the linewidth for the most intense Raman-active modes in both HP-RS experiments under hydrostatic and non-hydrostatic conditions. We have found no major change on increasing pressure that could be indicative of a pressure-induced ETT in this compound. Only a small increase of the RS background is observed above 4 GPa which could be indicative of the progressive metallization of the material above this pressure as will be discussed in the next section.

Electronic band structure calculations

Taking into account that ETTs are very subtle transitions (they are $2^{1/2}$ transitions in Ehrenfest notation) whose occurrence could be difficult to evidence by XRD or RS measurements, we have performed *ab initio* band-structure calculations in α-As_2Te_3 at HP in order to identify possible changes of the band extrema that could be related to a pressure-induced ETT. We show in **Fig. 7** the electronic band structure at different pressures. As can be seen, the electronic structure at 0 GPa exhibits an indirect bandgap (theoretical value around 0.7 eV) with the conduction band minimum (CBM) located close to the L point of the BZ and three almost degenerate valence band maxima (VBM) located in different directions close to the A point of the BZ. This result is in good agreement with recent calculations [Zhao 2016], but in disagreement with other ones [Zhang 2016, Deng 2015]. In any case, all reported theoretical DFT results for α-As_2Te_3 at 0 GPa underestimate the experimental bandgap value at room pressure, which is estimated to be experimentally between 0.82 and 0.92 eV [Popescu 2000, Fayek 2007].

The indirect bandgap progressively closes at HP in good agreement with recent results [Zhao 2016, Zhang 2016]. Around 1 GPa, our calculations show that the bandgap remains indirect with a value above 0.4 eV and that the CBM changes from the L point to the V point. No major changes occur in the electronic band structure above this pressure. Our calculations indicate that the indirect bandgap of α-As_2Te_3 closes completely around 4 GPa undergoing a pressure-induced trivial semiconductor-metal transition and no other major change occurs at higher pressures.

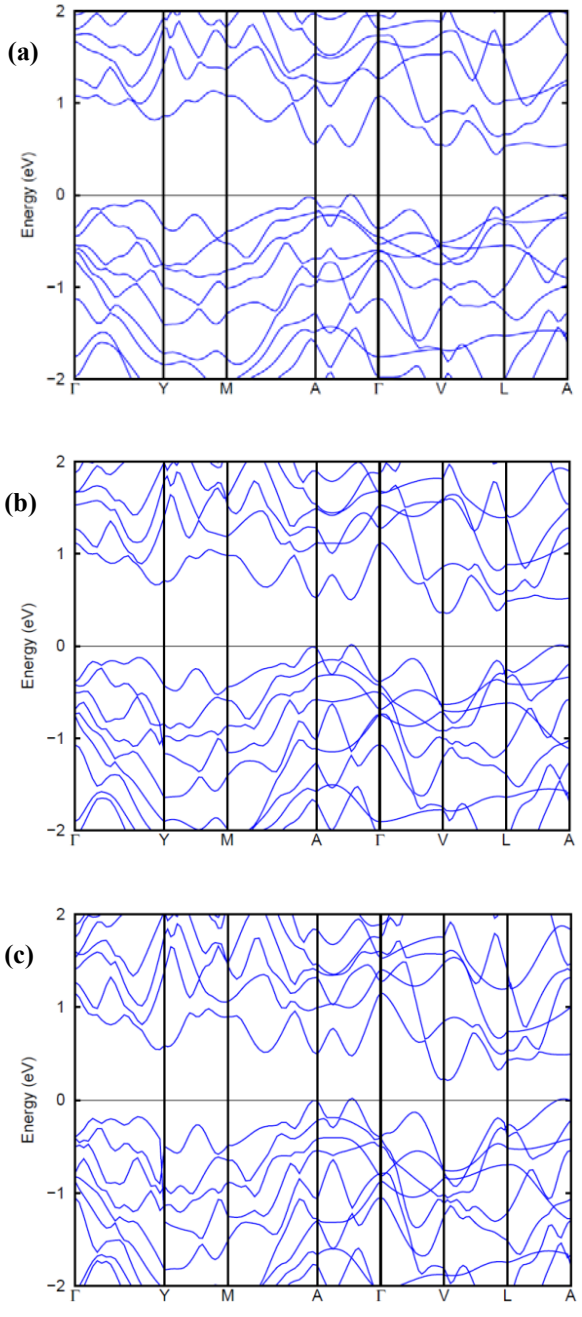
(a)
(b)
(c)
Energy (eV)
2
1
0
−1
−2
Γ
Y
M
A
Γ
V
L
A

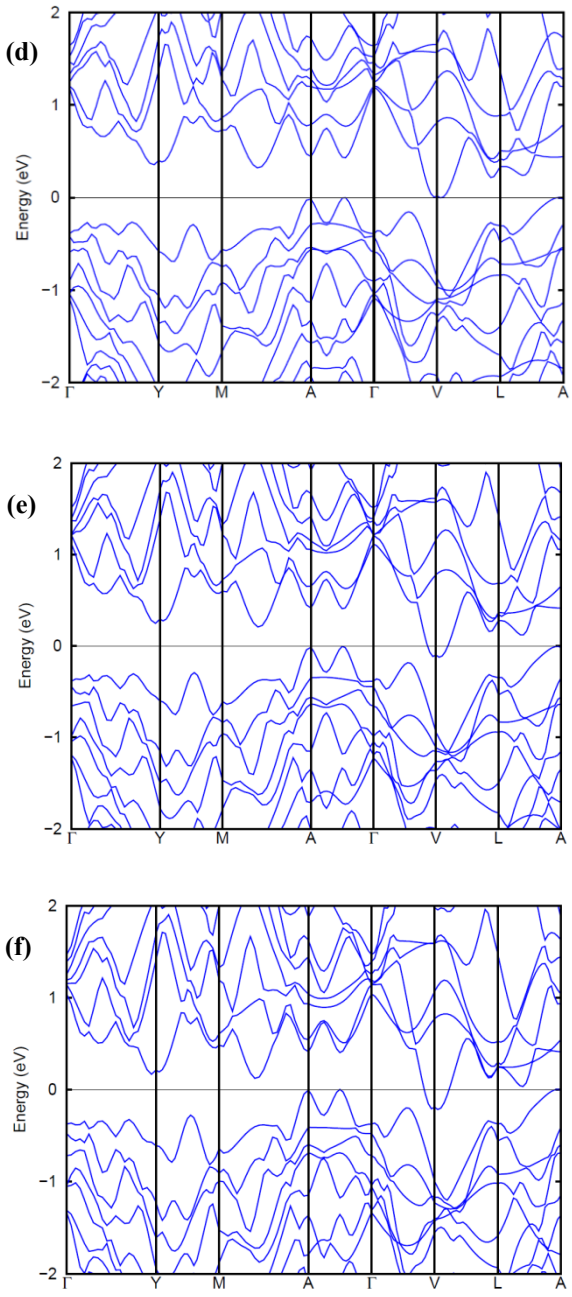

Figure 7. Calculated band structure of α-As_2Te_3 at different pressures: **(a)** 0 GPa, **(b)** 1 GPa, **(c)** 2 GPa, **(d)** 4 GPa, **(e)** 6 GPa, and **(f)** 8 GPa.

Therefore, due to the underestimation of the theoretical bandgap in DFT calculations, it is reasonable to assume that the actual closing of the bandgap takes place at a slightly larger pressure (around 6-7 GPa). This closing could explain the anomalies observed in thermopower measurements in this pressure range [Scheidemantel 2005] and is in good agreement with the recent electric measurements and theoretical calculations of a recent report [Zhao 2016]. However, our results are in disagreement with another recent report that suggests two indirect-to-direct crossovers that have been incorrectly interpreted as IPTs [Zhang 2016] and whose calculations do not allow us to explain the electrical results recently obtained [Zhao 2016].

In summary, our theoretical electronic band structure calculations show that α-As_2Te_3 is a semiconductor with an indirect bandgap above 0.7 eV at room pressure, whose energy decreases with increasing pressure until it becomes a semimetal above 4-6 GPa. Only a change in the location of the CBM in the BZ is observed around 1 GPa which could lead to a pressure-induced ETT; however, the bandgap at this pressure is too high (probably above 0.5 eV) to result in a strong modification of the electronic density of states near the Fermi level. Therefore, we conclude that there is no evidence for a pressure-induced ETT in α-As_2Te_3 and that the changes in the resistance of α-As_2Te_3 measured by Scheidemantel *et al*. (2005) between 1 and 2 GPa and above 6 GPa match with the changes in the electronic band structure here reported. However, on the light of the present results and the discrepancies observed among the different calculations, we must say that more precise calculations including SOI should be performed to shed further light on the pressure dependence of the electronic band structure of α-As_2Te_3.

V. CONCLUSIONS

We have studied the structural, vibrational, and electronic properties of α-As_2Te_3 at room temperature and high pressure. We have observed that there is a stronger interlayer compressibility in α-As_2Te_3 than in α-Sb_2Te_3 and α-Bi_2Te_3, which can be explained due to the larger lone electron pair effect of As than Sb and Bi. In fact, we have shown that the structure of α-As_2Te_3 can be understood as an intermediate structure between that of Sb_2Se_3 and α-Sb_2Te_3. Strong changes in the monoclinic β angle and in the axial compressibilities are observed in the region between 2 and 4 GPa, which are related to the strengthening of the interlayer van der Waals bonds in this pressure range. This feature was demonstrated by the change of the direction of the maximum compressibility given by the analysis of the compressibility tensor. Furthermore, we have observed that polyhedral units around As cations in α-As_2Te_3 become more regular with increasing pressure and show a small rotation in order to accommodate pressure in a clear tendency to increase the coordination with increasing pressure of both non-equivalent As atoms. Our *ab initio* theoretical simulations predict that the β phase, where As atoms are in true 6-fold coordination, is thermodynamically more stable than the α phase above 1 GPa. However, no phase transition to the β phase has been observed at ambient temperature even above 17 GPa; however, a phase transition to the γ phase has been observed. The lack of

observation of the phase transition from α-As_2Te_3 to β-As_2Te_3 at ambient temperature is likely because it is a highly reconstructive first-order phase transition, which can be frustrated due to the presence of a high kinetic energy barrier and lately hidden by the phase transition towards a γ polymorph.

Our Raman scattering measurements and lattice dynamics calculations support the stability of the α phase up to 12 GPa and show small changes in the region between 2 and 4 GPa, consistent with the progressive changes of the interatomic distances with increasing pressure. Phonon dispersion curves at different pressures do not show any soft mode that evidences a pressure-induced second-order IPT. Additionally, changes in the RS spectrum, which could be indicative of a pressure-induced ETT, have not been observed. This result is in agreement with theoretical calculations of the electronic band structure, which show that α-As_2Te_3 is an indirect semiconductor with a bandgap above 0.7 eV that shows a change of the conduction band minimum close to 1 GPa. A closing of the indirect bandgap occurs with increasing pressure, which suggests an experimental semiconductor-to-metal transition above 6 GPa.

Supporting information

Supporting Information provides an analysis of the vibrational properties of α-As_2Te_3 at ambient pressure and at high pressure under non-hydrostatic conditions. Besides, details of the structural evolution of compressed α-As_2Te_3, showing the evolution of the theoretical and experimental Wyckoff free coordinates, the interatomic distances and the polyhedral distortion under pressure is provided. On the other hand, an extensive description of the experimental and theoretical isothermal compressibility tensor together with all the information extracted from it and the evolution of the calculated enthalpy of the α and β polymorph of As_2Te_3 vs pressure is given. This material is available free of charge via the Internet at http://pubs.acs.org.

Acknowledgments

This work has been performed under financial support from projects MAT2013-46649-C4-2-P, MAT2013-46649-C4-3-P, MAT2015-71070-REDC, FIS2013-48286-C2-1-P, and FIS2013-48286-C2-2-P of the Spanish Ministry of Economy and Competitiveness (MINECO), and to the Department of Education, Universities and Research of the Basque Government and UPV/EHU (Grant No. IT756-13). This publication is also fruit of "Programa de Valoración y Recursos Conjuntos de I+D+i VLC/CAMPUS" and has been financed by the Spanish Ministerio de Educación, Cultura y Deporte as part of "Programa Campus de Excelencia Internacional" through projects SP20140701 and SP20140871. Finally, authors thank ALBA Light Source for beam allocation at beamline MSPD.

References

[Aggarwal 2002] I. D. Aggarwal and J. S. Sanghera. Development and Applications of Chalcogenide Glass Optical Fibers at nrl. *J. Optoelectron. Adv. Mater.* **2002**, *4*, 665-678.

[Alekberov 2014] R. I. Alekberov, S. I. Mekhtiyeva, G. A. Isayeva, and A. I. Isayev. Raman Scattering in As-Se-S and As-Se-Te Chalcogenide Vitreous Semiconductors. *Semiconductors.* **2014**, *48*, 800-803.

[Angel 2004-2011] R. J. Angel. http://www.rossangel.com/text_strain.htm

[Aoki, 1980] K. Aoki, O. Shimomura, S. Minomura, N. Koshizuka, and T. Tsushima. Raman Scattering of Trigonal Se and Te at Very High Pressure. *J. Phys. Soc. Jpn.* **1980**, *48*, 906-911.

[Birch 1938] F. Birch. The Effect of Pressure Upon the Elastic Parameters of Isotropic Solids, According to Murnaghan's Theory of Finite Strain. *J. Appl. Phys.* **1938**, *9*, 279-288.

[Blöchl 1994] P.E. Blöchl. Projector Augmented-Wave Method. *Phys. Rev. B: Condens. Matter Mater. Phys.* **1994**, *50*, 17953−17979;

[Brazhkin 2014] V. V. Brazhkin, and A. I. Orlov. High-Pressure Thermoelectric Characteristics of Bi_2Te_3 Semiconductor with Different Charge Carrier Densities. *JETP Lett.* **2014**, *99*, 283-285.

[Canepa 2011] P. Canepa, R. M. Hanson, P. Ugliengo, and M. Alfredsson. J-ICE: a New Jmol Interface for Handling and Visualizing Crystallographic and Electronic Properties. *J. Appl. Crystallogr.* **2011**, *44*, 225-229.

[Carron 1963] G. J. Carron. The Crystal Structure and Powder Data for Arsenic Telluride. *Acta Crystallogr.* **1963**, *16*, 338-343.

[Chen 2009] Y. L. Chen, J. G. Analytis, J-H. Chu, Z. K. Liu, S-K. Mo, X-L. Qi, H. J. Zhang, D. H. Lu, X. Dai, Z. Fang, et al. Experimental Realization of a Three-Dimensional Topological Insulator, Bi_2Te_3. *Science* **2009**, *325*, 178-181.

[Deng 2015] H. Deng. Theoretical Prediction of the Structural, Electronic, Mechanical and Thermodynamic Properties of the Binary α-As_2Te_3 and β-As_2Te_3. *J. Alloys Compd.* **2015**, *656*, 695-701.

[Dewaele 2004] A. Dewaele, P. Loubeyre, and M. Mezouar. Equations of State of Six Metals above 94 GPa. *Phys. Rev. B* **2004**, *70*, 094112.

[Efthimiopoulos 2013] I. Efthimiopoulos, J. M. Zhang, M. Kucway, C. Park, R. C. Ewing, and Y. Wang. Sb_2Se_3 under Pressure. *Sci. Rep.* **2013**, *3*, 2665.

[Efthimiopoulos 2014] I. Efthimiopoulos, J. Kemichick, X. Zhou, S. V. Khare, D. Ikuta, and Y. Wang. High-Pressure Studies of Bi_2S_3. *J. Phys. Chem. A* **2014**, *118*, 1713-1720.

[Efthimiopoulos 2016] I. Efthimiopoulos, C. Buchan, and Y. Wang. Structural Properties of Sb_2S_3 under Pressure: Evidence of an Electronic Topological Transition. *Sci. Rep.* **2016**, *6*, 24246.

[Errandonea 2014] D. Errandonea, C. Popescu, S. N. Achary, A. K. Tyagi, and M. Bettinelli. In situ High-Pressure Synchrotron X-ray Diffraction Study of the Structural Stability in NdVO4 and LaVO4. *Mater. Res. Bull*. **2014**, *50*, 279-284.

[Fauth 2013] F. Fauth, I. Peral, C. Popescu, and M. Knapp. The New Material Science Powder Diffraction Beamline at ALBA Synchrotron. *Powder Diffr.* **2013**, *28*, S360−S370.

[Fayek 2007] S. A. Fayek, M. R. Balboul, and K. H. Marzouk. Optical, Electrical and Thermal Studies on $(As_2Se_3)_{3-x}(As_2Te_3)_x$ Glasses. *Thin Solid Films.* **2007**, *515*, 7281-7285.

[Hammersley 1996] A. P. Hammersley, S. O. Svensson, M. Hanfland, A. N. Fitch, and D. Hausermann. Two-Dimensional Detector Software: From Real Detector to Idealised Image or Two-Theta Scan. *High Pressure Res.* **1996**, *14*, 235−248.

[Haussühl 2007] S. Haussühl. *Physical Properties of Crystals. An Introduction*. (Wiley-VCH, Weinheim, **2007**).

[Hohenberg 1964] P. Hohenberg and W. Kohn. Inhomogeneous Electron Gas. *Phys. Rev.* **1964**, *136*, B864-B871.

[Hoshino 1996] H. Hoshino, T. Miyanaga, H. Ikemoto, S. Hosoyawas, and H. Endo. The Semiconductor-Metal Transition of Liquid Arsenic-Selenium Mixtures at High Temperatures and High Pressures. *J. Non-Cryst. Solids.* **1996**, *205-207*, 43-47.

[Hsieh 2009] D. Hsieh, Y. Xia, D. Qian, L. Wray, F. Meier, J. H. Dil, J. Osterwalder, L. Patthey, A. V. Fedorov, H Lin, et al. Observation of Time-Reversal-Protected Single-Dirac-Cone Topological-Insulator State in Bi_2Te_3 and Sb_2Te_3. *Phys. Rev. Lett.* **2009**, *103*, 146401.

[Hwang 2001] H.Y. Hwang, G. Lenz, M.E. Lines, and R.E. Slusher. US Patent No 6.208.792 (**2001**).

[Ibáñez 2016] J. Ibáñez, J. A. Sans, C. Popescu, J. López-Vidrier, J. J. Elvira-Betanzos, V. P. Cuenca-Gotor, O. Gomis, F. J. Manjón, P. Rodríguez-Hernández, and A. Muñoz. Structural, Vibrational, and Electronic Study of Sb_2S_3 at High Pressure. *J. Phys. Chem. C* **2016**, *120*, 10547.

[Kanishcheva 1982] A. S. Kanishcheva, Y. N. Milhailov, and A. P. Chernov. Refinement of the Crystal Structure of Arsenic Telluride As_2Te_3. *Inorg. Mater.* **1982**, *18*, 796-799.

[Kirkinskii 1974] V. A. Kirkinskii and V. G. Yakushev. The System As-Te at high Pressures. *Izves. Akad. Nauk SSSR, Neorg. Mat.* **1974**, *10*, 1431-1435; idem, *Inorg. Mater.* **1974**, *10*, 1230-1233.

[Kirshenbaum 2013] K. Kirshenbaum, P. S. Syers, A. P. Hope, N. P. Butch, J. R. Jeffries, S. T. Weir, J. J. Hamlin, M. B. Maple, Y. K. Vohra, and J. Paglione. Pressure-Induced Unconventional Superconducting Phase in the Topological Insulator Bi_2Se_3. *Phys. Rev. Lett.* **2013**, *111*, 087001.

[Klotz 2009] S. Klotz, J-C. Chervin, P. Munsch, and G. Le Marchand. Hydrostatic Limits of 11 Pressure Transmitting Media. *J. Phys. D: Appl. Phys.* **2009**, *42*, 075413.

[Kong 2014] P. P. Kong, F. Sun, L. Y. Xing, J. Zhu, S. J. Zhang, W. M. Li, Q. Q. Liu, X. C. Wang, S. M. Feng, and X. H. Yu. Superconductivity in Strong Spin Orbital Coupling Compound Sb_2Se_3. *Sci. Rep.* **2014**, *4*, 6679.

[Kovanda 2003] V. Kovanda, M. Vicek, and H. J. Jain. Structure of As–Se and As–P–Se Glasses Studied by Raman Spectroscopy. *J. Non-Cryst. Solids.* **2003**, *326-327*, 88-92.

[Kresse 1993] G. Kresse and J. Hafner. Ab Initio Molecular Dynamics for Liquid Metals. *Phys. Rev. B: Condens. Matter Mater. Phys.* **1993**, *47*, 558−561.

[Kresse 1996a] G. Kresse and J. Furthmüller. Efficiency of ab-initio Total Energy Calculations for Metals and Semiconductors Using a Plane-wave Basis Set. *Comput. Mat. Sci.* **1996**, *6*, 15-50.

[Kresse 1996b] . Kresse and J. Furthmüller. Efficient Iterative Schemes for ab initio Total-energy Calculations Using a Plane-wave Basis Set. *Phys. Rev. B: Condens. Matter Mater. Phys.* **1996**, *54*, 11169-11186.

[Kresse 1999] G. Kresse and D. Joubert. From Ultrasoft Pseudopotentials to the Projector Augmented-wave Method. *Phys. Rev. B: Condens. Matter Mater. Phys.* **1999**, *59*, 1758-1775.

[Kristofik 1985] J. Kristofik, J. J. Mares, and V. Smid. The Effect of Pressure on Conductivity and Permittivity of As_2Te_3-Based Glasses. *Phys. Stat. Sol. A.* **1985**, *89*, 333-345.

[Kroumova 2003] E. Kroumova, M. I. Aroyo, J. M. Pérez-Mato, A. Kirov, C. Capillas, S. Ivantchev, and H. Wondratschek. Bilbao Crystallographic Server: Useful Databases and Tools for Phase-Transition Studies. *Phase Transitions* **2003**, *76*, 155-170.

[Larson 2004] A. C. Larson and R. B. von Dreele. General Structure Analysis System (GSAS). *LANL Report*. **2004**, *86*, 748.

[Lindberg 2013] G. P. Lindberg, R. E. Tallman, R. Lauck, M. Cardona, X. Liu, J. K. Furdyna, and B. A. Weinstein. Effects of Pressure on Photo-Induced Formation of Se and Te Clusters in II–VI Compounds. *Phys. Status Solidi B.* **2013**, *250*, 711− 715.

[Liu 2013] G. T. Liu, L. Zhu, Y. M. Ma, C. L. Lin, and J. Liu. Stabilization of 9/10-Fold Structure in Bismuth Selenide at High Pressures. *J. Phys. Chem. C* **2013**, *117*, 10045-10050.

[Lukic 2003] S. R. Lukic, D. M. Petrovic, S. J. Skuban, Lj. Radonjic, and Z. Cvejic. Formation of Complex Structural Units and Structure of As-S-Se-Te-I Glasses. *J. Opt. Adv. Mater.* **2003**, *5*, 1223-12229.

[Lundegaard 2003] L. F. Lundegaard, R. Miletich, T. Balic-Zunic, and E. Makovicky. Equation of State and Crystal Structure of Sb_2S_3 between 0 and 10 GPa. *Phys. Chem. Minerals.* **2003**, *30*, 463-468.

[Lundegaard 2005] L. F. Lundegaard, E. E. Makovicky, T. Boffa-Ballaran, and T. Balic-Zunic. Crystal Structure and Cation Lone Electron Pair Activity of Bi_2S_3 between 0 and 10 GPa. *Phys. Chem. Minerals.* **2005**, *32*, 578-584.

[Madan 1988] A. Madan, and M. P. Show. *The Physics and Application of Amorphous Semiconductors*. (Academic Press: Boston-San Diego, **1988**).

[Manjón 2013] F. J. Manjón, R. Vilaplana, O. Gomis, E. Pérez-González, D. Santamaría-Pérez, V. Marín-Borrás, A. Segura, J. González, P. Rodríguez-Hernández, and A. Muñoz. High-Pressure Studies of Topological Insulators Bi_2Se_3, Bi_2Te_3, and Sb_2Te_3. *Phys. Status Solidi B* **2013**, *250*, 669-676.

[Mao 1986] M. K. Mao, J. Xu, and P. M. Bell. Calibration of the Ruby Pressure Gauge to 800 kbar under Quasi-Hydrostatic Conditions. *J. Geophys. Res.* **1986**, *91*, 4673−4676.

[Mendoza-Galván 2000] A. Mendoza-Galván, E. García-García, Y. V. Vorobiev, and J. González-Hernández. Structural, Optical and Electrical Characterization of Amorphous Se_xTe_{1-x} Thin Film Alloys. *Microelectron. Eng.* **2000**, *51-52*, 677-687.

[Momma 2011] K. Momma and F. Izumi. VESTA 3 for Three-dimensional Visualization of Crystal, Volumetric and Morphology Data. *J. Appl. Crystallogr.* **2011**, *44*, 1272-1276.

[Morin 2015] C. Morin, S. Corallini, J. Carreaud, J. B. Vaney, G. Delaizir, J. C. Crivello, E. B. Lopes, A. Piarristeguy, J. Monnier, C. Candolfi, et al. Polymorphism in Thermoelectric As_2Te_3. *Inorg. Chem.* **2015**, *54*, 9936-9947.

[Nielsen 2015] M. B. Nielsen, P. Parisiades, S. R. Madsen, and M. Bremholm. High-Pressure Phase Transitions in Ordered and Disordered Bi_2Te_2Se. *Dalton Transactions* **2015**, *44*, 14077-14084.

[Nolas 2001] G. S. Nolas, J. Sharp, and J. Goldsmid. *Thermoelectrics*. (Eds. Springer: Berlin, **2001**).

[Ovsyannikov 2015] S. V. Ovsyannikov, N. V. Morozova, I. V. Korobeinikov, L. N. Lukyanova, A. Y. Manakov, A. Y. Likhacheva, A. I. Ancharov, A. P. Vokhmyanin, I. F. Berger, O. A. Usov, et al. Enhanced Power Factor and High-Pressure Effects in $(Bi,Sb)_2(Te,Se)_3$ Thermoelectrics. *Appl. Phys. Lett.* **2015**, *106*, 143901.

[Pal 2014] K. Pal, and U. V. Waghmare. Strain Induced Z_2 Topological Insulating State of β-As_2Te_3. *App. Phys. Lett.* **2014**, *105*, 062105.

[Parlinski 1997] K. Parlinski, Z. Q. Li, and Y. Kawazoe. First-Principles Determination of the Soft Mode in Cubic ZrO_2. *Phys. Rev. Lett.* **1997**, *78*, 4063−4066.

[Parthasarathy 1985] G. Parthasarathy, and E. S. R. Gopal. Effect of High Pressure on Chalcogenide Glasses. *Bull. Mater. Sci.* **1985**, *7*, 271-302.

[Perdew 1996] J. P. Perdew, K. Burke, and M. Ernzerhof. Generalized Gradient Approximation Made Simple. *Phys. Rev. Lett.* **1996**, *77*, 3865-3868

[Pereira 2012] A. L. J. Pereira, L. Gracia, D. Santamaría-Pérez, R. Vilaplana, F. J. Manjón, D. Errandonea, M. Nalin, and A. Beltrán. Structural and Vibrational Study of Cubic Sb_2O_3 at under High Pressure. *Phys. Rev. B.* **2012**, *85*, 174108.

[Pereira 2014a] A. L. J. Pereira, O. Gomis, J. A. Sans, J. Pellicer-Porres, F. J. Manjón, A. Beltrán, P. Rodríguez-Hernández, and A. Muñoz. Pressure Effects on the Vibrational Properties of α-Bi_2O_3: an Experimental and Theoretical Study. *J. Phys.: Condens. Matter*. **2014**, *26*, 225401.

[Pereira 2014b] A. L. J. Pereira, J. A. Sans, O. Gomis, F. J. Manjón, P. Rodríguez-Hernández, A. Muñoz, C. Popescu, and A. Beltrán. Isostructural Second-Order Phase Transition of β-Bi_2O_3 at High Pressures: an Experimental and Theoretical Study. *J. Phys. Chem. C.* **2014**, *118*, 23189-23201.

[Piermarini 1973] G. J. Piermarini, S. Block, and J. D. Barnett. Hydrostatic Limits in Liquids and Solids to 100 kbar. *J. Appl. Phys.* **1973**, *44*, 5377-5382.

[Pine 1971] A. S. Pine and G. Dresselhaus. Raman Spectra and Lattice Dynamics of Tellurium. *Phys. Rev. B.* **1971**, *4*, 356-371.

[Popescu 2000] M. A. Popescu. *Non-crystalline chalcogenides*. (Dordrecht, Kluwer Academic Publishing. **2000**).

[Ramesh 2014] K. Ramesh. Pressure Dependence of Glass Transition in As_2Te_3 Glass. *J. Phys. Chem. B* **2014**, *118*, 8848-8853.

[Richter 1973] W. Richter, J. B. Renucci, and M. Cardona. Hydrostatic Pressure Dependence of First-Order Raman Frequencies in Se and Te. *Phys. Status Solidi B.* **1973**, *56*, 223-229.

[Rodríguez-Fernández 2016] C. Rodríguez-Fernández, C. V. Manzano, A. H. Romero, J. Martín, M. Martín-González, M. Morais de Lima Jr, and A. Cantarero. The Fingerprint of Te-rich and Stoichiometric Bi_2Te_3 Nanowires by Raman Spectroscopy. *Nanotechnology.* **2016**, *27*, 075706.

[Sakai 1977] N. Sakai, and H. Fritzsche. Semiconductor-Metal and Superconducting Transitions Induced by Pressure in Amorphous As_2Te_3. *Phys. Rev. B* **1977**, *15*, 973-978.

[Sanghera 2006] J. S. Sanghera, I. D. Aggarwal, L. B. Shaw, C. M. Florea, P. Pureza, V. G. Nguyen, and F. J. Kung. Nonlinear Properties of Chalcogenide Glass Fibers. *J. Optoelectron. Adv. Mater.* **2006**, *8*, 2148-2155.

[Sans 2016c] J. A. Sans, F. J. Manjón, A. L. J. Pereira, R. Vilaplana, O. Gomis, A. Segura, A. Muñoz, P. Rodríguez-Hernández, C. Popescu, C. Drasar, et al. Structural, Vibrational, and Electrical Study of Compressed BiTeBr. *Phys. Rev. B: Condens. Matter Mater. Phys.* **2016**, *93*, 024110.

[Scheidemantel 2003] T. J. Scheidemantel, and J. V. Badding. Electronic Structure of β-As_2Te_3. *Solid State Commun.* **2003**, *127*, 667-670.

[Scheidemantel 2005] T. J. Scheidemantel, J. F. Meng, and J. V. Badding. Thermoelectric Power and Phase Transition of Polycrystalline As_2Te_3 under Pressure. *J. Phys. Chem. Solids.* **2005**, *66*, 1744-1747.

[Scherrer 2005] H. Scherrer and S. Scherrer. "Thermoelectric Properties of Bismuth Antimony Telluride Solid Solutions." in *Thermoelectrics Handbook: Macro to Nano*. Ed. D.M. Rowe (CRC Press: Boca Raton, FL, **2005**).

[Shimojo 2002] F. Shimojo, K. Hoshino, and Y. Zempo. Atomic and Electronic Structures in Liquid Arsenic Telluride by ab initio Molecular Dynamics Simulations. *J. Phys.: Condens. Matter.* **2002**, *14*, 8425-8433.

[Shu 1986] H. W. Shu, S. Jaulmes, and J. Flahaut. System As/1bTe - Obtention and Structural Study of a new Variety of As_2Te_3, Metastable. *Mater. Res. Bull.* **1986**, *21*, 1509-1514.

[Sorb 2016] Y. A. Sorb, V. Rajaji, P. S. Malavi, U. Subbarao, P. Halappa, S. C. Peter, S. Karmakar, and C. Narayana. Pressure-Induced Electronic Topological Transition in Sb_2S_3. *J. Phys.: Condens. Matter.* **2016**, *28*, 015602.

[Stergiou 1985a] A. C. Stergiou and P. J. Rentzeperis. Hydrothermal Growth and the Crystal Structure of Arsenic Telluride, As_2Te_3. *Z. Kristallogr*. **1985**, *172*, 139-145.

[Stordeur 1995] M. Stordeur. "Valence Band Structure and the Thermoelectric Figure-of-Merit of $(Bi_{1-x}Sb_x)Te_3$ Crystals." in *CRC Handbook of Thermoelectrics*, Ed. D.M. Rowe (CRC Press: Boca Raton, FL, **1995**).

[Struzhkin 2008] V. V. Struzhkin, A. F. Goncharov, R. Caracas, H-K Mao, and R. J. Hemley. Synchrotron Infrared Spectroscopy of the Pressure-Induced Insulator-Metal Transitions in Glassy As_2S_3 and As_2Se_3. *Phys. Rev. B: Condens. Matter Mater. Phys.* **2008**, *77*, 165133.

[Taylor 1975] P. C. Taylor, S. G. Bishop, and D. L. Mitchell. Infrared Properties of AsxTe1-x Glasses, *Solid State Commun.* **1975**, *16*, 167-170.

[Thornburg 1973] D. D. Thornburg. Physical Properties of the $As_2(Se,Te)_3$ Glasses. *J. Electron. Mater.* **1973**, *2*, 495-532.

[Toby 2001] B. H. Toby. EXPGUI, A Graphical User Interface for GSAS. *J. Appl. Crystallogr.* **2001**, *34*, 210−213.

[Toscani 1991] S. Toscani. J. Dugue, R. Ollitrault, and R Ceolin. Polymorphism of As_2Te_3: Structural Studies and Thermal behavior of Rhombohedral β-As_2Te_3. *Thermochim. Acta*, **1991**, *186*, 247-251.

[Tverjanovich 2012] A. Tverjanovich, K. Rodionov, and E. Bychkov. Raman Spectroscopy of Glasses in the As-Te System. *J. Solid State Chem.* **2012**, *190*, 271-276.

[Usuki 1996] T. Usuki, K. Saitoh, M. Endo, and O. Uemura. Short-range Order of Amorphous and Liquid As-Te-I System, *J. Non-Cryst. Solids* **1996**, *205-207*, 184-188.

[Vaney 2015] J. B. Vaney, J. Carreaud, G. Delaizir, A. Piarristeguy, C. Morin, E. Alleno, J. Monnier, A. P. Gonçalves, C. Candolfi, A. Dauscher, et al. High-Temperature Thermoelectric Properties of Sn-Doped β-As_2Te_3. *Adv. Electron. Mater.* **2015**, *1*, 1400008.

[Vilaplana 2011b] R. Vilaplana, D. Santamaría-Pérez, O. Gomis, F. J. Manjón, J. González, A. Segura, A. Muñoz, P. Rodríguez-Hernández, E. Pérez-González, V. Marín-Borrás, et al. Structural and Vibrational Study of Bi_2Se_3 under High Pressure. *Phys. Rev. B: Condens. Matter Mater. Phys.* **2011**, *84*, 184110.

[Vilaplana 2013] R. Vilaplana, O. Gomis, F. J. Manjón, H. M. Ortiz, E. Pérez-González, J. López-Solano, P. Rodríguez-Hernández, A. Muñoz, D. Errandonea, V. V. Ursaki, et al. Lattice Dynamics Study of $HgGa_2Se_4$ at High Pressures. *J. Phys. Chem. C.* **2013**, *117*, 15773-15781.

[Walsh 2011] A. Walsh, D. J. Payne, R. G. Egdell, and G. W. Watson. Stereochemistry of Post-Transition Metal Oxides: Revision of the Classical Lone Pair Model. *Chem. Soc. Rev.* **2011**, *40*, 4455-4463.

[Wang 2015] B. T. Wang, P. Souvatzis, O. Eriksson, and P. Zhang. Lattice Dynamics and Chemical Bonding in Sb_2Te_3 from First-Principles Calculations. *J. Chem. Phys.* **2015**, *142*, 174702.

[Yakushev 1986] V. A. Yakushev and V. A. Kirkinskii. New Polymorphic Modification of Arsenic Telluride, Produced at high Pressures. *Dokl. Akad. Nauk SSSR* **1969**, *186*, 882-884; idem, *Dokl. Phys. Chem.* **1986**, *186*, 369-371.

[Yu 2015] Z. H. Yu, L. Wang, Q. Y. Hu, J. G. Zhao, S. Yan, K. Yang, S. Sinogeikin, G Gu, and H-K. Mao. Structural Phase Transitions in Bi_2Se_3 under High Pressure. *Sci. Rep.* **2015**, *5*, 15939.

[Zallen 1971] R. Zallen, M. L. Slade, and A. T. Ward. Lattice Vibrations and Interlayer Interactions in Crystalline As_2S_3 and As_2Se_3. *Phys. Rev. B.* **1971**, *3*, 4257-4273.

[Zhang 2009] H. Zhang, C-X. Liu, X-L. Qi, X. Dai, Z. Fang, and S-C. Zhang. Topological Insulators in Bi_2Se_3, Bi_2Te_3 and Sb_2Te_3 with a Single Dirac Cone on the Surface. *Nature Phys.* **2009**, *5*, 438-442.

[Zhang 2014] J. K. Zhang, Y. H. Han, C. L. Liu, X. Zhang, F. Ke, G. Peng, Y. M. Ma, Y. Z. Ma, and C. X. Gao. Semiconductor-to-metal Transition of Bi_2Se_3 under High Pressure. *Appl. Phys. Lett.* **2014**, *105*, 062102.

[Zhang 2015] H. Y. Zhang, Y. Cheng, M. Tang, X. R. Chen, and G. F. Ji. First-Principles Study of Structural, Elastic, Electronic and Thermodynamic Properties of Topological Insulator Sb_2Te_3 under Pressure. *Comput. Mater. Sci.* **2015**, *96*, 342-347.

[Zhang 2016] Y. H. Zhang, Y. M. Ma, A. H. Geng, C. Y. Zhu, G. T. Liu, Q. Tao, F. F. Li, Q. L. Wang, Y. Li, X. Wang, et al. Pressure-Induced Electronic Phase Transitions of α-As_2Te_3. *J. Alloys Compd.* **2016**, *685*, 551-558.

[Zhao 2013] J. Zhao, H. Liu, L. Ehm, D. Dong, Z. Chen, and G. Gu. High-Pressure Phase Transitions, Amorphization, and Crystallization Behaviors in Bi_2Se_3. *J. Phys.: Condens. Matter* **2013**, *25*, 125602.

[Zhao 2015a] K. Zhao, Y. Wang, Y. Sui, C. Xin, X. J. Wang, Y. Wang, Z. G. Liu, and B. S. Li. First Principles Study of Isostructural Phase Transition in Sb_2Te_3 under High Pressure. *Phys. Stat. Sol. RRL.* **2015**, *9*, 379-383.

[Zhao 2015b] K. Zhao, Y. Wang, C. Xin, X. J. Wang, Y. Wang, Z. G. Liu, and B. S. Li. First Principles Study of Isostructural Phase Transition in Sb_2Te_3 under High Pressure. *Phys. Status Solidi RRL.* **2015**, *9*, 379-383.

[Zhao 2016] J. G. Zhao, L. X. Yang, Z. H. Yu, Y. Wang, C. Y. Li, K. Yang, Z. G. Liu, and Y. Wang. Structural Phase Transitions and Metallized Phenomena in Arsenic Telluride under High Pressure. *Inorg. Chem.* **2016**, *55*, 3907.

[Zhu 2013] J. Zhu, J. L. Zhang, P. P. Kong, S. J. Zhang, X. H. Yu, J. L. Zhu, Q. Q. Liu, X. Li, R. C. Yu, and R. Ahuja. Superconductivity in Topological Insulator Sb_2Te_3 Induced by Pressure. *Sci. Rep.* **2013**, *3*, 2016.

SUPPORTING INFORMATION

Structural, Vibrational and Electronic Study of α-As_2Te_3 under Compression

V.P. Cuenca-Gotor, J.A. Sans, J. Ibáñez, C. Popescu, O.Gomis, R. Vilaplana, F.J. Manjón, A. Leonardo, E. Sagasta, A. Suárez-Alcubilla, I.G. Gurtubay, M. Mollar, and A. Bergara

Lattice dynamics of α-As_2Te_3 at room pressure

The RS spectrum of α-As_2Te_3 at room pressure has a close similarity to RS spectra reported in glasses containing As and Te atoms which show vibrational frequencies below 200 cm^{-1}. Modes between 150 and 160 cm^{-1} were attributed to Te-Te vibrations as in amorphous Te [Mendoza-Galván 2000, Usuki 1996, Tverjanovich 2012, Alekberov 2014]. Modes between 175 and 195 cm^{-1} have been attributed to As-Te vibrations [Usuki 1996, Tverjanovich 2012, Alekberov 2014, Taylor 1975, Lukic 2003]. Finally, modes between 230 and 240 cm^{-1} have been attributed to amorphous As [Tverjanovich 2012, Taylor 1975]. The mode whose frequency is around 195 cm^{-1} is in good agreement with RS measurement in As_2Se_3, whose highest vibrational modes is around 250 cm^{-1} [Zallen 1971] as already commented by Tverjanovich et al. [Tverjanovich 2012]. These two modes scale perfectly with the square root masses of Se and Te, thus giving support to the assignment of the mode around 195 cm^{-1} to the stretching vibrations of As-Te.

Visualization of the vibrational modes of α-As_2Te_3 at Γ calculated from *first principles* using the VASP code can be performed with the J-ICE software [Canepa 2011]. This visualization has allowed us to further understand the complex lattice dynamics of this compound as it was previously done for monoclinic α-Bi_2O_3 [Pereira 2014a]. In general, we have observed that the motion of atoms is very complex and no modes related to isolated molecular units can be identified in monoclinic As_2Te_3. Modes with frequencies above 160 cm^{-1} are dominated by the vibration of light As atoms; modes with frequencies between 100 and 150 cm^{-1} are mainly determined by the vibration of heavy Te atoms; and modes with frequencies below 100 cm^{-1} are collective or lattice modes of vibration where groups of As and Te atoms move in or out of phase. As matter of example **Figure S1** shows the atomic vibrations in four Raman-active vibrational modes. The highest vibrational Raman mode A_g^{10} mode shows the strong movement of As atoms in the *a*-*c* plane [**Fig. S1(a)**]; the A_g^7 mode [**Fig. S1(b)**] corresponds to an almost pure vibration of Te atoms; the lowest B_g^1 mode [**Fig. S1(c)**] corresponds to a half shear mode between alternated layers with atoms vibrating along the *b* axis (note that the structure is shifted in this view to see the atom movements along the *b* axis perpendicular to *a* and *c* axis); and the A_g^1 mode [**Fig. S1(d)**] is the lowest-frequency Raman mode. In this complex monoclinic layered structure, there is no

pure shear mode of the layers either in the *a*-*c* plane or along the *b* axis (either Raman or IR-active).

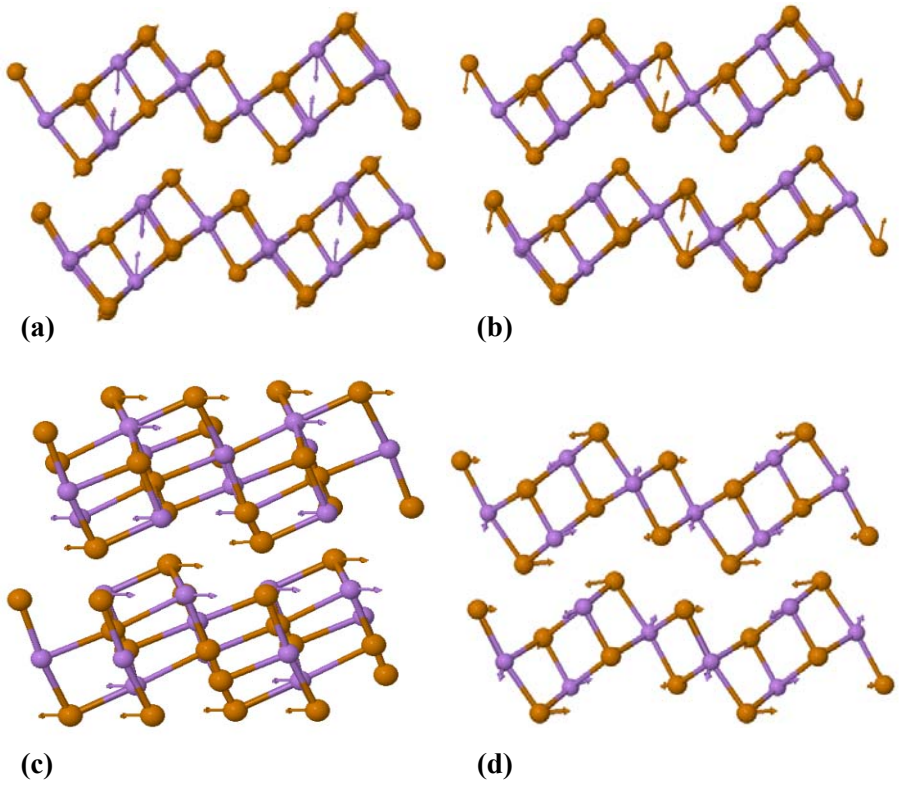

Figure S1. Scheme of atomic vibrations (As atoms are violet circles and Te atoms are orange circles) in some Raman-active vibrational modes of α-As_2Te_3: **(a)** A_g^{10} mode (optical mode of highest frequency), **(b)** A_g^7 mode (pure vibration of Te atoms), **(c)** B_g^1 mode (half shear mode along *b* axis), and **(d)** A_g^1 mode (optical mode of lowest frequency which is not a pure shear mode in the *a*-*c* plane).

Rietveld and LeBail analysis of HP-XRD measurements of α-As_2Te_3 under pressure

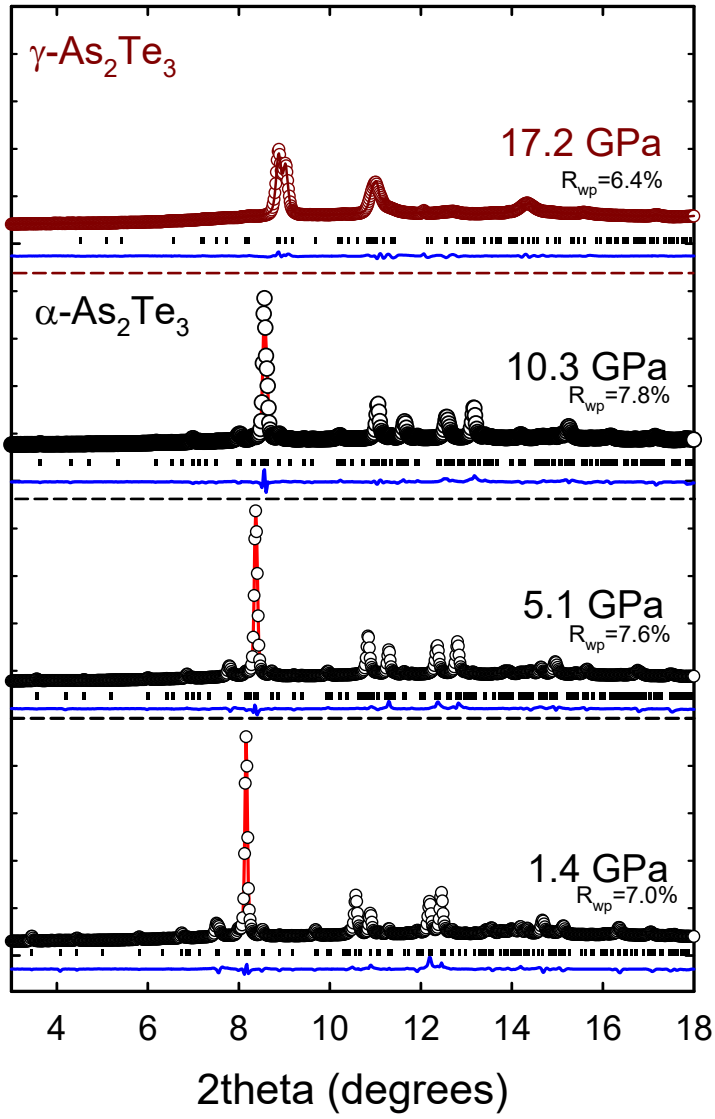

Figure S2. Rietveld refinement at two different pressures (1.4 and 5.1 GPa) and Le Bail refinement (10.3 GPa) for α-As_2Te_3. Le Bail analysis for γ-As_2Te_3 is also reported at 20 GPa. Experimental diffraction patterns are plotted as symbols, with the refined pattern as red lines and the residuals as blue lines. Vertical ticks represent theoretical position of the Bragg reflections both in α-As_2Te_3 and γ-As_2Te_3.

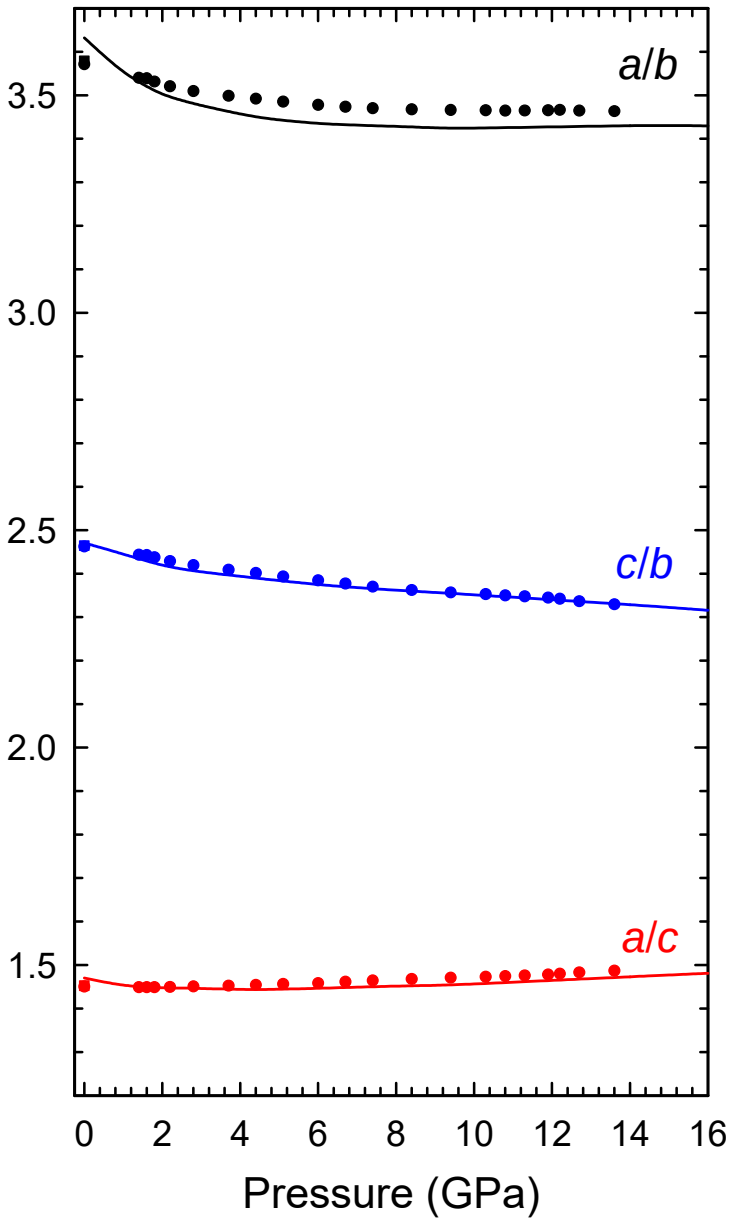

Figure S3. Experimental (symbols) and theoretical (solid lines) pressure dependence of the axial ratios of α-As_2Te_3 under compression. Squares correspond to data at ambient pressure taken from Carron (1963).

Calculation of the experimental and theoretical compressibility tensor at different pressures

The isothermal compressibility tensor, β_{ij}, is a symmetric second rank tensor that relates the state of strain of a crystal to the change in pressure that induced it [Haussühl 2007]. The tensor coefficients for a monoclinic crystal with *b* as the unique crystallographic axis are:

$$\beta_{ij} = \begin{pmatrix} \beta_{11} & 0 & \beta_{13} \\ 0 & \beta_{22} & 0 \\ \beta_{13} & 0 & \beta_{33} \end{pmatrix}$$

We have obtained the isothermal compressibility tensor coefficients for α-As_2Te_3 at several pressures using the IRE (Institute of Radio Engineers) convention for the orthonormal basis for the tensor: $e_3||c$, $e_2||b^*$, $e_1||e_2 \times e_3$. The tensor has been obtained with the finite Eulerian approximation as implemented in the Win_Strain package [Angel 2004-2011].

The change of the β monoclinic angle (always perpendicular to the *b* axis) with pressure implies that, in this monoclinic compound, the direction of the *a* axis changes with pressure assuming both *b* and *c* axis constant. Furthermore, the departure of this monoclinic angle from 90º indicates that the direction of maximum compressibility is not exactly that of the *a* axis. Therefore, in order to evaluate the direction of maximum compressibility as a function of pressure we have calculated and diagonalised the experimental and theoretical isothermal compressibility tensor, β_{ij}, at different pressures. The experimental and theoretical elements of this tensor at different pressures are reported in **Tables S1 and S2**, respectively, where the directions of the maximum, intermediate and minimum compressibility and the values of the compressibility along those directions are given by the eigenvectors (ev_i, i=1-3) and eigenvalues (λ_i, i=1-3), respectively.

First of all, we have to note that there is a reasonable good agreement between the experimental and calculated axial compressibilities (β_{ii} coefficients) at room pressure because $\beta_{11} > \beta_{33} > \beta_{22}$ in both cases. A diagonalization of the β_{ij} tensor at room pressure yields for our experiments the maximum, intermediate and minimum compressibilities $27.3(2.1)\cdot10^{-3}$, $14.0(1.1)\cdot10^{-3}$ and $4.7(4)\cdot10^{-3}$ GPa^{-1}, respectively; whereas for the case of our calculations the obtained values for the compressibilities are $38(3)\cdot10^{-3}$, $14.6(1.1)\cdot10^{-3}$ and $4.3(5)\cdot10^{-3}$ GPa^{-1}. These experimental (theoretical) results indicate that around 59% (67%) of the total compression at room pressure is being accommodated along the direction of maximum compressibility. Taking into account the eigenvector ev_1, the major compression direction at zero pressure occurs in the (0 1 0) plane at the given angle Ψ [see **Tables S1 and S2**] relative to the *c* axis (from *c* to *a*) or equivalently at an angle θ relative to the *a* axis (from *a* to *c*). In particular, the experimental major compression direction at room pressure is at θ =16.0(1.4)º from the *a* axis whereas for our calculations is at 5.5(7)º from the *a* axis. The direction of intermediate compressibility at room pressure given by eigenvector ev_2 is in the (0 1 0) plane perpendicular to the direction of maximum

compressibility, and the direction of minimum compressibility at room pressure given by eigenvector ev_3 is along the *b* axis.

As regards the behavior of the compressibility tensor under pressure, the most notable feature is that below 2.0 GPa the experimental compressibility of the *a* axis is higher than that of the *c* axis ($\beta_{11} > \beta_{33}$); however, at 2.0 GPa both compresibilities are similar, and beyond 3.0 GPa $\beta_{11} < \beta_{33}$ within experimental uncertainties. This behavior is because the *c* axis becomes more compressible than the *a* axis above 3.0 GPa. Furthermore, the decrease of the compressibility of the *a* axis with increasing pressure is so large that the compressibilities of the *a* and *b* axes become equal around 13 GPa ($\beta_{11} = \beta_{22}$). Correspondingly, the direction of maximum compressibility move away the *a* axis and approaches the *c* axis with increasing pressure; i.e., the θ angle increases. At 3.0 GPa the direction of maximum compressibility is closer to the *c* axis than to the *a* axis and at pressures beyond 5 GPa the direction of maximum compressibility is already very close to the *c* axis. Note that the results for the evolution of the theoretical tensor under pressure are similar to those obtained for the experimental tensor.

Table S1. Experimental isothermal compressibility tensor coefficients, β_{ij}, and their eigenvalues, λ_i, and eigenvectors, ev_i, for α-As_2Te_3 at several pressures. The results are given using the finite Eulerian method. The eigenvalues are given in decreasing value along a column.

P(GPa)	0.0	1.0	2.0	3.0	5.0
β_{11} (10^{-3} GPa^{-1})	26.8 (2.0)	16.5 (1.2)	11.5 (8)	8.7 (6)	5.8 (5)
β_{22} (10^{-3} GPa^{-1})	4.7 (5)	4.4 (4)	4.2 (3)	3.9 (3)	3.5 (3)
β_{33} (10^{-3} GPa^{-1})	14.5 (1.1)	12.5 (9)	11.0 (8)	9.8 (7)	8.0 (6)
β_{13} (10^{-3} GPa^{-1})	2.54 (22)	2.08 (18)	1.56 (15)	1.05 (12)	0.28 (9)
λ_1 (10^{-3} GPa^{-1})	27.3 (2.1)	17.4 (1.3)	12.9 (9)	10.4 (8)	8.0 (6)
ev_1 (λ_1)	(0.98,0,0.19)	(0.92,0,0.39)	(0.76,0,0.65)	(0.52,0,0.85)	(0.12,0,0.99)
λ_2 (10^{-3} GPa^{-1})	14.0 (1.1)	11.6 (9)	9.7 (7)	8.1 (6)	5.8 (5)
ev_2 (λ_2)	(-0.19,0,0.98)	(-0.39,0,0.92)	(-0.65,0,0.76)	(-0.85,0,0.52)	(-0.99,0,0.12)
λ_3 (10^{-3} GPa^{-1})	4.7 (4)	4.4 (4)	4.2 (3)	3.9 (3)	3.5 (3)
ev_3 (λ_3)	(0, 1, 0)	(0, 1, 0)	(0, 1, 0)	(0, 1, 0)	(0, 1, 0)
Ψ, θ (°)[a]	78.8 (1.4), 16.0 (1.4)	66.9 (1.2), 28.2 (1.2)	49.6 (2.3), 45.7 (2.3)	31.4 (2.9), 63.9 (2.9)	7.1 (2.4), 88.5 (2.4)

P(GPa)	7.0	9.0	11.0	13.0
β_{11} (10^{-3} GPa^{-1})	4.4 (4)	3.5 (3)	2.9 (3)	2.5 (3)
β_{22} (10^{-3} GPa^{-1})	3.2 (3)	2.9 (3)	2.7 (3)	2.5 (4)
β_{33} (10^{-3} GPa^{-1})	6.8 (5)	5.9 (4)	5.2 (4)	4.6 (4)
β_{13} (10^{-3} GPa^{-1})	-0.11 (9)	-0.18 (9)	-0.07 (9)	0.04 (9)
λ_1 (10^{-3} GPa^{-1})	6.8 (5)	5.9 (4)	5.2 (4)	4.6 (4)
ev_1 (λ_1)	(0.07,0,1.00)	(0.05,0,1.00)	(0.03,0,1.00)	(0.02,0,1.00)
λ_2 (10^{-3} GPa^{-1})	4.4 (4)	3.4 (3)	2.9 (3)	2.5 (3)
ev_2 (λ_2)	(-1.00,0,0.07)	(-1.00,0,0.05)	(-1.00,0,0.03)	(-1.00,0,0.02)
λ_3 (10^{-3} GPa^{-1})	3.2 (3)	2.9 (3)	2.7 (3)	2.5 (3)
ev_3 (λ_3)	(0, 1, 0)	(0, 1, 0)	(0, 1, 0)	(0, 1, 0)
Ψ, θ (°)[a]	-2.6 (2.3), 98.2 (2.3)	-4.2 (2.3), 99.7 (2.3)	-1.6 (2.4), 97.0 (2.4)	1.1 (2.4), 94.3 (2.4)

[a] The major compression direction occurs in the (0 1 0) plane at the given angles Ψ to the *c* axis (from *c* to *a*) and θ to the *a* axis (from *a* to *c*).

Table S2. Theoretical isothermal compressibility tensor coefficients, β_{ij}, and their eigenvalues, λ_i, and eigenvectors, ev_i, for α-As_2Te_3 at several pressures. The results are given using the finite Eulerian method. The eigenvalues are given in decreasing value along a column.

P(GPa)	0.0	1.0	3.0	4.0	5.0
β_{11} (10^{-3} GPa^{-1})	38 (3)	21.4 (1.6)	10.4 (7)	8.2 (6)	6.7 (5)
β_{22} (10^{-3} GPa^{-1})	4.3 (5)	4.2 (4)	3.9 (3)	3.8 (3)	3.7 (3)
β_{33} (10^{-3} GPa^{-1})	14.6 (1.1)	12.7 (9)	10.0 (7)	9.0 (6)	8.2 (6)
β_{13} (10^{-3} GPa^{-1})	-0.14 (2)	0.93 (9)	0.95 (9)	0.53 (7)	-0.005 (9)
λ_1 (10^{-3} GPa^{-1})	38(3)	21.5 (1.6)	11.2 (8)	9.2 (7)	8.2 (6)
ev_1 (λ_1)	(1.00,0,0.01)	(0.99,0,0.11)	(0.79,0,0.62)	(0.46,0,0.89)	(0.00,0,1.00)
λ_2 (10^{-3} GPa^{-1})	14.6 (1.1)	12.6 (9)	9.2 (7)	7.9 (6)	6.7 (5)
ev_2 (λ_2)	(0.01,0,1.00)	(0.11,0,-0.99)	(0.62,0,-0.79)	(0.89,0,-0.46)	(1.00,0,0.00)
λ_3 (10^{-3} GPa^{-1})	4.3 (5)	4.2 (4)	3.9 (3)	3.8 (3)	3.7 (3)
ev_3 (λ_3)	(0,1,0)	(0,1,0)	(0,1,0)	(0,1,0)	(0,1,0)
Ψ, θ (°)[a]	90.3 (7), 5.5 (7)	84.0 (5), 12.0 (5)	51.9 (1.9), 44.4 (1.9)	27.1 (2.8), 69.3 (2.8)	-0.2 (1.6), 96.6 (2.5)

P(GPa)	7.0	9.0	11.0	13.0
β_{11} (10^{-3} GPa^{-1})	4.9 (4)	3.9 (3)	3.2 (3)	2.7 (2)
β_{22} (10^{-3} GPa^{-1})	3.5 (3)	3.3 (3)	3.2 (4)	3.0 (4)
β_{33} (10^{-3} GPa^{-1})	6.9 (5)	6.0 (4)	5.3 (4)	4.8 (4)
β_{13} (10^{-3} GPa^{-1})	-0.34 (7)	-0.43 (7)	-0.54 (7)	-0.63 (8)
λ_1 (10^{-3} GPa^{-1})	7.0 (5)	6.1 (4)	5.4 (4)	4.9 (4)
ev_1 (λ_1)	(0.16,0,-0.99)	(0.19,0,-0.98)	(0.23,0,-0.97)	(0.27,0,-0.96)
λ_2 (10^{-3} GPa^{-1})	4.9 (4)	3.8 (3)	3.2 (7)	3.0 (4)
ev_2 (λ_2)	(0.99,0,0.16)	(0.98,0,0.19)	(0.97,0,0.23)	(0.96,0,0.27)
λ_3 (10^{-3} GPa^{-1})	3.5 (3)	3.3 (3)	3.1 (5)	2.5 (2)
ev_3 (λ_3)	(0,1,0)	(0,1,0)	(0,1,0)	(0,1,0)
Ψ, θ (°)[a]	-9.4 (1.7), 105.7 (1.7)	-11.1 (1.6), 107.3 (1.6)	-13.6 (1.7), 109.6 (1.7)	-15.9 (1.8), 111.8 (1.8)

[a] The major compression direction occurs in the (0 1 0) plane at the given angles Ψ to the *c* axis (from *c* to *a*) and θ to the *a* axis (from *a* to *c*).

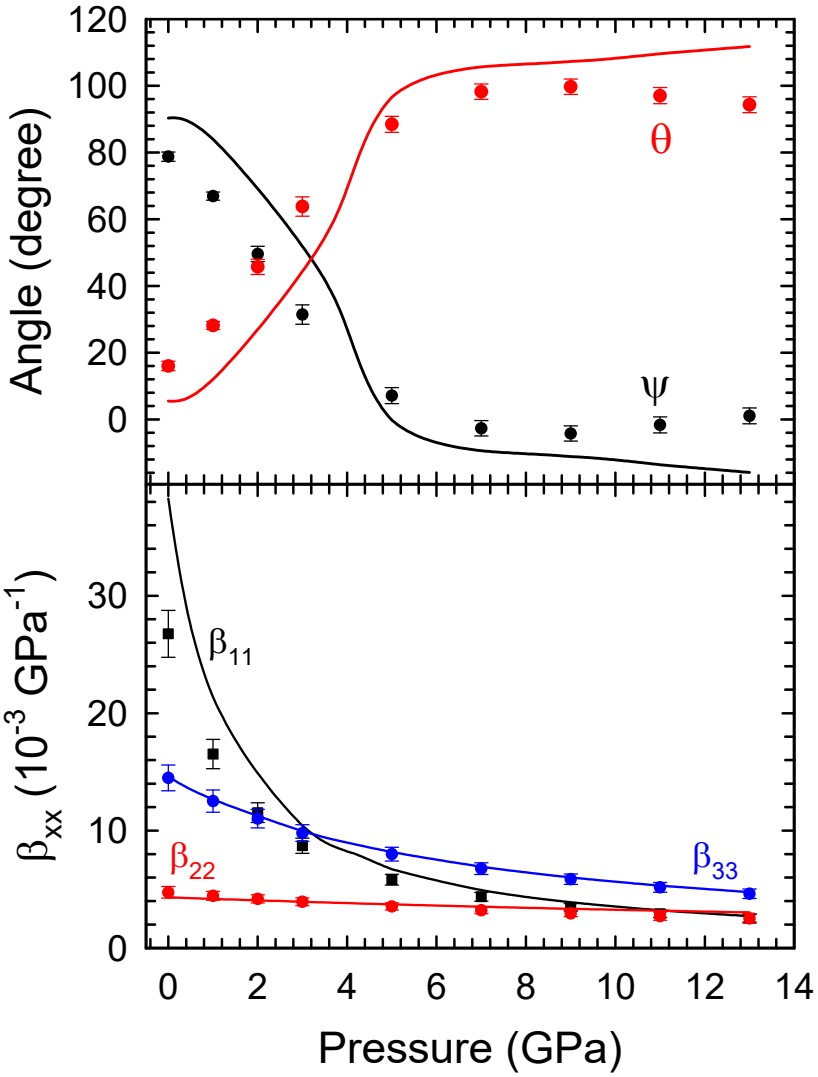

Figure S4. (a) Angle of maximum compressibility Ψ relative to the *c* axis (from *c* to *a*) or equivalently θ relative to the *a* axis (from *a* to *c*). **(b)** β_{xx} coefficients of the compressibility tensor that indicates the compressibility along the crystallographic axis. Solid lines represent the *ab initio* calculations and symbols data obtained from our experiments.

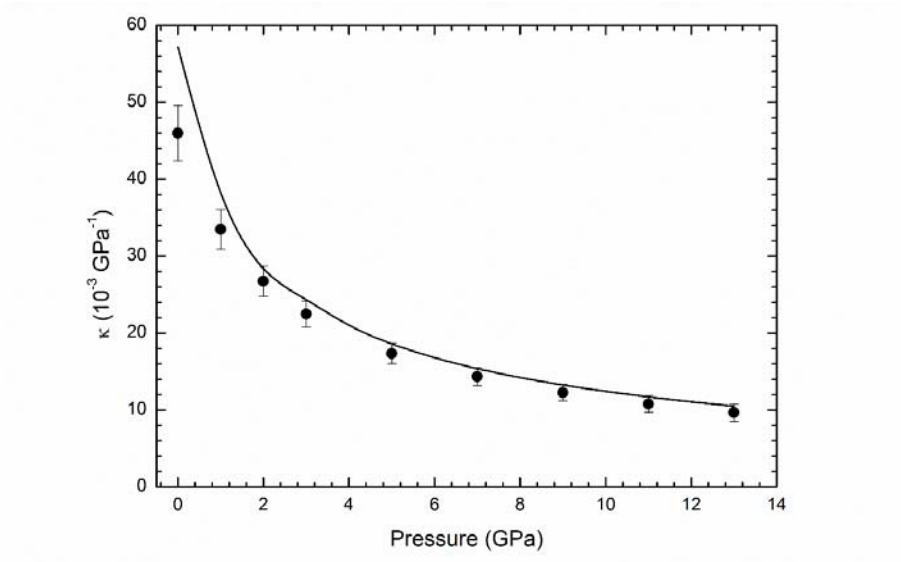

Figure S5. Experimental (symbols) and theoretical (curve) pressure dependence of the volume compressibility as obtained from the trace of the experimental and theoretical compressibility tensors at different pressures.

Pressure dependence of atomic coordinates and interatomic distances

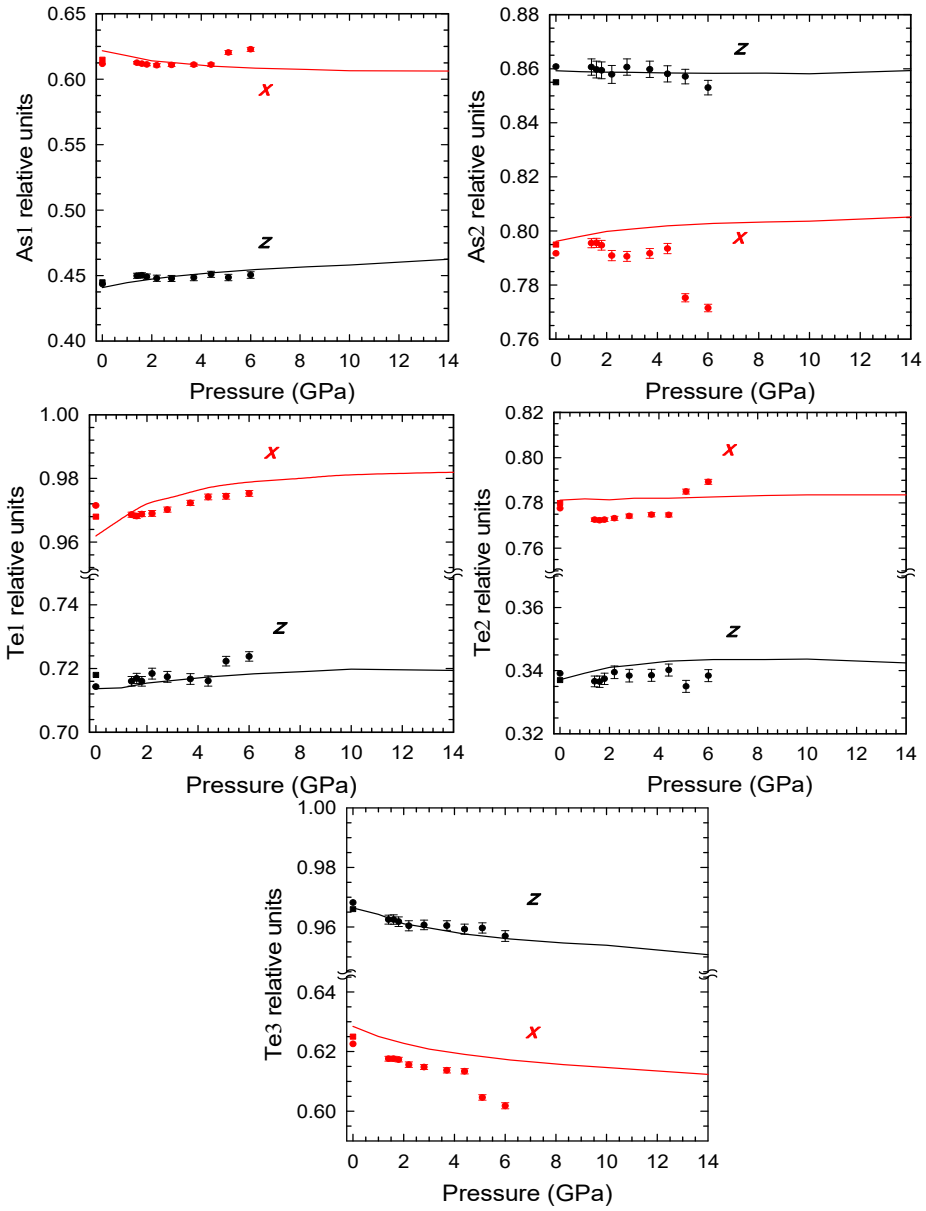

Figure S6. Pressure dependence of the experimental (symbols) and theoretical (lines) As1, As2, Te1, Te2 and Te3 *x* and *z* coordinates in α-As_2Te_3. Squares correspond to data at ambient pressure taken from Carron (1963).

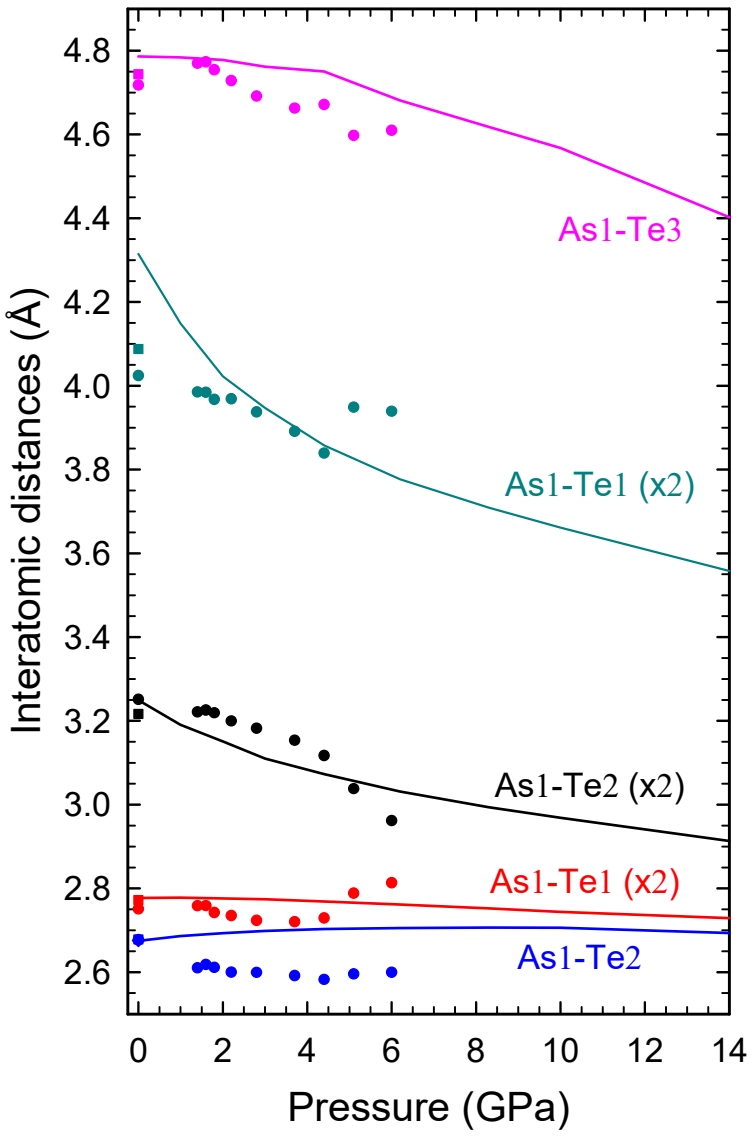

Figure S7. Pressure dependence of the experimental (symbols) and theoretical (lines) As1-Te distances. Squares correspond to data at ambient pressure taken from Carron (1963).

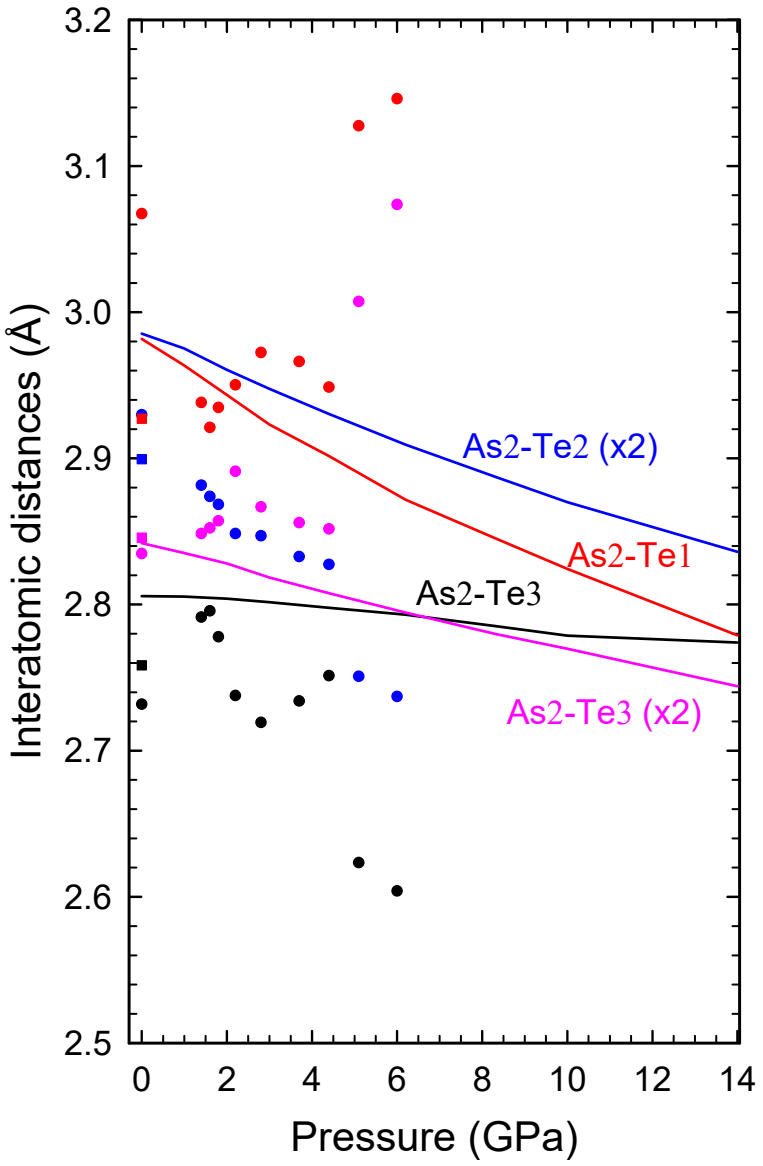

Figure S8. Pressure dependence of the experimental (symbols) and theoretical (lines) As2-Te distances. Squares correspond to data at ambient pressure taken from Carron (1963).

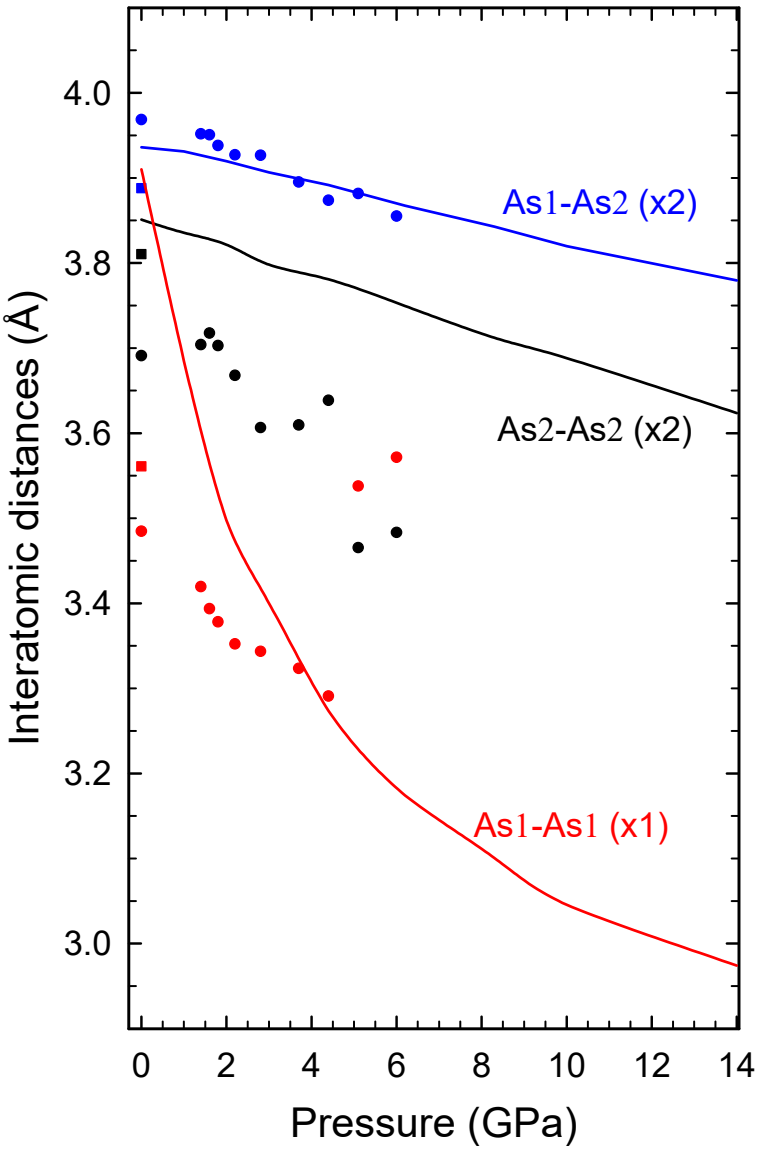

Figure S9. Pressure dependence of the experimental (symbols) and theoretical (lines) As-As distances. Squares correspond to data at ambient pressure taken from Carron (1963).

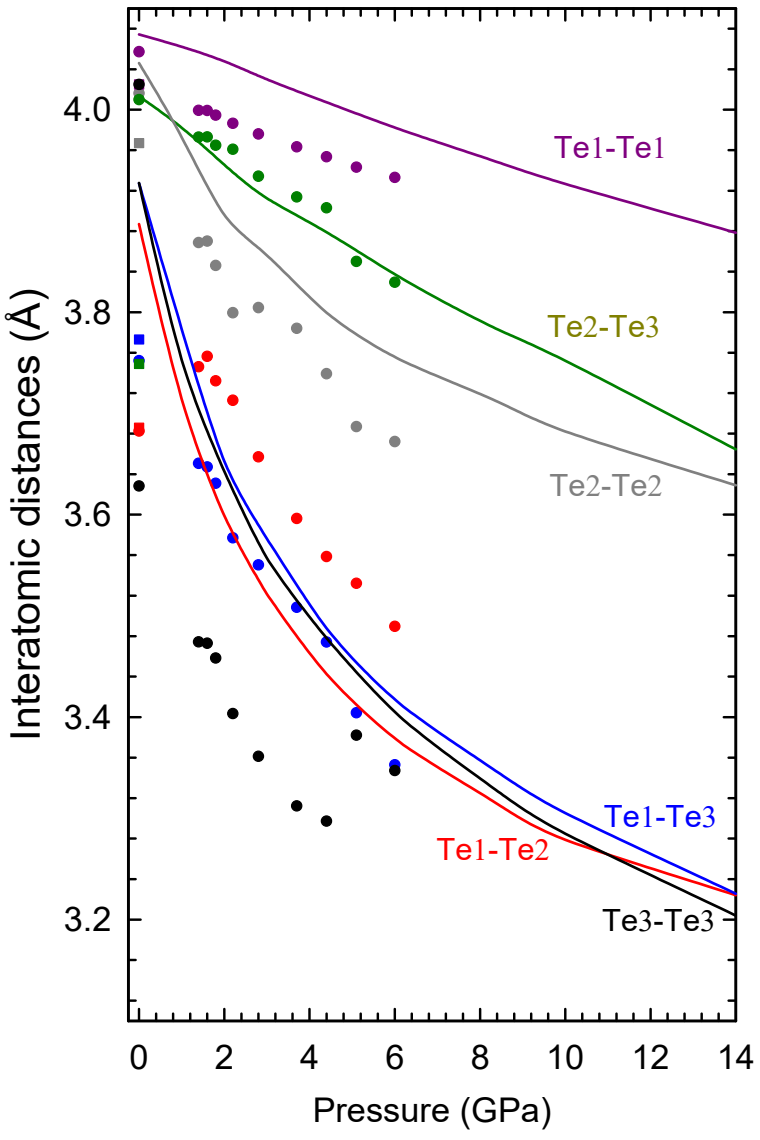

Figure S10. Pressure dependence of the experimental (symbols) and theoretical (lines) Te-Te distances. Squares correspond to data at ambient pressure taken from Carron (1963).

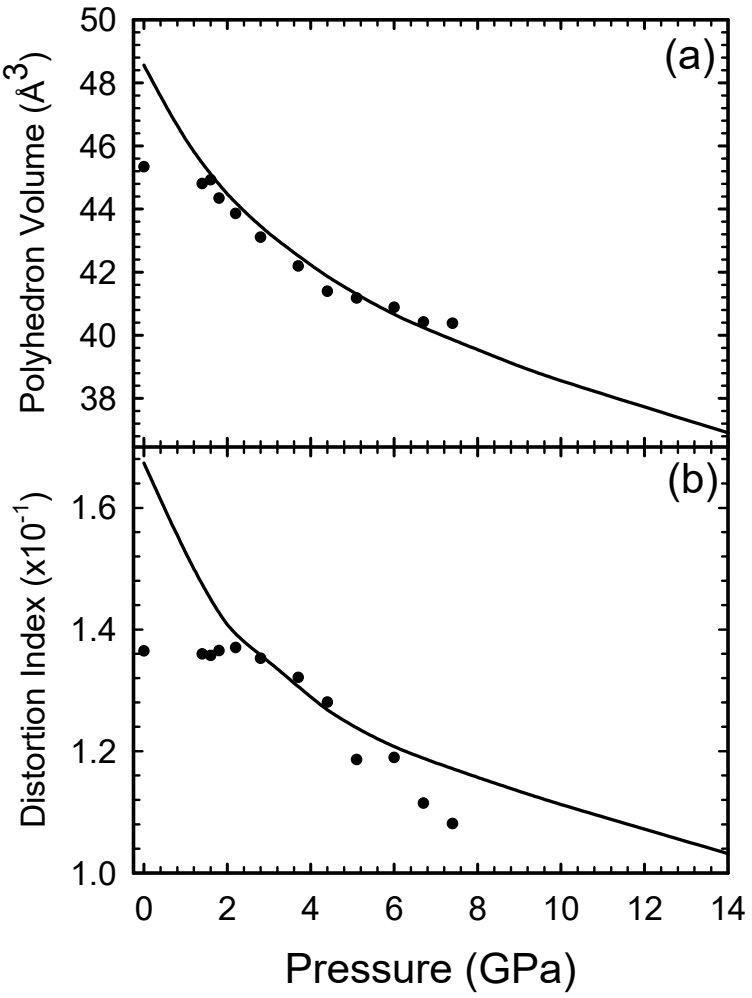

Figure S11. Pressure dependence of the experimental (symbols) and theoretical (lines) volume **(a)** and distortion index **(b)** of the As1 polyhedron.

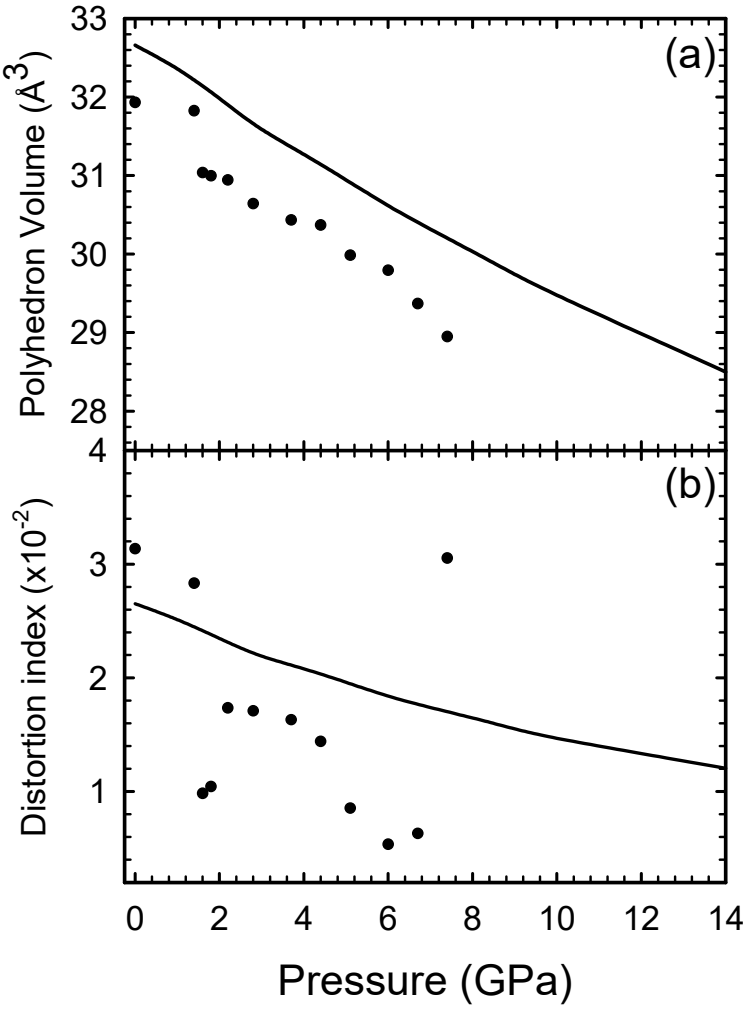

Figure S12. Pressure dependence of the experimental (symbols) and theoretical (lines) volume **(a)** and distortion index **(b)** of the As2 polyhedron.

Comparison of the structure of α-As_2Te_3 and its pressure behavior with other related group-15 sesquichalcogenides

It is interesting to compare the structure of α-As_2Te_3 and its pressure behavior with that of other group-15 sesquioxides and sesquichalcogenides in order to understand the role played by the As LEP in the structure of α-As_2Te_3. **Table S3** summarizes the experimental and theoretical BM-EoS of α-As_2Te_3, α-Sb_2Te_3, α-Bi_2Te_3 and orthorhombic Sb_2Se_3. As observed, the bulk modulus of α-As_2Te_3 is smaller than that of α-Sb_2Te_3 and α-Bi_2Te_3. This result is in good agreement with the larger activity of the LEP in As than in Sb and Bi tellurides and how this activity favors open structures with a large compressibility. In this way, it is easy to understand that the increase of the cation LEP activity in the series Bi-Sb-As explains that distorted structures caused by the cation LEP are present in Bi_2X_3 (*X*= O, S), Sb_2X_3 (*X*= O, S, Se) and As_2X_3 (*X*= O, S, Se, Te) since cation LEP activity is different for different anions [Walsh 2011]. The comparison of compounds with the same anion, shows that the volume per unit formula rises when the atomic number of the cation increases, as expected by the increase of the cationic radius size. However, the LEP effect softens this increase allowing a small increment of the initial volume of α-As_2Te_3 compared with that observed in α-Sb_2Te_3. On the other hand, the bulk modulus of α-As_2Te_3 is similar to that of Sb_2Se_3.

It is also worthy to compare the compressibility of the different axes in these compounds [see **Table S4**]. The experimental compressibility of the *a* axis at room pressure in α-As_2Te_3 ($26.8(2)\cdot10^{-3}$ GPa^{-1}) can be compared to that of the *c* axis in α-Sb_2Te_3 (around $21.2\cdot10^{-3}$ GPa^{-1}) [Haussühl 2007] and α-Bi_2Te_3 (around $15.2\cdot10^{-3}$ GPa^{-1}) [Walsh 2011] since layers are mainly stacked along these directions in the different compounds. As observed, the interlayer compressibility of α-As_2Te_3 is larger than of α-Sb_2Te_3 and α-Bi_2Te_3. Again, this result is in good agreement with the larger Te-Te interlayer distance observed in As telluride than in Sb and Bi tellurides as expected by the larger cation LEP activity of As than that of Sb and Bi for the same anion. On the contrary, the intralayer compressibility at room pressure, which is mainly that of *b* axis in α-As_2Te_3 ($4.7(5)\cdot10^{-3}$ GPa^{-1}) and that of *a* axis in α-Sb_2Te_3 ($6.2\cdot10^{-3}$ GPa^{-1}) [Souza 2012] and α-Bi_2Te_3 ($8.4\cdot10^{-3}$ GPa^{-1}) [Polian 2011], is smaller than that of the other axes in the three compounds, as expected for the intralayer strong covalent A-Te (*A*= As, Sb, Bi) bonds.

An even closer comparison of axial compressibilities can be performed between α-As_2Te_3 and Sb_2Se_3 since the latter compound crystallizes in an orthorhombic layered structure (*Pnma* space group) isostructural to Sb_2S_3 and Bi_2S_3 and with similar tendency than α-As_2Te_3 to form needles extended along the *b* axis which are weakly linked to form extended layers. The structure of Sb_2Se_3 is more distorted than that of α-As_2Te_3 and has also two independent cations, Sb1 and Sb2. At room pressure, both cations are bonded to three Se atoms with short bonds (< 2.7 Å) and to four additional Se atoms with longer bonds (> 3.0 Å), giving rise to an apparent 7-fold coordination. Actually, the coordination at ambient pressure is much smaller. The shortest bonds give rise to distorted trigonal Sb_1Se_3 units and tetragonal Sb_2Se_5 pyramids, thus resulting in Sb1Se3E tetrahedra and Sb2Se5E octahedra (where E indicates the LEP of both Sb atoms) of quasi-4-fold and quasi-6-fold coordination,

respectively. Similar to Sb_2Se_3, the polyhedral units of α-As_2Te_3 could be described as As1Te5E octahedra and As2Te6 octahedra. From this perspective, it is observed that the cation LEP is active in both polyhedral units of Sb_2Se_3, but only in one polyhedral unit of α-As_2Te_3; i.e., the LEP activity of Sb in Sb_2Se_3 is larger than that of As in α-As_2Te_3. This different LEP activity is a consequence that the cation LEP activity depends on the anion and increases for lighter anions as already reported elsewhere [Walsh 2011].

Due to the larger cation LEP activity in Sb_2Se_3 than in α-As_2Te_3, the zigzag layers in Sb_2Se_3 are cut along the *c* axis [Deringer 2015]. Inside the needles extended along the *b* axis, intralayer Sb-Se distances are around 2.67 Å; a value similar to that of most intralayer As-Te bonds [**Figs. S6 and S7**]. These needles are separated from adjacent ones in a zigzag way by intermediate primary and secondary interchain distances (around 3.1 Å) mainly along the *c* axis. Finally, the layers formed by linked chains along *b* and *c* axes pile up along the *a* axis with large distances between layers (around 3.7 Å) [Deringer 2015]. In this way, the structure of Sb_2Se_3 results in a *b* lattice parameter around 4 Å, similar to that of α-As_2Te_3, while *a* and *c* lattice parameters are around 11.8 Å and 11.6 Å, respectively. The compresibilities of *a*, *b* and *c* axes in Sb_2Se_3 at room pressure are around $13.6 \cdot 10^{-3}$, $5.0 \cdot 10^{-3}$ and $9.3 \cdot 10^{-3}$ GPa^{-1} [Efthimiopoulos 2013] so they clearly scale with the lattice parameter values and with the Sb-Se distances along the different directions. This situation is the same already described for α-As_2Te_3 where the compressibility of the *a*, *b* and *c* axes at room pressure scale with the lattice parameters and with the interlayer Te-Te distance (around 3.8 Å), with the intralayer As2-Te distances (around 2.8 Å), and with the intralayer As1-Te distance (around 3.2 Å). The largest difference in axial compressibilities between α-As_2Te_3 and Sb_2Se_3 occurs along the *a* axis. This result must be ascribed to the different compressibility of van der Waals interlayer Te-Te distances than Se-Se distances since all three tellurides show larger interlayer compressibilities than the selenide Sb_2Se_3.

In summary, the structure of α-As_2Te_3 can be understood as intermediate between that of α-Sb_2Te_3 and Sb_2Se_3 in good agreement with what is expected from the activity of cation LEP in group-15 sesquichalcogenides.

Table S3. Experimental (Exp) and theoretical DFT-GGA (The) parameters of the BM-EoS of α-As_2Te_3, α-Sb_2Te_3, α-Bi_2Te_3 and Sb_2Se_3 at ambient pressure. Volumes per formula unit are taken for comparison of the different compounds.

Compound	V_0 (Å^3)	B_0 (GPa)	B_0'	Character
α-As_2Te_3	144.8	24	7.9	Exp[a]
	143.0	26	9.0	Exp[b]
	143.0	33	4.0(fixed)	Exp[b]
	142.6	38.4	4.0(fixed)	Exp[c]
	150.8	19.7	8.1	The[a]
	138.4	42.7		The[d]
α-Sb_2Te_3	159.7	40	4 (fixed)	Exp[e]
	159.7	30.2	9.4	Exp[f]
		45	4 (fixed)	Exp[g]
	159.9	36.1	6.2	Exp[h]
	157.5	54.7	4	Exp[i]
	158.1	41.0	5.2	The[j]
	159.9	33.1		The[k]
α-Bi_2Te_3	169.2	56.2	2.1	Exp[f]
		21.9*	17.1	Exp[l]
		38.2**	4.6	
	168.5	28.1*	13.8	Exp[m]
	168.5	36.3**	5.5	
	170.0	46.3	3.6	Exp[n]
		50.1	3.0	Exp[o]
	166.7	41.6	4.68	The[p]
	168.8	28.1		The[q]
		40.3		The[r]
Sb_2Se_3	136.4	30	6.1	Exp[q]

[a] This work, [b] [Zhao 2016], [c] [Zhang 2016], [d] [Deng 2015], [e] [Sakai 1977], [f] [Jacobsen 2007], [g] [Zhao 2011], [h] [Souza 2012], [i] [Ma 2012], [j] [Gomis 2011], [k] [Zhang 2015], [l] [Nakayama 2009], [m] [Polian 2011], [n] [Zhu 2011], [o] [Einaga 2011], [p] [Vilaplana 2011a], [q] [Ibarra-Hernández 2014], [r] [Feng 2014], [q] [Efthimiopoulos 2013]. * Values below 3 GPa. ** Values above 3 GPa.

Table S4. Lattice parameters (in Å) and compressibilities (in 10^{-3} GPa^{-1}) of α-As_2Te_3, α-Sb_2Te_3, α-Bi_2Te_3 and Sb_2Se_3 at ambient pressure. Values with same shadow color correspond to distances and compressibilities to be compared. Note that *c* lattice parameter of α-Sb_2Te_3 and α-Bi_2Te_3 has been divided by 2 because there are two times more layers along the unit cell of these compounds than along the *a* axis of α-As_2Te_3 and Sb_2Se_3.

Compound	*a*	χ_a	*b*	χ_b	*c*	χ_c
α-As_2Te_3[a]	14.55	26.8	4.03	4.7	9.96	14.5
Sb_2Se_3[b]	11.80	13.6	3.98	5.0	11.60	9.3
α-Sb_2Te_3[c]	4.27	6.2	4.27	6.2	15.19	21.2
α-Bi_2Te_3[d]	4.38	8.4	4.38	8.4	15.18	15.2

[a] This work, [b] [Efthimiopoulos 2013], [c] [Souza 2012], [d] [Polian 2011].

Ab-initio calculations of enthalpy vs pressure

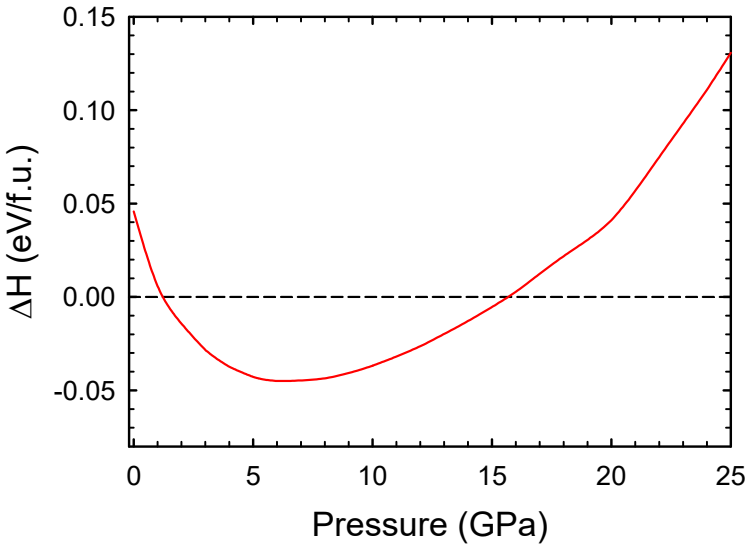

Figure S13. Enthalpy difference curves of the α (black dashed line) and β (red solid line) phases as a function of pressure with respect to the α-phase which has been taken as a reference.

Vibrational properties of α-As_2Te_3 at high pressures

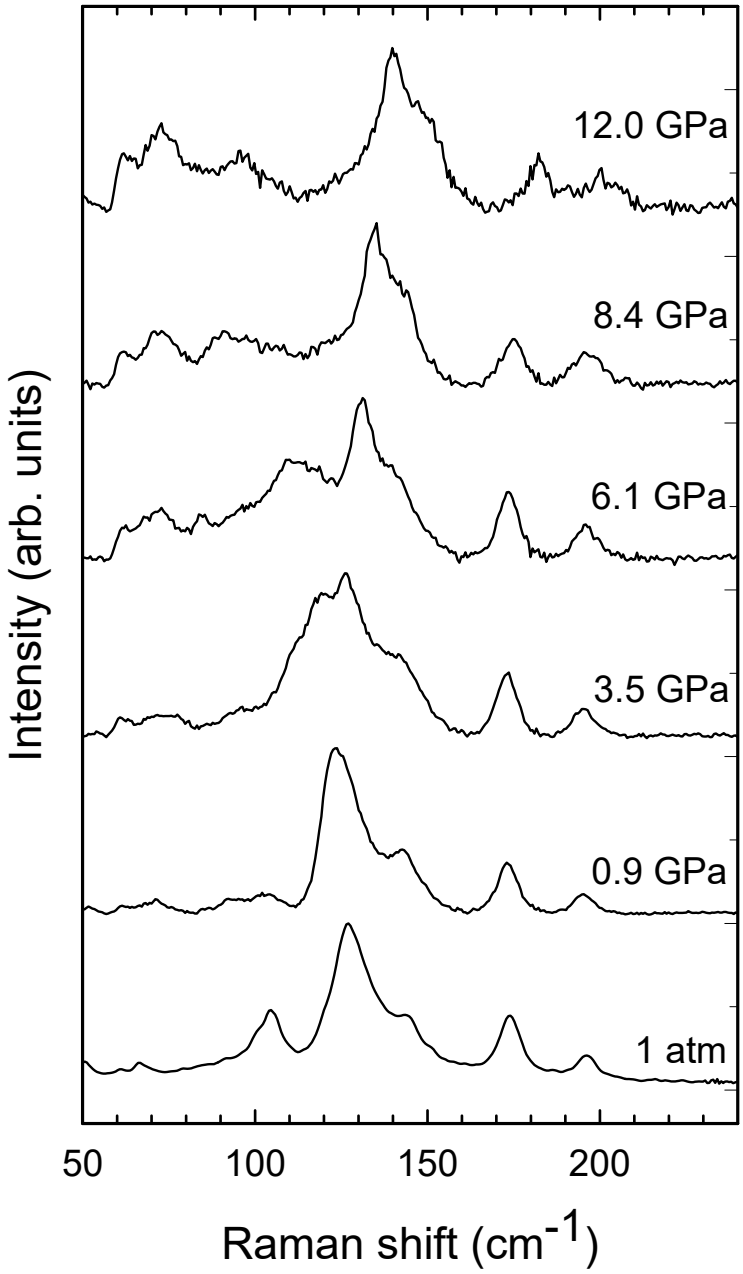

Figure S14. Room-temperature Raman spectra of α-As_2Te_3 at selected pressures under non-hydrostatic conditions.

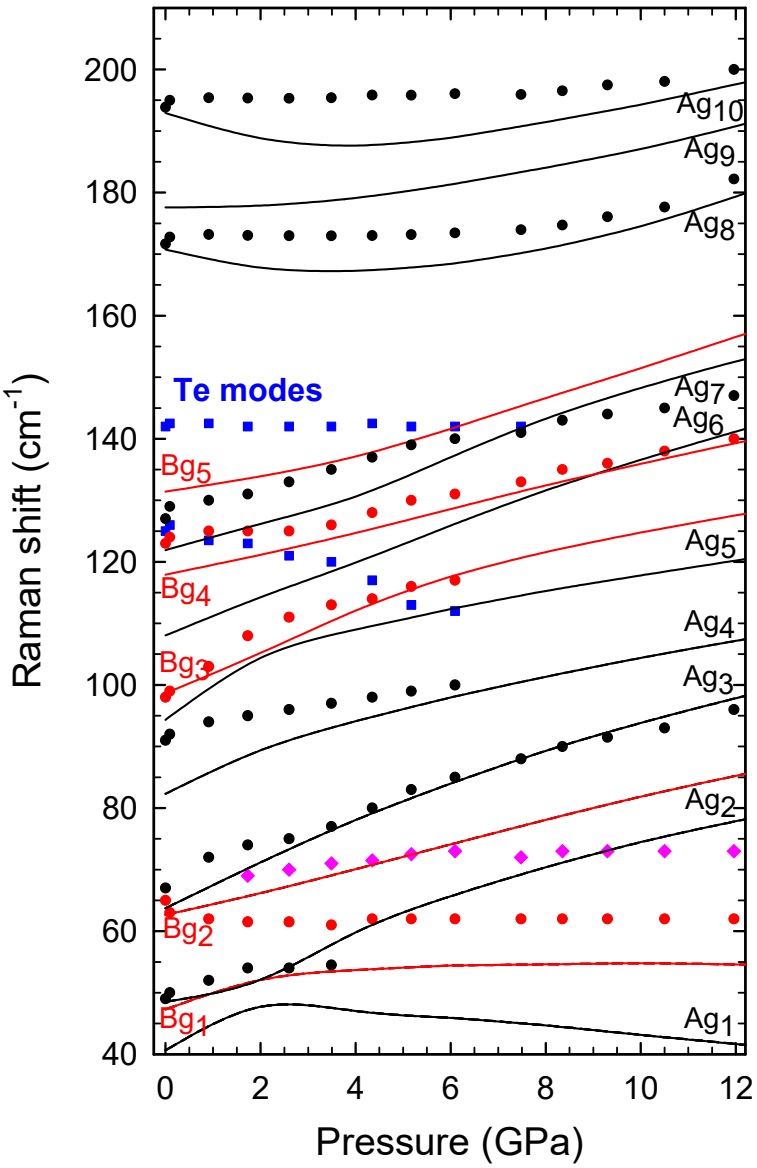

Figure S15. Experimental (symbols) and theoretical (lines) pressure dependence of the Raman-mode frequencies of α-As_2Te_3 under non-hydrostatic conditions. Different colors represent Raman-active modes of different symmetries.

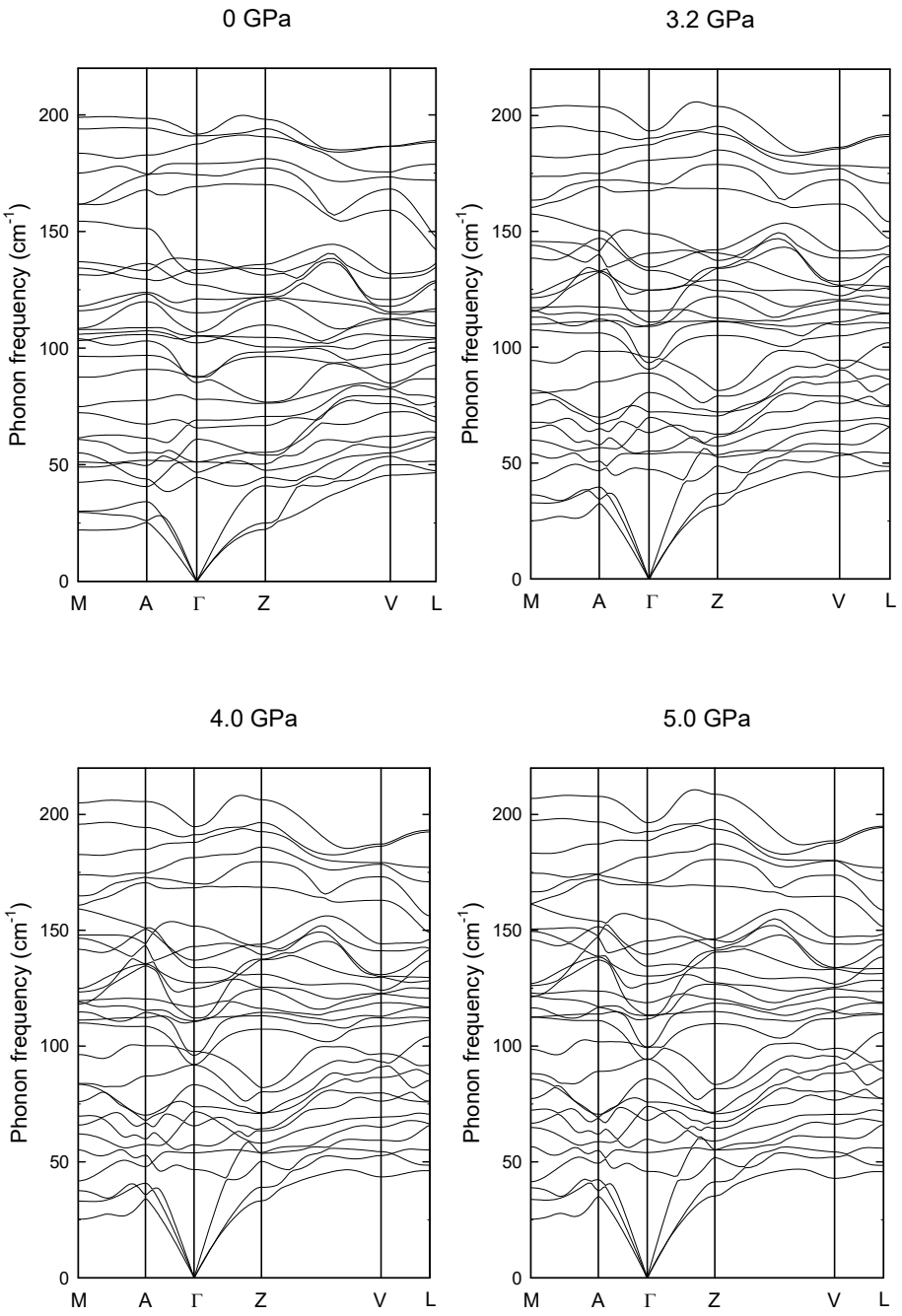
0 GPa
3.2 GPa
4.0 GPa
5.0 GPa
Phonon frequency (cm-1)
0
50
100
150
200
M
A
Γ
Z
V
L

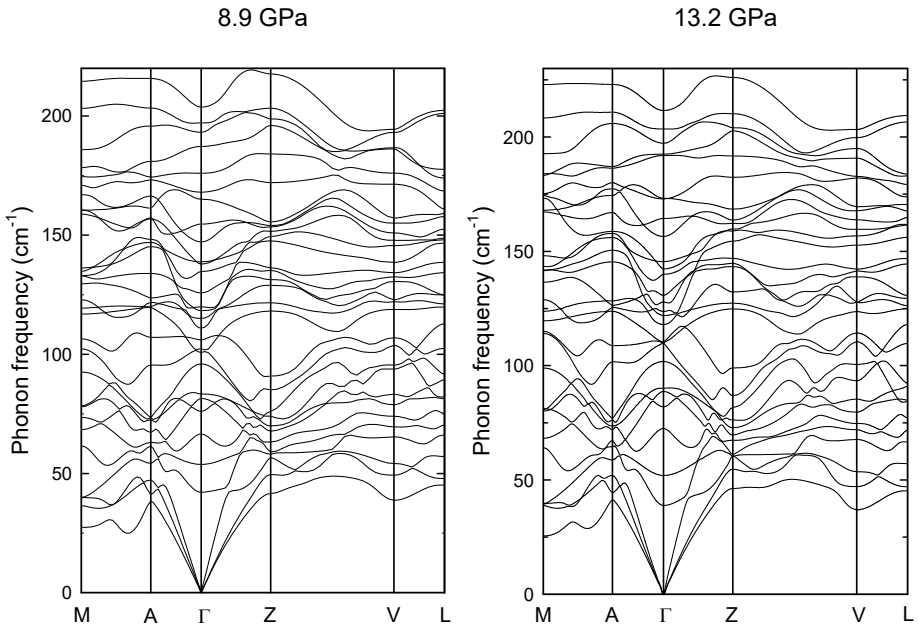

Figure S16. Theoretical phonon dispersion curves of α-As_2Te_3 at different pressures. No soft phonon mode is observed either at Γ or at any other point of the Brillouin zone.

References

[Alekberov 2014] R. I. Alekberov, S. I. Mekhtiyeva, G. A. Isayeva, and A. I. Isayev. Raman Scattering in As-Se-S and As-Se-Te Chalcogenide Vitreous Semiconductors. *Semiconductors.* **2014**, *48*, 800-803.

[Angel 2004-2011] R. J. Angel. http://www.rossangel.com/text_strain.htm

[Canepa 2011] P. Canepa, R. M. Hanson, P. Ugliengo, and M. Alfredsson. J-ICE: a New Jmol Interface for Handling and Visualizing Crystallographic and Electronic Properties. *J. Appl. Crystallogr.* **2011**, *44*, 225-229.

[Carron 1963] G. J. Carron. The Crystal Structure and Powder Data for Arsenic Telluride. *Acta Crystallogr.* **1963**, *16*, 338-343.

[Deng 2015] H. Deng. Theoretical Prediction of the Structural, Electronic, Mechanical and Thermodynamic Properties of the Binary α-As_2Te_3 and β-As_2Te_3. *J. Alloys Compd.* **2015**, *656*, 695-701.

[Deringer 2015] V. L. Deringer, R. P. Stoffel, M. Wuttig, and R. Dronskowski. Vibrational Properties and Bonding Nature of Sb_2Se_3 and their Implications for Chalcogenide Materials. *Chem. Sci.* **2015**, *6*, 5255-5262.

[Efthimiopoulos 2013] I. Efthimiopoulos, J. M. Zhang, M. Kucway, C. Park, R. C. Ewing, and Y. Wang. Sb_2Se_3 under Pressure. *Sci. Rep.* **2013**, *3*, 2665.

[Einaga 2011] M. Einaga, A. Ohmura, A. Nakayama, F. Ishikawa, Y. Yamada, and S. Nakano. Pressure-Induced Phase Transition of Bi_2Te_3 to a bcc Structure. *Phys. Rev. B*. **2011**, *83*, 092102.

[Feng 2014] S. Feng, S. M. Li, and H. Z. Fu. First-Principle Calculation and Quasi-Harmonic Debye Model Prediction for Elastic and Thermodynamic Properties of Bi_2Te_3. *Comp. Mat. Sci.* **2014**, *82*, 45-49.

[Gomis 2011] O. Gomis, R. Vilaplana, F. J. Manjón, P. Rodríguez-Hernández, E. Pérez-González, A. Muñoz, C. Drasar, and V. Kucek. Lattice Dynamics of Sb_2Te_3 at High Pressures. *Phys. Rev. B*. **2011**, *84*, 174305.

[Haussühl 2007] S. Haussühl. *Physical Properties of Crystals. An Introduction*. (Wiley-VCH, Weinheim, **2007**).

[Ibarra-Hernández 2014] W. Ibarra-Hernández, M. J. Verstraete, and J-Y. Raty. Effect of Hydrostatic Pressure on the Thermoelectric Properties of Bi_2Te_3. *Phys. Rev. B.* **2014**, *90*, 245204.

[Jacobsen 2007] M. K. Jacobsen, R. S. Kumar, A. L. Cornelius, S. V. Sinogeiken, and M. F. Nicol. High Pressure X-Ray Diffraction Studies of $Bi_{2-x}Sb_xTe_3$ (x = 0,1,2). *AIP Conf. Proc.* **2007**, *955*, 171-174.

[Lukic 2003] S. R. Lukic, D. M. Petrovic, S. J. Skuban, Lj. Radonjic, and Z. Cvejic. Formation of Complex Structural Units and Structure of As-S-Se-Te-I Glasses. *J. Opt. Adv. Mater.* **2003**, *5*, 1223-12229.

[Ma 2012] Y. M. Ma, G. T. Liu, P. W. Zhu, H. Wang, X. Wang, Q. L. Cui, J. Liu, and Y. M. Ma. Determinations of the High-Pressure Crystal Structures of Sb_2Te_3. *J. Phys: Condens. Matter*. **2012**, *24*, 475403.

[Mendoza-Galván 2000] A. Mendoza-Galván, E. García-García, Y. V. Vorobiev, and J. González-Hernández. Structural, Optical and Electrical Characterization of Amorphous Se_xTe_{1-x} Thin Film Alloys. *Microelectron. Eng.* **2000**, *51-52*, 677-687.

[Nakayama 2009] A. Nakayama, M. Einaga, Y. Tanabe, S. Nakano, F. Ishikawa, and Y. Yamada. Structural Phase Transition in Bi_2Te_3 under High Pressure. *High Pressure Res.* **2009**, *29*, 245-249.

[Pereira 2014a] A. L. J. Pereira, O. Gomis, J. A. Sans, J. Pellicer-Porres, F. J. Manjón, A. Beltrán, P. Rodríguez-Hernández, and A. Muñoz. Pressure Effects on the Vibrational Properties of α-Bi_2O_3: an Experimental and Theoretical Study. *J. Phys.: Condens. Matter*. **2014**, *26*, 225401.

[Polian 2011] A. Polian, M. Gauthier, S. M. Souza, D. M. Triches, J. Cardoso de Lima, and T. A. Grandi. Two-Dimensional Pressure-Induced Electronic Topological Transition in Bi_2Te_3. *Phys. Rev. B.* **2011**, *83*, 113106.

[Sakai 1977] N. Sakai, and H. Fritzsche. Semiconductor-Metal and Superconducting Transitions Induced by Pressure in Amorphous As_2Te_3. *Phys. Rev. B* **1977**, *15*, 973-978.

[Souza 2012] S. M. Souza, C. M. Poffo, D. M. Triches, J. C. de Lima, T. A. Grandi, A. Polian, and M. Gauthier. High Pressure Monoclinic Phases of Sb_2Te_3. *Physica B*. **2012**, *407*, 3781-3789.

[Taylor 1975] P. C. Taylor, S. G. Bishop, and D. L. Mitchell. Infrared Properties of AsxTe1-x Glasses, *Solid State Commun.* **1975**, *16*, 167-170.

[Tverjanovich 2012] A. Tverjanovich, K. Rodionov, and E. Bychkov. Raman Spectroscopy of Glasses in the As-Te System. *J. Solid State Chem.* **2012**, *190*, 271-276.

[Usuki 1996] T. Usuki, K. Saitoh, M. Endo, and O. Uemura. Short-range Order of Amorphous and Liquid As-Te-I System, *J. Non-Cryst. Solids* **1996**, *205-207*, 184-188.

[Vilaplana 2011a] R. Vilaplana, O. Gomis, F. J. Manjón, A. Segura, E. Pérez-González, P. Rodríguez-Hernández, A. Muñoz, J. González, V. Marín-Borras, V. Muñoz-Sanjosé, et al. High-Pressure Vibrational and Optical Study of Bi_2Te_3. *Phys. Rev. B: Condens. Matter Mater. Phys*. **2011**, *84*, 104112.

[Walsh 2011] A. Walsh, D. J. Payne, R. G. Egdell, and G. W. Watson. Stereochemistry of Post-Transition Metal Oxides: Revision of the Classical Lone Pair Model. *Chem. Soc. Rev.* **2011**, *40*, 4455-4463.

[Zallen 1971] R. Zallen, M. L. Slade, and A. T. Ward. Lattice Vibrations and Interlayer Interactions in Crystalline As_2S_3 and As_2Se_3. *Phys. Rev. B.* **1971**, *3*, 4257-4273.

[Zhang 2015] H. Y. Zhang, Y. Cheng, M. Tang, X. R. Chen, and G. F. Ji. First-Principles Study of Structural, Elastic, Electronic and Thermodynamic Properties of Topological Insulator Sb_2Te_3 under Pressure. *Comput. Mater. Sci.* **2015**, *96*, 342-347.

[Zhang 2016] Y. H. Zhang, Y. M. Ma, A. H. Geng, C. Y. Zhu, G. T. Liu, Q. Tao, F. F. Li, Q. L. Wang, Y. Li, X. Wang, et al. Pressure-Induced Electronic Phase Transitions of α-As_2Te_3. *J. Alloys Compd.* **2016**, *685*, 551-558.

[Zhao 2011] J. G. Zhao, H. Z. Liu, L. Ehm, Z. Q. Chen, S. Sinogeikin, Y. S. Zhao, and G. Gu. Pressure-Induced Disordered Substitution Alloy in Sb_2Te_3. *Inorg. Chem.* **2011**, *50*, 11291-11293.

[Zhao 2016] J. G. Zhao, L. X. Yang, Z. H. Yu, Y. Wang, C. Y. Li, K. Yang, Z. G. Liu, and Y. Wang. Structural Phase Transitions and Metallized Phenomena in Arsenic Telluride under High Pressure. *Inorg. Chem.* **2016**, *55*, 3907.

[Zhu 2011] L. Zhu, H. Wang, Y. Wang, J. Lv, Y. Ma, Q. Cui, Y. Ma, and G. Zou. Substitutional Alloy of Bi and Te at High Pressure. *Phys. Rev. Lett.* **2011**, *106*, 145501.

Capítulo 3

Discusión de los resultados

Como se ha visto a lo largo del presente documento, el propósito de esta tesis doctoral es el estudio de las propiedades estructurales, mecánicas, electrónicas y vibracionales de los compuestos de tipo As_2X_3. En esta tesis se han estudiado la arsenolita pura (As_4O_6), el compuesto resultante al medir la arsenolita con He como medio transmisor de presión (MTP) a altas presiones ($As_4O_6 \cdot 2He$), el oropimente (α-As_2S_3) y el telururo de arsénico (α-As_2Te_3). Para llevar a cabo estas investigaciones se han realizado experimentos de espectroscopia Raman y difracción de rayos X (DRX) sobre las muestras en polvo y monocristal de dichos materiales, a temperatura ambiente, tanto a presión ambiente como a altas presiones, complementados con cálculos teóricos *ab initio* para su contraste.

En el estudio publicado en el **primer artículo** sobre la arsenolita, se ha sometido a este compuesto a altas presiones empleando diferentes MTP (He, mezcla de metanol-etanol 4:1 y aceite de silicona), así como sin MTP. En los resultados obtenidos de los diferentes experimentos de DRX, se observa un aumento progresivo del ángulo de Bragg para todos los picos de difracción de esta estructura cúbica con el aumento de la presión, como se espera debido a la disminución de las distancias entre planos cristalográficos cuando se contrae el volumen de la celda unidad sometida a compresión. La ausencia de nuevos picos a alta presión indica claramente que no se produce una transición de fase en el rango de presión estudiado. El As_4O_6 comprimido con metanol-etanol, aceite de silicona y sin MTP, revela la aparición de una amorfización progresiva inducida por presión que viene dada por el progresivo aumento de la anchura de los picos de Bragg a partir de una cierta presión crítica. Sin embargo, al comprimir la arsenolita con He, no hay evidencia de esta amorfización hasta la máxima presión alcanzada en el experimento (29,4 GPa), excepto por un ligero aumento en la anchura de los picos de Bragg a las presiones más elevadas, probablemente debido a una pérdida parcial de hidrostaticidad en el helio.

Los parámetros de red y las posiciones atómicas de la arsenolita se han obtenido mediante refinamiento Rietveld en un amplio rango de presión debido a la calidad relativamente alta de nuestros patrones experimentales de DRX, lo que ha llevado a una obtención precisa de la dependencia con la presión de estos. La ecuación de estado (EdE) de la arsenolita pura, obtenida de los experimentos de compresión usando metanol-etanol, aceite de silicona y sin MTP, da como resultado un módulo de compresión promedio a presión ambiente (β_0) de 7(2) GPa. Este valor está en buena concordancia con la EdE obtenida de los datos teóricos y con el valor de β_0 obtenido a partir de los datos experimentales del As_4O_6 comprimido con He por debajo de 3 GPa.

En los experimentos de dispersión Raman (DR) bajo presión, se observa un aumento progresivo de las frecuencias de los modos activos Raman relativos a la arsenolita con el aumento de la presión, independientemente del MTP no penetrante utilizado y coincidiendo con los resultados sin MTP. La ausencia de nuevos picos a altas presiones indica claramente que no se produce una transición de fase en el rango de presión estudiado, observándose únicamente el desdoblamiento de algunos modos en la muestra comprimida sin MTP. Muchos modos Raman, especialmente en los experimentos sin MTP y con la mezcla de metanol-etanol, experimentan un

ensanchamiento asimétrico progresivo por encima de 10 GPa. Este ensanchamiento es probablemente causado por dos razones: i) El aumento de las interacciones intermoleculares, es decir, el aumento de las interacciones entre las unidades moleculares del As_4O_6, vecinas, que finalmente resulta en una interacción tan grande que produce el inicio de la amorfización inducida por presión, por encima de 15 GPa, o ii) La pérdida de hidrostaticidad de los MTP a partir de esa presión. No se observa tal ensanchamiento de los modos Raman en el experimento realizado con He hasta 30 GPa.

A la vista de los resultados experimentales y teóricos, se puede observar que la compresión de la arsenolita con He exhibe un comportamiento sorprendente por encima de 3 GPa. El volumen de la celda unitaria disminuye al aumentar la presión de manera similar al de la EdE de la arsenolita pura por debajo de 3 GPa, pero por encima de esa presión se produce un salto en la EdE, coherente con un aumento de volumen al entrar el He a formar parte de la estructura. Este salto en la curva *P*-*V* del As_4O_6 comprimido con He se observa en la comparación con las curvas *P*-*V* de la arsenolita pura comprimida con otros MTP. Así, el volumen observado a 3 y 5 GPa es similar, lo que se puede explicar como una compensación entre la disminución de volumen con la presión y el aumento de volumen debido a la incorporación y captura del He.

En el estudio vibracional, cuando la arsenolita es comprimida con He no se observan nuevos picos relativos a la formación de otras fases. Por otro lado, las frecuencias siguen la misma dependencia de la presión que en el resto de los experimentos por debajo de 3 GPa. Sin embargo, por encima de 3 GPa, casi todos los modos Raman sufren un pequeño cambio en la frecuencia que es consistente con un aumento de volumen a esta presión. Así, podemos destacar la presencia de un *anticruce* a 5 GPa en el comportamiento de algunos modos activos Raman de la arsenolita pura. Esto se produce también en el $As_4O_6 \cdot 2He$ a 3 GPa y se vuelve a repetir a 11 GPa.

Una vez hemos comprobado que el He entra en la estructura de la arsenolita pura, nos preguntamos dónde y en qué cantidad. Por eso analizamos la evolución del volumen alrededor de posiciones cristalográficas vacías y que en principio deben seguir las mismas tendencias, tanto experimental como teórica, de la arsenolita pura (8*a*, 16*c* y 16*d*). La evolución de los volúmenes alrededor de estas posiciones Wyckoff (tanto experimental como teórica) muestra una clara evidencia de que el He se introduce en las posiciones 16*d* de la estructura entre 3-5 GPa, quedando atrapado en ellas. Estos resultados se ven confirmados con el análisis de la tendencia de las EdE teóricas simuladas incorporando el He en las distintas posiciones cristalográficas, siendo la EdE teórica del He atrapado en las posiciones 16*d* la que muestra una mejor concordancia con los resultados experimentales obtenidos entre 5 y 30 GPa. Además, la correlación entre el salto producido experimental y teóricamente con helio en y fuera de la posición *16d*, indica una ocupación total de estos huecos. Al estar todo el He en una posición cristalográfica se puede determinar que no es un mero atrapamiento de un material poroso donde el elemento atrapado está heterogéneamente distribuido, sino que en este caso, el helio está formando parte de la red cristalográfica.

En el análisis de los modos Raman, el cambio producido por la utilización de He como MTP es más perceptible en el *anticruce* del fonón que afecta a los modos T_{2g}^3 y T_{2g}^4 correspondientes a los modos de flexión As-O. Como ya discutimos anteriormente, estos modos sufren un *anticruce* aproximadamente a 4,5 GPa cuando se utiliza la mezcla de metanol-etanol como MTP, y de forma similar ocurre cuando se realiza el experimento sin MTP. Sin embargo, cuando la arsenolita se comprime utilizando He como MTP, estos modos se separan por encima de 3 GPa, retrasándose el *anticruce* hasta los 11 GPa, lo cual concuerda con nuestros cálculos teóricos incluyendo el He en las posiciones 16*d*.

Para comprender las diferencias en la estabilidad mecánica del As_4O_6 bajo presión, dependiendo del MTP utilizado, hemos analizado la evolución experimental y teórica de las dos distancias características As-As y As-O con el aumento de la presión. La modificación principal observada con la incorporación del He en la estructura de la arsenolita es el aumento de la distancia As-As más cercana entre unidades moleculares adyacentes (distancia As-As externa). En la compresión de la arsenolita pura, las distancias As-As internas y externas se vuelven casi iguales alrededor de 20 GPa, lo que lleva a fuertes repulsiones estéricas entre las diferentes unidades moleculares que dan lugar a la amorfización inducida por presión. Sin embargo, el atrapamiento del He en la arsenolita por encima de 3 GPa conduce a un aumento considerable de la distancia As-As externa, evitando así el aumento de las interacciones intermoleculares que hacen que la estructura cristalina de la arsenolita sea inestable. Esta característica explica la estabilidad de la arsenolita más allá de los 30 GPa, cuando se comprime con He, y sugiere que la estabilidad de la estructura molecular de la arsenolita está relacionada con la repulsión estérica entre los cationes As que organizan la formación de la estructura de tipo adamantano.

Los cálculos teóricos de la dependencia de la presión de las constantes elásticas y los coeficientes de rigidez elásticos en el As_4O_6 y el As_4O_6 con He en las posiciones 16*d* nos permiten comprender la diferente estabilidad mecánica de la arsenolita comprimida con diferentes MTP. Los criterios de estabilidad generalizada de Born revelan una inestabilidad de Born en la arsenolita debida a la violación del criterio M_2 a 19,7 GPa, una presión cercana a la observada experimentalmente para el inicio de la amorfización en nuestras medidas de DRX a alta presión sin MTP o con MTP distinto del He. Por otro lado, no se observa inestabilidad mecánica en el As_4O_6 con He en las posiciones 16*d*, incluso a 30 GPa, lo cual está totalmente de acuerdo con nuestros resultados experimentales.

Por último, hemos realizado estudios teóricos para discernir si el atrapamiento del He en la estructura de la arsenolita se limita a un simple posicionamiento del He en las posiciones 16*d* de la estructura o puede llevar a la modificación de otras propiedades, e incluso a la reacción con la arsenolita para la formación de un nuevo compuesto con estequiometría $As_4O_6 \cdot 2He$ por encima de 3 GPa. Para ello se han llevado a cabo cálculos teóricos de la estructura de bandas electrónicas del $As_4O_6 \cdot 2He$ a diferentes presiones, así como un análisis de la densidad de carga calculada para la arsenolita pura y la arsenolita con He en las posiciones 16*d* a diferentes presiones en busca de pequeñas interacciones del He con los átomos circundantes. Los resultados de estos cálculos teóricos muestran claras evidencias de

la creación de nuevos enlaces debidos a la reacción del He con la arsenolita. Así, respecto a la estructura electrónica de bandas del $As_4O_6{\cdot}2He$, se observa un claro carácter enlazante-antienlazante en la interacción de los niveles *4s* del As y *1s* del He. Dicha interacción aumenta de intensidad conforme aumenta la presión, llevando a unos niveles cada vez más separados y más curvados, incompatibles con un simple atrapamiento del helio. Por otro lado, el análisis de la densidad electrónica y su laplaciana en el punto crítico del enlace mediante el índice *Non-covalent Interactions* (NCI) nos muestra que la intensidad de esta interacción es similar a la de un enlace por puente de hidrógeno.

Una vez reportada la formación del compuesto $As_4O_6{\cdot}2He$ por encima de 3 GPa, se han ampliado los estudios anteriormente expuestos con el fin de mejorar la comprensión del comportamiento del As_4O_6 y del $As_4O_6{\cdot}2He$ bajo presión, centrándonos en el estudio de las propiedades vibracionales, elásticas y termodinámicas de ambos compuestos. Relativo al **segundo artículo**, la discusión de los resultados de los análisis de las evoluciones de los modos de vibración del As_4O_6 y del $As_4O_6{\cdot}2He$ bajo presión ha sido detallada en las páginas anteriores.

Para concluir el estudio de la dinámica de red, se reportan las curvas de dispersión de fonones a lo largo de las direcciones de alta simetría de la zona de Brillouin, obtenidas de los cálculos teóricos *ab initio*, para ambos compuestos a presiones seleccionadas, lo que nos permite analizar su estabilidad dinámica bajo compresión hidrostática. Se puede observar que no existe ninguna rama de fonones que sufra ablandamiento por debajo de frecuencia cero al aumentar la presión ni en el As_4O_6 hasta 34,7 GPa ni en el $As_4O_6{\cdot}2He$ hasta 35,5 GPa. Es por ello que podemos deducir que la estructura cúbica de ambos compuestos es dinámicamente estable al menos hasta esas presiones.

Al aplicar una tensión uniforme sobre una muestra cristalina, las propiedades elásticas se describen mediante los coeficientes de rigidez elástica, o coeficientes de tensión-deformación, que dependen directamente de la presión aplicada en el caso de que se produzca una compresión uniforme (presión hidrostática). En las relaciones entre estos coeficientes se basan las distintas constantes elásticas, que podemos estudiar en los materiales, como los módulos elásticos (módulo de compresión B, módulo de cizalladura o módulo elástico tangencial G, y módulo de Young o módulo elástico longitudinal E), el coeficiente de Poisson v, la dureza H, la densidad ρ, o las velocidades de transmisión de onda elástica longitudinal v_{lon}, transversal v_{trans} y media v_{med}.

Los valores calculados teóricamente para el módulo de compresión B_H, empleando la aproximación de Hill, son 9,8 (9,2) GPa para el As_4O_6 ($As_4O_6{\cdot}2He$), que están bastante de acuerdo con los valores de B_0 = 7,6 (6,4) GPa obtenidos de nuestros cálculos estructurales para el As_4O_6 ($As_4O_6{\cdot}2He$). Además, ambos valores son comparables a los valores experimentales de B_0 = 7(2) GPa y B_0 = 4(2) GPa, para el As_4O_6 y el $As_4O_6{\cdot}2He$ respectivamente. Dada la similitud de los resultados obtenidos por los tres métodos, podemos confiar en la exactitud de nuestros cálculos de constantes elásticas, y realizamos las comparaciones entre el resto de los valores obtenidos para el As_4O_6 y el $As_4O_6{\cdot}2He$.

Al comparar el módulo de compresión y el módulo de cizalladura, G_H = 9,3 (10,7) GPa para el As_4O_6 (As_4O_6·2He), observamos la diferencia entre el comportamiento elástico de ambos compuestos. En el As_4O_6 el módulo de compresión es mayor que el módulo de cizalladura, mientras que en el As_4O_6·2He se observa lo contrario, esto significa que el As_4O_6 es más resistente a la compresión que a los esfuerzos cortantes, mientras que el As_4O_6·2He es más resistente a los esfuerzos cortantes que a los de compresión.

El coeficiente de Poisson proporciona información sobre las características de las fuerzas de enlace y los enlaces químicos. El valor del coeficiente de Poisson, en la aproximación de Hill, es ν_H = 0,14 (0,08) para el As_4O_6 (As_4O_6·2He). Este valor indica que las fuerzas de enlace interatómico son predominantemente no centrales (ν < 0,25) y que el enlace direccional intramolecular e intermolecular es predominante a 0 GPa.

El cociente B_H/G_H es una relación simple que vincula empíricamente las propiedades plásticas de un material con sus módulos elásticos, de forma que una alta proporción de B_H/G_H está asociada con la ductilidad, mientras que una baja proporción corresponde a la fragilidad. El valor crítico para la relación B_H/G_H es alrededor de 1,75, límite entre los materiales dúctiles y los frágiles. En nuestro estudio, hemos encontrado valores de B_H/G_H a 0 GPa por debajo de 1,75 para ambos compuestos. Por lo tanto, ambos son frágiles a presión ambiente, siendo el As_4O_6·2He más frágil que el As_4O_6.

Una de las propiedades elásticas de los cristales con mayor importancia tanto para la ciencia de la ingeniería como para la física de los cristales es la anisotropía elástica, ya que está altamente relacionada con la posibilidad de inducir microrroturas en los materiales. Esta anisotropía se puede cuantificar con el factor de anisotropía Zener A, de forma que, si A = 1, no existe anisotropía, pero, cuanto más difiere este parámetro de 1, más elásticamente anisótropa es la estructura cristalina. Los valores para el As_4O_6 (As_4O_6·2He) son A = 1,15 (0,59), siendo el valor para As_4O_6 más cercano a 1 que para el caso del As_4O_6·2He, por lo que este último es más elásticamente anisótropo que el primero a 0 GPa.

En el análisis de la dependencia de la presión de los módulos elásticos B, G y E, el coeficiente de Poisson, la relación B/G y la anisotropía Zener A, en el As_4O_6 y el As_4O_6·2He, se puede observar que el módulo de compresión B_H aumenta con la presión alcanzando un valor máximo cercano a 115 GPa en ambos compuestos a 20 GPa. Por el contrario, los módulos de G_H y E_H aumentan con la presión hasta 9 GPa en el As_4O_6 y disminuyen para presiones mayores. Este comportamiento es diferente al del As_4O_6·2He donde tanto G_H como E_H aumentan con la presión hasta la presión máxima calculada (35,5 GPa).

Por otro lado, el coeficiente de Poisson muestra una curiosa dependencia con la presión en ambos compuestos. Así, aumenta fuertemente con la presión hasta 2 GPa y luego tiende a saturarse por encima de esta presión alcanzando un valor de 0,46 (0,32) a 20 GPa para el As_4O_6 (As_4O_6·2He). Estos valores indican un incremento de la ductilidad y del comportamiento metálico, es decir, la pérdida progresiva de la direccionalidad del enlace interatómico, al aumentar la presión en ambos

compuestos. La aproximación del coeficiente de Poisson del As_4O_6 a 0,5 (límite superior del coeficiente de Poisson) cerca de 20 GPa es probablemente debida a la tendencia del As_4O_6 a una inestabilidad mecánica. La relación *B/G*, que está relacionada con el coeficiente de Poisson, también aumenta con la presión en los dos compuestos, siendo el aumento moderado en el $As_4O_6{\cdot}2He$ y abrupto en el As_4O_6 por encima de 10 GPa, lo que sugiere la presencia de una inestabilidad mecánica en este último compuesto.

El factor de anisotropía Zener *A* también muestra un comportamiento bastante diferente en ambos compuestos. Aumenta considerablemente en el As_4O_6, especialmente por encima de 10 GPa, mientras que permanece casi constante (alrededor de 0,6) en el $As_4O_6{\cdot}2He$. Nuevamente, estos resultados indican que la anisotropía elástica aumenta notablemente en el As_4O_6 con la presión, pero permanece constante en el $As_4O_6{\cdot}2He$. Por lo tanto, el fuerte aumento de la anisotropía elástica en el As_4O_6 con la presión también podría entenderse como una señal de inestabilidad mecánica en la arsenolita a alta presión.

La dureza Vickers H_v, propiedad generalmente relacionada con las propiedades elásticas y plásticas de un material, es de 4,2 (5,8) GPa para el As_4O_6 ($As_4O_6{\cdot}2He$) a presión ambiente, siendo el $As_4O_6{\cdot}2He$ más duro que el As_4O_6. Como ambos compuestos tienen una dureza menor que 10 GPa se pueden considerar como relativamente blandos. En la evolución de la dureza con la presión se observa que el H_v disminuye a medida que aumenta la presión para ambos compuestos, siendo destacable la disminución en el caso del As_4O_6 donde H_v se aproxima a 0 GPa a una presión de 20 GPa. Este hecho está relacionado con el aumento de la ductilidad (relación *B/G*) con la presión estudiado anteriormente, de manera que ambos compuestos se ablandan a medida que la presión aumenta, en buena concordancia con el aumento de su ductilidad.

Finalmente, una propiedad elástica que es fundamental en el estudio de las Ciencias de la Tierra, para la interpretación de las ondas sísmicas, es la velocidad promedio de transmisión del sonido, v_m, que depende de las velocidades de las ondas elásticas transversales y longitudinales del material policristalino, v_{trans} y v_{lon}. Las velocidades de las ondas obtenidas, a 0 GPa, son v_m = 1678,0 (1838,1) m/s, v_{trans} = 1529,6 (1684,1) m/s y v_{lon} = 2359,8 (2495,3) m/s para el As_4O_6 ($As_4O_6{\cdot}2He$), siendo mayores para el $As_4O_6{\cdot}2He$ que para el As_4O_6 debido al mayor valor del módulo de cizalladura *G*, y a la densidad ρ ligeramente más pequeña, en el primero que en el último. El estudio de la evolución de las velocidades de las ondas elásticas con la presión muestra cómo la v_{lon} aumenta con la presión alcanzando los valores de 4725 (5580) m/s a 20 GPa para el As_4O_6 ($As_4O_6{\cdot}2He$). Un comportamiento similar es observado para las velocidades v_{trans} y v_{med} en el $As_4O_6{\cdot}2He$, mientras que las correspondientes v_{trans} y v_{med} aumentan en el As_4O_6 alcanzando sus valores máximos alrededor de los 6 GPa y disminuyendo por encima de esta presión.

Para concluir la discusión de los resultados obtenidos en el estudio de la arsenolita y el $As_4O_6{\cdot}2He$ bajo presión, se presentan los resultados de los parámetros que nos permiten comprender el comportamiento termodinámico de estos compuestos.

La temperatura de Debye, θ_D, es un parámetro fundamental para el estudio de las propiedades termodinámicas, que se correlaciona con muchas propiedades físicas de los sólidos, como el calor específico, las constantes elásticas y la temperatura de fusión. Los valores de θ_D a 0 GPa, utilizando la aproximación de Hill, son 196,2 (222,7) K para el As_4O_6 (As_4O_6·2He), ligeramente mayor en este último compuesto. En la evolución de la temperatura de Debye con la presión, se observa que θ_D sigue una tendencia similar a v_m, es decir, aumenta a bajas presiones en ambos óxidos y disminuye por encima de 8 GPa en el As_4O_6 mientras que aumenta en el As_4O_6·2He al menos hasta 35 GPa.

Por último, la conductividad térmica, κ, es la propiedad de un material que indica su capacidad para conducir el calor. Los valores de la conductividad térmica mínima, κ_{min}, a presión ambiente, usando la aproximación de Hill, son 0,36 (0,42) $Wm^{-1}K^{-1}$ para el As_4O_6 (As_4O_6·2He), por lo tanto, ambos materiales tienen una conductividad baja. La evolución de κ_{min} con la presión es muy similar a la de θ_D en ambos compuestos. Aumenta primero con la presión para disminuir posteriormente debido a la disminución de v_m con la presión, en el As_4O_6, mientras que aumenta con la presión hasta 35 GPa en el As_4O_6·2He. La disminución de κ_{min} con la presión en el As_4O_6 también puede explicarse por la disminución de la resistencia a la tracción del As_4O_6 a medida que la presión aumenta por encima de 9 GPa.

El siguiente compuesto estudiado en esta tesis ha sido el oropimente, **tercer artículo**, el cual ha resultado ser un material muy interesante en el desarrollo de nuestras investigaciones. Los primeros cálculos teóricos *ab initio*, para presiones hasta 12-15 GPa, se realizaron como un paso previo a la toma de datos experimentales en las fases oropimente (monoclínica) y anoropimente (triclínica) del sulfuro de arsénico (As_2S_3), sin embargo, los descubrimientos posteriores en el estudio experimental del oropimente necesitaron de una ampliación de dichos cálculos para facilitar la comprensión del comportamiento de este compuesto a altas presiones.

En primera instancia, la evolución de las distancias interatómicas con la presión en el oropimente y el anoropimente se reportaron, teniendo en cuenta las interacciones de van der Waals (vdW) entre las capas que forman estos compuestos, hasta la presión de 15 GPa. Se observó una disminución de las distancias entre átomos vecinos al aumentar la presión en ambos compuestos, excepto en el caso de la distancia entre el As1 y el S3, que tiene una tendencia claramente ascendente en el oropimente, mientras que, en el anoropimente, comienza con una disminución de la distancia hasta 11 GPa, presión a partir de la cual comienza a ascender.

Las curvas de energía-volumen (*E-V*) de ambas fases se han calculado empleando diferentes funcionales de intercambio y correlación de energía (XC), tanto incluyendo como sin incluir las interacciones de vdW, que muestran los efectos de las diferentes aproximaciones. En general, la inclusión de las interacciones de vdW disminuye el volumen de equilibrio y da como resultado curvas *E-V* con un mínimo mejor definido, en comparación con las curvas *E-V* sin considerar dichas interacciones vdW; es decir, la inclusión de las interacciones de vdW mejora la estabilidad del estado de presión cero. En este sentido se ha observado que los

funcionales PBEsol XC y PBE XC con la interacción de vdW proporcionan los resultados más cercanos a los valores experimentales de V_0.

Como cierre de la presentación de los primeros cálculos teóricos, se ha reportado la evolución de las frecuencias de los modos de los fonones en el centro de la zona de Brillouin (punto Γ) bajo presión para las dos fases. Los resultados de este trabajo han sido muy útiles para el estudio experimental y la tentativa de asignación de los modos de vibración posteriores.

En el **cuarto artículo** se presenta un estudio experimental y teórico del comportamiento del oropimente bajo presión (α-As_2S_3). Para comprender el comportamiento estructural de este compuesto bajo presión es conveniente tener presente que es un material laminar caracterizado por tener capas corrugadas (o en zigzag) extendidas a lo largo del plano *ac*, que están vinculadas por las interacciones vdW entre capas a lo largo del eje *b*. En condiciones ambientales, cada átomo As1 y As2 está unido por enlaces covalentes a un átomo S1, un S2 y un S3 a distancias de alrededor de 2,3 Å, lo que lleva a una coordinación triple del As. Además, cada átomo As1 y As2 tiene dos átomos vecinos de S en la misma capa que están alejados a distancias superiores a 3,0 Å y otros dos átomos vecinos de S en una capa adyacente a distancias superiores a 3,5 Å. Teniendo en cuenta la diferencia de las distancias As-S, podemos considerar la estructura del oropimente como una disposición de pirámides AsS_3 que forman unidades tetraédricas AsS_3E, donde E se refiere al par de electrones solitario (PES) del átomo de As. Por lo tanto, cada capa se puede describir alternativamente mediante una disposición de dos unidades AsS_3E tetraédricas, es decir, las formadas por los dos átomos de As no equivalentes, cada uno rodeado por tres átomos de S y el correspondiente PES del catión que apunta hacia el espacio intermedio entre las capas. El fuerte PES del As distorsiona la distribución electrónica y la geometría de las unidades poliédricas, lo que conduce a la estructura en capas del oropimente.

El espectro vibracional del oropimente a presión ambiente se caracteriza por la separación entre dos regiones de fonones: una región de baja frecuencia (por debajo de 200 cm^{-1}) y una región de alta frecuencia (por encima de 260 cm^{-1}), con una ausencia de fonones entre estas (gap fonónico). Entre los modos Raman medidos por debajo de 250 cm^{-1} y por encima de 280 cm^{-1}, los modos más intensos son los de la región de alta frecuencia entre 350 y 360 cm^{-1}.

Una característica interesante de las vibraciones atómicas asociadas a algunos modos activos Raman e infrarrojos es que estas evidencian que los átomos de la misma cadena espiral (As1, S1, As2 y S2) vibran en fase o fuera de fase, mientras que los átomos S3 que interconectan las cadenas espirales vibran de una manera bastante diferente a la de los otros cuatro átomos no equivalentes. Esta observación evidencia claramente la distribución en forma de cadena espiral de las capas del oropimente.

En el estudio de la evolución estructural del oropimente, hasta la presión de 26,6 GPa, los difractogramas obtenidos de las medidas de DRX de polvo muestran un aumento progresivo de la anchura de los picos de Bragg, que se puede explicar en el marco de una pérdida progresiva de las condiciones hidrostáticas. El análisis de Le

Bail a partir de estos difractogramas ha permitido la obtención de los parámetros de red del α-As_2S_3 a diferentes presiones, que han sido contrastados con los obtenidos en los cálculos teóricos *ab initio* (con y sin vdW) descritos anteriormente.

En la representación de la evolución con la presión del volumen de la celda unidad se observa una disminución continua del mismo, que concuerda con los datos teóricos con vdW hasta los 10 GPa, siendo más parecida a la simulación sin tener en cuenta la interacción vdW a partir de esta presión. Este resultado indica que el oropimente es más incompresible por encima de los 10 GPa, debido probablemente a la pérdida de las condiciones cuasi hidrostáticas del MTP (metanol-etanol 4:1) por encima de esta presión. La dependencia de la presión de los parámetros de red experimentales y teóricos del α-As_2S_3 hasta 26,6 GPa también muestra una disminución monótona y suave, sin cambios aparentes. La buena concordancia entre los cálculos teóricos y los resultados experimentales a temperatura ambiente, nos permite concluir que no se produce una transición de fase de primer orden en el rango de presiones estudiado. Además, la dependencia de la presión de los parámetros de red no evidencia anomalías en la región cercana a 10 GPa que pudieran ser indicativas de cualquier transición estructural.

El análisis de la compresibilidad axial en esta estructura monoclínica se ha realizado mediante el estudio teórico del tensor de compresibilidad isotérmico, β_{ij}, que relaciona el estado de tensión de un cristal con el cambio en la presión que lo indujo. De acuerdo con los resultados obtenidos, la compresibilidad a lo largo del eje *a* (eje espiral contenido en el plano de las capas) es algo mayor a la del eje *b* (eje perpendicular a las capas) y mucho más grande que la del eje *c* (contenido también en el plano de las capas) hasta la presión de 23 GPa. Este es un resultado inesperado para un cristal laminar cuyas capas se extienden en el plano *ac*, ya que normalmente el eje perpendicular a las capas es el más compresible. También es una clara indicación del carácter acicular (casi molecular) de las capas, siendo coherente con la naturaleza en forma de cadena espiral de las capas del oropimente y con la pequeña conectividad de las capas en espiral a lo largo del eje *a*. Curiosamente, alrededor de 23 GPa, se alcanza una regularización repentina de las tres compresibilidades axiales a aproximadamente el mismo valor con un rápido cambio de la dirección de máxima compresibilidad alrededor de esta presión. A 24 GPa, la dirección de máxima compresibilidad se encuentra a lo largo del eje *b* y, por encima de 27 GPa, la dirección de máxima compresibilidad se encuentra nuevamente dentro del plano *ac*, pero ahora está cerca del eje *c*. El cambio drástico de la dirección de máxima compresibilidad observada por encima de 23 GPa puede considerarse como la característica más significativa de la variación de las propiedades asociadas a la estructura de baja presión.

La dependencia teórica y experimental de las relaciones axiales con la presión (*c/a*, *b/a* y *c/b*) en el α-As_2S_3 muestran una tendencia monótona hasta 20 GPa, que se reproduce bien en nuestros cálculos teóricos que incluyen las interacciones de vdW. A partir de esta presión, las pendientes revelan un claro cambio de tendencia, donde las tres relaciones parecen volverse insensibles a la presión hasta 50 GPa, observándose un comportamiento similar en la dependencia con la presión del ángulo *β*. El cambio en la tendencia de *c/a* con la presión no necesariamente

garantiza un cambio en la densidad electrónica de los estados cerca del nivel de Fermi, que conduciría a una transición topológica electrónica (TTE), como se ha supuesto en otros trabajos, sino que puede ser indicativo de una transición de fase isoestructural (TFI) inducida por presión.

Para demostrar este hecho, hemos analizado la dependencia de la presión de los parámetros atómicos internos de las cinco posiciones atómicas no equivalentes del α-As_2S_3. Los resultados más notables son los observados para las tres coordenadas de los átomos As1 y As2, que muestran una clara tendencia hacia coordenadas fijas por encima de 18 (25) GPa, como se obtiene para los cálculos sin (con) vdW. Este resultado se produce a presiones similares a las que se observó el cambio de dirección de la máxima compresibilidad, lo que indica claramente una modificación del comportamiento del material en la fase de baja presión. Un resultado notable, derivado de la dependencia con la presión de las coordenadas atómicas, es la agrupación y regularización de muchas distancias interatómicas As-S teóricas alrededor de 18 (25) GPa. Como consecuencia, hay un aumento de la coordinación de As1 de 3, a 0 GPa, a más de cinco (5 + 2), por encima de 20 GPa, de forma que las unidades poliédricas del As1 (As2) del oropimente pasan de una coordinación triple a una coordinación siete (cinco) sin un cambio en el grupo espacial.

En resumen, la regularización de las compresibilidades axiales, la tendencia de las coordenadas libres del As hacia unas coordenadas fijas, y la similitud de las coordenadas *x* y *z* mostrada por las posiciones Wyckoff de los átomos As1, S2 y S3, indican la presencia de una TFI inducida por presión.

Para estudiar el efecto de la presión sobre las propiedades vibracionales del oropimente y comprender mejor su comportamiento a altas presiones, hemos realizado medidas de DR hasta 14,5 GPa, que se han comparado con los resultados teóricos previamente reportados. En el análisis de los espectros Raman, a temperatura ambiente y en condiciones hidrostáticas, podemos observar que el modo de frecuencia más alta de la región de bajas frecuencias, ubicado cerca de 200 cm^{-1} a presión ambiente, muestra un aumento de la intensidad a medida que aumenta la presión. Este hecho respalda el argumento de la ausencia de cualquier transición de fase de primer orden hasta la presión de 14,5 GPa, de acuerdo con nuestros resultados de DRX.

A pesar de la dificultad en la asignación de los modos de vibración, se ha realizado una tentativa de la misma mediante el estudio de la dependencia de la presión de los modos activos Raman en combinación con los cálculos de dinámica de red sobre la base de la correlación de las frecuencias y sus coeficientes de presión. Las frecuencias experimentales y teóricas de los modos activos Raman no muestran un comportamiento monótono simple al aumentar la presión, de hecho, muchos modos Raman exhiben un comportamiento complejo bajo presión con *cruces* y *anticruces* de modos con simetrías diferentes e iguales, respectivamente. Este complejo comportamiento se deriva de la presencia de 30 modos activos Raman en una pequeña región de frecuencias entre 30 y 400 cm^{-1}. A pesar del complejo comportamiento observado en nuestros modos teóricos activos Raman, varios modos experimentales han mostrado un comportamiento consistente con los modos

teóricos. En particular, hemos encontrado una reducción experimental con la presión en el gap de fonones, un *anticruce* de los modos Raman cerca de 150 cm^{-1} próximo a 2 GPa, y la división de varios modos Raman ubicados cerca de 350 cm^{-1}.

En un estudio más pormenorizado se observa que los modos rígidos de cizalla (o modos rígidos transversales) A_g^1 y A_g^2, localizados a 26 y 37 cm^{-1}, y el modo B_g (modo B_g^2), localizado a 69 cm^{-1}, muestran el mayor aumento relativo de frecuencia bajo presión (0,24, 0,13 y 0,15 GPa^{-1}, respectivamente). Además, el modo B_g^2 muestra los mayores coeficientes de presión experimentales y teóricos (10,5 y 10,3 cm^{-1}/GPa, respectivamente). Este resultado es bastante sorprendente porque, de hecho, se espera que el mayor coeficiente de presión corresponda al modo rígido de compresión (o modo rígido longitudinal) B_g^1, ubicado en 62 cm^{-1}, ya que este modo generalmente muestra frecuencias y coeficientes de presión mayores que los modos transversales en materiales laminados con interacciones vdW entre las capas. Esta dependencia anómala de la presión del modo longitudinal del oropimente se puede entender al considerar la existencia de un *anticruce* (que ya se produce a presión ambiente) entre los modos B_g^1 y B_g^2. De hecho, el coeficiente de presión del modo B_g^1 "desnudo" (si no se produjeran *anticruces* con modos de la misma simetría) es tan grande, cuando se compara con otros modos Raman, que este modo sufre *anticruces* con hasta cuatro modos B_g (hasta B_g^5) en el rango de presiones entre 0 y 15 GPa. Este *anticruce* nos permite explicar el pequeño coeficiente de presión del modo B_g^1 y el gran coeficiente de presión del modo B_g^2 del oropimente, debido al intercambio de caracteres entre ambos modos.

Otra característica sorprendente del oropimente es la gran cantidad de modos Raman que tienen coeficientes de presión negativos a presión ambiente. Este resultado es confirmado tanto por los datos experimentales como por los teóricos. Esta situación es bastante diferente a la observada en materiales con estructura similar al α-As_2S_3, ya que los tres ejes *a*, *b* y *c* del oropimente sufren una contracción bajo compresión, por lo que la explicación de los coeficientes de presión negativa no está relacionada con el alargamiento de ningún eje. Una explicación plausible para el ablandamiento de varios fonones en diferentes rangos de presión es el aumento de las distancias intracapa As1-S3, As2-S2 y As2-S3 (As1-S1) por encima de 0 (10) GPa. En particular, los cambios en el coeficiente de presión de algunos modos activos Raman experimentales y teóricos se han observado alrededor de 4 GPa en el α-As_2S_3, lo que podría atribuirse a los fuertes cambios de las distancias interatómicas alrededor de estas presiones.

En el estudio de los modos de vibración teóricos se observa un notable ablandamiento en la región entre 18 y 26 GPa, donde se prevé la TFI de acuerdo con nuestros cálculos. Para comprobar la posibilidad de que ocurra un TFI de segundo orden en el α-As_2S_3, hemos estudiado las curvas de dispersión de fonones calculadas a diferentes valores de presión. Al no observar ningún modo blando hasta 30 GPa, podemos concluir que la TFI inducida por presión que ocurre en el oropimente por encima de 20 GPa debe ser de un orden superior a 2, es decir, una TFI de origen electrónico, como las TTE inducidas por presión observadas en otros sesquicalcogenuros del grupo 15.

Para finalizar la visión del comportamiento del oropimente bajo presión, así como para completar la evaluación de la posibilidad de la existencia de una TTE inducida por presión en el oropimente, se han llevado a cabo los cálculos *ab initio* de estructura electrónica de bandas, a diferentes presiones, para identificar posibles cambios en el máximo de la banda de valencia (MBV) y el mínimo de la banda de conducción (MBC) que podrían estar relacionados con una TTE. Los resultados de estos cálculos muestran que el oropimente es un semiconductor a presión ambiente (gap indirecto teórico subestimado de 1,7 eV, experimental de 2,7 eV), con el MBV y el MBC ubicados a lo largo del segmento de alta simetría de las direcciones Y-Γ y Γ-Z, respectivamente.

Hay cambios considerables en el MBV y el MBC a altas presiones. Ambas bandas de valencia y conducción muestran una baja dispersión a través de la zona de Brillouin a 0 GPa, pero una alta dispersión por encima de 20 GPa. Las bandas planas a 0 GPa reflejan el carácter 2D del oropimente, mientras que las bandas altamente dispersas por encima de 20 GPa reflejan el carácter 3D del oropimente por encima de esta presión. Además, se produce una variación del MBV entre 20 y 30 GPa, con el MBV a 30 GPa desplazado a lo largo de la dirección Γ-Y de alta simetría. El cruce de una de estas bandas con el nivel de Fermi, observado por encima de 20 GPa, modifica la topología de la superficie de Fermi, lo que sugiere una posible TTE inducida por presión por encima de 20 GPa en el α-As_2S_3.

El gap indirecto calculado teóricamente muestra una fuerte disminución con la presión de 1,7 eV a 0 GPa a 0 eV a 26 GPa, evidenciando una transición semiconductor-metal por encima de 26 GPa. La disminución del gap electrónico muestra un coeficiente de presión teórico de -0.11 eV/GPa, que está muy de acuerdo con una estimación experimental previa del coeficiente de presión del gap óptico (-0.14 eV/GPa). Por lo tanto, nuestra estimación teórica de la dependencia de la presión del gap sugiere que la metalización de este material debe ocurrir muy por encima de los 40 GPa.

Los resultados obtenidos en el estudio de la dependencia de la presión de las propiedades estructurales, vibracionales, ópticas y eléctricas del α-As_2S_3 bajo presión, pueden ser entendidos a la luz de un caso especial de formalismo de enlace resonante, recientemente denominado como enlace metavalente. Este nuevo tipo de enlace está principalmente ubicado entre el enlace covalente tipo *p* y el enlace metálico, y es característico de un nuevo tipo de materiales denominados "metales incipientes", ya que muestran características cercanas a las de los metales. Estos materiales exhiben propiedades extraordinarias que los convierten en candidatos ideales para materiales con cambio de fase, materiales termoeléctricos y aislantes topológicos. Este tipo de enlace se produce en materiales en los que existe una deficiencia de electrones de valencia en la celda unidad para formar un gran número de enlaces, en cuyo caso, los pocos electrones de valencia disponibles deben compartirse (resonar) entre varios enlaces.

En particular, el comportamiento del oropimente entre 0 y 20 GPa se puede considerar como el proceso de cambio de un enlace covalente de tipo *p* hacia un enlace metavalente a altas presiones, y la igualdad de las distancias intracapa As-S

por encima de 18 (25) GPa, calculadas teóricamente sin (con) vdW, está de acuerdo con el cambio de la naturaleza de los enlaces As-S de covalente a metavalente. Para confirmar este hecho, hemos investigado el carácter enlazante del oropimente a diferentes presiones, estudiando por una parte la función de localización de electrones (FLE) a lo largo de las siete distancias As-S con los vecinos próximos, y por otra parte, el tensor dieléctrico y las cargas efectivas de Born. Los resultados obtenidos de estas investigaciones muestran que el comportamiento a altas presiones del oropimente, al igual que el de otros sesquicalcogenuros del grupo 15, se entiende perfectamente en el marco del enlace metavalente.

En el **quinto artículo** de la presente tesis se presenta un estudio experimental y teórico del telururo de arsénico bajo presión, el cual forma parte de los sesquicalcogenuros del grupo 15 que han sido ampliamente estudiados por sus destacadas propiedades termoeléctricas. De forma similar al oropimente, la fase α del As_2Te_3 presenta una estructura cristalina laminar compuesta por capas en zigzag apiladas principalmente a lo largo del eje *a*, que están unidas por débiles fuerzas de vdW. A su vez, las capas en zigzag están formadas por barras que se extienden a lo largo del eje *b*, que están unidas por fuerzas As-Te iónicas-covalentes débiles, principalmente a lo largo del eje *c*. En el α-As_2Te_3, los cinco átomos independientes (As1, As2, Te1, Te2 y Te3) ocupan las posiciones Wyckoff 4i, estando todos ellos localizados en los planos $y = 0$ e $y = 1/2$. Los dos átomos As1 y As2 independientes tienen una coordinación 5 y 6, respectivamente. En particular, los átomos de Te alrededor del As2 forman un octaedro distorsionado con distancias As-Te alrededor de 2,8 Å, mientras que los átomos de Te alrededor del As1 forman una pirámide de base cuadrada en una coordinación 3 + 2 con tres distancias As-Te alrededor de 2,7 Å y dos distancias alrededor de 3,2 Å.

Los patrones de DRX en polvo bajo presión del α-As_2Te_3, hasta 17,2 GPa, muestran cómo esta estructura monoclínica de baja presión se mantiene estable hasta 14 GPa. Por encima de esta presión se evidencia una transición estructural reversible a la fase γ-As_2Te_3. No se muestra una transición a una fase β-As_2Te_3 ni a una β'-As_2Te_3, ya que nuestro patrón DRX a 17,2 GPa es muy parecido a los obtenidos para los compuestos γ-Bi_2Te_3 y γ-Bi_2Se_3, compuestos monoclínicos similares al α-As_2Te_3.

Los refinamientos mediante el método de Rietveld hasta los 6 GPa y el análisis de Le Bail para presiones superiores, nos han permitido obtener los parámetros estructurales del α-As_2Te_3 a diferentes presiones, que han sido contrastados con los obtenidos en los cálculos teóricos *ab initio*. En la representación de la evolución con la presión del volumen de la celda unidad se observa una disminución monótona del mismo hasta los 14 GPa. La dependencia de la presión de los parámetros de red experimentales (hasta 14 Gpa) y teóricos (hasta 16 GPa) del α-As_2Te_3 también muestra una disminución monótona y suave. La buena concordancia entre los cálculos teóricos y los resultados experimentales a temperatura ambiente, nos permite concluir que no se produce una transición de fase de primer orden hasta 14 GPa. Además, la dependencia con la presión de los parámetros de red no evidencia anomalías en la región próxima a los 13 GPa que pudieran ser indicativas de una TFI, aunque la coexistencia de las fases de baja y alta presión del As_2Te_3 por encima de 13 GPa han podido inducir al error cometido en estudios estructurales previos.

En el estudio teórico y experimental de la dependencia con la presión de las relaciones axiales del α-As_2Te_3, se puede observar que existe un comportamiento monótono de la relación axial experimental *c/b*, que concuerda correctamente con nuestros cálculos teóricos. Por otro lado, las relaciones axiales teóricas *a/b* y *a/c* muestran una dependencia variable entre 2 y 4 GPa, con un claro cambio en la tendencia de las curvas en esta región que no es tan acusado en los resultados experimentales. A pesar de que en algunos estudios anteriores sobre sesquicalcogenuros del grupo 15 se han considerado los cambios en la dependencia con la presión de las relaciones axiales como una prueba de la aparición de una TTE inducida por presión, este hecho se ha cuestionado en trabajos más recientes. Como se ha comentado en el estudio del oropimente, el cambio de tendencia de la relación *a/c* puede originarse por un cambio en la relación de fuerzas entre capas / intracapa, y no necesariamente garantiza un cambio en la densidad electrónica de los estados cercanos al nivel de Fermi, que conduciría a una TTE, sin embargo, podría ser indicativo de una TFI inducida por presión.

Respecto a la evolución con la presión del ángulo cristalográfico β (siempre perpendicular al eje *b* y característico de las estructuras monoclínicas), se observa un cambio de tendencia en la pendiente por encima de 4 GPa, lo que implica que en el α-As_2Te_3 la evolución del eje *a* respecto al *c* cambia radicalmente con la presión, suponiendo que las direcciones de los ejes *b* y *c* permanecen constantes. Además, teniendo en cuenta que la dirección de máxima compresibilidad a presión ambiente no tiene por qué ser exactamente la del eje *a*, en estructuras monoclínicas, es decir, la dirección principal en la que se apilan las capas puede no coincidir con la dirección de máxima compresibilidad.

Para evaluar el cambio en la dirección de máxima compresibilidad en función de la presión, hemos calculado y diagonalizado los tensores de compresibilidad isotérmicos experimentales y teóricos, β_{ij}, a diferentes presiones. De acuerdo con los resultados obtenidos a presión ambiente, la mayor compresibilidad se da a lo largo del eje *a*, siendo el eje *b* el menos compresible con diferencia y la compresibilidad del eje *c* intermedia entre las de los ejes *a* y *b*. Las compresibilidades axiales experimentales (teóricas) indican que alrededor del 59% (67%) de la compresión total a presión ambiente se da a lo largo de la dirección de máxima compresibilidad. En particular, la dirección de mayor compresibilidad experimental a presión ambiente se encuentra a un ángulo θ =16,0(1,4)º respecto al eje *a*, mientras que los cálculos teóricos predicen que está a un ángulo θ =5,5(7)º respecto al eje *a*.

La evolución con la presión de los tensores de compresibilidad experimentales y teóricos es muy similar. La característica más notable es que la compresibilidad experimental del eje *a* es mayor que la del eje *c* por debajo de 2,0 GPa, como se espera de la fuerte compresión inicial de las débiles fuerzas de vdW presentes en el espacio entre capas adyacentes que se acumulan principalmente a lo largo del eje *a*. Ambas compresibilidades son similares a 2 GPa, y, por encima de 3 GPa, la compresibilidad experimental del eje *c* es mayor que la del eje *a*, dentro de las incertidumbres experimentales. Además, la disminución de la compresibilidad del eje *a* con el aumento de la presión es tan grande que las compresibilidades de los ejes *a* y *b* son iguales alrededor de 11 GPa. Estos resultados implican que el eje *c* se

vuelve más compresible que el eje *a* por encima de 3 GPa. De esta manera, la dirección de máxima compresibilidad se aleja del eje *a* y se acerca al eje *c* a medida que aumenta la presión, es decir, el ángulo θ aumenta con la presión. A 3 GPa, la dirección de máxima compresibilidad está más cerca del eje *c* que del eje *a*, y a presiones superiores a 5 GPa, la dirección de máxima compresibilidad ya está muy cerca del eje *c*.

A partir de los tensores de compresibilidad experimentales y teóricos a diferentes presiones podemos obtener la dependencia con la presión de la compresibilidad del volumen tanto experimental como teórica (traza del tensor). Como se ha comentado anteriormente, hay una evolución continua de la compresibilidad en función de la presión, por lo que no cabe sugerir la presencia de ninguna TFI de segundo orden inducida por presión.

Con el fin de comprender mejor el comportamiento bajo presión de los parámetros estructurales en el compuesto α-As_2Te_3 descrito anteriormente, hemos estudiado la dependencia con la presión experimental y teórica de los parámetros atómicos *x* y *z* de las posiciones Wyckoff para los átomos no equivalentes de As (As1 y As2) y de Te (Te1, Te2 y Te3), así como las principales distancias interatómicas. Se puede observar que todos los parámetros atómicos evolucionan de forma monótona entre la presión ambiente y 14 GPa. Es más, todas las posiciones atómicas están ubicadas en los planos $b = 0$ y 1/2 (coordenadas atómicas $y = 0$ o $y = 1/2$) a todas las presiones hasta 14 GPa, lo que sugiere que los cambios de los parámetros atómicos no muestran evidencia de ninguna transición de fase hasta 14 GPa. No se observa ningún aumento o disminución de la simetría de las posiciones atómicas teóricas en el rango de presiones estudiado, por lo que nuestros cálculos teóricos no admiten la existencia de ninguna TFI en el α-As_2Te_3.

De forma similar, las distancias experimentales y teóricas As-Te, As-As y Te-Te muestran una disminución monótona a medida que aumenta la presión. En general, existe una buena concordancia entre el comportamiento de las distancias interatómicas experimentales y teóricas. Los valores de las distancias refinadas son del mismo orden que los calculados teóricamente, lo que indica que el refinamiento es correcto; sin embargo, los errores en las posiciones de refinamiento Rietveld se propagan cuando se calculan las distancias interatómicas, especialmente al aumentar la presión, lo que explica las diferencias entre los datos experimentales y teóricos, especialmente a altas presiones. Por lo tanto, en lo que sigue, la discusión de la evolución con la presión de las distancias interatómicas se basará en la evolución de las distancias teóricas, que se han calculado en el rango completo de presiones desde 1 atm hasta 14 GPa.

Como continuación del análisis de las distancias interatómicas, nos centramos ahora en el estudio de las coordinaciones de los átomos de As en el α-As_2Te_3. Con respecto a la coordinación de los átomos As1, podemos observar que el As1 tiene una coordinación 5 (3 + 2) a presión ambiente, si consideramos todos los enlaces As-Te dentro de la capa, es decir, los enlaces As-Te dentro de la barra, por debajo de 3,0 Å, y los enlaces As-Te entre barras, por encima de 3,2 Å. Por encima de 6 GPa, se puede considerar que los átomos As1 pasan a tener una coordinación 5 real, ya

que todas las distancias interatómicas As-Te dentro de la capa tienen una longitud inferior a 3,0 Å. Por otro lado, las unidades poliédricas del As1 solo tienden a una coordinación 5 + 2 a presiones alejadas del rango de estabilidad de la fase de baja presión, si se consideran las distancias entre capas As1-Te1 (> 3,5 Å a 14 GPa). Con respecto a la coordinación de los átomos As2, se observa que el As2 tiene una coordinación 6 a presión ambiente, y las seis distancias As2-Te tienden a valores similares por encima de 6-7 GPa, lo que indica una regularización del octaedro distorsionado del As2 al aumentar la presión.

Las distancias interatómicas As-As y Te-Te en las capas y entre capas muestran diferentes comportamientos bajo presión. Las distancias dentro de la capa muestran una pequeña compresión, mientras que las distancias entre capas muestran una gran contracción hasta la presión de 3-4 GPa y una considerable saturación por encima de este rango de presión. Este efecto viene dado por las diferentes compresibilidades de los ejes *a*, *b* y *c* bajo presión, explicadas anteriormente. La fuerte compresión del eje *a* por debajo de 3 GPa está relacionada con la fuerte compresibilidad de las distancias Te-Te entre capas en este rango de presión. Por el contrario, el eje *b* es el eje menos compresible a cualquier presión debido a los fuertes enlaces As-Te dentro de la capa (< 3,0 Å) que se extienden a lo largo del eje *b*. Finalmente, la compresibilidad del eje *c* es intermedia entre la de los ejes *a* y *b* debido a la presencia de largas distancias As1-Te2 (> 3,2 Å) a presión ambiente. Por otro lado, las distancias Te-Te entre capas a presiones superiores a 3-4 GPa disminuyen a una tasa similar a las distancias Te-Te dentro de la capa, con la excepción de las distancias Te2-Te2 que se extienden principalmente a lo largo del eje *c*. Este resultado evidencia el endurecimiento de los enlaces entre capas y explica por qué el eje *a* no es el eje más compresible por encima de este rango de presión y por qué la dirección de máxima compresibilidad se acerca al eje *c* a medida que aumenta la presión, como demuestra el análisis del tensor de compresibilidad.

Para finalizar esta discusión sobre las propiedades estructurales del α-As_2Te_3, es interesante comparar la estructura de este compuesto y su comportamiento bajo presión con el de otros sesquicalcogenuros del grupo 15. Esta familia de compuestos cristaliza en varias estructuras cristalinas distorsionadas debido a la actividad del PES del catión, que aumenta en la serie Bi-Sb-As. Por lo tanto, el estudio del comportamiento del PES del As en el α-As_2Te_3 en altas presiones es crucial para comprender las propiedades de este compuesto y las de otros sesquicalcogenuros del grupo 15 sometidos a compresión.

La disminución del volumen de los diferentes poliedros Te alrededor de los átomos de As1 y As2 muestra un buen acuerdo entre los resultados experimentales y la evolución teóricamente simulada de estas unidades poliédricas. La disminución del índice de distorsión muestra que estos poliedros se vuelven más regulares a medida que aumenta la presión y evidencia una disminución de la actividad del PES del As a medida que aumenta la presión. Estos resultados están de acuerdo con los obtenidos en estudios anteriores en varios materiales relacionados con el Sb y el Bi. A la vista de estos resultados, podemos concluir que la estructura del α-As_2Te_3 y su comportamiento bajo presión pueden entenderse como intermedios entre los del

α-Sb_2Te_3 y Sb_2Se_3, en buena concordancia con lo que se espera de la actividad del PES del catión en los sesquicalcogenuros del grupo 15.

De esta manera, la no observación de una TFI de segundo orden inducida por presión en el α-As_2Te_3 es consistente con el hecho de que tampoco se ha observado TFI en los compuestos Sb_2Se_3, Bi_2S_3 y Sb_2S_3, los cuales presentan una estructura de capas en zigzag similar a la del α-As_2Te_3. Especulamos que la razón de la falta de TFI inducidas por presión en estos compuestos se debe a la gran flexibilidad estructural de las estructuras ortorrómbicas y monoclínicas, pues estas estructuras tienen muchos parámetros atómicos libres capaces de adaptarse a los cambios en la actividad del PES del catión debidos a la presión, a diferencia de las estructuras cúbica, tetragonal y romboédrica de los compuestos α-Sb_2O_3, β-Bi_2O_3 y α-Sb_2Te_3, respectivamente, que muestran una TFI de segundo orden inducida por presión.

En resumen, el aumento de la presión en la estructura del α-As_2Te_3 genera una contracción progresiva del espacio entre capas y una ligera rotación de las unidades poliédricas. Esto conduce a un aumento de la coordinación promedio de los cationes As y a una disminución de la distorsión de las unidades poliédricas alrededor de dichos cationes (debida a la disminución del efecto del PES del catión), pero sin modificar el parámetro *y* de las posiciones iniciales Wyckoff de los cinco átomos no equivalentes de la celda unidad.

Como se ha comentado previamente, las medidas de DRX del telururo de arsénico, bajo presión en condiciones quasi-hidrostáticas y a temperatura ambiente, no muestran una transición de la fase α a la fase β por encima de 8 GPa ni por encima de 14 GPa, a diferencia de lo reportado en estudios anteriores. Para aclarar la estabilidad de las fases α-As_2Te_3 y β-As_2Te_3, se han llevado a cabo los cálculos *ab initio* de la entalpía frente a la presión para ambas fases. Nuestros cálculos sugieren que la transición de la fase α a la fase β en el As_2Te_3 podría ocurrir a presiones relativamente pequeñas (> 1 GPa). Esto significa que, tal vez, la transición de fase se vea obstaculizada a temperatura ambiente y en condiciones quasi-hidrostáticas por una barrera de energía cinética alta, lo que sugiere que algo de energía térmica adicional sea necesaria para superar esta barrera energética. Este resultado explicaría las transiciones sugeridas en los estudios previos en los que se ha trabajado con unas presiones relativamente bajas pero con altas temperaturas, e incluso podría explicar las condiciones poco hidrostáticas en estos estudios. Además, la entalpía de la fase β es mayor que la de la fase α para presiones superiores a 15 GPa, por lo tanto, nuestros cálculos muestran que la fase β no es una fase competitiva a altas presiones. Esto puede explicar por qué hemos observado una nueva fase (γ) por encima de 14 GPa diferente a la β.

Con el fin de estudiar el posible efecto de la hidrostaticidad en la aparición de la transición de la fase α a la fase β en el As_2Te_3, hemos realizado medidas de DR a presión ambiente y bajo presión (en condiciones hidrostáticas y no hidrostáticas), que se han comparado con los resultados de los cálculos de dinámica de red para entender el comportamiento del α-As_2Te_3.

Las propiedades vibracionales del α-As_2Te_3 dan lugar a 15 modos activos Raman, 12 modos activos infrarrojos y 3 modos acústicos. Los modos A_u y B_g corresponden

a las vibraciones de los átomos a lo largo del eje *b*, mientras que los modos A_g y B_u corresponden a las vibraciones de los átomos en el plano *ac*. La totalidad de los modos activos Raman se desarrolla a bajas frecuencias, por debajo de 250 cm^{-1}, y genera un espectro vibracional a presión ambiente con picos muy anchos, lo cual dificulta su identificación, aun con el apoyo de los cálculos *ab initio*. Este espectro a presión ambiente está dominado por un modo cercano a 120 cm^{-1} y dos modos característicos entre 170 y 200 cm^{-1}.

Los espectros Raman del α-As_2Te_3, a temperatura ambiente y a presiones seleccionadas en condiciones hidrostáticas hasta 12 GPa, se corresponden claramente con los resultados de los cálculos teóricos del α-As_2Te_3 en este rango de presión. En general, las frecuencias teóricas de los modos activos Raman muestran un comportamiento complejo al aumentar la presión, con *cruces* y *anticruces* de modos con simetrías diferentes e iguales, respectivamente. Este complejo comportamiento se debe a la presencia de los 15 modos activos Raman en una pequeña región, entre 50 y 200 cm^{-1}, mencionada anteriormente. También se han observado pequeños cambios en el coeficiente de presión de algunos modos Raman teóricos en el rango entre 2 y 4 GPa en el α-As_2Te_3, que podrían atribuirse a los fuertes cambios observados en las distancias interatómicas alrededor de estas presiones, como ya se comentó en el estudio estructural. A pesar del comportamiento tan complejo observado teóricamente, se ha procedido a una asignación tentativa de los modos experimentales observados, que muestran un comportamiento consistente con los modos teóricos en los cambios de coeficientes de presión.

Hemos observado, además, dos modos Raman experimentales en el rango de 120 a 145 cm^{-1} cuya frecuencia disminuye al aumentar la presión. Las frecuencias y los coeficientes de presión negativos de estos modos son similares a las reportadas anteriormente para la fase trigonal del Te. En consecuencia, hemos asignado los modos localizados a presión ambiente cerca de 120 cm^{-1} y 140 cm^{-1} a los modos A_1 y E″ de los modos del Te cristalino. Esta situación ya ha sido observada en el estudio de compuestos que contienen Te y Se, y es debida al daño inducido por el láser en las medidas de los compuestos bajo presión. Sin embargo, estos modos ya no se observan a presiones superiores a 4-5 GPa, probablemente por la mejora en la conductividad térmica dentro de la celda de yunques de diamante al aumentar la presión, debida a la metalización del α-As_2Te_3.

Los espectros Raman del α-As_2Te_3, a temperatura ambiente y a presiones seleccionadas en condiciones no hidrostáticas hasta 12 GPa, así como la dependencia con la presión de los modos activos Raman, tampoco muestran ninguna transición de fase cerca de 6-8 GPa, lo que apoya la hipótesis de que la activación térmica a altas presiones es necesaria para forzar la transición de la fase α a la fase β en el As_2Te_3 a presiones relativamente bajas.

Para verificar si podría haber alguna TFI de segundo orden inducida por presión en el α-As_2Te_3, también hemos estudiado las curvas de dispersión de fonones teóricamente calculadas a diferentes presiones hasta 14 GPa, ya que una TFI de segundo orden debe estar relacionada con la presencia de un modo de fonón blando

de acuerdo con la teoría de Landau. Se puede observar que no existe ningún modo blando en la zona de Brillouin a cualquier presión, ya sea en el rango de 3 a 5 GPa o en el rango de 6 a 13 GPa. Por lo tanto, podemos concluir con seguridad que no hay TFI inducida por presión en el α-As_2Te_3 hasta 14 GPa, en contraposición a lo reportado recientemente por otros investigadores.

Finalmente, para verificar si podría haber una posible TTE inducida por presión en el α-As_2Te_3, también hemos estudiado la dependencia con la presión del ancho de línea de los modos activos Raman más intensos en ambos experimentos, en condiciones hidrostáticas y no hidrostáticas. No hemos encontrado ningún cambio importante, al aumentar la presión, que pueda ser indicativo de una TTE inducida por presión en este compuesto. Solo se observa un pequeño aumento del fondo de DR por encima de 4 GPa, lo que podría ser indicativo de la metalización progresiva del material por encima de esta presión.

Teniendo en cuenta que las TTE son transiciones muy sutiles (son transiciones $2^{1}/_{2}$ en notación Ehrenfest) cuya aparición podría ser difícil de evidenciar mediante mediciones de DRX o de DR, hemos realizado cálculos *ab initio* de la estructura de bandas electrónicas en el α-As_2Te_3 bajo presión, con el fin de identificar posibles cambios en los extremos de las bandas que podrían estar relacionados con una TTE inducida por presión. La estructura electrónica a 0 GPa muestra un gap indirecto (valor teórico subestimado de alrededor de 0,7 eV) con el MBC ubicado cerca del punto L de la zona de Brillouin, y tres MBV casi degenerados ubicados en diferentes direcciones cercanas al punto A de la zona de Brillouin.

El gap indirecto se cierra progresivamente al aumentar la presión. Alrededor de 1 GPa, nuestros cálculos muestran que el gap continúa siendo indirecto, con un valor superior a 0,4 eV, y que el MBC cambia del punto L al punto V. El gap indirecto del α-As_2Te_3 se cierra completamente en torno a 4 GPa. El α-As_2Te_3 sufre una transición trivial semiconductor-metal inducida por presión y no se produce ningún otro cambio importante a presiones más altas. Debido a la subestimación del gap teórico en los cálculos de teoría funcional de la densidad, es razonable suponer que el cierre real del gap se realiza a una presión ligeramente mayor (alrededor de 6-7 GPa). Sin embargo, el gap a esta presión es demasiado alto (probablemente por encima de 0,5 eV) como para provocar una fuerte modificación de la densidad electrónica de los estados cercanos al nivel de Fermi. Por lo tanto, concluimos que nuestros cálculos no muestran evidencia clara de una TTE inducida por presión en el α-As_2Te_3.

Capítulo 4

Conclusiones

Los principales resultados de las investigaciones realizadas a lo largo de los últimos años en el estudio de compuestos As_2X_3 han dado lugar a las publicaciones incluidas en esta tesis, con las que se ha avanzado en el análisis y comprensión de las propiedades de los sesquióxidos y sesquicalcogenuros de arsénico mediante la aplicación de la condición extrema de alta presión.

Hemos demostrado que la arsenolita (As_4O_6) es uno de los sólidos moleculares no hidratados con el módulo de compresibilidad más pequeño y que el He se incorpora a la estructura de la arsenolita en las posiciones Wyckoff 16*d* por encima de 3 GPa. Este atrapamiento del He ayuda a estabilizar la estructura molecular de la arsenolita, manteniendo las unidades de As_4O_6 separadas y evitando el proceso de amorfización inducida por presión (AIP) hasta al menos 30 GPa. La inesperada interacción de los átomos de He y As da como resultado la formación de un compuesto con estequiometría $As_4O_6 \cdot 2He$ (solo estable por encima de 3 GPa, ya que el He sale de la estructura de la arsenolita por debajo de esta presión) cuyas propiedades son diferentes de las del As_4O_6. Los resultados actuales allanan el camino para explorar la formación de compuestos mediante la captura y unión, inducidas por presión, de gases, pequeñas especies atómicas y moleculares en sólidos moleculares que tienen estructuras cristalinas abiertas, como las que se presentan en compuestos constituidos por cationes con pares de electrones solitarios (PES) activos. Además, estos resultados sugieren que la compresión de sólidos moleculares con gases nobles, como el helio, debe realizarse con precaución, ya que pueden producir resultados inesperados, en comparación con otros medios de transmisión de presión (MTP), debidos a la entrada (y posible reacción) de estos elementos con la estructura de los compuestos moleculares.

En el estudio experimental y teórico de la dinámica de red del As_4O_6 y el $As_4O_6 \cdot 2He$ hemos observado un comportamiento diferente a altas presiones en los modos activos Raman de ambos compuestos, que confirman la inclusión del He en las posiciones 16*d* de la estructura de la arsenolita por encima de 3 GPa. Por otro lado, tras el estudio de la estabilidad dinámica de la estructura cúbica de ambos compuestos, ha quedado demostrado que el As_4O_6 y el $As_4O_6 \cdot 2He$ son dinámicamente estables al menos hasta 34,7 y 35,5 GPa, respectivamente.

Además, hemos estudiado teóricamente el comportamiento elástico y termodinámico de ambos compuestos bajo presión y hemos observado que la mayoría de las propiedades de ambos compuestos son similares a bajas presiones. Las constantes elásticas y los coeficientes de rigidez elástica aumentan con el incremento de la presión en todo el rango de presión estudiado; sin embargo, los coeficientes de presión de los coeficientes de rigidez elástica B_{11} y B_{12} son bastante diferentes en ambos compuestos, lo que da como resultado un comportamiento a altas presiones completamente diferente en los módulos de cizalladura y de Young, la relación *B/G*, el coeficiente de Poisson, la dureza Vickers y la anisotropía Zener, en ambos compuestos. En este contexto, ambos compuestos son más resistentes a la compresión que a la deformación cortante ($B>G$) a todas las presiones. La velocidad de onda elástica promedio, la temperatura de Debye y la conductividad térmica mínima de ambos compuestos también son similares a bajas presiones, pero muestran un comportamiento diferente al aumentar la presión. Basándonos en el

comportamiento de los coeficientes de rigidez elástica bajo presión, hemos estudiado la dependencia con la presión de la estabilidad mecánica de la estructura cúbica en ambos compuestos y hemos observado que la estructura cúbica se vuelve mecánicamente inestable a 19,7 GPa en el As_4O_6, mientras que no hay inestabilidad mecánica en el $As_4O_6 \cdot 2He$ al menos hasta 35,5 GPa. Estos resultados concuerdan con los experimentos que muestran una amorfización inducida por presión (AIP) en el As_4O_6 por encima de 15-20 GPa, dependiendo del MTP utilizado, y con la observación experimental de la estructura cúbica del $As_4O_6 \cdot 2He$ hasta 30 GPa sin signos de AIP.

El comportamiento bajo presión de las estructuras laminares de las fases oropimente y anoropimente del As_2S_3 se ha investigado teóricamente por medio de cálculos *ab initio* realizados dentro de la teoría del funcional de la densidad (TFD). Las frecuencias de los fonones en el centro de la zona de Brillouin se han calculado utilizando el método de desplazamientos finitos, y se ha asignado la simetría de los modos, lo que servirá de apoyo en los posteriores estudios experimentales de dispersión Raman (DR) e infrarrojos de estas fases bajo compresión. El efecto de las interacciones de van der Waals (vdW) se ha investigado específicamente demostrándose su importancia en la respuesta estructural de estos compuestos y en la mejora de su estabilidad.

Las propiedades estructurales, vibracionales y electrónicas de la fase oropimente (α-As_2S_3) han sido estudiadas en condiciones ambientales y a altas presiones. Hemos observado que la estructura del oropimente, a presión ambiente, está compuesta por capas formadas por cadenas espirales de As-S, donde los átomos de As tienen una coordinación 3. Al aumentar la presión, la estructura sufre una fuerte compresión hasta 20 GPa, seguida de una transición de fase isoestructural (TFI) de origen electrónico, que conduce a una coordinación de los átomos de As mayor de 5 por encima de esa presión. La característica más sorprendente de esta TFI inducida por presión es que varias distancias de enlace As-S se vuelven iguales por encima de 20 GPa.

Se ha estudiado la dinámica de red del oropimente y se han descrito completamente todos los modos rígidos de capa y los modos principales dentro de las cadenas espirales y entre dichas cadenas. Nuestras mediciones y cálculos evidencian el reblandecimiento de muchos modos de vibración y la disminución del gap de fonones (se cierra por encima de 20 GPa) en alta presión. Además, nuestros cálculos confirman la metalización del material por encima de 26 GPa debida a la fuerte disminución del gap óptico, lo cual apoya la teoría de la metalización en laboratorio en condiciones hidrostáticas muy por encima de 50 GPa al considerar la subestimación del gap energético en nuestros cálculos *ab initio*.

Todos estos cambios están relacionados con la formación de enlaces metavalentes que se producen por encima de 20 GPa debido a la deslocalización de las nubes electrónicas, principalmente en el plano *ac* de las capas, sin la necesidad de una transición de fase estructural (TFE) de primer orden, como ocurre en los compuestos de Se y Te, pero similar a la observada en el compuesto GeSe, y reportados en otros trabajos anteriores. Se ha demostrado que los enlaces metavalentes ya se producen

en otros sesquicalcogenuros del grupo 15 a presión ambiente. El enlace metavalente completo se produce en los aislantes topológicos y en los buenos materiales termoeléctricos como el α-Bi_2Se_3, el α-Bi_2Te_3 y el α-Sb_2Te_3, con estructura en capas de tetradimita que cuentan con una coordinación 6 de los cationes. En estos compuestos, el enlace metálico se forma a altas presiones después de una transición de fase de primer orden que forma una estructura con una coordinación de los cationes mayor que en la fase original. Por otro lado, se produce un enlace metavalente parcial en el α-Bi_2S_3, el α-Sb_2S_3 y el α-Sb_2Se_3, con una estructura ortorrómbica *Pnma*, y en el α-As_2Te_3 con estructura monoclínica *C2/m*. Estos compuestos muestran una coordinación intermedia entre 3 y 6. En todos estos materiales, la presión aumenta la coordinación de los cationes, lo que conduce a una reducción considerable del gap y un ablandamiento parcial de los fonones consistente con el enlace metavalente. Finalmente, predecimos que se espera una situación similar a la del α-As_2S_3 para los polimorfos del As_2Se_3 y también en los trigonales de baja presión de Se y Te a altas presiones. Se espera que estos compuestos, que presentan una coordinación 3 a presión ambiente, exhiban un enlace metavalente a altas presiones.

En resumen, nuestros resultados en el α-As_2S_3 confirman que la presión es capaz de ajustar el enlace metavalente en los sesquicalcogenuros del grupo 15 con una fuerte actividad del PES, como ocurre en el oropimente, convirtiendo los semiconductores comunes en "metales incipientes" con prometedores cambios de fases, propiedades aislantes termoeléctricas y topológicas en condiciones extremas. Dado que el Sb_2Te_3 y el Bi_2Te_3 son aislantes topológicos y dos de los mejores materiales termoeléctricos conocidos en condiciones ambientales debido a sus enlaces metavalentes, este trabajo allana el camino para diseñar nuevos sesquicalcogenuros del grupo 15 y compuestos relacionados con propiedades aislantes termoeléctricas o topológicas, tanto a presión ambiente como en condiciones extremas.

Finalmente, en el estudio de las propiedades estructurales, vibracionales y electrónicas del α-As_2Te_3, a temperatura ambiente y altas presiones, hemos observado que existe una mayor compresibilidad entre las capas en el α-As_2Te_3 que en el α-Sb_2Te_3 y el α-Bi_2Te_3, lo que puede explicarse debido al mayor efecto del PES del catión As que en los cationes Sb y Bi. De hecho, hemos demostrado que la estructura del α-As_2Te_3 se puede entender como una estructura intermedia entre la del Sb_2Se_3 y el α-Sb_2Te_3. Así, se observan fuertes cambios en la tendencia con la presión del ángulo β y de las compresibilidades axiales en la región entre 2 y 4 GPa, que están relacionados con el fortalecimiento de los enlaces de vdW entre capas en este rango de presión. Esta característica ha quedado demostrada por el cambio en la dirección de máxima compresibilidad dada por el análisis del tensor de compresibilidad. Además, hemos observado que las unidades poliédricas alrededor de los cationes As en el α-As_2Te_3 se vuelven más regulares a medida que aumenta la presión y muestran una pequeña rotación para acomodarse a la presión, en una clara tendencia a aumentar la coordinación de ambos átomos de As no equivalentes con el incremento de la presión. Nuestras simulaciones teóricas *ab initio* predicen que la fase β, donde los átomos de As tienen una coordinación 6, es termodinámicamente más estable que la fase α por encima de 1 GPa. Sin embargo,

no se ha observado ninguna transición de fase a la fase β a temperatura ambiente, incluso por encima de 17 GPa, pero sí que se ha observado una transición de fase a la fase γ. La ausencia de la transición de fase del α-As_2Te_3 a β-As_2Te_3 a temperatura ambiente se debe a que esta es una transición de fase de primer orden altamente reconstructiva, que puede frustrarse debido a la presencia de una barrera de alta energía cinética y quedar oculta por la transición de fase a un polimorfo γ con una mejor barrera energética.

Concluyendo, nuestras mediciones de DR y nuestros cálculos de dinámica de red apoyan la estabilidad de la fase α hasta 12 GPa y muestran pequeños cambios en la región entre 2 y 4 GPa, consistentes con los cambios progresivos de las distancias interatómicas al aumentar la presión. Las curvas de dispersión de fonones a diferentes presiones no muestran ningún modo blando que evidencie una TFI de segundo orden inducida por presión. Además, no se han observado cambios en el espectro de DR, que podrían ser indicativos de una TTE inducida por presión. Este resultado está de acuerdo con los cálculos teóricos de la estructura de bandas electrónicas, que muestran que el α-As_2Te_3 es un semiconductor con un gap indirecto superior a 0,7 eV a presión ambiente, y que indican un cambio del mínimo de banda de conducción cerca de 1 GPa. El cierre del gap indirecto ocurre al aumentar la presión, lo que sugiere una transición experimental de semiconductor a metal por encima de 6 GPa.

Perspectivas futuras

Los objetivos principales de nuestro equipo de investigación son la síntesis y la caracterización de las propiedades estructurales, vibracionales, ópticas y electrónicas de materiales bajo condiciones extremas de presión y/o temperatura, poniendo un énfasis especial en aquellos materiales cuyas aplicaciones para la optoelectrónica sean de considerable valor, así como en minerales que puedan resultar de interés para la geofísica y la astrofísica.

Para el desarrollo de nuestro trabajo contamos con una red multidisciplinar colaborativa, formada por grupos de investigación nacionales e internacionales, entre los que cabe destacar a los grupos teóricos que complementan nuestros trabajos experimentales con los cálculos teóricos *ab initio*.

Nuestro equipo trabaja en varios frentes, siendo uno de ellos el estudio de la serie de polimorfos de sesquióxidos y sesquicalcogenuros: $(As,Sb,Bi)_2(O,S,Se,Te)_3$ y, en menor medida, $(Al,Ga,In)_2(O,S,Se,Te)_3$ y otros como el Sn_2S_3. En especial, se estudian los factores desencadenantes de las transiciones de segundo orden y de amorfizaciones inducidas por presión, así como las transiciones a aislante/superconductor topológico y las TTE inducidas por presión.

El análisis y la comprensión de las propiedades de los compuestos presentados en esta tesis ha supuesto un avance en el estudio de los sesquióxidos y sesquicalcogenuros del grupo 15. Sin embargo, este trabajo es solo una parte de un proyecto más ambicioso del que formo parte. Seguimos avanzando en los estudios de las propiedades estructurales, elásticas, vibracionales, ópticas y electrónicas de

sesquicalcogenuros a altas presiones, como los compuestos β-As_2S_3 (anoropimente), As_4S_4 (realgar), α-As_2Se_3, β-As_2Se_3, γ-As_2Se_3, β-Sb_2Se_3 y β-As_2Te_3.

Sobre este último compuesto, fase β del telururo de arsénico (del cual ya hemos reportado el estudio de la fase α), hemos obtenido los primeros resultados de nuestras investigaciones, que permiten la comparación del β-As_2Te_3 con el α-As_2Te_3, así como con otros sesquicalcogenuros del grupo 15. La estructura cristalina del α-As_2Te_3 es diferente a la de los compuestos α-X_2Te_3 (con X = Sb, Bi), que son comúnmente conocidos por sus buenas propiedades termoeléctricas y, más recientemente, como aislantes topológicos. Sin embargo, se sabe que en condiciones de alta presión y alta temperatura, el α-As_2Te_3 se transforma en una estructura romboédrica (fase β) que es isoestructural a α-X_2Te_3 (X = Sb, Bi). Por lo tanto, no es sorprendente que el β-As_2Te_3 haya sido propuesto recientemente para albergar también estados de superficie topológicos. La observación de la mejora de las propiedades termoeléctricas del As_2Te_3 con el incremento de la presión sugiere la síntesis de este compuesto a presión ambiente.

Por último, cabe mencionar que se están realizando también medidas y análisis preliminares del α-As_2Se_3 que permitirán corroborar nuestros resultados sobre el oropimente y sobre la naturaleza del enlace metavalente en los sesquicalcogenuros del grupo 15.

Bibliografía

[Ablain 2011] J. Ablain and H. The. Revisiting the differentiation paradigm in acute promyelocytic leukemia. *Blood*. **2011**, *117(22)*, 5795.

[Agency for Toxic Substances and Disease Registry 2005] Agency for Toxic Substances and Disease Registry. *Toxicological Profile for Arsenic (Update)*. (Atlanta, **2005**).

[Aggarwal 2002] I. D. Aggarwal and J. S. Sanghera. Development and Applications of Chalcogenide Glass Optical Fibers at nrl. *J. Optoelectron. Adv. Mater.* **2002**, *4*, 665-678.

[Alekberov 2014] R. I. Alekberov, S. I. Mekhtiyeva, G. A. Isayeva, and A. I. Isayev. Raman Scattering in As-Se-S and As-Se-Te Chalcogenide Vitreous Semiconductors. *Semiconductors.* **2014**, *48*, 800-803.

[Alfè 2009] D. Alfè. PHON: A program to calculate phonons using the small displacement method. *Computer Physics Communications.* **2009**, *180*, 2622−2633.

[Anderson 1963] O. L. Anderson. A simplified method for calculating the Debye temperature from elastic constants. *J. Phys. Chem. Solids*. **1963**, *24*, 909-917.

[Angel 2004-2011] R. J. Angel. http://www.rossangel.com/text_strain.htm

[Aoki 1980] K. Aoki, O. Shimomura, S. Minomura, N. Koshizuka, and T. Tsushima. Raman Scattering of Trigonal Se and Te at Very High Pressure. *Journal of the Physical Society of Japan*. **1980**, *48*, 906−911.

[Aroyo 2014] M. I. Aroyo, D. Orobengoa, G. de la Flor, E. S. Tasci, J. M. Pérez-Mato, and H. Wondratschek. Brillouin-zone database on the Bilbao Crystallographic Server. *Acta Crystallographica A*. **2014**, *70*, 126.

[Ballirano 2002] P. Ballirano and A. Maras. Refinement of the crystal structure of arsenolite, AS_2O_3. *Z. Kristallogr. NCS*. **2002**, *217*, 177.

[Bandyophadhay 1999] A. K. Bandyophadhay and D. B. Singh. Pressure induced phase transformations and band structure of different high pressure phases in tellurium. *Pramana*. **1999**, *52*, 303−319.

[Bartrip 1992] P. Bartrip. A "Pennurth of Arsenic for rat poison ": The Arsenic Act, 1851 and the prevention of secret poisoning. *Medical History*. **1992**, *36*, 53-69.

[Beattie 1970] I.R. Beattie, K.M.S. Livingston, G. A. Ozin, and D.J. Reynolds. Single-crystal Raman spectra of arsenolite (As_4O_6) and senarmonite (Sb_4O_6). The gas-phase Raman spectra of P_4O_6, P_4O_{10}, and As_4O_6. *J. Chem. soc. A.* **1970**, *449*.

[Beckstein 2001] O. Beckstein, J. E. Klepeis, G. L. W. Hart, and O. Pankratov. First-principles elastic constants and electronic structure of α-Pt_2Si and PtSi. *Phys. Rev. B.* **2001**, *63*, 134112.

[Bertoluzza 1972] A. Bertoluzza, M. A. Morelli, and C. Fogano. C. Investigation Using Raman and Infrared Spectroscopy of As_2O_3 Glass in Relation to

Crystalline Polymorphous Changes of Trioxide. *Lincei Rend. Sin. Fis. Mat. Nat.* **1972**, *52*, 932.

[Besson 1980] J. M. Besson, J. Cernogora, and R. Zallen. Effect of pressure on optical properties of crystalline As_2S_3. *Physical Review B.* **1980**, *22*, 3866−3876.

[Besson 1981] J. M. Besson, J. Cernogora, M. L. Slade, B. A. Weinstein, and R. Zallen. Pressure effects on the absorption edge, refractive index, and Raman spectra of crystalline and amorphous As_2S_3. *Physica B.* **1981**, *105*, 319−323.

[Birch 1938] F. Birch. The Effect of Pressure Upon the Elastic Parameters of Isotropic Solids, According to Murnaghan's Theory of Finite Strain. *Journal of Applied Physics*. **1938**, *9*, 279−288.

[Birch 1947] F. Birch. Finite Elastic Strain of Cubic Crystals. *Phys. Rev*. **1947**, *71*, 809.

[Blöchl 1999] P. E. Blöchl. Projector Augmented-Wave Method. *Physical Review B: Condensed Matter and Material Physics.* **1994**, *50*, 17953−17979.

[Bolotina 2013a] N. B. Bolotina, V. V. Brazhkin, T. I. Dyuzheva, Y. Katayama, L. F. Kulikova, L. V. Lityagina, and N. A. Nikolaev. High-pressure polymorphism of As_2S_3 and new AsS_2 modification with layered structure. *JETP Letters*. **2013**, *98*, 539-543.

[Bolotina 2013b] N. B. Bolotina, V. V. Brazhkin, T. I. Dyuzheva, L. M. Lityagina, L. F. Kulikova, N. A. Nikolaev, and I. A. Verin. Crystal structure of new AsS_2 compound. *Crystallogr. Rep*. **2013**, *58*, 61.

[Bondi 1968] A. Bondi. Van der Waals volumes and radii. *J. Phys. Chem.* **1968**, *68*, 441.

[Born 1940] M. Born. On the stability of crystal lattices. I. *I. Proc. Cambridge Philos. Soc.* **1940**, *36*, 160.

[Born 1954] M. Born and K. Huang. *Dynamical Theory of Crystal Lattices* (Oxford University Press, **1954**) p. 140.

[Brauer 1963] G. Brauer. *Handbook of Preparative Inorganic Chemistry* (Academic Press, **1963**).

[Brazhkin 2002] V. V. Brazhkin, A. G. Lyapin, and R. J. Hemley. Harder than diamond: Dreams and reality. *Philos. Mag. A.* **2002**, *82*, 231.

[Brazhkin 2010] V. V. Brazhkin, Y. Katayama, M. V. Kondrvin, A. G. Lyapin, and H. Saitoh. Structural transformation yielding an unusual metallic state in liquid As_2S_3 under high pressure. *Phys. Rev. B.* **2010**, *82*, 140202(R).

[Brazhkin 2014] V. V. Brazhkin, and A. I. Orlov. High-Pressure Thermoelectric Characteristics of Bi_2Te_3 Semiconductor with Different Charge Carrier Densities. *JETP Lett.* **2014**, *99*, 283-285.

[Bridgman 1914] P. W. Bridgman. The Coagulation of Albumen by Pressure. *Journal of Biological Chemistry*. **1914**, 19, 511-512.

[Brown 1965] A. Brown and S. Rundqvist. Refinement of the crystal structure of black phosphorus. *Acta Crystallographica*. **1965**, *19*, 684–685.

[Brumbach 1972] S.B. Brumbach and G.M. Rosenblatt. In-cavity Laser Raman Spectroscopy of Vapors at Elevated Temperatures. As_4 and As_4O_6. *J. Chem. Phys*. **1972**, *56*, 3110.

[Bundy 1955] F.P. Bundy, H.T. Hall, H.M. Strong, and R.H. Wentorf, Jr. Man-Made Diamonds. *Nature*. **1955**, *176*, 51.

[Burgio 2000] L. Burgio and R. J. H. Clark. Comparative pigment analysis of six modern Egyptian papyri and an authentic one of the 13th century BC by Raman microscopy and other techniques. *Journal of Raman Spectroscopy*. **2000**, *31*, 395-401.

[Canepa 2011] P. Canepa, R. M. Hanson, P. Ugliengo, and M. Alfredsson. J-ICE: a new Jmol interface for handling and visualizing crystallographic and electronic properties. *Journal of Applied Crystallography*. **2011**, *44*, 225−229.

[Caracas 2010] R. Caracas and T. B. Ballaran. Elasticity of $(K,Na)\cdot AlSi_3O_8$ hollandite from lattice dynamics calculations. *Phys. Earth Planet. Int*. **2010**, *181*, 21.

[Carron 1963] G. J. Carron. The Crystal Structure and Powder Data for Arsenic Telluride. *Acta Crystallographica.* **1963**, *16*, 338-343.

[Castro 2013] J. Castro Ramos, A.E. Villanueva Luna, y C.M. Ortiz Lima. Espectroscopia Raman y sus aplicaciones. *Óptica Pura y Aplicada*. **2013**, *46-1*, 83.

[Chattopadhyay 1982] T. Chattopadhyay, A. Werner, and H. G. von Schnering. Thermal expansion and compressibility of β-As_4S_3. *J. Phys. Chem. Solids*. **1982**, *43*, 919.

[Chen 2009] Y. L. Chen, J. G. Analytis, J-H. Chu, Z. K. Liu, S-K. Mo, X-L. Qi, H. J. Zhang, D. H. Lu, X. Dai, Z. Fang, et al. Experimental Realization of a Three-Dimensional Topological Insulator, Bi_2Te_3. *Science* **2009**, *325*, 178-181.

[Cheng 2017] H. F. Cheng, Y. Zhou, and R. L. Frost. Structure comparison of Orpiment and Realgar by Raman spectroscopy. *Spectroscopy Letters*. **2017**, *50*, 23−29.

[Chetty 1989] N. Chetty, A. Muñoz, and R. M. Martin. First-principles calculation of the elastic constants of AlAs. *Phys. Rev. B*. **1989**, *40*, 11934.

[Chinese Pharmacopoeia Committee 2005] Chinese Pharmacopoeia Committee. *Pharmacopoeia of China*. (People's Press, Beijing, China, **2005**)

[Clarke 2003] D. R. Clarke. Materials selection guidelines for low thermal conductivity thermal barrier coatings. *Surf. Coat. Technol*. **2003**, *163*, 67-74.

[Clayton 2010] J.D. Clayton. *Nonlinear Mechanics of Crystals, Solid Mechanics and Its Applications* (Springer, New York, **2010**) p. 177.

[Contreras-García 2008] J. Contreras-García, A. Martín Pendás, B. Silvi, and J. M. Recio. Useful applications of the electron localization function in high-pressure crystal chemistry. *Journal of Physics and Chemistry of Solids*. **2008**, *69*, 2204−2207.

[Contreras-García 2009] J. Contreras-García, B. Silvi, A. Martín Pendás, and J. M. Recio. Computation of local and global properties of the electron localization function topology in crystals. *Journal of Chemical Theory and Computation*. **2009**, *5*, 164–173.

[Contreras-García 2011a] J. Contreras-García, E. Johnson, S. Keinan, R. Chaudret, J. Piquemal, D. Beratan, and W. Yang. NCIPLOT: a program for plotting non-covalent interaction regions. *J. Chem. Theory Comput*. **2011**, *7*, 625.

[Contreras-García 2011b] J. Contreras-García, W. Yang, and E. Johnson. Analysis of Hydrogen-Bond Interaction Potentials from the Electron Density: Integration of Non-covalent Interaction Regions. *J. Phys. Chem. A* **2011**, *115*, 12983.

[Cuenca-Gotor 2016] V. P. Cuenca-Gotor, J. A. Sans, J. Ibáñez, C. Popescu, O. Gomis, R. Vilaplana, F. J. Manjón, A. Leonardo, E. Sagasta, A. Suárez-Alcubilla, I. G. Gurtubay, M. Mollar, and A. Bergara. Structural, Vibrational, and Electronic Study of α-As_2Te_3 under Compression. *Journal of Physical Chemistry C*. **2016**, *120*, 19340−19352.

[Cutler 1878] E. G. Cutler and E. H. Bradford. Action of iron, cod-liver oil, and arsenic on the globular richness of the blood. *The American Journal of the Medical Sciences*. **1878**, *75*, 74.

[De la Serna 2008] J. De la Serna, P Montesinos, E. Vellenga, C. Rayón, R. Parody, A. León, . Causes and prognostic factors of remission induction failure in patients with acute promyelocytic leukemia treated with all-trans retinoic acid and idarubicin. *Blood*. **2008**, *111(7)*, 3395.

[Debernardi 2001] A. Debernardi, C. Urlich, M. Cardona, and K. Syassen. Pressure Dependence of Raman Linewidth in Semiconductors. *Phys. Status Solidi B*. **2001**, *223*, 213.

[DeFonzo 1978] A. P. DeFonzo and J. Tauc. Network dynamics of 3:2 coordinated compounds, *Physical Review B*. **1978**, *18*, 6957−6972.

[Degtyareva 2007] O. Degtyareva, E. R. Hernández, J. Serrano, M. Somayazulu, H-K. Mao, E. Gregoryanz, and R. J. Hemley. Vibrational dynamics and stability of the high-pressure chain and ring phses in S and Se. *Journal of Chemical Physics*. **2007**, *126*, 084503.

[Deng 2015] H. Deng. Theoretical Prediction of the Structural, Electronic, Mechanical and Thermodynamic Properties of the Binary α-As_2Te_3 and β-As_2Te_3. *J. Alloys Compd*. **2015**, *656*, 695-701.

[Deringer 2015] V. L. Deringer, R. P. Stoffel, M. Wuttig, and R. Dronskowski. Vibrational Properties and Bonding Nature of Sb_2Se_3 and their Implications for Chalcogenide Materials. *Chem. Sci.* **2015**, *6*, 5255-5262.

[Dewaele 2004] A. Dewaele, P. Loubeyre, and M. Mezouar. Equations of State of Six Metals above 94 GPa. *Physical Review B.* **2004**, *70*, 094112.

[Ding 2016] W. Ding, Y. Tong, X. Zhang, M. Pan, and S. Chen. Study of Arsenic Sulfide in Solid Tumor Cells Reveals Regulation of Nuclear Factors of Activated T-cells by PML and p53, *Scientific Reports*. **2016**, *6*, 19793.

[Dong 2014] X. Dong *et al*. Stable Compound of Helium and Sodium at High Pressure. **2014**, arXiv:1309.3827v3.

[Drahota 2009] P. Drahota and M. Filippi. Secondary arsenic minerals in the environment: A review. *Environment International*. **2009**, *35*, 1243.

[Eastaugh 2004] N. Eastaugh, V. Walsh, T. Chaplin, and R. Sidall. *The Pigment Compendium. A Dictionary of Historical Pigments.* (Elsevier Butterworth-Heinemann, **2004**).

[Edwards 1961] A. L. Edwards and H. G. Drickamer. Effect of Pressure on the Absorption Edges of Some III-V, II-VI, and I-VII Compounds. *Physical Review*. **1961**, 122, 1149.

[Efthimiopoulos 2013] I. Efthimiopoulos, J. M. Zhang, M. Kucway, C. Park, R. C. Ewing, and Y. Wang. Sb_2Se_3 under Pressure. *Scientific Reports.* **2013**, *3*, 2665-2672.

[Efthimiopoulos 2014] I. Efthimiopoulos, J. Kemichick, X. Zhou, S. V. Khare, D. Ikuta, and Y. Wang. High-Pressure Studies of Bi_2S_3. *Journal of Physical Chemistry A.* **2014**, *118*, 1713-1720.

[Efthimiopoulos 2016] I. Efthimiopoulos, C. Buchan, and Y. Wang. Structural Properties of Sb_2S_3 under Pressure: Evidence of an Electronic Topological Transition. *Scientific Reports.* **2016**, *6*, 24246.

[Einaga 2011] M. Einaga, A. Ohmura, A. Nakayama, F. Ishikawa, Y. Yamada, and S. Nakano. Pressure-Induced Phase Transition of Bi_2Te_3 to a bcc Structure. *Phys. Rev. B.* **2011**, *83*, 092102.

[Errandonea 2014] D. Errandonea, C. Popescu, S. N. Achary, A. K. Tyagi, and M. Bettinelli. In situ High-Pressure Synchrotron X-ray Diffraction Study of the Structural Stability in NdVO4 and LaVO4. *Mater. Res. Bull*. **2014**, *50*, 279-284.

[Evens 2004] A. M. Evens, M. S. Tallman, and R. B. Gartenhaus. The potential of arsenic trioxide in the treatment of malignant disease: past, present, and future. *Leukemia Research*. **2004**, *28*, 891.

[Fauth 2013] F. Fauth, I. Peral, C. Popescu, and M. Knapp. The New Material Science Powder Diffraction Beamline at ALBA Synchrotron. *Powder Diffraction*. **2013**, *28*, S360−S370.

[Fayek 2007] S. A. Fayek, M. R. Balboul, and K. H. Marzouk. Optical, Electrical and Thermal Studies on $(As_2Se_3)_{3-x}(As_2Te_3)_x$ Glasses. *Thin Solid Films.* **2007**, *515*, 7281-7285.

[Feng 2014] S. Feng, S. M. Li, and H. Z. Fu. First-Principle Calculation and Quasi-Harmonic Debye Model Prediction for Elastic and Thermodynamic Properties of Bi_2Te_3. *Comp. Mat. Sci.* **2014**, *82*, 45-49.

[Fitzhugh 1997] E. W. Fitzhugh. *Orpiment and Realgar, in Artists' Pigments*. A Handbook of Their History and Characteristics, Vol 3, pp. 47−80 (Oxford University Press, **1997**).

[Forneris 1969] R. Forneris. The infrared and Raman spectra of realgar and orpiment. *American Mineralogist*. **1969**, *54*, 1062−1074.

[Frost 2002] R. L. Frost, W. N. Martens, and J. T. Kloprogge. Raman spectroscopic study of cinnabar (HgS), realgar (As_4S_4), and orpiment (As_2S_3) at 298 and 77K. *Neues Jahrbuch für Mineralogie. Mh. Jg.* **2002**, *10*, 469− 480.

[Frueh 1951] A. J. Frueh, Jr. The Crystal Structure of Claudetite (Monoclinic As_2O_3). *American Mineralogist.* **1951**, *36*, 833.

[García-Domene 2014] B. García-Domene, J. A. Sans, O. Gomis, F. J. Manjón, H. M. Ortiz, D. Errandonea, D. Santamaría-Pérez, D. Martínez-García, R. Vilaplana, A. L. J. Pereira, A. Morales-García, P. Rodríguez-Hernández, A. Muñoz, C. Popescu, and A. Segura. *Pbca*-Type In_2O_3: The High-Pressure Post-Corundum phase at Room Temperature. *J. Phys. Chem. C*. **2014**, *118*, 20545.

[Gasque 2013] L. Gasque Silva. Arsénico, el elemento inclasificable. *Educación Química*. **2013**, *24-2*, 495.

[Ghavamzadeh 2011] A. Ghavamzadeh, K. Alimoghaddam, S. Rostami, S.H. Ghaffari, M. Jahani, M. Iravani, S.A. Mousavi, B. Bahar, and M. Jalili. Phase II study of single-agent arsenic trioxide for the front-line therapy of acute promyelocytic leukemia. *Journal of Clinical Oncology*. **2011**, *29(20)*, 2753.

[Gibbs 2009] G. V. Gibbs, A. F. Wallace, D. F. Cox, P. M. Dove, R. T. Downs, N. L. Ross, and K. M. Rosso. Role of directed van der Waals bonded interactions in the determination of the structures of molecular arsenate solids. *J. Phys. Chem. A.* **2009**, *113*, 736.

[Gibbs 2010] G. V. Gibbs, A. F. Wallace, R. Zallen, R. T. Downs, N. L. Ross, D. F. Cox, and K. M. Rosso. Bond paths and van der Waals interactions in orpiment, As_2S_3. *J. Phys. Chem. A.* **2010**, *114*, 6550-6557.

[Gielen 2005] M. Gielen and E. R. Tiekink. *Metallotherapeutic Drugs and Metal-Based Diagnostic Agents.* (John Wiley & Sons, **2005**) p. 298.

[Gilliam 2003] S. J. Gilliam, C. N. Merrow, S. J. Kirkby, J. O. Jensen, D. Zeroka, and A. Banerjee. Raman spectroscopy of arsenolite: crystalline cubic As_4O_6. *J. Solid State Chem*. **2003**, *173*, 54.

[Gomis 2011] O. Gomis, R. Vilaplana, F. J. Manjón, P. Rodríguez-Hernández, E. Pérez-González, A. Muñoz, C. Drasar, and V. Kucek. Lattice Dynamics of Sb_2Te_3 at High Pressures. *Physical Review B: Condensed Matter and Materials Physics*. **2011**, *84*, 174305.

[Gomis 2014] O. Gomis, D. Santamaría-Pérez, J. Ruiz-Fuertes, J. A. Sans, R. Vilaplana, H. M. Ortiz, B. García-Domene, F. J. Manjón, D. Errandonea, P. Rodríguez-Hernández, A. Muñoz, and M. Mollar. High-Pressure Structural and Elastic Properties of Tl_2O_3. *J. App. Phys.* **2014**, *116*, 133521.

[Greaves 2011] G. N. Greaves, A. L. Greer, R. S. Lakes, and T. Rouxel. Poisson's ratio and modern materials. *Nat. Mater*. **2011**, *10*, 823.

[Grimme 2006] S. Grimme. Semiempirical GGA-type density functional constructed with a long-range dispersion correction. *Journal of Computational Chemistry*. **2006**, *27*, 1787-1799.

[Grimme 2010] S. Grimme, J. Antony, S. Ehrlich, and S. Krieg. A consistent and accurate *ab initio* parametrization of density functional dispersion correction (DFT-D) for the 94 elements H-Pu. *Journal of Chemical Physics*. **2010**, *132*, 154104.

[Grimwade 2009] D. Grimwade, J.V. Jovanovic, R.K. Hills, E.A. Nugent, Y. Patel, R. Flora, D. Diverio, K. Jones, H. Aslett, E. Batson, K. Rennie, R. Angell, R.E. Clark, E. Solomon, F. Lo-Coco, K. Wheatley, and A.K. Burnett. Prospective minimal residual disease monitoring to predict relapse of acute promyelocytic leukemia and direct pre-emptive arsenic trioxide therapy. *Journal of Clinical Oncology*. **2009**, *27(22)*, 3650.

[Grimvall 2012] G. Grimvall, B. Magyari-Köpe, V. Ozoliņš, and K. A. Persson. Lattice instabilities in metallic elements. *Rev. Mod. Phys*. **2012**, *84*, 945.

[Grund 2005] S. C. Grund, K. Hanusch, and H. Wolf. "Arsenic and Arsenic Compounds" in *Ullmann's Encyclopedia of Industrial Chemistry* (Wiley-VCH, **2005**). doi:10.1002/14356007.a03_113.pub2

[Grzechnik 1999] A. Grzechnik. Compressibility and Vibrational Modes in Solid As_4O_6. *J. Solid State Chem.* **1999**, *144*, 416.

[Guńka 2015a] P. A. Guńka, Z. Gontarz, and J. Zachara. Spatial dispersion of lone electron pairs?--experimental charge density of cubic arsenic(III) oxide. *Phys. Chem. Chem. Phys*. **2015**, *17*, 11020.

[Guńka 2015b] P. A. Guńka, K. F. Dziubek, A. Gladysiak, M. Dranka, J. Piechota, M. Hanfland, A. Katrusiak, and J. Zachara. Compressed Arsenolite As_4O_6 and Its Helium Clathrate $As_4O_6 \cdot 2He$. *Cryst. Growth Des*. **2015**, *15*, 3740.

[Guńka 2015c] P. A. Guńka, M. Dranka, M. Hanfland, K. F. Dziubek, A. Katrusiak, and J. Zachara. Cascade of High-Pressure Transitions of Claudetite II and the First Polar Phase of Arsenic(III) Oxide. *Crystal Growth & Design*. **2015**, *15*, 3950−3954.

[Hall 1960] H. T. Hall. Ultra-High-Pressure, High-Temperature Apparatus: the "Belt". *Review of Scientific Instruments.* **1960**, 31, 125.

[Hammersley 1996] A. P. Hammersley, S. O. Svensson, M. Hanfland, A. N. Fitch, and D. Hausermann. Two-Dimensional Detector Software: From Real Detector to Idealized Image or Two-Theta Scan. *High Pressure Research*. **1996**, *14*, 235−248.

[Haussühl 2007] S. Haussühl. *Physical Properties of Crystals. An Introduction.* (Wiley-VCH, Weinheim, **2007**).

[Hede 2007] K. Hede. Chinese folk treatment reveals power of arsenic to treat cancer, new studies under way. *Journal of the National Cancer Institute*. **2007**, *99*, 667.

[Heo 2014] J. Heo and W. J. Chung. *Rare-earth-doped chalcogenide glass for lasers and amplifiers*, in Chalcogenide Glasses: Preparation, Properties and Applications. (Woodhead Publishing, **2014**), pp. 347−380.

[Herman 2012] C. Herman. Cool as Helium. *Nat. Chem*. **2012**, *4*, 140.

[Hewak 2014] D. W. Hewak, N. I. Zheludev, and K. F. MacDonald. *Controlling light on the nanoscale with chalcogenide thin films*, in Chalcogenide Glasses: Preparation, Properties and Applications. (Woodhead Publishing, **2014**), pp. 471−508.

[Hill 1952] R. Hill. The Elastic Behaviour of a Crystalline Aggregate. *Proc. Phys. Soc. London A.* **1952**, *65*, 349.

[Hohenberg 1964] P. Hohenberg and W. Kohn. Inhomogeneous Electron Gas. *Physical Review*. **1964**, *136*, B864−B871.

[Hoppe 1979] R. Hoppe. Effective coordination numbers (ECoN) and mean Active fictive ionic radii (MEFIR). *Zeitschrift für Kristallographie*. **1979**, *150*, 23-52.

[Hoshino 1996] H. Hoshino, T. Miyanaga, H. Ikemoto, S. Hosoyawas, and H. Endo. The Semiconductor-Metal Transition of Liquid Arsenic-Selenium Mixtures at High Temperatures and High Pressures. *J. Non-Cryst. Solids.* **1996**, *205-207*, 43-47.

[Hsieh 2009] D. Hsieh, Y. Xia, D. Qian, L. Wray, F. Meier, J. H. Dil, J. Osterwalder, L. Patthey, A. V. Fedorov, H Lin, et al. Observation of Time-Reversal-Protected Single-Dirac-Cone Topological-Insulator State in Bi_2Te_3 and Sb_2Te_3. *Phys. Rev. Lett.* **2009**, *103*, 146401.

[Hwang 2001] H.Y. Hwang, G. Lenz, M.E. Lines, and R.E. Slusher. US Patent No 6.208.792 (**2001**).

[IARC 2004] International Agency for Research on Cancer. Some Drinking Water Disinfectants and Contaminants, including Arsenic. *Monographs on Evaluation of Carcinogenic Risk to Humans*. **2004**, *84*, 269.

[Ibáñez 2016] J. Ibáñez, J. A. Sans, C. Popescu, J. López-Vidrier, J. J. Elvira-Betanzos, V. P. Cuenca-Gotor, O. Gomis, F. J. Manjón, P. Rodríguez-Hernández, and A. Muñoz. Structural, Vibrational, and Electronic Study of Sb_2S_3 at High Pressure. *Journal of Physical Chemistry C*. **2016**, *120*, 10547-10558.

[Ibarra-Hernández 2014] W. Ibarra-Hernández, M. J. Verstraete, and J-Y. Raty. Effect of Hydrostatic Pressure on the Thermoelectric Properties of Bi_2Te_3. *Phys. Rev. B.* **2014**, *90*, 245204.

[Itié 1992] J. P. Itié, A. Polian, M. Grimsditch, and S. Susman. X-ray absorption spectroscopy Investigation of Amorphous and Crystalline As_2S_3. *Japanese Journal of Applied Physics*. **1992**, *32, Suppl. 2*, 719−721.

[Jacobsen 2007] M. K. Jacobsen, R. S. Kumar, A. L. Cornelius, S. V. Sinogeiken, and M. F. Nicol. High Pressure X-Ray Diffraction Studies of $Bi_{2-x}Sb_xTe_3$ (x = 0,1,2). *AIP Conf. Proc.* **2007**, *955*, 171-174.

[Jeanne 2010] M. Jeanne, V. Lallemand-Breitenbach, O. Ferhi, M. Koken, M. Le Bras, S. Duffort, L. Peres, C. Berthier, H. Soilihi, B. Raught, and H. de Thé. PML/RARA oxidation and arsenic binding initiate the antileukemia response of As_2O_3. *Cancer Cell*. **2010**, *18*, 88.

[Jensen 2003] J. O. Jensen, S. J. Gilliam, A. Banerjee, D. Zeroka, S. J. Kirkby, and C. N. Merrow. A theoretical study of As_4O_6: vibrational analysis, infrared and Raman spectra. *J. Mol. Str.: THEOCHEM*. **2003**, *664-665*, 145.

[Johnson 2010] E. Johnson, S. Keinan, P. Mori-Sánchez, J. Contreras-García, A. Cohen, and W. Yang. Revealing noncovalent interactions. *J. Am. Chem. Soc*. **2010**, *132*, 6498.

[Kampf 2011] A. R. Kampf, R. T. Downs, R. M. Housley, R. A. Jenkins, and J. Hyršl. Anorpiment, As_2S_3, the triclinic dimorph of orpiment. *Mineral. Mag*. **2011**, *75*, 2857-2867.

[Kanishcheva 1982] A. S. Kanishcheva, Y. N. Milhailov, and A. P. Chernov. Refinement of the Crystal Structure of Arsenic Telluride As_2Te_3. *Inorg. Mater*. **1982**, *18*, 796-799.

[Karki 2001] B. B. Karki, L. Stixrude, and R. M. Wentzcovitch. High-pressure elastic properties of major materials of Earth's mantle from first principles. *Reviews of Geophysics*. **2001**, *39*, 507.

[Kirkinskii 1974] V. A. Kirkinskii and V. G. Yakushev. The System As-Te at high Pressures. *Izves. Akad. Nauk SSSR, Neorg. Mat.* **1974**, *10*, 1431-1435; idem, *Inorg. Mater*. **1974**, *10*, 1230-1233.

[Kirshenbaum 2013] K. Kirshenbaum, P. S. Syers, A. P. Hope, N. P. Butch, J. R. Jeffries, S. T. Weir, J. J. Hamlin, M. B. Maple, Y. K. Vohra, and J. Paglione. Pressure-Induced Unconventional Superconducting Phase in the Topological Insulator Bi_2Se_3. *Phys. Rev. Lett.* **2013**, *111*, 087001.

[Klotz 2009] S. Klotz, J-C. Chervin, P. Munsch, and G. Le Marchand. Hydrostatic limits of 11 pressure transmitting media. *Journal of Physics D: Applied Physics*. **2009**, *42*, 075413.

[Koch 2007] I. Koch, S. Sylvester, V. W. Lai, A. Owen, K. J. Reimer, and W. R. Cullen. Bioaccessibility and excretion of arsenic in Niu Huang Jie Du Pian pills. *Toxicology and Applied Pharmacology*. **2007**, *222*, 357.

[Kong 2014] P. P. Kong, F. Sun, L. Y. Xing, J. Zhu, S. J. Zhang, W. M. Li, Q. Q. Liu, X. C. Wang, S. M. Feng, and X. H. Yu. Superconductivity in Strong Spin Orbital Coupling Compound Sb_2Se_3. *Sci. Rep.* **2014**, *4*, 6679.

[Kovanda 2003] V. Kovanda, M. Vicek, and H. J. Jain. Structure of As–Se and As–P–Se Glasses Studied by Raman Spectroscopy. *J. Non-Cryst. Solids.* **2003**, *326-327*, 88-92.

[Kozono 2018] S. Kozono, Y-M. Lin, H-S. Seo, B. Pinch, X. Lian, C. Qiu, M.K. Herbert, C-H. Chen, L. Tan, Z.J. Gao, W. Massefski, Z.M. Doctor, B.P. Jackson, Y. Chen, S. Dhe-Paganon, K.P. Lu, and X.Z. Zhou. Arsenic targets Pin1 and cooperates with retinoic acid to inhibit cancer-driving pathways and tumor-initiating cells. *Nature Communications*. **2018**, *9*, 3069.

[Krasil'nikov 2014] O. M. Krasil'nikov, M. P. Belov, A. V. Lugovskoy, I. Yu. Mosyagin, and Yu. Kh. Vekilov. Elastic properties, lattice dynamics and structural transitions in molybdenum at high pressures. *Computational Materials Science*. **2014**, *81*, 313.

[Kravchenko 1980] E. A. Kravchenko, A. V. Timofeeva, and G. Z. Virogradova. Crystals Modifications of Arsenic and Antimony Sulphides at High Pressure and Temperature. *Journal of Molecular Structure*. **1980**, *58*, 253−262.

[Kresse 1993] G. Kresse and J. Hafner. Ab Initio Molecular Dynamics for Liquid Metals. *Physical Review B*. **1993**, *47*, 558−561.

[Kresse 1994] G. Kresse and J. Hafner. Ab initio molecular-dynamics simulation of the liquid-metal–amorphous-semiconductor transition in germanium. *Phys. Rev. B*. **1994**, *49*, 14251.

[Kresse 1996a] G. Kresse and J. Furthmüller. Efficiency of *ab initio* Total-Energy Calculations for Metals and Semiconductors Using a Plane-wave Basis Set. *Computational Materials Science*. **1996**, *6*, 15-50.

[Kresse 1996b] Kresse and J. Furthmüller. Efficient Iterative Schemes for *ab initio* Total-energy Calculations Using a Plane-wave Basis Set. *Physical Review B: Condensed Matter and Materials Physics.* **1996**, *54*, 11169-11186.

[Kresse 1999] G. Kresse and D. Joubert. From Ultrasoft Pseudopotentials to the Projector Augmented-wave Method. *Physical Review B: Condensed Matter and Materials Physics.* **1999**, *59*, 1758-1775.

[Kristofik 1985] J. Kristofik, J. J. Mares, and V. Smid. The Effect of Pressure on Conductivity and Permittivity of As_2Te_3-Based Glasses. *Phys. Stat. Sol. A.* **1985**, *89*, 333-345.

[Kroumova 2003] E. Kroumova, M. I. Aroyo, J. M. Pérez-Mato, A. Kirov, C. Capillas, S. Ivantchev, and H. Wondratschek. Bilbao Crystallographic Server: Useful Databases and Tools for Phase-Transition Studies. *Phase Transitions*. **2003**, *76*, 155−170.

[Kulibekov 2003] A. M. Kulibekov, H. P. Olijnyk, A. P. Jephcoat, Z. Y. Salaeva, S. Onari, and K. R. Allakverdiev. Raman Scattering under Pressure and the Phase Transition in ε-GaSe. *Physica Status Solidi B.* **2003**, *235*, 517.

[Kyono 2013] A. Kyono. Ab initio quantum chemical investigation of arsenic sulfide molecular diversity from As_4S_6 and As_4. *Phys. Chem. Miner.* **2013**, *40*, 717.

[Larson 2004] A. C. Larson and R. B. von Dreele. General Structure Analysis System (GSAS). *LANL Report* **2004**, *86*, 748.

[Lazo 2003] G. Lazo, H. Kantarjian, E. Estey, D. Thomas, S. O'Brien, and J. Cortes. Use of arsenic trioxide (As_2O_3) in the treatment of patients with acute promyelocytic leukemia. *Cancer*. **2003**, *97*, 2218.

[Le Page 2002] Y. Le Page and P. Saxe. Symmetry-general least-squares extraction of elastic data for strained materials from ab initio calculations of stress. *Phys. Rev. B.* **2002**, *65*, 104104.

[Lee 2014] S. Lee, K. Esfarjani, T. F. Luo, J. W. Zhou, Z. T. Tian, and G. Chen. Resonant bonding leads to low lattice thermal conductivity. *Nature Communications*. **2014**, *5*, 3525.

[Lepore 2012] G. O. Lepore, T. Boffa Ballaran, F. Nestola, L. Bindi, D. Pasqual, and P. Bonazzi. Compressibility of β-As_4S_4: an in situ high-pressure single-crystal X-ray study. *Mineral. Mag*. **2012**, *76*, 963.

[Levi 2004] C. G. Levi. Emerging materials and processes for thermal barrier systems. *Curr. Opin. Solid State Mater. Sci*. **2004**, *8*, 77-91.

[Li 2015] C. W. Li, J. Hong, A. F. May, D. Bansal, S. Chi, T. Hong, G. Ehlers, and O. Delaire. Orbitally driven giant phonon anharmonicity in SnSe. *Nature Physics*. **2015**, *11*, 1063–1069.

[Lifshitz 1960] I. M. Lifshitz. Anomalies of Electron Characteristics of a Metal in the High Pressure Region. *Sov. Phys. JETP*. **1960**, *11*, 1130.

[Lin 2007] M. Lin, Z. Wang, and D. S. Zhang. Preparation of orpiment nanoparticles and their cytotoxic effect on cultured leukemia K562 cells. *Journal of Nanoscience and Nanotechnology*. **2007**, *7*, 490.

[Lin 2008] M. Lin, D. S. Zhang, H. Li, J. Ye, and L. X. Zhang. Anticancer effect of orpiment nanoparticles on K562 cells in vitro and its mechanism. *Nanotechnology and Precision Engineering*. **2008**, *6(1)*, 14.

[Lindberg 2013] G. P. Lindberg, R. E. Tallman, R. Lauck, M. Cardona, X. Liu, J. K. Furdyna, and B. A. Weinstein. Effects of Pressure on Photo-Induced Formation of Se and Te Clusters in II–VI Compounds. *Phys. Status Solidi B.* **2013**, *250*, 711− 715.

[Liu 2007] J. Liu, R. Goyer, and M. P. Waalkes. "Toxic effects of metals." in *Casarett and Doull's Toxicology – The Basis of Poisons, 7th Ed*. Ed. C. D. Klaassen (McGraw Hill, New York, **2007**, 931-979).

[Liu 2008] J. Liu, Y. Lu, Q. Wu, R. A. Goyer, and M. P. Waalkes. Mineral Arsenicals in Traditional Medicines: Orpiment, Realgar, and Arsenolite. *The Journal of Pharmacology and Experimental Therapeutics*. **2008**, *326*, 2-363.

[Liu 2011] Q. J. Liu, Z. T. Liu, and L. P. Feng. First-Principles Calculations of Structural, Elastic and Electronic Properties of Tetragonal HfO_2 under Pressure. *Commun. Theor. Phys*. **2011**, *56*, 779.

[Liu 2013] G. T. Liu, L. Zhu, Y. M. Ma, C. L. Lin, and J. Liu. Stabilization of 9/10-Fold Structure in Bismuth Selenide at High Pressures. *J. Phys. Chem. C* **2013**, *117*, 10045-10050.

[Liu 2019] K. X. Liu, L. D. Dai, H. P. Li, H. Y. Hu, L. F. Yang, C. Pu, M. L. Hong, and P. F. Liu. Phase Transition and Metallization of Orpiment by Raman Spectroscopy, Electrical Conductivity and Theoretical Calculation under High Pressure. *Materials*. **2019**, *12*, 784.

[Lockwood 2000] D.J. Lockwood. Raman Spectroscopy of Oxides of GaAs Formed in Solution. *J. Sol. Chem*. **2000**, *29*, 1039.

[Loubeyre 1993] P. Loubeyre, M. Jean-Louis, R. LeToullec, and L. Charon-Gerard. High pressure measurements of the He-Ne binary phase diagram at 296 K: Evidence for the stability of a stoichiometric $Ne(He)_2$ solid. *Phys. Rev. Lett*. **1993**, *70*, 178.

[Lu 2002] D. P. Lu, J. Y. Qiu, B. Jiang, Q. Wang, K. Y. Liu, Y. R. Liu, and S. S. Chen. Tetra-arsenic tetra-sulfide for the treatment of acute promyelocytic leukemia: a pilot report. *Blood*. **2002**, *99*, 3136.

[Lu 2014] Z. Lu and T. Hunter. Pin 1 and cancer. *Cell Research*. **2014**, *24*, 1033.

[Lucogsky 1972] G. Lucogsky. Comparison of the Long Wave Optical Phonons in Se and Te. *Physica Status Solidi B*. **1972**, *49*, 633−641.

[Lukic 2003] S. R. Lukic, D. M. Petrovic, S. J. Skuban, Lj. Radonjic, and Z. Cvejic. Formation of Complex Structural Units and Structure of As-S-Se-Te-I Glasses. *J. Opt. Adv. Mater*. **2003**, *5*, 1223-12229.

[Lundblad 1994] E. W. Lundblad. High pressure synthesis of diamond in Sweden in 1953. *AIP Conference Proceedings.* **1994**, 309, 503.

[Lundegaard 2003] L. F. Lundegaard, R. Miletich, T. Balic-Zunic, and E. Makovicky. Equation of State and Crystal Structure of Sb_2S_3 between 0 and 10 GPa. *Phys. Chem. Minerals.* **2003**, *30*, 463-468.

[Lundegaard 2005] L. F. Lundegaard, E. E. Makovicky, T. Boffa-Ballaran, and T. Balic-Zunic. Crystal Structure and Cation Lone Electron Pair Activity of Bi_2S_3 between 0 and 10 GPa. *Phys. Chem. Minerals.* **2005**, *32*, 578-584.

[Ma 2012] Y. M. Ma, G. T. Liu, P. W. Zhu, H. Wang, X. Wang, Q. L. Cui, J. Liu, and Y. M. Ma. Determinations of the High-Pressure Crystal Structures of Sb_2Te_3. *J. Phys: Condens. Matter*. **2012**, *24*, 475403.

[Machon 2006] D. Machon, P. F. McMillan, B. Xu, and J. J. Dong. High-Pressure Study of the β-to-α Transition in Ga_2O_3. *Phys. Rev. B.* **2006**, *73*, 094125.

[Madan 1988] A. Madan, and M. P. Show. *The Physics and Application of Amorphous Semiconductors*. (Academic Press: Boston-San Diego, **1988**).

[Maeda 2004] H. Maeda, S. Hori, H. Ohizumi, T. Segawa, Y. Kakehi, O. Ogawa, and A. Kakizuka. Effective treatment of advanced solid tumors by the combination of arsenic trioxide and L-buthionine-sulfoximine. *Cell Death & Differentiation*. **2004**, *11*, 737.

[Mamedov 2018] S. Mamedov and N. Drichko. Characterization of 2D As_2S_3 crystal by Raman spectroscopy. *MRS Advances*. **2018**, *3*, 385−390.

[Manjón 2013] F. J. Manjón, R. Vilaplana, O. Gomis, E. Pérez-González, D. Santamaría-Pérez, V. Marín-Borrás, A. Segura, J. González, P. Rodríguez-Hernández, and A. Muñoz. High-Pressure Studies of Topological Insulators Bi_2Se_3, Bi_2Te_3, and Sb_2Te_3. *Physica Status Solidi B*. **2013**, *250*, 669-676.

[Mao 1986] M. K. Mao, J. Xu, and P. M. Bell. Calibration of the Ruby Pressure Gauge to 800 kbar under Quasi-Hydrostatic Conditions. *Journal of Geophysical Research.* **1986**, *91*, 4673−4676.

[Marini 2012] C. Marini, D. Chermisi, M. Lavagnini, D. Di Castro, C. Petrillo, L. Degiorgi, S. Scandolo, and P. Postorino. High-pressure phases of crystalline tellurium: A combined Raman and ab initio study. *Physical Review B.* **2012**, *86*, 064103.

[Mathieu 1970] J. M. Mathieu and H. Poulet. Spectres de vibration de l'orpiment As_2S_3. *Bulletin de la Société Française de Minéralogie et de Cristallographie*. **1970**, *93*, 532−535.

[Matsumoto 2010] A. Matsumoto, Y. Koyama, and I. Tanaka. Structures and energetics of Bi_2O_3 polymorphs in a defective fluorite family derived by systematic first-principles lattice dynamics calculations. *Phys. Rev. B.* **2010**, *81*, 094117.

[Matsumoto 2011] A. Matsumoto, Y. Koyama, and I. Tanaka. Electronic structures of dynamically stable As_2O_3, Sb_2O_3, and Bi_2O_3 crystal polymorphs. *Phys. Rev. B.* **2011**, *83*, 214110.

[Mei 2007a] Q. Mei, R. T. Hart, C. J. Benmore, S. Amin, K. Leinenweber, and J. L. Yarger. The structure of densified As_2O_3 glasses. *J. Non-Cryst. Solids*. **2007**, *353*, 1755.

[Mei 2007b] Q. Mei, C. J. Benmore, E. Soignard, S. Amin, and J. L. Yarger. Analysis of high-energy X-ray diffraction data at high pressure: the case of vitreous As_2O_3 at 32 GPa. *J. Phys.: Condens. Matter*. **2007**, *19*, 415103.

[Mendoza-Galván 2000] A. Mendoza-Galván, E. García-García, Y. V. Vorobiev, and J. González-Hernández. Structural, Optical and Electrical Characterization of Amorphous Se_xTe_{1-x} Thin Film Alloys. *Microelectron. Eng.* **2000**, *51-52*, 677-687.

[Miller 2002] W. H. Jr. Miller, H. M. Schipper, J. S. Lee, J. Singer, and S. Waxman. Mechanism of action of arsenic trioxide. *Cancer Research*. **2002**, *62*, 3893.

[Minomura 1979] S. Minomura, K. Aoki, N. Koshizuka, and T. Tsushima. *The Effect of Pressure on The Raman Spectra in Trigonal Se and Te*. in High-Pressure Science and Technology (Springer, **1979**), p. 435.

[Momma 2011] K. Momma and F. Izumi. VESTA 3 for Three-dimensional Visualization of Crystal, Volumetric and Morphology Data. *Journal of Applied Crystallography*. **2011**, *44*, 1272−1276.

[Monkhorst 1976] H. J. Monkhorst and J. D. Pack. Special points for Brillouin-zone integrations. *Physical Review B*. **1976**, *13*, 5188.

[Morimoto 1954] N. Morimoto. The crystal structure of orpiment (As_2S_3) refined. *Mineralogical Journal*. **1954**, *1(3)*, 160-169.

[Morin 2015] C. Morin, S. Corallini, J. Carreaud, J. B. Vaney, G. Delaizir, J. C. Crivello, E. B. Lopes, A. Piarristeguy, J. Monnier, C. Candolfi, et al. Polymorphism in Thermoelectric As_2Te_3. *Inorg. Chem.* **2015**, *54*, 9936-9947.

[Mujica 2003] A. Mujica, A. Rubio, A. Muñoz, and R. J. Needs. High-pressure phases of group-IV, III–V, and II–VI compounds. *Rev. Mod. Phys.* **2003**, *75*, 863, and references therein.

[Mullen 1972] D. J. E. Mullen and W. Nowacki. Refinement of the crystal structures of realgar, AsS and orpiment, As_2S_3. *Zeitschrift für Kristallographie*. **1972**, *136*, 48-65.

[Nakayama 2009] A. Nakayama, M. Einaga, Y. Tanabe, S. Nakano, F. Ishikawa, and Y. Yamada. Structural Phase Transition in Bi_2Te_3 under High Pressure. *High Pressure Res.* **2009**, *29*, 245-249.

[National Research Council 1999] National Research Council, Subcommittee on Arsenic in Drinking Water, Committee on Toxicology, Board on Environmental Studies and Toxicology, and Commission on Life Sciences. *Arsenic in the Drinking Water*. National Academy Press (Washington, DC, **2005**).

[Nielsen 2015] M. B. Nielsen, P. Parisiades, S. R. Madsen, and M. Bremholm. High-Pressure Phase Transitions in Ordered and Disordered Bi_2Te_2Se. *Dalton Transactions* **2015**, *44*, 14077-14084.

[Niu 1999] C. Niu, H. Yan, T. Yu, H.P. Sun, J.X. Liu, X-S. Li, W. Wu, F.Q. Zhang, Y. Chen, L. Zhou, J.M. Li, X.Y. Zeng, R.R. Yang, M.M. Yuan, M.Y. Ren, F.Y. Gu, Q. Cao, B.W. Gu, X.Y. Su, G-Q. Chen, S.M. Xiong, T.D. Zhang, S. Waxman, Z-Y. Wang, Z. Chen, J. Hu, Z-X. Shen, and S.J. Chen. Studies on treatment of acute promyelocytic leukemia with arsenic trioxide: remission induction, follow-up, and molecular monitoring in 11 newly diagnosed and 47 relapsed acute promyelocytic leukemia patients. *Blood*. **1999**, *94*, 3315.

[Nolas 2001] G. S. Nolas, J. Sharp, and J. Goldsmid. *Thermoelectrics*. (Eds. Springer: Berlin, **2001**).

[Nye 1957] J. F. Nye. *Physical Properties of Crystals. Their Representation by Tensor and Matrices* (Oxford University Press, **1957**).

[Otero-de-la-Roza 2012] A. Otero-de-la-Roza, J. Contreras-Garcia, and E. R. Johnson. Revealing non-covalent interactions in solids: NCI plots revisited. *Phys. Chem. Chem. Phys.* **2012**, *14*, 12165.

[Ovsyannikov 2015] S. V. Ovsyannikov, N. V. Morozova, I. V. Korobeinikov, L. N. Lukyanova, A. Y. Manakov, A. Y. Likhacheva, A. I. Ancharov, A. P. Vokhmyanin, I. F. Berger, O. A. Usov, et al. Enhanced Power Factor and High-Pressure Effects in $(Bi,Sb)_2(Te,Se)_3$ Thermoelectrics. *Appl. Phys. Lett.* **2015**, *106*, 143901.

[Papatheodorou 1976] G. N. Papatheodorou and S. A. Solin. Vibrational excitations of As_2O_3. I. Disordered phases. *Phys. Rev. B.* **1976**, *13*, 1741.

[Pal 2014] K. Pal, and U. V. Waghmare. Strain Induced Z_2 Topological Insulating State of β-As_2Te_3. *App. Phys. Lett.* **2014**, *105*, 062105.

[Parlinski 1997] K. Parlinski, Z. Q. Li, and Y. Kawazoe. First-Principles Determination of the Soft Mode in Cubic ZrO_2. *Physical Review Letters.* **1997**, *78*, 4063−4066.

[Parthasarathy 1985] G. Parthasarathy, and E. S. R. Gopal. Effect of High Pressure on Chalcogenide Glasses. *Bull. Mater. Sci.* **1985**, *7*, 271-302.

[Perdew 1996] J. P. Perdew, K. Burke, and M. Ernzerhof. Generalized Gradient Approximation Made Simple. *Physical Review Letters*. **1996**, *77*, 3865−3868.

[Perdew 2008] J. P. Perdew, A. Ruzsinszky, G. I. Csonka, O. A. Vydrov, G. E. Scuseria, L. A. Constantin, X. Zhou, and K. Burke. Restoring the Density-Gradient Expansion for Exchange in Solids and Surfaces. *Physical Review Letters*. **2008**, *100*, 136406.

[Pereira 2012] A. L. J. Pereira, L. Gracia, D. Santamaria-Perez, R. Vilaplana, F. J. Manjon, D. Errandonea, M. Nalin, and A. Beltran. Structural and vibrational study of cubic Sb_2O_3 under high pressure. *Phys. Rev. B.* **2012**, *85*, 174108.

[Pereira 2013] A. L. J. Pereira, D. Errandonea, A. Beltran, L. Gracia, O. Gomis, J. A. Sans, B. Garcia-Domene, A. Miquel-Veyrat, F. J. Manjon, A. Muñoz, and

C. Popescu. Structural study of α-Bi_2O_3 under pressure. *J. Phys.: Condens. Matter*. **2013**, *25*, 475402.

[Pereira 2014a] A. L. J. Pereira, O. Gomis, J. A. Sans, J. Pellicer-Porres, F. J. Manjón, A. Beltrán, P. Rodríguez-Hernández, and A. Muñoz. Pressure Effects on the Vibrational Properties of α-Bi_2O_3: an Experimental and Theoretical Study. *J. Phys.: Condens. Matter*. **2014**, *26*, 225401.

[Pereira 2014b] A. L. J. Pereira, J. A. Sans, O. Gomis, F. J. Manjón, P. Rodríguez-Hernández, A. Muñoz, C. Popescu, and A. Beltrán. Isostructural Second-Order Phase Transition of β-Bi_2O_3 at High Pressures: an Experimental and Theoretical Study. *J. Phys. Chem. C.* **2014**, *118*, 23189-23201.

[Pereira 2018] A. L. J. Pereira, D. Santamaría-Pérez, J. Ruíz-Fuertes, F. J. Manjón, V. P. Cuenca-Gotor, R. Vilaplana, O. Gomis, C. Popescu, A. Muñoz, P. Rodríguez-Hernández, A. Segura, L. Gracia, A. Beltrán, P. Ruleova, C. Drasar, and J. A. Sans. Experimental and Theoretical Study of Bi_2O_2Se Under Compression. *Journal of Physical Chemistry C*. **2018**, *122*, 8853−8867.

[Pershagen 1981] G. Pershagen. The Carcionogenicity of Arsenic. *Enviromental Health Perspectives*. **1981**, *40*, 93.

[Pertlik 1978a] F. Pertlik. Strukturverfeinerung von Kubischem As_2O_3 (Arsenolith) mit Einkristalldaten. *Czech. J. Phys. B*. **1978**, *28*, 170.

[Pertlik 1978b] F. Pertlik. Verfeinerung der Kristallstruktur des Minerals Claudetit, As_2O_3 ("Claudetit I"). *Monatshefte für Chemie*. **1978**, *109*, 277-282.

[Piermarini 1973] G. J. Piermarini, S. Block, and J. D. Barnett. Hydrostatic limits in liquids and solids to 100 kbar. *Journal of Applied Physics*. **1973**, *44*, 5377−5382.

[Pine 1971] A. S. Pine and G. Dresselhaus. Raman Spectra and Lattice Dynamics of Tellurium. *Phys. Rev. B.* **1971**, *4*, 356-371.

[Pliny the Elder 1855] Pliny the Elder. *Naturalis Historia, Chapter 22*, edited by J. Bostock MD FRS, H. T. Riley, Esq., B.A. London. (Taylor and Francis, London, **1855**).

[Pliny 1938] Pliny the Elder. *Natural History I*, ed. by E. H. Warmington (Harvard University Press, Cambridge, **1938**, 147).

[Poirier 2000] J. P. Poirier. *Introduction to the Physics of the Earth's Interior* (Cambridge University Press, **2000**).

[Polian 2011] A. Polian, M. Gauthier, S. M. Souza, D. M. Triches, J. Cardoso de Lima, and T. A. Grandi. Two-Dimensional Pressure-Induced Electronic Topological Transition in Bi_2Te_3. *Phys. Rev. B.* **2011**, *83*, 113106.

[Popescu 2000] M. A. Popescu. *Non-crystalline chalcogenides*. (Dordrecht, Kluwer Academic Publishing. **2000**).

[Porto 1962] S. P. S. Porto and D. L. Wood. Ruby Optical Maser as a Raman source. *Journal of the Optical Society of America*. **1962**, *52*, 251−252.

[Properzi 2013] L. Properzi, A. Polian, P. Munsch, and A. Di Cicco. Investigation of the phase diagram of selenium by means of Raman spectroscopy. *High Pressure Research*. **2013**, *33*, 35−39.

[Pugh 1954] S. F. Pugh. XCII. Relations between the elastic moduli and the plastic properties of polycrystalline pure metals. *Philos. Mag*. **1954**, *45*, 823.

[Quadbeck 2007] H.-J. Quadbeck-Seeger. *World of the Elements – Elements of the World*. (Wiley-VCH, Weinheim, **2007**, 51).

[Radescu 2017] S. Radescu, A. Mujica, P. Rodríguez-Hernández, A. Muñoz, J. Ibáñez, J. A. Sans, V. P. Cuenca-Gotor, and F. J. Manjón. Study of the orpiment and anorpiment phases of As_2S_3 under pressure. *Journal of Physics: Conference Series*. **2017**, *950*, 042018.

[Ramesh 2014] K. Ramesh. Pressure Dependence of Glass Transition in As_2Te_3 Glass. *J. Phys. Chem. B* **2014**, *118*, 8848-8853.

[Ramos 2009] C.O. Ramos Peñafiel, H. Castellanos Sinco, E. Montaño, C. Martínez Murillo, P. Lavielle, y V. García Vidrios. Experiencia del tratamiento de leucemia promielocítica aguda (LAP) en el Hospital General de México: protocolo LAP 2001. *Revista de Hematología Mexicana*. **2009**, *10 (supl2)*, 57.

[Raty 2018] J-Y. Raty, M. Schumacher, P. Golub, V. L. Deringer, C. Gatti, and M. Wuttig. A Quantum-Mechanical Map for Bonding and Properties in Solids. *Advanced Materials*. **2018**, *31*, 1806280.

[Razzetti 1979] C. Razzetti and P. P. Lottici. Polarization analysis of the Raman spectrum of As_2S_3 crystals. *Solid State Communications*. **1979**, *29*, 361−364.

[Reuss 1929] A. Reuss. Berechnung der Fließgrenze von Mischkristallen auf Grund der Plastizitätsbedingung für Einkristalle. *Z. Angew. Math. Mech*. **1929**, *9*, 49.

[Richter 1973] W. Richter, J. B. Renucci, and M. Cardona. Hydrostatic Pressure Dependence of First-Order Raman Frequencies in Se and Te. *Phys. Status Solidi B.* **1973**, *56*, 223-229.

[Rodríguez-Fernández 2016] C. Rodríguez-Fernández, C. V. Manzano, A. H. Romero, J. Martín, M. Martín-González, M. Morais de Lima Jr, and A. Cantarero. The Fingerprint of Te-rich and Stoichiometric Bi_2Te_3 Nanowires by Raman Spectroscopy. *Nanotechnology.* **2016**, *27*, 075706.

[Rzepa 2010] H. S. Rzepa.The rational design of helium bonds. *Nat. Chem*. **2010**, *2*, 390.

[Saint-Exupéry 2010] A. de Saint-Exupéry. *El principito*. (Salamandra, **2010**, p. 50; 1ª edición: Éditions Gallimard, 1943).

[Sakai 1977] N. Sakai, and H. Fritzsche. Semiconductor-Metal and Superconducting Transitions Induced by Pressure in Amorphous As_2Te_3. *Phys. Rev. B.* **1977**, *15*, 973-978.

[Saleh 2012] G. Saleh, C. Gatti, L. Lo Presti, and J. Contreras-Garcia. Revealing Non-covalent Interactions in Molecular Crystals through Their Experimenatl Electron Densities. *Chem. Eur. J.* **2012**, *18*, 15523.

[Sanghera 2006] J. S. Sanghera, I. D. Aggarwal, L. B. Shaw, C. M. Florea, P. Pureza, V. G. Nguyen, and F. J. Kung. Nonlinear Properties of Chalcogenide Glass Fibers. *J. Optoelectron. Adv. Mater.* **2006**, *8*, 2148-2155.

[Sans 2015] J. A. Sans, F. J. Manjón, C. Popescu, V. P. Cuenca-Gotor, O. Gomis, A. Muñoz, P. Rodríguez-Hernández, J. Pellicer- Porres, A. L. J. Pereira, D. Santamaría-Pérez, and A. Segura. Helium ordered trapping in arsenolite under compression: Synthesis of $He_2As_4O_6$. **2015**, arXiv:1502.04279.

[Sans 2016a] J.A. Sans, F.J. Manjón, C. Popescu, V.P. Cuenca-Gotor, O. Gomis, A. Muñoz, P. Rodríguez-Hernández, J. Contreras-García, J. Pellicer-Porres, A.L.J. Pereira, D. Santamaría-Pérez, and A. Segura. Ordered helium trapping and bonding in compressed arsenolite: Synthesis of $As_4O_6 \cdot 2He$. *Phys. Rev. B.* **2016**, *93*, 054102.

[Sans 2016b] J.A. Sans, F.J. Manjón, C. Popescu, A. Muñoz, P. Rodríguez-Hernández, J.L. Jordá, and F. Rey. Arsenolite: a quasi-hydrostatic solid pressure-transmitting medium. *J. Phys: Condens. Matter*. **2016**, *28*, 475403.

[Sans 2016c] J. A. Sans, F. J. Manjón, A. L. J. Pereira, R. Vilaplana, O. Gomis, A. Segura, A. Muñoz, P. Rodríguez-Hernández, C. Popescu, C. Drasar, et al. Structural, Vibrational, and Electrical Study of Compressed BiTeBr. *Physical Review B: Condensed Matter and Materials Physics.* **2016**, *93*, 024110.

[Sanz 2005] M. Sanz, P. Fenaux, and F. Lo-Coco. Arsenic trioxide in the treatment of acute promyelocytic leukemia. A review of current evidence. *Haematologica*. **2005**, *90*, 1231.

[Sato 2011] T. Sato, N. Funamori, and T. Yagi. Helium penetrates into silica glass and reduces its compressibility. *Nat. Commun*. **2011**,*2*, 345.

[Scheidemantel 2003] T. J. Scheidemantel, and J. V. Badding. Electronic Structure of β-As_2Te_3. *Solid State Commun.* **2003**, *127*, 667-670.

[Scheidemantel 2005] T. J. Scheidemantel, J. F. Meng, and J. V. Badding. Thermoelectric Power and Phase Transition of Polycrystalline As_2Te_3 under Pressure. *J. Phys. Chem. Solids.* **2005**, *66*, 1744-1747.

[Scherrer 2005] H. Scherrer and S. Scherrer. "Thermoelectric Properties of Bismuth Antimony Telluride Solid Solutions." in *Thermoelectrics Handbook: Macro to Nano*. Ed. D.M. Rowe (CRC Press: Boca Raton, FL, **2005**).

[Scheuermann 1969] W. Scheuermann and G. J. Ritter. Raman spectra of cinnabar (HgS), realgar (As_4S_4) and orpiment (As_2S_3). *Zeitschrift für Naturforschung*. **1969**, *A 24*, 408−411.

[Shen 1997] Z-X. Shen, G-Q. Chen, J-H. Ni, X-S Li, S.M. Xiong, Q.Y. Qiu, J. Zhu, W. Tang, G.L. Sun, K.Q. Yang, Y. Chen, L. Zhou, Z-W. Fang, Y.T. Wang, J. Ma, P. Zhang, T-D- Zhang, S.J. Chen, and Z-Y Wang. Use of arsenic trioxide (As2O3) in the treatment of acute promyelocytic leukemia (APL): II. Clinical efficacy and pharmacokinetics in relapsed patients. *Blood*. **1997**, *89*, 3354.

[Shen 2004] J. C. Shen, K. Y. Liu, B. Jiang, X. J. Lu, and D. P. Lu. Effect of the tetra-arsenic tetra-sulfide (As_4S_4) on the corrected QT interval in the treatment of acute promyelocytic leukemia. *Zhonghua Xue Ye Xue Za Zhi*. **2004**, *25*, 359.

[Shen 2011] G. Shen, Q. Mei, V. B. Prakapenka, P. Lazor, S. Sinogeikin, Y. Meng, and C. Park. Effect of helium on structure and compression behavior os SiO_2 glass. *Proc. Natl. Acad. Sci. U. S. A.* **2011**, *108*, 6004.

[Shen 2013] S. Shen, X-F. Li, W.R. Cullen, M. Weinfeld, and X.C. Le. Arsenic binding to proteins. *Chemical Reviews*. **2013**, *113*, 7769.

[Shimojo 2002] F. Shimojo, K. Hoshino, and Y. Zempo. Atomic and Electronic Structures in Liquid Arsenic Telluride by ab initio Molecular Dynamics Simulations. *J. Phys.: Condens. Matter*. **2002**, *14*, 8425-8433.

[Shportko 2008] K. Shportko, S. Kremers, M. Woda, D. Lencer, J. Robertson, and M. Wuttig. Resonant bonding in crystalline phase-change materials. *Nature Materials*. **2008**, *7*, 653−658.

[Shu 1986] H. W. Shu, S. Jaulmes, and J. Flahaut. System As/1bTe - Obtention and Structural Study of a new Variety of As_2Te_3, Metastable. *Mater. Res. Bull.* **1986**, *21*, 1509-1514.

[Siddall 2018] R. Siddall. Mineral Pigments in Archaeology: Their Analysis and the Range of Available Materials. *Minerals*. **2018**, *8*, 201.

[Siebert 1954] H. Siebert. Struktur der Sauerstoffsäuren. *Zeitschrift für anorganische und allgemeine Chemie*. **1954**, *275*, 225−240.

[Smith 1973] J. D. Smith, J. C. Bailar, H. J. Emeléus, and R. Nyholm. *The Chemistry of Arsenic, Antimony and Bismuth*. (Pergamon Texts in Inorganic Chemistry, **1973**).

[Soignard 2008] E. Soignard, S. A. Amin, Q. Mei, C. J. Benmore, and J. L. Yarger. High-Pressure Behavior of As_2O_3: Amorphous-Amorphous and Crystalline-Amorphous Transitions. *Phys. Rev. B*. **2008**, *77*, 144113.

[Soignet 1998] S. L. Soignet, P. Maslak, Z-G. Wang, S. Jhanwar, E. Calleja, L.J. Dardashti, D. Corso, A. DeBlasio, J. Gabrilove, D.A. Scheinberg, P.P. Pandolfi, and R.P. Warrell. Complete remission after treatment of acute promyelocytic leukemia with arsenic trioxide. *The New England Journal of Medicine*. **1998**, *339*, 1341.

[Song 2013] Y. Song. New perspectives on potential hydrogen storage materials using high pressure. *Phys. Chem. Chem. Phys*. **2013**, *15*, 14524.

[Sorb 2016] Y. A. Sorb, V. Rajaji, P. S. Malavi, U. Subbarao, P. Halappa, S. C. Peter, S. Karmakar, and C. Narayana. Pressure-induced electronic topological transition in Sb_2S_3. *Journal of Physics: Condensed Matter*. **2016**, *28*, 015602.

[Souza 2012] S. M. Souza, C. M. Poffo, D. M. Triches, J. C. de Lima, T. A. Grandi, A. Polian, and M. Gauthier. High Pressure Monoclinic Phases of Sb_2Te_3. *Physica B*. **2012**, *407*, 3781-3789.

[Spurrell 1895] F. C. J. Spurrell. Notes on Egyptian Colours. *Archaeological Journal*. **1895**, *52:1*, 222-239.

[Srivastava 2011] P. Srivastava, H. Singh Mund, and Y. Sharma. Investigation of electronic properties of crystalline arsenic chalcogenides: Theory and experiment. *Physica B*. **2011**, *406*, 3083−3088.

[Stergiou 1985a] A. C. Stergiou and P. J. Rentzeperis. Hydrothermal Growth and the Crystal Structure of Arsenic Telluride, As_2Te_3. *Z. Kristallogr*. **1985**, *172*, 139-145.

[Stergiou 1985b] A. C. Stergiou and P. J. Rentzeperis. The crystal structure of arsenic selenide, As_2Se_3. *Z-Kristall*. **1985**, *173*, 185−191.

[Stordeur 1995] M. Stordeur. "Valence Band Structure and the Thermoelectric Figure-of-Merit of $(Bi_{1-x}Sb_x)Te_3$ Crystals." in *CRC Handbook of Thermoelectrics*, Ed. D.M. Rowe (CRC Press: Boca Raton, FL, **1995**).

[Struzhkin 2008] V. V. Struzhkin, A. F. Goncharov, R. Caracas, H-K Mao, and R. J. Hemley. Synchrotron Infrared Spectroscopy of the Pressure-Induced Insulator-Metal Transitions in Glassy As_2S_3 and As_2Se_3. *Phys. Rev. B: Condens. Matter Mater. Phys.* **2008**, *77*, 165133.

[Suárez 2014] L. Suárez, Y.N. Tamayo, I. Rodríguez, G. Hernández, y B.O. de la Uz. Tratamiento con trióxido de arsénico en pacientes con leucemia promielocítica aguda. *Medisan*. **2014**, *18(1)*, 25.

[Svensson 1974] C. Svensson. The crystal structure of orthorhombic antimony trioxide, Sb_2O_3. *Acta Crystallographica B*. **1974**, *30*, 458−461.

[Szymansky 1968] H.A. Szymansky, L. Marabella, J. Hoke, and J. Harter. Infrared and Raman Studies of Arsenic Compounds. *Appl. Spectros*. **1968**, *22*, 297.

[Taylor 1975] P. C. Taylor, S. G. Bishop, and D. L. Mitchell. Infrared Properties of AsxTe1-x Glasses, *Solid State Commun.* **1975**, *16*, 167-170.

[Thornburg 1973] D. D. Thornburg. Physical Properties of the $As_2(Se,Te)_3$ Glasses. *J. Electron. Mater*. **1973**, *2*, 495-532.

[Tian 2012] Y. Tian, B. Xu, and Z. Zhao. Microscopic theory of hardness and design of novel superhard crystals. *Int. J. Refract. Met. H*. **2012**, *33*, 93.

[Toby 2001] B. H. Toby. EXPGUI, A Graphical User Interface for GSAS. *Journal of Applied Crystallography*. **2001**, *34*, 210−213.

[Toscani 1991] S. Toscani. J. Dugue, R. Ollitrault, and R Ceolin. Polymorphism of As_2Te_3: Structural Studies and Thermal behavior of Rhombohedral β-As_2Te_3. *Thermochim. Acta*, **1991**, *186*, 247-251.

[Tuktabiev 2009] M. A. Tuktabiev, S. V. Popova, V. V. Brazhkin, A. G. Lyapin, and Y. Katayama. Compressibility and polymorphism of α-As_4S_4 realgar under high pressure. *J. Phys.: Condens. Matter*. **2009**, *21*, 385401.

[Tvergaard 1988] V. Tvergaard and J. W. Hutchinson. Microcracking in Ceramics Induced by Thermal Expansion or Elastic Anisotropy. *J. Am. Ceram. Soc*. **1988**, *71*, 157.

[Tverjanovich 2012] A. Tverjanovich, K. Rodionov, and E. Bychkov. Raman Spectroscopy of Glasses in the As-Te System. *J. Solid State Chem.* **2012**, *190*, 271-276.

[Ulrich 1996] C. Ulrich, M. Mroginski, A. R. Goñi, A. Cantarero, U. Schwarz, V. Muñoz, and K. Syassen. Vibrational Properties of InSe under Pressure: Experiment and Theory. *Physica Status Solidi B.* **1996**, *198*, 121.

[Usuki 1996] T. Usuki, K. Saitoh, M. Endo, and O. Uemura. Short-range Order of Amorphous and Liquid As-Te-I System, *J. Non-Cryst. Solids* **1996**, *205-207*, 184-188.

[Vaidya 1971] S. N. Vaidya and G. C. Kennedy. Compressibility of 18 Molecular Organic Solids to 45 kbar. *J. Chem. Phys*. **1971**, *55*, 987.

[Vaney 2015] J. B. Vaney, J. Carreaud, G. Delaizir, A. Piarristeguy, C. Morin, E. Alleno, J. Monnier, A. P. Gonçalves, C. Candolfi, A. Dauscher, et al. High-Temperature Thermoelectric Properties of Sn-Doped β-As_2Te_3. *Adv. Electron. Mater*. **2015**, *1*, 1400008.

[Vilaplana 2011a] R. Vilaplana, O. Gomis, F. J. Manjón, A. Segura, E. Pérez-González, P. Rodríguez-Hernández, A. Muñoz, J. González, V. Marín-Borrás, V. Muñoz-Sanjosé, C. Drasar, and V. Kucek. High-pressure vibrational and optical study of Bi_2Te_3. *Physical Review B: Condensed Matter and Materials Physics*. **2011**, *84*, 104112.

[Vilaplana 2011b] R. Vilaplana, D. Santamaría-Pérez, O. Gomis, F. J. Manjón, J. González, A. Segura, A. Muñoz, P. Rodríguez-Hernández, E. Pérez-González, V. Marín-Borrás, et al. Structural and Vibrational Study of Bi_2Se_3 under High Pressure. *Physical Review B: Condensed Matter and Materials Physics.* **2011**, *84*, 184110.

[Vilaplana 2013] R. Vilaplana, O. Gomis, F. J. Manjón, H. M. Ortiz, E. Pérez-González, J. López-Solano, P. Rodríguez-Hernández, A. Muñoz, D. Errandonea, V. V. Ursaki, et al. Lattice Dynamics Study of $HgGa_2Se_4$ at High Pressures. *J. Phys. Chem. C.* **2013**, *117*, 15773-15781.

[Voigt 1928] W. Voigt. *Lehrbuch der Kristallphysik* (B. G. Teubner, Leipzig, Germany, **1928**).

[Vos 1992] W. L. Vos, L. W. Finger, R. J. Hemley, J. Z. Hu, H. K. Mao, and J. A. Schouten. A high-pressure van der Waals compound in solid nitrogen-helium mixtures. *Nature*. **1992**, *358*, 46.

[Wallace 1967] D.C. Wallace. Thermoelasticity of Stressed Materials and Comparison of Various Elastic Constants. *Phys. Rev*. **1967**, *162*, 776.

[Wallace 1970] D. C. Wallace, "Thermoelastic theory of stressed crystals and higher-order elastic constants," in *Solid State Physics*, edited by F. S. Henry Ehrenreich, D. Turnbull, and F. Seitz (Academic Press, **1970**), vol. *25*, pp. 301–404.

[Walsh 2011] A. Walsh, D. J. Payne, R. G. Egdell, and G. W. Watson. Stereochemistry of post-transition metal oxides: revision of the classical lone pair model. *Chemical Society Reviews*. **2011**, *40*, 4455−4463.

[Wang 1993] J. Wang, S. Yip, S. R. Phillpot, and D. Wolf. Crystal instabilities at finite strain. *Phys. Rev. Lett*. **1993**, *71*, 4182.

[Wang 1995] J. Wang, J. Li, S. Yip, S. Phillpot, and D. Wolf. Mechanical instabilities of homogeneous crystals. *Phys. Rev. B*. **1995**, *52*, 12627.

[Wang 2012] H. Wang and M. Li. Unifying the criteria of elastic stability of solids. *J. Phys. Condens. Matter*. **2012**, *24*, 245402.

[Wang 2015] B. T. Wang, P. Souvatzis, O. Eriksson, and P. Zhang. Lattice Dynamics and Chemical Bonding in Sb_2Te_3 from First-Principles Calculations. *J. Chem. Phys.* **2015**, *142*, 174702.

[Ward 1968] A. T. Ward. Raman spectroscopy of sulfur, sulfur-selenium, and sulfur-arsenic mixtures. *Journal of Physical Chemistry*. **1968**, *72*, 4133−4139.

[Waxman 2001] S. Waxman and K. C. Anderson. History of the development of Arsenic Derivatives in Cancer Therapy. *The Oncologist*. **2001**, *6-2*, 3-10.

[Weber 1965] A. Weber and S. P. S. Porto. He-Ne Laser as a Light Source for High Resolution Raman Spectroscopy. *Journal of the Optical Society of America*. **1965**, *55*, 1033−1034.

[Weber 1983] G. Weber and H. G. Drickamer. The effecxt of high pressure upon proteins and other biomolecules. *Quarterly Reviews of Biophysics.* **1983**, 16, 89-112.

[Wei 2015] S. Wei . Active Pin1 as a target of all-trans retinoic acid in acute promyelocytic leukemia and breast cancer. *Nature Medicine*. **2015**, *21*, 457.

[Weigel 2012] C. Weigel, A. Polian, M. Kint, B. Rufflé, M. Foret, and R. Vacher. Vitreous Silica Distends in Helium Gas: Acoustic Versus Static Compressibilities. *Phys. Rev. Lett*. **2012**, *109*, 245504.

[Weir 1959] C. E. Weir, E. R. Lippincott, A. Van Valkenburg, and E. N. Bunting, Infrared Studies in the 1- to 15-Micron Region to 30,000 Atmospheres. *Journal of Research of the Natural Bureau of Standards.* **1959**, 63A, 55-62.

[Weir 1965] C. E. Weir. Compressibility of 11 Inorganic Materials. *J. Res. Natl. Bur. Stand., Sect. A*. **1965**, *69A*, 29.

[White 1967] W. B. White, F. Dachille, and R. Roy. High-pressure polymorphism of As_2O_3 and Sb_2O_3. *Z. Kristall*. **1967**, *125*, 450.

[Wuttig 2018] M. Wuttig, W. L. Deriger, X. Gonze, C. Bichara, and J-Y. Raty. Incipient Metals: Functional Materials with a Unique Bonding Mechanism. *Advanced Materials*. **2018**, *30*, 1803777.

[Xiang 2012] S. Xiang, Y. He, Z. Zhang, H. Wu, W. Zhou, R. Krishna, and B. Chen. Microporous metal-organic framework with potential for carbon dioxide capture at ambient conditions. *Nat. Commun*. **2012**, *3*, 954.

[Xu 2017] M. Xu, S. Jakobs, R. Mazzarello, J-Y. Cho, Z. Yang, H. Hollermann, D. S. Shang, X. S. Miao, Z. H. Yu, L. Wang, and M. Wuttig. Impact of Pressure on the Resonant Bonding in Chalcogenides. *Journal of Physical Chemistry C*. **2017**, *121*, 25447−25454.

[Yakushev 1986] V. A. Yakushev and V. A. Kirkinskii. New Polymorphic Modification of Arsenic Telluride, Produced at high Pressures. *Dokl. Akad. Nauk SSSR* **1969**, *186*, 882-884; idem, *Dokl. Phys. Chem.* **1986**, *186*, 369-371.

[Yu 2007] J. Yu, H. Qian, Y. Li, Y. Wang, X. Zhang, X. Liang, M. Fu, and C. Lin. Arsenic trioxide (As_2O_3) reduces the invasive and metastatic properties of cervical cancer cells in vitro and in vivo. *Gynecologic Oncology*. **2007**, *106*, 400.

[Yu 2015] Z. H. Yu, L. Wang, Q. Y. Hu, J. G. Zhao, S. Yan, K. Yang, S. Sinogeikin, G Gu, and H-K. Mao. Structural Phase Transitions in Bi_2Se_3 under High Pressure. *Sci. Rep.* **2015**, *5*, 15939.

[Zallen 1971] R. Zallen, M. L. Slade, and A. T. Ward. Lattice Vibrations and Interlayer Interactions in Crystalline As_2S_3 and As_2Se_3. *Physical Review B.* **1971**, *3*, 4257-4273.

[Zallen 1974a] R. Zallen and M. L. Slade. Rigid-layer modes in chalcogenide crystals. *Physical Review B*. **1974**, *9*, 1627−1637.

[Zallen 1974b] R. Zallen. Pressure-Raman effects and vibrational scaling laws in molecular crystals: S8 and As_2S_3. *Physical Review B*. **1974**, *9*, 4485−4496.

[Zallen 2004] R. Zallen. Effect of Pressure on Optical Properties of Crystalline As_2S_3. *High Pressure Research*. **2004**, *24*, 117−118.

[Zhang 2009] H. Zhang, C-X. Liu, X-L. Qi, X. Dai, Z. Fang, and S-C. Zhang. Topological Insulators in Bi_2Se_3, Bi_2Te_3 and Sb_2Te_3 with a Single Dirac Cone on the Surface. *Nature Phys.* **2009**, *5*, 438-442.

[Zhang 2010] X.W. Zhang, X.J. Yan, Z.R. Zhou, F.F. Yang, Z.Y. Wu, H.B. Sun, W.X. Liang, A.X. Song, V. Lallemand-Breitenbach, M. Jeanne, Q.Y. Zhang, H.Y. Yang, Q.H. Huang, G.B. Zhou, J.H. Tong, Y. Zhang, J.H. Wu, H.Y. Hu, H. de Thé, S.J. Chen, and Z. Chen. Arsenic trioxide controls the fate of the PML-RARalpha oncoprotein by directly binding PML. *Science*. **2010**, *328*, 240.

[Zhang 2014] J. K. Zhang, Y. H. Han, C. L. Liu, X. Zhang, F. Ke, G. Peng, Y. M. Ma, Y. Z. Ma, and C. X. Gao. Semiconductor-to-metal Transition of Bi_2Se_3 under High Pressure. *Appl. Phys. Lett.* **2014**, *105*, 062102.

[Zhang 2015] H. Y. Zhang, Y. Cheng, M. Tang, X. R. Chen, and G. F. Ji. First-Principles Study of Structural, Elastic, Electronic and Thermodynamic Properties of Topological Insulator Sb_2Te_3 under Pressure. *Comput. Mater. Sci.* **2015**, *96*, 342-347.

[Zhang 2016] Y. H. Zhang, Y. M. Ma, A. H. Geng, C. Y. Zhu, G. T. Liu, Q. Tao, F. F. Li, Q. L. Wang, Y. Li, X. Wang, et al. Pressure-Induced Electronic Phase Transitions of α-As_2Te_3. *J. Alloys Compd.* **2016**, *685*, 551-558.

[Zhao 2011] J. G. Zhao, H. Z. Liu, L. Ehm, Z. Q. Chen, S. Sinogeikin, Y. S. Zhao, and G. Gu. Pressure-Induced Disordered Substitution Alloy in Sb_2Te_3. *Inorg. Chem.* **2011**, *50*, 11291-11293.

[Zhao 2013] J. Zhao, H. Liu, L. Ehm, D. Dong, Z. Chen, and G. Gu. High-Pressure Phase Transitions, Amorphization, and Crystallization Behaviors in Bi_2Se_3. *J. Phys.: Condens. Matter* **2013**, *25*, 125602.

[Zhao 2015a] K. Zhao, Y. Wang, Y. Sui, C. Xin, X. J. Wang, Y. Wang, Z. G. Liu, and B. S. Li. First Principles Study of Isostructural Phase Transition in Sb_2Te_3 under High Pressure. *Phys. Stat. Sol. RRL*. **2015**, *9*, 379-383.

[Zhao 2015b] K. Zhao, Y. Wang, C. Xin, X. J. Wang, Y. Wang, Z. G. Liu, and B. S. Li. First Principles Study of Isostructural Phase Transition in Sb_2Te_3 under High Pressure. *Phys. Status Solidi RRL*. **2015**, *9*, 379-383.

[Zhao 2016] J. G. Zhao, L. X. Yang, Z. H. Yu, Y. Wang, C. Y. Li, K. Yang, Z. G. Liu, and Y. Wang. Structural Phase Transitions and Metallized Phenomena in Arsenic Telluride under High Pressure. *Inorg. Chem.* **2016**, *55*, 3907.

[Zhou 1996] Z. Zhou and B. Joós. Stability criteria for homogeneously stressed materials and the calculation of elastic constants. *Phys. Rev. B*. **1996**, *54*, 3841.

[Zhou 2016] X.Z. Zhou and K.P. Lu. The isomerase Pin1 controls numerous cancer-driving pathways and is a unique drug target. *Nature Reviews Cancer*. **2016**, *16*, 463.

[Zhu 2011] L. Zhu, H. Wang, Y. Wang, J. Lv, Y. Ma, Q. Cui, Y. Ma, and G. Zou. Substitutional Alloy of Bi and Te at High Pressure. *Phys. Rev. Lett.* **2011**, *106*, 145501.

[Zhu 2013] J. Zhu, J. L. Zhang, P. P. Kong, S. J. Zhang, X. H. Yu, J. L. Zhu, Q. Q. Liu, X. Li, R. C. Yu, and R. Ahuja. Superconductivity in Topological Insulator Sb_2Te_3 Induced by Pressure. *Sci. Rep.* **2013**, *3*, 2016.